Springer Water

Philippe Gourbesville
Jean A. Cunge
Guy Caignaert *Editors*

Advances in Hydroinformatics

SIMHYDRO 2014

Springer

Springer Water

More information about this series at http://www.springer.com/series/13419

Philippe Gourbesville · Jean A. Cunge
Guy Caignaert
Editors

Advances in Hydroinformatics

SIMHYDRO 2014

Springer

Editors
Philippe Gourbesville
University of Nice-Sophia Antipolis
Sophia Antipolis
France

Guy Caignaert
Arts et Métiers ParisTech
Lille, Paris
France

Jean A. Cunge
Society Hydrotechnique of France
La Tronche
France

ISSN 2364-6934 ISSN 2364-8198 (electronic)
Springer Water
ISBN 978-981-287-614-0 ISBN 978-981-287-615-7 (eBook)
DOI 10.1007/978-981-287-615-7

Library of Congress Control Number: 2015944448

Springer Singapore Heidelberg New York Dordrecht London

Printed on acid-free paper

Springer Science+Business Media Singapore Pte Ltd. is part of Springer Science+Business Media (www.springer.com)

Preface

Hydroinformatics defined as management of information related to the water sector using ICT tools is a large domain of engineering technology and sciences. Modelling and simulation are historically the points of departure for hydroinformatics and are one of the most important part of it. Neither the SimHydro cycle of international conferences nor the present book has the purpose or ambition to cover thematically the whole extent of the subjects. The purpose is to concentrate on a limited number of specific areas and subjects which are not usually considered as such during most global international conferences.

Modelling in fluid mechanics, hydraulics and hydrology, whether using digital tools or scale models, has reached sufficient maturity to be in daily use by engineers for analysis, design and for communication. Increasingly, complex cases can be handled thanks to ever-more sophisticated tools and increasingly abundant computing power. The emerging environment populated with new generation of sensors, using cloud-computing resources, is challenging the current practices of modelling and request innovation in methodology and concepts for a real integration into the decision-makings processes. At the same time, the request to integrate vulnerability and resilience dimension in the various engineering approaches is becoming more and more frequent.

With respect to these issues, however, a number of questions still remain open: coupling of models, data acquisition and management, uncertainties (both epistemic and random) of results supplied by models, use of 3D CFD models for complex phenomena and for large-scale problems…. All these points are continuously explored and investigated by researchers, scientists and engineers. Like in all scientific domains, most recent and advanced developments have to be discussed and shared regularly in a growing community. The SimHydro 2014 conference, following the two previous editions, has contributed to this objective by providing a platform for exchanges and discussion for the different actors in the water domain.

SimHydro is a permanent cycle of conferences held every 2 years, hosted by Polytech Nice Sophia and organised by the Société Hydrotechnique de France and its European partners. It aims, as the subject, at recent advances in modelling and hydroinformatics and at the participation and exchanges at European scale (it is

open to all other researchers and participants but the purpose is to maintain a specific platform for the region that was a birthplace of both domains). That is why the SimHydro language is English.

The latest SimHydro conference was held in Sophia Antipolis, France, from 11 to 13 June 2014. The conference was jointly organized by the Société Hydrotechnique de France (SHF), the Association Française de Mécanique (AFM) and the University of Nice Sophia Antipolis/Polytech Nice Sophia with the support of IAHR, the Environmental & Water Resources Institute (EWRI) of the American Society of Civil Engineers (ASCE) as well as Eau and DREAM clusters. The conference attracted 172 delegates from 42 (although most of them European) countries who participated in 16 sessions where 76 papers were presented. The programme was organised around four main themes:

- Theme 1: Modelling of fast hydraulic transients (dam and dyke breaking waves, storm waves, tsunamis, flash floods)
- Theme 2: Uncertainty in simulation, uncertainty of results of models
- Theme 3: Simulation and modelling of 3D near field phenomena in free surface flows (rivers, lakes and coastal areas)
- Theme 4: Simulation and modelling of multiphase flows: cavitation, bubbly flows, flows with particles

Within these general themes, topics like coupling of models, data assimilation and uncertainties, urban flooding, data and uncertainties in hydraulic modelling, model efficiency and real situations, new methods for numerical models, hydraulic machinery, 3D flows in the near field of structure, models for complex phenomena have been covered. The conference, by attracting researchers, engineers and decision makers, has promoted and facilitated the dialogue between communities with round tables where needs and expectations were discussed. Exchanges have been very fruitful on crucial questions related to sources of uncertainty in modelling, the state of the art in research and development in the domain of numerical fluid mechanics, the stakeholder's capacity to understand results, the means for dialogue directly or indirectly between the stakeholders and the model developers, the information's exchange between stakeholders and developers.

In order to contribute to this dialogue and to provide useful references, following the successful experience of 2012, the organisers of SimHydro 2014 have decided to elaborate this book. This volume gathers a selection of the most significant contributions received and presented during the conference. The objective is to provide the reader with an overview of the ongoing developments and the state of the art taking place in three major themes that are:

- Modelling: Floods and Inundations;
- Uncertainties, 3D Modelling and Models Coupling;
- Two-phase Flows and Cavitation.

Obviously, all dimensions of these themes cannot be covered in a single book. However, the editors are convinced that the contents may contribute to provide to

the reader essential references for understanding the actual challenges and developments in these areas of the hydroinformatics field.

This volume represents the sum of the efforts invested by the authors, members of the scientific committee and members of the organising committee. The editors are also grateful for the dedicated assistance of the reviewers who worked tirelessly behind the scene to ensure the quality of the papers. We hope this book will serve as a reference source on hydroinformatics for researchers, scientists, engineers and managers alike.

Sophia Antipolis
May 2015

Philippe Gourbesville
Jean A. Cunge
Guy Caignaert

Contents

Part I
Modelling: Floods and Inundations

2D and 3D Modelling in German Inland Waterways

Thomas Wenka, Thomas Brudy-Zippelius and Andreas Schmidt

1 Introduction

The German Federal Waterways and Shipping Administration (WSV) is responsible for the construction, operation and maintenance of the german waterways, including 23,000 km^2 of maritime and 7,350 km of inland waterways. The WSV is in charge for some 290 weirs, 450 lock chambers, 500 culverts, 1,600 bridges, 15 canal bridges, 8 barrages, 4 ship lifts and numerous other structures, such as groynes and riprap designed to support inland navigation. The total freight volume transported by inland navigation in Germany amounts to some 240 million tonnes annually, out of which cross-border traffic accounts for some 180 million tonnes—with an upward trend.

The principal challenges confronting waterways engineers today are the over-aging of a great part of the infrastructure constructions, the trend towards larger vessels, the persistent bed erosion processes in the freeflowing parts of the rivers, the optimisation of river training and sediment management, the possible impacts of climate change on navigation, and the need to incorporate ecological aspects, e.g. from the European Framework Directive on Water [1].

As waterways engineering consultant and expert, the Federal Waterways Engineering and Research Institute (BAW) supports the WSV and the Federal Ministry of Transport and Digital Infrastructure (BMVI) in the development and construction and the operation and maintenance of the waterways in Germany.

T. Wenka (✉) · T. Brudy-Zippelius · A. Schmidt
BAW, Kussmaulstr, 17, D-76187 Karlsruhe, Germany
e-mail: thomas.wenka@baw.de

T. Brudy-Zippelius
e-mail: thomas.brudy-zippelius@baw.de

A. Schmidt
e-mail: andreas.schmidt@baw.de

P. Gourbesville et al. (eds.), *Advances in Hydroinformatics*,
Springer Water, DOI 10.1007/978-981-287-615-7_1

The BAW supplies important contribution in the disciplines of structural engineering, geotechnical engineering and hydraulic engineering in inland and coastal areas to ensure that waterways in Germany meet ever tougher technical, economic and ecological demands. To sustain and improve the quality of its consulting services, the BAW conducts research and development (R&D) projects in the entire spectrum of waterways engineering.

For the various investigations in hydraulic engineering, numerous methods are used and developed, with an increasing proportion of numerical models. In this paper, examples are given for numerical simulation techniques of the Department of Hydraulic Engineering in Inland Areas used for daily project work as well as R&D.

2 Scales, Processes, Models

In numerical models of rivers and waterways, the main problems are caused by irregular boundary conditions, sediment transport and turbulence. The major problems in numerical models of hydraulic structures are due to interaction of design geometry and surrounding flow field, air entrainment and, again, turbulence. It is therefore not surprising that the scales captured in the models range from reach scale down to point scale, i.e. 100 km–0.1 m. Thus, very different models, using different methods, are necessary.

The purpose of this chapter is to give some insight with regards to the differences and similarities of the simulation techniques applied to waterways (Fig. 1) and currents in or around hydraulic structures (Fig. 2). Furthermore, the characteristics of the models with respect to their scales and processes are described in more detail.

In spite of the three-dimensional nature of the flow in most rivers, it is customary in river modelling to solve the so-called shallow water equations derived from depth-integrating the Navier–Stokes equations. Since the horizontal length scale is mostly much greater than the vertical length scale, it can be shown from the momentum equation that vertical pressure gradients are nearly hydrostatic and the vertical velocity component can be set to zero. In the 2D shallow water equations, the resultant velocity vector is determined from the depth-averaged horizontal

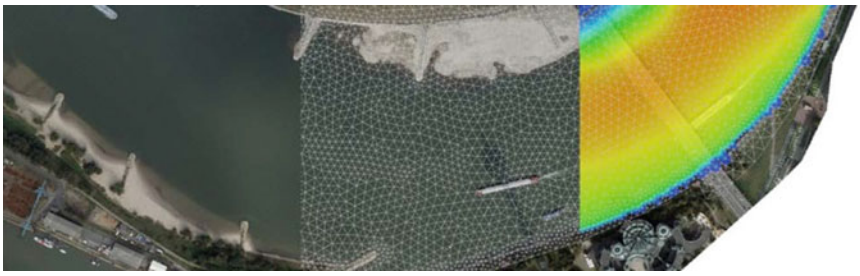

Fig. 1 Flow simulations in river engineering

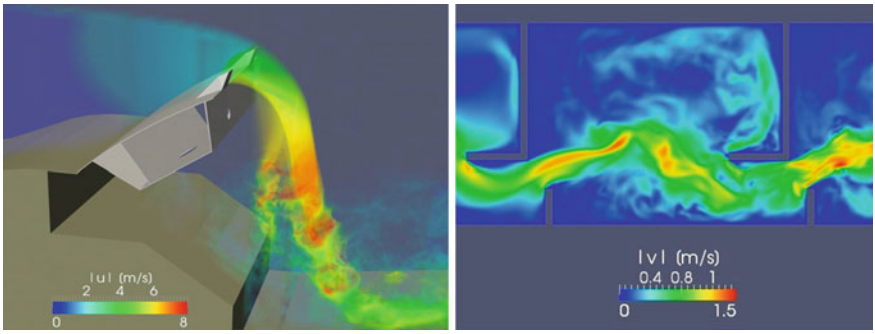

Fig. 2 Flow simulations in hydraulic structures—weir (*left*) and fish pass (*right*)

components and does not necessarily represent the velocity direction near the river bed. This can have a strong impact on the calculation of bed-load transport. The non-uniformity of the velocity over the flow depth, which is usually neglected in depth-averaged models, directly affects the suspended sediment and indirectly through the momentum exchange also the bed-load transport.

The so-called dispersion terms arising from depth-averaging can be of significance in depth-average calculations when secondary flows are present. The importance of these terms, and of the turbulent stresses, may be quantitatively of the same order. The share of the dispersion terms can be determined in comparison with 3D models. The user will not get rid of that problem when HLES (Horizontal Large Eddy Simulation or depth-averaged 2D-LES) is applied for simulating the turbulent motion. However, the benefit of HLES lies in a more precise definition of the effects of the large turbulent structures and in the cost-effective option of identifying these horizontal 2D structures with scales much larger than the depth comprising 2D turbulence. In the high-resolution 3D models, an application of LES is still very expensive. Despite the increasing importance of LES the simulations of practical problems are still performed with RANS models that have to be adapted to the particular problem.

At this point, a more detailed discussion of this very complex matter would go much too far. For simplicity, we have selected below our own organization of the scales as adapted to our practice, keeping the very descriptive schematization of scales in Church [2] in mind. As for the turbulence modelling and LES in hydraulics, we refer to the monographs of Rodi [3] and Rodi et al. [4]. To this end, it is necessary to distinguish between typical 2D or 3D applications, river or structure hydraulics and the level of turbulence model to be used. Generally, no all-in-one solution of a numerical code system suitable for every purpose exists today.

First, a rough classification for the two- and three-dimensional river flow models is made, which due to their length expansion is given in model length. Accordingly, macro-scale means model lengths which extend up to about 100 km. Here, low-resolution 2D depth-averaged models are occasionally used to calculate water

levels and main-channel/flood plain flow distribution and to answer morpho-dynamical or nautical questions even in the context of long-term simulations (tens of years). The adequate identification of phenomena in river bends, in large-scale vortices and of geometric shape influences (riverbed and structures) plays a role in, inter alia, planning and assessing processes of sediment management.

Where coarse 2D models are not sufficient, high-resolution 2D depth-averaged models and 3D models are used. These usually represent the meso-scale with horizontal grid resolutions from about 2 to 50 m. They usually have model lengths of up to about 10–50 km and are applied to quasi-steady states or short-to-medium spans of time. Phenomena such as velocity distributions, bed forms, flow resistance, navigability, and ship-induced waves can be determined in detail and require less parameterization. A typical example of a scaled approach involving extensive in situ data is the artificial grain feeding at the Lower Rhine River (see Sect. 4.1.1), where the morphological effects are being investigated in an approximately 46-km-long 2D model and additionally in a 3D model stretch of about 10 km that has been extracted from the former.

The microscale models with typical grid resolutions of roughly 0.01–5 m are applied for the mapping of processes and phenomena of turbulence in single- and multi-phase flows, local velocity distributions, forces and moments, the interaction of incipient motion and sediment transport, etc. In river engineering, it is the high-resolution models in the vicinity of river engineering structures for which an adequate representation of the geometry and of the turbulence is required. An example of this is the study of the ferry lane at Rees by means of a Horizontal Large Eddy Simulation (see Sect. 4.1.2). Models from the domains of hydraulic structures, interaction ship/ship as well as ship/waterway and the spreading of propeller jets are typically 3D models that are within the range of the microscale. Although the boundary geometry is not as arbitrary as in the alluvial waterways, the complexity of the design and the resulting-induced flow phenomena are a major challenge to the modelling process (see Sect. 4.2).

In 3D models, one of the major drawbacks is the necessity of choosing an appropriate turbulence model. Turbulence models are necessary, because it is still impossible to model the movement of the fluid down to its smallest scales. And yet, a typical grid for the problems to be solved with models of hydraulic structures has approximately 10 million computational cells.

Increasingly, grid-free methods are also being applied. The use of 3D particle models is described in the section on R&D (Chap. 5).

3 Numerical Methods and Computational Power

Again, a distinction must be made between the numerical codes for river engineering and hydraulic structures. For river engineering, the solution of the shallow water equations and various sediment transport formulas is the main focus. At the

BAW, different Finite Element (FE) and Finite Volume (FV) approaches are applied by use of the TELEMAC System, UnTRIM or Rismo 2D. The calculation of the water depth or the free surface is a standard part of the equation system. The problems referring to this often arise from the wetting and drying algorithm.

For flow simulations in and around hydraulic structures or relating to ship-waterway interaction, the solution of the Navier–Stokes equations and of turbulence closure models is given the highest priority. With the application of StarCCM + and OpenFoam, the BAW has one commercial and one Open Source code in use. The VOF method plays a major role in the calculation of the free surface.

Different methods have different strengths. So it is only logical to provide several numerical methods or codes. By applying several methods to the same problem, a mutual validation of the existing models is possible. In this regard, the trend in the department is towards in-house developments. This also has the advantage of being able to keep up with the continuous development of high-performance computers (HPC). Thus, the use of distributed memory parallel computers with domain decomposition (MPI-based) is always a challenge for the code developers. Also, the use of future computing platforms and processors (such as GPU) must be considered.

The current hardware facilities of the Department of Hydraulic Engineering in Inland Areas consist of two independent HPC:

- SGI ICE Altix 8400 EX:
  - 256 nodes at 2 Intel Westmere CPUs and 6 kernels each = 3072 comp. cores
- Bullx Blade System:
  - 126 nodes at 2 Intel Sandy Bridge CPUs and 8 kernels each = 2016 comp. cores
  - 8 nodes at 2 Nvidia Tesla GPUs each
  - 1 node at 2 MIC (Intel Xeon Phi) each.

4 Model Applications in Hydraulic Engineering

4.1 River Engineering

4.1.1 Artificial Grain Feeding at the Lower Rhine

The reach of the River Rhine between km 730.0 and km 776.5 (Fig. 3) has the sharpest river bends of the lower Rhine. Strong morphological dynamics and erosion calls for high maintenance efforts to ensure navigability. In order to improve the coordination and optimization of projected maintenance and artificial bed-load supply measures, a 2D depth-averaged model has been established. The

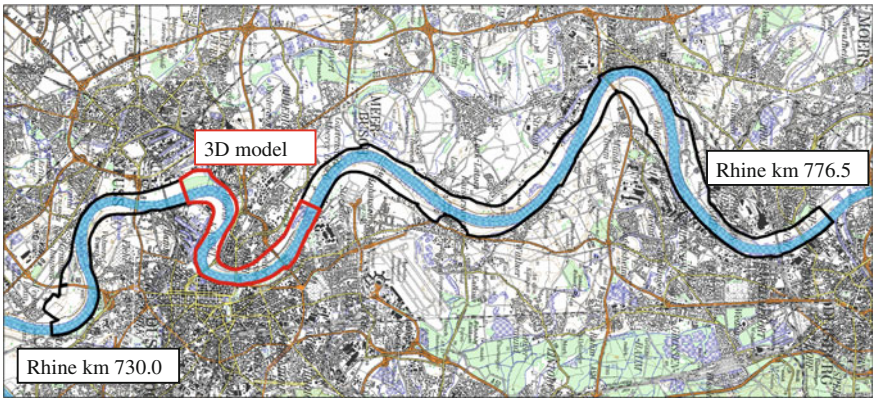

Fig. 3 Reaches of 2D and 3D model at the Lower Rhine

Finite Element-based numerical model consists of three modules: TELEMAC-2D solves the 2D shallow water equations; SISYPHE calculates the bed evolution based on the mass balance equation for sediment and considers grain gradation as well as the influence of secondary currents and gravitational effects to sediment transport flows; DredgeSim allows the controlling and timing of locally accurate dredging and dumping measures that can be automated for future prediction based on certain criteria.

For the evaluation of the flow model, the calculated flow velocities and lateral water levels were compared with ADCP measurements. For the calibration of the sediment transport model, freeze cores of the river bed were analysed in addition to sounding data and bed-load samples. Moreover, by adding separate fractions to the graded sediment transport model, the software allows the analysis of the spreading and the propagation of the dumped material. At first, predictions of the river bed evolution and sediment transport over a period of 10 years will be compared as precisely as possible with the field measurements. Later, the simulations should be able to predict the formation of point-bars at an early stage in order to ensure navigation in inland waterways.

Regarding the pronounced bends in the river, it was assumed that the secondary currents would have a significant effect on the hydraulic and morpho-dynamic processes. Therefore, a 3D sediment transport model was developed additionally for the central reach of the 2D model at Düsseldorf/Neuss (Rhine km 739 to Rhine km 749, Fig. 4). The comparison of the bed evolution and the depth-averaged flow velocities between the 2D and the 3D version of the model domain generally showed good agreement. However, there were local differences in the evolution of the bed level and the location of the point-bar at the transition of the bends. The simulations were also compared with data from in situ measurements, e.g. the mean fraction diameter by freeze cores, and 3D velocity measurements. The predictions of the models in which the bed deformation is calculated in curved alluvial channels under steady and unsteady flow conditions are discussed in [5, 6].

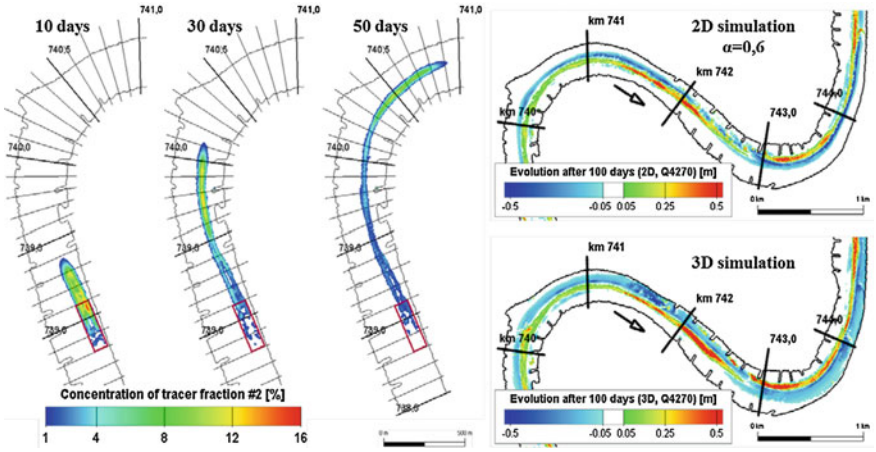

Fig. 4 Propagation speed of particular grain fractions/bed evolutions in 2D or 3D model

Figure 4 shows some first results of the simulations with grain feeding. The time-lapse picture on the left of Fig. 4 shows the propagation speed of tracer fraction #2 as part (of the initial concentration) of the artificial bed-load material supplied in the rectangular area at Rhine km 739.0. On the right, a comparison of the predicted bed evolution in the 2D- and the 3D-model respectively after 100 days of steady flow (Q = 4270 m^3/s) without any dredging and dumping is given.

4.1.2 Ferry Lane at Rees—Horizontal Large Eddy Simulation HLES

At the bend of the Rhine near Rees, the Federal Waterways and Shipping Administration has been building a flood channel that contributes significantly to the reduction of the substantial bed erosion and yields also in a reduction of the high water level of approx. 0.1 m in the upper reaches. Since a relocation of the ferry at Rees was out of the question, the ferry now has to cross the Rhine and the flood channel to get to the new pier on the opposite bank. Discharge measurements showed a relatively high flow rate in the ferry lane, causing a separation of the flow and an extensive recirculation zone (Fig. 5). In this context, a study of the flood channel outlet was conducted to investigate how conditions in the ferry lane with regard to sedimentation could be improved by structural measures [7].

Due to the problematic flow conditions, the selection of suitable river construction work was carried out under the premise that the flow separation and recirculation zone could be resolved. In order to calculate the extent of the recirculation zone as accurately as possible within the framework of a 2D depth-averaged flow model (Rismo2D), a horizontal large eddy simulation (HLES with Smagorinsky model) was adopted. The HLES required a very high spatial and temporal resolution of the flow field. Therefore, a time step of 0.05 s and in the area of the ferry lane an average point spacing of 0.25 m were chosen for the simulation.

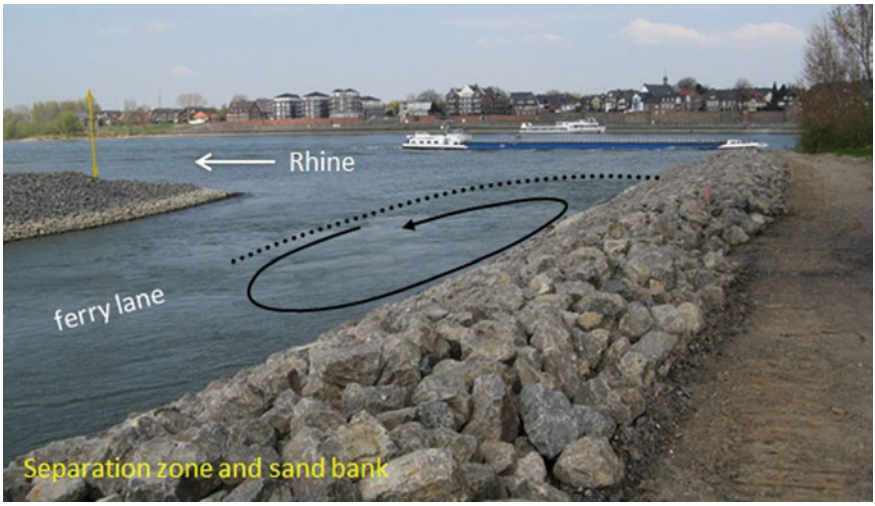

Fig. 5 Separation zone in the ferry lane opposite Rees

Some results of the flow simulation for the actual state are shown in Fig. 6, which represents a small section in the vicinity of the ferry lane. It shows the dimensionless rotation of the flow field calculated from the depth-averaged velocity field. By representing the rotation, the horizontal turbulent eddy structures become particularly clear (red represents a mathematically positive rotation counter-clockwise, blue a clockwise rotation).

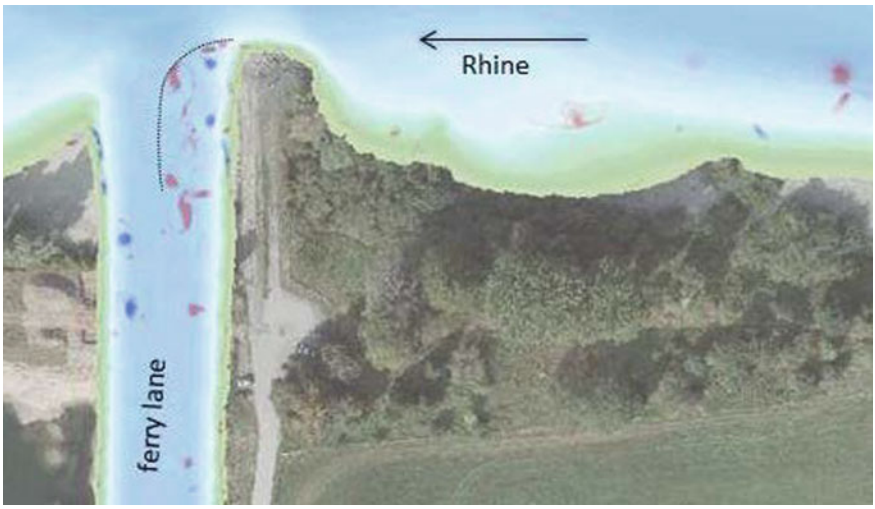

Fig. 6 Eddy motion of the flow simulation in the ferry lane opposite Rees

4.2 *Navigation Simulation and Modelling of Hydraulic Structures*

4.2.1 Ship Handling Simulation at the BAW: TMS Waldhof Accident

As a consistent enhancement of its navigational dynamics model method, the BAW has procured two ship handling simulators for the locations in Karlsruhe and Hamburg some years ago. Originally designed for the education and training of nautical personnel, the simulators are currently being extended by in-house model developments and upgraded to tools to answer waterways engineering issues. Especially in the inland area, the model procedures must be adapted to the specificities of the inland waterways. Since rowing machines and bow thrusters of inland vessels differ in large part from those of the sea-going vessels, additional model developments are needed.

A first severe test case for the "dynamic model" was the investigation of the accident of the inland tank barge (TMS) Waldhof. On 13 January 2011, the TMS Waldhof reached the stretch of the Rhine at the Loreley. The passage of this section was initially unremarkable until the vessel disappeared from radar screens around 4.42 am. As it turned out later, the ship had capsized at Rhine km 553.75 and drifted keel-up downstream until it ran aground at the entrance to the Loreley port on the right bank [8].

Figure 7 shows parts of the calculated velocity field for the investigated flood discharge in the immersive visualization system of the BAW. From the 3D flow model, the z-components of the velocities are identified at three cross sections along the ship. In order to visualize the flow effect on the TMS Waldhof, the ship was placed in the undisturbed flow field (calculated without interaction flow/vessel) in the area of the accident [9].

The inland simulator is currently being extended to include a highly accurate collision detection and a method for calculating ship-induced waves. With the help

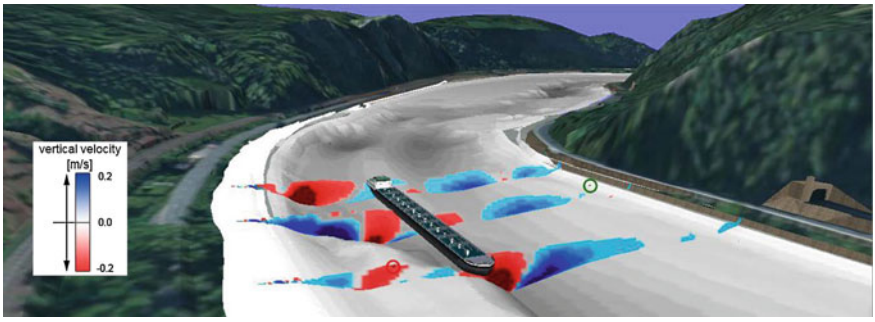

Fig. 7 Visualization of vertical flow velocities in the context of terrain and TMS Waldhof

of this wave model, the determination of the bank stress to wave action as well as the numerical model method for calculating the dynamic trimming and squats should be improved.

4.2.2 Numerical Investigations of Locks

For numerical investigations of locks, in many cases, tools of different dimensionalities are used in the different phases of the studies [10, 11]. For the studies described here and in more detail in [12], the 3D CFD solver StarCCM + (by CD-Adapco) was used, because several similar studies had been performed with this code in the BAW before. The solver computes the three-dimensional, transient, multi-phase Navier–Stokes (NS) equations for water and air, based on a Volume-of-Fluid (VOF) approach. This is in contrast to more sophisticated methods, in which the movement of air and water is treated with separate momentum equations [13].

In order to reduce maintenance costs for the valves and culverts, it was decided to replace the longitudinal filling system by a simple through-the-gates system at the so-called large locks of the lock complex located in Kiel-Holtenau. Consequently, the new gates had been equipped with valves for filling and emptying the chamber. For the numerical grid, attention was paid to local refinements near the valves, the exits of the culverts and the water surface (Fig. 8, left). Furthermore, prismatic layers were introduced along the ship hull in order to reproduce the friction accurately. In the computations, the changes to the computational grid due to the ship movement took substantial computing time. Thus, it was indispensable to use as coarse a mesh as possible, making it impossible to apply an LES-approach for the turbulence modelling. Hence, a RANS approach had to be used to model the dampening effect of the turbulence on the flow velocities. Here, the SST k-ω model by Menter [14] was selected.

Figure 8 shows the computed velocity field in a horizontal and a vertical cross section at the beginning of the filling process. The integration of the velocities in a cross section through the gate delivered the flow rates, which agree very well with the results of the laboratory model [12].

5 R&D Hydraulic Engineering

5.1 CFD Approaches for Modelling the Multi-phase Flow Phenomena in a Navigation Lock

When designing navigation locks with large lift heights, a compromise between a short operational time, limited hawser forces and acceptable construction costs must be reached. With a recently proposed filling-emptying system, a promising solution

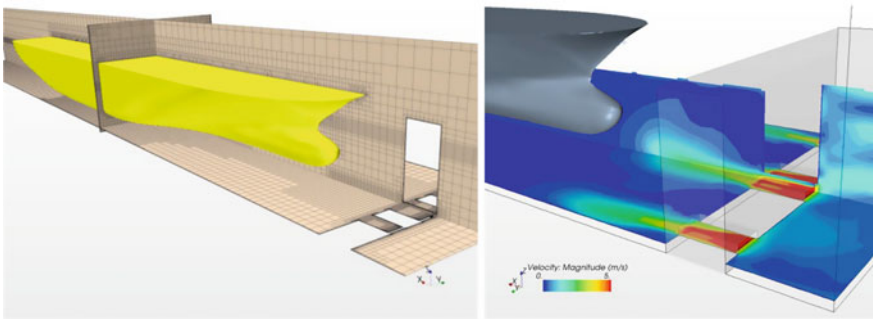

Fig. 8 Numerical mesh and velocity pattern around ship hull (lock Kiel-Holtenau) [12]

was presented [11], which significantly reduces the construction effort by avoiding side channels at the upstream and downstream heads. The new system includes a filling shaft, where the water drops over an edge and then plunges into a pool. With falling heights of up to 20 m and a width of approximately 14 m, high air entrainment is assumed to occur in the plunging pool. However, it has not been clarified whether the air can be detrained before entering the lock chamber, where it could cause severe disturbances to the ships in the chamber.

As can be seen from Fig. 9, in which the fraction of water "alpha" is illustrated, strong intermixing takes place, but the dispersed elements (drops and bubbles) cannot be depicted appropriately. Additionally, mass and momentum exchange between the two phases is not possible, since only one set of conservation equations for both phases can be solved. From that it also follows that both phases have the same velocity in each cell. It can be concluded that the VoF method would be suitable for the simulation of the smooth water surface from the upstream water and in the lock chamber, but the jet evolution as well as the air entrainment, transport and detrainment processes cannot be modelled satisfactorily. For modelling the lock filling process, in which air entrainment has to be taken into account, the VoF method can therefore not be used alone [13].

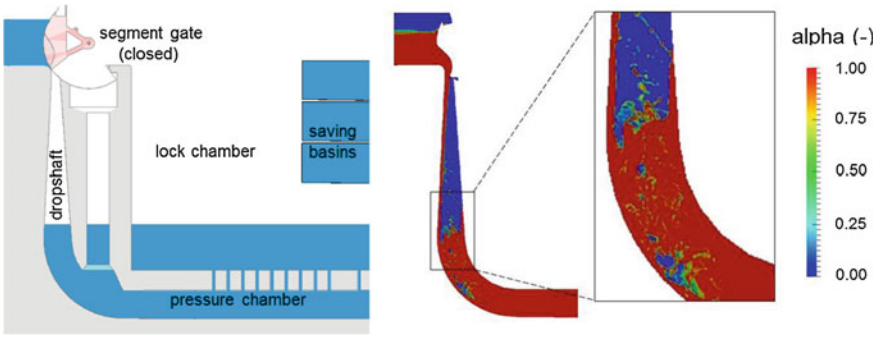

Fig. 9 Sketch of the new filling system and first results of a VoF simulation with interFoam [13]

For the simulation of the filling process of the lock, the "Toolbox OpenFOAM" is used. This freely available C++ library for the solution of partial differential equations is particularly useful here because, unlike most commercial CFD products, a direct intervention in the existing code is possible. Thus, the existing VoF-solver "interFoam" can be used as basis for the implementation of the so-called Algebraic Slip Mixture (ASM) model. According to [15], the VoF model has been extended by an equation for the velocity between the phases. Extensive testing and code optimizations are planned [16].

5.2 *Smoothed-Particle Hydrodynamics on GPU*

Hydraulic research on vertical-slot fish passes has shown that the hydraulic conditions within the pools of such facilities are mainly affected by the pool geometry and the slope of the fish pass. GPU-based SPH modelling represents an efficient numerical tool for the investigation of different geometry variants.

Simulations in a 9-pool, vertical-slot fish pass with GPUSPH, a high-performance CUDA implementation of the Smoothed Particles Hydrodynamics (SPH) numerical model for free surface flows [17], show promising results (Fig. 10). The results obtained by GPUSPH were compared with flow velocity and water level measurements from a laboratory model with identical geometry. Laboratory measurements were performed with an Acoustic Doppler Velocimeter (ADV), while the water level measurements were obtained by ultrasonic distance sensors mounted in each pool. Recent advances in the development of GPUSPH include the possibility to exploit multiple GPUs on one or more host nodes, making it possible to concurrently exploit hundreds of devices across a network and thus allowing the simulation of larger domains and/or higher resolutions. Due to these improvements, modelling of the filling and emptying of large ship lock with regard to the movement of the ship will be feasible.

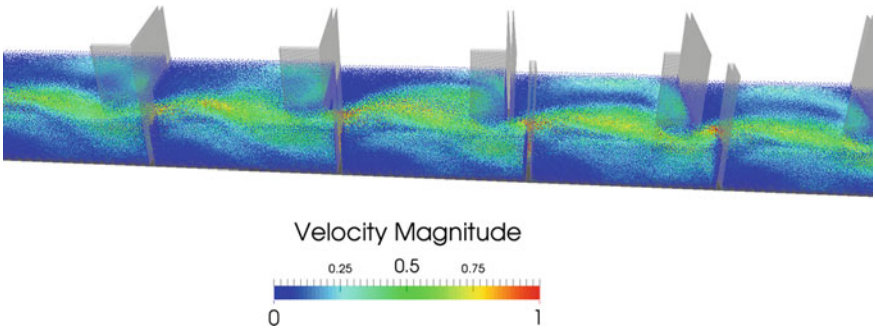

Fig. 10 Fish pass simulation with GPUSPH, 3.3 million particles on one GPU [17]

6 Outlook

Despite the progress in the past years in the field of two- and three-dimensional flow simulation, the developers and users are faced with major challenges in the next years. These affect not only the model development itself, but also the areas of benchmarking, pre- and post-processing, data analysis and data management. In addition, due to the rapid hardware development in the recent years, the testing and evaluation of software adjustments to new hardware architectures is an actual and challenging issue. In future, one main task will be to quantify the uncertainties in the input data and parameterizations to allow statements for the reliability of results on the basis of probability based methods. Also the coupling of methods has to be pushed. Numerous hydraulic engineering and water management issues will considerably benefit from advances e.g. in fluid-structure interaction, in a coupled simulation of flow and groundwater dynamics and in realistic simulations of the complex interaction of ship dynamics and flow in narrow waterways.

Acknowledgments This publication provides an overview of various current investigations performed in the Department of Hydraulic Engineering in Inland Areas. From a few of the publications cited in the references below, some passages were taken with the permission of the authors. For that the authors deserve our sincerest thanks.

References

1. Heinzelmann, C. (2010). Application of innovative methods in waterways engineering. *Proceedings of River Flow 2010, Braunschweig*.
2. Church, M. (2008). Multiple scales in rivers. *Proceedings of 6th International Gravel-Bed Rivers Workshop 2005*, *St. Jakob/Lienz*.
3. Rodi, W. (1993). *Turbulence models and their application in hydraulics* (3rd ed.). IAHR Monograph, Rotterdam: A.A. Balkema.
4. Rodi, W., Constantinescu, G., & Stoesser, T. (2013). *Large-eddy simulation in hydraulics.* Taylor & Francis: IAHR Monographs, CRC Press.
5. Wenka, T., Backhaus, L., & Brudy-Zippelius, T. (2014). Artificial bedload supply in waterways—numerical traceability. *Proceedings of 11th International Conference on Hydroscience and Engineering ICHE 2014, Hamburg* (to be published).
6. Backhaus, L., Riesterer, J., Brudy-Zippelius, T., & Wenka, T. (2014). Comparison of morphological predictions in the Lower Rhine River by means of a 2-D and 3-D model and in situ measurements. *Proceedings of River Flow 2014, Lausanne* (to be published).
7. BAW. (2012). Die Fährschneise an der Flutmulde Rees (The ferry lane at the flood channel near Rees, River Rhine). In *Annual Report 2011 of the Federal Waterways Engineering and Research Institute, Karlsruhe* (pp. 31–32).
8. Dettmann, T. (2013). Schiffsführungssimulatoren im Einsatz zur Ursachenermittlung von Havarien. *Conference Volume of the Colloquium "Havarie des TMS Waldhof—Bergung, Analysen, Einsichten",Karlsruhe*. 9th–10th April 2013.
9. Zentgraf, R., & Schlenker-Bohr, S. (2013). 3D-HN-Modellierung der Loreleystrecke als Bestandteil der Untersuchung zur Havarie des TMS Waldhof. *Conference Volume of the Colloquium "Havarie des TMS Waldhof—Bergung, Analysen, Einsichten", Karlsruhe.* 9th–10th April 2013.

10. Thorenz, C. (2009). Computational fluid dynamics in lock design—state of the art. *International Workshop on "Innovations in Navigation Lock Design", PIANC, Brussels.*
11. Thorenz, C. (2012). Ein neuartiges Füllsystem für Sparschleusen großer Höhe (A novel filling system for high lift locks). *Dresdner Wasserbauliche Mitteilungen: 35th Dresden Conference on Hydraulic engineering, 2012*.
12. Thorenz, C., & Anke J. (2013). Evaluation of ship forces for a through-the-gate filling system. *Proceedings of the 6th Intern. PIANC—SMART Rivers Conference 2013, Liège*.
13. Schulze, L., & Thorenz, C. (2013). Towards the CFD-modelling of multiscale-multiphase flow phenomena in a navigation lock. *Proceedings of the 6th International PIANC—SMART Rivers Conference 2013, Liège*.
14. Menter, F. R. (1994). Two-equation eddy-viscosity turbulence models for engineering applications. *AIAA Journal, 32*(8), 1598–1605.
15. Damiàn, S. M. (2013). An extended mixture model for the simultaneous treatment of short and long scale interfaces. *PhD Thesis, Universidad Nacional del Litoral, Argentina*.
16. Schulze, L., Thorenz, C., & Stamm, J. (2014). Entwicklung eines numerischen Ansatzes für die Modellierung von Lufteintrag und -transport in einem Schleusenfüllsystem. *Dresdner Wasserbauliche Mitteilungen: 37th Dresden Conference on Hydraulic Engineering, 2014*.
17. Rustico, E., Jankowski, J., Bilotta, G., Del Negro, C., Hérault, A., & Brudy-Zippelius, T. (2014). Multi-GPU, multi-node SPH implementation with arbitrary domain decomposition. *Proceedings of 9th SPHERIC International Workshop, 2nd–5th June 2014, Paris* (to be published).

Storm Events of Nice Bay: A Numerical Modeling of the Interactions Between Wave, Current, and Solid Transport

Rémi Dumasdelage, Olivier Delestre, Didier Clamond and Gourbesville Philippe

1 Introduction

Nice is located in the South–East of France on the French Riviera (Fig. 1). It is the fifth most populous city in France with nearly 1 million inhabitants. Moreover, tourism is one of the main economical activities in this region. Thus, the 4.5-km-long beach is a key element for this sector.

The erosion of neighboring pebble zones and the sediment transport by various rivers (Var, Paillon, Magnan) are at the origin of this gravel beach [5]. The main river, the Var, can carry away between 1 and 20 million tons of sediments per year. Most of these sediments are silty clays, and only 100,000 m^3 are gravels [11]. Some Var pebbles have been identified in the west part of the bay and are characterized by their lamellar shape. This shape explains their transport and their storage on the backshore, for more details see [10].

R. Dumasdelage (✉)
Department of the Environment, The Energy and the Sea of Nice Municipality,
59 Rue Beaumont, 06364 Nice Cedex 4, France
e-mail: remi.dumasdelage@ville-nice.fr

O. Delestre
Laboratoire J.A. Dieudonné and Polytech' Nice—Sophia, UMR CNRS 7351 UNSA,
06108 Nice Cedex 02, France
e-mail: olivier.delestre@polytechnice.fr

D. Clamond
Laboratoire J.A. Dieudonné, UMR CNRS 7351 UNSA, 06108 Nice Cedex 02, France
e-mail: didier.clamond@unice.fr

G. Philippe
I-CiTy Laboratory and Polytech' Nice—Sophia, URE 005, IMREDD 1-3 Bd Maître Maurice Slama, 06200 Nice, France
e-mail: philippe.gourbesville@unice.fr

P. Gourbesville et al. (eds.), *Advances in Hydroinformatics*,
Springer Water, DOI 10.1007/978-981-287-615-7_2

Fig. 1 Geographical orientation of Nice bay, with its two neighboring rivers the Papillon and the Var

Globally, the upper layer of the beach is dominated by very coarse gravels and small cobbles (5–10 cm in diameter). Coarse sand composes the lower level of the beach and can be observed after a storm on the intertidal zone [1]. Below the depth of 0 m, the clast size of the sea bed is decreasing progressively, and sand can be found between −5 and −10 m. A protected seaweed called *Cymodocee nodosa* grows at about 50 m off the shore (Fig. 2). This last parameter is a major limitation to the construction of coastal structures, because this seaweed must not be impacted by any human activities.

Regarding the climate, the South-East of France experiences intense autumn and winter storms [12]. They are defined by important wave heights (up to 4 m for a 10-year return period) and intense rainfalls implying big discharges in the neighboring rivers. Thus, high quantities of sediments are evacuated during floods [2]. This special configuration stresses the variability of the sediment transfers in terms of space and time in the studied area. The more frequent wave propagation directions are South–South–West and East–South–East [8]. The French Riviera is not subjected to substantial tide (<0.5 m for spring tides) and the surge level has been evaluated to 0.7 m NGF for a 10-year return period [8]. All these observations will help us later on to understand the beach dynamics and were primordial in order to build up an accurate numerical model.

The special configuration described above, as well as the urban development of the city, can be linked to explain the significant erosion phenomena observed in the studied area. Two main sediment transports exist along the shore and across the shore. These transports are the physical results of the natural setting of the bay. However, human activities increase their effects and their impacts, modifying the environment and the morphological nature of the beach.

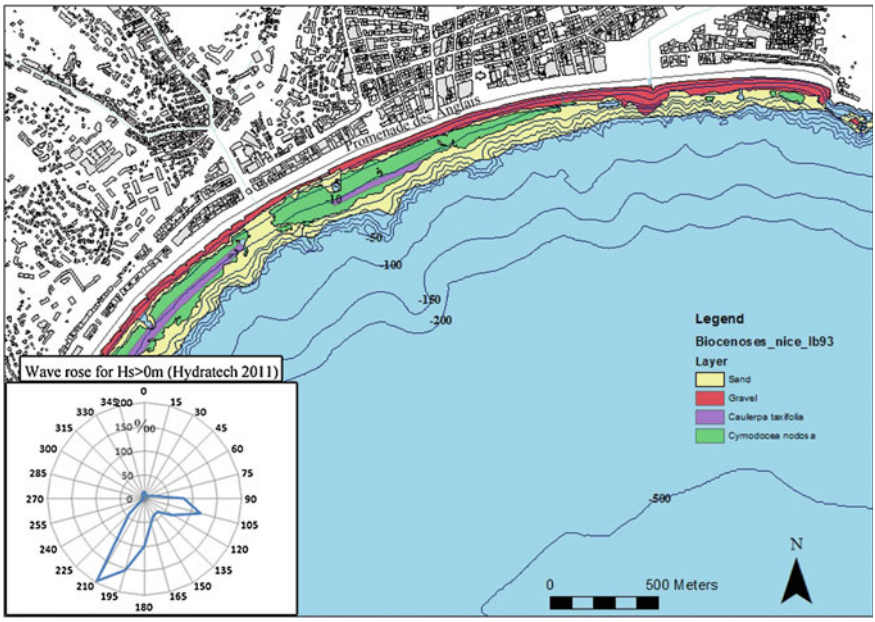

Fig. 2 Bathymetry of Nice Bay, sea *bottom* coverage and wave rose

Nice is defined by a steep continental margin and high value of the shoreface slope (Fig. 2). In fact between depths of 0 and −20 m the mean slope is around 10 % (with a beach step at the inner shoreface). At the depth of −20 m, the bathymetry is decreasing quickly until −100 m because of an abruptness (slopes are between 20 and 80 %) [12]. Thus, waves can propagate longer inshore before breaking. Combined with the low tide range, plunging waves are concentrated over a narrow and constant region of the beach. So, the high pressure and the important energy dissipation constitute the driving forces of the cross-shore gravel transport.

This downslope loss of materials is amplified by the wave reflection on the beach step [1]. In fact, this step forces waves to break at the base of the beach and so prevents the formation of a surf zone [3].

A second effect of the abrupt bathymetry is that the wave refraction is often incomplete. Thus, waves arrive at the beachface with a significant angle, creating a longshore current [4]. This current and the nearshore waves regime are at the origin of the longshore gravel transport.

Most of the time, these two sediment transports (cross and along the shore) have to be taken into account in order to understand the changes on the coastline.

During exceptional events, the extreme power of high plunging waves makes the cross-shore transport the major actor of the sediment mobility (Fig. 3).

However, it is important to stress that these transports do not fully explain the significant erosion phenomena faced by Nice's beach each year. Studies have shown that the total beach sediment losses is around 15,000 m^3/year and that the

Fig. 3 Example of the 2010 storm event in Nice

sediment budget of some part of the beach is around −5,000 m^3/year [12]. The anthropological action that experiences the French Riviera is at the origin of this erosion. Structures have been built on the neighboring streams. For instance, in the lower part of the Var, ten weirs have been constructed in order to raise up the river bed (previously lowered by extraction and urbanization of the flood plain). Thus, the bed load transport has almost completely stopped [7], implying a drastic decrease of the main gravel supply for Nice's beach. In addition, the modification of the Var delta which followed the building of Nice-Riviera airport in the 1940s can be compared to a huge groin that deviates the sediments towards the nearby bay (Fig. 1).

Urban development has also impacted directly the morphology of Nice beach. Between 1929 and 1958, the *Promenade des Anglais* has moved from a simple coastal pathway to a main 4 ways road indispensable to Nice traffic. Thus, a 3-m high seawall has been built at about 4 m from the coastline in order to protect the roads and to create a walkway along the sea. As a result, Nice backshore faced an important decrease and an amplification of the reflection phenomena during storms. This seawall stops some morphological process such as the roll-over of Nice beach and cuts off the storage of sediment capacity of the backshore [10].

The municipality has decided to artificially nourish the beach in order to stabilize its width. Since 1969, around 580,000 m^3 have been brought. According to Anthony and Cohen [1], the efficiency of this process is analyzed, so we will not discuss it further. Before 2006, the recharged material was provided by the construction sites and the gravelly bed of the Papillon river. So, the price of the artificial nourishments was only due to the transport of sediments. Since 2010, the municipality has to buy the gravels from a quarry around 100 km away, at the rate of 130 $/$m^3$. Therefore, the cost of these operations has increased, which forces the decision makers to find new solutions to the beach erosion.

In this context, we started a modeling approach to represent the natural phenomena that participate to erosion, such as the longshore current and the wave propagation. Finally, it enables us to study the interaction between them and the artificial structures.

2 Study Method

The numerical model has been built with TELEMAC, a free and open source system developed by EDF R&D's Laboratoire National d'Hydraulique et Environnement (LNHE). It is a powerful integrated modeling tool, composed of different simulation modules, such as TOMAWAC and TELEMAC2D.

TOMAWAC (TELEMAC-based Operational Model Addressing Wave Action Computation) aims at representing the sea states by solving the balance equation of the action density directional spectrum, for more details see [6, 9]. The code attempts to reproduce the evolution of this spectrum at each point of a spatial computational grid.

Concerning TELEMAC2D, it solves the Saint-Venant/shallow water equations in two space horizontal dimensions so as to provide mainly, values of the water height and mean horizontal velocity (averaged vertically) at each point of the grid. Our results are based on a resolution of the system with the finite element method.

In this study, TOMAWAC and TELEMAC2D have been coupled so that the interaction of the current and the waves could be taken into account. This direct coupling TOMAWAC-TELEMAC2D enables an exchange of variables between the two modules. Therefore, the action of the waves on the current and the current on the waves are represented. TELEMAC2D calculates current velocities and water depths and transmits them to TOMAWAC which in turn solves the wave action density equation by using these updated variables. Then TOMAWAC sends back to TELEMAC2D the new values of the wave driving forces that interfere with the current.

The spatial computational grid has been created with Blue Kenue. This software, developed by The National Research Council of Canada, provides tools to generate a triangular unstructured mesh (Fig. 4). Thus, different grids have been tried by changing the mesh density and the area of the study, in order to have an accurate representation of the phenomena with an acceptable time of simulation. The grid represented on Fig. 4 has been used to run the TOMAWAC model and is composed of 74,000 nodes. However, the coupling with TELEMAC2D required too much computation time, so the domain has been reduced by removing zone 3. The waves do not have any impact on the bottom in deep water, that is why we deleted this part of the grid (Fig. 4). The scenarios tested with this numerical approach are based on the previous study of the observed wave propagation directions (SSO and SE) and intensities. These data allowed us to set a JONSWAP spectrum on the boundaries.

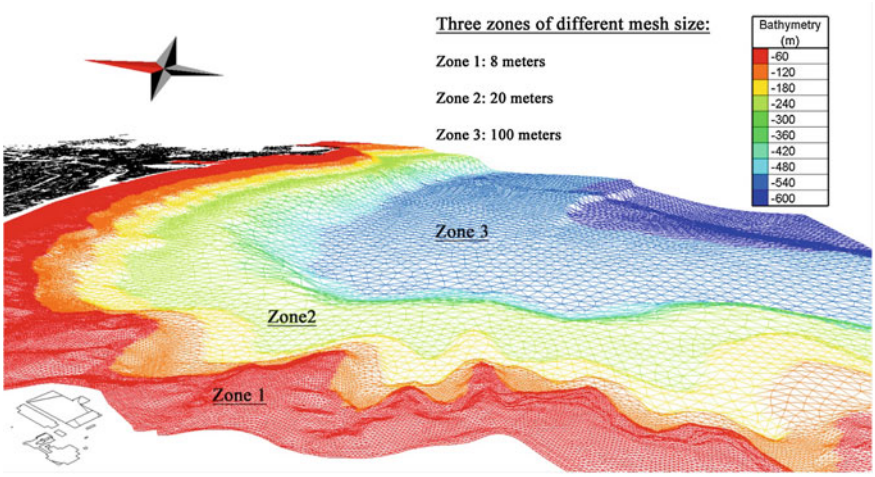

Fig. 4 TOMAWAC grid generated on Blue Kenue

3 Results and Discussion

3.1 TOMAWAC Results

Four wave directions of propagation have been tested on the model, N120, N140 (ESE-SE) and N180, N200 (S-SSW). The return period of the simulated storms is around 1 year, so the significant wave heights prescribed at the boundary of the grid are approximately 2.5 m (for ESE-SE swell) and 3.0 m (for S-SSW swell) [8]. Of course, source and dissipation terms have been configured to integrate the influence of some physical parameters, as for instance the bottom friction-induced dissipation, which occurs in shallow water. Other phenomena have been considered, like the white capping and the wave breaking dissipation.

As expected, because of its geographical orientation, a larger portion of Nice's beach is affected by the swell, when it comes from ESE-SE directions. However, the S-SSW swells are defined by more important wave heights and periods than the other swell directions. Therefore, even if the west part of the bay is protected, the east part is completely exposed to high wave heights.

A common phenomenon to all the swell directions can be observed near the coastline (around 30 m from the beach): an increase of the significant wave heights on some zones of the bay (Fig. 5). This can easily be explained by the bathymetry. Indeed, the geometrical refraction process forces the waves to propagate perpendicularly to the isobaths. Consequently, sub-marine caps create areas of high energy concentration (Fig. 5).

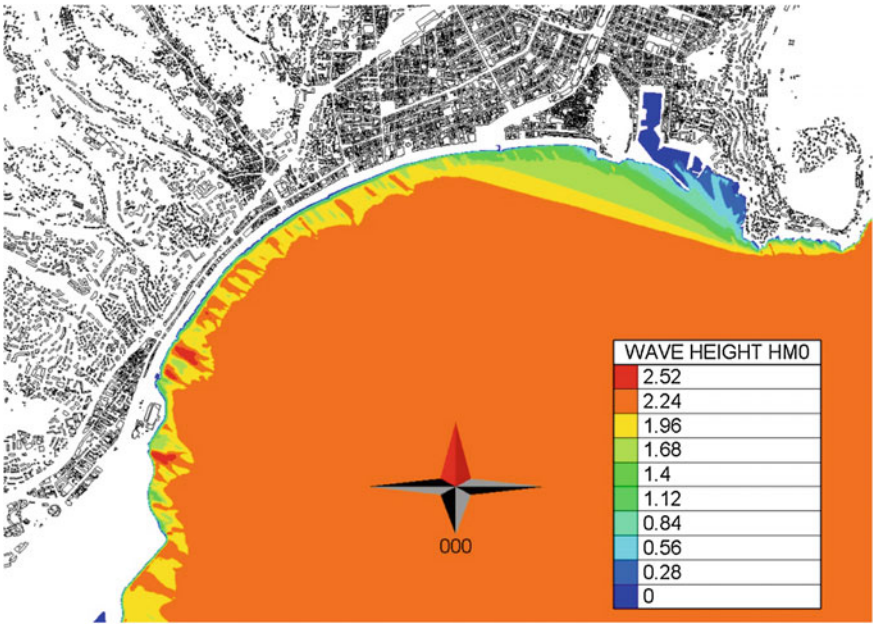

Fig. 5 TOMAWAC results for a 1-year return period event with a direction of swell N120

3.2 TELEMAC2D Results

The analysis of the current velocities results gives us more information about the potential sediment transport of a storm. Indeed, it allows us to interpret the effect of current patterns on the sediment dynamic. The event simulated in this second part is a little less important than 1-year return period events in terms of wave heights (Fig. 6). Yet, we can observe high values of the velocity with 1 m/s on some parts of the beach. They are observed in the middle of the bay, zone 1 (Fig. 6). These results are explained by the orientation of zone 1 compared to the near shore wave direction. A significant angle exists between the wave direction and the coastline of this zone. Thus, our comments in the introduction regarding the bathymetry are illustrated here. The refraction phenomena cannot be completed because of the late influence of the bathymetry on the wave direction, creating an alongshore current near the coastline.

In Zone 2, the current is coming from the East to the West with low velocity values. Two causes can be mentioned. The first one is, as seen before, the angle between the near shore wave direction of propagation and the beach orientation. In this case, the waves come nearly perpendicularly to the coast, thus the current velocity is lowered and oriented towards the East. The second one is the implanted

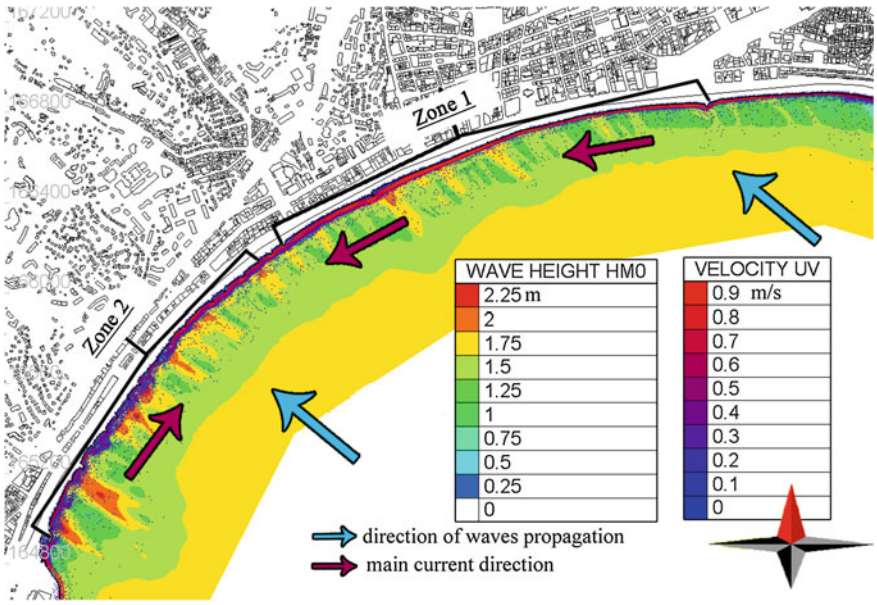

Fig. 6 Coupling TOMAWAC-TELEMAC2D results

groins in the west part of the bay. We can see that the velocity is still important in the east part of zone 2, but then it decreases progressively. This blocking action on the alongshore current is the first purpose of the groynes (Fig. 7).

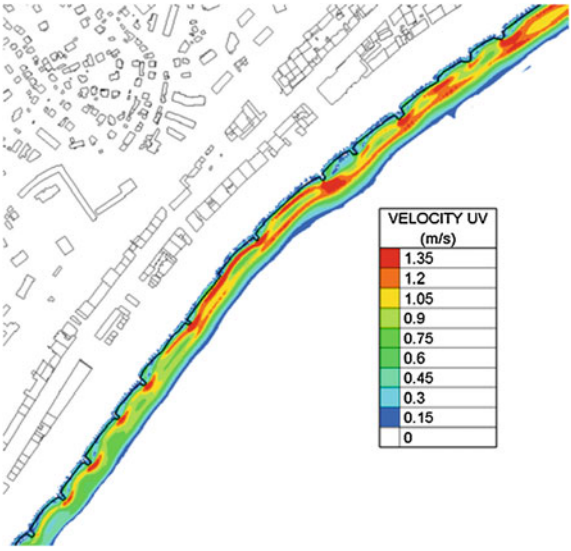

Fig. 7 Interaction of the current with the groynes

3.3 Validation and Prospects

Because of the lack of data, we could not validate accurately the wave and the current modeling results. Nevertheless, our findings have been compared with different local observations (storm damages, shape of the beach) with satisfactory results. For instance, after a South–East swell event, sediments have piled up on the west side of the groins (especially in the west part of zone 2, Fig. 8).

The final goal of this study is to model the sediment transport. So, we started to work on coupling TOMAWAC and TELEMAC2D with SISYPHE, the sediment transport module of TELEMAC. Thus, the data that needed to be acquired first concern the sediment motions. That is why we focused on obtaining these data and through them we tried to validate our waves and currents model.

Some simple correlation between the simulation results and the decrease of the beach width could be used to demonstrate the accuracy of the approach. In fact since 1950, Nice municipality has been measuring the beach width nearly 3 times a year. But this set of data is not well adapted to our modeling work.

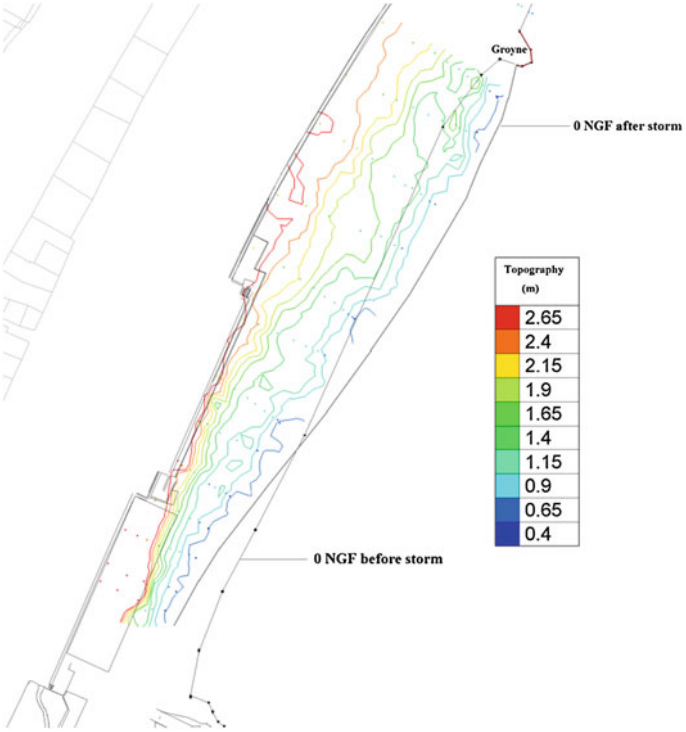

Fig. 8 Example of beach shape modifications after a South–East storm

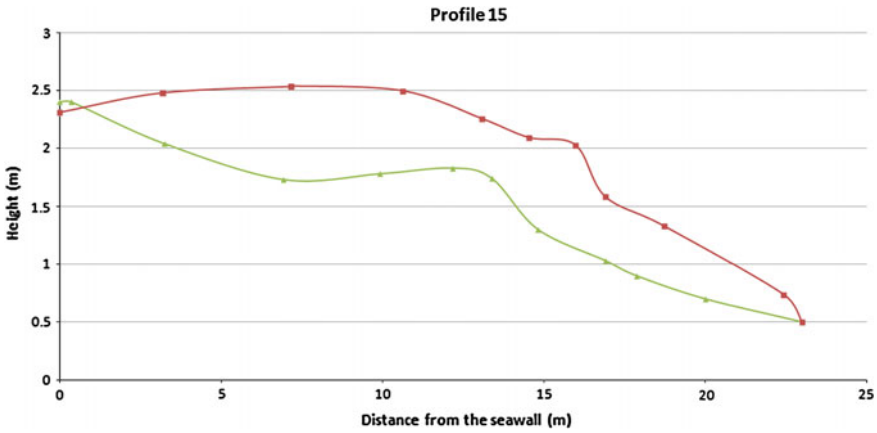

Fig. 9 Beach profile variations between the 10/12/13 (*green curve*) and the 06/01/14 (*red curve*)

In fact, the purpose of our simulations is to represent the action of the hydrodynamic forcing terms due to a short storm event (few hours). Several months separate two beach width field campaigns. Because of this time scale, the comparison between our results and the beach width data is not accurate.

Moreover, it is quite common that the beach experiences sediment losses or gains without any variation of the beach width (Fig. 9). In order to overcome these issues, we have started a new field campaign based on GPS measurements. The frequency of these measurements has been increased and varies depending on the storm events. Thanks to the GPS system, we are now able of capturing the beach profile motions and to characterize the variation of sediment volumes. However, more data need to be acquired before validating the previous model.

4 Conclusion

The goal of this paper was to present the erosion phenomena of Nice bay, and to illustrate some of its driving forces through a numerical model. The wave propagation simulations run on TOMAWAC have stressed the variable aspect of the significant wave heights along the coast, due to the special bathymetry of the domain. Thus, around sub-marine caps, concentrations of energy are observed and characterized by an amplification of the offshore wave height. As for the analysis of the currents modeled on TELEMAC2D, they have shown that the direction of the swell propagation directly impacts the direction and the intensity of the alongshore current. For instance, a South–East swell will create an East–West current, which is maximal around the center part of the bay. However, further work needs to be achieved before presenting concrete results of the gravel transport and to validate them.

Of course the phenomena illustrated by the model results were well known, but the major advantage of a modeling approach is to quantify them and furthermore, to understand their interactions with existing structures and future ones. The next step of this study will be to integrate structural solutions to reduce erosion and to analyze their effects by keeping in mind that such a model will not take into account all the complex phenomena of coastal erosion on a gravel beach.

Acknowledgment We wish to thank Mr. Bonnin, Mr. Ceruti, and Mr. Moretti from the environmental service of Nice for providing us all the data used in this paper and for economical support. We also thank Mr. Joubaud who has participated to the field measurement campaigns.

References

1. Anthony, E. J., & Cohen, O. (2011). Chronic offshore loss of nourishment on Nice beach, French Riviera: A case of over-nourishment of a steep beach? *Coastal Engineering, 58*, 374–383.
2. Anthony, E. J., & Julian, M. (1999). Source-to-sink sediment transfers, environmental engineering and hazard mitigation in the steep Var River catchment, French Riviera, Southeastern France. *Geomorphology, 31*, 337–354.
3. Austin, M. J., & Buscombe, D. (2008). Morphological change and sediment of the beach step on a macro-tidal gravel beach. *Marine Geology, 249*, 167–183.
4. Beau Devin, C., & Alesant, L. (1955). Etude systématique de la protection d'une plage par un brise-lame immergé, plage de Nice. NEYRPIC. Grenoble, R4181, 35 pp.
5. Cohen, O. (1993). *Stabilisation d'un cordon de galets par des rechargements: Exemple de la plage de Nice, Côte d'Azur*. Memoire de recherche en géographie: Université de Nice Sophia-Antipolis. 50 pp.
6. Goda, Y. (2000). *Random seas and design of maritime structures. Advanced series on Ocean Engineering* (Vol. 15, 2nd Edn.). Singapore: World Scientific, 443 pp.
7. Gourbesville, P. (2009). Le bassin venant du Var est la crue de 1994 [extrait]. 14 pp.
8. Hydratech (2012). Etude numérique de la courantologie aux abords des épis présents sur le littoral niçois. Ref : 01629290_Rév.C. 58 p.
9. Komen, G.J., Cavaleri, L., Donelan, M., Hasselmann, K., Hasselmann, S., Jansen, P.A.E.M. (1994). *Dynamics and modelling of ocean waves* (532 pp.). New York: Cambridge University Press.
10. Perez, S. (1991). *L'artificialisation du littoral et ses impacts sur la dynamique sédimentaire et la morphologie littorale (de Rauba Capeu à la Cagne)*. UFR Espaces et Cultures, Nice: Memoire de maîtrise en géographie. 168 pp.
11. Sage, L. (1976). La sédimentation à l'embouchure d'un fleuve côtier méditerranéen: le Var. Thése, doctorat de 3éme cycle, Université de Nice, 243 pp.
12. Sogreah (2009). Littoral entre Antibes et Cap d'Ail, bilan, analyse et préconisation sur le phénomène érosif. Contrat de Baie d'Antibes à Cap d'Ail, ref 1711764.

One-Dimensional Model for Sediment Transport: An Application to the Design of Silt Basins

Álvaro A. Aldama, Adalberto Vaca, Dunia González-Zeas, Xavier Coello-Rubio and Gustavo Luzuriaga

1 Introduction

The design of silt basins is commonly based on the use of simplistic methods for modeling suspended sediment transport. Such methods are based on the assumption that all suspended sediment particles follow a straight path in their motion through a silt basin, thus ignoring the turbulent and spatial heterogeneity of sediment transport phenomena. Experimental studies developed by Vanoni [1], Vanoni and Nomicos [2], Cellino and Graf [3] and Peng et al. [4] support the hypothesis that the turbulence is cushioned by the suspended sediment, thereby increasing cross-sectional spatial heterogeneity. Such effects may be modeled through the introduction of the dispersion component in sediment transport models, thus providing a more realistic representation of the sedimentation processes. It is the opinion of the authors of this paper that it is important to highlight the significance of introducing the dispersion component and evaluating its effect on sediment removal.

Many researchers have accounted for the effect of the dispersion component in suspended sediment modeling through its introduction in the physically based

Á.A. Aldama (✉)
Independent Consultant, Mexico, Mexico
e-mail: alvaro.aldama@gmail.com

A. Vaca · D. González-Zeas · X. Coello-Rubio
Association CFE-PYPSA-CVA-ICA, Quito, Ecuador
e-mail: adalberto.vaca@gyfccs.com

D. González-Zeas
e-mail: duniapgz@yahoo.com.mx

X. Coello-Rubio
e-mail: xavier.coello@gyfcces.com.ec

G. Luzuriaga
Hydroelectric Coca Codo Sinclair, Public Company, Quito, Ecuador
e-mail: gustavo.luzuriaga@cocacodosinclair.gob.ec

P. Gourbesville et al. (eds.), *Advances in Hydroinformatics*,
Springer Water, DOI 10.1007/978-981-287-615-7_3

advection–dispersion equation [5–8]. The main difficulty thereof has been the estimation of the dispersion coefficient. Several parameterizations of this coefficient have been proposed [9–11].

This paper proposes a one-dimensional model for suspended sediment transport that incorporates the dispersion component. The proposed model is applied to the design of the settling basins of the Coca Codo Sinclair (CCS) hydropower station located in Ecuador. The main objective of this study is to evaluate and compare the results produced by the proposed model with those generated by a simplistic model, in terms of sediment removal efficiency, with the underlying idea of improving settling basins design practice. The specific objectives of the paper are: (1) to evaluate different parameterizations of the dispersion coefficient, (2) to perform sensitivity analysis of the proposed model based on dimensionless parameters, and (3) to apply the proposed model and a simplistic model to a case study, in order to evaluate and compare their predictions of sediment removal efficiency.

2 Methodology

Different components are integrated in order to address the aspects related to the design of the silt basins of an intake complex. A one-dimensional model is proposed with the understanding that the consideration of the dispersion coefficient could improve the design of the hydraulic structures, in comparison those based on a simplistic method. As summarized in Fig. 1, the methodology entails the following four steps: (1) to evaluate different alternative parameterizations of the longitudinal dispersion coefficient, (2) to analyze the performance of the simplistic model with respect to the proposed model in simulating suspended sediment transport, (3) to assess the significance of the dispersion component through a sensitivity analysis, and (4) to apply and compare the results of both the simplistic and the proposed model in terms of the sediment removal efficiency of the silt basins for the case study.

2.1 Dispersion Coefficient

The longitudinal dispersion coefficient is an important parameter that is used to account for cross-sectional velocity and concentration distribution heterogeneities in the transport of sediments in rivers and streams. Numerous empirical equations have been developed in order to predict the longitudinal dispersion coefficient in natural streams and channels [12]. Nonetheless, the nonuniformities of the channels can have a significant influence on the distribution of the velocity, consequently, the dispersion coefficients vary depending on the channel, its location, and flow rate [13]. Having said that, it is essential to consider different dispersion coefficients provided by the literature in order to evaluate the most adequate and reliable for silt basins design.

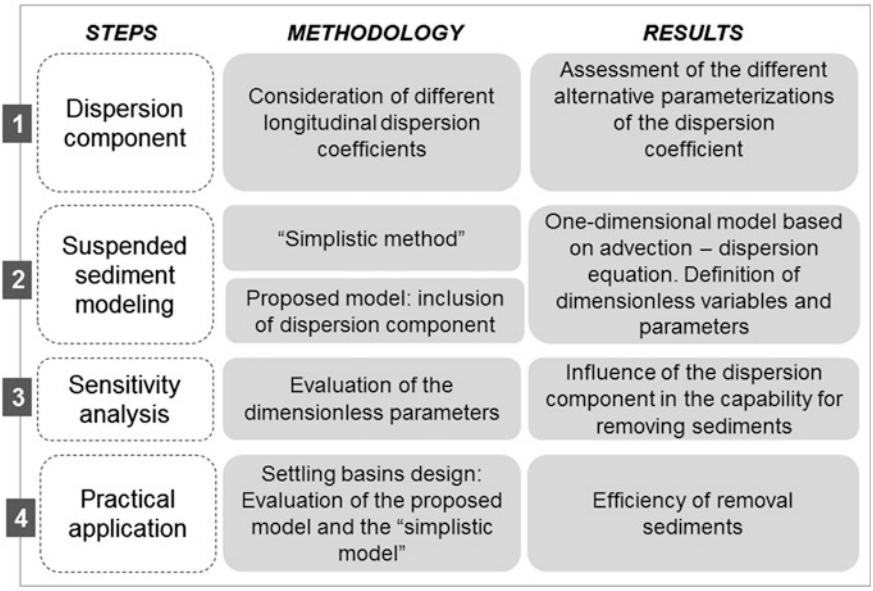

Fig. 1 Proposed methodological approach

Table 1 shows some of the existing equations that have been used in this study in order to predict the dispersion coefficient. According to the table, D_l is the longitudinal dispersion coefficient, H the average water depth, W the width of the channel, U the cross-sectional mean flow velocity, and U_* the shear velocity.

Table 1 Existing equations to calculate longitudinal dispersion coefficients

Source	Equation
Elder [14], Taylor [15]	$D_l = 5.93HU_*$
Lui [16]	$D_l = \alpha \frac{U^2W^2}{HU_*} \quad \alpha = 0.18\left(\frac{U_*}{U}\right)^{1.5}$
Fischer [17]	$D_l = 0.011\frac{U^2W^2}{HU_*}$
Seo and Cheong [10]	$D_l = 5.915HU_*\left(\frac{W}{H}\right)^{0.620}\left(\frac{U}{U_*}\right)^{1.428}$
Koussis and Rodríguez-Mirasol [18]	$D_l = 0.6\frac{U_*W^2}{H}$
Kashefipour and Falconer [7]	$D_l = 10.612HU\frac{U}{U_*}$
Sahay and Dutta [11]	$D_l = 2HU_*\left(\frac{W}{H}\right)^{0.96}\left(\frac{U}{U_*}\right)^{1.25}$

2.2 Suspended Sediment Modeling

2.2.1 One-Dimensional Transport Model

A cross-sectional average of the three-dimensional transport equation results in the following one-dimensional advection–dispersion–reaction (ADR) equation, in accordance with the theoretical background established by Taylor [15], Elder [14, 19] and Fischer et al. [17]:

$$\underbrace{\frac{\partial CA}{\partial t}}_{\text{storage}} + \underbrace{\frac{\partial CUA}{\partial x}}_{\text{advection}} = \underbrace{\frac{\partial}{\partial x}\left(D_\ell A \frac{\partial C}{\partial x}\right)}_{\text{dispersion}} \underbrace{-w_s \overline{c_b} W}_{\text{settling}} + \underbrace{\int_\Gamma (\overline{c'v'} n_y + \overline{c'w'} n_z) d\ell}_{\text{resuspension}} \tag{1}$$

where the physical interpretation of each term appears in the same equation follows: A is the cross-sectional area of a river or a channel, C is the cross-sectionally averaged sediment concentration, U the cross-sectionally averaged flow velocity, D_l the dispersion coefficient, x and t denote space and time, respectively, w_s the fall velocity of the sediment particles, W the width of the free surface, v' and w' represent turbulent fluctuations of the velocity components in the transverse and vertical directions, respectively, n_y and n_z are the components of the unit normal vector to τ (solid border of the integration area) in the transverse and vertical directions, respectively, dl is an arc differential, $\overline{c_b}$ is the concentration at the boundary of the channel, where the overbar represents an average in the Reynolds sense [20] and c' represents the concentration turbulent fluctuation. The first term on the right of the Eq. (1), represents the longitudinal dispersion of the suspension, which accounts for the velocity and concentration distributions cross-sectional heterogeneities.

2.2.2 Advection–Reaction Model

In a settling basin, the flow can be assumed as steady and uniform. Additionally, in a conservative way, the concentration in the bottom, $\overline{c_b}$, can be replaced by the cross-sectional mean sediment concentration, C. Finally, since the longitudinal velocities will be relatively small, the resuspension can be neglected. Therefore, Eq. (1) can be simplified as:

$$U\frac{dC}{dx} = D_l \frac{d^2C}{dx^2} - \frac{w_s C}{H} \tag{2}$$

where H is the hydraulic depth. Furthermore, letting $C \equiv C_v$, neglecting the dispersion term, and taking into account the boundary condition $C_v(0) = C_0$, Eq. (3) is obtained:

$$C_v(L) = C_0 \exp\left(-\frac{w_s L}{q}\right) \tag{3}$$

where L denotes the length of the settling basin and $q \equiv UH$ is the flow rate per unit width. Equation (3) corresponds to the well-known equation presented in Vanoni [21].

Due to the fact that Eq. (3) ignores dispersion, it will be referred to as advection–reaction (AR) model.

2.2.3 Simplistic Model

The simplistic model has been used in many projects throughout the world in order to design settling basins. Nonetheless, it is important to highlight that these methods are based on the following assumptions: (a) the particles move horizontally with the average velocity of the flow and vertically with the fall or sedimentation velocity, (b) the vertical travel time T_v, and the horizontal travel time T_h, of a particle located at the free surface at the upstream of the settling basin are equal, as shown in the following equations:

$$T_h = \frac{L_d}{U} \tag{4}$$

$$T_v = \frac{H}{w_s} \tag{5}$$

$$T_h = T_v \Rightarrow L_d = \frac{UH}{w_s} \tag{6}$$

where L_d is the length of the settling basin, U the cross-sectional mean flow velocity, H the hydraulic depth, and w_s the fall velocity of the sediment particles.

According to a one-dimensional perspective of mass conservation, when only advection and settling are accounted for:

$$\rho UAC_L = \rho UAC_0 - \rho w_s WLC^* \tag{7}$$

where ρ is the liquid density, U the cross-sectional mean flow velocity, C_L the downstream concentration, C_0 the upstream concentration, w_s the fall velocity of the sediment particles, W the width, and C^* a representative mean concentration of settling particles along the settling basin.

If the sediment concentration downstream of the settling basin is $C_L = 0$, the Eq. (7) can be written as follows:

$$L = \frac{UA}{w_s W}\frac{C_0}{C^*} = \frac{UH}{w_s}\frac{C_0}{C^*} \tag{8}$$

where the last step implies that a rectangular cross section has been assumed.

A reasonable approximation of the sediment concentration to the representative mean value is given by the trapezoidal rule, as follows:

$$C^* = \frac{C_0 + C_L}{2} = \frac{C_0}{2} \tag{9}$$

Therefore,

$$L = 2\frac{UH}{w_s} = 2L_d \tag{10}$$

In other words, the required length would be twice the value computed by employing the simplistic model. In fact, the only way in which $L = L_d$ is to assume that $C^* = C_0$. This assumption is clearly invalid, since it neglects the fact that the concentration of sediment gradually decreases along the length of the silting basin as a consequence of settling. Therefore, the simplistic method is inconsistent with the principle of mass conservation and therefore should be rejected, given that it is conceptually wrong. Actually, it may be shown that if the basin is subdivided into N reaches of length $\Delta x = L/N$ and an analogue of Eq. (7) is applied to each reach, after taking the limit as $N \to \infty$, the Vanoni solution, Eq. (3) is produced.

2.2.4 Proposed Model

On the basis of Eq. (2), let the following dimensionless variables be defined:

$$\tilde{C} = \frac{C}{C_0} \tag{11}$$

$$\tilde{x} = \frac{x}{L} \tag{12}$$

where C_0 is the upstream sediment concentration and L the length of the settling basin.

Substituting Eqs. (11) and (12) in Eq. (2), the following dimensionless transport equation is obtained:

$$\frac{1}{P_e}\frac{d^2\tilde{C}}{d\tilde{x}^2} - \frac{d\tilde{C}}{d\tilde{x}} - S_e\tilde{C} = 0 \tag{13}$$

where P_e and S_e represent the Pécléct number and the sedimentation number, respectively, defined as follows:

$$P_e = \frac{UL}{D_l} \tag{14}$$

$$S_e = \frac{w_s}{U}\frac{L}{H} = \frac{w_s}{U}\frac{L}{h} \tag{15}$$

where, in the case of a rectangular section, the depth h and the hydraulic depth H coincide, as is shown in Eq. (15).

The upstream and downstream boundary conditions are defined as follows:

$$\tilde{C}(0) = 1 \tag{16}$$

$$\frac{d\tilde{C}}{dx}(1) = 0 \tag{17}$$

Then, the problem to be solved consists of Eq. (13) subject to the boundary conditions given by Eqs. (16) and (17). Equation (13) admits the following particular solution:

$$\tilde{C}_p(\tilde{x}) = \exp(m\tilde{x}) \tag{18}$$

Substituting Eq. (18) in Eq. (13), the following characteristic equation is obtained:

$$\frac{1}{P_e}m^2 - m - S_e = 0 \tag{19}$$

which one has the following solutions:

$$m_1 = \frac{P_e}{2}\left[1 + \sqrt{\left(1 + \frac{4}{p_e}\frac{w_s}{U}\frac{L}{H}\right)}\right] \tag{20}$$

$$m_2 = \frac{P_e}{2}\left[1 + \sqrt{\left(1 + \frac{4}{p_e}\frac{w_s}{U}\frac{L}{H}\right)}\right] \tag{21}$$

Therefore, the general solution of Eq. (13) is given by:

$$\tilde{C}(\tilde{x}) = k_1 \exp(m_1\tilde{x}) + k_2 \exp(m_2\tilde{x}) \tag{22}$$

Using Eq. (22) in the boundary conditions of Eqs. (16) and (17), the following results are obtained:

$$k_1 = \frac{1}{1 - \frac{m_1 \exp m_1}{m_2 \exp m_2}} \tag{23}$$

$$k_2 = \frac{\frac{m_1 \exp m_1}{m_2 \exp m_2}}{1 - \frac{m_1 \exp m_1}{m_2 \exp m_2}} \tag{24}$$

Substituting Eqs. (23) and (24) in Eq. (22) and applying different algebraic operations, the dimensionless concentration downstream of the settling basins is obtained as follows:

$$\tilde{C}(\tilde{x}) = \exp\left(\frac{P_e}{2}\tilde{x}\right) \frac{(1-\alpha)\exp\left(-\frac{P_e}{2}\alpha\right)\exp\left(\frac{P_e}{2}\alpha\tilde{x}\right) - (1+\alpha)\exp\left(\frac{P_e}{2}\alpha\right)\exp\left(-\frac{P_e}{2}\alpha\tilde{x}\right)}{(1-\alpha)\exp\left(-\frac{P_e}{2}\alpha\right) - (1+\alpha)\exp\left(\frac{P_e}{2}\alpha\right)} \tag{25}$$

where Eqs. (20) and (21) have been used and the following parameter has also been introduced:

$$\alpha = \sqrt{\left(1 + 4\frac{S_e}{P_e}\right)} \tag{26}$$

According to Eq. (25), the reduction factor of the concentration along the settling basin is given by:

$$\tilde{C}(1) = \frac{2\alpha}{(1+\alpha)\exp\left[-\frac{P_e}{2}(1-\alpha)\right] - (1-\alpha)\exp\left[-\frac{P_e}{2}(1+\alpha)\right]} \tag{27}$$

Then, the removal efficiency will be:

$$\eta = 1 - \tilde{C}(1) \tag{28}$$

Moreover, when the Pécléct number approaches to infinity, the proposed model corresponds with the solution of Vanoni [21], given by Eq. (3), as shown in the following expression:

$$\lim_{P_e \to \infty} \tilde{C}(1) = \exp(-S_e) = \exp\left(-\frac{w_s}{U}\frac{L}{H}\right) = \exp\left(-\frac{w_s L}{q}\right) \tag{29}$$

2.3 Sensitivity Analysis

The sensitivity analysis of the model is related to the identification of the most important parameters with respect to the model results. A sensitivity analysis of the

Eqs. (25) and (27) is carried out through the values of the dimensionless parameters P_e and S_e. The sensitivity of the model to the parameter S_e is evaluated, maintaining constant the parameter P_e. This is done for different values of P_e, with the aim of evaluating the influence of the dispersion component on the capability for removing sediments. On the other hand, the dimensionless concentration along the silt basins is obtained for different values of the parameter P_e and keeping constant the parameter S_e. This allows to assess the influence of the fall velocity in the capability for removing sediments for different values of S_e.

Due to the fact that P_e depends on the dispersion coefficient, accordingly with Eq. (20) and taking into account that the dispersion component implies the existence of an additional flow entering upstream of the silt basin, it is possible to infer that, a lower value of P_e supposes a lower sediment removal, given that the dispersion coefficient is greater. On another note, a greater value of S_e, supposes a greater fall velocity, as a result, the capability of sediment removal is greater.

3 Practical Application

The case study involves the settling basins of the Coca Codo Sinclair (CCS) hydroelectric station, a run-of-river project under construction in the Coca River, located in the northeastern of Ecuador. This river is a branch of the Napo River and belongs to the Amazon River system. The intake complex is located on the Coca River, about 1 km downstream of the confluence of the Quijos River and the Salado River with a catchment area of 3600 km^2, as shown in Fig. 2.

The project is going to generate 1500 MW of maximum power, through eight Pelton turbines of 187.5 MW each, which implies 8631 GWh of annual average energy. Due to the large amount of highly abrasive sediment carried by the Salado

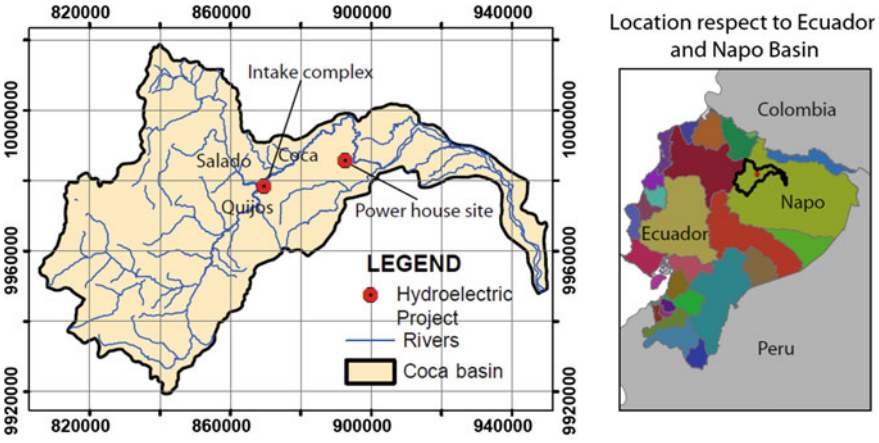

Fig. 2 Map of the hydropower project location

Table 2 Grain size and settling velocity of the sediment

Diameter (ϕ) (mm)	0.05	0.06	0.07	0.10	0.25	0.5	2.00
Settling velocity (w_s) (m/s)	0.0037	0.0048	0.0056	0.008	0.035	0.07	0.181
Percentage of particles (%)	6	2	2	10	12	20	48

River, the construction of the settling basins plays an important role in controlling sediments, in order to guarantee the efficiency of the turbines during the hydroelectric station operation. The inflow in the intake complex is 222 m^3/s that will be conducted through a headrace tunnel until a balancing reservoir for hourly regulation and then feed the pressure pipes that carry the liquid to the power house. The grading and settling velocity of the sediments at the intake complex of the case study are as indicated in the Table 2.

According to the project specifications, the settling basins should be designed to deposit 100 % of the particles greater than 0.25 mm. Hence, it is important to analyze the efficiency of the silt basins for sediment removal in order to satisfy this specification. The channel parameters of the settling basins took the following values: width (W) = 13 m, depth (H) = 9.90, flow (Q) = 222 m^3/s. A composite Manning's roughness factor, n, was taken to consider the roughness of the concrete walls channel (n_c = 0.015) and the roughness of the bottom bed (n_b = 0.020). Several alternatives of settling basins design have been evaluated with the primary goal of defining the most suitable design from the economical and technical point of view. An important aspect to be considered is the topographic characteristics in the project area and specifically the available space for the location of the settling basins in order to establish the final option design. Table 3 summarizes the different combinations of number of settling basins and their respective length, in order to test the efficiency of removing sediments.

Table 3 Evaluated design options

Description	Design options								
	1	2	3	4	5	6	7	8	9
Number of settling basins (N_S)	7.0	8.0	9.0	10.0	11.0	12.0	13.0	14.0	15.0
Length of each settling basin (L) (m)	175.0	150.0	140.0	130.0	120.0	110.0	100.0	95.0	90.0

4 Results

4.1 Evaluation of the Longitudinal Dispersion Coefficient

Seven equations of the dispersion coefficient have been evaluated in order to determine the influence of this coefficient in the capability for removing sediments (Table 1). The predictions of the dispersion coefficients using different parameterization alternatives show interesting results as is shown in Table 4. A significant variability is observed in the values of the dispersion coefficient for the different equations. Nonetheless, according to the analyzed design options presented in Table 3, all the equations agree with decreasing of dispersion coefficient when increasing the number of settling basins. Note that the increase of the number of settling basins causes a decrease of the cross-sectional average longitudinal velocity U, causing lower values of the dispersion coefficient.

Additionally, it is recommended to carry out experiments in order to define the most reliable alternative parameterization in correspondence with the experimental data, which is not an objective of this paper, but it will be considered for future research. However, from a conservative point of view and taking into consideration the effectiveness of each dispersion equation on sediment removal, as is presented in Table 5, the Fischer coefficient dispersion has been selected as the most reliable in this study.

Another factor with an important influence in the longitudinal dispersion coefficient is the roughness of the channel. Figure 3 shows the values of the Fischer dispersion coefficient versus the variation of the roughness coefficient for the different design options. The results show a decrease of the dispersion coefficient when increasing roughness. From the physical point of view, a greater roughness implies a more efficient mechanism of momentum transfer, which tends to homogenize the velocity distribution. Consequently, if the walls of the silt basins have a greater roughness, the dispersion coefficient will be lower, augmenting the removal efficiency of the sediments.

4.2 Analysis of the Degree of Sensitivity to the Dimensionless Parameters

In order to evaluate the sensitivity of the proposed model to the dimensionless parameters, Fig. 4a highlights the results obtained as a function of the parameters P_e and S_e. Similarly, a comparison with the results obtained by Vanoni solution is made. It is possible to appreciate that in all cases, the solutions that take into consideration the effect of the dispersion component are more unfavorable than the Vanoni solution, which implies a lower removal. This is not surprising, since the dispersive term supposes the existence of an additional flow entering upstream of the settling basins. On another note, when Péclét number is lower, which means a

Table 4 Values of the longitudinal dispersion coefficients for different equations and different design options

Source	Dispersion coefficients (D_l) for the different design options (m^2/s)								
	1	2	3	4	5	6	7	8	9
Elder [14], Taylor [15]	0.71	0.62	0.55	0.50	0.45	0.41	0.38	0.36	0.33
Lui [16]	0.18	0.16	0.14	0.13	0.11	0.10	0.10	0.09	0.08
Fischer et al. [17]	1.21	1.06	0.94	0.85	0.77	0.71	0.65	0.61	0.57
Seo and Cheong [10]	74.37	65.08	57.84	52.06	47.33	43.38	40.05	37.19	34.71
Koussis and Rodríguez-Mirasol [18]	0.12	0.11	0.10	0.09	0.08	0.07	0.07	0.06	0.06
Kashefipour and Falconer [7]	679.34	594.42	528.38	475.54	432.31	396.28	365.80	339.67	317.03
Sahay and Dutta [11]	15.77	13.80	12.27	11.04	10.04	9.20	8.49	7.89	7.36

Table 5 Efficiency of sediment removal for particles between 0.25 and 0.5 mm, for the 9 design alternatives and using different parameterization of the longitudinal dispersion coefficient

Dispersion coefficient	Efficiency of sediment removal (%)								
	1	2	3	4	5	6	7	8	9
Elder [14], Taylor [15]	99.03	98.89	99.07	99.16	99.19	99.15	99.05	99.11	99.14
Lui [16]	99.27	99.18	99.34	99.43	99.47	99.46	99.41	99.47	99.50
Fischer et al. [17]	98.80	98.59	98.79	98.88	98.89	98.82	98.66	98.72	98.74
Seo and Cheong [10]	63.44	59.05	58.74	57.78	56.18	53.93	51.02	50.35	49.38
Koussis and Rodríguez-Mirasol [18]	99.29	99.21	99.37	99.46	99.49	99.49	99.44	99.50	99.53
Kashefipour and Falconer [7]	15.40	13.24	13.02	12.55	11.85	10.97	9.93	9.68	9.34
Sahay and Dutta [11]	90.06	88.09	88.22	87.95	87.27	86.15	84.51	84.25	83.76

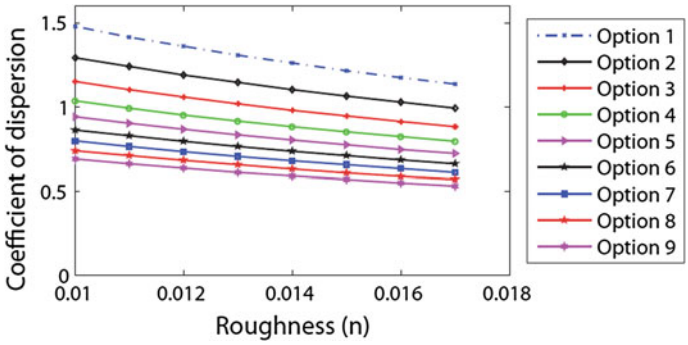

Fig. 3 Contrast between roughness n and the Fischer coefficient of dispersion for the design options

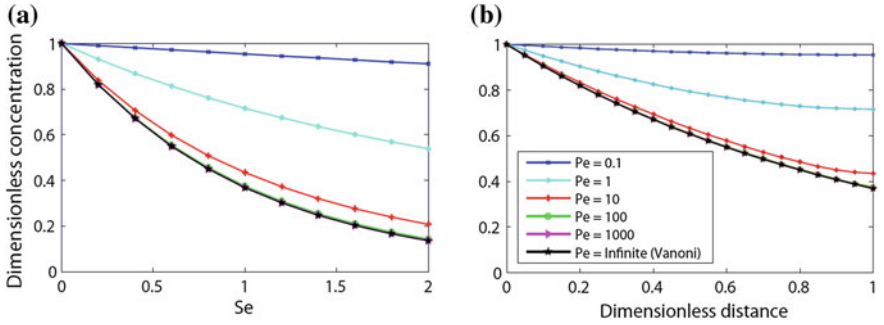

Fig. 4 Dimensionless concentration: **a** as function of parameters P_e and S_e and **b** along the silt basin for different values of P_e and with $S_e = 1$

higher dispersion coefficient, the capability for removing sediments decreases. Moreover, as the sedimentation number increases the capability of sediment removal increases as well due to a greater fall velocity of the particles. Figure 4b shows the distribution of the dimensionless concentration along the settling basins for different values of the Pécléct number and a sedimentation number equal to 1. In a similar way, it is observed that the concentration decreases along the length of the settling basins. The decreasing of the concentration is greater when the sedimentation number increases as is presented in Fig. 4a. Therefore, when P_e is lower, the capability of sediment removal decreases, and when S_e is greater, the capability of sediment removal increases.

In accordance with the Eq. (29), when P_e tends to infinity, the proposed model concurs to Vanoni solution, given that the dispersion component is too small. Consequently, the solutions that incorporate the dispersion component imply a lower capability for removing sediments.

4.3 Efficiency of Sediments Removal

With regard to the efficiency of the silt basins for sediment removal, Table 6 summarizes the results obtained when applying the proposed model using the Fischer dispersion coefficient and Table 7 shows the results when the method of Vanoni is used and therefore, the dispersion component is omitted. As an example, the results of the design option 2 (8 silt basins of 150 m length) are shown:

With reference to the results of Tables 6 and 7, and in accordance with the project specification related to deposit 100 % of particles greater than 0.25 mm, both, the proposed model and Vanoni method do not meet the specification with values of 98.59 and 99.27 %, respectively. Nevertheless, the proposed model implies a more unfavorable solution and, therefore a smaller sediment removal efficiency in comparison with the simplistic method, given that it overestimates the capability of the silt basin for sediment removal.

4.4 Evaluation of the Settling Basins Design

In view of the above results, a new set of design options were analyzed, such that the efficiency of removal is 100 % for the particles greater than 0.25 mm. Figure 5a shows a combination of the length and number of settling basins that satisfy the project specification. As could be expected, a greater number of silt basins required lower length. Nonetheless, the resulting lengths for low numbers of silt basins are

Table 6 Efficiency of sediment removal applying the proposed model and using Fischer longitudinal dispersion coefficient

Diameter (mm)	Input percentil	Settling velocity (m/s)	Reduction factor[a]	Output percentil	Efficiency (%)
0.1 a 0.25	15	0.035	0.106	1.589	89.41
0.25 a 0.5	25	0.07	0.014	0.353	98.59
0.5 a 2	60	0.181	0.000	0.004	99.99
TOTALES	100			1.946	98.05

[a]Reduction factor = Upstream concentration/downstream concentration

Table 7 Efficiency of sediment removal applying simplistic method of Vanoni

Diameter (mm)	Input percentil	Settling velocity (m/s)	Reduction factor[a]	Output percentil	Efficiency (%)
0.1 a 0.25	15	0.035	0.085	1.282	91.45
0.25 a 0.5	25	0.07	0.007	0.183	99.27
0.5 a 2	60	0.181	0.000	0.000	100,00
TOTALES	100			1.465	98.53

[a]Reduction factor = Upstream concentration/downstream concentration

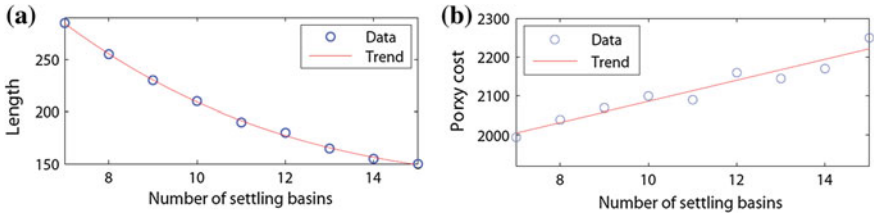

Fig. 5 **a** Design combinations with a removal efficiency of 99 % for particles ranging between 0.25 and 0.5 mm. **b** Proxy cost of the optimal design

too large. Likewise, the number of silt basins for small lengths are too high. This suggests relaxing somewhat the required removal efficiency. But before turning to this point, it should be emphasized that most of the cost of excavation and construction of silt basins will be proportional to the product of the number of silt basins by its length (assuming that the cross section remains constant), which is considered as a proxy cost. In Fig. 5b the behavior of the proxy cost as function of the number of silt basins is shown. It can be seen that with a lower number of silt basins, the cost tends to be lower too. Then, the number of silt basins should be kept as low as possible.

In the case study, some factors such as: the limited available space for the intake complex, the use of a flushing system of greater efficiency, and the existence of a balancing reservoir downstream of the silt basins that will also retain sedimentation particles, have permitted to relax the requirement for 100 % removal of particles between 0.25 and 0.5 mm by a lower removal efficiency. Taking into consideration the above factors, the most convenient combination selected for the case study has been the design option 2, ensuring that the turbines will not be affected in their operation.

5 Conclusion

A one-dimensional model for suspended sediment transport is proposed in order to improve silting basin structures design. The mathematical analysis of the simplistic method (developed in Sect. 2.2.3) has shown that this method is inconsistent with the principle of mass conservation and therefore, is conceptually wrong. Despite the significant progress and excellent work in recent years related to dispersion processes, there is still uncertainty as to what parameterization is the most adequate for silting basins design. Thus, it is essential to perform experimental and prototype studies. On the other hand, it has been demonstrated that the inclusion of the longitudinal dispersion coefficient produces more unfavorable results in terms of sediment removal in comparison with the advection–reaction model of Vanoni, whose results tend to overestimate the capability of the silt basins for sediment removal. In a similar way, it is advisable that the walls of the silt basins have a

greater roughness, given that this decreases the dispersion coefficient and increases the efficiency of sediment removal. In accordance with the available space for the implantation of the silt basins of the case study and from the economic and technical perspective, it is not feasible to construct silt basins that remove 100 % of the suspended sediment greater than 0.25 mm. However, the most suitable design option has been defined in order to ensure an efficient turbine operation.

Acknowledgements The authors acknowledge the support given by the Public Company Hydroelectric Coca Codo Sinclair, Ministry Coordinator of Strategic Sectors and the Ministry of Electricity and Renewable Energy of Ecuador.

References

1. Vanoni, V. (1946). Transportation of suspended sediment by water. *Transactions of ASCE, 111*, 67–133.
2. Vanoni, V., & Nomicos, G. N. (1960). Resistance properties of sediment laden streams. *Transactions of ASCE*, 1140–1175.
3. Cellino, M., & Graf, W. H. (1999). Sediment laden flow in open channels under non-capacity and capacity condition. *Journal of Hydraulic Engineering ASCE, 125*(5), 455–462.
4. Peng, L., Cheng, L., & Huang, J. (2001). *Study of the structure of flow in open channel with suspended sediment*. Beijing, China: XXIX Congress of IAHR.
5. Uncles, R., Elliot, R., & Weston, S. (1985). Dispersion of salt and suspended sediment in a partially mixed estuary. *Estuaries, 8*, 256–269.
6. Gerritsen, H., Vos, R. J., van der Kaaij, T., Lane, A., & Boon, J. G. (2000). Suspended sediment modelling in a shelf sea (North Sea). *Coastal Engineering, 41*, 317–352.
7. Kashefipour, S., & Falconer, R. (2002). Longitudinal dispersion coefficients in natural channels. *Water Research, 36*, 1596–1608.
8. Cui, G., & Yanagi, T. (2007). Dispersion of suspended sediment originated from the Yellow River in the Bohai Sea. *Coastal Marine Science, 31*, 9–18.
9. Fischer, H. B. (1967). The mechanics of dispersion in natural streams. *Journal of Hydraulic Division, ASCE, 93*(HY6), 187–215.
10. Seo, I. W., & Cheong, T. S. (1998). Predicting longitudinal dispersion coefficient in natural streams. *Journal of Hydraulic Engineering ASCE, 124*, 25–32.
11. Sahay, R. R., & Dutta, S. (2009). Prediction of longitudinal dispersion coefficients in natural rivers using genetic algorithm. *Hydrology Research, 40*(6), 544–552.
12. Swamee, P., Pathak, S., & Sohrab, M. (2000). Empirical relations for longitudinal dispersion in streams. *Journal of Hydraulic Engineering ASCE, 126*, 1056–1062.
13. Wallis, S. G., & Manson, J. R. (2004). Methods for predicting dispersion coefficients in rivers. *Proceeding of the Institution of Civil Engineers, 157*, 131–141.
14. Elder, J. W. (1959). The dispersion of marked fluid in turbulent flow. *Journal of Fluid Mechanics, 5*, 544–560.
15. Taylor, G. I. (1954). The dispersion of matter in turbulent flow through a pipe. *Proceedings of the Royal Society of London, Series A, 223*, 446–448.
16. Liu, H. (1977). Predicting dispersion coefficient of streams. *Journal of the Environmental Engineering Division, 103*(1), 59–69.
17. Fischer, H. B., List, E., Koh, R., Imberger, J., & Brooks, N. (1979). *Mixing in inland and coastal waters*. New York, USA: Academic Press.
18. Koussis, A., & Rodríguez-Mirasol, J. (1998). Hydraulic estimation of dispersion coefficients for stream. *Journal of Hydraulic Engineering ASCE, 124*, 317–320.

19. Taylor, G. I. (1953). Dispersion of soluble matter in solvent flowing slowly through a tube. *Proceedings of the Royal Society of London, Series A, 219*, 186–203.
20. Aldama, A. (1990). *Filtering techniques for turbulent flow simulation*. Heidelberg, Germany: Springer Verlag.
21. Vanoni, V. (1975). Sedimentation Engineering (ed.). *Manuals and reports on engineering practice* (N°54, 22–25 and 582–583). New York: ASCE.

Evaluation of Flow Speed in Urbanized Areas and Flood Hazard Mapping in Flood Risk Prevention Schemes

Arnaud Koch, Kévin Corsiez, Jérôme Defroidmont and Manuel Philippe

1 Introduction

Since 1995, flood prevention schemes[1] are one of the main tools used to manage natural risks in France, first, in order to preserve natural flood expansion zones, and second to reduce the vulnerability of urbanized areas. The elaboration of such schemes requires to intersect on one side the flood risk, which is the representation of a natural phenomenon, for events which have at least a 100-year return period; and on the other side, mapping the properties, which identifies natural zones to preserve, and urbanized areas where prescriptions taking the risk levels into account have to be defined.

This article aims at comparing different hydraulic numerical approaches used for simulation flooding in urbanized areas for 100-year return period events, in order to produce flood hazard mapping.

In such configurations, the flooding is disturbed by the presence of numerous obstacles (walls, fences, buildings, embankments, etc.) and water flows in priority

[1]Plan de Prévention du Risque inondation, in French.

A. Koch (✉)
Quentin Strappazzon, Marc Delbec, Prolog Ingenierie, 3-5 rue de Metz, 75010 Paris, France
e-mail: koch@prolog-ingenierie.fr

K. Corsiez · J. Defroidmont · M. Philippe
Direction Departementale des Territoires et de la Mer du Nord, 62 Bld. de Belfort, CS 90007, 59042 Lille, France
e-mail: kevin.corsiez@nord.gouv.fr

J. Defroidmont
e-mail: jerome.defroidmont@nord.gouv.fr

M. Philippe
e-mail: manuel.philippe@nord.gouv.fr

P. Gourbesville et al. (eds.), *Advances in Hydroinformatics*,
Springer Water, DOI 10.1007/978-981-287-615-7_4

in the main communication axes (streets, roadways), while progressively flooding properties and buildings.

A precise representation of these disturbed flows will allow to have a better characterization of the flood hazard by taking into account the flow speed. This will have two advantages, first, allowing to identify the dangerous zones with high flow speeds, where the urbanization will have to be controlled, and second to give accurate information for crisis management planning.

This case study has been realized for the *Direction Départementale des Territoires et de la Mer du département du Nord (DDTM59)*, a state institution in charge of the elaboration of flood prevention schemes.

This shows that such precise approaches are economically and technically viable and operational, as long as precise topographical data are available at a large scale, which is made possible since a few years by aerial acquisition methods such as LIDAR.

The next sections detail successively: the principle of intersecting the flood hazard and the soil occupation to define prevention objectives, the different methods used to characterize flood hazard and their limits in urbanized areas, and finally the different methods for the evaluation of flow speed and direction, and their impact on the computed flood hazard.

2 The Principle of Intersecting Flood Hazard and Land Cover in an Objective of Risk Prevention

Taking natural risks into account in urban and territory planning is one of the key actions of any risk prevention policy.

Natural risk prevention schemes have been created in France by the "Barnier Law" of 1995. Their goal is to control land use and urban planning. Urban planning documents have to take them into account, and mayors have the responsibility to apply their directives, in order to diminish the vulnerability of the territory and make it more adapted to natural phenomena. These schemes also contribute to improving the knowledge about risks and make people more aware about risks.

These schemes comprise a mapping, dividing the properties into different type zones, called regulatory zoning. They also comprise a set of rules associated to these zones in function of the flood hazard. The regulatory zoning is produced by intersecting a mapping of the flood hazard for a 100-year return period event (computed by crossing the flow speed and flood depth) and a mapping of the land use, which shows two main zones, the Currently Urbanized Areas (CUA) and the Natural and Unbuilt Areas (NUA) also identified as Flood Expansion Zones. This intersection leads to the definition of different zones where different prevention objectives and regulatory rules will apply (Fig. 1).

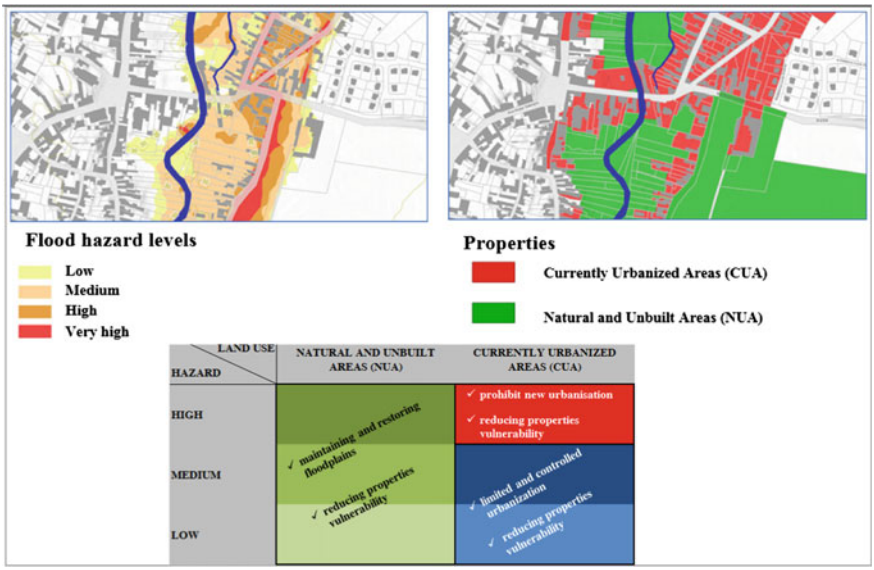

Fig. 1 Principle of the flood hazard and land use intersection, leading to the definition of prevention objectives (example of the rules applied for the DDTM59)

3 Methods of Characterization of the Flood Hazard and Their Limits in Urbanized Areas

3.1 The Definition of the Reference Flood Hazard

The flood hazard used as a reference in the flood prevention schemes has to represent a 100-year return period event at the least.

Different methods can be applied to define this flood hazard:

- *The historical approach*. Consisting of the delimitation of limits of floods occurred in the recent or distant past, as long as this is at least a 100 return period event, and as long as flood testimonies and traces are sufficient to retrace a flood envelope;
- *The hydro-geomorphological approach*. Consisting of the analysis of the floodplain forms, in order to identify the different morphological features of the floodplain (river bed, floodplain, etc.);
- *The hydraulic modelling*. Used to simulate the propagation of flood waves.

The flood hazard is then usually defined by different classes (low, medium, high, etc.), computed in function of the flood depth or by a combination of various variables (depth, speed, flood duration) (Fig. 2).

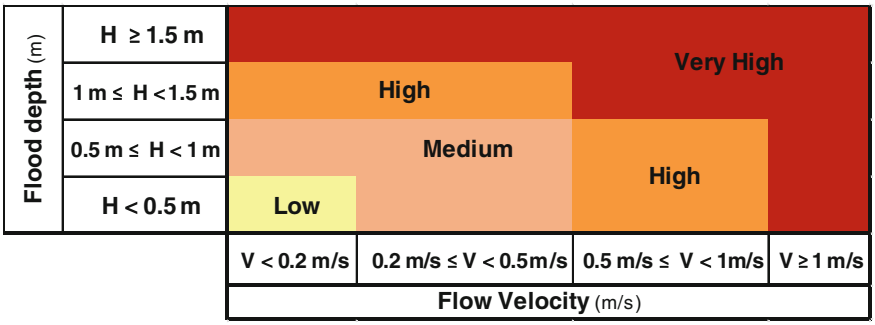

Fig. 2 Example of the definition of classes of flood hazard based on flood depth and speed

3.2 *The Specificities of Urbanized Areas*

Flood hazard characterization in urbanized areas is specific for multiple reasons:

- *In terms of prevention*. These places concentrate economical and social values, and accordingly this is where people need to have a better understanding of the dangers, and work out a better prevention and vulnerability reduction policy;
- *In terms of town and urban planning and development*. These sectors also concentrate numerous projects of urban extension, adaptation or renewal. It is crucial to take risks levels into account when designing these projects;
- *In terms of crisis management*. When a flood occurs, it will be crucial first to reorganize the town in order to cut the flooded roads and avoid a paralysis of the town, and second to rescue disaster victims. The identification of roads flooded with high speed flows, potentially impracticable by rescue vehicles, allows the planning of a more efficient crisis management plan;
- *In terms of method*. It is a challenge to accurately reproduce the specific urban configurations, with main axes concentrating the flow and numerous obstacles diverting it, in order to produce in the end a reliable mapping of the flood hazard.

3.3 *Limits of the Historical Approach*

The historical approach is essential in a flood prevention scheme. It allows to retrieve in archives flood testimonies, illustrations, photographs and eventually mappings of past events.

This preliminary step usually allows to initiate contact with local elected officials and work on culture and risk awareness. In the best case, when an event has been particularly well documented, either because there has been a considerable extent, or because it is still recent, flood marks will have been measured and marked. The altitudes or depths available on these markers can be used to reconstruct a water long section and a flood envelope by crossing with altimetry data (Fig. 3).

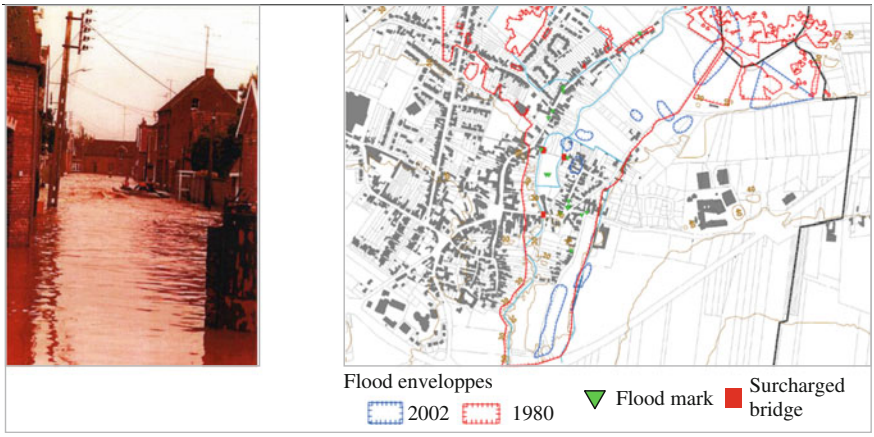

Fig. 3 From historical information to the mapping of historical floodable areas

For the mapping of the reference flood hazard in a flood prevention scheme, the limits of the historical approach are well known. They are mainly related to the heterogeneity of the evidences and the information density which is not the same everywhere. It is often difficult to reconstruct a continuous flood limit across the study area. The information density is insufficient to account for variations in flow within urbanized areas.

3.4 Limits of the Hydro-geomorphological Approach

The hydro-geomorphological approach is often used in addition to the historical approach. By combining historical information, the geological map, the analysis of landforms, etc., it is possible to reconstruct a hold of the envelope major floods, and by crossing this envelope with a Digital Terrain Model, to produce a mapping of the water depths (Fig. 4).

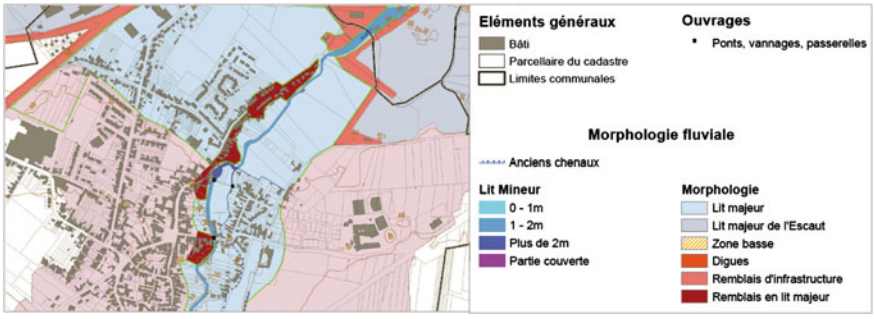

Fig. 4 The hydro-geomorphological map

The hydro-geomorphological approach for flood hazard mapping is widely used in France as part of the development of flood risk prevention schemes. However, the method has many known limits on areas substantially altered because of the artificial streams, loss of natural boundaries between different river beds and urbanization.

Furthermore, this approach does not provide an estimate of flow velocity.

3.5 Limits of Classical Hydraulic Approach

Hydraulic modelling is also regularly used to produce a mapping of the flood hazard. In many cases, and up to very recently, the models were restricted to 1D approaches.

In urban areas, a 1D schematization of flows is not adapted to the complexity of the reality. To reproduce this complexity, it would be necessary to build a network of fictitious arms representing the main roads and secondary axes flow, connected to basins representing storage into flooded properties.

Besides the complexity of the development of such a 1D model, this approach is not able to reproduce the dynamics of propagation of water within a district. At best, 1D modelling can allow for a more precise and accurate estimation of submersion heights compared to the other two approaches mentioned above.

4 New Methods for the Evaluation Flow Speed in Urban Areas

1D/2D modelling method provides solutions for modelling floods in urbanized areas. This approach is the most relevant to this day, its flexibility allows first to cover a large study area and second to represent fine flows in areas of complex topography, while controlling the costs and time spent to produce the results.

The riverbed of rivers is represented by a 1D approach, the hydrodynamic calculation taking place on a series of cross sections; the floodplain is represented in 2D, by an adaptive triangular mesh.

4.1 Equations and Numerical Scheme

4.1.1 1D Model

The governing model equations of the 1D model are the Saint-Venant equations [1], dealing with the conservation of mass and momentum. These equations are solved with the Preissmann 4-point scheme [2], the method is implicit.

4.1.2 2D Model

The shallow water equations (SWE), that is, the depth-average version of the Navier-Stokes equations, are used for the mathematical representation of the 2D flow. The SWE assume that the flow is predominantly horizontal and that the variation of the velocity over the vertical coordinate can be neglected, which is an acceptable hypothesis regarding the context of the study.

Turbulence contributions are not currently modelled, its effect being considered to be included in the energy loss due to the bed resistance and modelled via the Mannings n parameter.

The conservative formulation of the SWE is essential in order to preserve the basic fundamental quantities of mass and momentum. This type of formulation allows the representation of flow discontinuities and changes between gradually and rapidly varied flow.

The conservative SWE are discretised using a first-order finite volume explicit scheme. The scheme that is used to solve the SWE is based upon the Gudunov numerical scheme, with the numerical fluxes through the boundaries of the control volumes computed using the standard Roe's approximate Riemann solver [3]. Finite volume methods are generally considered to have a number of advantages in terms of conservativeness, geometric flexibility and conceptual simplicity.

As the scheme is an explicit solution, it does not require iteration to achieve stability within defined tolerances like the 1D scheme. Instead, for each element, the required time step is calculated using the Courant-Friedrichs-Lewy condition in order to achieve stability.

The management of cell wetting and drying, which is essential in the context of flood modelling, is performed using a threshold depth as a criteria to determine whether a cell is wet and the velocity is set to zero if the depth is below the threshold value (by default = 0.001 m). This allows to avoid the formation of artificially high velocities in wetting/drying areas.

The use of an unstructured mesh to represent the 2D zone together with the scheme used allows robust simulation of rapidly varying flows (shock capturing) as well as supercritical and transcritical flows. This flexibility allows to deal with the problems of urban flooding, where the flow is perturbed by numerous obstacles. The references [3, 4] show, at a smaller scale, the validity of using this kind of numerical approaches to deal with the problems encountered.

4.1.3 1D/2D Linking

Banks overtopping is calculated as a flow over a jagged or irregular weir. The flow is calculated by splitting the calculation into determining flows over segments using an integrated form of the weir equation for dry, free and drowned, forward and reverse modes.

These flow and associated matrix coefficients are then summed together subject to stability constraints, to give values over the entire bank [5].

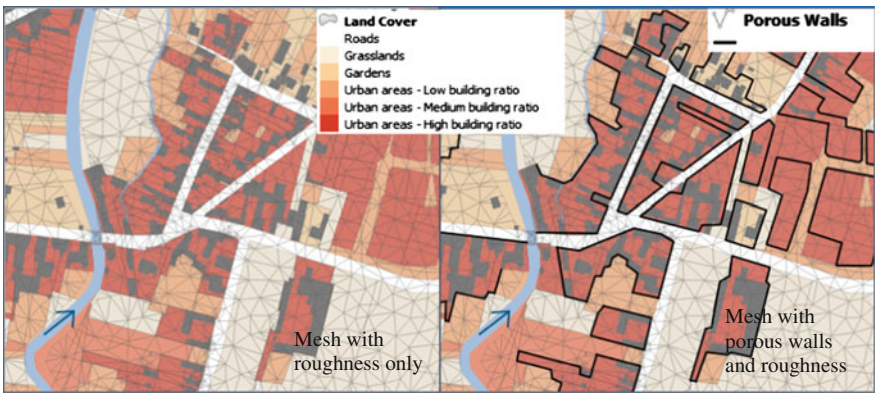

Fig. 5 Examples of computational meshes

4.2 Methodology Implementation

Modelling urbanized areas involves consideration of obstacles, including buildings, in the computational mesh, while allowing flooding of all areas. Two approaches were tested to develop the most appropriate methodology:

Method # 1. Consideration of obstacles in the form of areas of significant roughness. Defining areas of roughness is based on data from land use; the layout of the mesh calculation follows the boundaries of these areas.
Method # 2. The mesh is designed to take the roughness into account, as the previous method, and also integrates the obstacles related to the presence of buildings in the form of walls having a porosity allowing the flood to spread in low points. To limit the number of calculation meshes, these blocking elements are applied to property boundaries instead of building limits (Fig. 5).

4.3 Results

This paragraph presents the differences between the results produced by the two approaches. A baseline without any element of age representing the buildings is also presented to show the need to take into account in all cases obstacles, following one of the methods described (Fig. 6).

The illustration above shows the maximum extent of flooding, the maximum water depth and the velocity vectors at the peak of the flood. It is clear that the integration of obstacles in the modelling brings significant differences. Thus, in the case # 0, not incorporating any obstacle, the flow follows primarily the topography and is not impacted by the buildings.

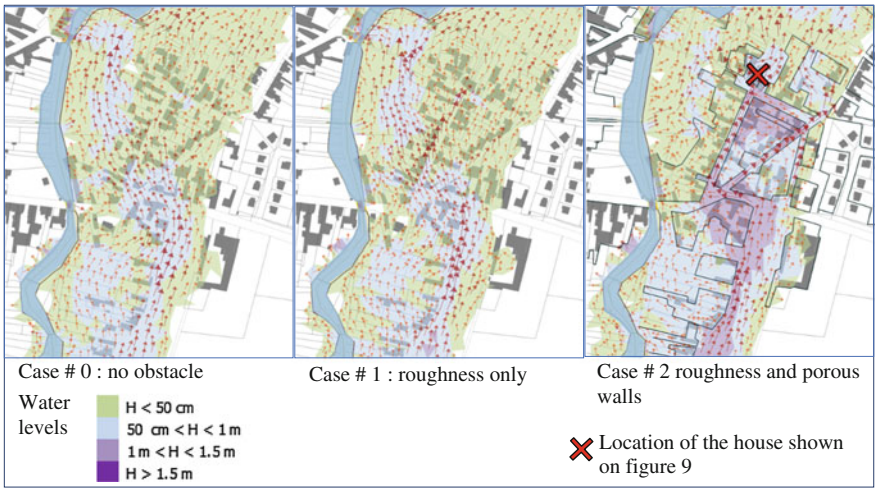

Fig. 6 Comparison of the results

Case # 1, taking into account the obstacles only in the form of a high roughness already shows a deflection of flows via the main axes formed by the two streets in "V" shape on the right bank of the river, even if a major part of the flow is still following the topography and passing through the densely built area.

Case # 2, taking into account the porous borders (shown in black) shows that the flow is focused in the streets, however, allowing a flood of land located behind the buildings. In terms of overall impact, this approach leads to increased levels of submersion in flooded streets and upstream, and an increase in flow velocity.

The choice of approach has a direct impact on the flood hazard which is produced by acting on both the flow speed and the water depths.

The following illustration shows the flood hazard calculated by intersecting the depth and the flow speed, based on the grid defined in Fig. 2. We note that the different approaches modify the contours of the different classes of hazard, and therefore impact the recommendations and obligations arising from the procedure in terms of urban planning.

4.4 Method Validation

The following photographs show flooding in the study area in the 1980s. The event recorded was slightly less than a 100 return period event. On the left can be recognized the two "V" shape streets shown on the map views (the view is inverted relative to the map). The high flow rates are displayed on the press clipping, detectable by the presence of waves, especially visible in the lower part of the photograph. This shows that the model reproduces the observed flooding, with high

speed through the streets, and flooding in calm waters in the plot's back areas. In the photograph on the right, one can see at the bottom of the image a flooded house (marked by a cross) just below the window sill. A field visit showed that it corresponded to a water level of about 80 cm. In Fig. 7, only the scenario with porous barriers can restore water levels of the same order of magnitude (the map shows depth around 1 m, for a 100 return period event, when the other methods show depths under 50 cm, less than the recorded event) (Fig. 8).

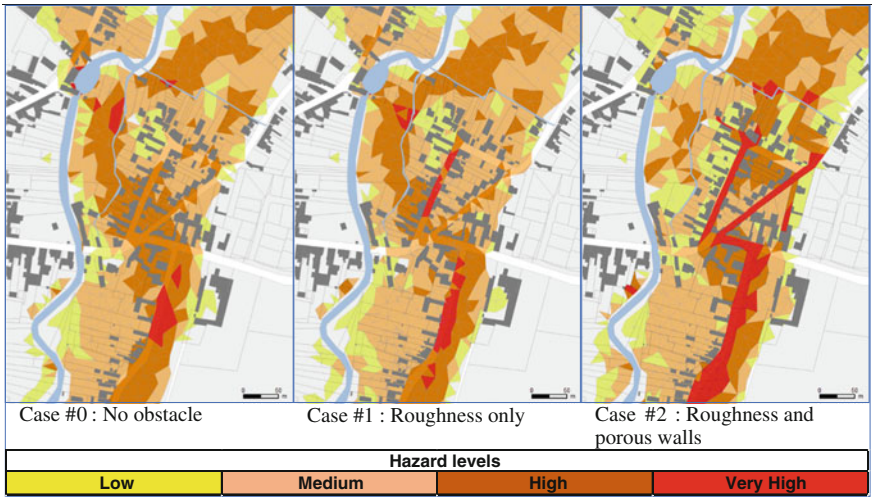

Fig. 7 Flood hazard resulting from the different approaches

Fig. 8 Press clipping: photographs of a flood occured in the study area

5 Conclusion

The accurate evaluation of the flood hazard in an urban environment is an important challenge in terms of risk prevention, on the one hand to better identify the possible high-speed danger zones that could endanger human lives during events of high magnitude, and second to be able to define the most appropriate rules taking the risk into account in urban planning.

Two-dimensional modelling has always been the most suitable to represent complex floodings that can occur in urban areas, the assumptions related to 1D approaches being often inadequate.

This paper compares different methods of representation of flows in a district, taking into account, in particular, the blocking effects associated with different urban obstacles and built plots. The results show that this new accurate approach leads to significant differences from previous approaches, and better represents the reality of these disturbed and complex flows. The latter approach taking into account the buildings' blockage has been used in the context of the development of hazards maps on some flood prevention schemes underway in northern France.

For a long time, the main obstacles to the adoption of these approaches were the technical difficulties to implement them, especially for the generation of the computational mesh, as well as computation times unsuited to economic constraints of technical studies.

The evolution of computer hardware and modelling tools can make viable the adoption of these accurate technics to produce flood hazard maps, while maintaining realistic computation time, especially by exploiting the multiprocessor architectures and GPU computers calculations. The 1D/2D coupled model presented in this paper covers more than 100 km of waterways and ten urbanized areas, for a calculation time of about 4 days for a 100 return period event.

However, it is clear that this approach requires dense and accurate topographical data. The development of large-scale surveys such as LIDAR today allows to generalize this approach to any territorial subject to the risk.

Acknowledgments The Rivers /Risk section at Prolog Ingénierie particularly wishes to thank the "Security Risks and Crisis" service at DDTM 59 for its support and confidence throughout these studies.

References

1. de Sain-Venant, B., Yen, B.C. (1973). Open channel flow equations revisited. *Journal of the Engineering Mechanics Division ASCE, 99*, No EM5.
2. Preissmann, A. (1961). *Propagation des intumescences dans les canaux et rivieres*. Presented at the 1st Congress of the French Association for Computation, Grenoble, France.
3. Alcrudo, F., Mulet-Marti, J. (2005). Urban inundation models based upon the Shallow Water equations. Numerical and practical issues Marrakesh July 2005. In F. Benkhaldoun, D. Ouazar,

& S. Raghay (Eds.), *Proceedings of Finite Volumes for Complex Applications IV. Problems and Perspectives* (pp 1–12). Paris: Hermes Science Publishing.
4. Dottori, F., Todini, E. (2012). *Testing a simple 2D hydraulic model in an urban flood experiment, Hydrological Processes*. Published on-line doi:10.1002/hyp.9370.
5. Evans, E.P., von Lany, P.H. (1983): A mathematical model of overbank spilling and urban flooding. Published in *Hydraulic Aspects of Floods and Flood Control*, London, UK.

Deterministic Hydrological Model for Flood Risk Assessment of Mexico City

Rafael B. Vargas and Philippe Gourbesville

1 Introduction

Every year, Mexico City is affected by severe flooding events, which are affecting deeply the urban environment and the 20 million inhabitants. This situation is becoming more and more serious and represents a major risk for the population. The actual situation is the result of a complex process that combines hydrological characteristics and urban development.

Mexico City is located in the Southern part of the Basin of Mexico, an extensive high mountain valley at approximately 2,200 m above sea level and surrounded by mountains reaching over 5,000 m above sea level. This valley is commonly referred to as the Valley of Mexico [15]. The Mexico City catchment was originally an endoreic basin and the only way of runoff evacuation were through evaporation. After a series of large floods, which occurred in 1604, it was decided to build an artificial outlet for the basin, and a channel was constructed as well as a tunnel of almost 7 km of length [8]. Before the works were finished, several flood events occurred, especially between 1629–1635, when an estimated total of 30,000 people died and a similar number left the City. After this event, the idea to relocate the city was explored [7]. In 1900, works were concluded for a channel that would drain the Texcoco Lake out of the basin, this channel is called Gran Canal, or Great Channel. This system worked well until the soil subsidence affected the slope of the channel and decreased its efficiency. Until the year 2002, the slope of the Great Channel

R.B. Vargas · P. Gourbesville (✉)
Polytech Nice Sophia, Nice Sophia Antipolis University, URE 005 Innovative City, 930 Route de Colles, 06903 Sophia Antipolis, France
e-mail: philippe.gourbesville@unice.fr; gourbesv@unice.fr

R.B. Vargas
e-mail: gordonbotija@gmail.com

P. Gourbesville et al. (eds.), *Advances in Hydroinformatics*,
Springer Water, DOI 10.1007/978-981-287-615-7_5

allowed the water to flow by gravity, however, after 2002, pumps are being used to force the water out of the basin [13]. However, the discharge capacity of the great channel decreased from 90 to 12 m^3/s in 30 years. This decrease has been ascribed to the sinking of more than 4 m, which in average the City suffered from 1975 to 2007. In a study carried out by Carrillo, the cause of this subsidence was found to be the extraction of groundwater through wells [4]. Because the sinking is uneven in the City, there are problems with the drainage system to work correctly due to the decrease and loss of slope. Furthermore, in the subsoil of Mexico City, alluvial materials are present, comprised especially of gravels and sands. This materials form the aquifer exploited for the supply of the City's inhabitants. The aquifer is covered by clay materials working as an aquitard with very low permeability of around 10^{-7} –10^{-9} m/s. All these factors have contributed to frequent flooding during the rainy season between June and September, when most of the 700 mm of rainfall concentrate [12].

From 1930 to 1960 thousands of kilometers of drainage ducts were constructed as well as a system of dams to regulate the discharges in the west of the City. In addition, several pumping stations were installed with a cumulative capacity of more than 100 m^3/s and the rivers crossing the City were enclosed in ducts to avoid flooding. For example, the Mixcoac, Piedad and Magdalena rivers, which drain the catchment in a direction predominantly from West to East, are first intercepted by the drain system by gravity and after by the great channel through the use of pumps. According to Dominguez [7], the problem of flood control in the Mexico City valley can generally be divided into local and global processes. The first are caused by rain events, which in Mexico City are typically heavy and of short duration, and the second are related to more persistent and generalized rain events, which fortunately occur less frequently, but require a solution urgently due to the high potential to cause damages. Moreover, the main factors found to cause flooding in Mexico City are:

- Development of sewer system slower than the development of the city;
- Quick growth of population causing increasing imperviousness;
- Climate change that induce shift of rainy season;
- Inadequate river regulation;
- City expansion in high-risk areas.

In such context, it is essential for the local authorities to develop an assessment of the flood risks and then to define a global strategy for the City. However and as already mention, the hydrological monitoring within the Mexico basin is limited especially regarding the runoff processes. The knowledge on the hydraulic structures implemented for collecting the runoff is also limited and no flood maps are available for the City. The challenge is then to evaluate the flood processes with an appropriate model able to produce a first assessment for every area of the Mexico basin.

2 Proposed Methodology

In most of the cases, urban flooding problems are analyzed through data collection on rainfall events and runoff on surface and in drainage networks. With such available data, the classical approach combines a hydrological model with a hydraulic model—most of the time 1D—able to simulate the runoff and propagation processes. In the case of the Mexico basin, the data are not available and the approach has to be reviewed by implementing an alternative concept.

In order to overcome the difficulties and to produce a tool able to support operational management, a potential alternative approach is to implement a deterministic distributed hydrological model. This type of model has the reputation to request a tremendous quantity of data in order to produce simulations and results. However, due to the physically based approach, most the variables could be reasonability estimated through physically meaningful hypothesis. In addition, several authors have underlined the major importance of an accurate description, within the model; of the topography properly represented through a DEM [10]. The introduction of additional variables allows improving gradually the efficiency of the model and the quality of the simulations.

For the Mexico City Valley, the suggested methodology is based on the implementation of deterministic hydrological model with the Mike She modeling system [6]. The analysis will evaluate the discharges in several rivers of the City and compare the estimated values with gauged data to see whether the model can represent the full hydrological process with sufficient accuracy for the operational management of the catchment.

MIKE SHE is an integrated fully distributed physically based hydrological modeling system developed by DHI [6]. It simulates water flow in the entire land based phase of the hydrological cycle from rainfall to river flow, via various flow processes such as overland flow, infiltration into soils, evapotranspiration from vegetation and ground water flow. For the Mexico City basin, the model is based only on the most relevant variables, which may produce results with a reasonable accuracy. In order to define the most efficient approach, three models were considered with different levels of complexity:

1. A first basic hydrological model has been developed with a minimal data set. To construct the basic model of the Mexico City catchment, the following components were included:
    - a Digital Elevation Model (DEM) with a resolution of 5 m provided by the Institute of Statistics and Geography of Mexico (INEGI);
    - the daily rainfall values from the measuring stations available and for the duration of the simulation period;
    - and a river network composed with cross sections extracted from the DEM.

2. A second model for the Hondo river sub-catchment in Mexico City with all of the above components and also distributed roughness values used for runoff according to vegetation types.
3. Finally, a third model for the Hondo river sub-catchment including all of the above components, plus the land use component and the unsaturated zone component.

The accuracy of the three models to represent the hydrological processes is assessed by quantification and evaluation of the root mean squared error RMSE and of the Nash Sutcliffe coefficient E, represented in formulas (1) and (2) respectively:

$$RMSE = \sqrt{\frac{\sum_{i=1}^{n}\left(X_{obs,i} - X_{model,i}\right)^2}{n}}; \tag{1}$$

$$E = 1 - \frac{\sum_{i=1}^{n}\left(X_{obs,i} - X_{model,i}\right)^2}{\sum_{i=1}^{n}\left(X_{obs,i} - \bar{X}_{obs}\right)^2}\,[2] \tag{2}$$

where X_{obs} is observed values and X_{model} is modeled values at time/place *i*.

In addition, the evaluation of the model is also carried out by visual inspection of the hydrographs. The calibration of the model is conducted by a trial and error procedure in which the influence of the different parameters is analyzed after several simulations and parameters were set differently before the following simulation until results are sufficiently close to observed data. The performance of the model is considered acceptable at $R2 > 0.7$ and $RMSE > 2$.

3 Application to Mexico Basin

The analysis is focused on the local flood problems in the high surrounding areas of the West of the City. In this part of the basin, the rivers mentioned before still flow naturally. At the same time, urban growth has caused an increase in runoff and discharges to the rivers. The analysis concerns also the low areas where the discharges accumulate naturally, especially when the drainage network is working at maximum capacity. The methodology proposed was applied to the three model cases described. In this section, the characteristics of the catchment are described, the available data are listed, the development of each model is explained in detail and the results of the simulations are presented.

3.1 Description of Catchment

The study area has a size of 2800 km^2 and has a population of approximately 20 million inhabitants. It includes the West part of the metropolitan area of Mexico City. The rivers modeled in are the San Javier, Tlalnepantla, Hondo, Tacubaya, Mixcoac, Piedad and Magdalena, and the channels included are the Great Channel, the National canal, and the Remedios. Only the rivers in the West of the City were modeled because these supply the largest part of the discharge especially the Magdalena, Mixcoac, Hondo and Tacubaya. The Fig. 1 shows the Mexico City catchment, and the hydro meteorological network.

3.2 Available Data

The following data are available:

- a DEM with 5 m resolution provided by the Institute of Statistics and Geography;
- the river and drainage network as shape files;
- cross sections extracted from the DEM within the GIS environment and geometry of open channel sections;
- daily rainfall values for 44 stations and their location;
- daily evaporation values for the 5 gauging stations (Aquiles Serdan, Molinito, Magdalena, San Bartolome, Huixquilucan);
- land use polygons (shape files) for agricultural land, forests, grassland and urban area;

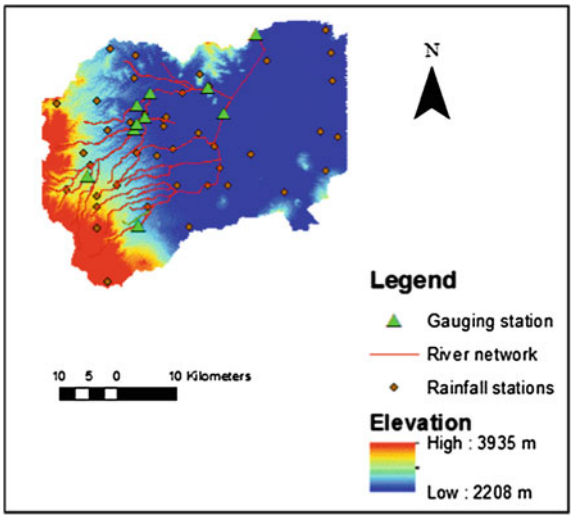

Fig. 1 The Mexico City catchment and the hydro meteorological network

- polygons (shape files) for seven types of soils;
- observed average daily discharge for the 11 hydrometric stations (San Bartolo, Molinito, Molino blanco, Conde, San Juan, Santa Teresa, Arboledas, Etchegaray, Puente de Vigas, Calacoaya, Gran canal);
- roughness coefficients (Strickler coefficients) associated to different vegetation covers.

3.3 Development of the Models

A basic model for the Mexico City catchment was created. The components of the model are the following:

- Model domain: According to the Water Commission of Mexico (CONAGUA), there are 730 hydrologic catchments in Mexico. The analysis is focused on the catchment RH26 dp, which contains Mexico City.
- Topography: The digital elevation model has a resolution of 5 m. To speed up the simulations, a 90 m resolution version of the DEM associated with a projection in UTM zone 14 N was generated and used in the topography component of MIKE SHE. It should be noted that the geometry of the catchment is the most important factor in a model, and a good quality DEM can assure a good representation of the hydrological processes.
- Precipitation and evaporation rates: Historical observed precipitation and evaporation data from 44 stations in the Valley of Mexico were obtained from the surface waters division of the National Water Commission (CONAGUA). In order to distribute the rainfall over the catchment the Thiessen approach has been used. The Thiessen polygons were generated in GIS from the point shape file of the stations. The polygons were added to MIKE SHE model in order to define the precipitation spatial distribution. Several studies suggest a minimum number of rainfall stations per square kilometer. For example, Segond et al. [17] recommends that for largely rural catchments a network of 16 rain gauges is acceptable for 1000 km^2, and between 4 and 7 stations for 80–280 km^2. Figure 2 shows the rainfall distribution for the 44 stations in the Mexico City climatological network. The gauging station density is considered acceptable for the use of the Thiessen polygon distribution method, which consists of drawing a polygon around each gauge with the boundaries at a distance halfway between gauge pairs [9].
- River network: The hydrographic river network consists of a linear shape file system, including lines central to water bodies, and also contain important channels that give continuity to the flow of natural streams. A network file was completed in MIKE 11 and 27 branches were included. All branches were defined as regular branches.
- Cross sections: The cross sections were evaluated using the River Bathymetry Toolkit and exported to use as raw data in the cross section editor of MIKE 11.

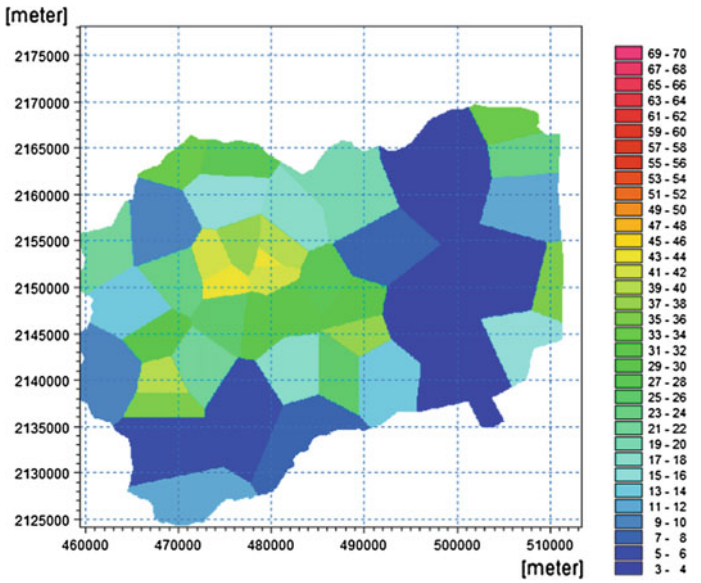

Fig. 2 Thiessen polygon codes distribution for 44 rainfall stations in the Mexico City catchment

One cross section was created for every 1000 m approximately. The open channel cross-section geometry were obtained and applied to the corresponding lengths of the river network.

- Daily average observed discharge data were obtained for 11 stations for the year of 1981 and used to create time series and compared with simulated discharges. At the initial stage, discharge boundary conditions were set to 0.1 m^3/s in all river upstream ends to avoid the initial drying of the bed. Available data of discharge were used to compare with simulated discharges. The water level boundary was set to a constant value in the outlet of the Great Channel based on the bed level.
- A uniform Strickler roughness value of 20 was used for the overland component of MIKE SHE, and a uniform value of 30 for all river beds, defined in the hydrodynamic module of MIKE 11.

For the second model covering the Hondo catchment, a model of Hondo sub-catchment was constructed including river network, rainfall, topography, and a map of distribution of the Strickler number based on vegetation data. The Fig. 3 shows the location of the Hondo sub-catchment in the catchment of Mexico City and the hydro meteorological network. The model area is 173 km^2.

Furthermore, in the second model, the Strickler coefficients have been distributed over the Hondo river basin according to the vegetation types. The overall distribution is presented on the Fig. 4.

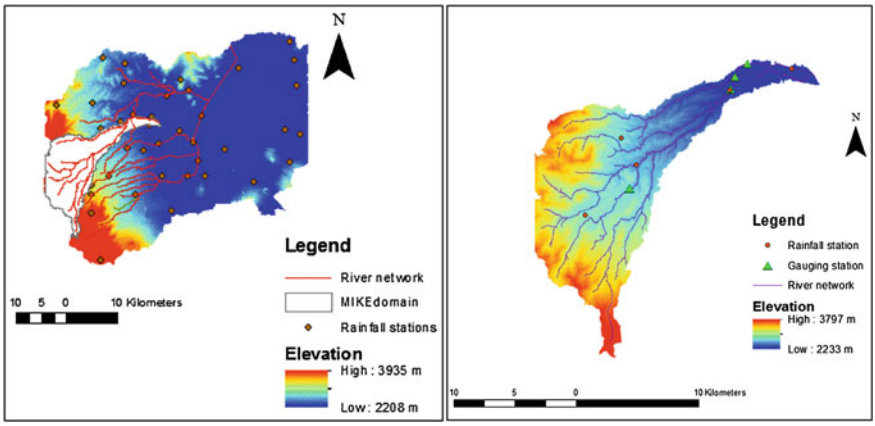

Fig. 3 Location of Hondo sub-catchment in the Mexico City catchment and River Hondo sub-catchment with hydro meteorological monitoring network

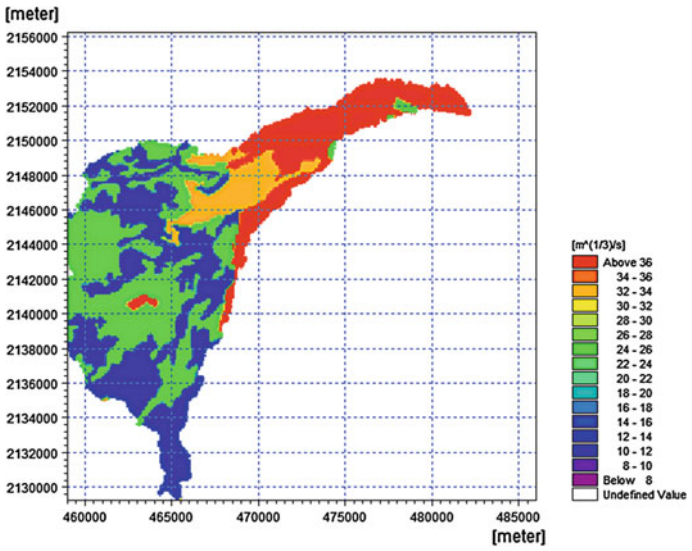

Fig. 4 Distribution of Strickler coefficient in Hondo catchment

In addition, five rainfall stations were used for the Hondo model, and Thiessen polygons were created in GIS and added to MIKE SHE. The used rainfall distribution is shown on Fig. 5. The model was applied for the same period and the resulting hydrograph was compared to observed values in Molino Blanco station.

For the third model covering the Hondo catchment, the unsaturated zone (UZ), evaporation and land use components of MIKE SHE were included in addition to

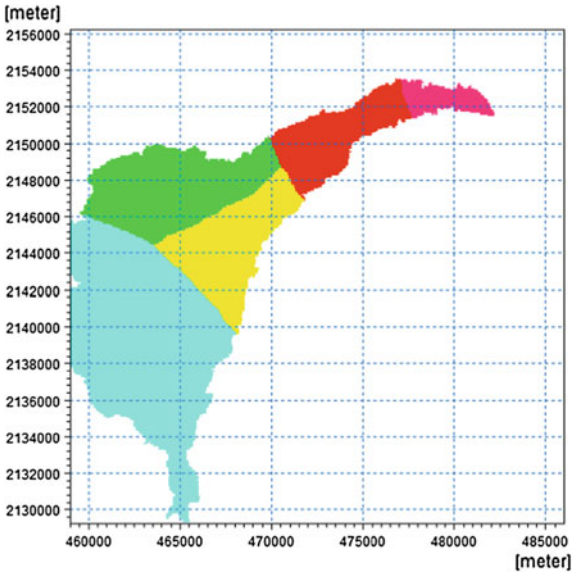

Fig. 5 Thiessen polygon rainfall distribution of 5 stations in Hondo River sub-catchment

the same Strickler number distribution of model 2. The used rainfall distribution for model 3 is the same as in model 2.

The land use information was extracted from digital maps and added to the land use module of the model.

The 2-layer set-up was chosen in MIKE SHE for the unsaturated zone, and 6 types of soils were included in this set-up. The soil type polygons were obtained from INEGI.

Other values necessary for the MIKE SHE modules of land use and unsaturated zone, such as permeability of soils, leaf area index of vegetation, root depth, Strickler coefficients, water content and hydraulic conductivity of soils, were found in different publications, documents and articles. Figure 6 shows the soil types boundaries.

For all models, a period of 1 year was chosen (1981) when data were available for all rainfall and gauging stations. The simulation time step was 10 s in MIKE 11 (hydraulic component of Mike She). The time step control values used, necessary to control the simulation in MIKE SHE, are listed below (Table 1).

The setup of the various models was successful and a series of simulations was done to calibrate the model. The purpose of calibration is to confirm that the model is able to reproduce the hydrological processes with reasonable accuracy. However, it is a complex procedure due to the large amount of model parameters involved, and the computational requirements for simulations. Therefore, calibration is considered one of the most time consuming phases when building a hydrological model [18].

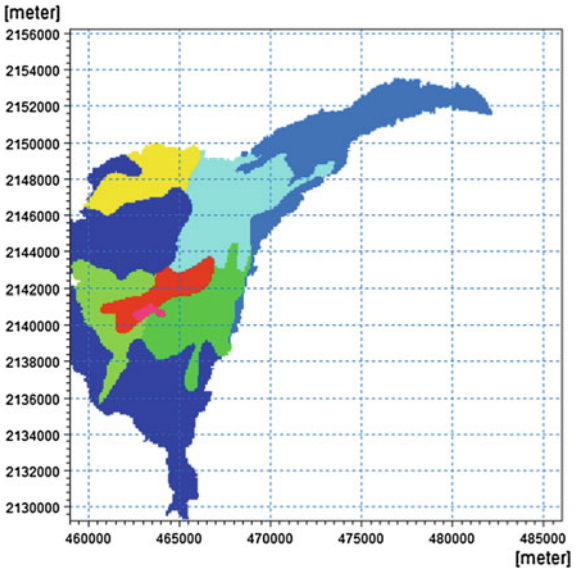

Fig. 6 Boundaries of the 6 different types of soils used in the River Hondo set-up

Table 1 Values for the control of time steps during the MIKE SHE simulation

Initial time step	6 h
Max allowed overland time step	12 h
Max allowed UZ time step	24 h
Increment of reduced time step length	0.05
Max precipitation depth per time step	20 mm
Max infiltration amount per time step	10 mm
Input precipitation rate requiring own time step	1 mm/hr

4 Results

The predictive capability of the model set-up was evaluated by comparing the resulting hydrographs against independent observed data. The results of the three types of models described in the methodology are presented in the following paragraphs.

Model 1: The model of Mexico City catchment includes topography, rainfall and river network. Figures 7 and 8 show the resulting hydrographs from the simulation of the Mexico City catchment model compared with observed values for Molino Blanco stations in river Hondo and St. Teresa station in river Magdalena respectively. The resulting RMSE and E values can be seen in Table 2. The E coefficients the St. Teresa station did not achieve the mark of 0.7 but achieved the value of 2 for RMSE. Both coefficients achieved the mark in Molino Blanco station.

In Molino Blanco station, the resulting hydrograph is remarkably close to the observed data, however, there are important discrepancies in the months of June,

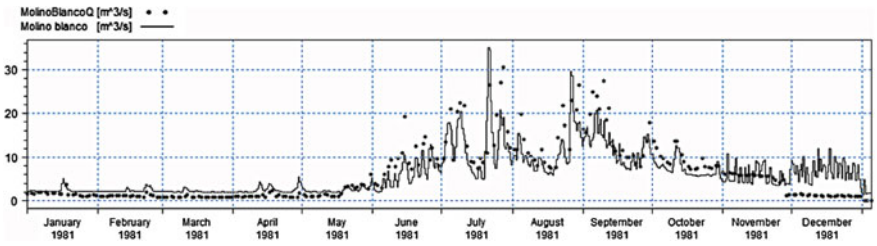

Fig. 7 Molino Blanco station simulated discharge against observed discharge for the Mexico City catchment model

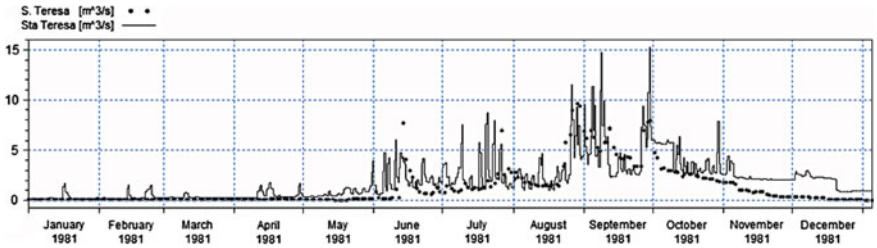

Fig. 8 St. Teresa station simulated discharge against observed discharge for the Mexico City catchment model

Table 2 Statistical coefficients of the MIKE SHE model of Mexico City catchment

	St. Teresa	Molino Blanco
RMSE	2	3.34
E	−0.03	0.73

July, August and September. Also during December, the model did not stabilize. This may be caused by different factors and all the variables in the model should be carefully analyzed to determine their influence on the result.

In St. Teresa station, the results follow successfully the main processes and trends but the model doesn't succeed to present properly the intensity of several flood events appearing during September and October in the Magdalena River. The representation of the processes in this model may be too coarse, and do not integrate enough variables for representing the hydrological behavior of the catchment.

Model 2: For the model of the Hondo river sub-catchment, the Strickler coefficients have been distributed over the basin according to the vegetation types.

The model applied for the same period and the resulting hydrograph was compared to observed values in Molino Blanco station. The hydrograph can be seen in Fig. 9. The model produced a value of 0.71 for the E coefficient and 3.48 for the RMSE coefficient.

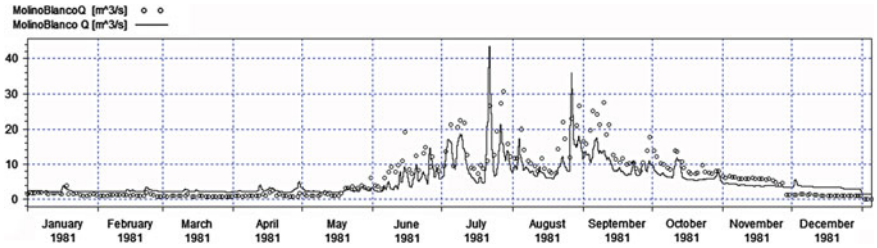

Fig. 9 Molino Blanco simulated discharge against observed discharge Hondo sub-catchment model including the effects of vegetation in Strickler coefficient

The results of model 2 followed relatively well the main trends of the observed data, and it stabilized well in the month of December. However, this model has a consistent difference between the gauged data, especially from July to September. This could be caused by errors when implementing the Strickler coefficients related to vegetation cover.

Model 3: The third model for the river Hondo sub-catchment includes the land use component and the unsaturated zone component. The model was simulated and result were obtained of RMSE = 3.05 and E = 0.77. The Fig. 10 represents simulated discharges in Molino Blanco gauging station compared to observed values.

The results of model 3 follow effectively the main trends of the observed data. The representation of the processes includes the effects of soil types and land use. These variables provide a benefit for representing the hydrological behavior of the catchment compared to the first two models, however, an important difference is located in July and August, when an excess of simulated discharge takes place.

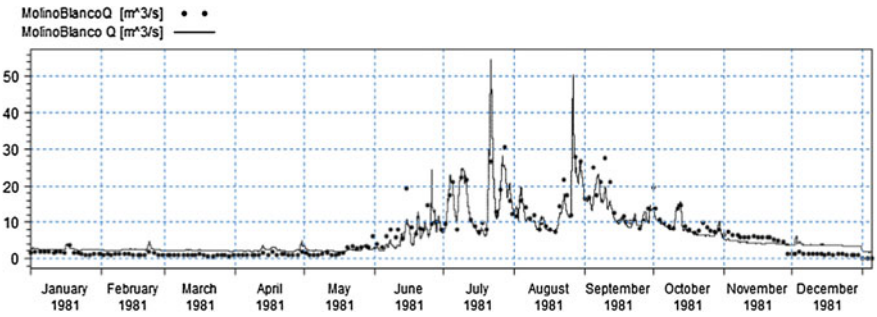

Fig. 10 Molino Blanco station simulated discharge against observed discharge in Hondo River catchment model with unsaturated zone and land use components

Table 3 Statistical coefficients of the three models of study

	Molino Blanco	
Model 1	RMSE	3.34
	E	0.73
Model 2	RMSE	3.48
	E	0.71
Model 3	RMSE	3.05
	E	0.77

5 Conclusions

The statistical coefficient values in Molino Blanco station for the three models are listed in Table 3. As the St. Teresa station was not assessed in models 2 and 3, its results are not included in this table.

Three deterministic hydrological models were constructed and used with the data available from Mexican institutions. Results have been compared with discharges recorded at gauging stations. This was done with the aim of testing the premise that a deterministic hydrological model could be an efficient tool for representing the hydrological processes in a catchment when data and resources are limited. It can be inferred from Table 3 that the coefficients for all models met the goals of accuracy in Molino Blanco station.

Model 1 has results reasonably close to the observed data; however, the discrepancies in the months of June, July, August and September reduce the accuracy of the model. Furthermore, in December, the model did not stabilize. If the cause for this loss of stability could be found and fixed, the result would improve considerably for this model.

Model 2 obeyed relatively well the main trends of the observed data. In addition, it stabilized during the last months of simulation, as opposed to model 1. However, the results present a regular difference between the gauged data, especially from July to September. This could be caused by errors when implementing the Strickler coefficients related to vegetation cover. Therefore, an analysis of the Strickler values applied is recommended to improve the results of this model.

Model 3 produced results that follow effectively the main trends of the observed data. The unsaturated zone and land use components provide a benefit when representing the hydrological behavior of the catchment. However, an important difference is observed in July and August, when an excess of simulated discharge takes place. The different variables incorporated that conform the unsaturated zone and land use sections should be analyzed to try to find the causes of this difference.

Nevertheless, model 3 provided the best result when representing the hydrological processes of the Hondo River catchment. Therefore, model 3 is recommended for hydrological studies of the Mexico City catchment and its sub-catchments; at least until the issues associated to models 1 and 2 can be resolved.

The importance of the deterministic approach has been demonstrated for the Mexico City basin. The developed tool may allow the managing authorities to establish a first diagnostic on the runoff processes that may generate flooding events. The distributed model allows generating, for a specific rainfall event associated to a given return period, the hydrograph to consider for protection design and population awareness. The following step will have to concentrate on the risk evaluation and the damages assessment.

Acknowledgments The authors would like to thank the Surface Water department of the National Water Commission of Mexico CONAGUA and the Institute of Geography and Statistics INEGI for the data provided for this study.

References

1. Baró-Suárez, J., Díaz-Delgado, C., & Esteller-Alberich, M. (2007). Flood damage curves in residential and agricultural areas of Mexico. Part II: Case study in Lerma River catchment'. *Ingeniería hidráulica en México, XXII*(3), 71–85.
2. Baró-Suárez, J., Díaz-Delgado, C., Esteller-Alberich, M., & Calderón, G. (2007). Flood damage curves in residential and agricultural areas of Mexico. Part I: Methodology. *Ingeniería hidráulica en México, XXII*(1), 91–102.
3. Boyle, S., Tsanis, I., & Kanaroglou, P. (1998). Developing geographic information systems for land use impact assessment in flooding conditions. *Journal of Water Resource Planning and Management, 124*(2), 89–98.
4. Carrillo, N. (1969). The sinking of Mexico City and Proyect Texcoco. VII International Congress of Soil Mechanics, SHCP edn.
5. Conagua. (2012). *Water Atlas of Mexico*. México: Semarnat.
6. DHI. http://www.crwr.utexas.edu/gis/gishyd98/dhi/mikeshe/Mshemain.htm.
7. Dominguez, R. (2000). Floodings in Mexico city, issues and proposed solutions. Revista digital universitaria, UNAM. Vol. 1, No. 20. ISSN 1607-6079, 30 September 2000.
8. Dutta, D., Herath, S., & Musiake, K. (2003). A mathematical model for flood loss estimation. *Journal of Hydrology, 277*(1–2), 24–49.
9. Goovaerts, P. (2000). Geostatistical approaches for incorporating elevation into spatial interolation of rainfall. *Journal of Hydrology, 228,* 110–130.
10. Guinot, V., & Gourbesville, P. (2003). Calibration of physically based models: back to basics? *Journal of Hydroinformatics, 5*, 233–244.
11. Jonkman, S. N., Bočkarjovab, M., Kokc, M., & Bernardinid, P. (2008). Integrated hydrodynamic and economic modelling of flood damage in the Netherlands. *Ecological Economics, 66*, 77–90.
12. Lesser, J. M., & Cortes, M. A. (1998). The sinking of the terrain of Mexico City and its implications on the drainage system. Ingeniería hidráulica en México, Septemper–December, México.
13. Luege, J. L. (2012). Hydrological sustainability program. IV International Legal Colloquium on Water, Conagua, México.
14. Messner, F., Penning-Rowsell, E., Green, C., Meyer, V., Tunstall, S., & van der Veen, A. (2007). Evaluating flood damages: guidance and recommendations on principles and methods.
15. National academy of sciences. (1995). *Mexico City's Water Supply: Improving the Outlook for Sustainability*. Washington, D.C: National Academy Press.

16. Penning-Rowsell, E. C., & Chatterton, J. B. (1977). *The benefits of flood alleviation. A manual of assessment techniques*. London: Belhaven Technical Press.
17. Segond, M. L., Wheater, H., & Onof, C. (2007). The significance of spatial rainfall representation for flood runoff estimation. *Journal of Hydrology, 347*, 243–259.
18. Vazquez, R. F., Feyen, L., Feyen, J., & Refsgard, J. C. (2002). Effect of grid size on effective parameters and model performance of the MIKE SHE code. *Hydrological Processes, 16*(2), 355–372.

Community-Based Flood Vulnerability Index for Urban Flooding: Understanding Social Vulnerabilities and Risks

Mae Brigitt Bernadel L. Villordon and Philippe Gourbesville

1 Introduction

According to the World Risk Report released by the United Nations University Institute for Environment and Human Security, the Philippines is ranked third globally in terms of disaster risk.[1] Typhoon which usually followed by flooding in some areas is one of those disaster risk that is frequency occurring in the Philippines, twenty or more typhoons visits the country every year leaving devastations in many forms. It is a global phenomenon and due to climate change, this will continue. Urban fluvial flooding in particular caused havoc in many aspects in the society particularly to human health, infrastructure and the economy of the country. Moreover, it has become a usual scenario especially in underdeveloped and the developing countries. However, this phenomenon is also occurring in developed countries though less more frequent than those previous countries mentioned. Flooding poses a serious challenge to the economic development and the lives of the people particularly the residents of a rapidly expanding towns and cities in developing countries. Its causes are shifting and their impacts are accelerating against the backdrop of increasing demographics, urbanization trends and climate change. The current and projected levels of flood impacts give urgency to the need to make flood risk management in urban settlement a high priority on the political and policy agenda. It is therefore important to conduct studies related to

[1]United Nations University Institute for Environment and Human Security (UN World Risk Index) [11].

M.B.B.L. Villordon (✉) · P. Gourbesville
Polytech Nice Sophia, Nice Sophia Antipolis, URE 005 Innovative City,
930 Route Des Colles, 06903 Sophia Antipolis, France
e-mail: villmae1@euroaquae.eu

P. Gourbesville
e-mail: gourbes@unice.fr

P. Gourbesville et al. (eds.), *Advances in Hydroinformatics*,
Springer Water, DOI 10.1007/978-981-287-615-7_6

vulnerability and resilience at the community level so issues on health and disaster risks will be addressed appropriately.

Public health risk in urban fluvial flooding are usually been overlooked, undermined and only very little attention is given. In Dumaguete City alone, there was no study similar to this that was conducted. This would therefore hopefully serve as a baseline study. Fecal pollution of water particularly human fecal sources are the most relevant source of human illnesses globally especially during flooding event and rainy season. Exposure and ingestion of fecally-contaminated water and other routes of transmission are responsible for a variety of diseases such as diarrhea, liptospirosis, and bites from dengue mosquitoes which demands special attention. Diarrheal and other waterborne diseases still rank among the leading causes of morbidity worldwide and in the Philippines. According to the World Health Organization, each year diarrhea kills around 760,000 children under the age of five and is the second leading cause of death among that age group. Worldwide, there are nearly 1.7 billion cases of diarrheal disease ever year.[2] In the surveillance report of 2013 by the DOH, a total of 1,174 liptospirosis cases have been reported nationwide from January 1, 2013 to September 17, 2013. This is 78.74 % lower compared to the same period last year (5,522).[3] A total of 117,658 dengue fever cases from January 1 to September 7, 2013 were reported nationwide. This is 5.25 % lower compared to the same period last year's (124,173) cases and mostly coming from regions VI and IV-A.[4] Though the figures of the surveillance report in 2013 were lower than the previous years, yet these recent statistics is still very alarming. Given this high incidences of diarrhea, leptospirosis, and dengue fever cases, it is therefore important to conduct studies that would provide better understanding how each households perceives, relates and employs their attitudes and practices towards personal hygiene and protection, and to environmental sanitation.

According to the 2012 Philippines Disaster Report, a total of 471 natural and human-induced disasters were reported in the Philippines in 2012.[5] 1,615 people were killed, and more than 2.8 million families or 12 million people were affected, and caused over Php 39.9 billion in economic damages. In terms of frequency, flood topped the list with 143 reported incidents, or 30 % of the total number of disaster events monitored in 2012. Given this high-risk status of the Philippines to hazards in general, it is surprising to find that there were very few comprehensive place-specific vulnerability and resilience assessments performed at the local level in the Philippines which accounts on social vulnerability specifically on how the community people respond to these kind of phenomenon and to the impacts of global warming. Such kinds of studies and assessment should be conducted so such gaps will be addressed properly. This study was an exploratory step towards

[2]WHO (World Health Organization) [12].

[3]DOH (Department of Health) [4].

[4]DOH (Department of Health) [5].

[5]CDRC (Citizens' Disaster Response Center): [3].

assessing flood vulnerability and resilience, a rapid assessment of the Knowledge, Attitudes, and Practices (KAP) of the community people towards flood resilience, health, environmental sanitation and including their socio-demographic profile and governance. These are important factors to be assessed in order to established correlations and relationships in understanding social vulnerabilities and its indicators so it can be incorporated in hydroinformatics. Determining flood vulnerability index (FVI) varies from one country to another. There is no single gold standard used worldwide. Measuring vulnerability and resilience is important, it mirrors how well are the people adapting to climate change and its impacts, how are the resilience programs implemented and facilitated by the local government units. Perhaps it is also important to note that gauging vulnerability may have a number of different reasons but understanding the context of people's vulnerability to hazards and why they are vulnerable in the first place, seems to be more useful for making a difference in their lives.

2 Motivation and Objectives

Several studies on disaster risk, flood vulnerability and resilience index have been conducted worldwide. Here is a brief review.

2.1 The Bündnis Entwicklung Hilft (Alliance Development Works) and United Nations University Institute for Environment and Human Security (UNU-EHS)

On behalf of the Bündnis Entwicklung Hilft (Alliance Development Works), the UNU-EHS in Bonn, Germany has developed the WorldRiskIndex in 2011 and calculated the risk values for 173 countries worldwide.[6] The WorldRiskIndex in this report was measured on the basis of four components namely; exposure to natural hazards or a climatic stimulus, susceptibility, coping and adaptive capacities. According to this report, the Philippines ranked 3rd among those highest with a score of 24.32 % on the disaster risk from all the 173 countries surveyed. However, this report has failed to include some of the important component which has theoretical and practical significance due to lack of relevant data. These four sub-categories are, housing situation, social networks, disaster preparedness/early warning and adaptation strategies were not integrated into the overall calculation of the WorldRiskIndex in 2011 which are deemed to be relevant and significant. Thus,

[6]United Nations University Institute for Environment and Human Security (UN World Risk Index) [11].

this research study focuses on these items and among others so we would have a thorough understanding why the community people are vulnerable or resilient in the first place.

2.2 The United Nation Development Programme (UNDP)

In 2004, the United Nation Development Programme (UNDP) also published a Global Report on Reducing Disaster Risk: A Challenge for Development. Countries with low Gross Domestic Product (GDP) per capita, low local density of population and high physical exposure were associated with high levels of risk in floods.[7] Part of the recommendations from this report is to address the gaps in knowledge for disaster risk assessment. A clear understanding of the depth and extent of hazard, vulnerability and disaster loss are primary steps towards a concerted and coordinated global action in disaster risk reduction along with appropriate governance and risk indexing from sub-regional areas which in turned encourages the researcher to consider these components at the local level. It is very important and vital to address these gaps in knowledge for disaster risk and vulnerability assessment. Measuring the KAP of the respondents from preparedness to recovery, and as well as the KAP on the exposures of the microorganisms in focus and would give us a clue how community people perceived in these kinds of phenomenon which are translated into their attitudes and practices before, during or after any catastrophic events such as typhoons and flooding.

2.3 A Flood Vulnerability Index for Coastal Cities and Its Use in Assessing Climate Change Impacts

A FVI for coastal cities was developed by Balica et al. in [1] using the system's components namely, the hydro-climatic component, socio-economic and the politico-administrative components.[8] It has been conducted to nine cities around the world. However, indicators in the socio-economic components such as the detailed description of the households in terms of their educational attainment, housing conditions, social networks, family income and property insurances were not included which are parts of the susceptibility and resilience category. Moreover, the knowledge, attitudes and practices of the households were also not taken into consideration which could also influence the vulnerability of those target population. In this same way, some indicators for the politico-administrative components such as good governance, sustainable community livelihood and among others

[7]UNDP (United Nation Development Programme) [10].

[8]Balica et al. [1].

should have been included. Thus, this study focuses and gives attention to these factors and indicators in developing this FVI for urban flooding.

2.4 The 2012 Philippine Disaster Report

The 2012 Philippines Disaster Report presents information on disasters that occurred in the Philippines in 2012 and a review of the major disaster that occurred within the country for the past decade. According to this report, compared to the 2011 data, 2012 posed a 9 % increase in the number of disaster events recorded. Reviewing the figures of the extent of devastation of the different natural disasters that has occurred in the Philippines in recent years particularly that of flooding and typhoon events, the researcher has been taking considerations on how vulnerable or resilient the community people are. It is very important to conduct studies that would give us a comprehensive view why the same scenario of devastation and sometimes even worse than the previous one is repeating. Is our government serious about implementing those measures, do we have enough resources and equipment and training, are our communities responsive, have we done something with our infrastructures that would make it resilient, and why is recovery is too inefficient and too slow in most cases, these and many other similar concerns were addressed in this study.

2.5 Motivation and Objectives for Developing of the Vulnerability Index for Urban Flooding

In May 27, 2010, former President Gloria Macapagal Arroyo signed into law the Disaster Risk Reduction and Management Act of 2010 or RA 10121, to amend the three-decade Presidential Decree 1566, the old Disaster Management Law of the Philippines. RA 10121 institutionalizes the Disaster Risk Reduction and Management system not only in the National Government but also to all local government units in the country. In 2011, the Dumaguete City Council passed SP Resolution No. 118, Ordinance No. 63 Series of 2011 which established the Local Disaster Risk Reduction and Management Office (LDRRMO) to strengthen the effectiveness of the various protective and emergency services in the City. The LDRRMO is the coordinator of all activities and actions related to disaster risk management and is also an operational unit responsible for functions and services not presently performed or not adequately performed by existing units, offices and organizations. In spite that the Philippines has a very good National and Local Disaster Risk Reduction and Management Council Structure yet there have been cases where emergency response and disaster recovery during and after a typhoon or flooding had experienced some delays due to some political issues or gaps

among concerted actions from numerous actors across multiple sectors. It is important to know why such gaps exists thus soliciting surveys from LGU's and NGO's is a way of connecting these gaps. Concerted actions and coordination among authorities at all levels (national, provincial, municipal and community) and among other partners are critical to ensure that the resources are mobilize accordingly. On the other hand, most assessments conducted by the Local Disaster Risk Reduction and Management Council (LDRRMC) were mainly focused on the damage of physical structures, height of flood, number of families affected and deaths. There were no thorough assessments in terms of how vulnerable and resilient the community people in terms of their perception and action towards flood preparedness, response, recovery and their response to adaptation strategies.

Most studies on vulnerability and resilience revolves around national data or on a per country description but fails to cover some of the important components from the local settings, for instance, survey on housing conditions which are not included in the computation in global assessment because of insufficient data, very time-consuming and cost-intensive but they should have been included in the susceptibility component because they are highly significant. Also, items like disaster preparedness and early warning, social network and adaptation strategies should also be taken into account because of their high significance in the component. Other items that influence the occurrence of disease outbreaks were also incorporated which are believed to be highly significant in the resilience and vulnerability index at the community level. Furthermore, the community people's knowledge, attitude, and practices towards flood resilience and disease outbreaks were gauge to be able to have a thorough assessment.

Through this study, the FVI of Dumaguete City will be established. Vulnerable communities will be identified and map. But what is even more important is for us to understand why the community people are vulnerable in the first place. This research will allow us to pinpoint the weak points and strong points of the socio-behavioral and politico-administrative components particularly on the perception and behavior of the community people in their way of coping and adapting to the effects of global warming and its impact. The aim of this study is to improve the limitation of the previous WorldDisasterIndex and other similar studies by developing new indicators and components for FVI that will be useful in the community level.

3 Concepts and Components

3.1 Key Concepts and Components for Flood Vulnerability Index (FVI)

This section provides an overview of the selected components and indicators in the development and calculation of FVI. This study was done locally and the researcher

has based the analysis to the following components: Hydro-climatic, Socio-economic, Socio-behavioral and Politico-administrative components which are general and relevant to the local level. The individual indicators of each of the components will be made mention below. There are 3 important factors to consider all throughout the components which determine the vulnerability index. These factors are exposure, susceptibility and resilience. In addition, the concept of vulnerability will also be described below to facilitate a complete understanding of the concepts and components.

3.1.1 Exposure

Exposure in its core meaning in natural hazard research refers to entities exposed and prone to be affected by a hazard event. These entities include persons, resources, infrastructure, production, goods, services or ecosystems and coupled social-ecological systems.[9]

The selection for the sub-indicators for exposure was based primarily on the local threats that exposed the household respondents to river flooding and possible disease outbreak that goes with it. Within the FVI, exposure is related to the likelihood of acquiring and being affected by such phenomenon. The actual practices of the people prior and during the flooding events, the established land use and structural design, and the infrastructures mirror the exposure of certain populations to flooding events.

3.1.2 Susceptibility

Generally, susceptibility is understood as the likelihood of suffering harm and damages in case of the occurrence of a natural hazard.[10] In this study, susceptibility relates to system and individual characteristics, including the individual level of education, housing conditions, their attitude regarding the risk that they live with (before the flood), the institutions that are involved in mitigating and reducing the effects of the hazards and the existence of possible measures, like flood hazard maps and early warning systems to be used during the floods. This paper defines susceptibility as the elements exposed within the system, which influences the probabilities of being harmed at times of hazardous floods.

[9]United Nations University Institute for Environment and Human Security (UN World Risk Index) [11].

[10]United Nations University Institute for Environment and Human Security (UN World Risk Index) [11].

3.1.3 Resilience

Resilience is the capacity of any kind of system, community, society or environment, potentially exposed to hazards to adapt to any change, by resisting or modifying itself, in order to maintain or to achieve an acceptable level of functioning and structure.[11] Resilience is therefore analyzed through a political, administrative, environmental and social organizational evaluation.[12] In this study, the resilience factor is composed of the coping capacities and adaptive capacities of the individuals, communities and the government that may contribute in reducing the impacts of river flooding and disease outbreaks, and the transformation of societies and socio-ecological systems for long term adaptation to negative impacts of natural hazards and climate change through direct actions and resources.

3.1.4 Vulnerability

Vulnerability is considered as the extent of harm which can be expected under certain conditions of exposure, susceptibility, and resilience. More specifically in the case of floods, a system is susceptible to floods due to exposure in conjunction with its capacity/incapacity to be resilient, to cope, recover or adapt to the extent. Some of the exposed populations are protected from flooding by various structural and non-structural measures that are part of the resilience strategy. On the other hand, some of them have none, or only weak, flood defenses and the exposed populations are more often subject to flooding with the consequent disruption, economic loss and loss of life.[13] In this research, vulnerability is the result of the interplay of the indicators in the exposure, susceptibility and resilience category.

3.2 Components of Flood Vulnerability Index (FVI)

This part deals with the description of the components and its indicators as used on the local scale to capture the aspects of exposure, susceptibility, and resilience as well as their aggregation to the local FVI. In this study the indicators vary but were chosen based on the same concept as the WorldRiskIndex Report and the study of Balica et al. on the development of FVI for Coastal City. This study is trying to fill those categories that were not included in the global scale, for instance, housing conditions, disaster preparedness and early warning, social networks, property insurance, KAP of respondents on flood resilience and exposure to microorganism

[11]Pelling [9] The vulnerability of cities; natural disaster and social resilience. Earthscan Publications, UK.

[12]Di Mauro [6].

[13]Balica et al. [1].

such as that of *E.coli*, Liptospirosis and Dengue fever mosquito, the different adaptation strategies such as integration of post-risk assessments, sustainable community livelihood, relocation site projects and health programs for the prevention against diarrhea, leptospirosis and dengue fever which are facilitated by the LGU's and as well as some NGO's.

3.2.1 Hydro-Climatic Component

In spite that the hydro-climatic component is part of the natural river system as being hazard dependent, the following indicators were considered since they have a direct interaction between these components. The average number of typhoons that passes through the country is 20 but not all of it passes through the Visayan region, thus, in this case only 50 % of the total is being considered (susceptibility). Furthermore, this component includes the frequency and height of flooding, the houses reached by flood waters and those houses that were not located on elevated areas near the river (exposure). The land use management and structural design (resilience) is taken into consideration being a positive measure and influences the vulnerability of the area in one way or another.

3.2.2 Socio-Economic Component

The socio-economic component is part of the socio-economic system which can determine the individual's vulnerability in terms of its social and economic status. The indicators in this component predisposes these certain groups to what extent they will be affected. The socio-economic component is pertaining to their educational attainment, housing conditions (susceptibility); social networks and water treatment practice, income and property insurances (resilience) and as well as to those factors that would predispose them to certain vulnerability such as no access to improved sanitation and water sources, presence of rats and waterlogged in the vicinity, open disposal of animal waste and the unwillingness to vacate (exposure) from the hazard area.

3.2.3 Socio-Behavioral Component

This component is an added component not found in many studies on FVI. The researcher believed that it is as equally important to study the respondent's knowledge, attitude and practices (KAP) related to these events. The respondent's KAP predisposes them to the cause and effects of this phenomenon. From what they know (knowledge-resilience); how they perceived or what is their opinion and general view (attitude-susceptibility) to such environmental threat, and what they actually do (practices-exposure) are very important to consider because the

interplay of these factors influences the actual and direct effects of flooding and the occurrence of possible disease outbreaks.

3.2.4 Politico-Administrative Component

The politico-administrative component includes land use management and structural design, and the rivers natural resources and natural features management and program, these comprises the indicators for exposure. The local government's governance including those from the national and other NGO's are also included (susceptibility) which affects the extent of vulnerability in the area. Along with these indicators, the government's adaptation capacities are highly considered because of their strong influences to the extent of vulnerability. It is important to know how far the government has done its adaptive and coping measures in facing the different impacts of climate change. Post-risk assessment and integration, sustainable community livelihood, relocation site project, health and prevention programs for *E.coli*, Liptospirosis and Dengue fever infection are all part of the adaptive measures (resilience) for long term adaptation.

The relationship between flood vulnerability components, indicators and factors is illustrated in Table 1. The availability of data, the importance of certain indicators and the condition that all FVIs computed must be dimensionless for the purposes of comparison that would lead to the formulation of the equations for each vulnerability component.

The Catchment Area and Population

The Philippines is an archipelago of 7,107 islands with a population of 96.71 million as of 2012. On average, 20 typhoons/year pass through the country and 2–3 of these passes through the Visayas and Mindanao region. Dumaguete City is part of the Visayas region, the study area of this research and is located 9°18'28" north latitude and 123°18'28" east longitude. It has a population of 120,883 people as of the 2010 Population census. Dumaguete City is a second class city and has an entire area of 3,426 hectares divided into 30 communities or barangays. The City's topography is generally flat from 2 to 6 km from the shoreline. Its slope increases gently upwards to the adjoining municipality of Valencia. The highest ground elevation is located at the boundary of the municipality of Valencia, about 100 m (300 ft) above mean sea level. About 93 % of the land has slopes of less than 3 %. The remaining areas have 3–5 % slope. The Banica River Watershed (BRW) forms an elongated channel of approximately 18 km from the mouth of Banica River in Dumaguete City to Casaroro Falls in Valencia. The difference in elevation from Dumaguete's shoreline to the peak of the watershed is 1,580 m. The straight course of Banica River and high gradient signify a short residence time for surface runoff and hence, a great risk and occurrence of flashfloods and riverbed drying. At the Dumaguete-Valencia boundary in Barangay Balugo, the watershed is approximately 2.0 km wide. The river becomes slower as the gradient decreases and discharges at Poblacion 1 (Tinago) just south of Dumaguete poblacion into the

Table 1 Relationship between components and indicators

Flood vulnerability components	Vulnerability indicators		
	Exposure Abb.	Susceptibility Abb.	Resilience Abb.
A. Hydro-climatic components	A. Frequency of Flooding (FF)	A. Number of Typhoons per year (50 %) (NTY)	A. Land Use Management And Structural Design (LUMSD)
	B. Height of flooding (HF)		
	C. Houses reached by floods (HRF)		
	D. Houses not on elevated area (HNE)		
B. Social components	A. Open disposal of animal waste (ODAW)	A. Educational Attainment (High School Level and below) (EA)	A. Water Treatment or Sterilization Practice (WT)
	B. Unwillingness to vacate and be relocated (UVR)		B. Social Networks (SN)
C. Economic components	A. Houses with NO access to improved sanitation (HNIS)	A. Housing Conditions (semi-concrete, tent light materials, and plastic materials) (HC)	A. Family Income (3000–10,000) (FI)
	B. Houses with NO access to an improved water source (HNIW)		B. Property Insurance (PI)
	C. Presence of rats in the vicinity (PRV)		
	D. Presence of water logged areas in the vicinity (PWLV)		
D. Socio-Behavioral Components	A. PRACTICES of households on flood resilience (hazards, risks, exposure, preparedness, response, recovery, coordination, adaptation strategies) (PHFR)	A. ATTITUDE of households on flood resilience (hazards, risks, exposure, preparedness, response, recovery, coordination, adaptation strategies) (AHFR)	A. KNOWLEDGE of households on flood resilience (hazards, risks, exposure, preparedness, response, recovery, coordination, adaptation strategies) (KHFR)
	B. PRACTICES of households on E.coli (nature of E.coli, mode of transmission, prevention, signs and symptoms, it is fatal, treatment, financial cost of treatment) (PHEC)	B. ATTITUDE of households on E.coli (nature of E.coli, mode of transmission, prevention, signs and symptoms, it is fatal, treatment, financial cost of treatment) (AHEC)	B. KNOWLEDGE of households on E.coli (nature of E.coli, mode of transmission, prevention, signs and symptoms, it is fatal, treatment, financial cost of treatment) (KHEC)

(continued)

Table 1 (continued)

Flood vulnerability components	Vulnerability indicators		
	Exposure Abb.	Susceptibility Abb.	Resilience Abb.
	C. PRACTICES of households on Liptospirosis (same factors with letter B above) (PHL)	C. ATTITUDE of households on Liptospirosis (same factors w/letter B above) (AHL)	C. KNOWLEDGE of households on Liptospirosis (same factors w/letter B above) (KHL)
	D. PRACTICES of households on Dengue Fever (same factors with letter B above) (PHDF)	D. ATTITUDE of households on Dengue Fever (same factors with letter B above) (AHDF)	D. KNOWLEDGE of households on Dengue Fever (same factors with letter B above) (KHDF)
E. Politico-Administrative Components	A. Land Use & Management & Structural Design (LUMSD)	A. Governance (Warning and Evacuation, Emergency Response, Disaster Recovery) (G)	A. Post-risk Assessment and Integration (PRAI)
			B. Sustainable Community Livelihood Prog. (SCLP)
	B. The River's Natural Resources & Natural Features Management and Program (RNRMP)		C. Relocation Site Project (RSP)
			D. Health & Prevention Program of E.coli, Liptospirosis & DF (HPP)

Mindanao Sea. There are basically two types of soil in the BRW, namely: clay to sandy clay loam in the upper watershed and sandy loam in the lowlands. In the lowlands, soil is slightly susceptible to erosion but in the uplands, there are pockets wherein soils are highly, moderately and slightly susceptible to erosion. Dumaguete City has two seasons, namely; the dry and wet seasons. The wet season covers the period from June to November, and the dry season starts from December to May, the hottest being April and May. The average maximum temperature is 34.31 °C and the average minimum temperature is 22.85 °C for the past years. The relative humidity of the locality for the past years was 78.75 % with the month of December registering the highest. In the summer months sections of Banica River in Balugo, Candau-ay, and Cadawinonan are dry for months. At the poblacion where river discharges to the seas, the river during this period is dry and seawater flows inward about 1 km into the river channel. There is a big difference in the flow measurements between Candau-ay and Batingiuel sections of Banica River, which is attributed to high infiltration rates in Batinguel section.[14]

[14]Institutionalization of the Rehabilitation of BANICA River Watershed [7].

4 Formulation of Flood Vulnerability Index (FVI) for Urban Flooding

A total of 361 household respondents from the 12 communities and 30 respondents from the Local Government Units (LGU's) and Non-Governmental Organizations (NGO's) in Dumaguete City Philippines, were surveyed through sets of questionnaires and interviews from March 2013 to July 2013. The FVI is calculated using appropriate indicators from the five components namely: hydro-climatic, social, economic, socio-behavioral, and the politico-administrative components. Table 1 shows the relationship between components and their corresponding indicators. The selection of the indicators relates among other things, to the aspects of the eight Millennium Development Goals and the Hyogo Framework for Action (2005–2015) of the United Nations. The respondents evaluated none of the suggested variables as irrelevant but some were, of course, judged more important than others. However, after thorough weighing of the variables, for most cases, not significantly different from equal weights hence, the researchers decided to use equal weights in many of the components at the moment and to reassess the weighting of the indicators at a potential later project stage, within the process of fully testing the proposed index.

Depending on the nature of the answer to the question, each question was given a corresponding score. For questions that require a yes or no answer: Yes = 1, No = 0. For questions that require very lightly, lightly, seriously and very seriously answer: very lightly = 1, lightly = 2, seriously = 3, very seriously = 4. For questions that require excellent, very well, good, poor and very poor answer: excellent = 5, very well = 4, good = 3, poor = 2, very poor = 1. To determine the composite score which is expressed in percent, the sum of the item scores were divided by the highest possible score and then multiplied by 100.

The data were summarized per barangay (political/community unit) in frequency tables and their corresponding relative frequencies (%) as well the average of scores whenever appropriate. Variations in responses are expressed as standard deviation. For the calculation of the FVI each of the components (hydro-climatic, social, economic, socio-behavioral, and politico-administrative) is computed based on the general flood vulnerability index (FVI) formula (Eq. 1).

$$\mathrm{FVI} = \frac{\mathrm{E}^{*}\mathrm{S}}{R} \tag{1}$$

The general formula for FVI is computed by categorizing the indicators to the factors to which they belong (exposure (E), susceptibility (S) and resilience (R)). The indicators of exposure and susceptibility are multiplied and then divided by the resilience indicators, because indicators representing exposure and susceptibility increase the flood vulnerability and are therefore placed in the numerator. The

resilience indicators decrease flood vulnerability and are thus part of the denominator.[15]

The FVI for the hydro-climatic, social, economic, socio-behavioral and politico-administrative components are expressed as follows (Eqs. 2–9) and Eqs. 10 and 11 is the formula for computing the total FVI.

$$\mathrm{FVI}_{\mathrm{hydro-climatic}} = f\frac{\mathrm{FF,\ HF,\ HRF,\ HNE\ *\ NTY}}{\mathrm{LUMSD}} \tag{2}$$

$$\mathrm{FVI}_{\mathrm{social}} = f\frac{\mathrm{ODAW,\ UVR\ *\ EA}}{\mathrm{WT,\ SN}} \tag{3}$$

$$\mathrm{FVI}_{\mathrm{economic}} = f\frac{\mathrm{HNIS,\ HNIW,\ PRV,\ PWLV\ *\ HC}}{\mathrm{FI,\ PI}} \tag{4}$$

$$\mathrm{FVI}_{\mathrm{socio-behavioral\ on\ flood\ resilience}} = f\frac{\mathrm{PHFR\ *\ AHFR}}{\mathrm{KHFR}} \tag{5}$$

$$\mathrm{FVI}_{\mathrm{socio-behavioral\ on\ E.coli}} = f\frac{\mathrm{PHEC\ *\ AHEC}}{\mathrm{KHEC}} \tag{6}$$

$$\mathrm{FVI}_{\mathrm{socio-behavioral\ on\ Liptospirosis}} = f\frac{\mathrm{PHL\ *\ AHL}}{\mathrm{KHL}} \tag{7}$$

$$\mathrm{FVI}_{\mathrm{socio-behavioral\ on\ Dengue\ fever}} = f\frac{\mathrm{PHDF\ *\ AHDF}}{\mathrm{KHDF}} \tag{8}$$

$$\mathrm{FVI}_{\mathrm{politico-administrative}} = f\frac{\mathrm{RNRMP\ *\ G}}{\mathrm{SCLP,\ RSP,\ HPP}} \tag{9}$$

$$\text{Total FVI} = \frac{\text{Hydro-climatic + Social + Economic + Socio-Behavioral + Politico-Administrative}}{5} \tag{10}$$

$$\begin{aligned}\text{Total FVI} = \Bigg\{ &\left(\frac{FF, HF, HRF, HNE * NTY}{LUMSD}\right) + \left(\frac{ODAW, UVR * EA}{WT, SN}\right) \\ &+ \left(\frac{HNIS, HNIW, PRV, PWLV * HC}{FI, PI}\right) + \left(\frac{PHFR * AHFR}{KHFR}\right) \\ &+ \left(\frac{PHEC * AHEC}{KHEC}\right) + \left(\frac{PHL * AHL}{KHL}\right) + \left(\frac{PHDF * AHDF}{KHDF}\right) \\ &+ \left(\frac{RNRMP * G}{SCLP, RSP, HPP}\right)\Bigg\}\end{aligned} \tag{11}$$

[15]Cendrero and Fischer [2] A procedure for assessing the environmental quality of coastal areas for planning and management. J Coast Res 13:732–744.

The integrated FVI is a method to combine multiple aspects of a system into one number. On a global perspective, the results will be presented in values between 0 and 100 % for better comprehension: 100 % being the highest vulnerability found in the samples studied and 0 % the lowest vulnerability. The FVI percentile ratings are as follows with its corresponding interpretation: 0–19 % very low; 20–39 % low; 40–59 % medium; 60–79 % high; 80–100 % very high vulnerability. Here is how the FVI will be interpreted: A very low FVI indicates that the community is very well prepared for a flood event. A low FVI also indicates that the community is well prepared for a flood event. A medium FVI indicates that more work could be done to improve the resilience in this category. A high FVI indicates that the community should pay specific attention to this category and should make efforts to address the areas of high vulnerability rating. A very high FVI indicates that the community should really pay specific attention to this category and should make more efforts to address the areas of very low rating.

* Regardless if the community/city has a HIGH, MEDIUM, or LOW Flood Vulnerability Index, one should learn about and investigate the weaknesses identified during the process.

5 Tables and Figures

The Overall FVI of the twelve communities examined is 39.34 %. Tabuc-tubig is the most vulnerable to urban river floods (53.39 %). Its vulnerability is owing to its high vulnerability index in economic and hydro-climatic components and low resilience to the latter. Poblacion 8 ranks 2nd in the overall result mainly because it has very high vulnerability to exposure (hydro-climatic factors). Barangay 2 (Lukewright) is next in line. It has high vulnerability to hydro-climatic exposure and politico-administrative components. Though the socio-behavioral is relatively low in vulnerability but it is still significant considering that it ranks highest in that component among all the twelve communities. Barangay Balugo ranks 4th mainly because of high economic vulnerability and low resilience to hydro-climatic exposures and significantly higher in the politico-administrative index. Poblacion 1 (Tinago) is rank 5th, Bagacay on the 6th whom both similarly owing to high economic vulnerability, but for Bagacay it is significantly higher than the rest in terms of socio-behavioral component vulnerability. Batinguel ranks 7th, largely due to its very high economic vulnerability index and considerably high in the hydro-climatic exposure factors. Junob is on the 8th rank owing to its high economic vulnerability. Taclobo is on the 9th rank, showing a considerable vulnerability in hydro-climatic exposure. Barangay Candau-ay, Cadawinonan and Calindagan are the least vulnerable among the twelve communities respectively. All these three latter communities have very good resilience in most of the components examined (Fig. 1).

The values of the hydro-climatic component indicators were used for Eq. 2. In this study, the researcher included susceptibility and resilience in computing for the

hydro-climatic component simply because its susceptibility and resilience factors influence the extent of vulnerability to these kinds of exposures thus it is considered in this study. The result of the hydro-climatic component is shown in Table 2. Six (6) indicators were used to determine the hydro-climatic FVI values.

After examining the hydro-climatic components, it can be seen that Poblacion 8 (82.07 %) is the most vulnerable. This can be attributed to a slightly lower values in the land use and management and structural design as part of its resilience strategies wherein the other leading communities for instance Batinguel, ranks first in terms of exposure it has a slightly higher values for its the land use and management and structural design thus in the overall vulnerability index for hydro-climatic component it only ranks 4th. Tabuc-tubig and Barangay 2 (Lukewright) follows next to Poblacion 8 respectively. Those who are in the top 3 follows the same pattern wherein, the land use and management and structural design values are low to medium and with very high exposures in terms of the height of flooding and the number of houses reached by floods. Poblacion 1 (Tinago) ranks 5th with a very high exposure to floods in terms of height in flooding but has a high value in the land use and management and structural design (resilience) thus putting it in a much lower vulnerability. The least vulnerable communities are Barangay Balugo (37.03 %) and Calindagan (37.76 %). However, this does not imply that these communities are not vulnerable to fluvial flooding. All these communities have already been subjects to urban river flooding for the past years with loss of lives and significant cost of damaged from properties. Its reason for its least vulnerability is attributed to low exposure to flood waters wherein most houses of Balugo community were situated on an elevated area while Calindagan has very high values for the land use and management and structural design.

The values of the social component indicators were used in Eq. 3, as described above. The results of the social component are shown in Table 2. There are five indicators from this component, belonging to all factors of vulnerability, but assigned correspondingly as exposure factor, susceptibility and resilience factors and were used to determine the social FVI values. These indicators were the following: open disposal of animal waste, unwillingness to vacate and be relocated, educational attainment (high school level and below), water treatment or sterilization practice, and social networks. These 5 indicators have an effect on flood exposure and possible disease outbreak before, during and after any flood event which is another major focus of this study. Using these indicators, Tabuc-tubig (39.13 %) stands out to be the most vulnerable to possible disease outbreak due to its high values of practice in open disposal of animal waste (95.00 %) and with very low values for water treatment or sterilization practice (20.00 %). Barangays Balugo and Cadawinonan follow respectively. Unwillingness to vacate with extremely low values makes Balugo vulnerable to future urban river flooding and with similar reasons for Cadawinonan. Batinguel and Barangay 2 (Lukewright) are the least vulnerable to fluvial flooding when it comes to social component for the following reasons: it has very good scores for water treatment practices and with very good social networks among their neighborhoods and with a very high

Table 2 The overall FVI and FVI of the 5 components

Community	Overall FVI (%)	H/dro-CIimatic FVI (%)	Serial FVI (%)	Eocnonic FVI (%)	Socio-Behavioral FVI (%)	Politico-Administrative FVI (%)
Tabu-tubig	53.39	74.19	39.13	100	3.96	49.69
Junob	36.57	41.585	13.59	100.00	13.25	13.43
Poblacion 1 (Tinago)	42.62	60.15	17.65	100	13.12	22.18
Caliridagan	23.37	37.76	22.27	48.24	7.10	1.47
Balugo	48.32	37.03	38.21	100.00	10.15	56.15
Poblacion 2 (Lukewright)	48.53	67.14	9.30	94.77	25.59	45.83
Poblacion 8	48.67	82.07	16.49	92.43	9.53	42.85
Cada Winnonan	26.70	43.75	28.03	27.79	11.45	22.50
Bagacay	41.22	50.37	18.08	100.00	15.72	21.93
Taclobo	31.83	55.31	23.93	39.75	6.88	33.26
Candau-ay	31.11	49.18	24.48	52.30	13.51	16.06
Batinguel	39.73	62.73	6.08	100.00	8.76	21.10

educational attainment and Barangay 2 (Lukewright) follows the same pattern of results. Communities along the river have high social resilience.

There are 12 indicators for the socio-behavioral component. The values were computed using Eqs. 5–8 and the results are shown in Table 2. Using these indicators Barangay 2 (Lukewright) with a score of 25.59 % is the most vulnerable when it comes to KAP to flood resilience and KAP to prevention and management of diseases from E.coli, Liptospirosis and Dengue Fever. It is followed by Bagacay and Candau-ay respectively. In spite that Barangay 2 showed a very high knowledge score (resilience) yet still ranks to be the most vulnerable due to high bad attitude (susceptibility) scores which is (68.62 %). It follows the same pattern for those next in rank except that it's bad practice (exposure) rather than attitude that scores high in those cases. On the other hand, the least vulnerable community is Tabuc-tubig (3.96 %) followed by Taclobo and Calindagan respectively. The common pattern for this is usually, knowledge (resilience) score is sufficiently high and with extremely low bad attitude (susceptibility) or extremely low bad practices (exposure) against flood resilience and in the exposure of those diseases associated with flooding.

The politico-administrative component of this study shows the involvement of institutional organizations in the flood management process, including those policies and programs that were laid prior to any catastrophic events and its long term adaptation strategies. These institutional organizations are composed of the following: the LGU's from each of the communities studied, the Local Disaster Risk Reduction Management Council (DRRMC) of the City, the Provincial Disaster Risk Reduction Management Council (PDRRMC) of the Province of Negros Oriental and some of the NGO's in Dumaguete City, namely; the Silliman Volunteer for Fire and Rescue Unit (SUVFRU), One Rescue EMS, the GIZ, and the CNDR-SMART. The computation of the values uses Eq. 9 above.

As seen in Table 2, the most vulnerable politico-administrative is Barangay Balugo (56.19 %) followed by Tabuc-tubig and Barangay 2 respectively. This is due to low resilience score in some of the indicators under this component, like for instance, the post-risk assessment and integration (42.50 %) and sustainable community livelihood (47.50 %) and it follows the same for Tabuc-tubig and Barangay 2 where the lowest score for sustainable community livelihood (resilience) is 37.50 % respectively. The latter 2 Barangays were consistent as they are highly exposed to flood hazards (hydro-climatic component) ranking 2nd and 3rd as well though surprisingly Balugo ranks the least exposed community in terms of flood hazard and its hydro-climatic component due to its high elevation from the river banks thus they have less frequency when it comes to flooding and being flooded yet in this component it ranks to be the most vulnerable to politico-administrative components simply because it also ranks second (57.03 %) for its exposure indicator and low resilience scores. Barangay Calindagan is the least vulnerable to this component with very high scores (76.29 %) on its resilience strategies. Moreover, it also has good governance score which is (91.78 %). Thus, making it the least vulnerable community when it comes to politico-administrative components. Junob

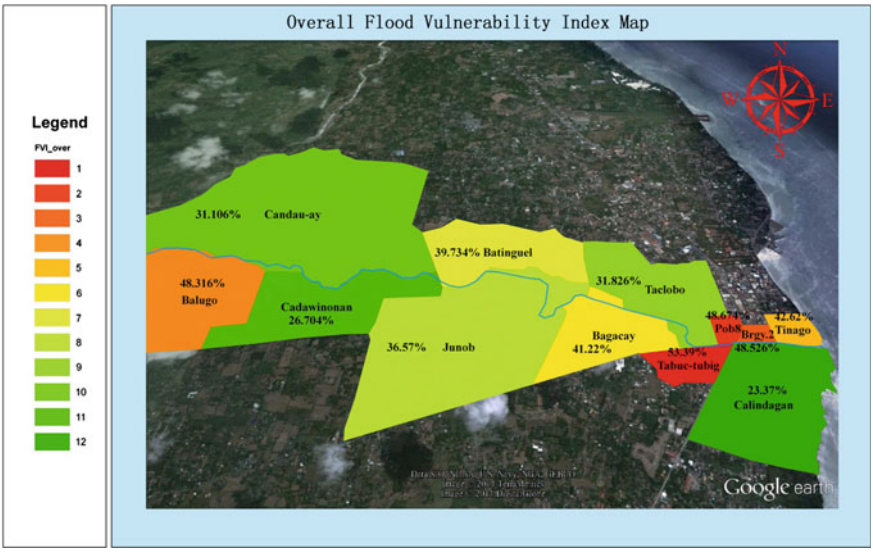

Fig. 1 The overall flood vulnerability index for the 12 communities

and Candau-ay follows respectively. Junob shows low exposure scores with good governance and high resilience. Same is true to Barangay Candau-ay, it follows the same pattern with Barangay Junob respectively (Fig. 2).

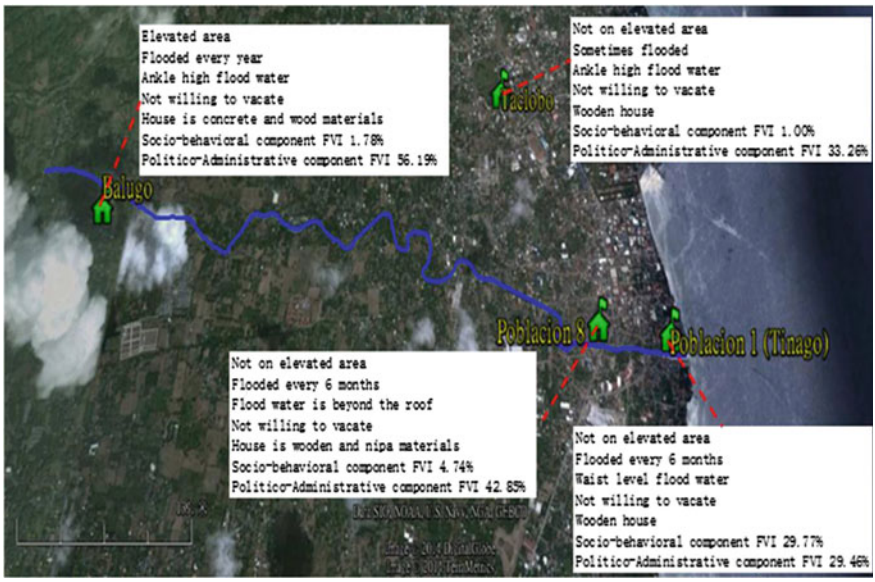

Fig. 2 The household respondents at glance

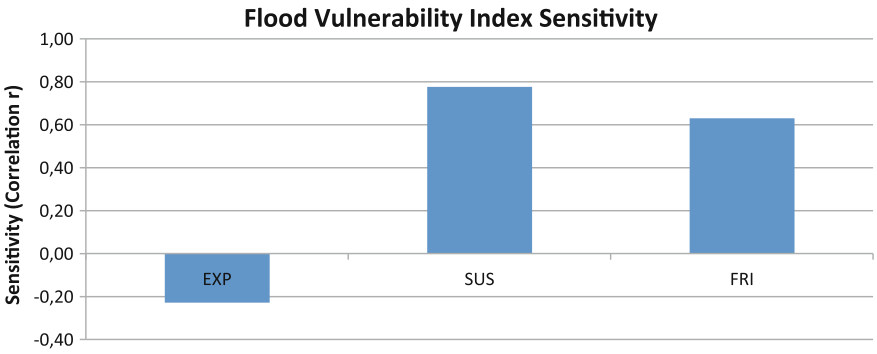

Fig. 3 Flood vulnerability index sensitivity

Table 3 Flood vulnerability index: pearson product moment correlation matrix (r)

	FVI	EXP	SUS	FRI
FVI		–0.2281	**0.7760**	**0.6305**
EXP	–0.2281		–0.1747	0.6054
SUS	**0.7760**	–0.1747		0.5024
FRI	**0.6305**	0.6054	0.5024	

Here is a brief view of the household respondents in reference to their location from the river, the scenarios during flooding events, housing conditions and their vulnerability to the different components (Fig. 3, Table 3).

The mark values are correlation values (r) that are significant (at alpha = 0.05). The FVI in this study is significantly sensitive to susceptibility and flood resilience variables.

6 Conclusions

The results of the FVI of the 5 components and the overall FVI are summarized in Table 2. A new FVI was developed in this study that incorporates the hydro-climatic components, the socio-economic factors and perspectives of the community people in terms of its knowledge, attitude, and practices towards flood resilience, hygiene practices and disease outbreaks. The politico-administrative component was also included since it could have a profound effect in all of these components in the long run.

The conclusion of this study covers four aspects and advantages: (1) The FVI methodology and use. The advantage of developing this FVI can make the community and the government aware of the different vulnerabilities that each community has and at the same time, this can be used as a network of knowledge to learn from each other and to increase the resilience of each community and which

progress needs to be prioritized. With the FVI, the impacts can be predicted in different scenarios. In this way, it helps policymakers, environmental, water and disaster agencies to define what measurements must be taken and possible allocation for adaptation and reduction of flood vulnerability in urban areas. FVI is a powerful tool for mapping of vulnerable areas in the city. (2) FVI baseline results. Using these indicators one can clearly compare the vulnerabilities of communities in a thorough perspective which can later be used between cities and countries in the world. The focus of publishing the study is more of the holistic approach rather than just a political per se. (3) Local Authority and Stakeholders Involvement. For a FVI to be widely accepted, local authorities, community people and the non-governmental agencies has to be involved in the weighting of the indicators which this study has accomplished. It is only through this involvement that the interconnectedness of several indicators and local specificities will be thoroughly captured. (4) FVI Sensitivity. The FVI in this study is significantly sensitive to susceptibility and flood resilience variables. Precisely, the community people are vulnerable in the first place because of these variables.

As this study deals particularly on local-based indicators methodology in producing a FVI, for future studies, an interdisciplinary approach by bringing engineering and social approaches together is recommended to help in assessing flood vulnerable areas or other types of natural calamities.

After an in-depth study of this newly developed FVI for Dumaguete City, there is a need to increase awareness towards adaptation measures by raising anticipatory mentality of the local population towards flood preparedness and adaptation strategies; a change of behavior towards caring for the environment; and a sense of awareness in the importance of good hygiene practices; and the collaboration between the LGU's, multiple stakeholders, local and international organizations and the community people must be realised so measurements that would lessen the vulnerability and impact would be undertaken.

Acknowledgments The first author acknowledges the support from the European Commission Erasmus Mundus Mobility with Asia: 2010-2362/001-EM Action 2 and Silliman University. The help and support of Prof. Philippe Gourbesville is very much appreciated. Profound thanks to my colleagues for their comments and support to help improved this paper, the Local Disaster Risk Reduction and Management Office, and the City Planning & Development Office of Dumaguete City for providing some information.

References

1. Balica, S. F., Wright, N. G., & van der Meulen, F. (2012). *A Food Vulnerability Index for Coastal Cities and Its Use in Assessing Climate Change Impacts*. http://download.springer.com/static/pdf/308/.
2. Cendrero, A., & Fischer, D. W. (1997). A procedure for assessing the environmental quality of coastal areas for planning and management. *Journal of Coastal Research, 13*, 732–744.
3. CDRC (Citizens' Disaster Response Center). *The 2012 Philippines Disaster Report*. http://www.cdrc-phil.com/wp-content/uploads/2009/08/PDR-2012.pdf.

4. DOH (Department of Health) (2013). http://www.doh.gov.ph/sites/default/files/leptoup36.pdf.
5. DOH (Department of Health) (2013). http://www.doh.gov.ph/sites/default/files/dengue36.pdf.
6. Di Mauro, C. (2006). Regional vulnerability map for supporting policy definitions and implementations. *ARMONIA Conference "Multi-hazards: Challenges for Risk Assessment, Mapping and Management"*, *Barcelona*.
7. Institutionalization of the Rehabilitation of BANICA River Watershed (2000).
8. Google Earth Map. Image Lands at Data SIO, NOAA, U.S. Navy, NGA, GEBCO. Image Copyright 2014 DigitalGlobe.
9. Pelling, M. (2003). *The vulnerability of cities; natural disaster and social resilience*. UK: Earthscan Publications.
10. UNDP (United Nation Development Programme) (2004). *A Global Report Reducing Disaster Risk: A Challenge for Development*. http://www.undp.org/content/dam/undp/library/.
11. United Nations University Institute for Environment and Human Security (UN World Risk Index) (2011). *Governance and Civil Society*. http://www.ehs.unu.edu/file/get/9018.
12. WHO (World Health Organization) (2013). http://www.who.int/mediacentre/factsheets/fs330/en/.

Evaluation of Adaptation Strategies for Urban Flooding in Central Taipei City in Taiwan

Ming-Hsi Hsu, Chih-Hung Chen, Wen-Cheng Liu, Tsang-Jung Chang, Albert S. Chen, Michael J. Hammond, Slobodan Djordjević and David Butler

1 Introduction

Flooding often causes both tangible and intangible damage. Many countries have endeavoured to improve their understanding of flooding such that decision makers can adopt adequate measures to reduce flood damage [7]. The effectiveness of these alternatives is usually evaluated through the reduction of risk after implementing the measures.

The spatial and temporal distributions of risk are typically non-homogenous. To investigate risk in a large area, we need to understand how the hazard and damage can vary temporally and spatially. Field survey or remote sensing, during or after an event, or computer modelling is often applied to assess flood damage. White [13] was among the first researchers to develop and apply depth-damage curves (DDCs) to represent flood damage. White [14] developed to synthetic DDCs through a hypothetical analysis. Some studies combined the loss estimation model with flood inundation model to estimate the flood damage [3, 9]. McBean et al. [8] argued that flood damage functions should include other flood damage influencing factors, such as the existence of effective, timely flood early warning, duration of flooding

M.-H. Hsu · C.-H. Chen · T.-J. Chang
Department of Bioenvironmental Systems Engineering, National Taiwan University, 10617 Taipei, Taiwan

M.-H. Hsu · W.-C. Liu (✉)
Department of Civil and Disaster Prevention Engineering, National United University, 36003 Miaoli, Taiwan
e-mail: wcliu@nuu.edu.tw

W.-C. Liu
Taiwan Typhoon and Flood Research Institute, National Applied Research Laboratories, 10093 Taipei, Taiwan

A.S. Chen · M.J. Hammond · S. Djordjević · D. Butler
University of Exeter, England, UK

P. Gourbesville et al. (eds.), *Advances in Hydroinformatics*,
Springer Water, DOI 10.1007/978-981-287-615-7_7

and flood velocity, and suggested correcting the flood damage based on weighted DDCs; in contrast, Grigg [4] thought DDCs should be applied to estimate damage without any correction for these additional factors.

In Taiwan, the National Science and Technology Center for Disaster Reduction (NCDR) has established the national flood potential database [2], which was aimed to help the government developing flood disaster mitigation strategies. Nevertheless, the flood potential information only indicates possible locations of flood hazard under certain scenarios. A further investigation is required to convert hazard information into risk, by taking the effect of climate change into account, such that the decision makers can easily determine and prioritise the strategies to prevent hazards and mitigate the impacts.

2 Case Study Area

Taipei City is located at the downstream floodplain of the Danshuei River Basin. The Digital Elevation Model (DEM) of Taipei City shown in Fig. 1 displays that the northeast region is mountainous with elevation above 400 m, the southeast and south areas have few hills, and the northwest part is alluvial floodplain with elevation below 5 m. The Danshuei River and its tributary, the Sindian River, flow along the west boundary of Taipei City. Another tributary, the Keelung River, passes through Taipei City from east to west and converges into the Danshuei River.

Taipei City developed quickly between 1968 and 1991, which consequently attracted more investment and residents. The population rose fast and reached the peak 2.72 million in 1991. Table 1 lists the land zoning for urban development planning of Taipei City. Only 134 km^2 is flat land suitable for urban development. The remaining areas are covered by hills, slope land and low-lying land, which were not adequate for urbanisation.

High raised levees were built along the banks of rivers in order to protect the Central Taipei Area (CTA) from the 200-year flood. The high density of houses alongside the banks of the Danshuei River prevented the broadening plan. Therefore, utilising flood diversion, the Erchong Floodway was constructed to mitigate the floods of Sindian River and Dahan River.

The storm sewer system, shown in Fig. 2, is composed of 26 main drainage networks which were designed for a rainfall of 5-year return period. During storm events, the water stages in rivers are typically higher than the stages of storm sewer and overland flows. Draining the surface runoff by gravity is not possible such that pumping stations were constructed at the outlets of drainage networks. The total capacity of the pumping stations is around 840 m^3/s. Although the CTA is protected against the river flooding as large as 200-year return period, surcharging from storm sewers may cause serious inundation if the precipitation is more than 5-year return period. Based on earlier studies [5], Manning's roughness coefficient had been calibrated by land use. The grid size of the inundation model is 40 m × 40 m.

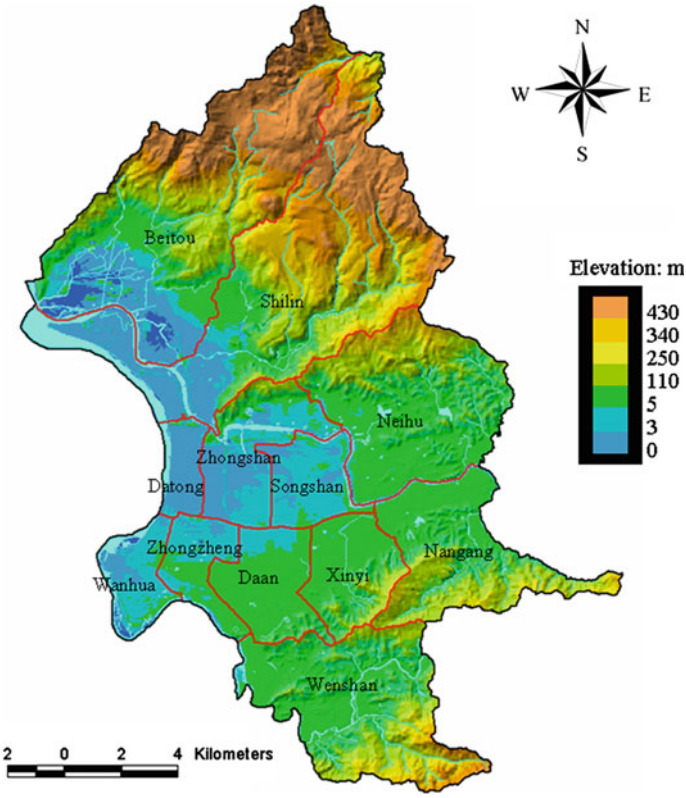

Fig. 1 Digital elevation model, river system, and administrative districts in Taipei City

Table 1 Land zoning of the Taipei City based on urban development plan

Land Zoning		Area (ha)	Total area (ha)
For urban development	Residential zone	3,837	13,394
	Industrial zone	452	
	Commercial zone	919	
	Public facilities zone	7,123	
	Others[a]	1,063	
Not for urban development	Agricultural and scenic zones	804	13,786
	Conservation zone	11,351	
	Water covering zone	1,631	

[a] Including Administrative zone, cultural and education zone, zone for specific purposes, airport, recreation zone and others

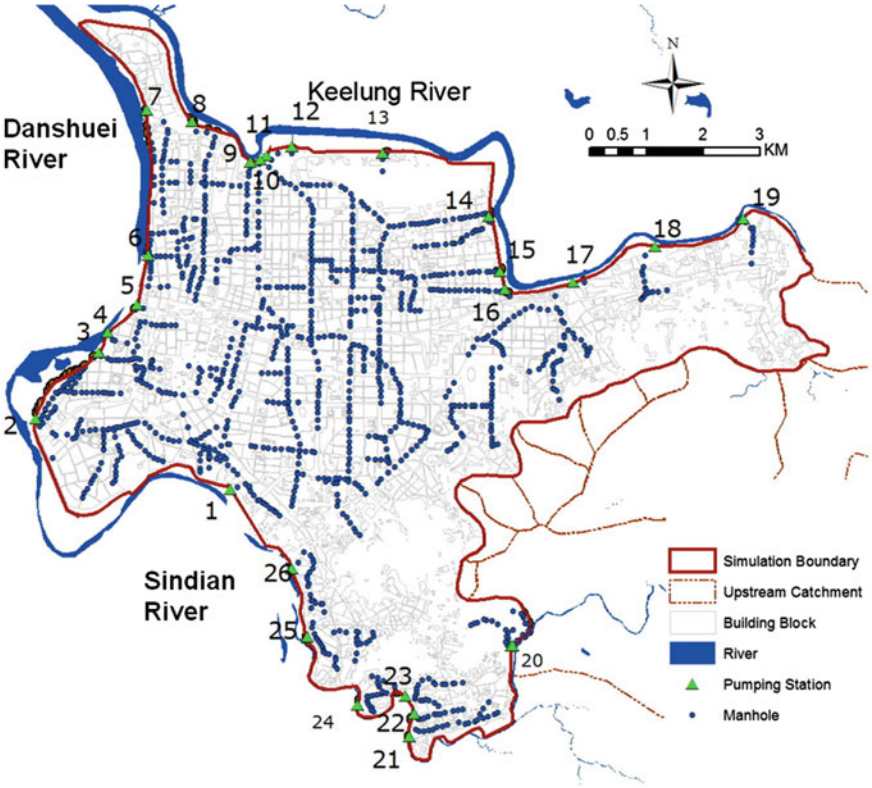

Fig. 2 The storm drainage system in the Central Taipei City

3 Methodology

3.1 Modelling Tools

This study is part of the Collaborative Research of Flood Resilience in Urban Areas (CORFU) and we adopted the modelling framework developed within CORFU for flood impact assessment. The DHI's MIKE FLOOD model was applied to hydraulic modelling in this study. The MIKE FLOOD contains various modules for solving different hydrodynamic problems, including rainfall-runoff, pipe flow, overland flow, and pollution transport. The 1D flow dynamic in sewer networks is solved by the MIKE URBAN while as the 2D overland flow is simulated by the MIKE 21. The 1D sewer and the 2D overland flows are coupled to simulate the complex flow movements between the drainage system and the ground surface in urban environment. The modelling results from the MIKE FLOOD can be directly fed into the tool developed by Hsu et al. [6] to estimate the damage of corresponding flood events.

3.2 Model Verification

On 16 and 17 September 2001, Typhoon Nari swept through Taiwan with a historical-high rainfall record in northern Taiwan. The torrential rainfall caused the most serious flood damage in Taipei for decades. The flash flood of the Keelung River flowed from a levee gap near the pumping station No. 19 and flooded the downtown Taipei. Many pumping stations were submerged by flooding water, and were paralysed. Figure 3 shows the flooded areas, which are more than 30 cm in water depth marked with dark colour, released by the Taipei City Government [10]. The lowlands along the Keelung River were almost entirely inundated. Thousands of building basements and the two subway systems, the Taipei Rail Transit System and the Mass Rapid Transit System, were filled by the deluge. The total amount of damage was estimated to be 45.34 million USD [1]. The hourly rainfall records of the gauges nearby the CTA were used in numerical simulation. The simulated flooded area shown in Fig. 4 is close to the surveyed area.

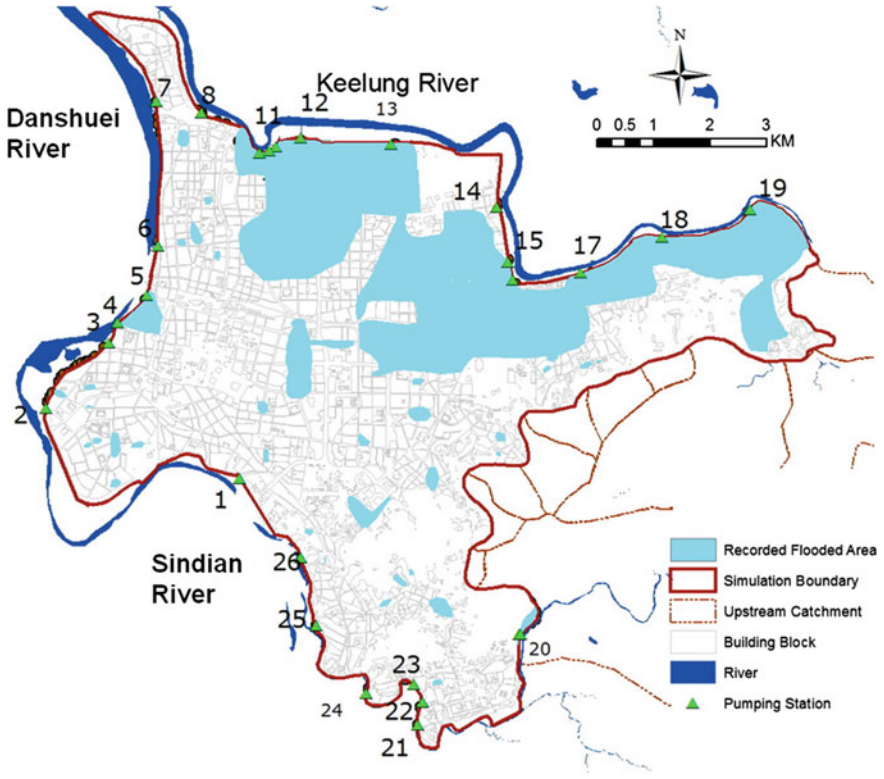

Fig. 3 Investigated flooded areas of typhoon Nari in CTA

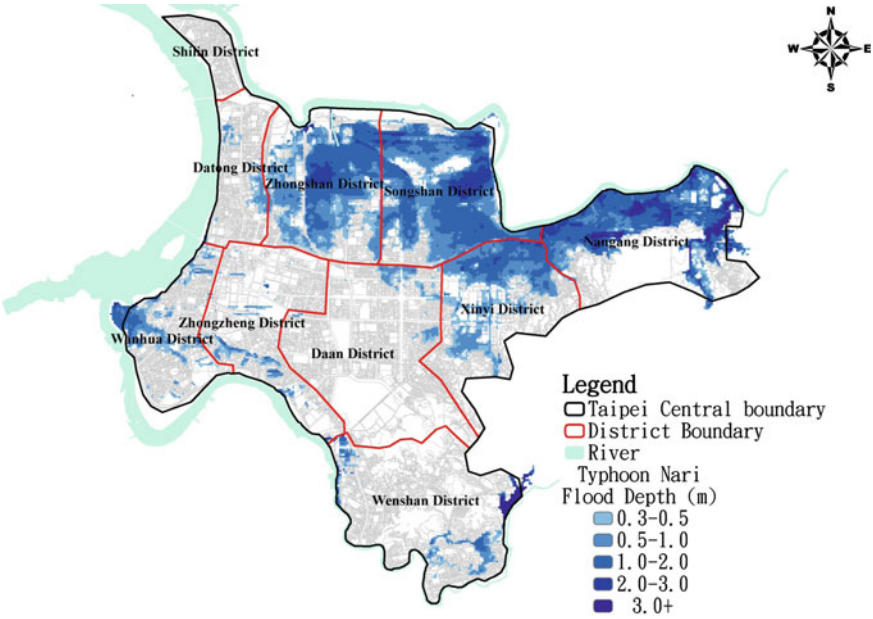

Fig. 4 Simulated flooded areas of typhoon Nari in downtown Taipei

3.3 Precipitation Frequency Analysis

According to the government report [12], we chose the design rainfall of the Taipei station with return periods of 10, 25, 100 and 200-year, as shown in Table 2, as the rainfall input of urban flood model. Based on the report, GCM model was adopted to simulate CO2 emission under difference scenarios. The adjustment factors of hourly rainfall for future climate change scenarios to baseline in the period of 2020–2039 are shown in Table 3. The rainfall depth and the adjustment factors are applied to of design rainfall to generate the new hyetographs that represent the rainfall patterns under the future climate change scenarios.

Table 2 Rainfall depth (mm) for different durations and different return periods at Taipei station

Duration (hr)	Return Period (year)									
	1.1	2	5	10	20	25	50	100	200	500
24	105.2	167.2	247.8	305.7	362.2	380.2	435.7	490.7	545.3	616.9
48	135.6	199.3	295.7	368.3	440.7	464.1	536.4	608.8	681.0	776.6
72	153.1	219.2	321.7	399.4	477.3	502.4	580.4	658.4	736.4	839.6

Table 3 Climate change factors for hourly rainfall under different return periods

Scenario	Return period (year)							
	2	5	10	20	25	50	100	200
A2	1.21	1.18	1.17	1.17	1.17	1.17	1.18	1.20
A1B	1.14	1.12	1.12	1.12	1.12	1.13	1.13	1.14
B1	1.05	1.03	1.03	1.03	1.03	1.03	1.03	1.04

3.4 Adaptive Strategies for Climate Change

For the Taipei case study, a combination of different future scenarios of climate, adaptive capacity and socioeconomic aspects is considered. In general, hazard and vulnerability are two factors for the risk analysis. This works in the way that if one of the factors was reduced, the degree of risk will be going down. With reduction to both factors at the same time in metropolitan area, the less risk of flood disaster will be taken. In this study, the adaptive strategies for climate change, including (1) increasing water retention in urban areas, (2) reducing social vulnerability in flooding areas, are investigated.

Following the recommendations of the guidelines, one of the scenarios will be a "baseline" scenario, in which no adaptation strategies and no population growth, but it considers no climate change in Taipei City. The other scenarios will consider a range of probable future, including climate change, population growth pathways and different adaptive capacities.

There will be one socioeconomic pathway for population growth and future climate situations (A1B). Taking into account, the studied area is totally developed and is unlikely to vary essentially until 2039; different scenarios for land use changes will not be considered. The Central Taipei shape file representing the land use types in the area will be the same for all future scenarios, representing the 2039 land use situation. In the report, we applied the medium population growth to show the result, and considering the population change in the future, we constitute some possible combinations, and the following sections present a brief description of these scenarios that will be finally modelled.

4 Model Application

4.1 Flood Hazard Assessment

We simulated the design rainfall events with return periods of 10, 25, 100 and 200-year for both baseline and A1B scenarios, assuming no urban growth. The water depth 0.3 m was used to illustrate the flooded area. The flood extents, as shown in Table 4, of 10-year event for the baseline and the A1B scenarios were 101 and 135 ha, respectively. The flooding area for the A1B climate change scenario was 33 % more than the baseline scenario, due to the 12 % increase of total rainfall

for the 10-year return period event. The maximum change of flooding extents, which was 42 %, between the baseline and A1B scenarios occurred for the 100-year event, caused by 13 % increase of total rainfall. For the 200-year event, although the total rainfall was 14 % more for the A1B scenario, the increased flood extent was only 39 %. It was due to the total rainfall of baseline scenario had exceeded the design standard and resulted in extensive flooding area. Although the A1B scenario had 13 % more of total rainfall and caused 205 ha increase in flooding area, the relative change of flood area was less than the 100-year event, because the baseline scenario had a larger flood area.

In this study, we proposed the adaptive strategy is the use of public facilities to enhance the retention capacity. The design retention capacity made by Taipei City government in 2011. The flooding area for the future was 33, 35, 30 and 27 % more than the baseline scenario, due to the increase of total rainfall for the 10, 25, 100 and 200-year return period event.

Figure 5 shows that, for the 200-year event, the flooding areas in Zhongshan, Songshan and Xinyi districts increased more significantly than other districts for the A1B scenario. Adaptive will reduce some flooded areas.

4.2 Tangible Damage Assessment

We considered that human activities, which are related to the types of land use, are the major factor that affects the level of loss once a flooding is occurring. Wang [11] collected the data of a field survey from the flooded areas in Taipei city, and of flood loss claims for tax relief from the government revenue office after a major typhoon event in 2001. Wang associated the damage information with the land use types, which were classified into residential, commercial (retailer, service), industrial (manufacturing, wholesaler) and cultural zones, and developed the DDCs shown in Fig. 6.

We evaluated the flood damage for both climate scenarios and different return periods using the DDCs and the flood maps as mentioned in the previous section. Figure 7 shows the flood damage map for 200-year event of the baseline. There is an obvious flooding damage in the Datong, Zhongshan, Songshan and Xinyi districts because these districts have more flooding areas than others. The Xinyi district has large business and commercial zones such that the flood damage is the worst.

To evaluate the increase of flood impact due to climate change, we compared the hydraulic modelling and damage assessment results. The simulated flood area is summarised in five depth groups, and Table 5 shows that flood areas for the 200-year event of the A1B scenario in all groups are higher than the areas for same return period event of the baseline scenario. Table 6 shows the total direct flood damage of different return period events in the CTA for both the baseline and the A1B scenarios. The climate change could increase the direct flood damage by 38, 44 and 46 % more than the baseline scenario for 10, 25, 100, and 200-year events, respectively. If we proposed the adaptive strategy to enhance the retention capacity,

Table 4 Flood area and percentage with different return periods in CTA

Return period (year)	Flooded area (ha)			Relative increase of flooded area (%)	Relative reduce of flooded area (%)
	Baseline	A1B scenario	Adaptive		
10	101	135	134	33	33
25	191	266	258	39	35
100	385	548	500	42	30
200	526	731	669	39	27

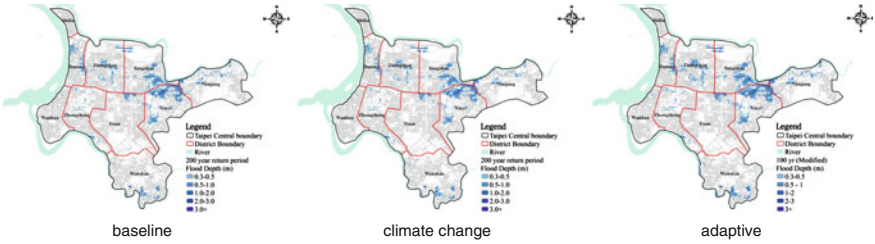

Fig. 5 Flood map of 200-year return period under baseline climate change and adaptive conditions

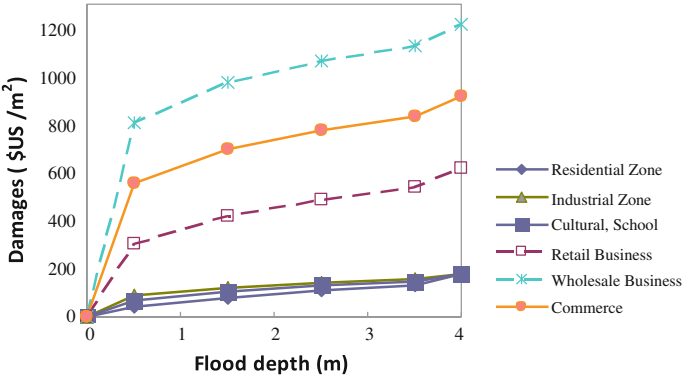

Fig. 6 Depth-damage curves for residential, commercial, industrial and cultural zones in Taipei City [11]

the adaptive strategy could reduce the direct flood damage by 0.3, 4.3, 18.8 and 41.3 million USD for 10, 25, 100, and 200-year events.

Figures 8, 9, 10 and 11 show all scenarios of the return of period in 10, 25, 100 and 200-year, including baseline, future (A1B), adaptation scenarios. Count the quantity the population live in the high-risk (level 4 and level 5) regions for each scenarios, shown in Table 7, that would appear the result if the urban has implement the

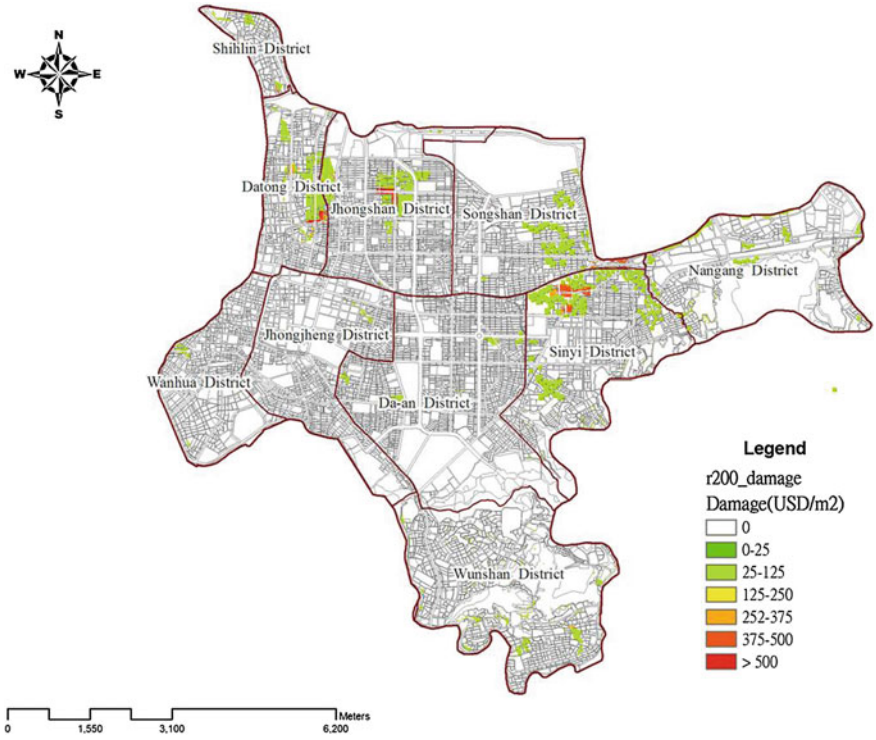

Fig. 7 Flood damage map with 200-year return period

Table 5 Flood area with different depths of 200-year event in CTA

Flood depth (m)	Flooded area (ha)		Relative increase of flooded area (%)
	Baseline	A1B scenario	
0.3–0.5	284.00	366.24	29
0.5–1.0	207.52	304.96	47
1.0–2.0	30.08	52.80	76
2.0–3.0	2.24	4.16	86
3.0+	2.08	2.72	31
Total	525.92	730.88	39

adaptation measures or not. The risk of future (A1B) is the most serious than other scenarios. Wenshan and Xinyi district are higher than other districts, due to the high ratios of the SVI and higher flood depth.

In 10-year return of period, future (A1B) has 4.56 % dwellers (0.11 million) at high-risk regions. When increasing water retention, the adaptation could reduce to 4.18 % dwellers (99 thousand) at high-risk regions. In 25-year return of period,

Table 6 The total direct flood damage with different return periods in CTA

Return period (year)	Total direct damage (million USD)			Relative increase of damage (%)	Reduce of damage (million USD)
	Baseline	A1B scenario	Adaptive		
10	32.5	44.7	44.4	38	0.3
25	63.4	92.7	88.4	46	4.3
100	135.7	198.1	179.3	46	18.8
200	194.6	279.4	238.1	44	41.3

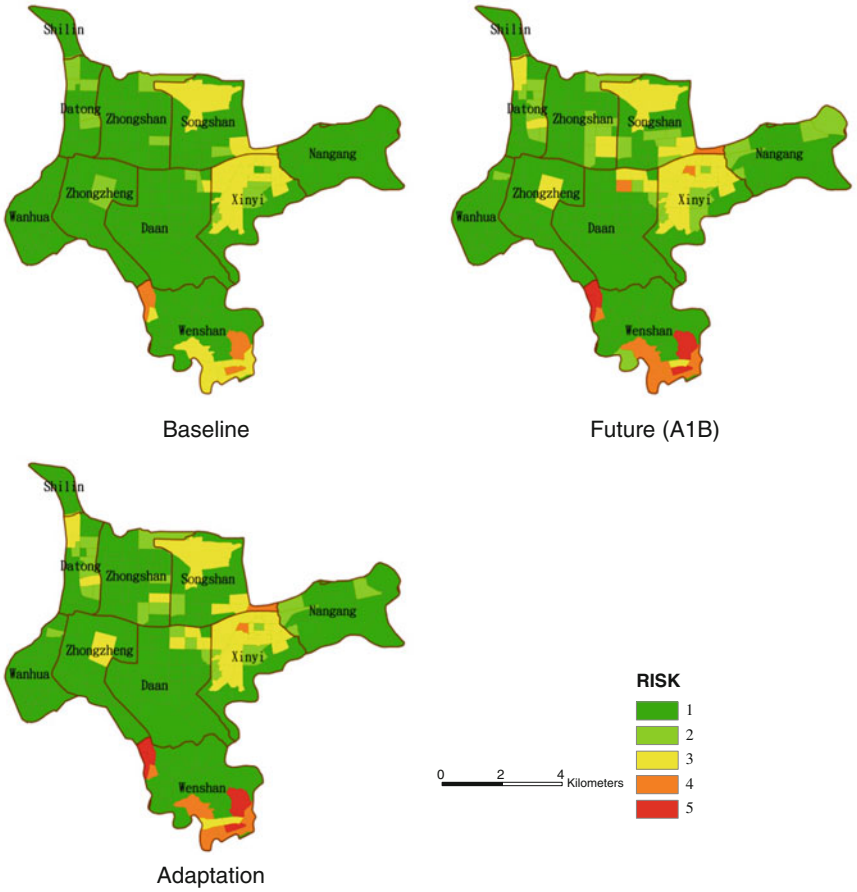

Fig. 8 Risk Map of 10-year return period

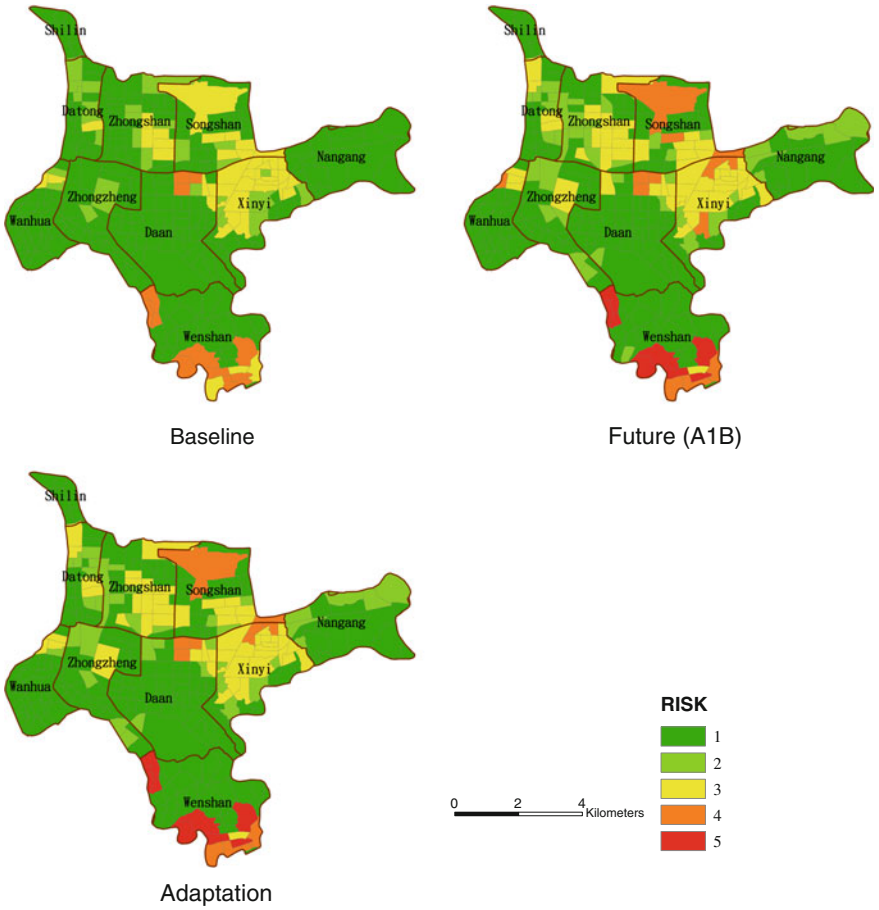

Fig. 9 Risk Map of 25-year return period

scenario of baseline has 2.93 % dwellers who are at high-risk regions. And scenario of future (A1B) increases to 7.44 % dwellers (0.18 million) at high-risk regions. The adaptation could reduce to 6.35 % dwellers (0.15 million) at high-risk regions. In 100-year return of period, scenario of baseline has 4.12 % dwellers at high-risk regions. And scenario of future (A1B) increases to 11.92 % dwellers (0.28 million) who are at high-risk regions. The adaptation could reduce to 11.62 % dwellers (0.27 million) at high-risk regions. In 200-year return of period, scenario of baseline has 4.95 % dwellers at high-risk regions. And scenario of future (A1B) increases to

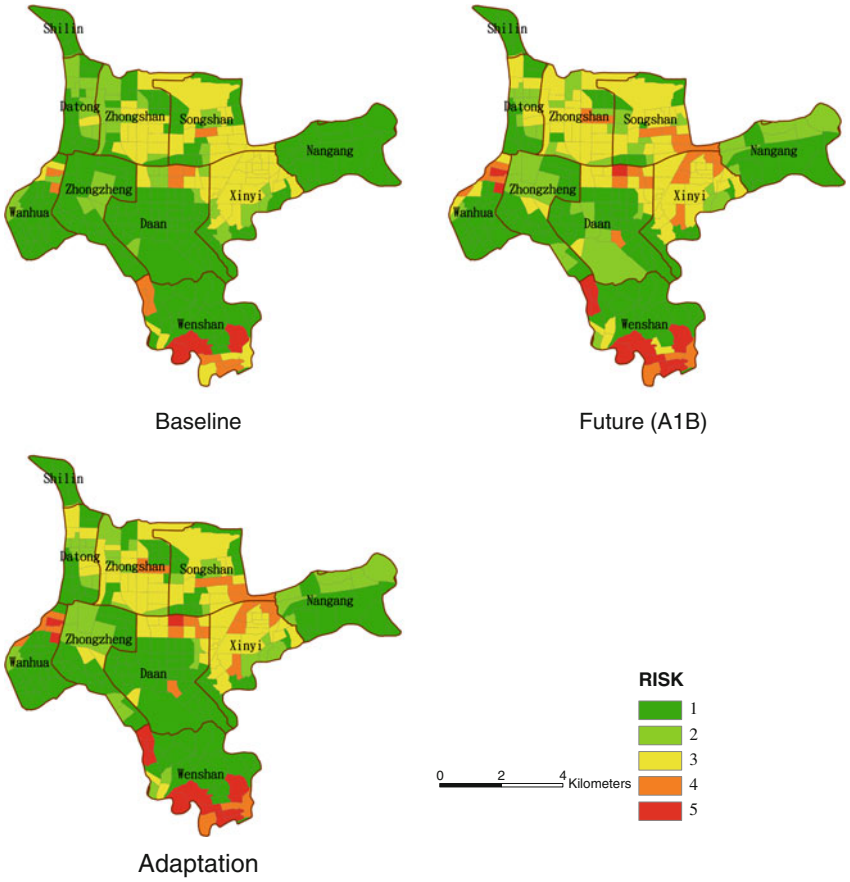

Fig. 10 Risk Map of 100-year return period

16.32 % dwellers (0.39 million) at high-risk regions. The adaptation could reduce to 14.53 % dwellers (0.34 million) at high-risk regions.

Finally, no matter what scenarios, the villages are at very high-risk regions (level 5), there are in Wenshan district, due to the high ratios of the SVI and higher flood depth (the depth of flood is above 1.0 m).

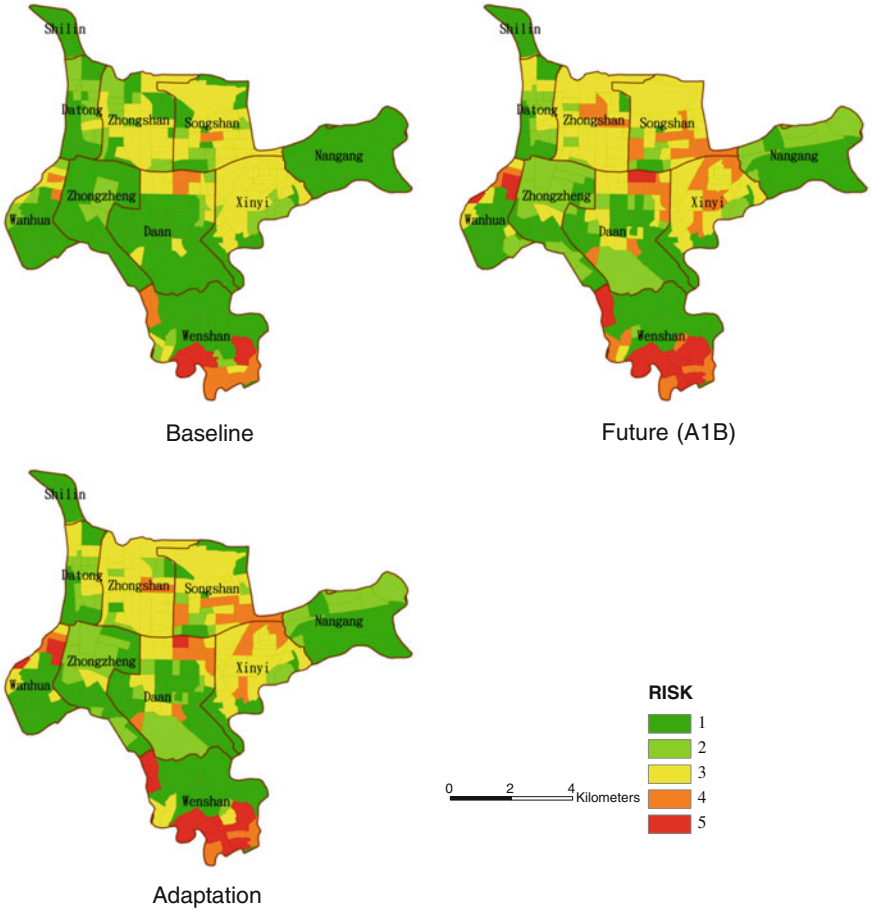

Fig. 11 Risk Map of 200-year return period

Table 7 Population in the high-risk regions of CTA

Scenario	Return of period				Total population of CTA
	10 (year)	25 (year)	100 (year)	200 (year)	
Baseline	47,841	78,214	110,238	132,242	2,673,226
Future (A1B)	107,956	176,076	282,151	386,150	2,366,814
Adaptation	99,003	150,390	274,972	343,893	

5 Conclusions

In the study, we compared the pluvial flooding extents and damage of the CTA under the baseline and the A1B climate scenarios. The hydraulic modelling was carried out by using the DHI MIKE FLOOD model, which integrates the 1D sewer network and the 2D overland flow models. The flood damage was evaluated using the hydraulic modelling results and the CORFU flood damage assessment tool. Rainfall events with different return periods for both the baseline and the A1B scenarios were adopted for modelling. The results show that the flooded area could be up by 40 % and the damage would be 37.5–45 % more due to the increased rainfall due to the climate change. The adaptive strategy could reduce the flooded area and the direct flood damage would also reduced by 0.3–41.3 million USD for 10, 25, 100, and 200-year events. With the adaptive by reducing social vulnerability in flooding areas, the area and population in the high-risk regions could be reduced, too. This methodology can be combined with envisaged changes in urbanisation and with any resilience measures, to analyse possible future impacts more comprehensively.

Acknowledgement The work is supported by the National Science Council, Taiwan (NSC 99-2915-I-002-120) and the CORFU project, funded by the European Commission through Framework Programme 7, Grant Number 244047.

References

1. Chang, H. K. (2004). Disaster recovery and management of Taipei Metro after typhoon Nari. *The 2nd Asian crisis management conference* (pp. 157–187). Taipei, Taiwan: Taipei Fire Department.
2. Chen, A. S., Hsu, M. H., Teng, W. H., Huang, C. J., Yeh, S. H., & Lien, W. Y. (2006). Establishing the database of inundation potential in Taiwan. *Natural Hazards, 37*(1–2), 107–132.
3. Dutta, D., Herath, S., & Musiakec, K. (2003). A mathematical model for flood loss estimation. *Journal of Hydrology, 277*(1–2), 24–49.
4. Grigg, N. S. (1996). *Water resources management*. McGrawHill: Wiley Online Library.
5. Hsu, M. H. (1992). Simulation of inundation with overflow on Levee along Keelung river. In *The CCNAA-AIT joint seminar on prediction and damage mitigation of meteorologically induced natural disasters, Taipei, Taiwan*.
6. Hsu, M. H., Tsai, M. Y., Lin, Y. C., Chen, A. S., Hammond, M. J., & Djordjević, S. et al. (2012). Flood damage assessment in Taipei city Taiwan. In *9th International Conference on Urban Drainage Modelling*, *Belgrade, Serbia, 4th–6th Sep 2012*.
7. James, L. D., & Hall, B. (1986). Risk information for floodplain management. *Journal of Water Resources Planning and Management-Asce, 112*(4), 485–499.
8. McBean, E. A., Gorrie, J., Fortin, M., Ding, J., & Moulton, R. (1988). Adjustment factors for flood damage curves. *Journal of Water Resources Planning and Management-Asce, 114*(6), 635–646.
9. Smith, D. I. (1994). Flood damage estimation—a review of urban stage-damage curves and loss functions. *Water SA, 20*(3), 231–238.

10. Taipei City Government. (2001). *The reconstruction plan for the damage caused by typhoon Nari*. Taipei, Taiwan.
11. Wang, R. Y. (2003). Establishment of systematic models for flood damage evaluation, Taipei, Taiwan. In *WRA, Hydrological Year Report of Taiwan, Republic of China 2006*. Water Resource Agency, Ministry of Economics Affairs.
12. Water Resources Agency. (2011). *Assessing the impact of climate change on hydrological risk*. Taipei, Taiwan.
13. White, G. (1945). *Human Adjustment to Floods: Department of Geography Research Paper No. 29*. Chicago, IL: The University of Chicago.
14. White, G. F. (1964). *Choice of Adjustments to Floods: Department of Geography Research Paper No. 93*. Chicago: University of Chicago Press.

Improvement to the Treatment of the Wave Setup Along Open Boundaries in the Swan Wave Model

Hafedh Hajji and Delphine Cariou

1 Introduction

Nearshore areas are subjected to complex processes due to gravity of water waves inducing nearshore circulations. Waves propagating in shallow-waters are modified by coastal effects such as shoaling, refraction, diffraction, dissipation, and wave-current interaction. The associated energy and momentum are propagated in the same direction, but only the energy is dissipated. The excess of momentum flux, never dissipated, is transferred to the water column resulting in a slope of the water surface to balance the momentum flux.

To compute the characteristics of wave propagations as well as the wave-induced setup near-shore, GlobOcean uses the third-generation wave model that SWAN developed at Delft University of Technology [1].

The SWAN gives satisfactory results, but for some applications it is necessary to adapt or to improve the source code which is made available by the developers.

The calculation of the increase of mean sea level during hurricanes and deep depressions is a major difficulty in storm modeling. Consequently, the wave setup is an important aspect of research to enhance the evaluation of shoreline risks of damage to coastal infrastructure. Its value can reach 20 % of input waves, depending on the configuration.

In the present paper, the treatment of the wave setup with SWAN is briefly introduced. A particular emphasis is made to show the inconvenience encountered by using the currently available procedure to take into account wave setup on the open boundary limits when SWAN is nested to SWAN. The new numerical method

H. Hajji (✉) · D. Cariou
Draguignan, France
e-mail: hafedh.hajji@globocean.fr

D. Cariou
e-mail: delphine.cariou@globocean.fr

P. Gourbesville et al. (eds.), *Advances in Hydroinformatics*,
Springer Water, DOI 10.1007/978-981-287-615-7_8

is then presented. The benefits of using the improved SWAN code on embedded grids are shown through a particular storm study.

Thus, in Sect. 2, the storm 'Xynthia' is presented as well as wave setup produced along the shoreline based on empirical solutions. In Sect. 3, the difficulties in simulating this extreme event using the SWAN-SWAN nesting are shown. In Sect. 4, the theoretical and numerical aspects of wave setup as they are defined in the SWAN model are briefly introduced, our solution to improve the wave setup treatment of the boundary conditions is presented and finally, the results are analyzed. The last Sect. 5 contains some concluding remarks.

2 Storm 'Xynthia'

2.1 The Weather Conditions

On the 28th of February 2010, the French west coast was subjected to a strong meteorological depression named 'Xynthia'. It produced a powerful storm surge, flooding the Pertuis Charentais coast (See Figs. 1 and 2). The storm 'Xynthia' was one of the most important meteorological disasters in several decades in France: on a human level with 47 victims and on an economic level with widespread submerged areas [2].

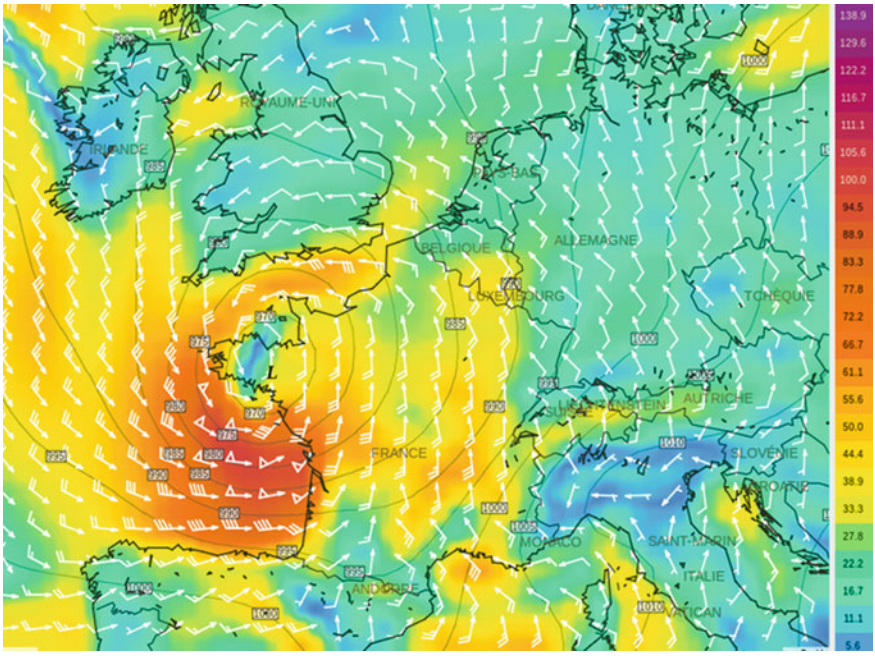

Fig. 1 Wind fields (km/h) and isobars (hPa), from NOAA, the 28th of February 12 h

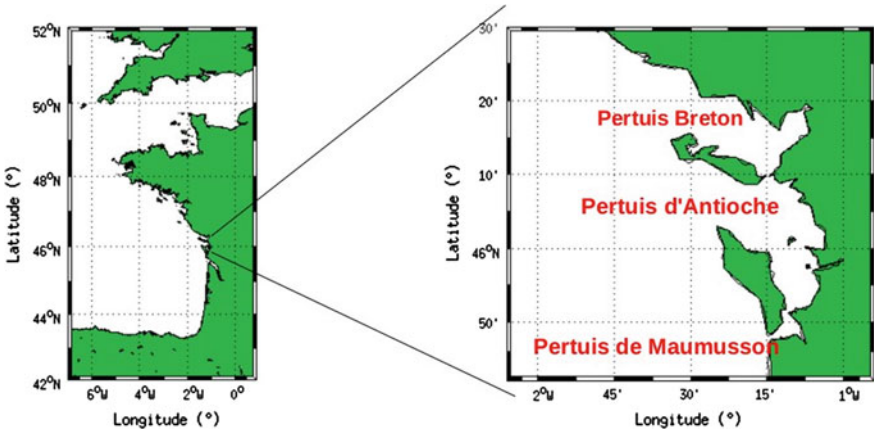

Fig. 2 Location of the Pertuis charentais coast

The damage caused by Xynthia was studied by EGIS Ports, whose activity involves engineering structures to be resilient against exceptional sea states including those predicted to arise in time due to climate change. EGIS Ports inquiries are focused on the high storm surge observed during this event, due to the conjunction of various natural phenomena: First, a strong tidal coefficient (102) corresponding to the storm passage increased the sea level. Then, a deep depression with strong wind fields blowing over from the open sea, during the storm, reinforced the storm surge (the lowest pressure observed during the storm was about 970 hpa and the highest gust of wind speed observed was 130 km/h from a westerly direction, on the 28th of February, on the Pertuis area, (see Fig. 1). Next, the topography of Pertuis is favorable to strong surge phenomena: The presence of the 'île de Ré' and the 'île d'Oléron' is responsible for a Venturi effect accentuating wind flows in the Pertuis. Finally, the high sea-states arriving perpendicular to the coast provoked an important wave setup.

2.2 *Estimation of the Wave Setup in the Pertuis During Xynthia Based on Empirical Methods*

Unlike SWAN which uses an approximation of the equation of motion, many authors based on laboratory and field measurements of wave setup, have suggested empirical formulae to estimate wave setup at or near the shoreline. Most of these formulae are based on wave nonlinearity which depends on the parameters H/L0 and h/L0 where H is the wave height, L0 is the wave-length in deep-water and h is the depth.

Yanagishima and Katoh [3] developed for their beach slope (1–60) an empirical solution linking the wave setup to the deep-water significant wave height (H_{os}) and wavelength (L_{os}):

$$\eta = 0.0520 H_{os} \left(\frac{L_{os}}{H_{os}}\right) \tag{1}$$

which is also formulated in term of the Iribarren number (ς_0):

$$\eta = 0.27 H_{os} (\varsigma_0)^{0.4} \tag{2}$$

The authors found reasonable agreement with the theory of Goda [4].

Raubenheimer et al. [5] based on field measurements across the surf zone from the shoreline to 5 m of water depth proposed the following formula:

$$\eta = (0.019 + 0.003(\beta_f)^{-1}) H_{os} \tag{3}$$

where β_f is the average slope across the surface zone.

Stockdon et al. [6], provided an empirical parameterization for wave setup under any natural beach conditions as follow:

$$\eta = 0.35 \beta_f \sqrt{H_0 L_0} \tag{4}$$

Assuming that $\tan(\beta_f) \approx \beta_f$, their expression in terms of the Iribarren Number gives:

$$\eta = (0.35 \varsigma_0) H_{os} \tag{5}$$

More recently, Goulay [7] uses the deep-water rms wave height (H_{rms}) and the Iribarren Number as follows:

$$\eta = 0.35 H_{\text{rms}} (\varsigma_0)^{0.4} \tag{6}$$

In addition, graphical methods were established to calculate the wave setup:

The U.S. Army Corps of Engineers 1984 Shore Protection Manual (SPM) gives the non-dimensional wave setup versus the deep-water wave steepness and the profile slope at mid depth in the surf zone (see Fig. 3a).

Goda [4] also presented a graphical method to calculate the static and dynamic wave setups due to irregular waves. The guidance gives the nondimensional wave setup versus deep wave steepness and relative depth within the surface zone (see Fig. 3b).

These empirical formulations were used to estimate the wave setup on two transects in front of the 'Hôtel du Département'. Difficulties in choosing a representative bathymetric profile were mainly due to the complex topography of the studied domain. Thus, two closed transects were chosen to evaluate the wave setup. Figure 4 shows the transects (1) and (2) studied from the open sea to the 'Hôtel du Département' and Table 1 gives the wave and depth characteristics of the offshore point of the two transects. We note that transect (1) is located inside a bay whereas transect (2) is lies along a relatively steep gradient in depth. Thus, transect (2) is more exposed to wave-breaking.

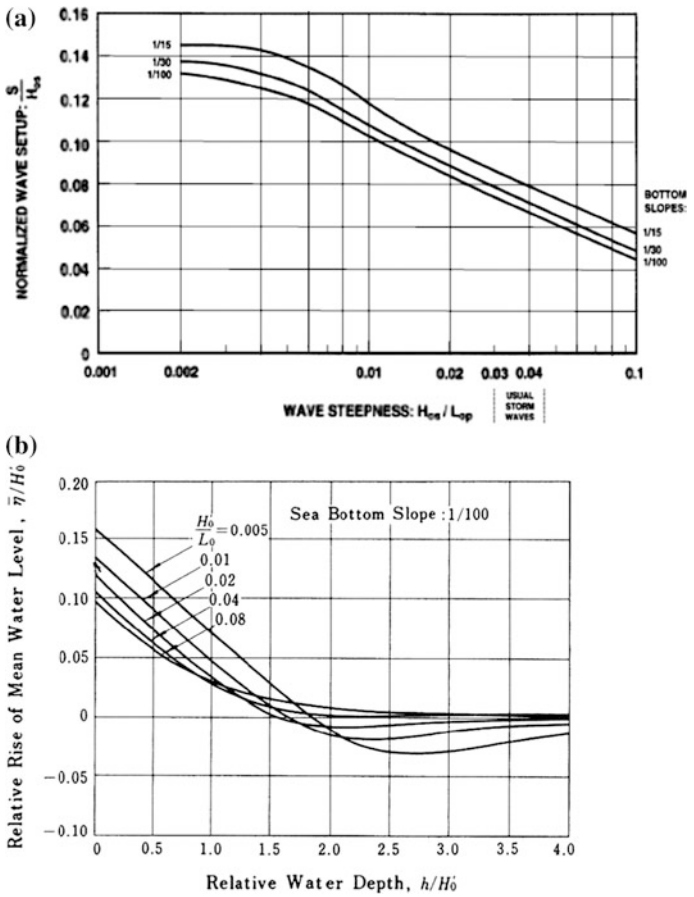

Fig. 3 **a** Nondimensional wave setup versus deep-water steepness and profile slope (see SPM 1984). **b** Nondimensional wave setup versus deep-water steepness and profile slope: profile slope = 1/100 [4]

At the starting point of the profiles, the Hs is about 1.8 and 1.9 m for transect (1) and transect (2), respectively. The equivalent deep-water wavelength is about 205 m for both points. Computing the equivalent deep-water significant wave height using a de-shoaling coefficient, the deduced wave steepness are about 0.0087 for the northern transect 1 and 0.0093 for the southern transect 2. Using the SPM and Goda recommendations, the following non-dimensional wave setups are obtained:

$$\eta/H_0 = 0.11 \tag{7}$$

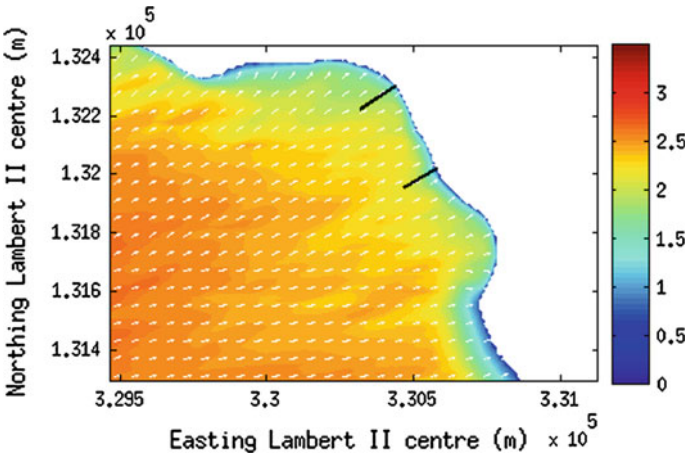

Fig. 4 Hs (m), Transect 1 (north) and 2 (south) used to estimate the wave setup based on empirical methods

Table 1 Characteristics of the first point of the transects 1 and 2

	Transect 1	Transect 2
Hm0	1.78 m	1.91 m
Tp	11.5 s	11.5 s
Depth	5.9 m	5.1 m
Slope	4 %	4 %
Distance	137 m	130 m

Table 2 Wave setup in meter estimated near-shore line of transects (1) and (2) using different empirical methods

Empirical solution	Transect 1	Transect 2
Yanagishima and Katoh: Eq. 1	0.24	0.25
Raubenheimer et al.: Eq. 3	0.16	0.18
Stockdon et al.: Eqs. 4 or 5	0.29	0.27
Gourlay: Eq. 6	0.32	0.33
SPM	0.20	0.20
Goda	0.21	0.21

$$\eta/H_0 = 0.12 \tag{8}$$

The two methods give a similar normalized wave setup.

Table 2 gives the wave setup estimated using empirical solutions near the shorelines of transects (1) and (2). The empirical methods results vary from 0.5 to 0.32 m for transect (1) and from 0.06 to 0.33 m for transect (2).

SPM, Goda and Yanagishima wave setup values are much closer and Stockdon et al. and Gourlay gave the highest values whereas Raubenheimer et al. gave the

smallest wave setup. Note that these authors have mentioned that their solutions estimating the wave setup for water depths greater than 1 m but the theory was found to under-predict water in shallow water (h < 1 m).

A simulation was undertaken with SWAN version 40.91 without modification of the source code and with no wave setup imposed at the boundary limit of the local grid. The resulting wave setup and Hs obtained along the two transects are presented in Fig. 5a, b.

On the shoreline (depth ≈ 1 m) of transect (1), the wave setup calculated by the model is about 0.11 m whereas on the shoreline (depth ≈ 1 m) of transect (2) is more sensible to wave-breaking, the SWAN computed a wave setup of 0.24 m. The maximum wave setup calculated on this concerned beach was 0.27 m and on average, the wave setup varies between 0.1 and 0.2 m along the still water shoreline of this beach (See Fig. 6). Consequently, the empirical methods produce similar approximations of wave setup compared to the SWAN wave model.

3 Difficulties in Simulating the Wave Setup Using Swan to Swan Nesting

The wave setup represents an important part of the surge during the Xynthia storm. Thus, EGIS Ports were interested in inquiring this parameter near the shoreline.

SWAN includes an optional command SETUP which activates the wave-induced set-up computation, modifying the water level taken into account by the model. When configuring SWAN-SWAN nesting, SWAN reads the wave boundary conditions in the relevant output file of the parent grid that are then transferred to the child grid. However, the wave setup information is not transmitted in this file. When the wave setup is involved, the user can impose only one value of wave setup in the child grid. The given value will not cover the open boundaries, but is applied at the deepest point of the open limit of the computational grid: the forced wave setup of 0.07 m is applied on the deepest point of the computational grid and is then propagated to the coast. Consequently, to reproduce the wave setup propagation in a complex wave model with embedded grids, the user has to read the wave setup at the boundary of deepest point of the child grid, in the parent grid and impose it at the deepest point of the limit of the child grid. This tedious work necessary to propagate the wave setup by the user between the grid simulations is inaccurate because the wave setup is not imposed on the entire boundary limit of the child grid and is irreproducible from an user to another because the user can choose to be more or less conservative depending on the value chosen by them.

To overcome this shortcoming, a solution was suggested to facilitate the transfer of wave setup simulated on the parent grid into the child grid without the intervention of the user, and as a consequence to increase the accuracy of the wave setup simulations.

This new version was then applied and validated in stationary and non-stationary modes through a reproduction of the Xynthia wave propagation. Figure 7 shows the bathymetry offshore of the ‘Hôtel du Département’. The dimensions of this

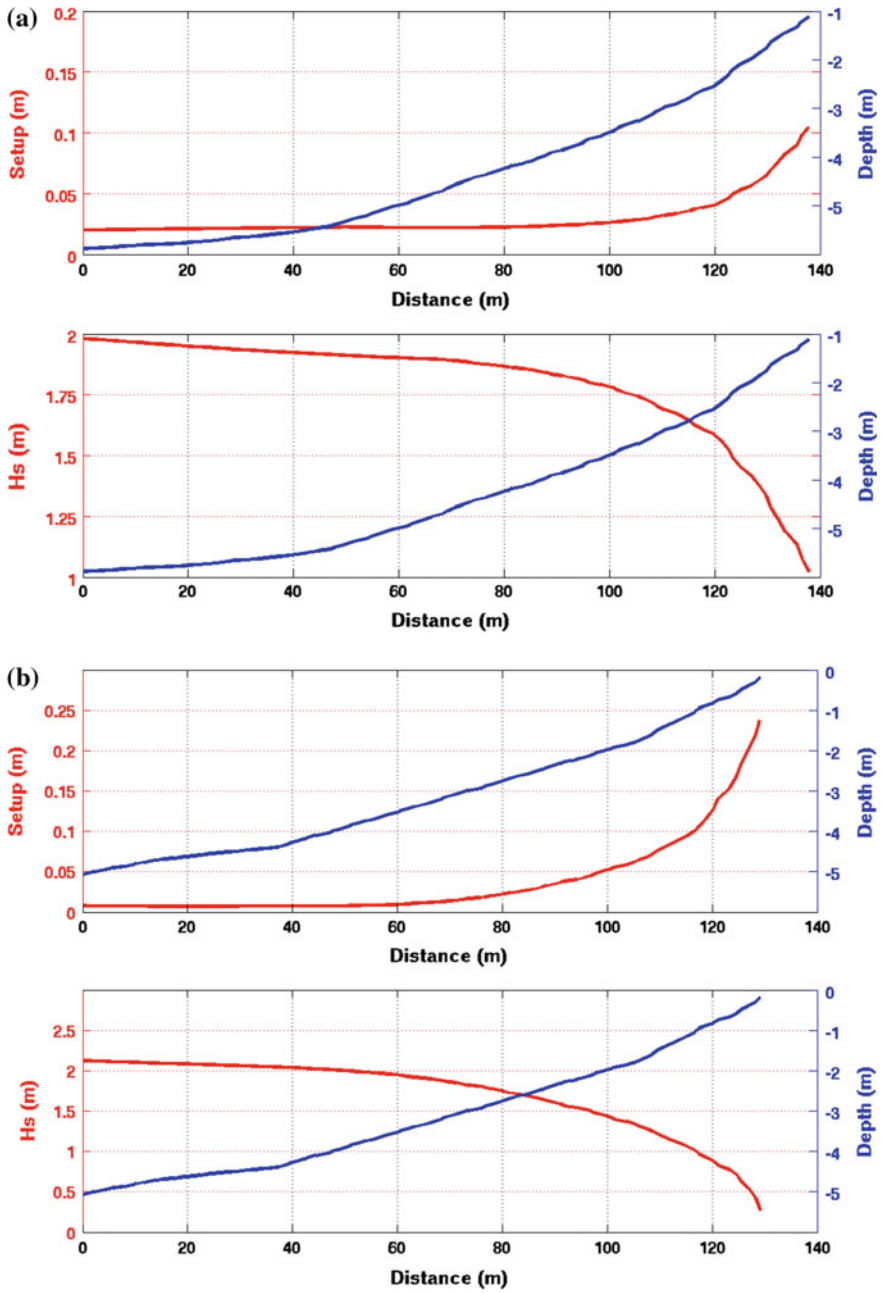

Fig. 5 **a** Evolution of the wave setup and Hs with the depth along the selected transect (1), SWAN version 40.91. **b** Evolution of the wave setup and Hs with the depth along the selected transect (2), SWAN version 40.91

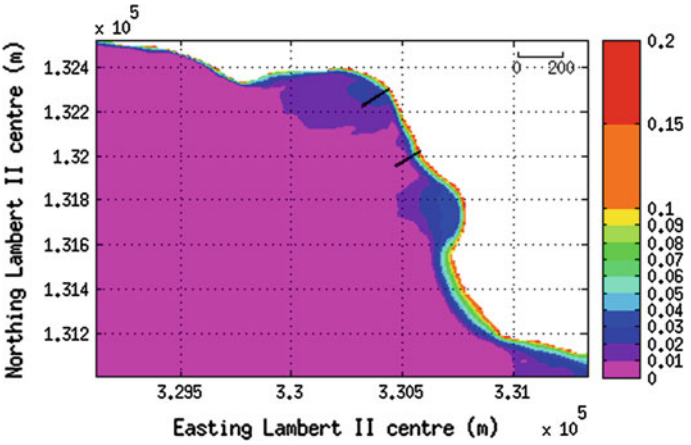

Fig. 6 Wave setup in meter in front of the "Hôtel du Département", SWAN version 40.91

Fig. 7 Bathymetric grid (m) of the global offshore grid

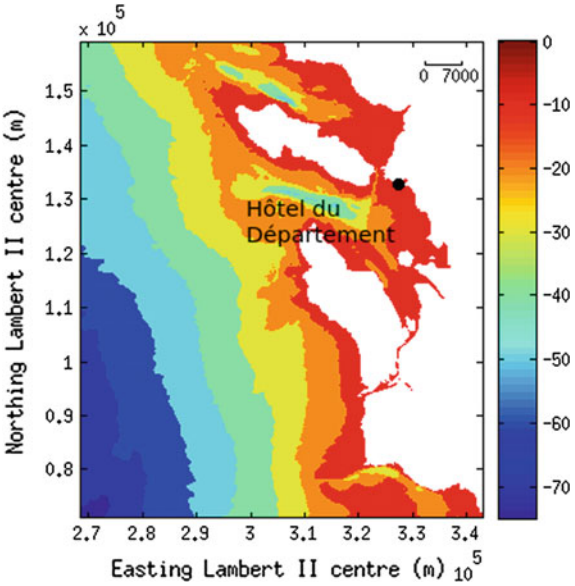

bathymetric grid were used to propagate the Xynthia storm with the nearshore wave model SWAN into the entrance of the Pertuis. The storm 'Xynthia' brought to the Pertuis coast a sea-state of Hs = 7.5 m with Tp = 11.4 s on the open sea in the direction of the coast. Wavelength at an infinite depth is about 200 m. The wave setup, which is a phenomenon occurring in shallow water is already pertinent considering this wavelength in these depths.

Consequently, the wave setup has to be considered from the global grid to the local grid to reproduce correctly this phenomenon. The transfer of the wave setup

from the parent grid to the child grid is essential. This specific event generated a very significant wave setup, accumulated offshore throughout the period in question and propagated towards the Pertuis coast. This will be shown in the next section.

4 Reproduction of the Wave Setup During Xynthia with the Modified Swan Version

4.1 Implementation of the Wave Setup in Swan

Wave setup is the increase of water level within the surf zone due to the transfer of wave-related momentum to the water column during wave-breaking.

After deleting from the equation of motion all terms involving current velocities, SWAN retains equilibrium between the wave-induced force and the gradient of the water table:

$$F_k + gd\frac{\partial \varsigma}{\partial x_k} = 0, \tag{9}$$

where ζ is the setup, d the depth and F_k is the wave-induced force.

Equation (9) can be used directly to compute the setup if one is concerned only by one-dimensional case. In order to reduce the number of equations to one, SWAN uses the observation by Dingemans [8] that wave-driven currents are mainly due to the divergence-free part of the wave forces whereas the setup is mainly due to the rotation-free part of the force field. Therefore, SWAN takes the divergence of Eq. (9) to obtain the following elliptic partial differential equation for ζ:

$$\frac{\partial F_k}{\partial x_k} + \partial(gd\frac{\partial \varsigma}{\partial x_k})/\partial x_k = 0 \tag{10}$$

This Poisson equation needs one boundary condition in each point of the boundary of the computational domain. Two types of boundary conditions are foreseen; the first one is used on the open boundaries and on the shoreline, defined as the line where the depth is zero:

$$F_n + gd\frac{\partial \varsigma}{\partial n} = 0 \tag{11}$$

It is not possible to use this boundary condition on all boundary points because there remains an unknown constant. So at one point, for which we take the boundary point with the largest depth, the setup is assumed to be 0: ζ = 0.

The second type of boundary condition with given value of ζ is also used in nested models. The setup computed in the larger model is used as boundary

condition in the nested model. In the child grid, the setup is given in all points of the outer boundary. On shorelines inside the area again Eq. (5) is used.

When boundary conditions are obtained from a coarse grid SWAN run (generated in the previous SWAN run with command NESTOUT) only wave spectra are transferred to the nested grid. If on all points of the outer boundary of the child grid, the wave-induced setup is significant and differs from point to point, one cannot consider this variability since only one value has to be given to the child grid. To take the advantage of the previous SWAN run and the variability of the wave setup produced on the all boundary points, the SWAN code was modified accordingly. As with the wave spectra given by the coarse domain, the setup values are transferred to the child grid.

4.2 *Xynthia Modeling*

A first reproduction of the propagation of the storm 'Xynthia' in the Pertuis Charentais was undertaken with version 40.91 of SWAN. Three embedded grids were necessary to transfer the sea-states from the open sea to the 'Hotel du

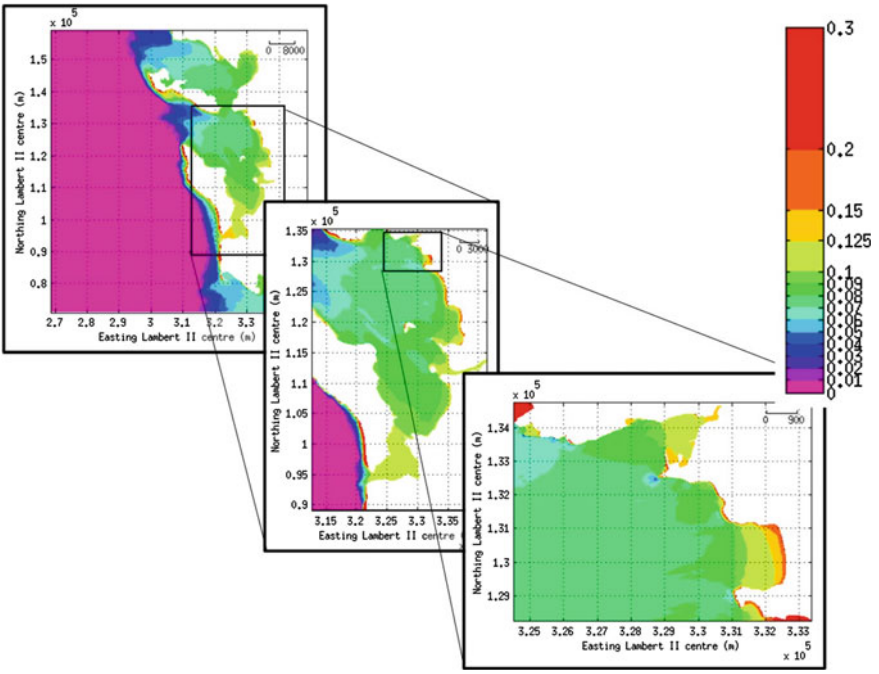

Fig. 8 Wave Setup propagation (m) in the Pertuis with swan v40.91

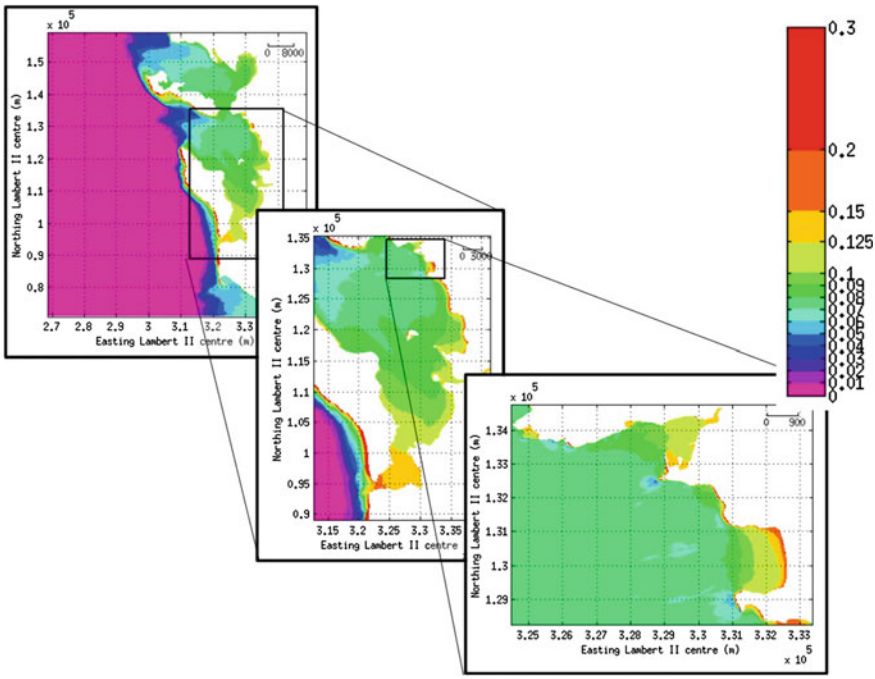

Fig. 9 Wave Setup propagation (m) in the Pertuis with SWAN (updated version)

Département' passing by the Pertuis d'Antioche. With this SWAN version, the wave setup at the deepest point at the boundary of the child grid was read on the parent grid and applied 'manually' on the child grid. This inaccurate way to propagate the wave setup from a grid to another is conservative: The user can apply a high setup to be secure on the wave setup reproduction on the study location. Figure 8 shows the wave setup fields through the three embedded grids.

Another reproduction of the propagation of the Xynthia storm was then undertaken with the updated version of SWAN. The same three grids were used to transfer the sea-states from the open sea to the 'Hotel du Département' passing by the Pertuis d'Antioche. With this SWAN version, the wave setup at the boundary points of the child grid is read in the output file of the parent grid and propagated to the study location. Figure 9 shows the wave setup fields obtained with the updated version of SWAN.

This new way to take into account the wave setup throughout different grids is more accurate because this method is automatic and there is no intervention of the user between the grids. In addition, the exact wave setup is read at the boundary points of the child grid, contrarily to the first version in which the user impose the wave setup at the deepest point of the boundary limit. Figure 10 shows the evolution of the wave setup at the boundary limit between the parent and child grid.

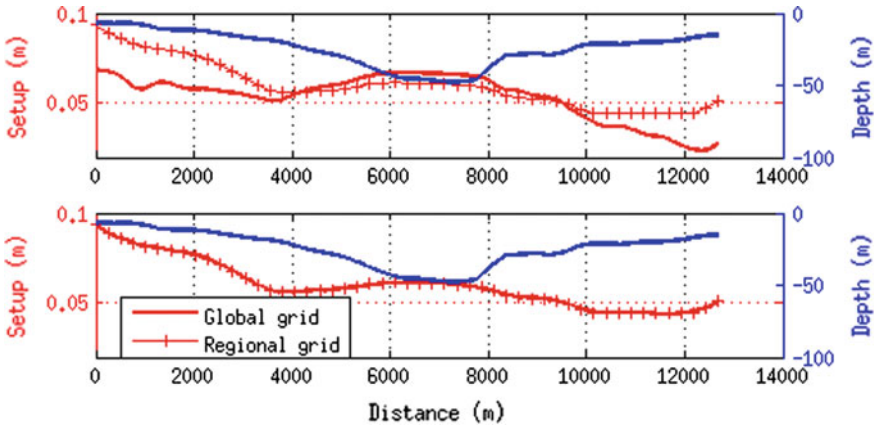

Fig. 10 Evolution of the wave setup and the depth along the transect separating the Global and regional grid (*top* SWAN v40.91; *bottom* SWAN updated version). The depth is illustrated with *blue line* whereas the setup is shown in continuous red line for parent grid and in cross *red line* for child grid

The first curve of Fig. 10 shows the evolution along the transect on the parent grid (continuous line) and the child grid (cross-line) with the first manual version. The imposed wave setup of 0.07 m is applied at the deepest point of the transect. The setup is re-calculated along the transect depending on the depth. The second curve shows the same figure obtained with the new automated version of SWAN.

5 Conclusions

In the present paper, the difficulties in simulating wave setup when SWAN code is used in nested applications are highlighted by considering a case study based on the 2010 storm 'Xynthia'.

A first analysis of empirical formulations found in the literature and adapted to our study location was undertaken. Such formulations confirmed that the wave setup is reasonably reproduced by SWAN in this specific event.

After this succinct validation of the setup simulation with SWAN 2D on the Xynthia case, the new solution to improve the treatment of wave setup along open boundaries in SWAN model is presented. The use of this updated code in studying the case of Xynthia provides a real benefit in the accuracy and ability to simulate this parameter. Consequently, this new version of SWAN opens up new possibilities for simulating various storms with embedded grids taking into account the wave setup without the intervention of the user, leading to more robust and reproducible results.

GlobOcean is developing its modeling tools to use unstructured grids to reproduce the sea-states with SWAN. This kind of grids would improve the setup simulations.

Acknowledgements GlobOcean would like to thank the EGIS ports authorities who supported this work.

References

1. http://swanmodel.sourceforge.net.
2. International News. (2010). "AIR Estimates Windstorm Xynthia Insured Losses at $2 to $4.1 Billion". *AIR Worldwide* (Wells Publishing, Inc.). Retrieved March 18, 2010, ClaimsJournal.com
3. Yanagishima, S., & Katoh, K. (1990). Field observation on wave setup near the shoreline, Proceedings of the 25th International Conference on Coastal Engineering. Vol. 1 (pp. 95–108). ASCE: New York, Chapter 7.
4. Goda, Y (2000). *Random seas and design of maritime structures* (p. 443). World Scientific Publishing Co.
5. Raubenheimer, B. R., Guza, T., & Elgar, S. (2001). Field observations of wave-driven setdown and setup. *Journal of Geophysical Research, 106*(C3), 4629–4638.
6. Stockdon, R. A., Holman, P. A., Howd, A. H., & Sallenger, Jr. (2006). Empirical parameterization of setup, swash, and runup. *Coastal Engineering, 53*, 573–588.
7. Gorlay, M. R. (1992). Wave setup, run-up and beach water table: Interaction between surf zone hydraulics and groundwater hydraulics. *Coastal Engineering, 17*, 93–144.
8. Dingemans, M. W., Radder, A. C., & de Vriend, H. J. (1978). Computations of the driving forces of wave- induced currents. *Coastal Engineering, 11*, 539–563.

Construction of the Numerical Wave Databases Anemoc-2 on the Mediterranean Sea and the Atlantic Ocean Through Hindcast Simulations Over the Period 1979–2010

Anne-Laure Tiberi-Wadier, Amélie Laugel and Michel Benoit

1 Introduction

From 2003 to 2007, CEREMA (Centre for expertise and engineering on risks, urban, and country planning, environment, and mobility, Brest, France) and EDF R&D LNHE (National Hydraulic and Environment Laboratory, Chatou, France) have been collaborating to build two continuous wave databases through numerical hindcast simulations. The first one covers the North-East part of the Atlantic Ocean, the English Channel, and the North Sea [2, 3]. The second one covers the Mediterranean Sea [12, 13].

These first versions of the databases, called ANEMOC, for "Atlas Numérique d'Etats de Mer Océanique et Côtier" (i.e. Numerical Atlas of Oceanic and Coastal Sea States), are available through Internet since 2008 (see: http://anemoc.cetmef.developpement-durable.gouv.fr/). Wave climate analyses were performed based on the simulated time series (distributions of individual sea-state parameters, seasonal effects, estimation of extreme values, etc.). These data have been used in a number of research projects and engineering studies.

In order to ameliorate these results, and complementary to other wave databases [5, 6], from 2010 to 2013, these institutes continued their collaboration, through the

A.-L. Tiberi-Wadier (✉)
Centre D'Étude et D'expertise Sur Les Risques, La Mobilité et L'Aménagement (CEREMA),
155 Rue Pierre Bouguer, BP 5, 29280 Plouzané Cédex, France
e-mail: Anne-Laure.Tiberi-Wadier@cerema.fr

A. Laugel · M. Benoit
Laboratoire D'Hydraulique Saint Venant (CEREMA, EDF R&D, ENPC),
6 Quai Watier, BP 49, 78401 Chatou, France
e-mail: Amelie.Laugel@edf.fr

M. Benoit
e-mail: Michel.Benoit@edf.fr

P. Gourbesville et al. (eds.), *Advances in Hydroinformatics*,
Springer Water, DOI 10.1007/978-981-287-615-7_9

Saint-Venant Laboratory, in order to create new versions of these wave databases called ANEMOC-2. Following improvements have been made:

i. The Atlantic model covers a larger area: main parts of the Atlantic Ocean, from 63°S to 80°N;
ii. The temporal coverage of the atlases is larger: 32 years, from 1979 to 2010;
iii. Wave spectrum discretization is finer: 36 directions and 32 frequencies (from 0.0345 to 0.66 Hz, corresponding to periods from 1.5 to 29 s);
iv. The resolution of the wind field used for forcing the wave model is finer in time and space: 1 h and 0.312° × 0.312° resolution;
v. The computational grids are refined: resolution of about 800 m to 1 km along the French coasts.

This article presents the construction of the wave models ANEMOC-2 and their associated results. The methodology is described, focusing with more details and results on the Mediterranean model of ANEMOC-2, then results of both Mediterranean Sea and Atlantic Ocean atlases are expressed. Section 2 presents the setup of the models and wind data used as forcing. Section 3 is devoted to the calibration step using altimetry data, and highlights the accuracy of the wave model ANEMOC-2 compared to satellite measurements. In Sect. 4, comparisons of the wave simulations with buoy measurements are achieved, first for the validation step and then focusing on particular storm events. Finally, conclusion and perspectives are exposed in Sect. 5.

2 Setup of the Wave Models

2.1 The Spectral Wave Code TOMAWAC

The simulations are performed with the numerical wave model TOMAWAC [1], which is a third generation spectral model, solving the wave action density balance equation. TOMAWAC is a module of TELEMAC-MASCARET hydro-informatics suite (www.opentelemac.org). It models the evolution in space and time of the directional wave spectrum under unsteady wind forcing. It can take into account the input of energy from the wind, nonlinear wave-wave interactions, dissipation due to white-capping, bottom friction, and depth-induced breaking in shallow water. TOMAWAC is very suitable for coastal modeling applications as the computations are performed on unstructured irregular grids. This allows refining the computational mesh in areas of interest and in case of complex bathymetry and shoreline.

For the present version of ANEMOC-2, tidal and current effects are not taken into account. The models are run with water depths corresponding to the mean tidal level. The wave spectrum is divided into 32 frequencies (from 0.034 to 0.66 Hz, i.e., from 1.5 to 29 s) and 36 directions (constant angular resolution of 10°). All ANEMOC-2 models have been constructed over 32 years (1979–2010).

Regarding physical processes, the Mediterranean model and the oceanic Atlantic model include the effects of wind input, nonlinear wave-wave interactions, and dissipation due to white-capping. Bottom friction dissipation and dissipation through depth-induced breaking are taken into account for the Atlantic coastal model only.

A set of seven sea state parameters are calculated from the directional spectra and stored on output with a 1-hour resolution: (i) significant wave height, (ii) energetic period, (iii) mean period, (iv) peak period, (v) mean direction, (vi) angular spreading, and (vii) wave power.

2.2 The Mediterranean Wave Model

The Mediterranean wave model covers the whole Mediterranean Sea, from 30° to 46° North in latitude, and from 6° West to 37° East in longitude. The size of the mesh is variable. It is about 800 m along the French coasts, from 3 to 8 km along the Spanish and Italian coasts, about 25 km along North Africa coasts and a maximum resolution of 50 km is imposed over the rest of the domain. The mesh is composed of 15,343 nodes and 28,159 elements. Bathymetry data are derived from the Europe base (LEGOS). Figure 1 represents the mesh used in the simulations and the associated mean sea level bathymetry.

No wave spectrum is imposed at the boundaries of this model. We consider that the waves are generated only inside the model due to wind forcing.

The computational time step for this model is 100 s. Each year is simulated independently, starting the simulation on the 22nd of December of the previous year to initialize the model. It takes about 30 h to simulate a whole year by performing a parallel computation on 12 processors.

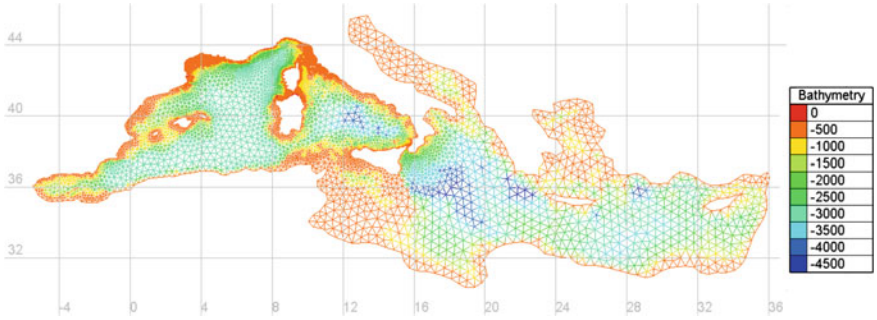

Fig. 1 Bathymetry, resolution and spatial domain of the Mediterranean model of ANEMOC-2

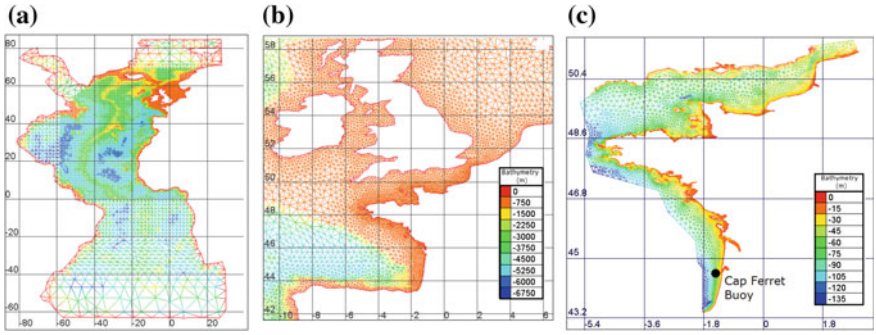

Fig. 2 Bathymetry, resolution and spatial domains of Oceanic **a**, **b** and Coastal **c** meshes of ANEMOC-2. Black node locates of the Cap Ferret buoy

2.3 The Atlantic Wave Models

The Atlantic Ocean is modeled by means of two unstructured nested grids. The first grid covers the Atlantic Ocean (Fig. 2a) from 63°S to 80°N with a resolution of 1.875° in the southern hemisphere, increasing up to 0.6° in the North East Atlantic to finally match with 20 and 10 km resolution along the European and French coasts, respectively (Fig. 2b). This "oceanic" grid provides wave spectra boundary conditions to the second mesh, named "coastal" grid and focusing on the Atlantic, English Channel, and North Sea French coasts (Fig. 2c). The coastal grid covers the English Channel and reaches the UK coast with a resolution of 3 to 4 km. It also covers the Atlantic and North Sea French shoreline from the 100 m depth isobaths and reaches the French coast with a 1 km resolution. Both grids have been constructed at mean sea level using Gebco (www.gebco.net) and Europe (LEGOS) bathymetric databases. The oceanic mesh comprises 13,426 nodes and 22,548 elements, while the coastal one comprises 16,295 nodes and 29,018 elements.

The time steps for the oceanic and coastal models are 300 and 180 s, respectively. One-year simulation lasts about 8 and 12 h for the each model on a 24 processors computer.

2.4 Wind Data Used to Force the Models

The wave models are forced with the 10 m wind fields from the Climate Forecast System Reanalysis (CFSR) database [15] from the National Oceanic and Atmospheric Administration (NOAA). Wind components are provided every hour, on a regular grid with resolution of 0.312° over a period of 32 years, from 1979 to

2010. Their high spatial and temporal resolutions promote their use as an alternative to reanalysis with a 6-hour time resolution. Therefore, a better representation of the storm events is expected, in particular regarding the times of the peak of the storms. These wind fields are linearly interpolated on the computational grids shown on Figs. 1 and 2.

3 Calibration of the Wave Models

3.1 General Methodology and Data

In the study, the numerical wave models have been calibrated by comparing the results of the simulations with the altimeter measurements from the GlobWave database ([14], www.globwave.org). This database provides altimeter observations of calibrated significant wave height H_{m0} for a set of eight satellites, over the period 1985–2014.

For the calibration step, simulations results of H_{m0} are linearly interpolated in space and time on the satellite tracks. Once this collocation step is achieved, two sets of data are considered: the observed series (x_i), and the simulated series (y_i). To assess and quantify the matching between both, four statistical parameters are calculated, as defined in Table 1. These statistical parameters are computed on various domains with different sizes: the whole computational domain, or sub-domains in areas of interest, or at the scale of cells of 0.5° × 0.5° or 1° × 1°.

Several methods have been tested to optimize calibration: (i) test of different combinations of physical laws implemented in TOMAWAC concerning generation, dissipation and energy transfer, (ii) modification of the coefficients in the physical laws, (iii) calibrating wind fields by comparison quantile/quantile with scatterometers measurements, and (iv) adjusting the elevation of the wind imposed in the model.

After comparing these various options, we decided not to modify the wind fields but to select the most accurate physical source and sink terms (option (i) above), and if necessary modifying their default parameters and setting (option (ii) above).

Table 1 Statistical parameters used to compare series of simulations results (y_i) with reference date (x_i)

Bias	Root mean square error (RMSE)	Scatter index	Symmetric slope
$\frac{1}{n}\sum_{1}^{n}(y_i - x_i)$	$\sqrt{\frac{1}{n}\sum_{1}^{n}(y_i - x_i)^2}$	$\sqrt{\frac{\sum_{1}^{n}(y_i - x_i)^2}{\sum_{1}^{n} x_i^2}}$	$\sqrt{\frac{\sum_{1}^{n} y_i^2}{\sum_{1}^{n} x_i^2}}$

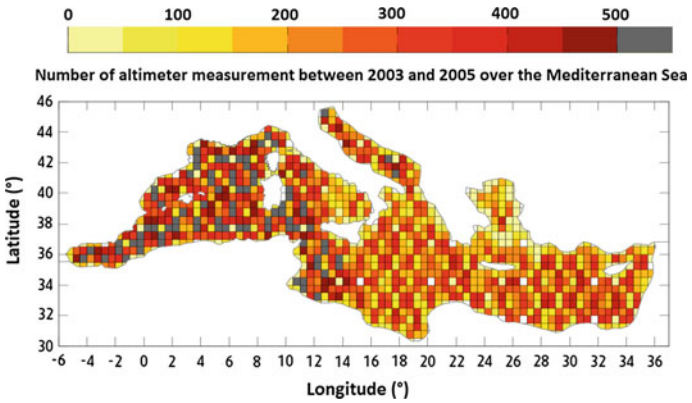

Fig. 3 Number of altimeter measurements from ENVISAT and ERS-2 between 2003 and 2005 over the Mediterranean Sea

3.2 Calibration of the Mediterranean Model

3.2.1 Altimeter Data Used for the Calibration

In order to calibrate the Mediterranean wave model, observations of H_{m0} from satellites Envisat (2002–2012) and ERS-2 (1995–2009) are used. Indeed, these satellites offer a good spatial coverage over the Mediterranean Sea of about 80 km between tracks, with a return period of 35 days.

Figure 3 shows the number of satellite measurements per cells of 0.5° × 0.5° in size over the Mediterranean Sea during the period 2003–2005. This figure shows that altimeter measurement coverage is dense enough to allow the calculation of statistics, especially on the west Mediterranean area (more than 200/300 measurements over each cell of 0.5° × 0.5°).

The selected parameterization of the Mediterranean model ANEMOC-2 corresponds to: (i) Janssen parametrization [9, 10] for the wind-wave induced generation, (ii) Discrete Interaction Approximation [8] for the nonlinear quadruplet interactions and (iii) Komen et al. parameterization [11] for the white-capping dissipation. In this formulation, the dissipation coefficient has been lowered to 3.2 and the weighting coefficient to 0.4. Indeed, the modification of these two coefficients avoids too much underestimation of the wave height.

3.2.2 Maps of Statistical Parameters

As results, the plots of Fig. 4 represent the statistical parameters calculated for the significant wave height H_{m0} between ANEMOC-2 results and the altimeter measurements, on cells of 0.5° × 0.5° over the period 2003–2005 on the west Mediterranean Sea which is our area of interest.

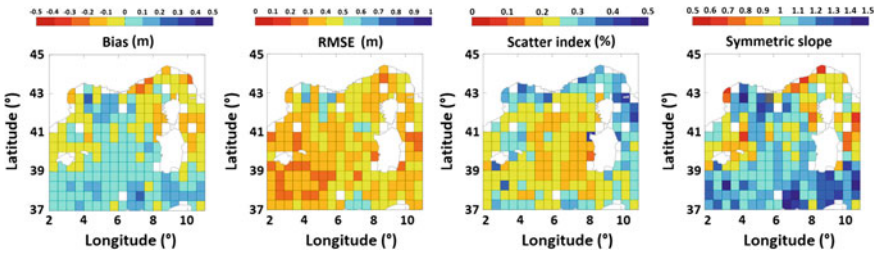

Fig. 4 Bias, RMSE, scatter index and symmetric slope between ANEMOC-2 H_{m0} wave height and the altimeters measurements over the period 2003–2005

In comparison with altimeter data, ANEMOC-2 has a negative bias in the area around Corsica, at the East of Marseille and along the Italian and Spanish coast. This means that the wave model slightly underestimates the altimeters observations in these areas. On the contrary, it presents a positive bias in the area of the Lion Gulf and more generally offshore, corresponding to a slight overestimation of H_{m0} from the wave model. However, ANEMOC-2 results show a bias between −10 and 10 cm over a large area, which is quite a good approximation of the observations.

The analysis provided by the other statistical indices corroborates these results. At the South of the Balearics, the root mean square error (RMSE) is between 25 and 30 cm. It increases and reaches about 50 cm near the French coast, and occasionally exceeds 50 cm. The scatter index shows a variation similar to that of the RMSE. The statistics are better offshore than in coastal areas. It is about 10 to 25 % offshore, and reaches 25 to 35 % near the French coast. The higher values are at the East of Corsica (45 % locally). The values calculated for the symmetric slope are similar to the values of the bias, and so confirm the areas of overestimation and underestimation of the wave atlas.

This difference between offshore and coastal area could be explained by two reasons: (i) the complex orography of the Mediterranean coast involves complications for the simulation of atmospheric forcing in a first time, and then for the simulation of shallow water physical processes in the wave model and (ii) the altimetry observations are biased in the vicinity of the shoreline because of the instrument initialization needed in case of altimeter path from the land to the ocean. Therefore, the validation step provided by means of coastal buoy will help to define the accuracy of ANEMOC-2 in coastal area.

3.2.3 Scatter Plots

The comparison between altimeter measurements and simulation wave fields has shown that depending on the areas, the wave model does not offer the same characteristics. Figure 5 represents the scatter plots for simulations wave height and altimeter measurements over the period 2003–2005. Three different areas are considered, which are shown by the plots of Fig. 5a, d, g. Green points represents

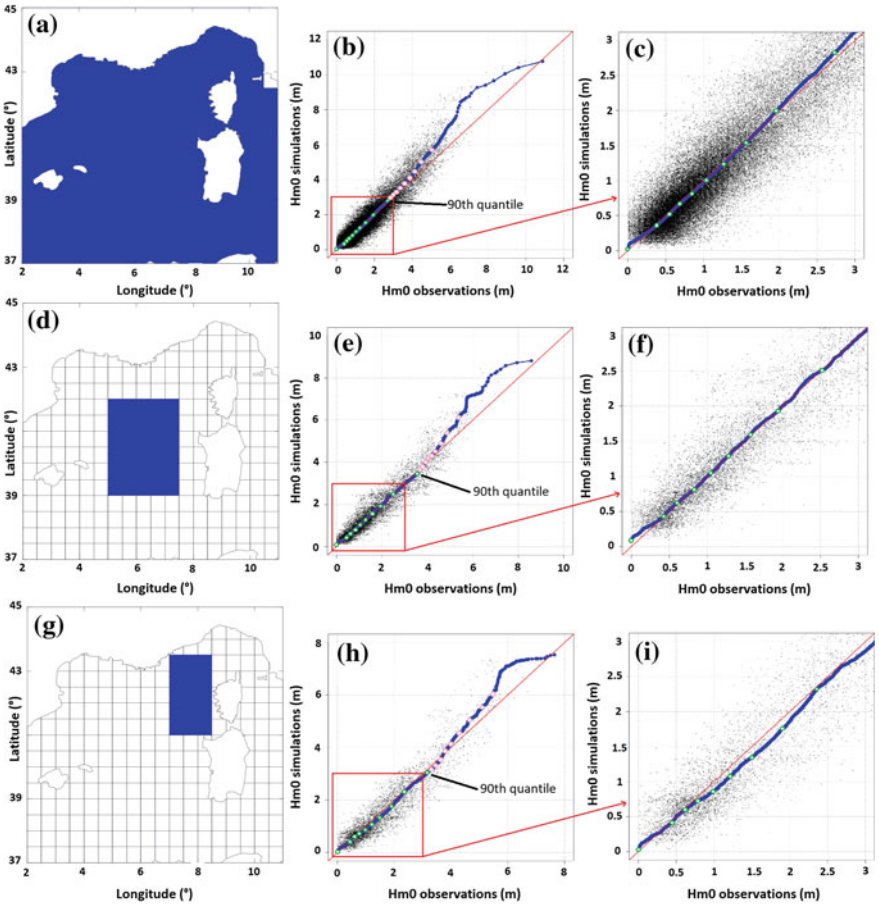

Fig. 5 Scatter plots of simulations wave height H_{m0} and altimeter measurements over three areas of the Mediterranean Sea

from the 10th to the 90th percentile and pink points represents from the 91th to the 99th percentile. The 90th percentile is indicated with an arrow. In each line of graphics, the first figure represents the area considered for the calculation (Fig. 5a, d, g), the second one represents the scatter plot for the whole distribution (Fig. 5b, e, h), and the last one (Fig. 5c, f, i) represents a zoom focusing on the waves height inferior to 3 m, corresponding approximately to the 80th or 90th percentile.

In the first area, the scatter plot shows that ANEMOC-2 results are very good up to the 90th percentile. From the 90th to the 95th percentile, we see a moderate overestimation. The overestimation is larger for waves higher than the 95th percentile. The tail of the distribution (values higher than the 99th percentile) is not very well modeled. The overestimation is 3.6 % for the 90th percentile and it is about 13 % for the 99th percentile.

In the second area in which the bias is positive, the scatter plot shows that ANEMOC-2 results are good up to the 96th percentile. For higher values, we see a moderate overestimation. For the 90th percentile, we see 2 % of underestimation. The overestimation is about 14 % for the 99th percentile.

Finally, the third area in which the bias is negative, the scatter plot shows that ANEMOC-2 slightly underestimates the wave values between the 40th and the 93th percentile. For the higher percentiles, we always notice an overestimation, but less than in the second area.

3.3 Calibration of the Atlantic Model

The calibration of the Atlantic model was performed over the period 2000–2009 with the GlobWave altimeters [14] from Topex/Poseidon, ERS-2, Geosat Follow On, Envisat, Jason-1, and Jason-2. It allowed to select the best parameterization of TOMAWAC for this oceanic model, which corresponds to the combination of the Janssen model [9, 10] for the wind-wave induced generation, the so-called BAJ parameterization [4] for the white-capping dissipation and the Discrete Interaction Approximation (DIA) for the nonlinear quadruplet interactions [8]. The parameterization of the coastal model is similar for these three physical processing, while dissipation terms from Thornton and Guza [16] and from the JONSWAP campaign [7] are respectively added for the bathymetric breaking and the bottom friction processes.

As a result of the calibration step, Fig. 6 illustrates the bias between the ANEMOC-2 H_{m0} and the six altimeters observations over the period 2007-2009 focusing on the Bay of Biscay and North Sea areas over a grid a 1° × 1°. Over the North East Atlantic Ocean, the bias varies between ± 10 cm which corresponds to a quite good reproduction of the H_{m0}. To be more specific, the bias value is −6 cm in the Bay of Biscay and −5 cm in the North Sea area, corresponding, respectively, to scatter index of 12 and 13 % and to RMSE of 37 and 34 cm. Therefore, this analysis characterizes the slight underestimation of the H_{m0} from ANEMOC-2 in comparison to the altimeter observations.

4 Validation of the Models Against Buoy Data

4.1 General Methodology

After the calibration step, the simulation results were validated by comparison with uncorrelated measurements from buoy data. The data sets used here are fully independent from the ones used in the previous section.

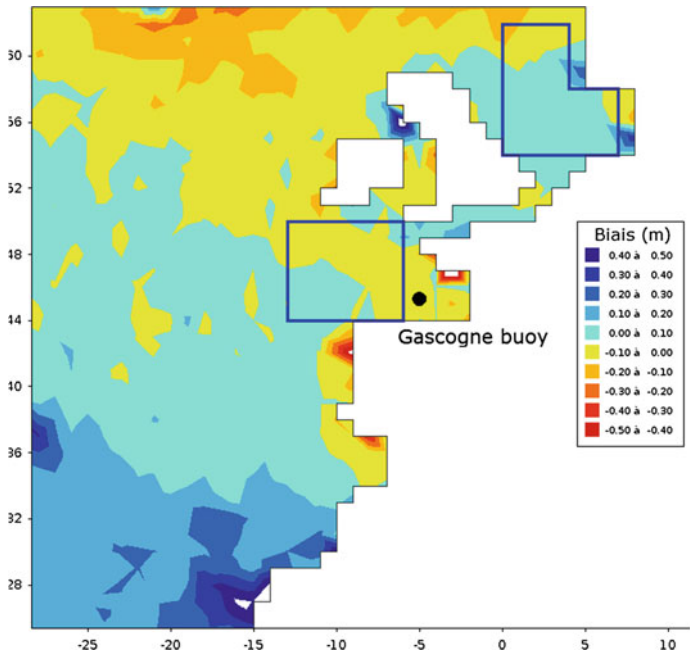

Fig. 6 Spatial repartition of the bias (m) between H_{m0} from ANEMOC-2 and GlobWave altimeters over the period 2007–2009 focusing on the Bay of Biscay and North Sea areas over a grid of 1° × 1° resolution. Black node locates of the Gascogne buoy

4.2 Validation of the Mediterranean Model

4.2.1 Buoy Data Used for the Validation

To validate the Mediterranean model, 23 buoys located in the west Mediterranean Sea have been used (see Fig. 7). Table 2 shows their period of measurement beginning in 1998, where dark colors represent an annual temporal coverage greater than 50 %. Each color corresponds to the databases providing observations: Candhis and Météo-France along the French coast, RON (*Rete Ondametrica Nazionale*) along the Italian coast and XIOM (*Xarxa d'Instrumentacion Oceanografica I Meteorologica*) along the Spanish coast.

4.2.2 Statistical Parameter Calculated with Buoy Data

Table 3 shows the statistical parameters bias, RMSE, scatter index, and symmetric slope calculated over the period 2002–2008 with the available buoy data during this period. White cells correspond to the significant wave height H_{m0}, and gray ones to the mean period T_{02}.

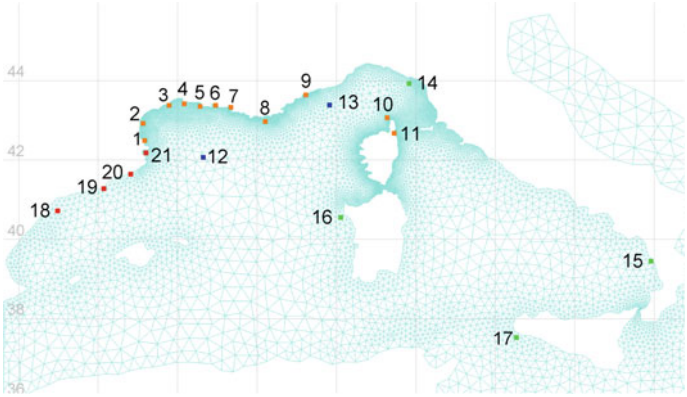

Fig. 7 Buoys location in the West Mediterranean Sea

Table 2 Temporal coverage of buoy measurements used for the validation step of the Mediterranean model of ANEMOC-2

Buoy	French buoys (candhis database)													Météo France buoys		Italian buoys				Spanish buoys			
	Banyuls	Leucate	Sete Marseillan	Sete Frontignan	Sete	Espiguette	Camargue	Port de Bouc	Marseille	Porquerolles	Nice	Cap Corse	Bastia	Lion	Cote d'azur	La Spezia	Cetraro	Alghero	Mazara	Tortosa	Llobregat	Blanes	Rosas
Buoy number	1	2	3	3	3	4	5	6	7	8	9	10	11	12	13	14	15	16	17	18	19	20	21
1998																							
1999																							
2000																							
2001																							
2002																							
2003																							
2004																							
2005																							
2006																							
2007																							
2008																							
2009																							

The bias between simulations and buoy measurements is low for the significant wave height, except on Porquerolles, Nice, and Cap Corse buoys, for which the bias is negative and quite important (between −13 and −41 cm). Apart from these three buoys, the accuracy of simulation results is homogeneous. Bias is almost always negative on buoys. RMSE shows errors between 3 and 8 cm for coastal buoys, which is satisfactory. Scatter index is about 30 to 40 %. Symmetric slope is often equal or lower than 1, which reflects the underestimation trend of the database on the buoys.

Table 3 Statistical parameters between simulations results and in situ observations over the period 2002–2008

Buoys/Statistic indices		Bias		RMSE		Scatter index		Symmetric slope	
		H_{m0} (cm)	T_{02} (s)	Hm^0 (cm)	T_{02} (s)	H_{m0} (%)	T_{02} (%)	H_{m0}	T_{02}
Offshore buoys	Lion	5	−1.4	22	1.1	25	31	1.1	0.7
	Azur	−4	−1.8	11	2.5	28	43	1.0	0.7
French buoys (Candhis database)	Banuyls	−9	−0.8	7	0.5	31	26	1.0	0.9
	Leucate	−13	−0.6	7	0.9	36	30	0.9	0.9
	Sète	−9	−0.6	5	0.6	30	27	0.9	0.9
	Sète Frontignan	−9	−1.0	4	1.2	30	36	0.9	0.8
	Espiguette	−11	−0.6	8	0.8	29	27	1.0	0.9
	Camargue	−5	−0.7	5	0.4	28	24	1.0	0.8
	Port-de-Bouc	1	−0.7	3	0.5	26	27	1.1	0.8
	Marseille	−6	−1.1	7	0.9	41	36	0.9	0.7
	Porquerolles	−41	−0.8	26	0.4	39	22	0.7	0.8
	Nice	−13	−1.2	5	0.7	37	33	0.8	0.8
	Cap Corse	−19	−0.6	24	0.7	30	21	0.9	0.9
	Bastia	−8	−1.0	3	0.4	37	30	0.9	0.8
Italian buoys (RON database)	Alghero	−3	−0.8	8	2.0	20	32	1.0	0.8
	Cetraro	1	−1.1	6	3.4	26	43	1.0	0.7
	La Spezia	−13	−0.5	6	1.5	28	30	0.9	0.9
	Mazara	1	−0.7	7	1.0	20	26	1.0	0.9

We can notice that the statistical parameters highlight better simulations of the significant wave height than the mean period. As example, the negative bias between T_{02} simulations and observations is approximately −1 s for the coastal buoys, and reaches −1.8 s for the offshore buoys.

4.2.3 Scatter Plot for the Comparison with Buoy Data

Figure 8 shows scatter plots for the simulation wave height H_{m0} and data of Banyuls, Camargue, Nice and Azur buoys.

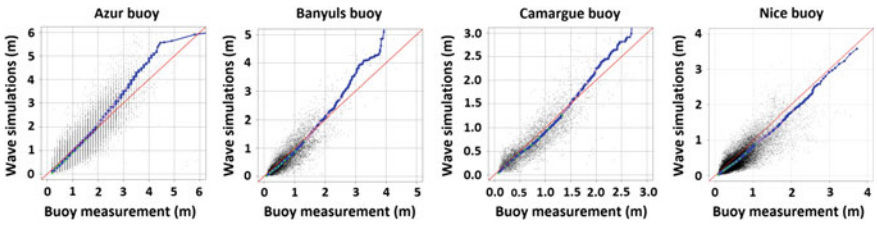

Fig. 8 Scatter plots between wave height H_{m0} simulations and measurements of offshore and coastal buoys over the period 2002–2008 (see temporal coverage of buoy measurements Table 2)

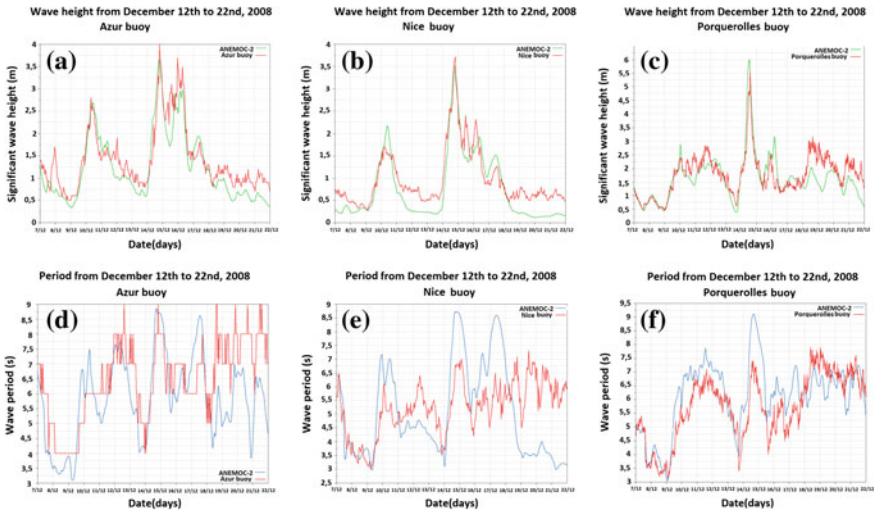

Fig. 9 Comparison of ANEMOC-2 results and in situ observations during the storm from 7th to 22nd of December, 2008. Configurations **a**, **b**, and **c** correspond to H_{m0} at Azur, Nice, and Porquerolles buoys, respectively, and configurations **d**, **e**, and **f** correspond to T_{02} at Azur, Nice and Porquerolles buoys, respectively

For the three buoys Camargue, Banyuls, and Azur, even if the global bias is slightly negative, the tail of the distribution (for the wave height higher than the 90th percentile for Azur, and than the 95th percentile for the two others) is overestimated. On the contrary, Nice buoy tends to underestimate the whole distribution. On this buoy, simulations seem to show a constant bias for all the wave height.

4.2.4 Study of a Storm Event: From 7th to 22nd of December, 2008

Figure 9 compares significant wave height H_{m0} and mean period T_{02} calculated by the wave model and measured by the offshore buoy Azur (−2430 m), and the two coastal buoys Nice (−270 m) and Porquerolles (−90 m)—see location Fig. 7. Figure 9 a–c compare the H_{m0} for ANEMOC-2 and in situ observations, and Fig. 9d–f compare T_{02}. Figure 9a and d represents Azur buoy, 9b, e represent Nice buoy and 9c, f represent Porquerolles buoy.

In offshore and coastal areas, a good agreement is observed between ANEMOC-2 and buoys measurements for both H_{m0} and T_{02}. During this storm, peaks of H_{m0} coincide with peaks measured by the buoys. We can notice a slightly underestimation of the simulations after the peak of the event.

Variations of wave period are also well simulated on the three buoys. However, at the end of the event, the model underestimates the period on Azur and Nice buoys ($\sim$2 s). Near the coast, for Nice and Porquerolles buoys, period is overestimated at the peaks of the event ($\sim$2 s).

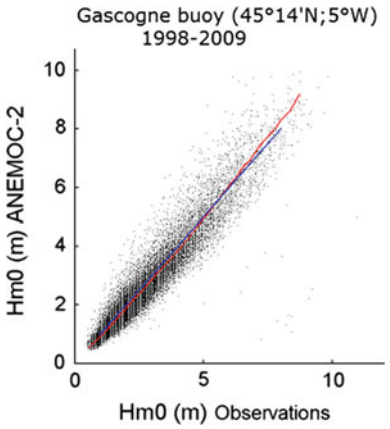

Fig. 10 Quantile-quantile diagram of ANEMOC-2 H_{m0} (m) and Gascogne buoy observations built over the period 1998–2009

4.3 Validation of the Atlantic Model

4.3.1 Comparison with Buoy Data

Météo-France and Candhis buoys have been used to validate the oceanic and coastal models over the period 1996-2009. As example, the quantile-quantile diagram (Fig. 10) of the H_{m0} at the Gascogne buoy (see location Fig. 6) indicates the good correspondence between simulations and in situ observations until 7 m, then ANEMOC-2 tends to overestimate the highest value of H_{m0}.

At coastal locations, the validation step informs about the good reproduction of the H_{m0} and the mean period T_{02} along the Atlantic shoreline, while results slightly degrade along the English Channel and North Sea where wave-current interactions should be taken into account as tidal effects are significant in these areas.

4.3.2 Study of a Storm Event: From 6th to 16th of February, 2009

The night between 9th and 10th of February 2009, the storm Quinten hit the Atlantic French coast with strong winds reaching 140 km/h at La Pointe du Raz (Brittany). Figure 11 shows the ability of the ANEMOC-2 significant wave height H_{m0} and mean period T_{02} to reproduce the wave climate during this extreme event at two locations: the Gascogne buoy (−4500 m, see location Fig. 6) and the Cap Ferret buoy (−54 m, see location Fig. 2c). Configurations Fig. 11a, b compare the H_{m0} of ANEMOC-2 and in situ observations in both offshore and coastal areas. In addition, configurations Fig. 11c, d compare the T_{02} between simulations and observations for both locations.

A general good agreement can be found between ANEMOC-2 and observations for H_{m0} and T_{02} in oceanic and coastal areas. Between 6th and 16th of February 2014, in situ observations characterized the storm Quinten by two peaks of H_{m0},

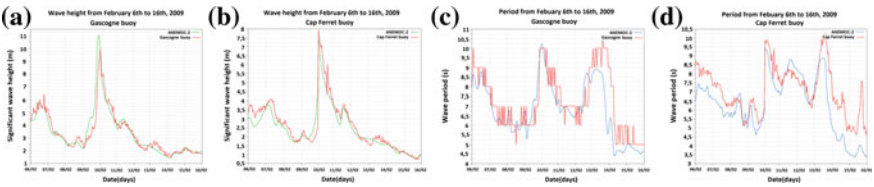

Fig. 11 Comparison of ANEMOC-2 results and in situ observations during the Quinten storm (6th to 16th of February 2009). Configurations **a** and **b** correspond to H_{m0} at Gascogne and Cap Ferret buoys, respectively and configurations **c** and **d** correspond to T_{02} at Gascogne buoy and Cap Ferret respectively

also well reproduced by ANEMOC-2. The highest of both peaks reaches a H_{m0} of about 10 m at the Gascogne buoy and up to 8 m at the Cap Ferret buoy. For this storm, it can be seen that ANEMOC-2 slightly overestimate the peak of H_{m0} ($\sim$1 m) at Gascogne buoy, and slightly underestimate it at the Cap Ferret buoy (0.60 m). In addition, mean period T_{02} from ANEMOC-2 reproduces quite well the variations of the observations, while its value slightly underestimates them ($\sim$1 s).

5 Conclusion

Two new numerical wave databases, called ANEMOC-2, have been built over the period 1979–2010 covering the Mediterranean Sea and the Atlantic Ocean, and focusing on the French coasts. They provide several wave parameters (significant wave height H_{m0}, mean period T_{02}, peak period T_p, mean direction θ_m,…) with a high spatial (800 m to 1 km along the French coasts) and temporal (1 h) resolution. The methodology developed to construct these databases has been explained, focusing on the Mediterranean model: parameterization of the TOMAWAC wave model, calibration and validation steps by means of altimetry and in situ observations, respectively. Their analyses provide an assessment of many characteristics of both databases. For example, in offshore areas, the comparison with altimeter wave heights shows that the absolute value of the bias is lower than 10 cm over large areas. This bias also informs that in the Bay of Biscay and in the eastern part of Corsica, ANEMOC-2 slightly underestimates mean values of H_{m0}, while the wave atlases slightly overestimates them in the south of France and North Sea areas. In addition, the validation step shows that the bias on the Mediterranean coastal buoys is almost always negative, while it remains acceptable with a bias lower than 10 cm for most of cases.

Furthermore, ANEMOC-2 ability to reproduce extreme wave climate has been highlighted by analysis of two particular storm. For five locations, numerical simulations and in situ observations of H_{m0} and T_{02} have been compared. On the one hand, the study of Quinten storm peak shows that the Atlantic model tends to overestimates highest values of H_{m0} at some places, as seen at the Gascogne buoy for instance, while it also appears to slightly underestimate the H_{m0} highest value at

other places, as seen on the coastal Cap Ferret buoy. On the other hand, the study has shown that the Mediterranean model slightly overestimates the highest H_{m0} even in areas where the mean values of H_{m0} are slightly underestimated. Therefore it will not cause any underestimation of H_{m0} highest values, which is a highly valuable characteristic.

Finally, ANEMOC-2 databases will benefit from future improvements. For example, wave-current interactions will be taken into account in the coastal model around the Atlantic, English Channel, and North Sea French coast where tidal effects are important. The spectral decomposition will also be applied to better separate and characterize the wind sea and swell components. Lastly, ANEMOC-2 databases will be updated by means of CFSRv2 reanalysis for the years 2011 and following ones.

Acknowledgements The authors thank the NOAA for the provision of the CFSR reanalysis used in this work. Institutes IFREMER, Météo-France, CEREMA, ISPRA (RON), XIOM, LEGOS, and GEBCO are thanked, respectively for altimeter and scatterometer observations, in situ observations and bathymetric databases.

References

1. Benoit, M., Marcos, F., & Becq, F. (1996). Development of a third generation shallow-water wave model with unstructured spatial meshing. *Proceedings of 25th Conference on Coastal Engineering*, Orlando (FL, USA), ASCE, pp. 465–478.
2. Benoit, M., & Lafon, F. (2004). A nearshore wave atlas along the coasts of France based on the numerical modelling of wave climate over 25 years. *Proceedings of 29th Conference on Coastal Engineering* (ICCE'2004), Lisbonne (Portugal), pp. 714–726.
3. Benoit, M., Lafon, F., & Goasguen, G. (2008). Constitution et exploitation d'une base de données d'états de mer le long des côtes françaises par simulation numérique sur 23 ans. Base ANEMOC en Atlantique—Manche—Mer du Nord. *European Journal of Environmental and Civil Engineering, 12*(1–2), 35–50.
4. Bidlot, J.-R., Janssen, P. A. E. M., & Abdalla, S. (2007). A revised formulation of ocean wave dissipation and its model impact. ECMWF Tech. Rep. Memo. Reading.
5. Charles, E., Idier, D., Thiebot, J., le Cozannet, G., Pedreros, R., Ardhuin, F. et al. (2012). Present wave climate in the Bay of Biscay: Spatiotemporal Variability and trends from 1958 to 2001. *Journal of Climate, 25*, 2020–2039. doi:10.1175/JCLI-D-11-00086.1.
6. Dodet, G., Bertin, X., & Taborda, R. (2010). Wave climate variability in the North-East Atlantic Ocean over the last six decades. *Ocean Modelling, 31*, 120–131.
7. Hasselmann, K. et al. (1973). Measurements of wind-wave growth and swell decay during the Joint North Sea Wave Project (JONSWAP). Deutschen Hydrographischen Zeitschrift.
8. Hasselmann, S., & Hasselmann, K. (1985). Computations and parameterizations of the nonlinear energy transfer in gravity-wave spectrum. Part I: a new method for efficient computations of the exact nonlinear transfer integral. *Journal of Physical Oceanography, 15*, 1369–1377.
9. Janssen, P. (1989). Wave induced stress and the drag of air flow sea waves. *Journal of Physical Oceanography, 19*, 745–754.
10. Janssen, P. (1991). Quasi-linear theory of wind-wave generation applied to wave forecasting. *Journal of Physical Oceanography, 21*, 1631–1642.

11. Komen, G. J., Hasselmann, S., & Hasselmann, K. (1984). On the existence of a fully developed wind-sea spectrum. *Journal of Physical Oceanography, 14*, 1271–1285.
12. Morellato, D., & Benoit, M. (2009). Construction d'une base de données d'états de mer le long des côtes françaises méditerranéennes par simulations rétrospectives couvrant la période 1979–2008. Colloque CM2, Tunis, décembre 2009.
13. Morellato, D., & Benoit, M. (2010). Constitution of a numerical wave data-base along the French Mediterranean coasts through hindcast simulations over 1979–2008. Colloque AIPCN MMX Congress 2010, Liverpool, Mai 2010.
14. Queffeulou, P., & Croize-Fillon, D. (2009). La mesure satellite de hauteur de vague par altimètre. Etat des lieux, application à la climatologie et à la modélisation des états de mer. *Proc. AMA 2009. Les Ateliers de Modélisation de l'Atmosphère*, Toulouse.
15. Saha, S., et al. (2010). The NCEP climate forecast system reanalysis. *Bulletin of the American Meteorological Society, 91*, 1015–1057.
16. Thornton, E. B., & Guza, R. T. (1983). Transformation of wave height distribution. *Journal of Geophysical Research, 88*, 5925–5938.

Evolution of Surge Levels Inside Harbour Basins: The Case of Le Havre Harbour

Vanessya Laborie, Philippe Sergent and François Hissel

1 Introduction

The Office of Major Risks of the Seine Estuary (ORMES), the Greater Maritime Port Council of Le Havre (GPMH) and CEREMA, among others, decided to carry out common studies on submersions inside the urban and the industrial port area of Le Havre. A Technical Commission for the Study and Evaluation of Maritime Submersions in the Seine Estuary was created to improve the collective knowledge on physical processes linked to maritime surge levels that may occur in the future or that already took place in the past.

The objectives of the project are:

- to get a better knowledge of water levels and wave heights near the coast;
- to determine the location of water entrance in inlands and to calculate the volumes of waters inside harbour basins, at the mouth of the Seine Estuary and in storage areas of the floodplain;
- to get better knowledge of the exposure of elements at stake to submersion hazard.

That is why a hydrodynamic model of surge levels and associated submersions in the Seine bay has been built, in order to: improve the knowledge about the interactions between waves, currents, tide and surge levels inside the Seine Estuary

V. Laborie (✉)
Laboratoire Saint-Venant (EDF R&D, CETMEF, École Des Ponts ParisTech), CEREMA, 134, CS 60039, 60280 Route de Beauvais, Margny Lès Compiègne, France
e-mail: vanessya.laborie@cerema.fr

V. Laborie · P. Sergent · F. Hissel
CEREMA, 134, CS 60039, 60280 Route de Beauvais, Margny Lès Compiègne, France
e-mail: philippe.sergent@cerema.fr

F. Hissel
e-mail: francois.hissel@cerema.fr

P. Gourbesville et al. (eds.), *Advances in Hydroinformatics*,
Springer Water, DOI 10.1007/978-981-287-615-7_10

and in harbour basins; bring better knowledge about the phenomenon of submersion waves in harbours and, in particular, about harbour seiches and amplification of the surge level signal from the sea to the harbour basins.

2 Study Site and Description of the Numerical Model

The study site is the Seine Bay. A two-dimensional numerical model of the Seine Estuary based on the shallow water equations has been developed, based on an existing model of downstream Seine, in order to simulate water levels at the mouth of the river and in the estuary and to evaluate the ability of the numerical model to reproduce harbour seiches in the harbour basin called René Coty. This model, whose bathymetry has been updated for the current study with more recent data provided by the GPMR and the GPMH and for the south-eastern part of the model with EMODNET data [1], has initially been built and used to assess the impact of new buildings in the harbour Port 2000 [2] and is based on TELEMAC2D [3].

The model covers the entire Seine bay up to Tancarville bridge on the Seine river. As shown in Fig. 1, its maritime boundary takes an east to west direction from Antifer to Ouistreham. Upstream, the model takes into account water levels or flow rates of the Seine River at Tancarville.

This two-dimensional model does not take into account overflow from the stream beds of the Seine river to the floodplain. The model features 96876 finite elements and is composed of 49740 nodes. Its mesh is represented in Fig. 1. It is about 55 km long from east to west and 45 km long from south to north.

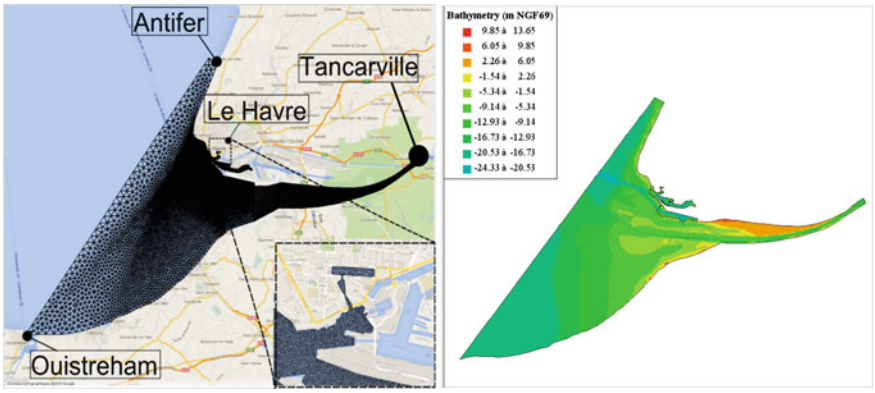

Fig. 1 Extension and location of the numerical model of the Seine Estuary (on the *left*) and bathymetry of the numerical model (on the *right*)

3 Data and Simulation Parameters

In a first step, some input data have been collected to feed the model for storms Johanna, which occurred in 2008 (March, 10th) and Xynthia in 2010 (February 27 and 28). To study seiches, the additional storm event of 2004 was also investigated. Three kinds of data have been collected: winds and pressure fields upon the interest area, the tide signal at the maritime boundary and water levels of the Seine river at Tancarville.

3.1 River Flow and Water Levels of the Seine River

At the eastern part of the model, at Tancarville bridge, water levels were given by the port of Rouen for 2004, 2008 and 2010. Forcing the numerical model with flow discharges instead of water levels at Tancarville bridge was also tested with no obvious benefit on the quality of results in the area of Le Havre harbour.

3.2 Winds and Pressure Fields

The winds and pressure fields considered for this study are CFSR (Climate Forecasting System Reanalysis) data provided by the NOAA (American National Oceanic and Atmospheric Administration). The resolution of the climatic model is about 0.312 and the temporal step is 1 h [4]. CFSR data were spatially interpolated on our study area to feed the model with the intensity and direction of the wind at each node of the mesh of the numerical model.

3.3 Maritime Boundary Conditions

The global signal at the maritime boundary of the model, located on a line linking Ouistreham and Antifer, as shown in Fig. 1, is the sum of two components: the predicted tide and the meteorological surge level. Both have been provided by a numerical model for surge levels on the Atlantic coast developed in Saint-Venant hydraulics laboratory and described in [4]. This numerical model has been calibrated on maregraphic data observed in 18 harbours located along the French coastline and for 10 events among which Johanna, Xynthia and 2004 storms. It is forced by the NEA (North East Atlantic) atlas (Prior solution) provided by LEGOS and, as the numerical model of the Seine bay, it uses CFSR winds and pressure fields.

4 Calibration of the Numerical Model on Johanna and Xynthia Storms

4.1 Calibration Methodology

The calibration of the numerical model consists in the adjustment of numerical parameters, which are the friction coefficient and the influence coefficient of the wind, to minimize some statistical indicators evaluating the difference between water levels predicted by the numerical model at several locations in the Seine Bay (6 locations for Xynthia event and 7 locations for Johanna storm). These calibration points are represented in Fig. 2.

The statistical indicators are: the absolute difference between observations and rephased numerical results (i.e., considering that the peaks of both signal, calculated and observed, occur at the same time), the elapsed time between the moment at which the numerical model predicts high tides and low waters and the moment at which they were really observed, the difference between water levels at the storm peak and the standard deviation of the error of water levels obtained for peaks at low waters and high tides. The two former indicators are the most important considered in the following of the study.

4.2 Calibration on Johanna Storm

The first event on which the numerical model of the Seine Bay was calibrated is Johanna, which occurred on 9 and 10 March 2008. It reached north-west Europe during high tide coefficients and provoked a lot of damage [5].

Calculations are realised on the time slice between 4th and 13th March 2008. The duration of simulations is about 10 days, i.e. 776,700 s and the storm peak occurred at about 560,000 s after the beginning of simulation. Figure 3 presents results obtained near Port 2000, as shown in Fig. 2.

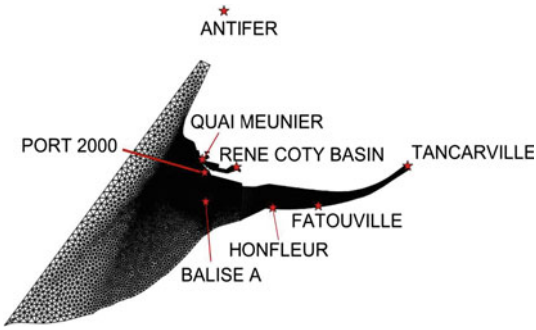

Fig. 2 Location of available maregraphic data for the calibration of the numerical model of the Seine Bay for Johanna and Xynthia events

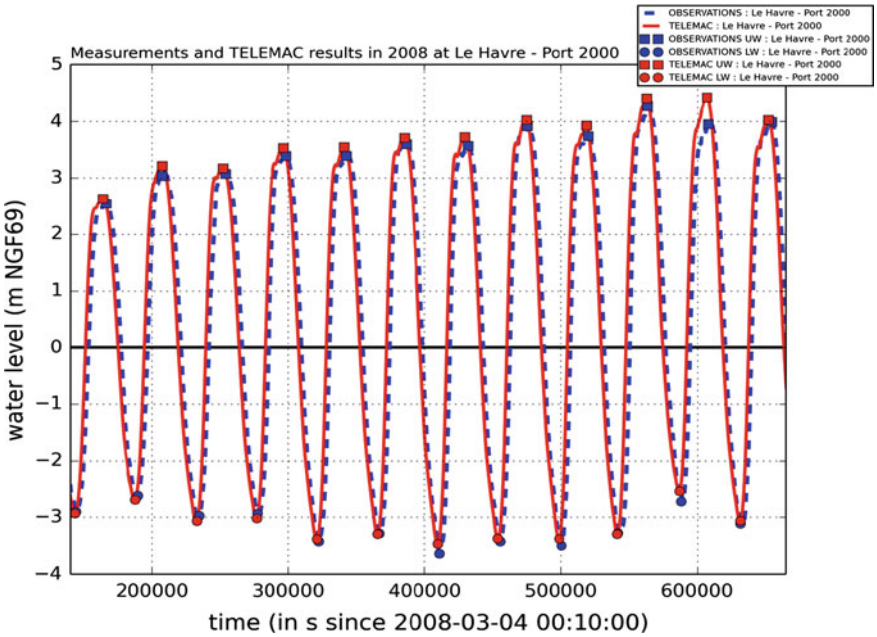

Fig. 3 Comparison between measurements and numerical results at Port 2000 for Johanna storm (*UW* = high tides; *LW* = low waters)

Table 1 summarizes the calibration results in terms of indicators for Johanna, as already described in Sect. 4.1.

As water levels at Tancarville are the measurements, the fact that the error there is 0 is normal.

For other calibration points, the average error is less than 5 cm, except for Antifer, Fatouville and Port 2000, where it reaches 15 cm. As the bad representation of one peak can roughly influence the average error and considering both the standard deviation of numerical results around observations which is about 10 cm and the error at the peak storm, which is smaller than 15 cm except at Fatouville, the numerical model can be considered as calibrated for Johanna storm. It can be noticed that water levels are particularly well represented by the numerical model during this event at Honfleur, Balise A and Quai Meunier.

4.3 Calibration on Xynthia Storm

The second event on which the numerical model of the Seine Bay was also calibrated (together with Johanna to improve the results for both events) is Xynthia, which occurred on 27th and 28th February 2010. Xynthia was a severe European windstorm, with a powerful storm surge topped by battering waves up to 7.5 m

Table 1 Results for Johanna event in terms of indicators evaluating the difference between TELEMAC numerical results and observations at high tide peaks

Location	Maximum error (m)	Minimum error (m)	Average error (m)	Standard deviation of the error (m)	Absolute error for the storm peak (m)
Tancarville	0.0	0.0	0.0	0.0	0.0
Fatouville	0.33	−0.10	0.13	0.11	0.31
Honfleur	0.34	−0.12	0.01	0.12	−0.03
Balise A	0.26	−0.15	−0.03	0.11	0.09
René Coty basin	0.30	−0.11	0.01	0.11	0.12
Quai Meunier	0.40	−0.05	0.05	0.11	0.00
Port 2000	0.47	0.04	0.15	0.10	0.13
Antifer	0.53	0.10	0.21	0.10	0.20

high, hitting at high tide, which crossed Western Europe between 27th February and 1st March 2010. It reached a minimum pressure of 967 mb on 27th February. In France, at least 51 people were killed, with 12 more said to be missing [6].

Calculations are realised on the time slice between 24th February and 2nd March 2010. The duration of simulations is about 7 days, i.e. 518,400 s and the storm peak occurred at about 377,400 s after the beginning of the simulation. Figure 4 represents the minimum and maximum errors between TELEMAC results and observations at eight locations at high tides and the error at the storm peak for Xynthia storm.

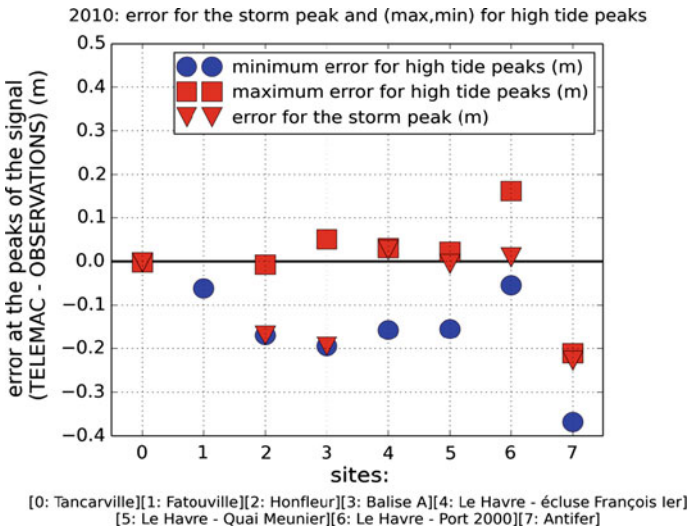

Fig. 4 Comparison between measurements and numerical results at eight sites for Xynthia storm at high tides

Table 2 Results for Xynthia event in terms of indicators evaluating the difference between TELEMAC numerical results and observations

Location	Maximum error (m)	Minimum error (m)	Average error (m)	Standard deviation of the error (m)	Absolute error for the storm peak (m)
Tancarville	0.0	0.0	0.0	0.0	0.0
Fatouville	0.42	−0.06	0.10	0.17	0.42
Honfleur	−0.01	−0.17	−0.08	0.07	−0.17
Balise A	0.05	−0.20	−0.06	0.09	−0.20
Quai Meunier	0.02	−0.16	−0.04	0.07	−0.01
Port 2000	0.16	−0.05	0.05	0.07	0.01
Antifer	−0.21	−0.37	−0.28	0.07	−0.23

Table 2 summarizes the calibration results in terms of indicators for Xynthia, as already described in Sect. 4.1.

As Fig. 3 and Table 2 stress it out, the numerical model is well adjusted at high tides, particularly at Le Havre Quai Meunier at the storm peak. The average error is less than 10 cm at each validation point, except at Antifer. Nevertheless, the only way to fit better with Antifer observations would be the calibration of the numerical model of surge levels along the Atlantic Coast at Antifer. Indeed, Antifer belongs to the maritime boundary of the numerical model of the Seine Bay and the tide signal at this point is the tide signal calculated by the surge levels' numerical model.

4.4 Conclusions About the Calibration of the Numerical Model of the Seine Estuary

As Tables 1 and 2 show, numerical results for Johanna and Xynthia storms show an average error smaller than 5 cm at le Havre Quai Meunier and in René Coty harbour basin. The absolute error at the storm peak is less than 1 cm at the former location for both storm events and around 10 cm inside of the latter for Johanna. Indeed, no data was available at this location for Xynthia.

As the purpose of the study was to study the processus of the seiches inside of Le Havre harbour, the numerical model of the Seine Bay fed by the numerical model of surge levels on the Atlantic Coast and CFSR data was considered to be calibrated.

5 Study of Seiches Inside of "Rene Coty" Harbour Basin

As data in René Coty harbour basin were available for 2008 (Johanna) and 2004 events, the processes of seiches inside the harbour basin named René Coty were studied for these two events. Johanna is described in Sect. 4.2 and in [5]. The 2004

event, which occurred from 16th December to 20th December 2004, is a storm which generated 130 km/h winds and hit northern France, including Paris, killing 6 people and leaving thousands of homes without power [7].

5.1 Definition and Characterization of a Seiche

Seiches are long-period standing oscillations in a partially closed basin or in a locally isolated part of a basin. The resonant (eigen) periods of seiches are determined by basin geometry and depth and in natural basins may range from tens of seconds to several hours. The set of seiche eigenfrequencies (periods) and associated modal structures are a fundamental property of a particular basin and are independent of the external forcing mechanism [8]. The period of the seiche can coaresely estimated by the following formula :

$$\frac{4L}{\sqrt{(gh)}}, \tag{1}$$

where L is the length of the basin (in m), g the gravity (9.81 m/s^2) and h the water depth (m) inside the basin.

Furthermore, the fact that the signal amplitude increases at the back of the harbour basin is normal, as the signal at the entrance of the harbour (Quai Meunier) corresponds to water levels just outside of it.

5.2 Identification of Seiches Inside of René Coty Harbour Basin

In addition to the usual components of water level, harbour seiches (as well as wave setup and runup) can increase the elevation reached by water during a storm [9]. Figure 5 represents the instantaneous surge levels for 2008 event at two specific locations in Le Havre Harbour: at the entrance of the harbour near "Quai Meunier" and inside of René Coty harbour basin. It also represents the difference between both signals.

Figure 5 shows that seiche effects (longitudinal and transverse oscillations determined by the basin dimensions) can be observed in Le Havre Harbour with amplitudes of 0.3 m or more (0.41 m for 2008). The seiche peaks correspond to the surge levels peaks and are therefore linked to meteorological processes. Differences in the maximum water level observed during 2004 and 2008 events between the René Coty Harbour basin tide gauge in Le Havre harbour and the other gauge near may be attributable to seiche effects induced by the storm surge. The peak water level during Johanna storm in René Coty harbour basin is 0.14 m higher than the peak near Le Havre Quai Meunier.

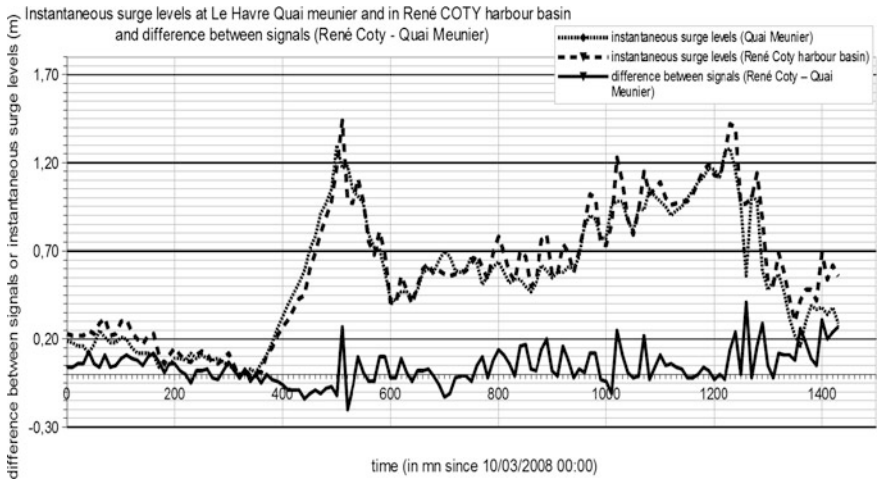

Fig. 5 Observed instantaneous surge levels at Le Havre Quai Meunier and in René Coty harbour basin and identification of the existence of a seiche phenomenon in René Coty harbour basin during 2008 storm event

It can be noticed that, in the case of René Coty basin, formula (1) leads to a signal period equal to 40 mn (L = 6 km and h = 10 m) which is in good adequation with that deduced from observations.

5.3 *Numerical Simulation of Seiches in Le Havre Harbour for Johanna Storm Event*

Figure 6 shows the difference in water levels between René Coty harbour basin and Quai Meunier obtained with measurements and with the numerical model of the Seine Bay. The amplitude of the oscillations calculated by the numerical model is widely underestimated, whereas the frequency is quite similar. Moreover, it can be noticed that the maxima for the numerical model occur at the same time as surge levels' maxima, as it is observed. The fact that amplitude is underestimated can be linked to the smoothing the numerical model realises on surge levels' oscillations, as it can be seen in Fig. 7 which represents the observed and calculated surge levels at Quai Meunier for 2008 storm event. The diffusive character of the semi-implicit numerical scheme used in TELEMAC2D can explain the smoothing of both oscillations.

Several issues have to be investigated to find the explanation to this phenomenon:

- considering the way a pure signal imposed at the entrance of the harbour propagates and if seiches occur;

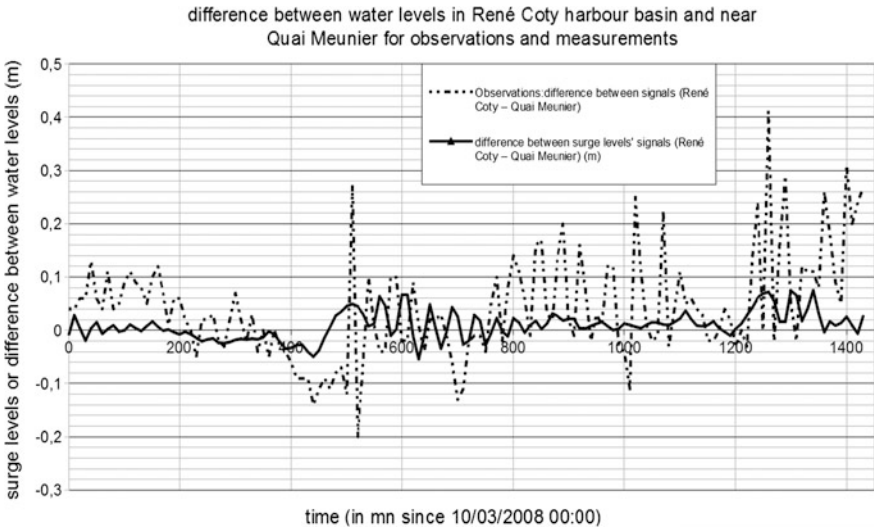

Fig. 6 Comparison between seiches values obtained with observations and numerical results for Johanna storm

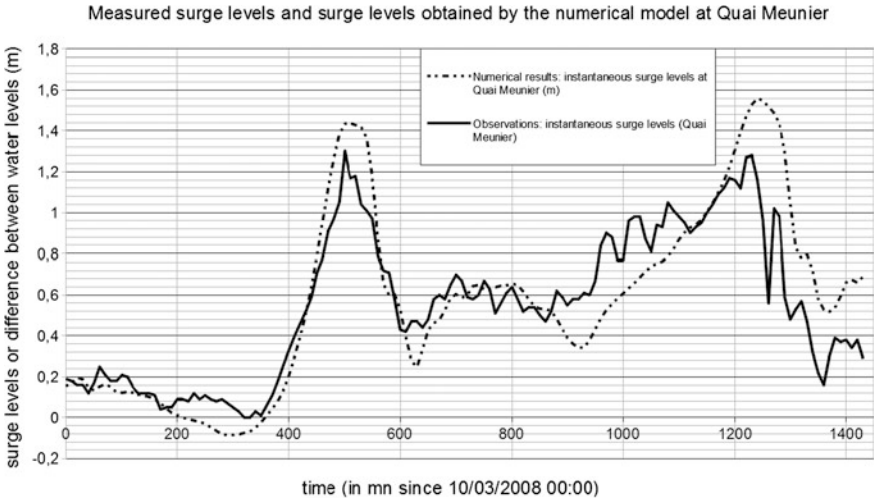

Fig. 7 Observed and calculated surge levels at Quai Meunier for Johanna storm

- considering other locations outside of the harbour to see if oscillation occurs despite the fact they are not located in a place where oscillations should be generated. A numerical artificial apparition of seiches should then be suspected;
- testing other mesh refinement or model extension to see if a better representation of seiches is then obtained with another numerical model.

6 Conclusions

A numerical model of the Seine estuary based on TELEMAC2D has been built to study the evolution of surge levels from the ocean to the harbour area of Le Havre and, in particular, evaluate the amplification of the global signal and the apparition of seiche inside René Coty harbour basin. It was calibrated on the Johanna and Xynthia storm events and was used to draw the evolution of surge levels from the ocean to Le Havre (quai Meunier) and then compare the signal obtained inside René Coty harbour basin. As shown by measurements, numerical results stress out the apparition of an oscillating signal which is added to the signal at the entry of the Harbour. If surge levels are well reproduced, the real oscillations are smoothed. The process of amplification of seiche inside the port in René Coty Harbour basin is still underestimated by the model and further numerical investigations must be realised to reproduce the magnitude of these harbour oscillations.

Acknowledgments and Thanks We would like to thank the Greater Maritime Port Councils of Le Havre (GPMH) and Rouen (GPMR) for bathymetric and observation data they provided for the needs of this study. The sea level observations of Le Havre—Quai Meunier are the property of SHOM and GPMH and are available on the REFMAR website (http://www.refmar.shom.fr).

References

1. http://www.emodnet-hydrography.eu/.
2. Boyer, B. (2012). Convention GPMH-CETMEF. *Projet de création d'une châtière, rapport de courantologie*, décembre (47 p.).
3. Hervouet J. M. (2006). *Hydrodynamics of free surface flows* (390 p.). Chichester: Wiley.
4. http://www.cfs.ncep.noaa.gov/cfsr/.
5. Levy, F. (2013). *Construction d'un modèle de surcotes sur la façade atlantique*, rapport provisoire, avril 2013.
6. http://www.en.wikipedia.org/wiki/List_of_European_windstorms.
7. Cariolet et al. (2010). *Aspects météo-marins de la tempête du 10 mars 2008 en Atlantique et en Manche*, Norois, *215*(2), 11–31.
8. Rabinovich, A. B. (2009). Seiches and harbour oscillations. In Y. C. Kim (Ed.), *Handbook of Coastal and Ocean Engineering*. Singapore: World Scientific.
9. Forbes, D. L., Manson, G. K., Charles, J., Thompson, K. R., & Taylor, R. B. (2009). *Halifax harbour extreme water levels in the context of climate change: scenarios for a 100-year planning horizon*. Geological Survey of Canada, open file 6346, p. 26.

Characteristics of Sumatra Squalls and Modelling of the Squall-Generated Waves

Duy Khiem Ly, Cheng Ann Tan and Qiang Ma

1 Introduction

There have been historical records of squall lines leading to disasters in the ocean. It was narrated that in 1878, the British frigate Eurydice was attacked by a squall line and quickly sank together with its crew. Another large battleship, Mermaid, from Russia had the same fate when faced with a squall line in the Baltic Sea in 1893. On-land observations of severe squall lines in the early twentieth century also recorded one that hit San Francisco in 1910, with peak wind speed of 28 m/s, causing strong tremor within a short period. Another squall line was recorded in Moscow in 1937. It had maximum wind speed of 35 m/s, collapsed many houses and uprooted many trees [1]. One of the earliest definitions related to the squall line can be found in the book of Nalivkin [2]. It briefly described the concept of "squall storm" as a sudden and significant growth in the average wind speed without air rotation in the areas of strong storms with clouds and rain.

Tropical squall lines were initially introduced to the scientific community through reports of meteorologists involved in weather forecasting in West Africa [3]. A typical squall line in the tropics was described to contain a row of

D.K. Ly (✉)
Energy Research Institute, Nanyang Technological University, CleanTech One, 1, CleanTech Loop, #06-09, Singapore S637141, Singapore
e-mail: dkly@ntu.edu.sg

C.A. Tan
DHI Water and Environment (S) Pte. Ltd, CleanTech One, 1 CleanTech Loop, #03-05, Singapore S637141, Singapore
e-mail: tca@dhigroup.com

Q. Ma
Laboratoire Innovative City, Polytech Nice Sophia, 930 Route Des Colles, 06903 Sophia-Antipolis, France
e-mail: qiang.ma1987@gmail.com

P. Gourbesville et al. (eds.), *Advances in Hydroinformatics*,
Springer Water, DOI 10.1007/978-981-287-615-7_11

Cumulonimbus clouds at the edge of a broad downdraft region. The downdraft region was positioned under a precipitating trailing anvil cloud which was eliminated from the Cumulonimbus towers. The squall line associated with a frontal-like temperature decrease usually foreran the downpour rain from the row of Cumulonimbus clouds by just a few minutes [4].

Cloud solving simulations were carried out using COAMPS with a 3 km horizontal grid to perceive the origin of the squall phenomenon in the Sumatra island [5]. The modelling results confirmed that line convection is initiated by warm sea surface temperature, and the key factor intensifying and directing the Sumatra squall is the diurnal circulations driven by the difference in temperature between land and sea. The outcome also revealed that the high relieves along west Sumatra and north-west Malaysia alter the wind direction from westerly to north-westerly, triggering low-level convergence with the south-west summer monsoon. Another study presented the consistency between coincident and collocated weather radar data and radar images of a Sumatra squall obtained by the European Remote Sensing (ERS) satellite over the southern coast of Singapore [6]. The rain rate in the region of heavy rainfall estimated from the ERS backscatter signature appeared to be in agreement with the one obtained from the weather radar data.

In general, there is a limitation of observation in network and high-resolution observed data, making it difficult to further study the generation and propagation of the Sumatra squall. The present paper does not attempt to further describe the physics of squalls. Rather, the objective is to study the resulting effect of squalls on wave generation. There were evidences of squall line surge which caused large freak waves of up to 6 m high to strike the Daytona Beach in 1992 [7]. In the local context, the risk of such squall-generated waves on the coastal structures of Singapore has never been studied. The study aims first to find out the characteristics of Sumatra squalls and then perform wind-wave simulation to investigate the resulting waves generated by Sumatra squalls. The results help to evaluate the potential impact of the squall-generated waves on coastal structures and offshore activities in Singapore.

2 Methodology

Sumatra squalls were first characterised by synthesising previous knowledge about the physics of squall lines in tropical regions.

In the next stage, a mesoscale meteorological model (WRF) was used to downscale and simulate the Sumatra squall propagation. The downscaled model was calibrated and validated against measured wind data at several weather stations to acquire the most precise wind dataset for the wind-wave model. Other modelling parameters of the wind-wave model such as wave breaking coefficient, bottom roughness value and white capping coefficient were assumed from previous wind-wave simulations having similar domain area and using the same modelling tool—MIKE 21 Spectral Wave (Mike 21 SW) model. The wind-wave model was

run afterwards and its outputs were used to depict the wave profile and the impact caused by the wave.

A wind dataset of the Sumatra squall is featured by three wind field parameters: squall speed (V_f), peak wind intensity (U_p) and squall width (W_s). The wind dataset obtained from WRF model allowed us to find out the importance of these parameters. The last stage of the study involved producing synthetic wind datasets by changing the values of V_f, U_p and W_s to create many scenarios from their various combinations. Each synthetic wind dataset corresponds to each scenario of the wind-wave model. All these scenarios of the wind-wave model were then run to explore how influential the three parameters were in the wave generation process.

3 Characteristics of Sumatra Squalls

3.1 Definition

Sumatra squalls are recorded yearly, mainly between March and November [8]. They are defined by the National Environmental Agency (NEA) as lines of thunderstorms formed over Sumatra island in Indonesia or the Malacca Strait usually at night and travelling eastward to reach Singapore and Malay Peninsula during sunrise. Sumatra squalls are accompanied by strong gusts (i.e. temporary increase in wind speed) and heavy rains of about one to two hours as they sweep across the island [6]. They can reach up to hundreds of kilometres in length, often oriented from north to south, occasionally from east to west, with several-hour lifespan. Gusts of 11.0–25 m/s, intense enough to uproot trees, together with the highest daily rainfall of up to 134 mm were measured during the passages of some Sumatra squalls in the past [9]. Figure 1 represents the formation and movement of one Sumatra squall observed in 2006.

3.2 Distinct Formation

The origin of Sumatra squalls can be explained by the special geographic locations of surrounding islands. Particularly, the narrow Strait of Malacca separates the Malay Peninsula on the east and the island of Sumatra on the west. The formation of squall lines is detected in unstable atmospheric environments. When there are strong winds (which often occur during the south-west monsoon) blowing across the mountain range in Sumatra, mountain waves on the leeward side are created, causing an unstable atmosphere. Likewise there were findings that small atmospheric disturbances over the sea in the middle and/or northern part of Malacca Strait also lead to instability of the air [10]. Furthermore, relatively warmer water from the Malacca Strait may supply extra source of moisture for convective

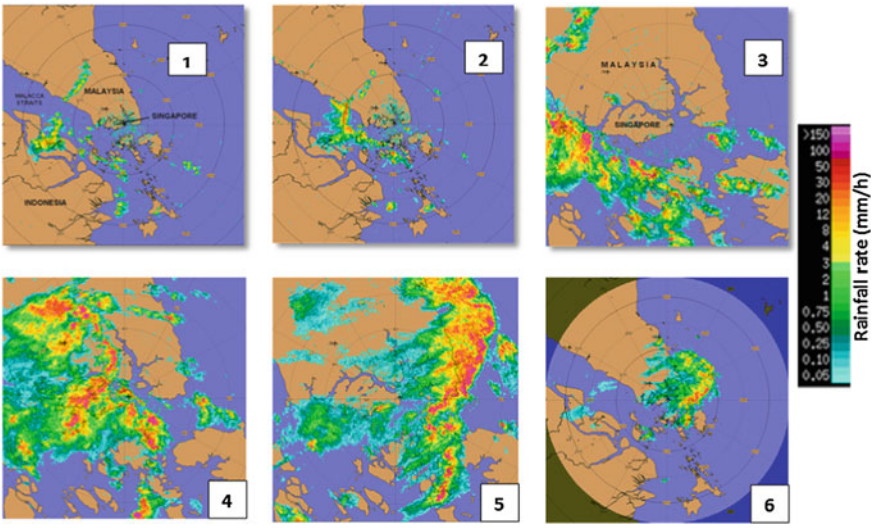

Fig. 1 Radar images showing the passage of a Sumatra Squall over Singapore (from *1* to *6*)

development. As the atmosphere becomes highly unstable, thunderclouds grow in situ and merge into squall lines. The squall lines steered by the westerly, southerly or south-westerly winds (between 2 and 4 km height), then propagate towards Singapore and the west coast of Malay Peninsula [11, 12]. In general, convergence of air stream over a large area and at levels lower than 1 km is the foremost condition for the development of Sumatra squalls. The other propitious conditions to trigger the squall lines include high moisture, moderate low-level wind shear in a typical tropical temperature profile with mild lapse rate.

3.3 Structure and Dynamics

A squall line in the tropics mostly comprises of a convective region forming at the leading edge and a region of trailing stratiform rain, or sometimes called a stratiform region, to the rear [13]. The conceptual model of a typical squall line in vertical cross section is depicted in Fig. 2. The squall line boundary as recognised by weather radars is represented by the thick black line (radar echo boundary). The visible boundaries of the clouds are indicated by the scalloped line, part of which (cloud top) lies above the radar echo boundary. The two stippling areas, enclosed by heavy grey curves, are radar bright band areas where the radar detects high precipitation particles. For tropical squall lines, maximal radar reflectivity is usually returned by convective cells at low levels. Within the convective region, the mature cells initiate an intense updraft that part of it can rise till the cloud top. The updraft is accompanied by a downdraft from mid to upper levels, leading to heavy

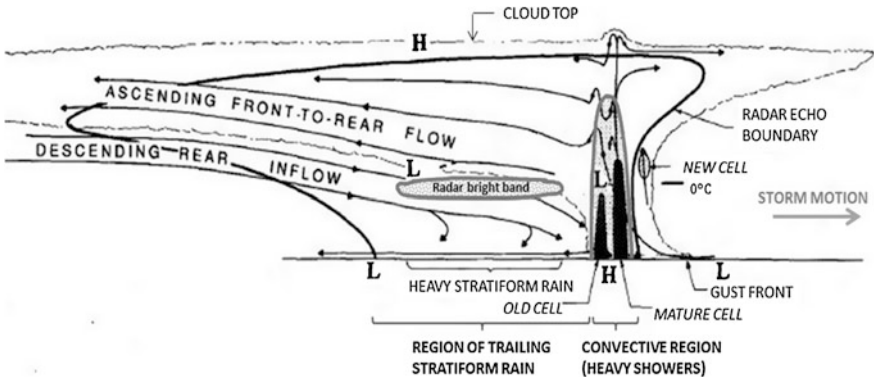

Fig. 2 Conceptual model in a vertical cross section through a squall line (adapted from [14])

convective showers. The old cells also create the similar process but at weaker intensity. New cells are produced right ahead of the convective region. H and L are to indicate areas of high (cold) and low (warm) pressure fields respectively [14].

In addition, an overall upward motion of air is found to start near the gust front, passing through the convective region and going up gradually in the stratiform region at the mid to upper levels. This can be explained by the strength imbalance between the cold pool below the convective region and the low-level shear. On the other hand, air also flows downward from the rear side towards the gust front. The flow results from air acceleration at mid-levels, caused by the low pressure field creating a horizontal pressure gradient. Large CAPE (Convective Available Potential Energy) value usually enhances this rear-to-front flow, which can fuel the gust front. Wind speed in general increases gradually from the rear to the convective region. After the wind passes the gust front, its speed drops dramatically [6].

4 Simulating the Sumatra Squall on 2 April 2012

4.1 Selection of the Event

In the early morning of 2 April 2012, a violent Sumatra squall spread over Singapore within 1.5 h, bringing heavy downpour. The heaviest rainfall of 95.2 mm/h was observed in the central area [15]. Figures 3 and 4 are 'zoom-in' charts merely for a period of 5 min, describing how fast the wind fluctuated within seconds in terms of speed and direction. The squall gusts during the period of interest seemed to blow eastward, following the movement of the squall. The squall on 2 April was selected to study because it met the interest of an intense squall and the availability of the measured wind data used for calibrating and validating the downscaled WRF model.

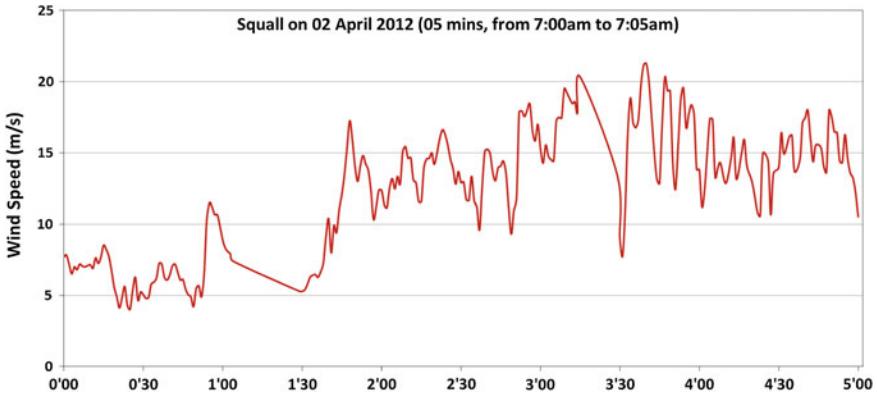

Fig. 3 Highest squall gusts observed at Pengerang weather station

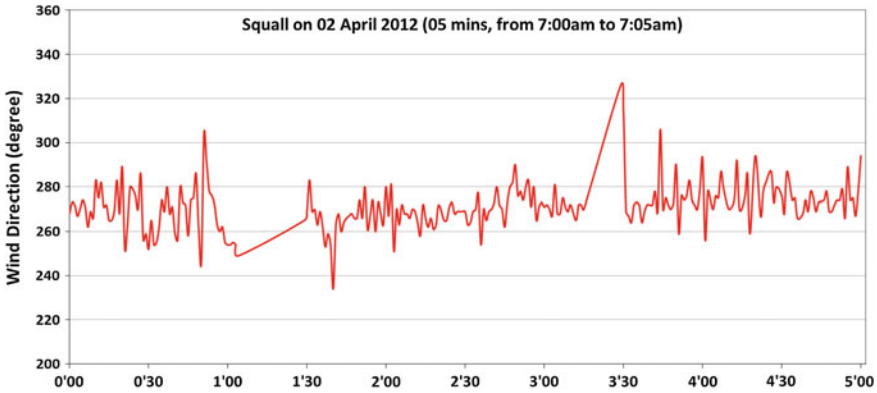

Fig. 4 Change in direction of the highest squall gusts observed at Pengerang weather station

4.2 Model Set-up

The model has three closed boundaries (illustrated by pink lines in Fig. 5), which are located sufficiently far from Singapore according to local fetch-limited condition for fully developed wave heights (i.e. 200 km wind fetch). Furthermore, the Malacca Strait is included extensively due to the fact that the squall line originated from Sumatra island, passing the strait before sweeping across Singapore. In addition, there are three points described by three orange dots under Singapore land on the map in Fig. 5. These points are to be studied later. One of the points was named Pengerang (PGRN) because its location is right at the Pengerang weather

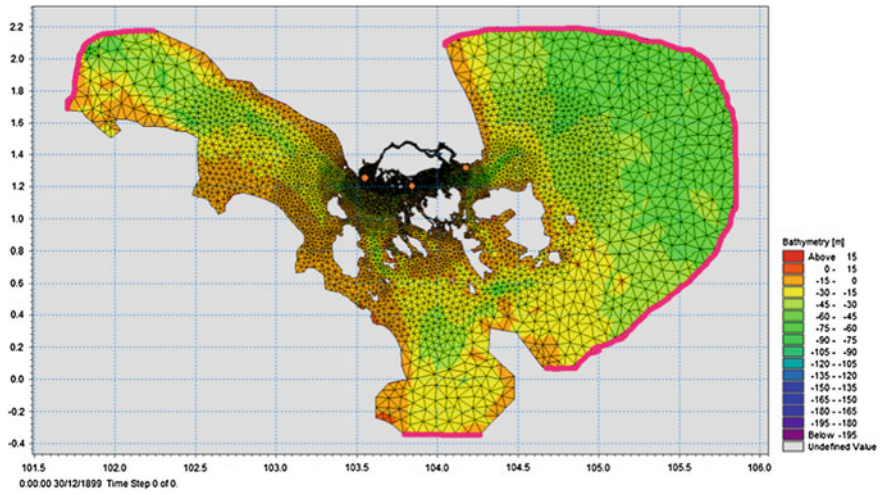

Fig. 5 Model area showing flexible mesh elements and the three studied points along Singapore coastline

station. The remaining two points, West and South, were named after their directions from Singapore. The bathymetry was obtained from compiled Admiralty charts developed by C-MAP and, where available, updated with more detailed local bathymetry that were approved and provided by local surveyors and agencies. The simulation period was 60 h, covering 1 day before and 1 day after the squall occurrence on 2 April 2012. The thickness of the unstructured mesh was tested deliberately to acquire an optimal mesh configuration which both optimised the resources and maintained the necessary accuracy. In total it has 9861 nodes and the spatial resolution ranges from about 9000 m offshore to 450 m approaching the coastline of Singapore.

4.3 Results and Discussions

Figures 6 and 7 represent the half an hour interval evolution of important wave parameters during the period when the squall swept over the island. Waves in the coastal zone of Singapore have very low height and period in normal conditions. When the squall line appeared, the wave height increased, ranging from more than 1.5 m offshore to around 0.5 m near the coastline. The peak wave period result fell within the range between 2 and 5 s. The squall-generated swell waves stemming from the Strait of Malacca entered the sea area in the west of Singapore with

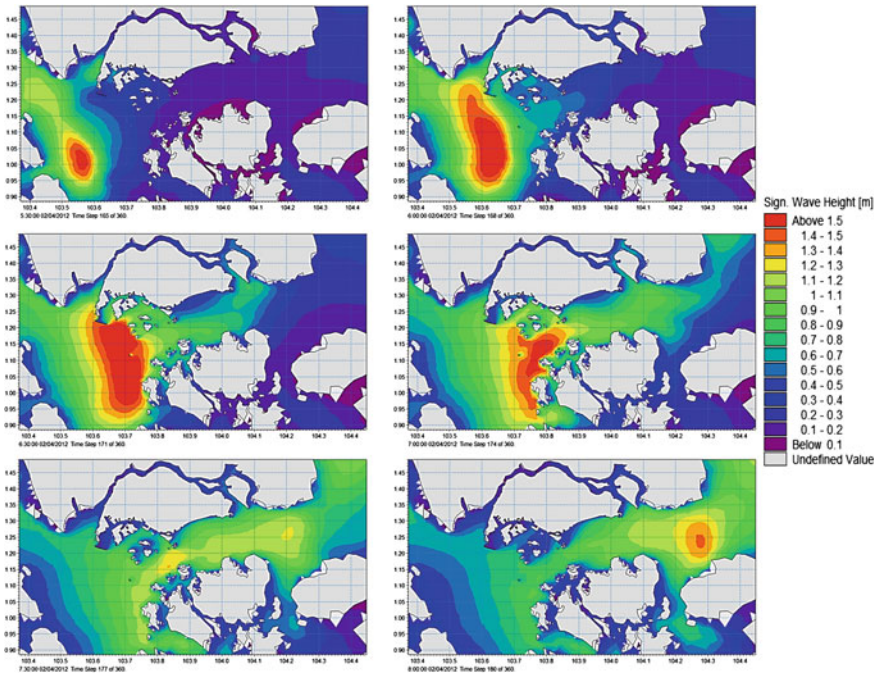

Fig. 6 The evolution every 30 min of significant wave height during the period when the squall approached and left Singapore (5.30–8 am) (order to view: *left* to *right*, *top* to *bottom*)

reduced height and period because the neighbouring islands of Karimunbesar and Kundur acted as barriers dissipating wave energy considerably. The farther the squall moved into the Strait of Singapore, the more wave energy was dissipated because of obstructions from other surrounding islands. As a result, the wave height decreased gradually from west to east. It is obvious that the squall on 2 April 2012 did not create high waves near the shoreline of Singapore.

The part above the black solid line in Fig. 8 shows the "safe zone" where the wave height was always lower than 1 m during the whole squall event. Furthermore, the Strait of Johor can be considered incapable of being affected by the squall line. The three studied locations are not within the "safe zone", and their significant wave height profiles are displayed in Fig. 9. The peak was formed when the squall arrived at the location. At Pengerang the maximum significant wave height ($H_S$max) was around 0.96 m, and at the other locations $H_s$max was lower than 1.4 m.

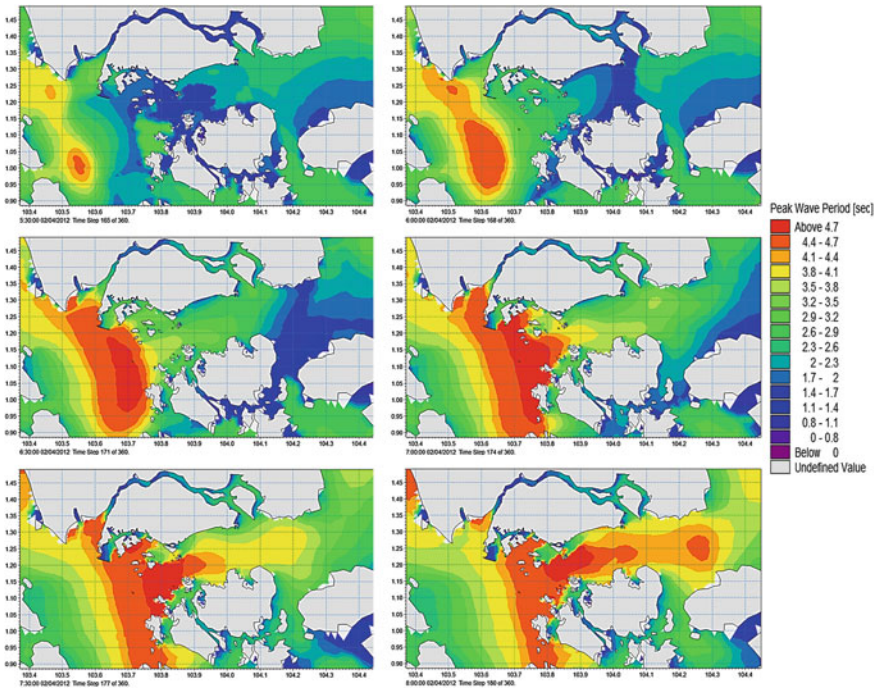

Fig. 7 The evolution every 30 min of peak wave period during the period when the squall approached and left Singapore (5:30 to 8:00 am)

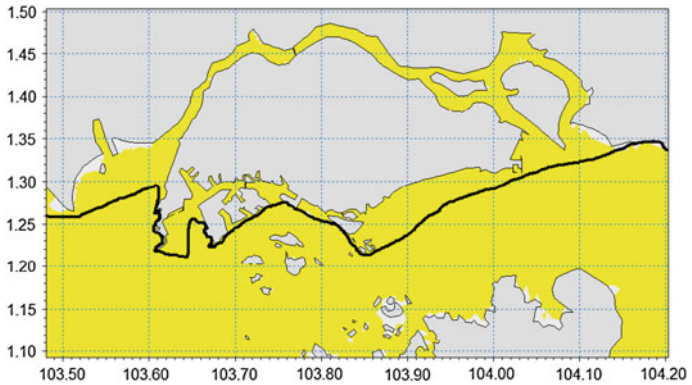

Fig. 8 The coastal zone of Singapore where wave height was always less than 1 m (*upper* part of the *black line*)

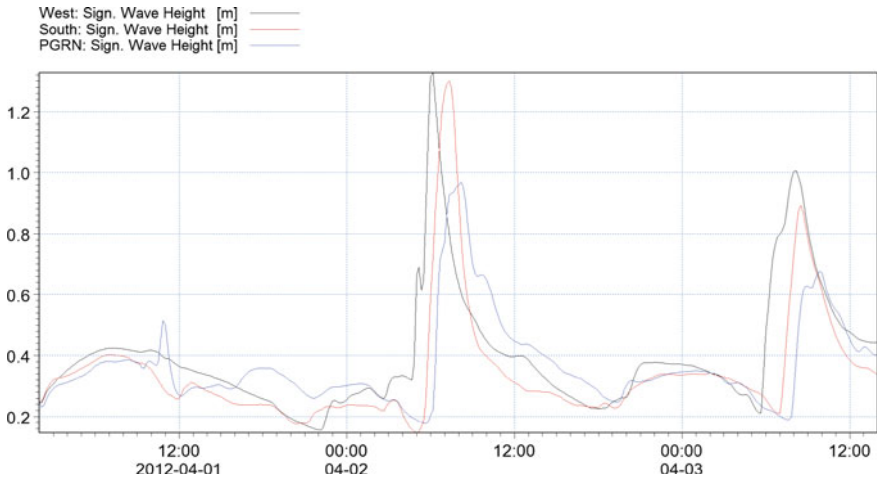

Fig. 9 Modelled significant wave height at the three studied points

5 Applying Synthetic Wind Field for the Wave Model

5.1 Synthetic Wind Field

There are three wind field parameters of the Sumatra squall that have significant impact on the generation of ocean waves. They are squall speed V_f (km/h), peak wind intensity in the squall U_p (m/s) and squall width W_s (km). V_f is the forward velocity of the squall line, indicating how fast the squall line commutes from its origin to Singapore. U_p refers to the highest wind intensity during the squall event. And W_s is defined as squall width, indicating the cover width of the squall (2D view) where one standing at any point within can "feel" the squall. WRF data of the Sumatra squall on 2 April 2012 were analysed to find out the characteristics of the three wind field parameters during the squall event. The knowledge was then applied to create synthetic wind fields to input into the wave model. Different scenarios of synthetic wind fields were created from different combinations of the parameters' values. The idea of running wave model with large number of scenarios of synthetic wind field was to understand the sensitivity of V_f, U_p and W_s towards wave generation.

Initially, manual check on the WRF wind data was performed to learn how the squall line moved along the modelled domain horizontally, namely from Sumatra island and Malacca Strait to Singapore. U_p of 20.0706 m/s was detected to occur at the cell between row 60 and column 102 at 4.30 am (Fig. 10). Therefore, row 60 was selected to observe the wind profile. The blue line in Fig. 11 illustrates the modelled wind profile along row 60 at the moment when the wind reached its highest peak. The horizontal axis indicates the length of the domain via grid number unit, from grid 0 to grid 196 and the grid spacing is 3 km. The vertical axis contains

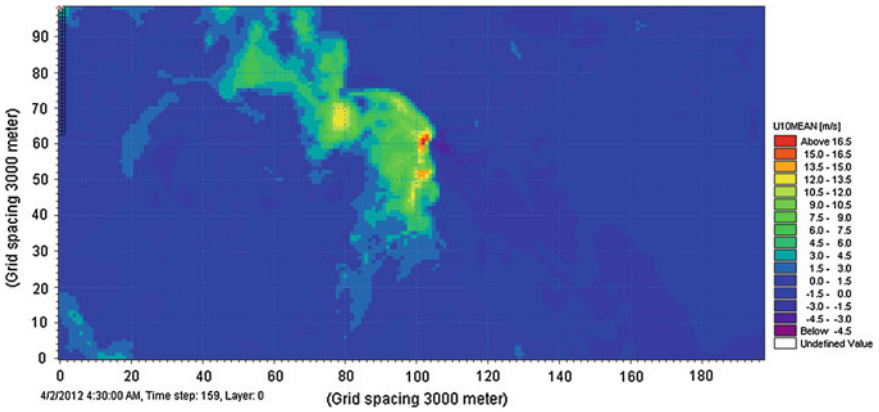

Fig. 10 Sumatra squall's wind field (with grid format) obtained by WRF model showing the peak of wind intensity

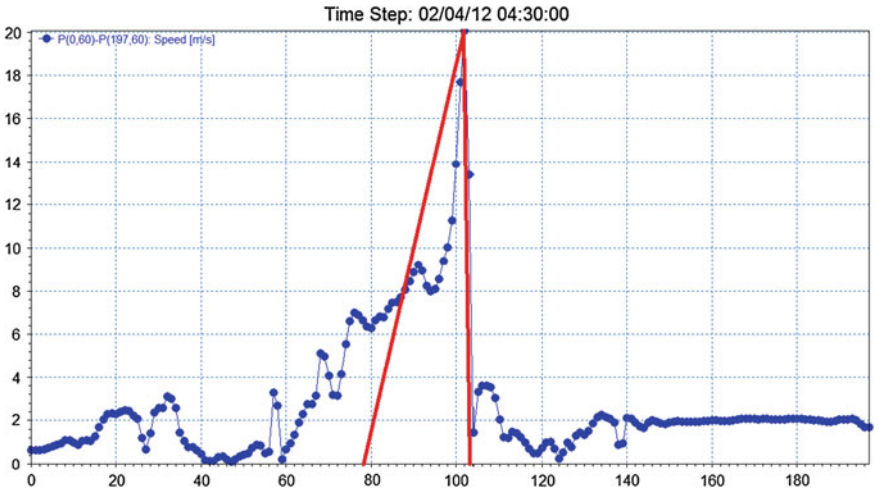

Fig. 11 East to West wind profile extracted from WRF model including the peak wind intensity versus the synthetic east-to-west wind profile

Table 1 Important features of Sumatra squall and their values used in creating different scenarios of synthetic wind field

Squall speed (km/h)	10	20	30		
Peak wind intensity (m/s)	10	15	20	25	
Squall width (km)	50	60	70	80	90

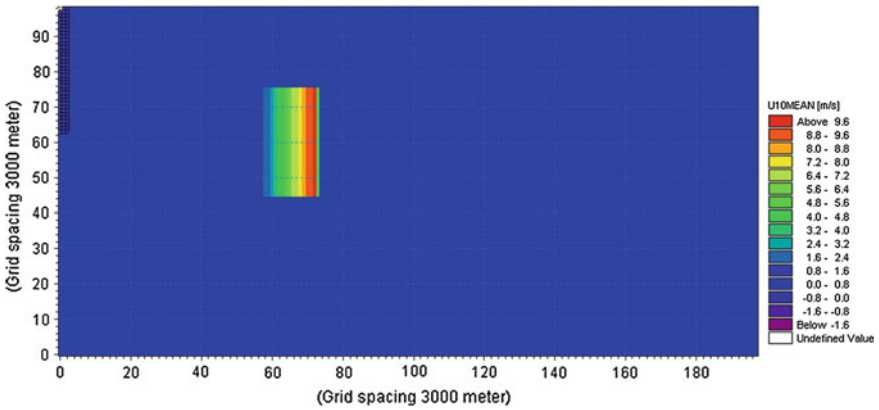

Fig. 12 An example of the synthetic wind field showing wind intensity distribution

the values of wind intensity in m/s. The red line in Fig. 11 represents an example of the profile of the synthetic wind field in terms of W_s and U_p. Triangular shape was considered as an optimal way to imitate the profile of the squall wind. W_s was tested with five values within the range between 50 and 90 km/h. U_p was varied from 10 to 25 m/s, and V_f had three values of 10, 20 and 30 km/h to be used. Table 1 lists out all values of the three parameters applied to create the scenarios. In total, 60 scenarios of synthetic wind field were created, corresponding to 60 scenarios of wind-wave simulation.

Following the WRF modelled wind dataset of the Sumatra squall, the north-to-south length of the synthetic wind field was selected to be 120 km. The wind direction was nevertheless assumed to be 270° constantly, conforming to the movement of the squall line. In other words, it meant the wind always blew eastward. In addition, areas not covered by the squall were assumed to have no wind, as shown in Fig. 12. This was to ensure no disturbance; the resulting wave is caused merely by the squall wind.

5.2 *Results and Discussion*

Apart from the input wind dataset, other parameter settings for the MIKE 21 wave model remained the same. Results from all simulations applying different synthetic wind fields show that wave height is highly sensitive to U_p, less sensitive to V_f and least sensitive to W_s. Tables 2, 3 and 4 provide $H_s$max acquired from all scenarios of synthetic wind fields at the three studied locations. It can be seen that $H_s$max increases dramatically following the growth of U_p. Conversely, it only rises slightly when W_s grows. Besides, $H_s$max is relatively sensitive to V_f, but in a totally different manner. This will be discussed further in the next paragraph. The sensitivity

Table 2 Maximum significant wave height at the west point obtained from all scenarios

Speed (km/h)		10				20				30			
Intensity (m/s)		10	15	20	25	10	15	20	25	10	15	20	25
Width (km)	50	0.915	1.733	2.715	4.011	0.605	1.579	2.946	4.923	0.482	0.965	1.834	3.945
	60	0.938	1.773	2.79	4.163	0.634	1.65	3.03	5.078	0.505	1.022	2.007	4.273
	70	0.957	1.808	2.865	4.313	0.661	1.705	3.108	5.159	0.525	1.075	2.152	4.444
	80	0.976	1.849	2.958	4.538	0.695	1.763	3.204	5.221	0.548	1.149	2.312	4.761
	90	0.987	1.872	3.02	4.735	0.721	1.798	3.271	5.259	0.563	1.2	2.418	4.904

Table 3 Maximum significant wave height at the South point obtained from all scenarios

Speed (km/h)		10				20				30			
Intensity (m/s)		10	15	20	25	10	15	20	25	10	15	20	25
Width (km)	50	0.8143	1.618	2.5558	3.7292	0.5294	1.2873	2.328	3.8131	0.4102	0.8941	1.6438	2.8593
	60	0.8324	1.6518	2.6034	3.8144	0.5671	1.3587	2.4394	3.9842	0.449	0.9592	1.7731	3.0594
	70	0.846	1.6781	2.6408	3.8865	0.5938	1.4105	2.5251	4.1085	0.4772	1.0186	1.8758	3.2044
	80	0.8597	1.706	2.6935	3.9773	0.625	1.4667	2.6124	4.2215	0.5128	1.0875	1.9835	3.3792
	90	0.868	1.7242	2.7275	4.0412	0.6455	1.5018	2.6647	4.2801	0.5301	1.1299	2.0484	3.4767

Table 4 Maximum significant wave height at Pengerang obtained from all scenarios

Speed (km/h)		10				20				30			
Intensity (m/s)		10	15	20	25	10	15	20	25	10	15	20	25
Width (km)	50	0.7669	1.4455	2.2069	3.1375	0.4749	1.062	2.0265	3.1928	0.3856	0.7835	1.3987	2.2114
	60	0.7847	1.4821	2.2512	3.2247	0.5001	1.1297	2.1105	3.352	0.413	0.8386	1.4968	2.364
	70	0.7991	1.5135	2.2893	3.2964	0.5235	1.1822	2.1758	3.4712	0.4347	0.8922	1.5727	2.4995
	80	0.8142	1.5478	2.3332	3.38	0.5521	1.2381	2.2434	3.5807	0.46	0.9482	1.6585	2.6688
	90	0.8232	1.5685	2.3638	3.4368	0.5691	1.2798	2.2839	3.6357	0.4752	0.9825	1.7206	2.7904

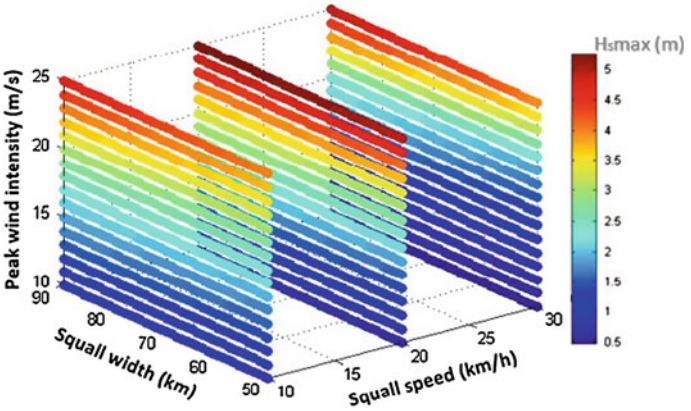

Fig. 13 Interpolated maximum significant wave height as a function of squall speed, squall width and peak wind intensity

of the three parameters can be seen more clearly through Fig. 13 which was drawn in 3D after interpolating $H_s$max results of all scenarios at the west point. In particular, knowing the relationship of the W_s and U_p versus $H_s$max, the values of $H_s$max could be interpolated linearly to have more data points, using the original modelled results of 60 scenarios collected from Table 2. This interpolation task including 3D plotting was done by applying MATLAB.

$H_s$max is directly proportional to U_p and W_s. The relationship is, however, different in the case of V_f. In order to fully understand this relationship, new scenarios from additional combinations of V_f (15, 18, 22.5, 24, 27 km/h) and U_p (17.5 and 22.5 m/s) were run to obtain more values of $H_s$max. Figure 14 reveals that if U_p is higher than 15 m/s, one should expect $H_s$max occurs when V_f falls within the range between 20 km/h and 25 km/h. With U_p less than 15 m/s, there is little risk that the wave height can endanger the coastline of Singapore. For a given value of U_p, $H_s$max increases gradually as a function of V_f till reaching a peak, after which $H_s$max decreases considerably. The reason for this behaviour is that when V_f is fast, the waves will be left behind the squall and no swell will be present ahead of the squall. On the contrary, when V_f is relatively slow, the dominant waves will surpass the squall and form swell ahead of its front [16]. The maximum wave conditions were proven to happen when the group wave velocity of the waves becomes slightly larger than the storm speed. The group wave velocity is defined as the velocity at which wave energy is transmitted. In shallow water the group wave velocity is equal to the wave celerity, and in deep water the group wave velocity is only a half of the wave celerity [17].

This can also be elaborated further using the approach of an equivalent fetch [16]. The process of wave energy transfer is governed by the intensity of the wind, the wind fetch and the length in time that the wind blows. Large waves with sufficiently long period can be generated only if the fetch is large. For slowly moving squall line, because the group wave velocity is greater than V_f, waves

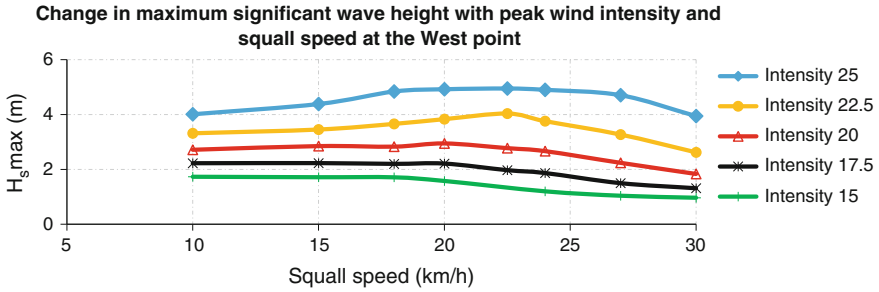

Fig. 14 Maximum significant wave height as a function of squall speed and peak wind intensity. (Squall width is fixed at 50 km)

generated in the intense wind regions to the front of the squall line move ahead of the squall line and encounter generally a short equivalent fetch. For fast moving squall line the converse situation happens with the waves being left behind the squall line. And if there is an optimal combination of V_f and the group wave velocity, waves will have the maximum equivalent fetch, spending maximum time in the intense wind region, and thereupon creating the biggest values of the significant wave height.

6 Conclusions

Sumatra squalls are understood as lines of thunderstorms followed by intense gusts and heavy rains originating from Sumatra island or the Malacca Strait and moving eastward to Singapore. Their formation requires airstream to converge over a large area and at altitude lower than 1 km. High moisture and moderate low-level wind shear in a tropical temperature area having mild lapse rate are other crucial factors to develop the squall lines. Sumatra squalls include a convective region appearing at the leading edge and a stratiform region to the rear. Wind speed grows gradually from the back to the gust front and then decreases substantially.

The study selected one Sumatra squall to investigate its impact on wave generation. A wind-wave model was built, of which the main forcing was the squall wind dataset imported from the downscaled WRF model after being calibrated and validated. The simulation results allowed us to determine the wave profile during the squall event and areas possibly considered safe from the high waves. Furthermore, a large number of wind fields were created synthetically by varying three wind field parameters of the squall line: V_f, U_p and W_s. Experiment simulations with different synthetic wind fields showed that U_p is the most sensitive parameters affecting the wave height, followed by V_f and $W_{s,}$ respectively. Moreover, W_s is directly proportional to $H_s$max with given values of V_f, U_p. Similarly, U_p is directly proportional to $H_s$max with given values of V_f, W_s.

However, the relationship between V_f and $H_s$max is not the same. For fixed values of U_p and W_s, $H_s$max increases gently as a function of V_f till reaching a peak, after which $H_s$max decreases considerably.

References

1. Arsen'ev, S. A., & Shelkovnikov, N. K. (2010). Soliton theory of squall storms. *Moscow Univeristy Physics Bulletin, 65*(5), 412–416.
2. Nalivkin, D. V. (1969). *Hurricanes, Storms, Tornadoes*. Leningrad, Russia: Nauka.
3. Houze, R. A., Jr. (1977). Structure and dynamics of a tropical squall-line system. *Monthly Weather Review, 105*, 1540–1566.
4. Hamilton, R. A., & Archbold, J. W. (1945). Meteorology of Nigeria and adjacent territory. *Quarterly Journal of Royal Meteorite Social, 71*, 231–262.
5. Yi, L., & Lim, H. (2006). Semi-idealized COAMPS simulations of sumatra squall lines: the role of boundary forcing. Solid Earth, Ocean science and Atmospheric science. In W. H. Ip, & Y. T. Chen (Eds.), (Vol. 9, pp. 111–124) *Advances in Geosciences*, World Scientific.
6. Lin, I.-I., Alpers, W., Khoo, V., Lim, H., Tian, K. L., & Kasilingam, D. (2001). An ERS-1 synthetic aperture radar image of a tropical squall line compared with weather radar data. *IEEE Transactions on Geoscience and Remote Sensing, 39*(5), 937–945.
7. Sallenger, A. H., List, J. H., Gelfenbaum, G., Stumpf, R. P., & Hansen, M. (1995). Large wave at Daytona Beach, Florida, explained as a squall-line surge. *Journal of Coastal Research, 11*(4), 1383–1388.
8. National Environmental Agency. (2002). "Sumatra" squalls. Retrieved on March 27, 2013, from http://cms.nea.gov.sg/sumatra_squalls.aspx.
9. National Environmental Agency. (2011). Annual Weather Review 2011. Retrieved on March 27, 2013, from http://app2.nea.gov.sg/annual_review_new.aspx.
10. Yi, L., & Koh, T. H. (2007). Analysis and prediction of Sumatra squall lines. *Paper presented at 22nd Conference on Weather Analysis and Forecasting/18th Conference on Numerical Weather Prediction*, Utah, US.
11. Malaysian Meteorological Department. (2012). Squall line. Retrieved on March 28, 2013, from http://www.met.gov.my/index.php?option=com_content&task=view&id=72&Itemid=160&limit=1&limitstart=1&lang=english.
12. National Environmental Agency. (2009). *Weather-wise Singapore*. National Environment Agency, Singapore: Meteorological Services Division.
13. Liu, L., Zhuang, W., Zhang, P., & Mu, R. (2010). Convective scale structure and evolution of a squall line observed by C-band Dual Doppler Radar in an arid region of Northwestern China. *Journal of Advances in Atmospheric Sciences, 27*(5), 1099–1109.
14. Houze, R. A., Jr, Rutledge, S. A., Biggerstaff, M. I., & Smull, B. F. (1989). Interpretation of Doppler weather radar displays of midlatitude mesoscale convective systems. *Bulletin American Meteorite Social, 70*, 608–619.
15. Chua, G. (2012). *Wet, wet, wet: Violent thunderstorms cause traffic snarls*. The Straits Times: Retrieved from http://www.straitstimes.com.
16. Young, I. R. (1988). Parametric hurricane wave prediction model. *Journal of Waterway, Port, Coastal and Ocean Engineering 114*(5), 639–652.
17. Reeve, D., Chadwick, A., & Fleming, C. (2010). *Coastal Engineering processes, theory and design practice* (2nd ed.). London: Spon Press.

Validation and Test Cases for a Free Surface SPH Model

Louis Goffin, Sébastien Erpicum, Benjamin J. Dewals, Michel Pirotton and Pierre Archambeau

1 Introduction

Numerical methods in hydraulics can be separated into two categories. On the one hand we have grid-based methods and on the other hand we have meshfree methods [17]. In the meshfree methods category, SPH is one the most used. Smoothed-particle hydrodynamics was first introduced in the field of astrophysics by Gingold and Monaghan [6] and Lucy [20] in 1977 but is now used in hydraulics [3, 12, 23], structure dynamics [1], solid mechanics [26], etc.

Nowadays, the method is still under development but a wide range of problems can be modeled: it is used in many fields of application and implemented in the well-known open-source program SPHysics [8, 9]. The goal of this paper is to identify some undesired effects linked to the SPH method as well as to give some validation benchmark. We will first introduce the SPH method in the frame of open-channel quasi-incompressible flows. Then, various implementation aspects that developers can encounter will be presented. The main part of this paper will focus on validation test cases. They will highlight some issues linked to the SPH method and the answers given recently. Finally, a brand-new test case will be described.

2 The SPH Method

The main principle of the SPH method, as explained in [21], is based on the approximation of a function

L. Goffin (✉) · S. Erpicum · B.J. Dewals · M. Pirotton · P. Archambeau
Hydraulics in Environmental and Civil Engineering (HECE), University of Liege (ULg), Allée de la Découverte 9 (B52/3), B-4000 Liège, Belgium
e-mail: l.goffin@ulg.ac.be

P. Gourbesville et al. (eds.), *Advances in Hydroinformatics*,
Springer Water, DOI 10.1007/978-981-287-615-7_12

$$\langle f(\mathbf{x})\rangle = \int_{\Omega} f(\mathbf{x}')W(\mathbf{x}-\mathbf{x}',h)d\mathbf{x}' \tag{1}$$

where f is a function, W a smoothing function, Ω the domain where f is defined, and h the smoothing length. The particle approximation can be applied to Eq. (1):

$$\langle f(\mathbf{x}_a)\rangle = \sum_{b=1}^{N} \frac{m_b}{\rho_b} f(\mathbf{x}_b)W_{ab} \tag{2}$$

where the subscripts a and b refer, respectively, to the current particle and the neighbor particles, N is the number of neighbors, m is the mass of a particle, ρ its density, and $W_{ab} = W(\mathbf{x}_a - \mathbf{x}_b, h)$.

For more details about the establishment of this formalism, the reader can refer to [18] or [7].

2.1 Equations and Smoothing Functions

Newtonian fluids are ruled by Navier–Stokes equations. When the SPH formalism is applied to these equations, we obtain the density continuity

$$\frac{D\rho_a}{Dt} = \sum_{b=1}^{N} m_b \mathbf{u}_{ab} \nabla_a W_{ab} \tag{3}$$

where the speed $\mathbf{u}_{ab} = \mathbf{u}_a - \mathbf{u}_b$, and a derived form of the conservation of momentum

$$\frac{D\mathbf{u}_a}{Dt} = -\sum_{b=1}^{N} m_b \left(\frac{p_b}{\rho_b^2} + \frac{p_a}{\rho_a^2} + \Pi_{ab}\right)\nabla_a W_{ab} + \mathbf{F} \tag{4}$$

where p is the pressure, Π_{ab} an artificial viscosity term, and $\mathbf{F}$ the body forces.

The smoothing function W in Eqs. (3) and (4) are most often a cubic spline [24], a Gaussian [6] or a quadratic function [13]. In this paper, we will use exclusively a cubic spline.

2.2 Time Integration Scheme

The time integration scheme used in this work is a Runge–Kutta 22 scheme (abbreviated RK22):

$$\begin{aligned} y_{i+1} &= y_i + h((1-\theta)k_1 + \theta k_2) \quad ; \quad k_1 = f(t_i, y_i) \quad ; \\ k_2 &= f(t_i + \frac{1}{2\theta}h, y_i + \frac{1}{2\theta}hk_1) \end{aligned} \tag{5}$$

with $\theta = 0.5$ and where $t_{i+1} = t_i + h$ and $f(t_i, y_i) = y_i'$. Another RK22 scheme is obtained with $\theta = 1$ and the Euler scheme is obtained for $\theta = 0$. These three integration schemes are compared for a dam break on dry bed in Sect. 3.

In the SPH literature, the Leapfrog scheme is often used for its stability [29].

2.3 Some Implementation Aspects

In order to implement a SPH code, the developer must be aware of some particularities of the method.

As the smoothing functions are most often supported on a compact, the sum in the Eqs. (3) and (4) can be limited to some particles within a given distance to the computed particle (smoothing length). In order to determine these neighbors, there are basically three possibilities [18]: (a) all-pair search algorithm, (b) linked list algorithm, and (c) tree search algorithm. The second procedure is the fastest one as its speed is of the order of N. However, if a variable smoothing length in space is used, the third algorithm is more appropriate.

Concerning the smoothing length, it can be variable in time and/or in space. s being the initial spacing between the particles, the initial smoothing length $h_0 = 1.2$ s but it can range from 1 to 2 s. In this work, we chose a coefficient of 1.2 which is a good compromise between the computational efficiency and the number of particles included in a support domain. In order to deal with the variable distance between particles, the smoothing length can be updated at every time step [24]:

$$h = h_0 \left(\frac{\rho_0}{\rho_m}\right)^d \tag{6}$$

where d is the number of dimensions and ρ_m the mean density. It is obvious that the density is not likely to be homogenous in the whole domain. A possibility would be to have an adaptive smoothing length in space. However, such a method requires more precautions as Newton's third law might be violated as highlighted in [25].

The speed of sound plays an important role in any numerical fluid simulation. In fact, it rules the time step. In the case of free surface flows Monaghan [22] shows that the initial speed of sound can be taken at $c_0 = 10\sqrt{gH}$ where H is the maximum depth. It allows larger time steps and thus a quicker resolution. However, it introduces an artificial compressibility.

Boundaries can be modeled using different methods, including (a) ghost particles [26], (b) repulsive particles [22], and (c) dynamic particles [2]. For this work, dynamic particles were used for their flexibility and ease of use. We can model

complex shapes, thanks to this kind of particles. However, there is no consensus in the SPH community about boundary conditions. It is one of the *grand challenges* on the SPH European Research Interest Community (SPHERIC).

Concerning initialization, particles can be set in a Cartesian grid or in a staggered way. Once their position is chosen, their pressure can be calculated. In most situations, the initial pressure is taken to the hydrostatic pressure. The pressure is not a direct variable in an SPH simulation but is related to the density. This link can be made, thanks to

$$p = B\left(\left(\frac{\rho}{\rho_0}\right)^{\gamma} - 1\right) \tag{7}$$

where $B = c_0^2\rho_0/\gamma$ and γ is set around 7. Equation (7) was introduced by Monaghan [22] and is based on Tait's equation [4] which is based on experimental measures. According to Violeau [28], the mass of a particle is set according to its volume $V_a = s^d$ and its density: $m_a = V_a\rho_a$. Considering hydrostatic pressure at the beginning of the simulation leads to particles having different masses. This mass, however, remains unchanged during the whole simulation.

3 Test Cases and Undesired Effects

In order to be validated, a code must pass some test cases. These test cases allow the developer to point his possible mistakes but also to realize the weakness of a method. This section will focus on some test cases and the conclusions that can be made. The characteristics of every test case are given in Table 1 in the order in which each test case appears.

Table 1 Characteristics of each test case

	TC 1	TC 2	TC 3	TC 4	TC 5
Nb fixed part. [−]	6196	9894	60402	236390	73614
Nb mob. part. [−]	35836	47175	123750	668160–767691	400200–504531
h_0 [m]	0.024	0.024	0.024	0.012	0.024
α [−]	0.05	0.2–0.01	0.5	0.05	0.01
Simul. time [s]	5	7	2	5	5

3.1 Tank of Still Water

This test case is simply a box that contains an amount of water with free surface. The particles are initially set with hydrostatic pressure and without velocity. It is supposed that the particles will not move and will keep their initial pressure. The results are not as expected. Figure 1 shows the pressure distribution in the fluid at different times of the simulation. Tests were made with a correction of the kernel gradient but no improvements were noticed.

In order to explain this phenomenon, let us take the problem in another way: how could we set the particles in order to have an initial equilibrium? The answer can be obtained by solving a system

$$Am = b \tag{8}$$

where m is a vector that contains the masses of the particles, b is a vector that contains the body forces that act on a particle and

$$A_{a,b} = -\left(\frac{p_b}{\rho_b^2} + \frac{p_a}{\rho_a^2}\right)\nabla_a W_{ab} \tag{9}$$

System (8) indicates that the variation of velocity of a particle should be equal to zero according to Eq. (4). The boundary conditions can be handled by adding a reaction force (that is determined iteratively) to the boundary particles.

Matrix A in system (8) is antisymmetric which makes it singular for an odd number of particles. This leads to impossibility to solve the system. We can conclude that an initial equilibrium can be found only for an even number of particles.

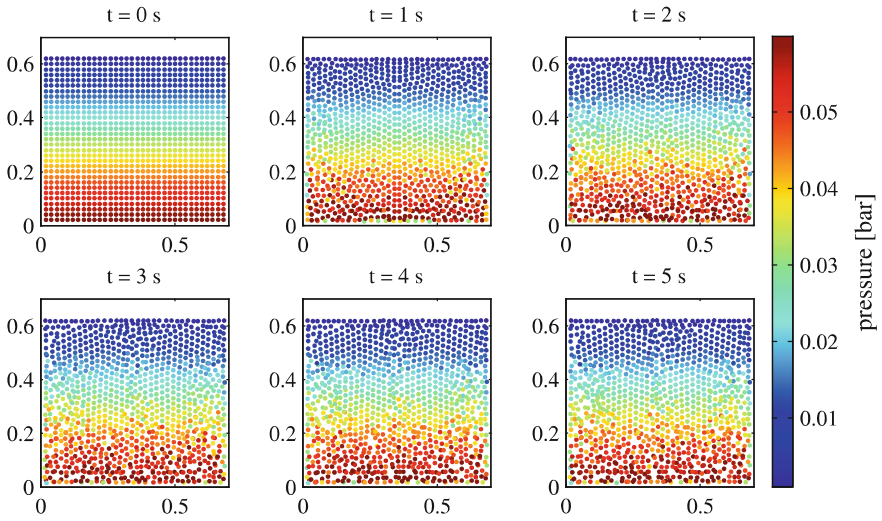

Fig. 1 Even if initially the pressure is hydrostatic, it is becoming less uniform with time

Even when this condition is satisfied, the masses are not linearly distributed and some oscillations appear. The reader may find more information and examples in [7].

3.2 Spinning Tank

A spinning cylindrical tank of water presents a free surface that has the equation

$$z(r) = \frac{r^2\omega^2}{2g} + z_0 - \frac{\omega^2 R^2}{6g} \tag{10}$$

where (z, r) are cylindrical coordinates, ω is the rotation speed, R the radius of the tank, and z_0 the z coordinate of the free surface when the tank is at rest. When using the assumption made by Monaghan [22] about the speed of sound, the free surface is below what was expected (see Fig. 2 left).

A speed of sound closer to reality avoids compressibility inconsistency. However, the time steps are much smaller and the computation time is greatly increased. For the example of Fig. 2, the computation time was multiplied by 24 when taking c_0 = 1480 m/s.

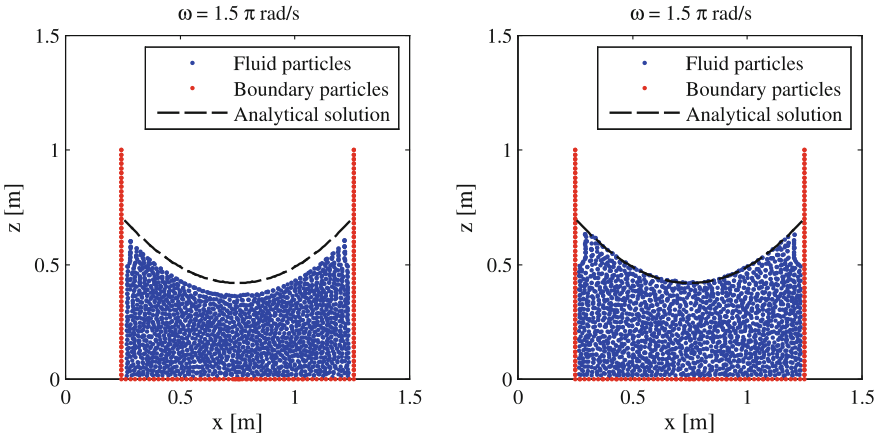

Fig. 2 On the *left*-hand side, c_0 is taken at 50 m/s which leads to an over compressibility. On the *right*-hand side, c_0 is equal to 1480 m/s as in reality, which leads to good results according to theory

3.3 *Dam Break on a Dry Bed*

A well-known test case is the dam break on a dry bed. It was performed in many articles such as in [2, 10]. It is based on the experiments of Koshizuka and Oka [14]. They measured the position of the front as well as the shape of the wave. The position of the wave front is measured dimensionless. The initial situation can be represented in 2-D as shown in Fig. 3a.

When taking a closer look at the interface between the fluid and the boundary, two observations can be made: (1) a gap is observed when a thin layer of fluid flows on a horizontal boundary (Fig. 3b) and (2) some particles stay attached to the walls of the domain (Fig. 3c). When a particle enters in the support domain of a boundary particle, a repulsive force is created which creates a gap equal to the support radius. When particles are moving away from each other, the artificial viscosity creates an attracting force between them. If this attracting force is greater than the gravity, some particles stay attached to the boundary.

The results of a numerical simulation can be compared to Koshizuka and Oka's experiment. Figure 4 gives this comparison. In order to avoid particles attached to the boundaries and consequently undesired attracting forces, a symmetry condition can be used. The effect of a symmetry condition for low number of particles is also plotted in Fig. 4. As it can be observed, the results are improved.

Recent works on the viscosity treatment [27] and the boundary conditions [5] may lead to better results.

The accuracies of time integration schemes used for this work are compared in Fig. 5. Concerning the execution time, the RK22 schemes are only 21 % slower than the Euler scheme. This is due to the fact that only the distance between neighbors is re-evaluated for the correcting step. The search of neighbors is performed only for the main step.

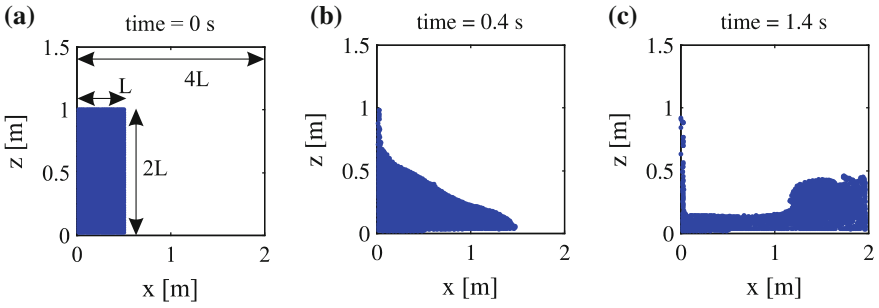

Fig. 3 The initial geometry that is plotted in figure **a** can be improved by doubling the size of the domain according to x in order to add a symmetry condition (and a symmetric dam break). A thin gap between the fluid and the boundary can be observed in figure (**b**). On figures **b** and **c**, some particles stay attached to the left wall. These behaviors can be explained, thanks to the repulsive and attracting forces that are generated by the dynamic particles

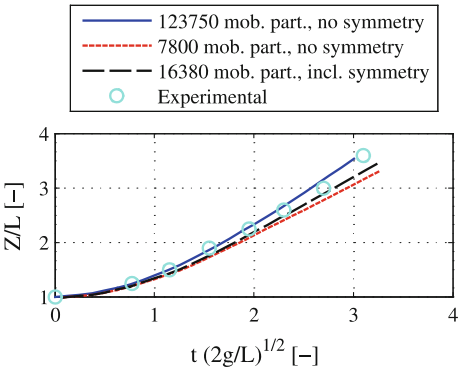

Fig. 4 Dimensionless comparison between experimental and numerical results. Z is the position of the front regarding the left boundary. The numerical results match well with the experimental ones. Better results are obtained with a larger amount of particles. However, for low numbers of particles, good results can be obtained when considering a symmetry condition

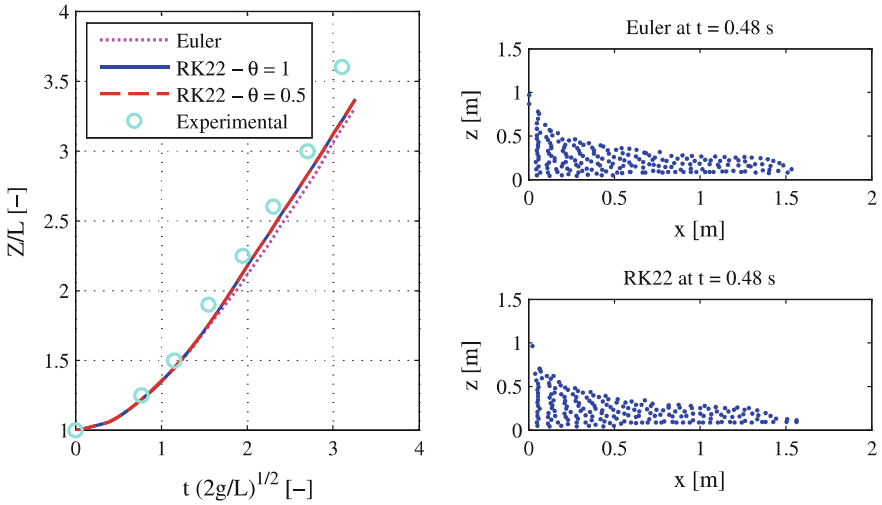

Fig. 5 The RK22 integration scheme gives better results than the Euler scheme

3.4 Flow Over a Spillway

This section will compare results of a steady flow over a spillway from a physical model to SPH results. In order to this, open boundaries must be implemented. These boundary conditions allow inflow and outflow in specific regions of the domain. Information about implementing this kind of boundaries can be found in [15]. When implemented, an inflow can be imposed upstream and particles are deleted when they leave the domain downstream. Initially, the free surface is set at the

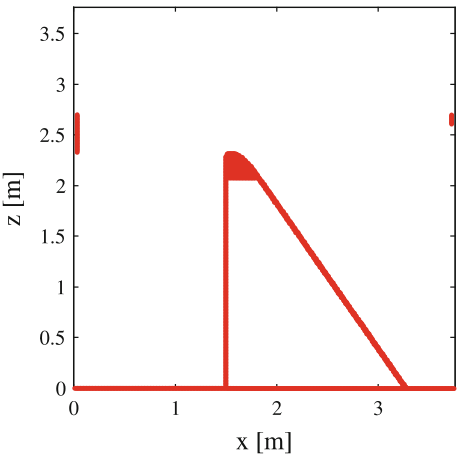

Fig. 6 Position of boundary particles and geometry of the spillway crest according to WES standard

height of the crest. The flow is considered steady when the head is stabilized upstream. The shape of the spillway crest is designed according to the WES standard. In order to avoid effects from the bottom of the domain, the crest is positioned at 2.32 m from the bottom. The numerical model has the same dimensions as the physical model in lab (see Fig. 6). A comparison between the speed profiles will be done for an inflow of 125 l/s per meter of crest. This inflow is the design discharge of the spillway.

A reduction of section at the top of the crest can be observed (see Fig. 7). This effect is due to high repulsive forces coming from the interaction with boundary particles.

According to experimental measurements of velocity (using LS-PIV), numerical and experimental velocity profiles over the crest are compared in Fig. 8. A velocity profile in SPH can be obtained by considering a zone that extends a little to the left and to the right of the considered section. It can be seen in Fig. 8 that before the crest ($x/H_d < 0$) the speeds are close to experimental measurements but after the crest ($x/H_d \geq 0$) the results are not conforming to experimental measures. This

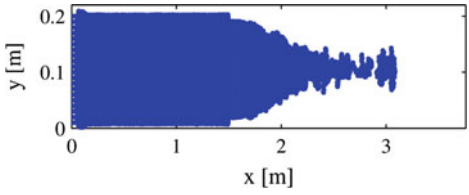

Fig. 7 When the water overtops the spillway, the lateral boundary particles exert a repulsive force on the fluid particles which repels them from the borders

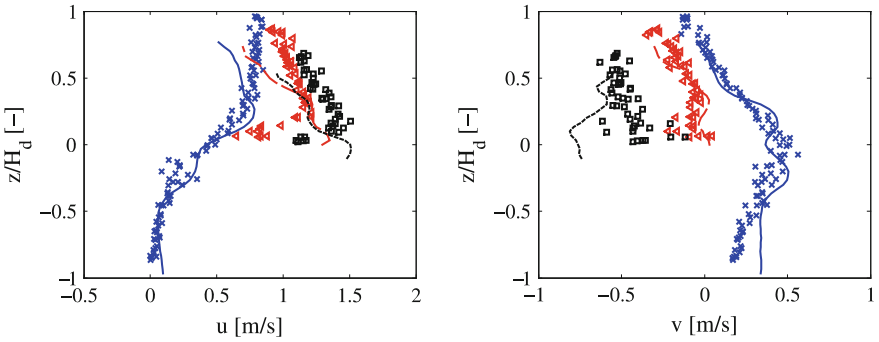

Fig. 8 Horizontal (u) and vertical (v) speed profiles at $x/H_d = -0.5$ (*plain line* and *crosses*), $x/H_d = 0$ (*dashed line* and *triangles*), and $x/H_d = 0.5$ (*dotted line* and *squares*). *Lines* are for experimental measures and shapes for numerical results

behavior can be explained by (a) too important viscous effects on the spillway, (b) the behavior of the dynamic particles which create too strong repulsive forces, and (c) the reduction of section at the crest due to the boundary particles. Once more, better boundary conditions and a more appropriate viscous term would lead to more quantitative results.

3.5 Shape of Flow Over a Weir

Another test case can consist in comparing the shape of a nape of flow over a weir to an analytical profile. This analytical profile can be digitalized from [11]. The resulting polynomials are given by (11) and (12) for, respectively, the upper nape and the lower nape.

$$\frac{z}{H} = -0.04\left(\frac{x}{H}\right)^3 - 0.2\left(\frac{x}{H}\right)^2 - 0.26\left(\frac{x}{H}\right) + 0.88 \quad -1 \le \frac{x}{H} \le 2 \tag{11}$$

$$\frac{z}{H} = -0.33\left(\frac{x}{H}\right)^4 + 1.18\left(\frac{x}{H}\right)^3 - 1.90\left(\frac{x}{H}\right)^2 + 0.84\left(\frac{x}{H}\right) \; 0 \le \frac{x}{H} \le 1.5 \tag{12}$$

In order to avoid effects from the bottom of the domain, we considered a weir's height of 2.3 m. The theoretical profiles and the one obtained numerically are compared in Fig. 9. Due to viscous tensions, these two different approaches do not fit well. There is also an influence from the boundary particles on the section of flow over the weir as it was observed in the previous test case (Fig. 7).

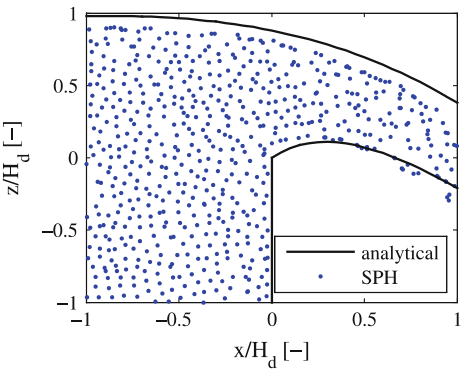

Fig. 9 The SPH does not fit so well with the analytical profiles

4 Conclusion

Even if the SPH method was introduced more than 35 years ago, it is still under large developments. However, a simple model can be obtained quickly. This paper is based on a master thesis in which a 3-D SPH code was implemented [7]. The goal of this paper was to present some test cases useful to validate a program. According to our experience, we pointed out some undesired effects that are not well referenced yet in the literature. Recent developments introduce new possibilities to deal with the undesired effects shown in this paper.

The still tank test case showed that an initial equilibrium state is impossible in some situations. The next test case concerned a spinning tank. It showed that the usual assumption of a low speed of sound can lead to an overcompressibility. In order to avoid this, a pressure Poisson equation is one of the possibilities [16]. The dam break test case pointed that the dynamic boundary particles can cause undesired effects such as attracting forces. Finally, the flows over a spillway and a weir emphasized the fact that boundaries have a large effect on SPH simulation. We are currently working on a 2-D code that should improve the situation [19]. However, boundary conditions are still a difficulty in SPH.

Aknowledgments The authors are grateful for the data provided and the fruitful discussions with Dr. Yann Peltier.

References

1. Canor, T., & Denoël, V. (2013). Transient Fokker-Planck-Kolmogorov equation solved with smoothed particle hydrodynamics method. *International Journal for Numerical Methods in Engineering, 94*(6), 535–553.
2. Crespo, A. J. C., Gómez-Gesteira, M., & Dalrymple, R. A. (2007). Boundary conditions generated by dynamic particles in SPH methods. *Computers, Materials and Continua, 5*(3), 173–184.

3. Dalrymple, R. A., & Knio, O. (2001). *SPH modelling of water waves*. Sweden: ASCE.
4. Dymond, J. H., & Malhotra, R. (1988). The Tait equation: 100 years on. *International Journal of Thermophysics, 9*(6), 941–951.
5. Ferrand, M., et al. (2013). Unified semi-analytical wall boundary conditions for inviscid, laminar or turbulent flows in the meshless SPH method. *International Journal for Numerical Methods in Fluids, 71*(4), 446–472.
6. Gingold, R. A., & Monaghan, J. J. (1977). Smoothed particle hydrodynamics-theory and application to non-spherical stars. *Monthly Notices of the Royal Astronomical Society, 181*, 375–389.
7. Goffin, L. (2013). *Development of a didactic SPH model*. Liege: University of Liege (ULg).
8. Gomez-Gesteira, M., et al. (2012). SPHysics—development of a free-surface fluid solver—Part 2: Efficiency and test cases. *Computers and Geosciences, 48*, 300–307.
9. Gomez-Gesteira, M., et al. (2012). SPHysics—development of a free-surface fluid solver—Part 1: Theory and formulations. *Computers and Geosciences, 48*, 289–299.
10. Gomez-Gesteira, M., et al. (2010). State-of-the-art of classical SPH for free-surface flows. *Journal of Hydraulic Research, 48*(1), 6–27.
11. Hager, W., & Schleiss, A. (2009). *Traité de Génie Civil, Volume 15—Constructions Hydrauliques—Ecoulements Stationnaires.* Switzerland: PPUR-Presses Polytechniques Romandes.
12. Jánosi, I. M., et al. (2004). Turbulent drag reduction in dam-break flows. *Experiments in Fluids, 37*(2), 219–229.
13. Johnson, G. R., Stryk, R. A., & Beissel, S. R. (1996). SPH for high velocity impact computations. *Computer Methods in Applied Mechanics and Engineering, 139*(1), 347–373.
14. Koshizuka, S., & Oka, Y. (1996). Moving-particle semi-implicit method for fragmentation of incompressible fluid. *Nuclear Science and Engineering, 123*(3), 421–434.
15. Lastiwka, M., Basa, M., & Quinlan, N. J. (2009). Permeable and non-reflecting boundary conditions in SPH. *International Journal for Numerical Methods in Fluids, 61*(7), 709–724.
16. Lind, S. J., et al. (2012). Incompressible smoothed particle hydrodynamics for free-surface flows: A generalised diffusion-based algorithm for stability and validations for impulsive flows and propagating waves. *Journal of Computational Physics, 231*(4), 1499–1523.
17. Liu, G. (2003). *Mesh free methods: moving beyond the finite element method*. New York: CRC Press.
18. Liu, G. G.-R., & Liu, M. (2003). *Smoothed particle hydrodynamics: a meshfree particle method*. Singapore: World Scientific.
19. Lodomez, M. (2014). *Determining the characteristics of a free jet in 2-D by the SPH method*. Liege: University of Liege (ULg).
20. Lucy, L. B. (1977). A numerical approach to the testing of the fission hypothesis. *The astronomical journal, 82*, 1013–1024.
21. Monaghan, J. J. (1988). An introduction to SPH. *Computer Physics Communications, 48*(1), 89–96.
22. Monaghan, J. J. (1994). Simulating Free Surface Flows with SPH. *Journal of Computational Physics, 110*(2), 399–406.
23. Monaghan, J. J., & Kos, A. (1999). Solitary waves on a cretan beach. *Journal of Waterway, Port, Coastal and Ocean Engineering, 125*(3), 145–154.
24. Monaghan, J. J., & Lattanzio, J. C. (1985). A refined particle method for astrophysical problems. *Astronomy and Astrophysics, 149*, 135–143.
25. Nelson, R. P., & Papaloizou, J. C. (1994). *Variable smoothing lengths and energy conservation in smoothed particle hydrodynamics.* arXiv preprint astro-ph/9406053.
26. Randles, P. W., & Libersky, L. D. (1996). Smoothed particle hydrodynamics: Some recent improvements and applications. *Computer Methods in Applied Mechanics and Engineering, 139*(1–4), 375–408.

27. Violeau, D. (2009). Dissipative forces for Lagrangian models in computational fluid dynamics and application to smoothed-particle hydrodynamics. *Physical Review E—Statistical, Nonlinear, and Soft Matter Physics*, *80*(3).
28. Violeau, D. (2012). *Fluid Mechanics and the SPH method: theory and applications*. Oxford: Oxford University Press.
29. Violeau, D., & Leroy, A. (2014). On the maximum time step in weakly compressible SPH. *Journal of Computational Physics, 256*, 388–415.

Uncertainty Analysis of Hydrodynamic Modeling of Flooding in the Lower Niger River Under Sea Level Rise Conditions

Zahrah N. Musa, Ioana Popescu and Arthur Mynett

1 Introduction

Natural processes consist of a combination of complex subprocesses and conditions. Models aim to represent the natural phenomena through simplified approximations of the physical processes in a reliable way. Flood modeling is therefore formulated in dimensions representing different types of flow simplified for practical purposes. Depending on the flow channel properties, averaging is done such that flow can be modeled in one dimension (1D, e.g., flow in a pipe, stream), two dimensions (2D, e.g., flow in a shallow lake, coastal waters), and three dimensions (3D, e.g., wind-driven currents on open water). The reliability of modeling results depends on several elements such as the input data, modeling assumptions, case study scenario, model choice, etc. Errors in measurement of input data, data processing, and interpretation of output data introduce measurement uncertainties that affect model output.

Hydrodynamic modeling of flooding in river channels and floodplains is based on the principles of continuity and momentum of the flow system. For an open

Z.N. Musa (✉) · I. Popescu
Department of Integrated Water Sytems and Governance, UNESCO-IHE, Westvest 7, 2611AX Delft, The Netherlands
e-mail: z.musa@unesco-ihe.org

I. Popescu
e-mail: i.popescu@unesco-ihe.org

A. Mynett
Department of Water Science and Engineering, UNESCO-IHE, Westvest 7, 2611AX Delft, The Netherlands
e-mail: a.mynett@unesco-ihe.org

A. Mynett
Department of Civil Engineering, Technical University, Stevinweg 1, 2628 CN Delft, The Netherlands

P. Gourbesville et al. (eds.), *Advances in Hydroinformatics*,
Springer Water, DOI 10.1007/978-981-287-615-7_13

channel in unsteady flow for a control volume the mass flow in minus the mass flowing out should be the same as the change of volume in time. The momentum equations represent the balancing of forces acting on a water control volume [2]. To model river dynamics and the effects of floods, the flow process is simulated along the routes used by the river. Consequently, hydrodynamic flood models use measured river discharge/water level data, friction parameters, topographic information, river geometry, etc. [10]. These factors can contain sources of distortion that make the data discontinues and unreliable, ultimately affecting the modeling results. Additional uncertainty can also be introduced after the model output has been generated if result interpretation requires spatial relations via GIS. Errors in georeferencing, data resampling, and other GIS processing can affect output reliability.

SOBEK hydrodynamic modeling tool, which is based on the full 1D Saint Venant equations for unsteady flow, is used in this study to model the effect of sea level rise (SLR) on flooding in the lower Niger River. Thus the model assumes that all variations of velocity in the vertical directions and across channel are negligible, giving rise to uniform flow in all directions.

This paper is divided into four parts. It starts with a brief introduction to hydrodynamic modeling and the concept of uncertainty in models. The second part summarizes the hydrodynamic modeling approach used for the Niger delta, and discusses the method used to quantify the model uncertainty. The results of the uncertainty analysis of the various modeling scenarios are presented, and conclusions are made based on the results.

1.1 Analyzing Uncertainty

Uncertainty bounds of model results represent the lack of sureness about the outcome of the physical process. It indicates that the model output cannot be assessed uniquely. The main types of modeling uncertainties are structural, parametric, and stochastic [7]. The difference between them is in the source of the uncertainty and determines how each is analyzed and measured. Structural uncertainty comes from the researcher's lack of knowledge on which model to use, parametric uncertainty comes from using parameters with unsure values, and stochastic uncertainty describes the randomness observed in nature which makes parameter values to vary.

Stochastic uncertainty is considered to be irreducible and is characterized using probability density function (PDF) and other statistical measures like variance, standard deviation, etc., which describe its variability. Structural and parametric uncertainties are both considered to be subjective, and reducible with increasing data and knowledge/information. Reducible uncertainty is characterized using fuzzy set theory, rough set theories, interval mathematics, etc. Notwithstanding this division, many cases in nature contain variables that are not explicitly reducible or irreducible, therefore, the same methods are often used to quantify different kinds of uncertainty, etc. [7].

One of the most commonly used methods for analyzing uncertainty is the Monte Carlo probability-based method. Monte Carlo involves generating random samples of uncertain variables from their distributions, and using the values in the model to produce multiple sets of outputs. The outputs are then analyzed for their statistical properties and probability distribution to get the uncertainty. The Monte Carlo method is considered very robust because it estimates the complete probability distribution of model output of nonlinear systems [1].

Monte Carlo simulation however requires random sampling which increases exponentially with parameter vector, making it computationally expensive when sampling for many parameters [6]. This difficulty is being addressed through optimization techniques like Latin Hypercube sampling, Consecutive sampling, DREAM algorithm, GLUE, etc. The GLUE technique, for example, uses likelihood measures to reduce the number of parameters by weighting them according to their effect on the model output [8]. However, in low-dimensional cases where only 2–3 parameters are sampled, pure random sampling method is used, in which all vectors are sampled independently of each other and the model runs are independent.

1.2 Case Study

The study area is the lower Niger River basin located in Nigeria. The Niger River basin (Fig. 1) covers nine African countries (Guinea, Niger, Cote D'voire, Chad, Burkina Faso, Mali, Benin, Cameroon, and Nigeria) and supports a population of over 100 million people [11]. At its lower end the Niger River merges with the

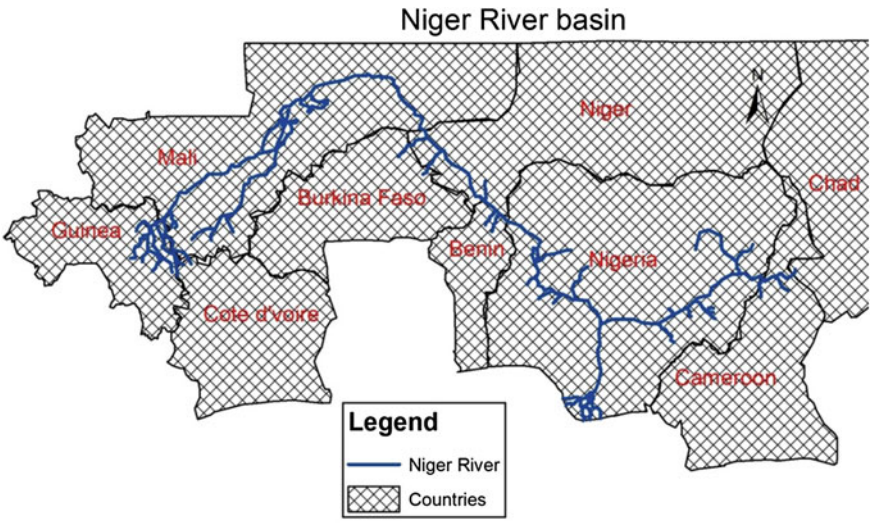

Fig. 1 The Niger River basin showing the tributaries and the member countries

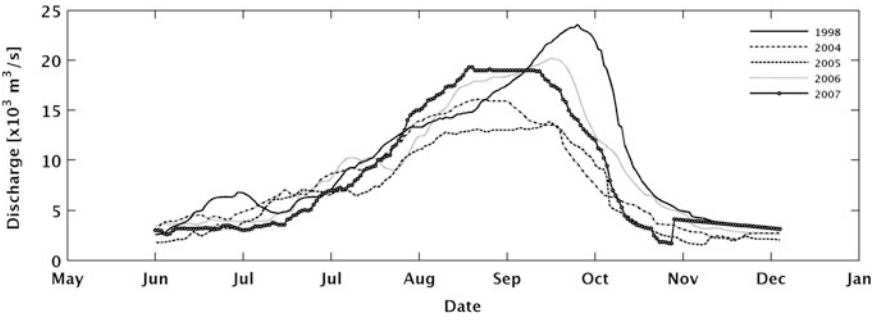

Fig. 2 Flow at the Lokoja gauging station, Nigeria

Benue River, which is its largest tributary, at Lokoja Nigeria. The now larger river flows south and later bifurcates into the Forcados (46 % of flow) and Nun (54 % of flow) rivers as it flows through the lower Niger delta.

The lower Niger delta region is low lying with an area of approximately 20,000 km^2 and 450 km of coastline. It consists of several creeks, estuaries, distributaries of the Niger River, as well as a stagnant mangrove swamp [12]. The delta is subsiding at an estimated rate of 25–125 mm/year due to the exploration of oil and gas from over 500 oil wells located onshore [9].

The hydrology of the lower Niger River basin is such that the rainy season starts in May causing water levels to rise steadily in the river, which leads to flooding in the downstream areas from July to October (Fig. 2). Consequently, river levels in the lower Niger delta show low flow periods from December to April, a high flow period from April to October, and a gradually declining flow period between October and December [4].

2 Methodology

The methodology consists of modeling the Lower Niger River based on five scenarios of sea level rise and quantifying the uncertainty of the results using probability-based analysis methods.

2.1 The Hydrodynamic Model

1D and 1D/2D hydrodynamic SOBEK models of flooding on the Niger River were set up (Fig. 3) with discharge data as upstream boundary conditions and tidal water level data as downstream boundary conditions. Based on data availability for different flow conditions in the Niger River, five modeling scenarios were simulated to evaluate the interaction of Niger River flooding with downstream rise in sea levels

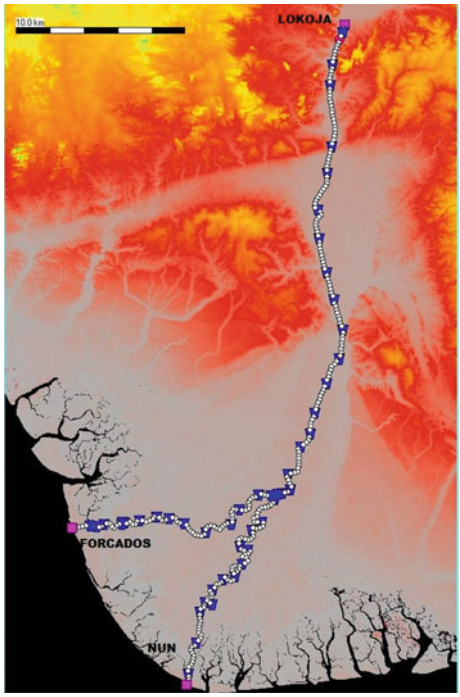

Fig. 3 SOBEK model setup of the Lower Niger River

through effects on flooding extent, flooding time, and water depth. The modeling scenarios were:

Scenario 1: Sea level rise with normal year flow from upstream
Scenario 2: Sea level rise with a flooding year flow from upstream
Scenario 3: Sea level rise with flash floods from upstream
Scenario 4: Sea level rise with subsidence and flooding year flow from upstream
Scenario 5: Sea level rise with subsidence and flash floods from upstream.

The models were run for the years 1998, 2005, 2006, and 2007. Data for 2006 and 2007 were used to simulate flooding due to rainfall/runoff because, the lower Niger River flooded in 2006 and 2007 due to high amounts of rainfall in the basin between July and September (Fig. 2). Data for 1998 was used to simulate flash flooding because, in 1998 flooding in the Niger river was modified by a dam break from upstream, which caused flash flooding in the channel [4]. Data for 2005 was used to simulate normal flow.

To simulate the scenarios the boundary conditions are varied downstream at the mouths of rivers Forcados and Nun using sea level rise (SLR) values adopted from the Rahmstorf [5] predicted values of 5.4–15.05 mm/year. The values are projected for the year 2030 as 0.12–0.45 m; and for 2050 as 0.23–0.65 m. Scenarios with land subsidence were varied downstream by adding land subsidence values to SLR values. Land subsidence values for the Niger delta are linearly projected for the

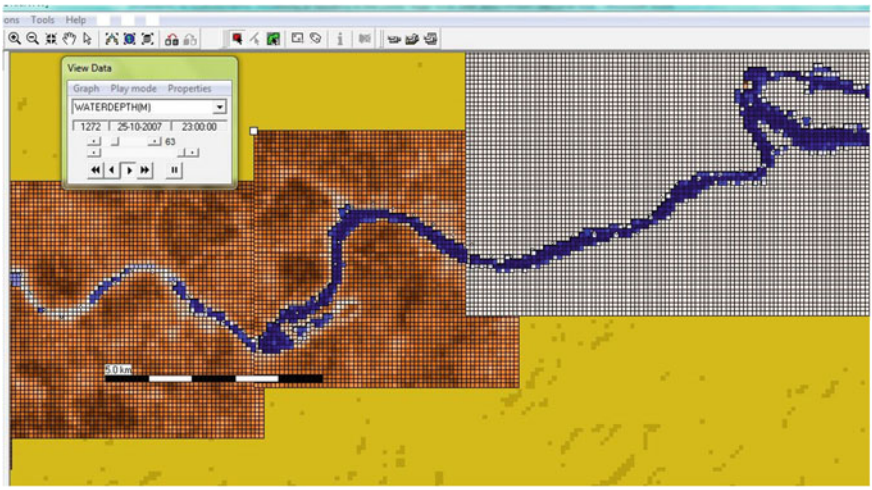

Fig. 4 SOBEK 1D/2D result of 2007 flooding along the Forcados River (*blue* areas on the grid show flooded areas)

years 2030 and 2050 from the estimated subsidence values of 25–125 mm/year for the Niger delta.

The simulations are done using the upper and lower SLR and subsidence limits for 2030 and 2050. Figure 4 shows a 1D/2D simulation result of the 2007 flood event at the bifurcation of River Niger with downstream SLR value of 0.65 m by 2050. The simulation results indicate that with SLR, flooding from the Niger River will affect more areas upstream of the Forcados and Nun rivers and increase water depths in the flooded areas around the Forcados River. Furthermore, there will be earlier onset of floods at the areas closest to the coast. Detailed information on the hydrodynamic model is available from [3].

2.2 *Probability-Based Uncertainty Analysis*

The SLR values used in this study are based on predicted SLR values from [5]. Although scientists have made such predictions based on past measurements and informed possible scenarios, the rate of the future SLR is uncertain. Therefore, our use of predicted SLR range and more so estimated land subsidence values in this study have introduced uncertainties in the hydrodynamic model which need to be quantified.

Probability-based uncertainty analysis is used to determine the uncertainty range of the modeling output which show the possible effects of SLR on the Niger delta. Pure random sampling is used to generate values from the projected 0.12–0.65 m SLR (by 2030–2050), and 0.7–6.25 m land subsidence values (by 2030–2050) for the Niger delta. 25 1D simulations of each scenario are run using the random values

generated. The simulations have a period of June to October of each year, and hourly time steps (giving an average of 3727 time steps). We use uniform distributions for the SLR and land subsidence values over the entire study area. Due to long simulation time (or otherwise a need for networked computation) only single scenario computations are done with the SOBEK 1D/2D overland flow module; the outputs compared with the range of 1D results.

The results are exported as .csv files into Microsoft excel, the data for the selected nodes are transposed for the 25 instances of each model scenario and used to generate hydrographs that are analyzed for parameter uncertainty propagated through the model. The full scenario analysis of the model output uncertainty is done using histogram analysis, summary statistics, and percentile ranging.

3 Results and Discussion

For each scenario run, uncertainty analysis is carried out on the last cross section at the mouth of rivers Nun and Forcados. The uncertainty analysis results are presented below:

3.1 Simulations with Sea Level Rise

3.1.1 Scenario 1: SLR with Normal Flow

Figure 5 shows the result of 25 simulations of the 1D model under normal flow conditions with SLR (ranging from 0.12–0.65 m). Results indicate that with higher SLR values, initial water depths in the channel (in June) are much higher than the values without SLR. From [3], the effect of SLR on normal flow from the Niger River represented by the 2005 data values, shows that rise in sea levels will cause

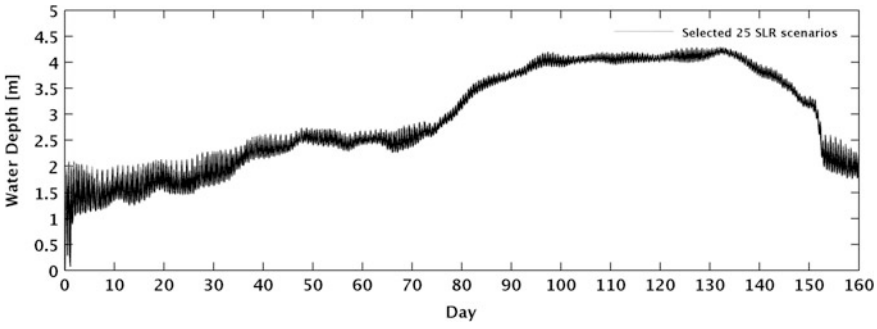

Fig. 5 Nun River: 2005 'normal flow' with downstream SLR

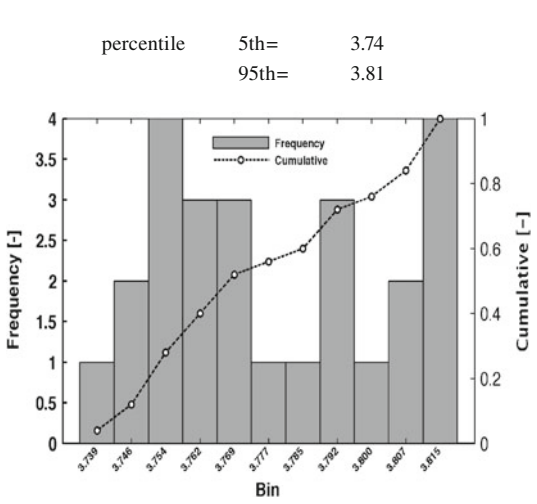

Mean	3.78
Standard Error	0.01
Median	3.77
Mode	#N/A
Standard Deviation	0.03
Sample Variance	0.00
Kurtosis	-1.37
Skewness	0.23
Range	0.08
Minimum	3.74
Maximum	3.82
Sum	94.38
Count	25.00

Fig. 6 Histogram and analysis of 'normal flow' with downstream SLR; Nun River

the flooding of areas around the Nun River which under 'normal' conditions does not overflow its banks in the rainy season.

The analysis of uncertainty, shown in Fig. 6, indicates that with SLR and normal flow, the water depth will range between 3.74 and 3.82 ± 0.01 with a 95 % probability that it will not be higher than 3.8 m above mean sea level. This implies that with 'normal' flow conditions and SLR (up to 0.65 m), there will be some flooding due to the change in sea level, but water depths at the downstream end of river Nun will not significantly change between 2030 and 2050.

3.1.2 Scenario 2: SLR with Flooding Year Flow from Upstream

The 1D/2D simulation results of the 2006 flood indicate changes in water depth for all levels of SLR in 2030 and 2050 for the Forcados River [3]. This result is also seen in the 2006 flood hydrographs in Fig. 7, which presents a harmonized computation of water levels with little difference between the 25 computed values.

The analysis of the result uncertainty (Fig. 8) implies that at the downstream of Forcados River all levels of SLR will produce high water levels (between 7.44 and 7.47 m). The standard error for the computation is 0.0 and there is only a 5 % probability of the water level being higher than the maximum water level.

3.1.3 Scenario 3: SLR with Flash Floods from Upstream

The 1D/2D simulation for SLR with flash flooding was done using the 1998 flood data. The results for SLR values of 0.12–0.41 m (by 2030) show no significant

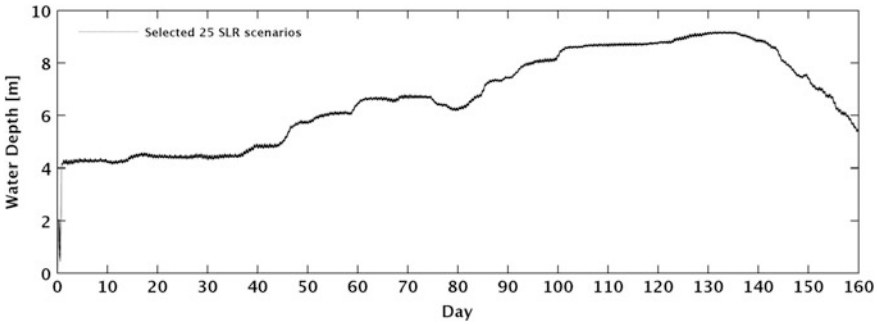

Fig. 7 2006 flood with downstream SLR for Forcados River

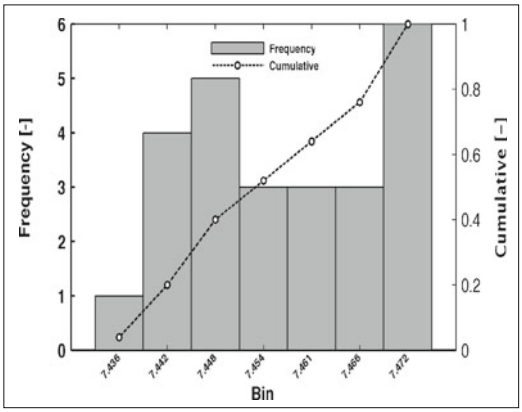

Mean	7.45
Standard Error	0.00
Median	7.45
Mode	#N/A
Standard Deviation	0.01
Sample Variance	0.00
Range	0.04
Minimum	7.44
Maximum	7.47
Sum	186.34
Count	25.00

Percentile	5% =	7.44
	95% =	7.47

Fig. 8 Histogram and analysis of 2006 flood simulation with downstream SLR; Nun River

effects. For SLR of 0.65 m by 2050, the results show continued flooding in the channel from July such that the recession in water level in August (as in the case for low SLR) still allows enough water to flood the area [3].

The 25 hydrographs used for uncertainty analysis (Fig. 9) show that the water depth during the August recession period (indicated by the arrow) is high at higher SLR values.

The histogram for the 1998 flooding at river nun (Fig. 10) shows very little difference between the minimum and maximum water levels, with 90 % of the water levels lying between the minimum and maximum values. Thus with high magnitude SLR and flash flood, increase in water levels in the Nun River will last for a significant length of time.

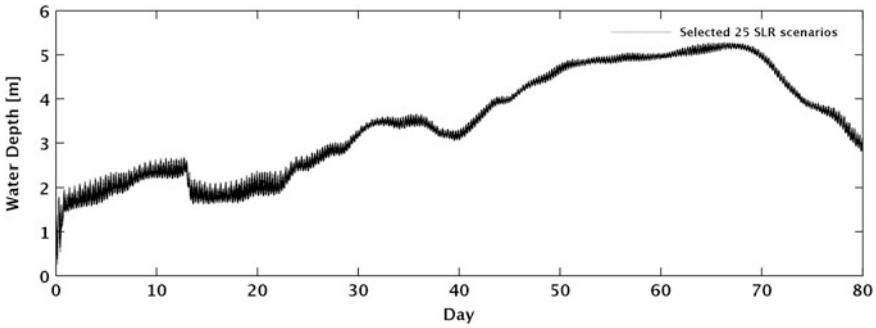

Fig. 9 1998 flood on the Nun River with SLR

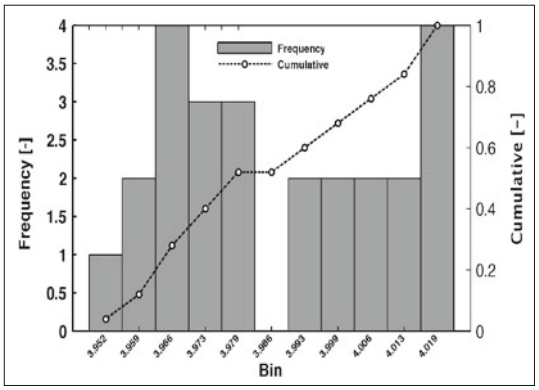

Mean	3.98
Standard Error	0.00
Median	3.98
Mode	#N/A
Standard Deviation	0.02
Sample Variance	0.00
Range	0.07
Minimum	3.95
Maximum	4.02
Sum	99.61
Count	25.00

percentile	5% =	3.95
	95% =	4.02

Fig. 10 Histogram and analysis of simulation results at downstream Nun River with the 1998 flood and SLR

3.2 Simulations with Sea Level Rise and Land Subsidence

Due to oil and gas extraction, subsidence levels in the Niger delta have been estimated to range from 25 to 125 mm/year [9]. We generated random values within this range and added them to the downstream tidal water levels with SLR projections.

3.2.1 Scenario 4: SLR with Subsidence and Flooding from Upstream

The simulation results for 2007 flood with SLR and land subsidence shows high water depths at the mouth of River Forcados [3]. In line with simulation results, the 25 hydrographs generated for uncertainty assessment show distinct water depths,

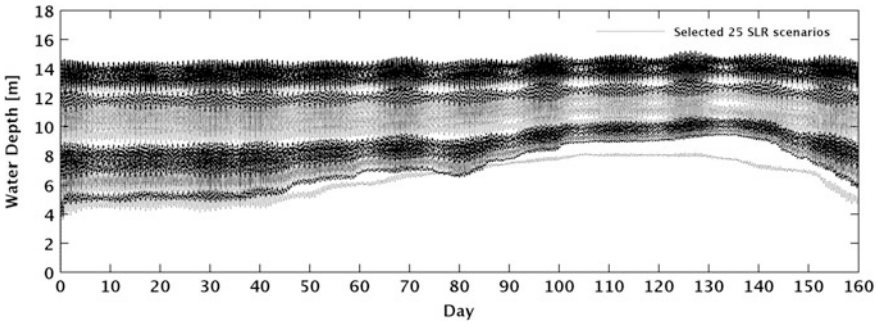

Fig. 11 2007 flood on the Forcados River with SLR and subsidence

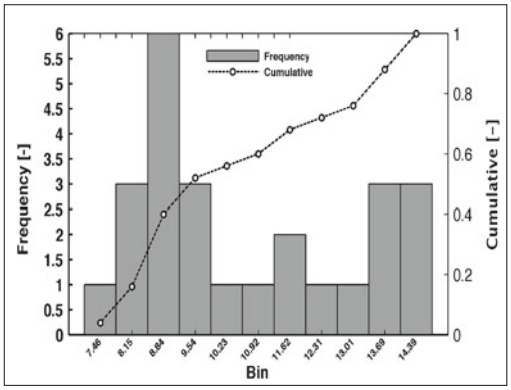

Mean	10.46
Standard Error	0.47
Median	9.43
Mode	#N/A
Standard Deviation	2.37
Sample Variance	5.60
Range	6.93
Minimum	7.46
Maximum	14.39
Sum	261.48
Count	25.00

percentile	5% =	7.83
	95% =	14.31

Fig. 12 Histogram and analysis of 2007 flood simulation with SLR and land subsidence at Forcados River

which maintain an almost constant value for all time steps at higher subsidence levels. In Fig. 11 there is no drop in water depths in the entire simulation period for water depths higher than 8 m.

From the uncertainty analysis in Fig. 12, there is 90 % probability that the water levels at downstream of Forcados will be between 7.8 and 14.3 m with land subsidence and SLR. The mean water level is 10.46 m, which implies that with subsidence the probability of inundation in the Niger delta is very high. The uncertainty for this simulation is high with a standard deviation of 2.37 m.

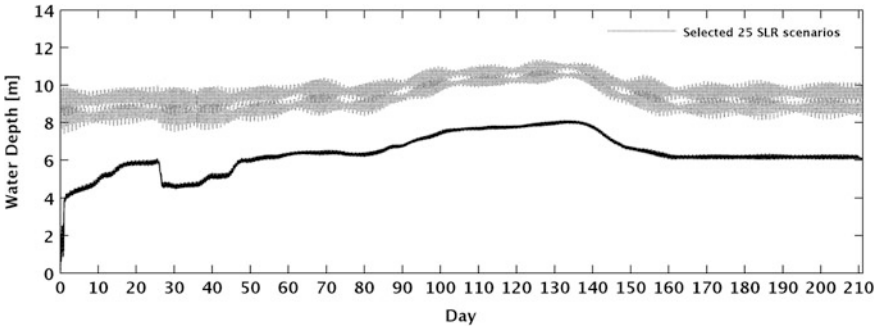

Fig. 13 1998 flood on the Forcados River with SLR and subsidence

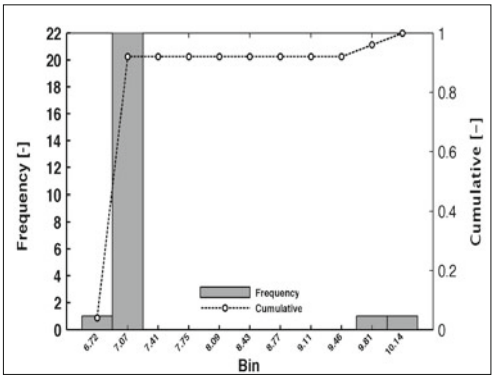

Mean	7.02
Standard Error	0.17
Median	6.79
Mode	6.81
Standard Deviation	0.84
Sample Variance	0.71
Range	3.42
Minimum	6.72
Maximum	10.14
Sum	175.51
Count	25.00

percentile	5% =	6.73
	95% =	8.93

Fig. 14 Histogram and analysis of 1998 flood simulation with SLR and land subsidence at Forcados River

3.2.2 Scenario 5: SLR with Subsidence and Flash Flooding from Upstream

The 1998 flash flood with land subsidence shows increase in water levels indicating the flash flood even at higher levels. Results of 1D/2D simulation of the 1998 flood with SLR and land subsidence shows a doubling of water depths in flooded areas around the Forcados river. This is indicated in the uncertainty analysis as the recession in water level from time step 503–1005 is absent at water levels higher than 8 m (Fig. 13).

The histogram (Fig. 14) shows a single spike at 7.07 m indicating maintenance of high water levels for 92 % of the simulations with 5 % chance of water levels surpassing 8.93 m. The uncertainty for this simulation is high with a standard deviation of 0.84 m.

4 Conclusion

The uncertainty analysis of hydrodynamic modeling of flooding in the lower Niger River with 25 simulations show low standard errors, indicating that the standard deviations are within acceptable ranges. The modeling results show that the effect of SLR for both rivers depends on the magnitude of the rise in sea levels. However, the Forcados River will be more affected by SLR than the Nun River which maintains a relatively low water depth even at all levels of SLR.

Due to the large range of estimated subsidence values, the uncertainty analyses of simulations with land subsidence show higher levels of uncertainty via high standard deviations and larger errors. Consequently, the simulations with land subsidence show a large difference between the maximum and minimum values. *Although the amount of subsidence is uncertain, the results indicate that with subsidence, the probability of flooding in the Niger delta is very high.*

In order to obtain good results with modeling approaches it is recommended that reliable subsidence values in the Niger delta be obtained via measurements and surveys undertaken at diverse sites. Such subsidence rates when obtained can show the rates at sites undergoing oil and gas extraction and those undergoing natural subsidence; thus better models of effects of subsidence can be developed for the Niger delta.

The uncertainty assessment results presented here show good agreement with the results obtained with single values of SLR and subsidence. Analysis of model uncertainty is very useful as it shows the level of reliability of a model output. It is therefore highly recommended.

References

1. Bobba, A. G., Singh, V. P., & Bengtsson, L. (1995). Application of unceratinty analysis to groundwater pollution modelling. *Journal of Environmental Geology, 26*, 89–96.
2. Chow, V. T. (1959). *Open channel hydraulics.* Singapore: Mcgraw-Hill, International Edition 1973.
3. Musa, Z. N., Popescu, I., & Mynett, A. (2014). Modelling the effects of sea level rise on flooding in the lower Niger River. *11 International Conference on Hydro-informatics, HIC 2014.* New York: HIC.
4. NDRMP. (2004). *Niger delta regional master plan: Environment and hydrology report*. Port Harcourt, Nigeria: NNDC.
5. Rahmstorf, S. (2007). A semi empirical approach to projecting future sea level rise. *Science, 315*(5810), 368–370.
6. Shrestha, D. L., Kayastha, N., & Solomatine, D. P. (2009). A novel approache to parameter uncertainty analysis of hydrological models using neural networks. *Hydrology, Earth Systems Science, 13*, 1235–1248.
7. Smith, E. (2002). Uncertainty analysis. In A. H. El-Shaarawi & W. W. Piegorsch (Eds.), *Encyclopedia of environmentrics* (Vol. 4, pp. 2283–2297). Chichester: John Wiley & Sons Ltd.

8. Stedinger, J. R., Vogel, R. M., Lee, S. U., & Batchelder, R. (2008). Appraisal of the Generalized Likelihood Uncertainty Estimation (GLUE) method. *WATER RESOURCES RESEARCH, 44*. doi:10.1029/2008WR006822.
9. Syvitski, J. P. (2008). Deltas at risk. *Sustainable Science, 3*, 23–32. doi:10.1007/s11625-008-0043-3.
10. Thompson, A., Yiping, G., & Moin, S. (2008). Uncertainty analysis of a two-dimensional hydrodynamic model. *Journal of Great Lakes Research, 34*(3), 472–484. doi:http://dx.doi.org/10.3394/0380-1330(2008)34[472:UAOATH]2.0.CO;2.
11. UNEP. (2010). *Africa water atlas. Division of Early Warning and Assessment (DEWA).* Nairobi, Kenya: United Nations Environment Programme (UNEP).
12. Uyigue, E. (2007). *Climate change in the Niger delta.* Retrieved from CIEL.ORG: www.ciel.org/Publications/Climate/CaseStudy_Nigeria_Dec07.pdf.

Fudaa-Crue and Crue10: Overview of New Concepts and Tools for Hydraulic Modelling

Pierre Balayn, Jean-Marc Battista and Frédéric Deniger

1 Introduction

CNR is France's leading producer of exclusively renewable energy, with 18 hydroelectric power plants along the Rhône River, providing a capacity of 3000 MW. In order to operate its plants, CNR has developed several hydroinformatic tools for study goals (such as checking concession-holder requirements and improving water management) and operational applications (e.g. real-time local development regulation, centralized operational forecast of energy production, simulation of flood propagation, operators training to manual control, etc.) [1]. A central tool, named Crue, is used to design and adapt each model to the specific needs of each application's hypothesis. It deals with 1-D looped-network hydraulic models with additional storage areas, along more than 500 km of French Rhône River.

Crue has been developed by CNR since the 1970s, initially for engineering purposes. A recent major update led to a new set of tools, including Fudaa-Crue modelling software and Crue10 computational core. The aim of this paper is to focus on some features of the new version of Crue, as an example of what modelling software may offer nowadays.

P. Balayn (✉) · J.-M. Battista · F. Deniger
Compagnie Nationale du Rhône, 2rue André Bonin, 69316 Lyon cedex 04, France
e-mail: p.balayn@cnr.tm.fr

J.-M. Battista
e-mail: j.battista@cnr.tm.fr

F. Deniger
e-mail: frederic.deniger@adexcel-consulting.com

P. Gourbesville et al. (eds.), *Advances in Hydroinformatics*,
Springer Water, DOI 10.1007/978-981-287-615-7_14

In this paper, four characteristics, maybe useful for other modelling softwares, are presented:

- The original packaging of the tool based on an open-source modelling software.
- The dynamic shared dictionary at the centre of the design.
- The comparison system and thus the automatic test-case library.
- The open and interactive documentary system.

This new version of Crue is a solid basis for new kinds of incoming studies, dealing with data assimilation [2] or uncertainty propagation [3]. Some tests have recently been done with Crue in these fields.

2 An Open Source Modelling Software

The Crue system is composed of two main parts: Fudaa-Crue modelling software and Crue10 computational core. Extra applications are also connected, such as the GIS modelling software GeoGAMA-Crue, the simulation component repository SYSSIH and the hydraulic model repository.

The inner part of the core is reused as a library component in every tool that needs 1D hydrodynamic computation in CNR's processes. The core is thus enhanced with regular developments (e.g. adaptive time steps). In order to guarantee its maintainability, it has been redesigned from Fortran to C++, with object conception for its higher levels. The core's source code is the property of CNR, but it can be shared with public partners through specific conventions.

On the other hand, the modelling software is an open-source development, in order to be freely shared with the hydraulic-modelling community. It is based on the Fudaa [4] framework. This Java framework has been held by a consortium including Cerema (former Cetmef), Irstea, EDF, Artelia and CNR, around hydraulic simulation. The main objectives of this framework are to pool user interface development and to allow communications between the different computational cores maintained by the consortium's partners.

Fudaa contains business layers for hydrodynamic computations, exploitation simulation (river and harbour), structures, etc., and common view layers for 1D, 2D and 3D representation. The Fudaa framework integrates open-source components, including Geotools (GIS toolkit), Apache POI (Microsoft Office files interoperability) and JGraphT (graph library). Thanks to the open-source approach, external libraries distributed under open-source licence can be reused in Fudaa applications.

Fudaa-Crue is also open source, with a public data object model. It is built on top of the Netbeans platform, distributed by Oracle, providing common application features like window management, actions linking, etc., and distribution packaging. Fudaa-Crue manages XML files under an XSD-control (the control files are also used by Crue10). Fudaa-Crue supports geographical design for modelling and results exploitation, and can also import and export shape files for GIS interoperability.

Fudaa and Fudaa-Crue are distributed under the GPLv2 licence and use a public software forge (sourceforge) to share the source code. To facilitate collaboration and new developers integration, development best practices are used: conventional build tool (Maven), public issue tracking system [5], public documentation site [6] and continuous integration. Once a year, the consortium's development and business teams are gathered to outline the last improvements and to introduce or prepare the next projects relative to the Fudaa framework.

The exchanges between the modelling software and the computational core rely on files. This allows different computational cores with the same modelling software. Furthermore, this weak link is useful for each part upgrades. As the data object model, the file structure is public and the XSD set is given (in order to control the XML files grammar) (Tables 1 and 2).

Many files are involved. Fortunately, the user does not have to manage them directly: Fudaa-Crue handles them in a coherent way. The files have been designed to carry only one nature of data at one level of modelling, in order to reuse them between several scenarios:

- Nature of data: network description, cross sections and beds, friction factors, structures description, numerical parameters, initial conditions, boundary condition types, boundary condition data (hydrogram and limnigram library), options for the network preprocessing, geometrical preprocessing, initial conditions preprocessing and hydraulic computation, results for each processing (preprocessings and hydraulic computation), logs for each processing.
- Level of modelling: the processing is carried out at the scenario-level, it can involve one or many models defined at the model-level, each model is composed of one or many submodels (in order to compose alternative models with more detailed versus synthetic parts) defined at the submodel-level; at the top level, the study-level allows to gather different scenarios.

3 An Interlinked Dictionary File

The computational core and the modelling software share a dictionary file (see CrueConfigMetier XML file on Fig. 1). It is dynamically interpreted at each run and is used to share data definitions.

It defines each variable (data or result) used, with a unique code. The information for each variable is read in the dictionary, and if not found, the initialization of the application aborts. Each variable bears the following information:

- A validity range: used to reject any out-of-range user's input and to alert (error level) on out-of-range output values.
- A usual range: used to check the user's input (warning message, but possible input) and to warn (warning level) on the output values.
- A nature, centralising some information:

Table 1 Example of variable definition. Crue's dictionary defines 195 variables

Variable	Nature	Validity range		Usual range		Signification
H	Nat_Z	−Inf	+Inf	0	+4000	Head on the cross section
J	Nat_Jx	0	+Inf	0	+0.03	Head slope on the cross section
K	Nat_K	0	+Inf	+8	+60	Strickler friction factor
L	Nat_Dy	0	+Inf	0	+Inf	Width of free surface on the cross section
P	Nat_Dy	0	+Inf	0	+Inf	Wetted perimeter
Q	Nat_Q	−Inf	+Inf	−15000	+15000	Discharge over the cross section
Qapp	Nat_Q	−Inf	+Inf	−15000	+15000	Discharge input (output if negative) at a node
R	Nat_Dz	0	+Inf	0	+100	Hydraulic radius on the cross section
S	Nat_S	0	+Inf	0	+Inf	Cross section area
Splan	Nat_Splan	0	+Inf	0	+Inf	Planimetric area of water on the branch
TempsLoi	Nat_Dt	0	3456000	0	3456000	Time period since the origin of the computation
Xp	Nat_X	0	+Inf	0	+Inf	Curvilinear abscissa of the cross section into the branch
Xt	Nat_X	−Inf	+Inf	−2500	+2500	Lateral abscissa of a point into the cross section
Y	Nat_Dz	0	+Inf	0	+100	Water elevation above Zf on the cross section
Z	Nat_Z	−Inf	+Inf	−15	+4000	Water surface level
Zg	Nat_Z	−Inf	+Inf	−15	+4000	Ground elevation of a point of the cross section
Zf	Nat_Z	−Inf	+Inf	−15	+4000	Lowest ground elevation of the cross section (thalweg)
Zimp	Nat_Z	−Inf	+Inf	−15	+4000	Imposed water surface level as a boundary condition

Table 2 Example of nature of variable definition. Crue's dictionary defines 56 natures of variables

Nature	Unit	Comparison threshold	Presentation precision
Nat_Z	mNGF	0,00001	0,00001
Nat_Jx	m/m	0,000001	0,000001
Nat_K	$m^{1/3}/s$	0,001	0,001
Nat_Dy	m	0,001	0,001
Nat_Q	m^3/s	0,0001	0,0001
Nat_Dz	m	0,00001	0,00001
Nat_S	m^2	0,0001	0,0001
Nat_Dt	s	0,001	0,001
Nat_Splan	m^2	0,01	0,01
Nat_X	m	0,001	0,001

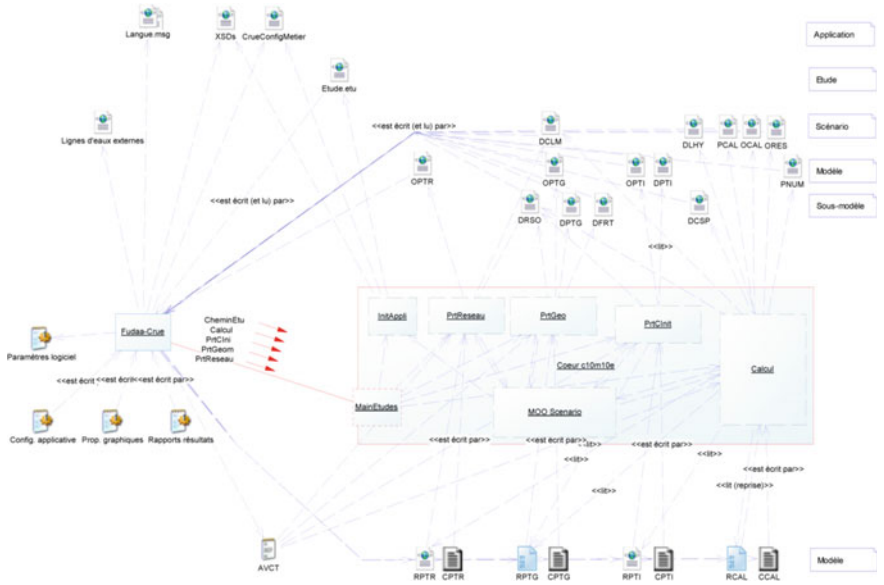

Fig. 1 Communication diagram between Fudaa-Crue modelling software and Crue10 computational core. It uses XML files (e.g. CrueConfigMetier, Etude.etu, DCLM, etc.), combined binary and XML files (e.g. RPTG, RCAL), CSV files (e.g. CPTR, CPTG, CPTI, CCAL), text files (e.g. AVCT), text INI files (e.g. ParamètresLogicels, etc.), but also (not shown here) GIS shapefiles and XSD files (associated with the XML files)

- A comparison threshold: used to compare (equality and inequality) two real variables of the same nature. All the code was written to implement these enhanced comparisons.
- A presentation precision: used to format the values presented in the user interface. Its value can be different from the comparison threshold.

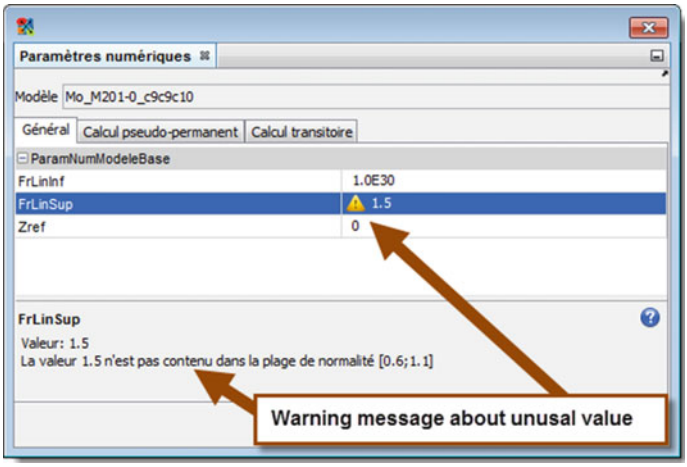

Fig. 2 Example of warning after an unusual user's input

Everywhere in the Crue applications, a given value is presented the same way to the user; furthermore, neither recompilation nor re-computation is needed to tune the applications' presentation of values.

- A unit: used to format the values presented in the user interface.

On this basis, both the computational core and the modelling software control the given and computed values and compose messages: users are warned about odd values and are helped in log interpretation (Fig. 2).

The dictionary also describes in a standardised way the "laws" (Y vs. X) used in the applications and their extrapolation behaviour. Obviously, each point value is checked according to the abscissa and ordinate variable. For example:

- Zg versus Xt for the profile definition, with no extrapolation allowed (an error occurs for an Xt value out of the definition range).
- Qapp versus TempsLoi for the upstream input hydrogram, with flat extrapolations (constant value, equal to the nearest point of the definition range).
- Zimp versus Q for the downstream ratting curve, with flat extrapolation for the low values of Q and interpolated extrapolations for the high values (interpolation according to the two nearest points of the definition range).

4 The Built-in Comparison System

The comparison system is called OTFA (Outil de Tests Fonctionnels Automatisés). It performs a set of systematic tree-tests comparison, regarding the comparison threshold of variable's nature.

This powerful feature detects only significant differences between two different scenarios. It is also used for automated non-regression tests on the test-case libraries. OTFA is usable as a non-GUI executable (batch) as well as in the Fudaa-Crue application.

The comparison system requires an XML file as the input data. This file defines the test campaign: a list of scenarios to process and then to compare (results and data are compared). Different operations could be done on the scenario before the comparison:

- Migrate from one version to another (useful for grammar migration over the test-case library).
- Perform a computation (a run).

The comparison is then performed on the last operation results.

For each line of the campaign, a computational core configuration must be defined. This configuration is composed by the dictionary file and the computational core executable. Thus it is also possible to compare the results of two different versions of the computational core system. The comparison produces two files:

- A report file with the logs of all performed tasks.
- A result file containing the detailed results of the comparison.

The Fudaa-Crue data object model was designed to perform automated comparison with data and results. Thanks to this design, all the definitions of the comparison tests can be made in a declarative way, as lists of comparison items; the corresponding applicative configuration files are very easy to tune, with no further development (Fig. 3).

A comparison item is defined in two parts: first, the selection of the objects to compare and then the type of comparison to perform. The objects to compare are selected thanks to XPath queries (path expressions used to select nodes in an XML document, applied on graphs of objects; the interpreter JXPath [7] from the Apache Software Foundation is used to perform this binding between XML and objects). Once the selection is done, several types of comparisons can be carried out:

- For single objects, comparison of their properties: objects of the same name are compared with one another, and so on for properties of the same name.
- For lists of objects, different options are available:
  - Search for list content differences: which objects names are in the first list and not in the second, and vice versa?
  - Order check: are the objects names ordered the same?

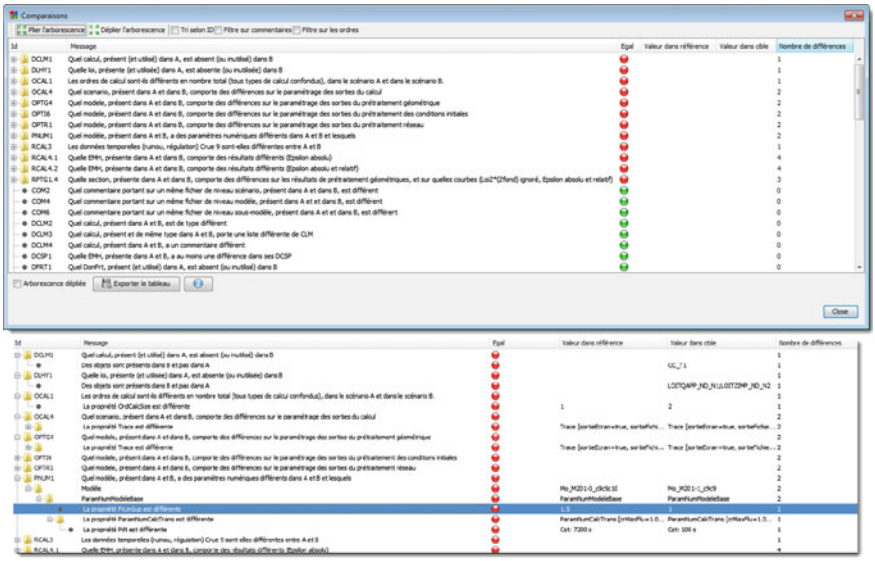

Fig. 3 *Above*, example of global results for a comparison between two scenarios on Fudaa-Crue's OTFA system (comparison items with differences are sorted first). *Below*, zoom on treeview details, for differences analysis

5 The Open Documentation System

Fudaa-Crue operates an online system of documentation on Crue (SyDoC). It was originally designed for the Fudaa-Crue and Crue10 project, but can be widely reused: CNR plans to use it for its other simulation tools.

As with other interactive help tools, it is a set of pages with navigation and search features (relying on HTML pages). But it was designed more like a Wiki. Its first remarkable characteristic is to concentrate wide spectrum documentation, with many links between:

- The user's manual, originally written by the Fudaa-Crue development team.
- The hydraulic modelling documentation (what are the hypotheses and limits, which equations are used, in which way, etc., and the dictionary with data definition, see Sect. 3), from the functional experts. In addition, a general free-surface flow course is being added (demonstrations of the different formulas, etc.).
- The numerical analysis documentation (how are the equations discretized, how is the system solved, etc.), from the numerical experts.
- The collaborative user's documentation, written by the users themselves; it allows users to comment on other documents, to share their experience and user's tips, to give some examples of alternative modelling techniques tested and their results.

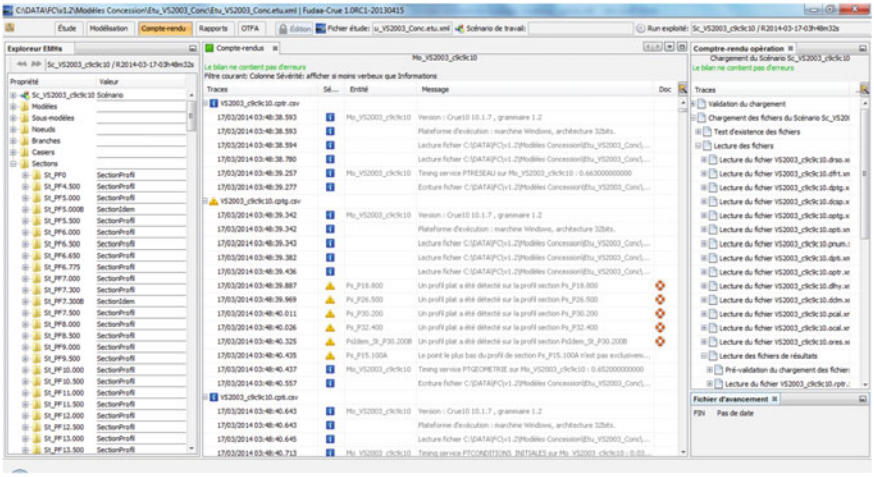

Fig. 4 In the *centre*, example of a log file as presented by Fudaa-Crue; the log lines are grouped by processing (up to 3 preprocessings and 1 hydraulic computation). A short message describes the log line; for more information, the user may click on the icon on the *right*, in order to jump into SyDoC

- The development generated documentations (Doxygen generated documentation for Crue10 computational core, and JavaDoc for Fudaa-Crue modelling software) can also be reached from SyDoC (but only for program developers).

Changes and additions pages may be proposed by each user. They are centralized and made by the documentation administrator, in order to maintain consistency. Fudaa-Crue offers useful features to look for dead links (integrity check) before publishing a new version of SyDoC's content.

SyDoC offers multilingual support: the user interface language can be chosen by the user in Fudaa-Crue's user configuration. The same language preference is used for the set of documentation. Thus, the documentation administrator has to maintain several documentation sets.

The second notable characteristic of SyDoC is the multiple ways to reach a page:

- Classic navigation features: hyperlink, undo/redo, search engine on key words, navigation from the menu.
- Help button on a specific frame of Fudaa-Crue: a specific help page is shown, with a description of the frame and links to tip pages.
- F1 key: the first page shown in SyDoC depends on Fudaa-Crue's active panel/frame (a configuration file binds each frame with a documentation page). This provides a contextual help, similar to the previous point.
- Core's execution logs: Fudaa-Crue presents Crue10's logs to the user. A documentation page can be specified for each different type of message (a configuration file binds each with a documentation page). It allows the user to click on the doc icon, and then to navigate SyDoC for additional explanation, advice or user's tip (Fig. 4).

6 Conclusions

CNR carried out a major update on his central hydraulic modelling tool. The new Crue system relies on notable features, presented here as an example of what modelling software could offer nowadays. These improvements needed a total rewriting of the codes (modelling software and computational core), with special attention to the design for long-term maintainability.

For any new project of simulation software, or if interested in using Fudaa-Crue modelling software, the following points should require attention:

- Design of the system, with shared and open-source parts.
- Object-oriented data modelling, relying on a shared data description.
- Built-in comparison system and test-case library.
- User interactive documentary system, as a central part of the system.

Acknowledgments This long-term work has been particularly supported by Jean-Robert Lagoutte, Laetitia Grimaldi and Robin Naulet, as CNR's project owner. Crue10 developments have been carried out by Astek Rhône-Alpes. The Fudaa framework part and Fudaa-Crue developments were entrusted to Frédéric Deniger. Jean-Marc Battista and Pierre Balayn provided the mastery of the project, respectively, on the technical and functional parts.

References

1. Grimaldi L., Bontron G. & Balayn P. (2012). Hydraulic modelling for Rhône river operation. *SimHydro 2012: New Trends in Simulation*, September 12–14, 2012, Sophia Antipolis.
2. Jean-Baptiste, N., Malaterre, P.-O., Dorée, C., & Sau, J. (2011). Data assimilation for real-time estimation of hydraulic states and unmeasured perturbations in a 1D hydrodynamic model. *Journal of Mathematics and Computers in Simulation, 81*(10), 2201–2214.
3. Nguyen, T., Richet, Y., Balayn, P., & Bardet L. (2013). Étude de la propagation d'incertitudes dans un modèle hydraulique 1D. *Événements extrêmes d'inondation: de l'étude de l'aléa à la gestion du risque pour les ouvrages hydrauliques*, novembre, 13–14, 2013, Lyon.
4. http://fr.wikipedia.org/wiki/Fudaa, http://sourceforge.net/projects/fudaa/.
5. https://fudaa-project.atlassian.net.
6. https://fudaa-project.atlassian.net/wiki/dashboard.action.
7. http://commons.apache.org/proper/commons-jxpath/.

AV2D: A Data-Driven Hydrological Forecasting Approach Based on Aggregate Variables

Wilfried Segretier and Martine Collard

1 Introduction

Natural risks represent a permanent threat for our modern society. Due to their generally unpredictable and potentially destructive nature, they have been widely studied for many years to help understanding their mechanisms. In this study, we focus on flood phenomena which can cause major damages in urbanized and industrial areas. Flash floods have the particularity to be very sudden and occur in small catchments with rugged topography and subject to large and localized precipitations. The Caribbean region contains mainly volcanic island and is concerned with tropical meteorological conditions including important storms and massive and localized rainfalls. Therefore, the anticipation of hydrological events represents a major problem for local authorities.

Classical hydrological forecasting systems mainly designed for larger and slower watersheds, as found in Europe, tends to be less efficient when applied to flash flood subject catchments. In order to overcome this problem, we propose the AV2D original approach consisting in the search for juries of aggregate variables as sets of parameters taking into account the hydrological dynamic over time periods thanks to statistical functions.

The work presented in this paper follows our preliminary works [7, 8]. A new case study of Caribbean watershed located in the island of Puerto Rico is considered.

This paper is organized in six sections. Section 2 presents an overview of hydrological predictive approach. Section 3 details the context and data related to

W. Segretier (✉) · M. Collard
LAMIA Laboratory, University of French West Indies and Guiana, Cayenne, French Guiana
e-mail: wilfried.segretier@univ-ag.fr

M. Collard
e-mail: martine.collard@univ-ag.fr

P. Gourbesville et al. (eds.), *Advances in Hydroinformatics*,
Springer Water, DOI 10.1007/978-981-287-615-7_15

the case study considered. Section 4 presents the AV2D approach that we propose in this work to address the problem of flash flood prediction. Finally, Sect. 5 presents the experiments and results obtained while Sect. 6 concludes and give some perspectives for future work.

2 Related Work

Hydrological forecasting approaches can be classified according to the way they represent physical processes underlying rivers or water streams activity.

Physically based models (PBM) typically use differential equations on flows to model the behavior of streams with respect to multiple parameters such as soil properties, topographical features, or evapotranspiration rates. They are sometimes called *spatially distributed models* since they use more or less accurate grid-based representations of river basins. They are generally very complex and their performances highly depend on the initialization of their parameters; thus, simpler approaches have been designed and have proved to provide more accurate performances in operational and short term flood forecasting [3, 10].

Conceptual or *semi-distributed models* can be seen as "simplifications" of PBM, since they are built on notions such as reservoirs filling and emptying, on approximations of parameters and on mathematical or empirical knowledge to model the hydrological dynamics of water streams.

Over the last 30 years, the democratization of more powerful computing devices led to new kind of models, known as *data-driven models* (DDM), inspired from different fields such as machine learning, artificial intelligence, or statistical analysis. A review of hydrological DDMs literature shows that most solutions in this domain have used Artificial Neural Networks (ANN), mostly for their ability to model nonlinear relationships [12]. However, ANNs acts as black box models, since they do not provide any easily interpretable explanation about their performances. Generally, stakeholders tend to trust models that express their predictions explicitly. In our work, the long-term objective is to design a decision making tool able to provide a comprehensible knowledge representation that explains why a flood or a nonflood is predicted. Thus, in this work, the first strong requirement was the *readability* of the models provided to end users that are experts in the hydrological domain.

3 Case Study

The watershed of the Gurabo River is a small watershed located in the north of the main island of Puerto Rico. Unlike the southern regions of the island, this area is very mountainous. The river is monitored by the *USGS Caribbean Water Science Center*. Thanks to several runoff measure stations positioned along the river course.

Fig. 1 Map of the Gurabo watershed

In this work, we considered the data of three of these stations—from up to down Rio Valenciano Nr Juncos (50056400), Rio Gurabo Blw El Mango (50055750), and Rio Gurabo. At Gurabo (50057000). The default record interval is 15 min. Figure 1 shows a map of the watershed. We can see the river stream in blue and the three stations considered circled in red. The river flows from the bottom of the image to the top.

3.1 Preprocessing

In a knowledge discovery from data (KDD) process, preprocessing represents a crucial step since it consists of cleaning, transforming, normalizing, or replacing the raw data. Indeed, real-world data are often noisy and organized in nonefficient way. Obviously, if the preprocessing step is well achieved, one can expect to find more easily the relevant information potentially hidden in the data.

A meticulous preanalysis of the two aforementioned raw datasets showed us that they were subjected to two main problems, namely the presence of:

- missing data due to unavailability of one or more station(s) during time periods ranging from few minutes to several months,
- and erroneous data corresponding to the records of malfunctioning stations (calibration problems, failing components, …).

The cleaning step involves the suppression of erroneous data, which could bias the data mining phase if they were kept, and filling of missing data. To do so, we followed a two-step methodology for the hydrological data (i.e., height level and runoff).

First, we eliminated in a semi-automatic way, thanks to a visualization tool that we developed specifically for this purpose, the most obviously erroneous data

periods. For instance, miscalibrated stations can produce negative values or irrealistic raises (for instance, from 10 to 1000 mm in one or two time steps).

Then, we tried to fill all the missing gaps, i.e., the originally missing values and the new gaps resulting from erroneous data suppression. To do so, we identified different situations depending on the length δgap of the gaps and/or on the hydrological activity observed in the *neighborhood* of concerned stations. By neighborhood, we mean spatial proximity, i.e., the activity observed on adjacent stations, or temporal proximity, i.e., the activity observed on the same station or on adjacent stations) before and after gaps. When δgap was:

- *short* (from 12 to 60 min), whatever the hydrological activity observed in the neighborhood, we adopted a linear interpolation strategy: the *i*th missing value di ($1 \leq i \leq n$) between two present values $d0$ and ($dn + 1$) is computed as $di = d0 + i * R$ with $R = (d(n + 1) - d0)/n$ and $n = (\delta gap/record\ interval) - 1$.
- *intermediate* (from 1 h to up to 6 days) and the activity observed in the neighborhood were quiet, i.e., no important raises or peeks, we also applied a linear interpolation as defined in (a);
- also *intermediate* but the activity observed in the neighborhood was not calm, i.e., at least one important peek observed, we used, when it was possible, nonlinear regression techniques such as ANN and expert knowledge to reproduce realistic data from observed data.
- *long* (more than 6 days) we did not replace the missing data since we estimated that the uncertainty was too important.

In order to apply automatic classification techniques for flash flood prediction on the hydro-meteorological data of this case study, we identified 70 hydrological events for the Gurabo River watershed, among which 28 flood events and 42 nonflood events. These events are characterized by the hydrological activity observed on an *event station* located in the area where we want to achieve prediction. When flood threshold values, provided for each station by experts of the basins are reached, we label the situation as a flood event (F) while nonflood events (N) correspond to the reaching of high values remaining under the thresholds, meaning that an activity is observed but do not lead to a flood. Since we are interested only in the conditions preceding events, the labels match the moment of over-passing a flood threshold value or reaching a high under threshold value. Next values are discarded.

We chose the *50057000* station as the event station because it presents the advantage to offer a good tradeoff between its proximity to the critical area and the number of events detected for its values. All the events have been selected in such a way that they are independent from each other, i.e., we checked that they were enough spaced in time so that the conditions of one do not influence another.

Regarding the construction of the final datasets, we associated each event to the values observed during time intervals [*t-k-prec, t-prec*] on all the stations, where t is the time of the event (flood threshold over-passing on event station) and *prec* is the *precocity* or *lead time* between the moment of prediction and the occurrence of the event. We use the term *measure stations* to refer to the stations at time *t-prec*.

Table 1 Dataset after transformation

Evt	$R^{\text{Station}_i}_{t-k-prec}$	$R^{\text{Station}_i}_{t-(k-1)-prec}$	...	$R^{\text{Station}_i}_{t-prec}$	...	$R^{\text{Station}_R}_{t-prec}$	Class F/N (t)
1	321	?	…	645	…	579	N
2	1235	1267	…	1678	…	2319	F
70	1567	1517	…	?	…	3299	F

Table 1 shows the structure of the datasets obtained after this transformation step. Each line stands for an event; the last column gives the corresponding class while all the other columns correspond to measure the station values.

3.2 *Exploratory Analysis*

The hydrological activity observed in Caribbean watersheds is very fast, leading to disastrous and hardly predictable flood events. Indeed, as we can see on Fig. 1, the catchments of this region have relatively small areas and contains steep slopes. Moreover, they are subject to tropical rainfalls and storms having the particularities to be massive and often localized. Figure 2a–d shows four typical examples of flood

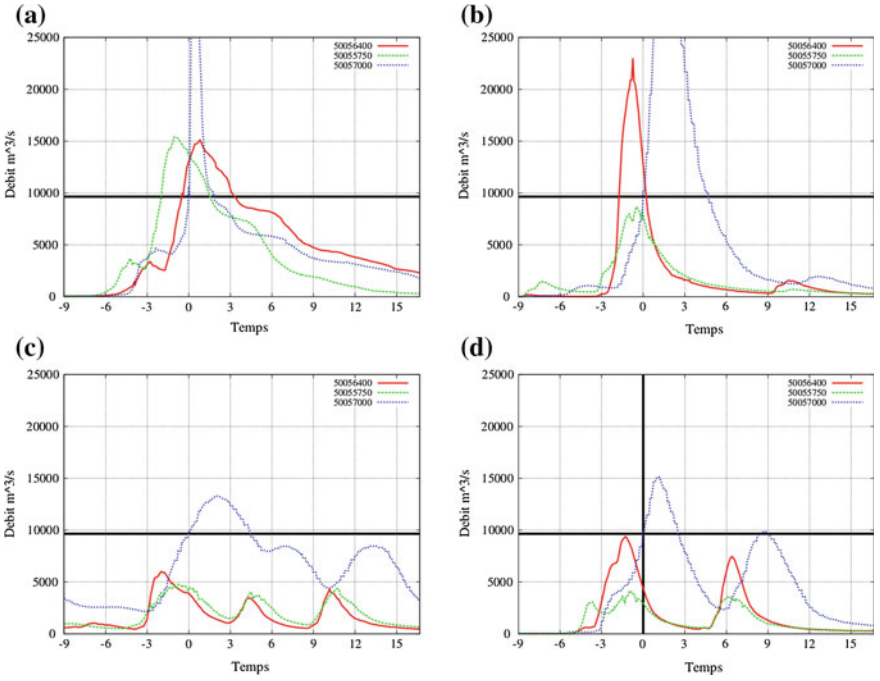

Fig. 2 Four typical hydrological events observed on the Gurabo watershed. **a** Gurabo 1. **b** Gurabo 2. **c** Gurabo 3. **d** Gurabo 4

events observed in the Gurabo watershed. The x-axis represents the evolution of time in hours—with hour 0, the time of the event, i.e., over-passing of flood threshold on 50057000 (Gurabo). The y-axis represents normalized hydrological measures (m^3⁄s). These figures confirm the rapidity and the magnitude of the hydrological behavior of the events observed. Moreover, we can see interesting correlations between the hydrological values observed at different locations by the different stations (the rises follow roughly the up to down order of the stations).

4 AV2D: Aggregate Variables Data-Driven Approach

4.1 Aggregate Variables

4.1.1 Definitions

In this work, we define an aggregate variable (AV) **structure** as a 4-uplet *(A, T, F, D)* in which:

- A is the set of attributes of the dataset,
- T is a set of time windows defined by some parameters and which can be associated with an attribute $a \in A$,
- F is a set of *aggregation* function f such as the mean, standard deviation, slope, minimum, maximum …,
- D is a set of decision functions d.

An aggregate variable is defined as an instance of this structure, thus a 4-uplet *(a, t, f, d)* ∈ A * T * F * D. We call *a, t, f* ,and *d* the *parameters* of an AV. We call *aggregate value* the result of the aggregation function of an AV. The decision function computed for this value allows us to know the class associated by the AV to the situation encountered.

For instance, let's consider the following simple AV structure in the context of transactional data:

- A = {"number of products purchased", "number of product sold"}
- T = {"January 2012", "February 2012", …, "December 2012"}
- F = {"Mean", "Standard deviation" }
- D the set of functions of the form: $d(x) = \begin{cases} A & \text{if } x \leq thresh \\ B & \text{if } x > thresh \end{cases}$

The aggregate variable *AV1* defined by:
a = "number of products purchased", t = "January 2012", f = Mean, $d = d1$ with $d1(x) = \begin{cases} A & \text{if } x \leq 453 \\ B & \text{if } x > 453 \end{cases}$ represents the mean of products purchased during the period of January 2012 and the prediction if this value is compared to 453. In a similar way, we can define the following AVs:

- *AV2*: a = "number of product sold", t = "March 2012", f = "Standard deviation", $d = d2$ with $\mathrm{d2(x)} = \begin{cases} A & \text{if } x \leq 11 \\ B & \text{if } x > 11 \end{cases}$
- *AV3*: a = "number of product sold", t = " January 2012", f = "Mean", $d = d3$ with $d3(x) = \begin{cases} A & \text{if } x \leq 790 \\ B & \text{if } x > 790 \end{cases}$

In an operational point of view, an AV is interpreted as follows: *if the result of the function f computed on the n instances of the attribute a associated to the time window t is included in a given value interval, then the class X is chosen by the AV.*

4.2 Hydrometeorological Aggregate Variables

In the context of hydrological events classification—Flood (F) or Non-flood (N)—we define the following AV structure:

- A is the set of attributes representing the values recorded by each hydrometeorological sensor available for the watershed considered,
- T is the set of time windows characterized by the two following parameters:

  (1) a precocity time *prec* corresponding to the prediction lead time, i.e., the time shift in minutes, between the last value observable and the beginning of the event to predict. Its value set is [*prec_min, prec_max*]; the timestep is 15 min.

  (2) an aggregation time *agg* corresponding to the time period during which the attribute values are considered for the computation of the aggregation value. This time period is adjacent to the precocity period. Its value set is [0, *agg_max*] with a timestep depending on the case study and sensor type.

  Figure 3 illustrates the use of these two parameters *prec* and *agg* in an AV.

- F = {"mean", "standard deviation", "minimum", "maximum", "slope"}
- D is the set of functions defined on [0, *agg_max*] such as: $\mathrm{d(x)} = \begin{cases} N & \text{if } x \leq tresh \\ F & \text{if } x > tresh \end{cases}$ with the parameter *tresh* representing a decision threshold.

4.2.1 Juries of Aggregate Variables

In order to face complex problems requiring more than single AVs to be efficiently modelized, we introduce the notion of *juries of AVs*. We define a jury of *AVs* of size n as a set of n AVs. It is noted: $Jn = \{(a1, t1, f1, d1), (a2, t2, f2, d2), \ldots, (an, tn, fn, dn)\} = \{AV1, AV2, \ldots, AVn\}$. Each AV in a jury can be derived from a different AV structure.

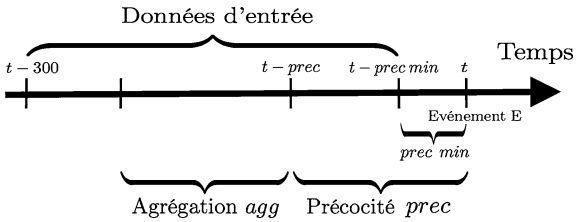

Fig. 3 Time aspect of an aggregate variable

Among different possible strategies to combine the answers of each AVs in a jury, we propose to use a majority vote scheme so that the final answer of a jury of size *n* is the most represented class. In comparison to a unanimity vote, this strategy presents the benefits to be computationally simpler and to preserve some diversity between the AVs of a jury. Indeed, if all the AVs have to choose the same class for the final answer, they will tend to be similar, while allowing some of them to be wrong sometimes let room for more diversity and possibly increase the performances: the AVs being wrong in a particular situation may be very useful in other situations.

A common problem in the implementation of data-driven approaches is the definition of strategies to deal with missing data in a dataset. In this work, we mainly considered two solutions. When the data corresponding to the measure sensor of one or many AVs are missing:

(1) the number of voting members is consequently reduced and the decision of the jury is given by the majority vote of the remaining AVs,
(2) a default answer is defined for the concerned AVs and the decision of the jury is given by the majority vote of all the AVs.

In the experiments presented in this paper, we follow the first approach.

4.2.2 Search for Optimal Solutions

For a given AV structure, the search for the best AVs, i.e., the quadruplets *(a, t, f, d)* allowing to obtain optimal classification performances, can be seen as a combinatorial optimization problem which search space |S_VA| is defined by the product:

$$|\mathrm{S\_VA}| = |\mathrm{A}| * |\mathrm{T}| * |\mathrm{F}| * |\mathrm{D}|.$$

Obviously, the size of this search space grows rapidly with the value set of each parameter, becoming impracticable for most real world applications.

Similarly, the search for best juries of AVs of size *n* boils down to the search of the best combinations {(*a*1, *t*1, *f*1, *d*1), (*a2, t2, f2, d2*), …, (*an, tn, fn, dn*)} through the search space defined by the product:

$|S\_Jn| = \prod_{p=1}^{n} |S\_VAp|$ with $|S\_VAp|$ the cardinal of the search space of the pth AV structure.

4.2.3 Evolutionary Approach

In order to address the complexity of the search for optimal solutions in such large search spaces, we propose to use stochastic solutions which have proven to be efficient in such situations where an exact approach to find optimal solutions is unknown. Indeed, they provide mechanisms to guide the search in order to find good solutions within relatively short execution times where an exhaustive search would require tremendous execution times (many years, centuries …). In the large family of stochastic methods, we chose Evolutionary Algorithms (EA) [1], mainly for their known abilities to deal with large class of problems.

In the following, we present the choices (problem dependant/independent operators, evolution parameters …) that we made for the implementation of our EA.

As seen before, an aggregate variable is a set of parameters (*a, t, f, d*) ∈ (*A, T, F, D,*) independent from each other. In this work, we use the notion of hydrometeorological aggregate variables defined by the AV structure shown in Sect. 1. In this structure, since a time window *t* \in *T* is characterized by the two values *prec* and *agg*, and a function *d* \in *D* is characterized by its decision threshold *thresh*, an AV can be encoded as the following sequence (*a, prec, agg, f, thresh*).

Similarly, a jury can be represented as the sequence {*AV*1, *AV*2, ..., *AVn*} of its AVs. Figure 4 illustrates this representation.

In an evolutionary process, the choice of the evolutionary operators is very important since they allow to evolve randomly initialized populations toward populations more adapted to the problem of solve among which optimal solutions may be found.

- *Multipoint crossover operator*: two levels of crossover points are considered. (1) the AV level, i.e., between AVs parameters, and (2) the jury level, i.e., between the AVs of a jury. After a random selection of possible such crossover points, VAs parameters and/or VAs are exchanged around them. We adopted a ROG strategy [6] consisting, when the crossover must be applied to two identical individuals (which would be useless), in returning a copy of the parents and

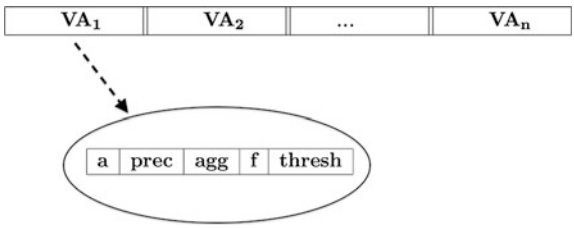

Fig. 4 Representation of a jury of AVs

a new randomly generated individual. This strategy presents the advantage of not affecting the search for optimal solution by increasing the diversity mostly when it is needed, i.e., when the population start to converge and thus the probability to select the identical individuals to cross is more important.

- *Uniform mutation operator*: A parameter is randomly chosen among a variable in the jury; then its value is changed either by a close value or a random value in its value space.
- *Selection*: we used a stochastic binary tournament which is a classical binary tournament operator with the particularity that the best individual has a probability p to be selected; otherwise the other one is selected. This strategy helps to reduce the selection pressure by allowing less-adapted individuals to survive, and then contributes to preserve a certain amount of diversity in the global population which is essential to prevent premature convergence.
- *Replacement*: we used an elitist generational replacement operator allowing to keep the best individual of the population for the next generation, avoiding the risk to decrease the quality of the population.

The evaluation is also a substantial part in an evolutionary process. Indeed, by allowing to estimate the quality of a solution regarding the problem to solve, it allows to know which ones are more or less close to optimal solution so they can be favored or not. In this work, we evaluate a solution by measuring its separative power regarding the two classes: Flood (F) and Non-flood (N). To do so, we consider combinations of the classical true positive, true negative, false positive, and false negative rates (the positive class is F and N is the negative class).

In this work, we considered the Information Value (IV): $IV = \Sigma\ (P(Si|A) - P(Si|B) * \log(P(S\_i|A)/P(S\_i|B))$ with $P(Si|X)$, the conditional probability that bin Si effectively corresponds to class X. In the present work, as we have two bins ([0, *tresh* [associated to class N and [*tresh*, $+\infty$[associated to class F), we have:

- $IV = \Sigma\ (P(Si|N) - P(Si|C) * \log(P(S\_i|N)/P(S\_i|C))$
- $IV = (TN - FN) * \log(TN/FN) + (FP - TP) * \log(FP/TP)$

with TN, TP, FP, FN $\in$]0,1[. When TN and TP tends to 1 and thus FP et FN tends to 0 we have:

- (TN – FN) tends to 1 and log(TN/FN) tends to $+\infty$,
- (FP – TP) tends to –1 and log(TN/FN) tends to $+\infty$,

thus IV tends to $+\infty$. In a similar way, we can show that when TN and TP tends to 0, IV also tends to $+\infty$. Indeed, this metric considers that the information offered perfect and inverse classifications are the same: only the class labels should be switched. The worst case is thus the random situation where TP = TN = FP = FN = 0.5 and IV = 0.

Table 2 Parameters used for classical data-driven techniques

Technique	Parameters used
MLP	Nb of layers: 1, Nb of nodes: $(\|attributes\| + \|classes\|)/2 = 202$ Learning rate: 0.3, momentum 0.2
C4.5	Minimum instances per leaf: 2, pruning: yes Confidence factor for pruning: 0.25
RF	Maximum depth: unlimited, Nb of trees generated: 10 Nb of features used in random selection: $log(\|attributes + 1\|)$
BFT	Minimum instances per leaf: 2, internal k fold cross-validation seed: random number, pruning strategy: post-pruning Separation criteria: Gini index
NB	Supervised discretization

5 Experiments and Results

Here we present the results obtained with the AV2D approach and compare them to those obtained with classical data-driven approaches commonly used, namely the decision trees C4.5 [5], Random Forest (RF) [2] and Best First Tree (BFT) [11], the naive bayes classifier (NB) [4], and the artificial neural network Multi-Layer Perceptron (MLP) [13]. Table 2 summarizes the parameters that we used for each of these techniques. These are the typical parameters mainly used to address similar problems.

The results obtained with the EA presented in the previous section were obtained with the following parameters:

- population size: 100,
- number of generations: 8000,
- selection operator: stochastic binary tournament with $p = 0.8$,
- generational replacement operator: elitism,
- mutation rate 0.001,
- crossover rate 0.75.

Due to the combinatorial explosion resulting from the increasing number of variables in a jury, we had to find a good tradeoff between complexity of the search space and efficiency of the models obtainable. We found after an exploratory analysis in which we compared the performances obtained with different jury sizes and GA parameters, as explained in [9], that the best tradeoff was a jury size of 3.

Given the low number of total instances in each case (70), we used a stratified 10-fold cross-validation technique to estimate the performance of each method. The performances are presented in terms of true negative, true positive, and weighted average rates:

$$- \text{TN rate} = \left(\sum_{i=1}^{k} \text{TP}_i\right)/\text{Total}_{\text{pos}}$$
$$- \text{TP rate} = \left(\sum_{i=1}^{k} \text{TN}_i\right)/\text{Total}_{\text{neg}}$$
$$- \text{W.Avg rate} = \left(\sum_{i=1}^{k} \text{TN}_i + \text{TP}_i\right)/(\text{Total}_{\text{pos}} + \text{Total}_{\text{neg}}$$

with TP_i, TN_i, respectively, the number of true positive and false positive in the *i*th k-fold cross validation iteration, and Total_pos, Total_neg, respectively, the total number of positive and negative instances.

Finally, since EA, MLP, RF, and BFT are stochastic methods, the results presented for them are averaged on 50 k-fold cross experiments. Standard deviation values on each rate are given in this case. Table 3 shows the performances obtained on the Gurabo case by standard data-driven techniques and AV2D. The first column shows the technique used, the second column gives the minimal precocity, while

Table 3 Performances of data-driven techniques for Gurabo River

Algorithm	Prec min	TN		TP		W. Avg	
		Avg	Std Dev	Avg	Std Dev	Avg	Std Dev
C4.5	60	73.80	–	57.10	–	67.10	–
	120	73.80	–	50.00	–	64.30	–
	180	66.7	–	42.90	–	57.10	–
	240	78.60	–	28.60	–	58.60	–
RF	60	72.28	4.46	61.06	7.60	67.80	3.77
	120	69.95	6.27	47.71	6.87	61.06	4.27
	180	67.57	5.83	43.15	5.71	57.80	4.33
	240	62.47	6.01	31.36	7.25	50.03	4.34
NB	60	76.2	–	82.10	–	78.60	–
	120	61.90	–	71.40	–	65.70	–
	180	**81.00**	–	32.10	–	61.40	–
	240	92.90	–	25.00	–	65.70	–
BFT	60	76.9	5.48	55.14	8.42	67.71	4.14
	120	74.10	4.69	45.79	7.85	62.77	3.66
	180	70.09	5.09	36.50	7.23	56.65	4.24
	240	81.34	7.22	18.00	7.28	56.00	3.74
MLP	60	**80.49**	2.77	65.35	5.32	74.42	3.01
	120	68.08	4.66	64.64	6.29	66.70	4.14
	180	68.56	5.31	46.44	5.30	59.71	3.31
	240	69.05	3.17	25.35	4.37	51.58	1.96
AV2D (IV)	60	77.81	5.43	**84.28**	5.97	**80.40**	3.91
	120	67.29	4.95	75.70	7.07	70.66	4..31
	180	59.90	4.50	54.71	13.20	57.83	5.03
	240	74.85	3.63	27.00	5.63	55.71	3.20

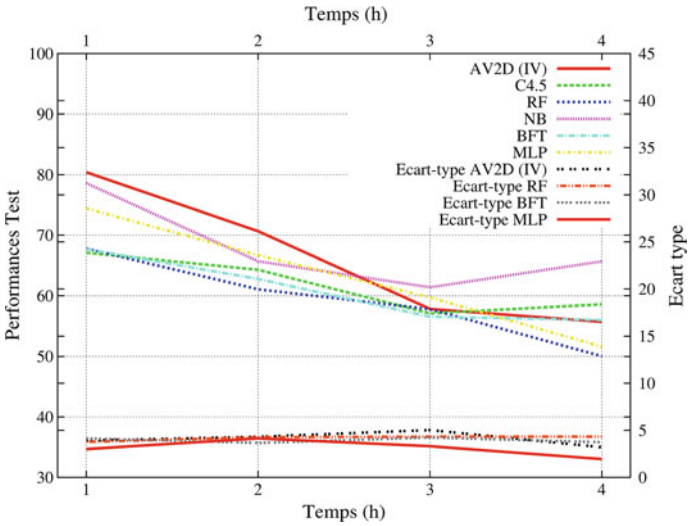

Fig. 5 Evolution of performances with minimal precocity values

the remaining columns give TN, TP, and W.Avg rates and their standard deviation when necessary. The Best results are bolded. As we could expect, best performances for each technique are obtained for lower values of prec min. AV2D obtain the bests W.Avg (80.40 %) and TP rates (84.28 %) for 60 min of minimal precocity.

Figure 5 summarizes graphically the results presented in Table 3.

6 Conclusion

In this paper, we presented AV2D, a data-driven hydrological classification approach based on combinations of aggregate variables acting as simple classifiers. We designed an EA to address the combinatorial optimization problem of searching such optimal combinations. We showed, through a comparison with standard data-driven techniques (ANN, decision trees) on a typical Caribbean watershed, that this new approach was able to provide very good performances in terms of classification accuracy, particularly for short term prediction.

Perspectives for future work include fitness landscape analysis in order to improve the evolutionary process, the use of other metaheuristics to find optimal juries of aggregate variables, the use of other kind of data such as radar rainfall, soil type, or tides data.

References

1. Back, T. (1996). *Evolutionary algorithms in theory and practice: Evolution strategies, evolutionary programming genetic algorithms*. Oxford: Oxford University Press.
2. Breiman, L. (2001). Random forests. *Machine Learning, 45*, 5–32.
3. Corzo, G., & Perez, P. (2009). *Hybrid models for hydrological forecasting: Integration of data-driven and conceptual modelling techniques*. London: Taylor and Francis Group.
4. John, G., & Langley, P. (1995). Estimating continuous distributions in bayesian classifiers. *Proceedings of the Eleventh Conference on Uncertainty in Artificial Intelligence* (pp. 338–345). Morgan Kaufmann.
5. Quinlan, J. R. (1993). *C4.5: Programs for machine learning*. San Mateo: Morgan Kaufmann.
6. Rocha, M., & Neves, J. (1999). Preventing premature convergence to local optima in genetic algorithms via random offspring generation. *Proceedings of the 12th International Conference on Industrial and Engineering Applications of Artificial Intelligence and Expert Systems: Multiple Approaches to Intelligent Systems, IEA/AIE'99* (pp. 127–136), Secaucus, NJ, USA: Springer-Verlag New York, Inc.
7. Segretier, W., Clergue, M., Collard, M., & Izquierdo, L. (2012). An evolutionary data mining approach on hydrological data with classifier juries. *IEEE Congress on Evolutionary Computation* (pp. 1–8).
8. Segretier, W., Collard, M., Brisson, L., & Symphor, J.-E. (2011). Variable optimization for flood prediction. *Ingénierie des Systèmes d'Information, 16*(3), 113–139.
9. Segretier, W., Collard, M., & Clergue, M. (2013). Evolutionary predictive modelling for flash floods. *2013 IEEE Congress on Evolutionary Computation (CEC)* (pp. 844–851).
10. Sene, K (2010). *Hydrometeorology: Forecasting and applications*. New York: Springer.
11. Shi, H. (2007). Best-first decision tree learning. Technical report, University of Waikato.
12. Solomatine, D. P., & Price, R. K. (2004). Innovative approaches to flood forecasting using data-driven and hybrid modelling. *Proceedings of the. 6th International Conference on Hydroinformatics*.
13. Werbos, P. J. (1974) Beyond Regression: New Tools for Prediction and Analysis in the Behavioral Sciences. PhD thesis, Harvard University.

Numerical Scheme for a Viscous Shallow Water System Including New Friction Laws of Second Order: Validation and Application

Olivier Delestre and Ulrich Razafison

1 Introduction

Free surface flows are described by the Navier-Stokes equations. It is well-known that the numerical resolution of these equations can be expensive. For this reason the shallow water equations (or Saint-Venant system [1]) are widely used in hydraulics and hydrology to simulate free surface flows. We can refer, for instance, to rain-water overland flows [2–5], river flows [6], flooding [7], dam breaks [8, 9], and also oceanography [10]. These equations are derived from the Navier-Stokes equations under the assumption that the ratio between the vertical and the horizontal scales is small. However, the friction laws that are obtained from this derivation, are not used in hydraulics and hydrology. In this context, the main friction laws used are the ones of Manning and Darcy-Weisbach types.

In this paper, we propose to derive the shallow-water equations with Manning or Darcy-Weisbach friction terms, starting from the Navier-Stokes equations with suitable wall-laws at the bottom boundary. Details of the derivation, which follows the ideas of [11, 12], will be presented in a forthcoming work. As an approximation of first order, we obtain the classical Shallow water model (without diffusion source term) with the classical Manning or Darcy-Weisbach laws. We next perform a second order approximation and we obtain a viscous Shallow water model with new friction laws of Manning or Darcy-Weisbach type. We then propose a numerical scheme for the new model which is mainly based on a well-balanced

O. Delestre
Laboratory J.A. Dieudonné CNRS UMR 7351 & Polytech Nice – Sophia,
UNSA, Arequipa, Peru
e-mail: delestre@unice.fr

U. Razafison (✉)
Laboratoire de Mathématiques, CNRS UMR 6623, Université de Franche-Comté,
16 Route de Gray, 25030 Besançon Cedex, France
e-mail: ulrich.razafison@univ-fcomte.fr

P. Gourbesville et al. (eds.), *Advances in Hydroinformatics*,
Springer Water, DOI 10.1007/978-981-287-615-7_16

finite volume method. Then we present analytical validation of the scheme on steady state reference solutions obtained following the main lines of [13]. Finally, this model is applied on real data.

2 Derivation of the Model

We give here the key points of the derivation of the model. Details will be given in a forthcoming work. First, we consider the 2D free surface Navier-Stokes equations

$$\begin{aligned} \frac{\partial u}{\partial x}+\frac{\partial w}{\partial z}&=0,\\ \frac{\partial u}{\partial t}+\frac{\partial u^2}{\partial x}+\frac{\partial uw}{\partial z}+\frac{\partial p}{\partial x}&=\frac{\partial \sigma_{xx}}{\partial x}+\frac{\partial \sigma_{xz}}{\partial z},\\ \frac{\partial w}{\partial t}+\frac{\partial uw}{\partial x}+\frac{\partial w^2}{\partial z}+\frac{\partial p}{\partial z}&=-g+\frac{\partial \sigma_{zx}}{\partial x}+\frac{\partial \sigma_{zz}}{\partial z}, \end{aligned} \tag{1}$$

where u and w are respectively the horizontal and the vertical components of the velocity, p is the pressure, σ is the viscosity tensor, Z is the topography variation and $g = 9.81\ \mathrm{m/s^2}$ is the gravity acceleration.

System (1) needs to be completed with conditions on the free surface and at the bottom. At the bottom $z = Z(x)$, a Manning or a Darcy-Weisbach formula is prescribed as follows

$$\sigma_{xz} = \mathrm{k}\frac{|u|u}{h^{\alpha}}, \tag{2}$$

where $\alpha \in (0, 1/3)$.

If $\alpha = 0$ (respectively $\alpha = 1/3$), then a Darcy-Weisbach type formula is obtained with $k = f/8$ (resp. $k = n^2 g$), where f (resp. n) is the Darcy-Weisbach (resp. Manning) roughness coefficient. This roughness coefficient depends mainly on the roughness of the soil, some values are tabulated in literature depending on the kind of ground considered [14]. Following the same lines as in [11, 12], the derivation of the Shallow Water system of first order is first obtained

$$\begin{aligned} \frac{\partial h}{\partial t}+\frac{\partial hu}{\partial x}&=0,\\ \frac{\partial hu}{\partial t}+\frac{\partial hu^2}{\partial x}+\frac{g}{2}\frac{\partial h^2}{\partial x}&=-k\frac{|u|u}{h^{\alpha}}-gh\frac{\partial z}{\partial x}. \end{aligned} \tag{3}$$

Then keeping smaller terms, and proceeding again as in [11, 12], a viscous Shallow Water system with new friction term of Darcy-Weisbach (resp. Manning) type is obtained

$$\begin{aligned} &\frac{\partial h}{\partial t}+\frac{\partial hu}{\partial x}=0,\\ &\frac{\partial hu}{\partial t}+\frac{\partial hu^2}{\partial x}+\frac{g}{2}\frac{\partial h^2}{\partial x}=-k\frac{h^{-\alpha}|u|u}{\left(1+\frac{k}{3\nu}|u|h^{1-\alpha}\right)^2}-g\,h\frac{\partial z}{\partial x}+4\nu\frac{\partial}{\partial x}\left(h\frac{\partial u}{\partial x}\right). \end{aligned} \tag{4}$$

3 Numerical Scheme

In order to solve systems (3) and (4), we use FullSWOF_1D software which stands for Full Shallow Water equations for Overland Flow in 1 space Dimension [3, 15]. It is an open source C++ codes, freely available from https://sourcesup.renater.fr/projects/fullswof-1d/. It is distributed under CeCILL-V2 free software license. The structure of the code is made to facilitate the development of new evolutions. This software solves the shallow water Eq. (3) thanks to a well-balanced finite volume method based on the hydrostatic reconstruction [16, 17]. This numerical method has good properties: water mass conservation, well-balanced property (at least preservation of lake at rest equilibrium) and positivity water height preservation. We have made some modifications in the sources to deal with system (4) as well. We will first give the main lines of the numerical method implemented in FullSWOF to solve system (3). Then we will explain the modification integrated in FullSWOF_1D to solve (4). In FullSWOF, the shallow water equations are solved thanks to a well-balanced finite volume scheme. The well-balanced property is achieved with the hydrostatic reconstruction, which is based on a general principle of reconstruction. We begin with a first order finite volume scheme for the homogeneous shallow water equations: choosing a positive and consistent numerical flux $F(U_L, U_R)$ (e.g. Rusanov, HLL, kinetic,… [2, 17]), it writes under the general form

$$\frac{U_i^{\text{star}}-U_i^n}{\Delta t}+\frac{F(U_i^n,\mathrm{U}_{i+1}^n)-F(U_{i-1}^n,\mathrm{U}_i^n)}{\Delta x}=0, \tag{5}$$

where Δt is the time step and Δx is the space step. The idea is to modify this scheme by applying the numerical flux to the reconstructed variables. Reconstruction can be used to get higher order schemes (MUSCL, ENO, …), and the higher order in time is obtained thanks to TVD-Runge-Kutta methods. The purpose of the hydrostatic reconstruction is to get a well-balanced scheme. It is designed to preserve at least steady states at rest ($u = 0$ and $h + Z = Cst$). When it is directly applied on the initial scheme, it gives a first order scheme, while coupling it with high order reconstruction increases the order of the scheme and thus its accuracy.

We now give the implementation of this method to get high order accuracy. The first step consists in performing a high order reconstruction (MUSCL, ENO, …). To deal properly with the topography source term $\partial_x z$, this reconstruction is applied on u, h and $h + z$. Thus we get the set of reconstructed variables (U_m, z_m) and (U_p, z_p), on which the hydrostatic reconstruction is applied

$$\begin{aligned} h_{\mathrm{i}+1/2\mathrm{L}} &= \max\left(h_{\mathrm{i}+1/2\mathrm{m}} + z_{\mathrm{i}+1/2\mathrm{m}} - \max\left(z_{\mathrm{i}+1/2\mathrm{m}}, z_{\mathrm{i}+1/2\mathrm{p}}\right), 0\right), \\ U_{\mathrm{i}+1/2\mathrm{L}} &= \left(h_{\mathrm{i}+1/2\mathrm{L}}, h_{\mathrm{i}+1/2\mathrm{L}} u_{\mathrm{i}+1/2\mathrm{m}}\right), \\ h_{\mathrm{i}+1/2\mathrm{R}} &= \max\left(h_{\mathrm{i}+1/2\mathrm{p}} + z_{\mathrm{i}+1/2\mathrm{p}} - \max\left(z_{i+1/2\mathrm{m}}, z_{\mathrm{i}+1/2\mathrm{p}}\right), 0\right), \\ U_{\mathrm{i}+1/2\mathrm{R}} &= \left(h_{\mathrm{i}+1/2\mathrm{R}}, h_{\mathrm{i}+1/2\mathrm{R}} u_{\mathrm{i}+1/2\mathrm{p}}\right) \end{aligned} . \tag{6}$$

The finite volume scheme (9) needs to be modified as follows

$$\frac{U_i^{\mathrm{star}} - U_i^n}{\Delta t} + \frac{F^n_{\mathrm{i}+1/2\mathrm{L}} - F^n_{i-1/2\mathrm{R}} - \mathrm{Fc}_i^n}{\Delta x} = 0, \tag{7}$$

where

$$\begin{aligned} F^n_{\mathrm{i}+1/2\mathrm{L}} &= F^n_{\mathrm{i}+1/2} + S^n_{\mathrm{i}+1/2\mathrm{L}}, \\ F^n_{\mathrm{i}-1/2\mathrm{R}} &= F^n_{\mathrm{i}-1/2} + S^n_{\mathrm{i}+1/2\mathrm{R}}, \end{aligned} \tag{8}$$

are left (resp. right) modifications of the numerical flux for the homogeneous system. In this formula, the numerical flux is now applied on the reconstructed variables $F^n_{\mathrm{i}+1/2} = F\left(U^n_{\mathrm{i}+1/2\mathrm{L}}, U^n_{\mathrm{i}+1/2\mathrm{R}}\right)$ and we take

$$S^n_{\mathrm{i}+1/2\mathrm{L}} = \begin{pmatrix} 0 \\ \frac{g h^2_{\mathrm{i}+1/2\mathrm{m}} - g h^2_{\mathrm{i}+1/2\mathrm{L}}}{2} \end{pmatrix} \quad , \quad S^n_{\mathrm{i}+1/2\mathrm{R}} = \begin{pmatrix} 0 \\ \frac{g h^2_{i-1/2\mathrm{p}} - g h^2_{i-1/2\mathrm{R}}}{2} \end{pmatrix}. \tag{9}$$

Finally, for consistency and well-balancing properties, a centered source term is added to the scheme

$$\mathrm{Fc}_i^n = \begin{pmatrix} 0 \\ -g \frac{h_{i-1/2\mathrm{p}} + h_{i-1/2\mathrm{m}}}{2} \left(z_{i+1/2\mathrm{m}} - z_{i-1/2\mathrm{p}}\right) \end{pmatrix}. \tag{10}$$

The chosen numerical strategy consists in the HLL flux (see [2, 17]) combined with a modified MUSCL reconstruction. It has shown to be the best compromise between accuracy, stability and CPU time cost [2]. The MUSCL reconstruction of a real variable s writes

$$s_{i-1/2\mathrm{p}} = s_i - \Delta x \,.\, \frac{Ds_i}{2}, s_{\mathrm{i}+1/2\mathrm{m}} = s_i + \Delta x \,.\, \frac{Ds_i}{2}, \tag{11}$$

with the minmod slope limiter

$$Ds_i = \min \mathrm{mod}\left(\frac{s_i - s_{i-1}}{\Delta x}, \frac{s_{\mathrm{i}+1} - s_i}{\Delta x}\right), \ \min \mathrm{mod}\,(x,y) = \begin{cases} \min(x,y) & \text{if } x,y \geq 0, \\ \max(x,y) & \text{if } x,y \leq 0, \\ 0 & \text{else.} \end{cases} \tag{12}$$

In order to keep the discharge conservation, the reconstruction of the velocity has to be modified as follows

$$u_{i-1/2\mathrm{p}} = u_i - \frac{h_{\mathrm{i}+1/2\mathrm{m}}}{h_i}\frac{\Delta x}{2}Du_i, u_{\mathrm{i}+1/2\mathrm{m}} = u_i - \frac{h_{\mathrm{i}-1/2\mathrm{p}}}{h_i}\frac{\Delta x}{2}Du_i. \tag{13}$$

We can notice that if we take $Ds_i = 0$, we recover the first order scheme in space. The friction term is treated numerically by a fractional step, with the following system

$$\partial_t U = \begin{pmatrix} 0 \\ -g\,h\,Sf \end{pmatrix}, \tag{14}$$

where Sf is the friction source term. This system is solved thanks to a semi-implicit treatment [18, 19]. As an example, for the Manning friction law, it writes

$$\begin{aligned} h^{\mathrm{n}+1} &= h^{\mathrm{star}}, \\ \frac{q^{\mathrm{n}+1} - q^{\mathrm{star}}}{\Delta t} &= -n^2 \frac{q^{\mathrm{n}+1}|q^n|}{h^n\left(h^{\mathrm{n}+1}\right)^{4/3}}. \end{aligned} \tag{15}$$

This method allows to preserve stability (under a classical CFL condition) and steady states at rest. Finally a TVD-Runge Kutta (Heun) method is applied to get second order in time. This is what has been currently developed in FullSWOF to solve system (3). To solve our new system (4), we have integrated the new friction laws treated with a semi-implicit treatment such as (15). A Crank-Nicolson method is used to deal with the diffusion source term. The obtained tridiagonal linear system is solved thanks to the LAPACK library (Linear Algebra PACKage [20]). We have to mention that these modifications of the code are not currently available on FullSWOF website.

4 Numerical Validations

4.1 Analytical Solutions

FullSWOF has been widely validated on analytical solutions implemented in SWASHES library [21, 22]. Keeping this philosophy in mind, we have developed some analytical solutions to validate our approach following the main lines of [13]. From (4), steady state solutions are constructed. At stationary equilibrium this system reduces into

$$q = C\,s\,t$$
$$\frac{\partial Z}{\partial x} = \frac{1}{gh}\left(\left(\frac{q^2}{h^2} - gh\right)\frac{\partial h}{\partial x} - \frac{k|q|q}{h^{\alpha+2}\left(1+\frac{k}{3\nu}|q|h^{-\alpha}\right)^2} + 4\nu\frac{q}{h}\left(\frac{1}{h}\left(\frac{\partial h}{\partial x}\right)^2 - \frac{\partial^2 h}{\partial x^2}\right)\right) \tag{20}$$

The above relation allows to compute topography corresponding to sufficiently smooth function for the free surface. For all the following tests, we will consider dry initial conditions ($h(t = 0, x) = 0$ m and $u(t = 0, x) = 0$ m/s), this allows to test the ability of the numerical to deal properly with wet/dry transitions and to catch steady state solutions. We will consider successively three kinds of regimes: subcritical (or fluvial), supercritical (or torrential) and transcritical, for both the new Manning and Darcy-Weisbach friction laws.

For each numerical result, we also compute the relative L^2- error at the final time between the reference and the computed water height.

4.2 Numerical Results

4.2.1 Subcritical Flow for Manning Friction Law

A 1000 m long channel is considered. The following water height is chosen and plotted on Fig. 1:

$$h_{ex}(x) = \left(\frac{4}{g}\right)^{1/3}\left(1 + \frac{1}{2}\exp\left(-16\left(\frac{x}{1000} - \frac{1}{2}\right)^2\right)\right). \tag{21}$$

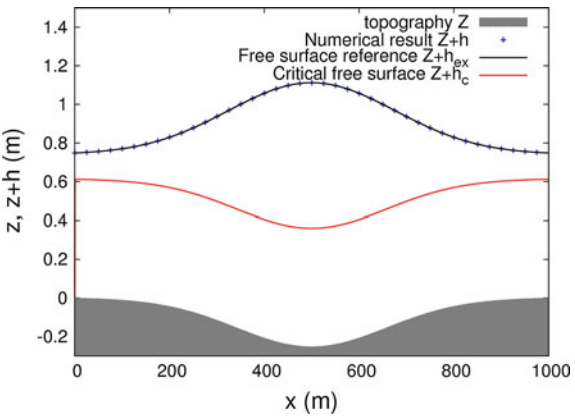

Fig. 1 Comparison between the numerical result $Z + h$ (plotted every 50 points) and the reference solution $Z + h_{ex}$ for subcritical flow and Manning friction law

At the inflow boundary $x = 0$, we impose a constant discharge q = 1.5 m^2/s. At the outflow $x = 1000$ m, we use the reference solution to impose the water height $h_{ex}(1000)$.

$$\text{Parameters}: \ n = 0.33, \ v = 10^{-6}, \ \Delta x = 0.5\,\text{m}, \ \Delta t = 0.02\ \text{s}.$$

We have represented the critical free surface $Z + h_c$ in red, where $h_c = (q^2/g)^{1/3}$ is the critical water height. This height allows to visualize the flow regime. We can notice that the subcritical stationary flow is perfectly catched by the numerical method (Fig. 1). The relative L^2- error is approximately 5.6384×10^{-5}.

4.2.2 Subcritical Flow for Darcy-Weisbach Friction Law

A 1000 m long channel is considered. We consider the water height defined by (21). At the inflow boundary $x = 0$, we impose a constant discharge $q = 1.5$ m^2/s. At the outflow $x = 1000$ m, we use the reference solution to impose the water height h_{ex} (1000) (Fig. 2).

$$\text{Parameters}: \ f = 0.25, \ v = 10^{-6}, \ \Delta x = 0.5\,\text{m}, \ \Delta t = 0.02\ \text{s}.$$

As for the Manning friction law (Sect. 4.2.1), we get a perfect agreement between the reference solution and the numerical solution. Moreover the relative L^2- error is also approximately 5.6384×10^{-5}.

4.2.3 Supercritical Flow for Manning Friction Law

A 1000 m long channel is considered. The following water height is chosen and plotted on Fig. 3:

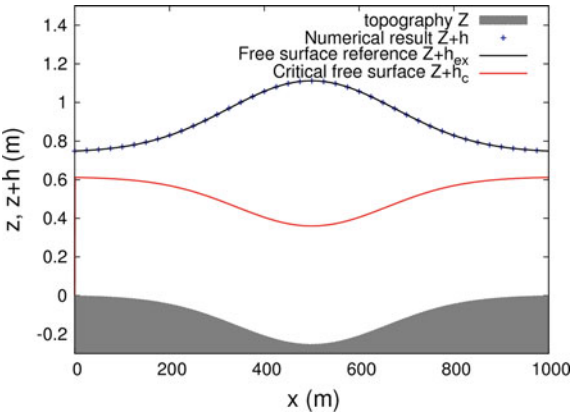

Fig. 2 Comparison between the numerical result $Z + h$ (plotted every 50 points) and the reference solution $Z + h_{ex}$ for subcritical flow and Darcy-Weisbach friction law

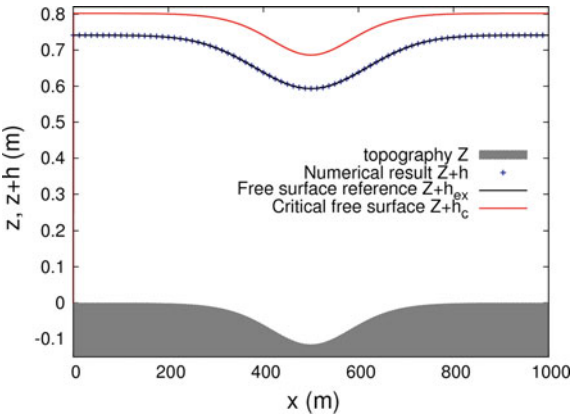

Fig. 3 Comparison between the numerical result $Z + h$ (plotted every 50 points) and the reference solution $Z + h_{ex}$ for supercritical flow and Manning friction law

$$h_{ex}(x) = \left(\frac{4}{g}\right)^{1/3}\left(1 - \frac{1}{5}\exp\left(-36\left(\frac{x}{1000} - \frac{1}{2}\right)^2\right)\right). \tag{22}$$

At the inflow boundary, we impose a constant discharge $q = 2.25\ \mathrm{m}^2/\mathrm{s}$ and a constant water height equal to the steady state reference solution at inflow $h_{ex}(0)$. The outflow boundary at $x = 1000$ m is let free (Neumann condition).

$$\text{Parameters}: \ n = 0.33,\ \nu = 10^{-6},\ \Delta x = 0.25\ \text{m},\ \Delta t = 0.02\ \text{s}.$$

On Fig. 3, we can notice that the numerical method allows to catch perfectly the torrential equilibrium for the Manning friction law. For this case, the relative L^2-error is approximately 1.4876×10^{-5}.

4.2.4 Supercritical Flow for Darcy-Weisbach Friction Law

A 1000 m long channel is considered. We consider the water height defined by formula (22). At the inflow boundary $x = 0$, we impose a constant discharge $q = 2.25\ \mathrm{m}^2/\mathrm{s}$ and a constant water height equal to the steady state reference solution at the income h_{ex} (0). The outflow boundary at $x = 1000$ m is let free (Neumann condition).

$$\text{Parameters}: \ f = 0.25,\ \nu = 10^{-6},\ \Delta x = 0.25\ \text{m},\ \Delta t = 0.02\ \text{s}.$$

Perfect agreement is observed between the reference solution and the numerical solution (Fig. 4) and the relative L^2-error is approximately $1.5.27 \times 10^{-5}$.

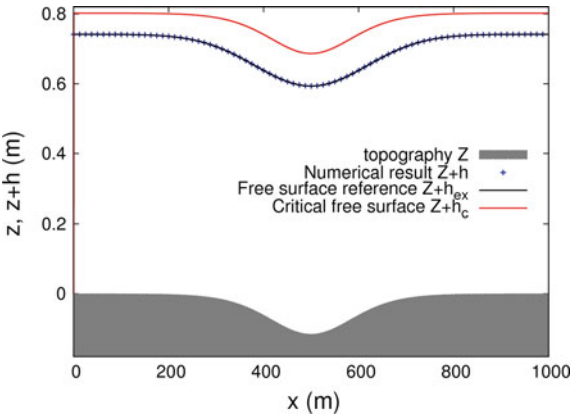

Fig. 4 Comparison between the numerical result $Z + h$ (plotted every 50 points) and the reference solution $Z + h_{ex}$ for supercritical flow and Darcy-Weisbach friction law

4.2.5 Transcritical Flow for Manning Friction Law

A 100 m long channel is considered. The following water height is chosen and plotted on Fig. 5:

$$h_{ex}(x) = \frac{1}{2}\cos\left(\frac{\pi}{100}x\right) + 1 \tag{23}$$

At the inflow boundary $x = 0$, we impose a constant discharge $q = 2.2\ \mathrm{m}^2/\mathrm{s}$. The outflow boundary at $x = 100$ m is let free (Neumann condition).

$$\text{Parameters}: \ n = 0.33,\ v = 10^{-6},\ \Delta x = 0.5\ \mathrm{m},\ \Delta t = 0.01\ \mathrm{s}.$$

Transcritical solutions might be difficult to catch numerically. We can see on Fig. 5, that this numerical difficulty is overcome by the scheme we have considered.

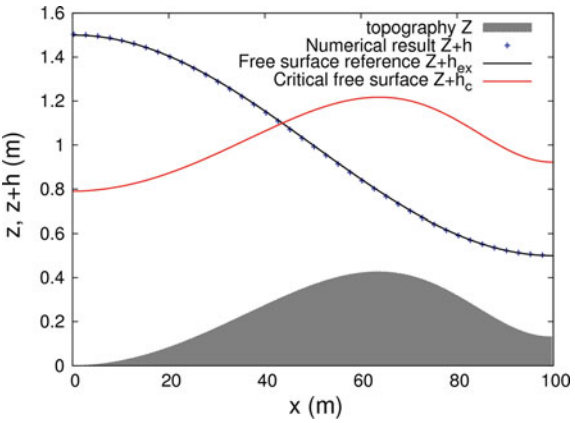

Fig. 5 Comparison between the numerical result $Z + h$ (plotted every 5 points) and the reference solution $Z + h_{ex}$ for transcritical flow and Manning friction law

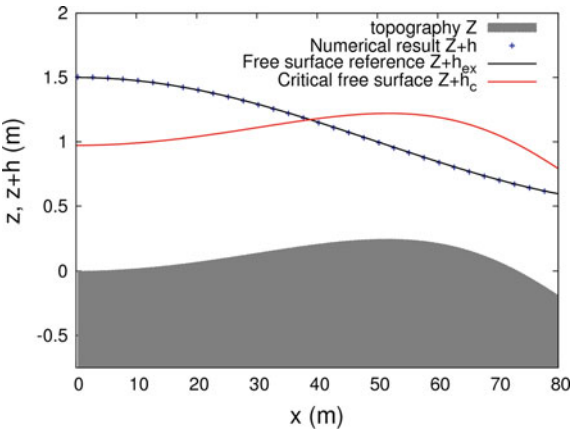

Fig. 6 Comparison between the numerical result $Z + h$ (plotted every 5 points) and the reference solution $Z + h_{ex}$ for transcritical flow and Darcy-Weisbach friction law

The equilibrium is perfectly obtained by the numerical method. The relative L^2-error is approximately 1.208×10^{-3}.

4.2.6 Transcritical Flow for Darcy-Weisbach Friction Law

A 80 m long channel is considered. We consider the water height defined by (23). At the inflow boundary $x = 0$, we impose a constant discharge $q = 3\ m^2/s$. The outflow boundary at $x = 80$ m is let free (Neumann condition).

$$\text{Parameters}: \ f = 0.25,\ v = 10^{-6},\ \ \Delta x = 0.5\,\text{m},\ \ \Delta t = 0.01\ \text{s}.$$

As for the Manning friction law (see Sect. 4.2.5), the transcritical steady state is perfectly reached by the numerical (as observed on Fig. 6) and the relative L^2- error is approximately 1.2885×10^{-3}.

We have validated our numerical method on various flow regimes. To complete this work, some convergence analysis and accuracy study need to be done. This will be considered in forthcoming work. We have to validate our model, this will be done in next section on real data.

5 First Attempt on Real Data

In this section, we aim at validating our model (4) on real data. For this case, an experimental flow over an inclined corrugated bottom (Fig. 7) is considered with an inflow discharge of $q = 3.9 \times 10^{-4}\ m^2/s$. Free surface profile is measured at steady state along a 55 cm long profile with a 0.5 mm resolution using the device described in [23]. A succession of transcritical transitions and hydraulic jumps is obtained.

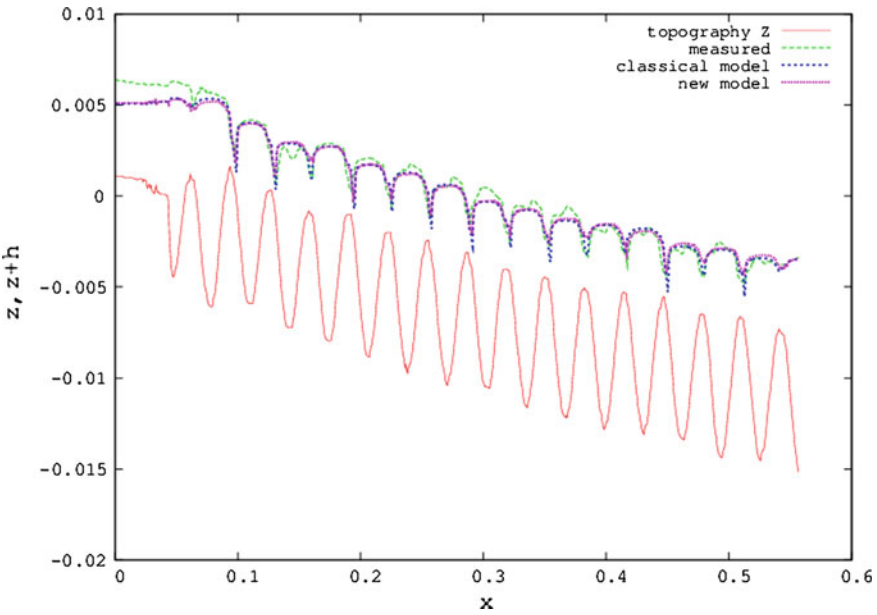

Fig. 7 Comparison between the two models against experimental data over a corrugated bottom

FullSWOF_1D has already been run on this data set [15]. It has been able to locate the hydraulic jumps correctly but the simulated solution has exhibited shocks steeper than the measured ones. In this work, we have considered successively system (3) and system (4) with Manning friction law. The length of the domain is $L = 0.557$ m, the space step length is $\Delta x = 5 \times 10^{-4}$ m. For system (4), the viscosity is $\nu = 2 \times 10^{-5}$.

On Fig. 7, we can notice that the hydraulic jumps are less steep with the new model (4) than with the classical model. The relative L^2- error on the water height between the experimental and the classical shallow water model is approximately 9.5872×10^{-2} and is closed to the one between the experimental and the new model which is approximately 9.4747×10^{-2}. More comparisons on real data will be necessary to completely validate this new model.

6 Conclusion and Perspectives

In this work, we have developed a new shallow-water system with diffusion source term and new Manning and Darcy-Weisbach friction laws. We have validated a numerical method adapted to this system on new various analytical solutions. This numerical method showed good agreement with the reference solutions. In forthcoming work, we will have to do convergence analysis. Then we have applied this

model on real data. This model seems to be more adapted than the classical shallow-water model. We will have to try other flow regimes to validate completely this new model.

Acknowledgements The authors whish to thanks the ANR-11-JS01-006-01 project CoToCoLa (Contemporary Topics on Conservation Laws), Carine Lucas for her advices and Frédéric Darboux for the data used in Sect. 4.2.

References

1. de Saint-Venant, A. J.-C. (1871). Théorie du mouvement non-permanent des eaux, avec application aux crues des rivières et à l'introduction des marées dans leur lit. *Comptes Rendus de l'Académie des Sciences, 73*, 147–154.
2. Delestre, O. (2010). Simulation du ruissellement d'eau de pluie sur des surfaces agricoles. PhD thesis University of Orléans, in french. http://tel.archives-ouvertes.fr/INSMI/tel-00531377/fr.
3. Delestre, O., Cordier, S., Darboux, F., Du, M., James, F., & Laguerre, C., et al. (2014). FullSWOF: A software for overland flow simulation. In P.Gourbesville, J. Cunge, & G. Caignaert, (Eds.), *Advances in Hydroinformatics*, Springer Hydrogeology (pp. 221–231). Springer: Singapore.
4. Esteves, M., Faucher, X., Galle, S., & Vauclin, M. (2000). Overland flow and infiltration modelling for small plots during unsteady rain: numerical results versus observed values. *Journal of Hydrology, 228*, 265–282.
5. Tatard, L., Planchon, O., Wainwright, J., Nord, G., Favis-Mortlock, D., Silvera, N., et al. (2008). Measurement and modelling of high-resolution flow-velocity data under simulated rainfall on a low-slope sandy soil. *Journal of Hydrology, 348*(1–2), 1–12.
6. Goutal, N., & Maurel, F. (2002). A finite volume solver for 1D shallow-water equations applied to an actual river. *International Journal for Numerical Methods in Fluids, 38*, 1–19.
7. Caleffi, V., Valiani, A., & Zanni, A. (2003). Finite volume method for simulating extreme flood events in natural flood events in natural channels. *Journal of Hydraulic Research, 41*(2), 167–177.
8. Alcrudo, F., & Gil, E. (1999). The Malpasset dam break case study. *Proceedings of the 4th CADAM Workshop, Zaragoza* (pp. 95–109).
9. Valiani, A., Caleffi, V., & Zanni, A. (2002). Case study: Malpasset dam-break simulation using a two-dimensional finite volume methods. *Journal of Hydraulic Engineering, 128*(5), 460–472.
10. Popinet, S. (2011). Quadtree-adaptive tsunami modelling. *Ocean Dynamics, 61*(9), 1261–1285.
11. Gerbeau, J.-F., & Perthame, B. (2001). Derivation of viscous Saint-Venant system for laminar shallow water; numerical validation. *Discrete and Continuous Dynamical Systems—Series S, 1*, 89–102.
12. Marche, F. (2007). Derivation of a new two-dimensional viscous shallow water model with varying topography, bottom friction and capillary effects. *European Journal of Mechanics B/Fluids, 26*, 49–63.
13. MacDonald, I., Baines, M. J., Nichols, N. K., & Samuels, P. G. (1997). *Journal of Hydraulic Engineering, 123*, 1041–1045.
14. Chow, V. T. (1959). *Open-channel hydraulics*. New York: McGraw-Hill.
15. Delestre, O., Darboux, F., James, F., Lucas, C., Laguerre, C., & Cordier, S. (Submitted). FullSWOF: A free software package for the simulation of shallow water flows. arxiv. org/abs/1401.4125.

16. Audusse, E., Bouchut, F., Bristeau, M.-O., Klein, R., & Perthame, B. (2004). A fast and stable well-balanced scheme with hydrostatic reconstruction for shallow water flows. *Journal of Scientific Computing, 25*(6), 2050–2065.
17. Bouchut, F. (2004). *Nonlinear stability of finite volume methods for hyperbolic conservation laws, and well-balanced schemes for sources*. Frontiers in Mathematics. Basel: Birkhauser.
18. Bristeau, M.-O., & Coussin, B. (2001). Boundary conditions for the shallow water equations solved by kinetic schemes. Inria report RR-4282.
19. Fiedler, R. F., & Ramirez, J. A. (2000). A numerical method for simulating discontinuous shallow flow over an infiltrating surface. *International Journal for Numerical Methods in Fluids, 32*, 219–240.
20. Anderson, E., Bai, Z., Bischof, C., Blackford, L.S., Demmel, J., & Dongarra, J., et al. (1999). *LAPACK Users' guide* (3rd ed.). Philadelphia: Society for Industrial and Applied Mathematics.
21. Delestre, O., Lucas, C., Ksinant, P.-A., Darboux, F., Laguerre, C., Vo, T. N. T., et al. (2013). SWASHES: A compilation of Shallow-Water analytic solutions for hydraulic and environmental studies. *International Journal for Numerical Methods in Fluids, 72*, 269–300. doi:10.1002/fld.3741.
22. Delestre, O., Lucas, C., Ksinant, P.-A., Darboux, F., Laguerre, C., & James, F., et al. (2014). SWASHES: A library for benchmarking in hydraulic. In p. Gourbesville, J. Cunge & G. Caignaert, (Eds.), *Advances in Hydroinformatics*, Springer Hydrogeology (pp. 233–243). Springer: Singapore.
23. Legout, C., Darboux, F., Nédélec, Y., Hauet, A., Esteves, M., Renaux, B., et al. (2012). High spatial resolution mapping of surface velocities and depths for shallow overland flow. *Earth Surface Processes and Landforms, 37*(9), 984–993. doi:10.1002/esp.3220.

A Modular Approach Dedicated to Dam-Break and Dam-Breaching Modelling

Frédéric Stilmant, Benjamin Dewals, Sébastien Erpicum, Michel Pirotton and Pierre Archambeau

1 Introduction

Dam-break flood waves often propagate on large areas and their interaction with hydraulic and non-hydraulic structures is often complex (overtopping, erosion, destruction, etc.). Dam-break hazard modelling is thus a task that is computationally demanding and affected with many uncertainties. As such, it requires an integrated tool that can handle both digital elevation models (DEMs) and hydraulic models, and that is versatile enough to enable the analysis of different scenarios. This tool must also be able to make the necessary post-processing of the results in order to provide decision-makers with relevant and objective information on dam-break flood risks.

This paper presents such an integrated tool, starting with the input data (Sect. 2) and goes through the hydraulic models (Sect. 3), the definition of scenarios (Sect. 4), the sensitivity and uncertainty analyses (Sect. 5) and the post-processing of the results (Sect. 6).

2 Input Data

2.1 Digital Elevation Model

DEMs are created from high-resolution laser altimetry data, distributed on a regular 1 × 1 m grid. These data require detailed processing, including field verification, before being used in hydrodynamic modelling. Raw altimetry data may not give a

F. Stilmant (✉) · B. Dewals · S. Erpicum · M. Pirotton · P. Archambeau
University of Liege (ULg), Hydraulics in Environmental and Civil Engineering (HECE),
Allée de la Découverte 9 (B52/3), 4000 Liège, Belgium
e-mail: f.stilmant@ulg.ac.be

P. Gourbesville et al. (eds.), *Advances in Hydroinformatics*,
Springer Water, DOI 10.1007/978-981-287-615-7_17

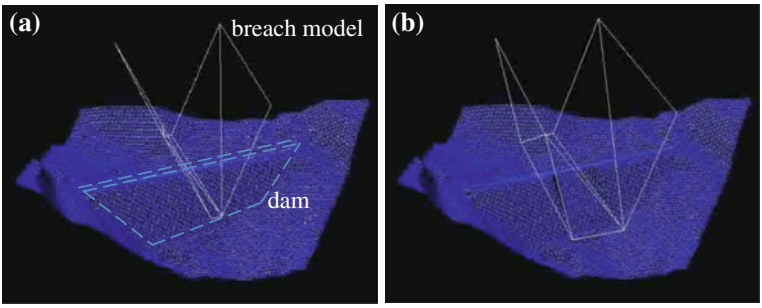

Fig. 1 Breach model applied to the DEM of a dam; **a** breach in the initial state, **b** breach during the opening process

correct description of features such as flood protection walls. They also do not contain information on some paths through which water is able to flow, like passages, under bridges, or conduits (Fig. 2). All these information must be included in the DEM as precisely as possible, given the resolution of the spatial discretisation. If the area under the threat of a dam-break is large, the resolution is lowered in order to limit the computational time to a reasonable value. However, different zones can be modelled with different grid sizes. Thus, the aggregation of the altimetry data can be made with limited impact on the most critical zones.

In the hydraulic modelling, the DEM is either fixed or evolving. In case of the instantaneous collapse of a dam, the structure is removed from the DEM at the beginning of the simulation and the DEM remains fixed. In case of a progressive collapse, a breach is initiated in the DEM and this breach is then increased during the simulation (Fig. 1). A breach model is defined by a set of points that define the three planes. The evolutions of the downstream points are fixed by a vertical and a lateral speed, while the evolutions of the upstream points are constrained by the critical slopes of the three planes. The breach model is used to erode the DEM until the non erodible bottom is reached. In the downstream valley, the DEM can also evolve due to the impacts of the dam-break wave on buildings. Buildings are identified by vector data and each of them can be removed from the DEM, if the action of the flow is sufficiently high to lead to their destruction. Finally, the DEM can also evolve due to erosion and deposition processes that are modelled with an optional sediment transport model fully coupled with the hydraulic model.

2.2 Roughness

The flow resistance induced by the interaction of the water with the ground is modelled with Manning's empirical formula. As mentioned hereafter, dam-break simulations generally use this formula to embed all diffusive effects, including turbulence. Thanks to the resolution of the DEM, the roughness formula however,

does not need to account for macro-roughness such as buildings. Manning's roughness coefficients are distributed throughout the area of interest according to land use. However, the extreme flows induced by a dam-break can significantly differ from the flow conditions for which the roughness coefficients have been validated. This questions the validity of the results given by the numerical model. Roughness coefficients are thus a source of uncertainty in the hydraulic modelling of dam-break hazard and the sensitivity analysis of the results to the roughness coefficients that should be part of the risk analysis [1].

3 Hydraulic Models

The purpose of the numerical model is to simulate highly transient flows that propagate on large areas and complex topographies. The challenge of providing the most precise flow modelling with a reasonable computational effort has led to the implementation of the modelling strategies described hereafter.

3.1 2D Depth-Averaged Model

3.1.1 Mathematical Model

The propagation of a dam-break-induced flood wave is mainly a two-dimensional phenomenon at the scale of the flooded area. As such, its modelling can be based on the depth-averaged equations of mass and momentum conservation, which ensures a good compromise between physical accuracy and computational effort. Moreover, as advective effects govern the flow, turbulence modelling can be avoided and all diffusive effects are integrated in the friction formula.

The depth-averaged equations assume that the flow propagates under atmospheric pressure, which is the most common situation. However, when the flood wave enters a tunnel or passes a bridge, the set of equations takes into account the fact that the flow can become pressurised (Fig. 2). A simulation of such mixed flows is performed within a unified framework [2, 3].

The depth-averaged model is able to take sediment transport into account, as well as erosion and deposition [4]. The interaction between the flow and hydraulic structures like dykes can thus be modelled in a coupled way. Nevertheless, evolving topography can also be prescribed as priori, e.g. in the case of a breaching process.

The model can be adapted to fluids other than water, which makes it possible to model the hazard, due to the failure of heaps of solid particles, e.g. fly-ash heaps [5].

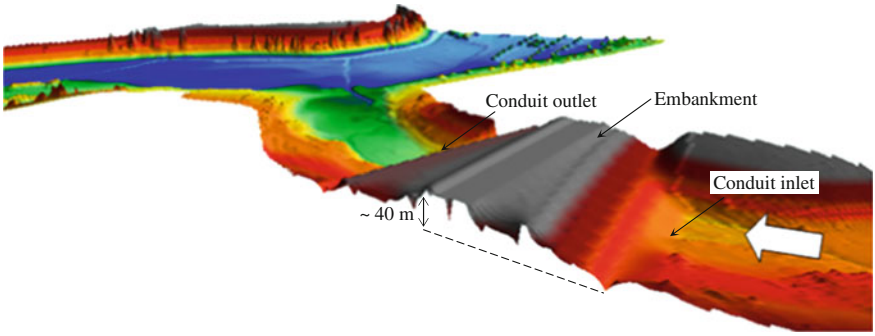

Fig. 2 Portion of a digital elevation model showing a road embankment placed across a valley, downstream of a dam (the *arrow* gives the streamwise direction). The digital elevation model has been modified in order to take into account the conduit through which the river flows. In this conduit, the flow becomes pressurised when the dam-break wave reaches the embankment. This structure has a considerable impact on the propagation of the flood wave

3.1.2 Numerical Model

The set of equations is solved with the WOLF 2D model [6]. The spatial discretisation is based on a finite volume scheme, with mass and momentum flux computed, thanks to a Froude-independent flux-vector splitting method. Time integration is achieved thanks to an explicit Runge-Kutta algorithm constrained by a Courant–Friedrichs–Lewy stability criterion. The numerical model ensures mass and momentum conservation, even in case of multiple cell dryings, and is able to capture shock waves adequately. It has been extensively validated over the past decade.

A dam-break-induced flood wave typically propagates for several kilometres along inhabited areas. This lays down the challenge of a sufficiently fine description of buildings, dykes, roads, bridges, etc., despite the large area of the zone affected by the flood. For this purpose, the spatial discretisation of the model follows a Cartesian grid in which the most critical zones can be described with a finer mesh size. Moreover, at each time step, the computation domain is limited to the flooded area in order to avoid unnecessary computations. Table 1 gives examples of computational domains for Belgian dams.

Table 1 Examples of computational domains for Belgian dams

Dam	Length of the DEM (km)	Grid size (m)
Plate-Taille	~90	8
Vesdre	~50	5
Ry de Rome	~45	4

3.2 Lumped Model

Reservoirs can be modelled thanks to an overall continuity equation and a stage–storage curve that link the water stage evolution to the inflow and outflow discharges. This lumped model, which neglects momentum effects, is valid provided that the inflow volume remains low enough in comparison to the storage volume and that the wave propagation time in the reservoir remains low enough in comparison to the characteristic time of the inflow hydrograph [7]. The lumped model can be coupled with the depth-averaged model. This is of prominent interest in case of a complex of dams or in case of progressive breaching processes; the computational effort is thus reduced in zones where a 2D model is not necessary according to the focus of the study.

4 Scenarios

Owing to the probabilistic nature of dam-breaks, the definition of failure scenarios is a central issue for the modelling of dam-break hazard. A 'worst-case' scenario is often not unique and is moreover unable to give a comprehensive picture of the risk associated with a dam-break. As a complete probabilistic approach, it is far from being feasible, and sensitivity analyses must be carried out to handle the uncertainties that affect these phenomena.

4.1 Single-Structure Failure Scenarios

The total collapse of concrete dams is almost instantaneous; its numerical simulation is thus straightforward. On the other hand, the collapse of rockfill dams is progressive and the assumption of an instantaneous collapse is conservative, but far from realistic. The simulation of a progressive collapse is, however, affected by many uncertainties on the initiation and progression of the breaching process. The initiation may be induced by an overtopping of the dam or a structural failure such as piping [8]. The progression of the breaching process is caused by the erosive effect of the water rushing through the breach. Such a phenomenon can be simulated thanks to a hydraulic model coupled with a sediment transport model. An empirical model can also be used (Fig. 1) that prescribes the evolution of the shape of the breach based on the characteristics of the structure (mainly the volume of the reservoir), regardless of the flow conditions within the breach. Though simpler, this last approach still ensures a strong connection between the flow and the evolving topography.

The uncertainties affecting the failure scenario require sensitivity analyses because the worst-case scenario is not unique. For instance, a modification in the

location of the initial breach (Fig. 3) can result in worse downstream maximum water depths in some zones and, at the same time, reduced maximum water depths in other zones. Moreover, in the example given in Fig. 3, the first scenario (breaching initiated in the centre of the dam) leads to the shorter wave-arrival time (–2 min), while the second scenario (breaching initiated on the right side of the dam) leads to the larger peak discharge (+20 %). Thus, the results of all scenarios have to be combined when generating the risk maps.

The worst-case scenarios are not enough to comprehensively assess the threat induced by a dam in the downstream valley because of less damageable but more failures can also occur, e.g. failures affecting penstocks, valves or gates. The definition of the risk involves all these failures. Their numerical simulations are performed with the help of physically-based lumped models that generate the

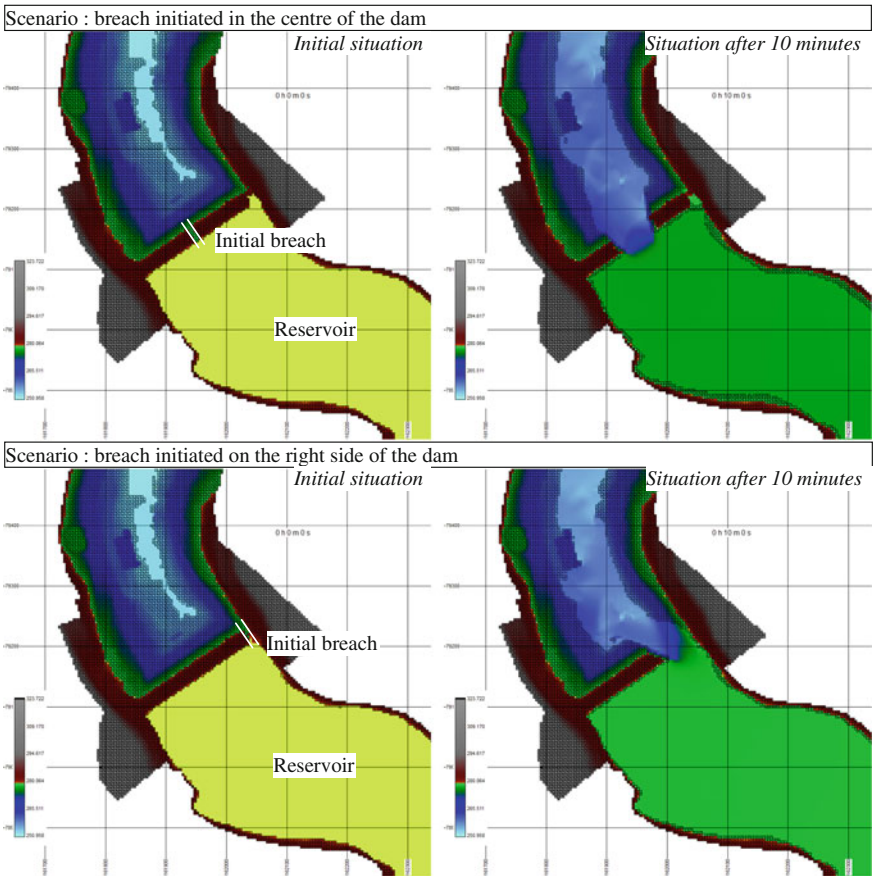

Fig. 3 Dam-breaching scenarios with breaching process initiated at two different locations. Colours give the elevation of the free surface (in metres); dry cells are hatched

necessary hydrographs. For instance, the hydrograph induced by the failure of a valve is deduced from the continuity equation applied to the reservoir together with Bernoulli's equation applied along the conduit affected by the failure.

4.2 *Domino Effects*

4.2.1 Collapse of Several Hydraulic Structures

The wave induced by a dam failure is likely to damage other hydraulic structures located downstream, may be dams, mobile dams, or dykes (Figs. 2 and 4—where the embankment is, in this case, not a 'hydraulic' structure). As this possibility makes the analysis much more complex, a specific methodology is then applied [7]. When a dam-break wave reaches a structure, the hydrodynamic impact of the wave is assessed in order to determine whether the structure is likely to fail or not. The simulation is then continued with the corresponding assumption on the structural behaviour. The simulation can then take advantage of the possible creation of a new

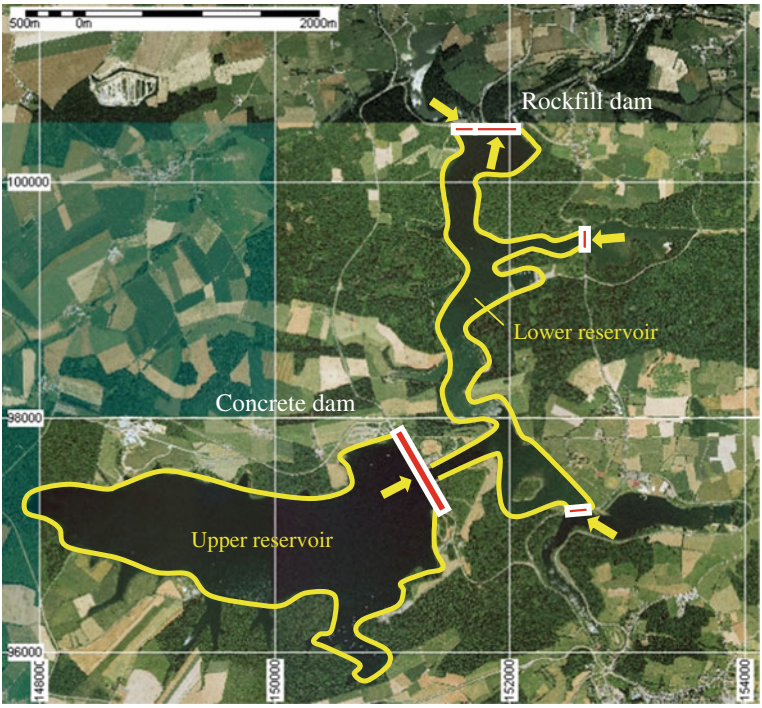

Fig. 4 Eau d'Heure dam complex (Belgium). The contours of the two main reservoirs are displayed in *yellow*

control section which uncouples the upstream and downstream flows. If present, backwater effects are however handled properly.

When assumptions are made on the structural behaviour of several structures, the question regarding the definition of a worst-case scenario becomes even more complex. For instance, in case of a series of successive mobile dams hit by a dam-break wave, the higher water depths are reached within the scenario in which all mobile dams successfully sustain the wave impact, while the shorter wave-front-arrival times are reached within the scenario in which successive mobile dams fail at the time when they are hit.

The interaction between different hydraulic structures, make sensitivity analyses even more important to perform. For the same reason, they are also more complex and require more computational time. The consequence, the methodology makes the best of a lumped model, which is used as a complement to the distributed numerical model presented above or even as a substitute for it when the dynamics of the wave are slow enough. The lumped model is based on the continuity equation applied to the whole reservoir of a downstream dam and gives the hydrograph at the corresponding structure. It can be used to efficiently analyse the influence of the parameters which describe a breaching process.

4.2.2 Collapse of Buildings

Non-hydraulic structures such as buildings have an influence on the propagation of dam-break-induced flood waves. Their obstructive effect tends to slow down the wave propagation and to increase the water depth. However, the impact of the wave is likely to destroy these obstacles, which has an influence on the subsequent flow, as the destruction of hydraulic structures has. Thus, it is necessary to take this possibility into account when modelling dam-break waves propagating over dense urban areas.

In the numerical simulations, the destruction of buildings is determined on the basis of threshold values for water depth, flow velocity and unit discharge. At each time step, the characteristics of the flow-field in the surroundings of each building are compared to the threshold values. When the failure threshold is reached for a given building, the digital elevation model is modified so as to take into account an instantaneous collapse of the structure. Buildings larger than the grid size are supposed to be destroyed cell by cell.

5 Sensitivity and Uncertainty Analyses

There are many sources of uncertainty in a risk analysis. Some of them are due to the inherent variability of physical phenomena and must be handled with a probabilistic approach, while others are due to a lack in knowledge [1]. In the last case,

uncertainty analyses are necessary to give an objective insight in confidence that can be granted to the results.

Uncertainty analysis goes beyond sensitivity analysis in so far as it considers the uncertain parameters as random variables that are described through a probability density. The results given by an uncertainty analysis are probability densities of the characteristics of the flow fields.

The Monte-Carlo method is often seen as the reference method to take the random nature of model parameters into account. This method is applied in three steps: a set of values that follow the probability density of the random variable is first generated; the model is then run for each value of this random sample; the probability densities of the model results are finally deduced. The main constraint to this method is the computational time because a larger number of model runs is required to properly describe the input and output probability densities with random samples.

The stochastic response surface method gets around the constraint of computational time by reducing the time required for one model run. To this aim, the distributed numerical model is replaced with a response surface, i.e. an analytical function that links a given result (local flow-field parameter, wave-front position, etc.) to the model parameters. The response surface is created thanks to a limited number of model runs and can be seen as an interpolation of the model results. As such, it cannot handle discontinuous phenomena properly [9].

The stochastic response surface method is able to give percentiles and confidence intervals on results that have been identified as very sensitive to uncertain model parameters. Figure 5 gives an example, in which the stochastic response surface method gives an interesting insight in the respective influence of two uncertainty sources (the digital elevation model and the roughness coefficient) on the maximum water depth reached in a locality downstream of a dam.

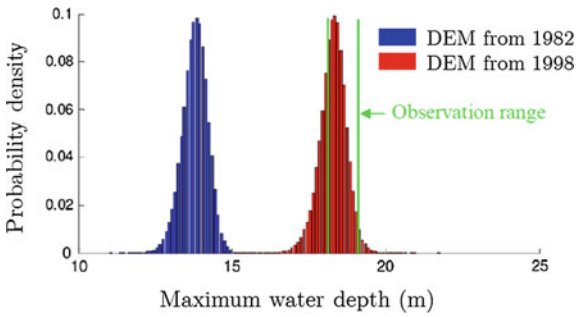

Fig. 5 Results generated thanks to the stochastic response surface method, with a roughness coefficient considered as a random variable. The probability density of the maximum water depth in a dam-break-induced flood wave is plotted for two available digital elevation models

6 Post-processing

The aim of the post-processing phase is to provide the decision-makers with relevant information for setting up appropriate crisis management (warning systems, rescue planning) and town-planning policies. The ultimate aim is to save lives and to mitigate the consequences of a dam-break. The relevant information consists of danger maps and risk analyses.

6.1 Graphical User Interface

The graphical user interface is a key tool for the analysis and the communication of the numerical results. One-, two- and three-dimensional views and animations of the unsteady flow fields helps in understanding the phenomena, verifying the numerical results, identifying the sensitive zones, comparing the scenarios, locating the results on aerial photographs, etc. These tasks are of prominent importance but are made difficult by the amount of data to process. Hence there is a need for an efficient and integrated tool.

6.2 Danger Maps

The flow model generates a series of danger maps including maximum water depths, maximum unit discharges, maximum velocities and wave-front-arrival times. These maps are created during the simulation and updated at each time step for best precision. However, they can also be created by post-processing the flow-field results. In both the cases, these maps are raw data that have to be treated in order to take uncertainty into account.

The uncertainty that affects the results is not restricted to the uncertainty on model parameters presented in previous section, but it also includes the uncertainty on the topographic data and the uncertainty on the flow model in itself. At present, computing power as well as methodological issues makes a probabilistic approach of the problem unrealistic. Uncertainty is thus taken into account through a safety coefficient.

The application of a safety coefficient to danger map is not a trivial procedure, when considering the problem of the spatial extent of the zone affected by the dam-break-induced flood wave. An increase in water depths must logically be coupled with an increase in the spatial extent of the inundated area. If the application of the safety coefficient lead water depths to overpass a protection structure like a dyke, then the flooded area is likely to increase disproportionately. Nevertheless, the increase in the flood extent can be based on a purely geometrical method, e.g. a fast marching method [10].

6.3 Risk Analysis

The aim of risk analysis is to assess the potential social and economic impacts of a dam-break. This is achieved by combining hydrodynamic modelling with land use data and vulnerability indicators. This kind of risk analysis is similar to flood risk analyses [11], with the difference that potential loss of lives are a much more important concern.

7 Conclusions

Over the past decades, dam-break modelling has taken advantage of increasing computational power and new model developments which have improved the accuracy of the numerical simulations. As more details are accounted for in the numerical simulations, the processing and verification of the input data and the results have become more dependent on efficient interfaces. Nevertheless, computational time is still felt as a limiting constraint, especially when facing the problem of sensitivity and uncertainty analyses. These analyses should, however, not be neglected. They are of prominent importance because of the unavoidable uncertainties that affect the flow model, the input data and the scenarios. The approach that has been presented here makes the best of several models (distributed numerical model, lumped models, surface response) integrated within a single interface to provide decision-makers with relevant and objective information.

References

1. Merz, B., & Thieken, A. H. (2009). Flood risk curves and uncertainty bounds. *Natural Hazards, 51*, 437–458.
2. Kerger, F., Archambeau, P., Dewals, B., Erpicum, S., & Pirotton, M. (2012). Three-phase bi-layer model for simulating mixed flows. *Journal of Hydraulic Research, 50*(3), 312–319.
3. Nguyen, V. N., Erpicum, S., Dewals, B., Pirotton, M., & Archambeau, P. (2012). Experiment investigations of 2D stationary mixed flows and numerical comparison, In P. Rutschmann, M. Grünzner & S. Hötzl (Eds.), *2nd IAHR Europe Conference*, Munich, Germany.
4. Dupont, E., Dewals, B., Archambeau, P., Erpicum, S., & Pirotton, M. (2007). Experimental and numerical study of the breaching of an embankment dam. In G. D. Silvio & S. Lanzoniin (Eds.), *32nd IAHR Biennial Congress—Harmonizing the Demands from art and Nature*, IAHR: Venise, Italy.
5. Stilmant, F., Pirotton, M., Archambeau, P., Erpicum, S., & Dewals, B. (2014). Can the collapse of a fly ash heap develop into an air-fluidized flow?—Reanalysis of the Jupille accident (1961). *Geomorphology* (In Press).
6. Erpicum, S., Dewals, B., Archambeau, P., & Pirotton, M. (2010). Dam-break flow computation based on an efficient flux-vector splitting. *Journal of Computational and Applied Mathematics, 234*, 2143–2151.

7. Dewals, B., Erpicum, S., Detrembleur, S., Archambeau, P., & Pirotton, M. (2011). Failure of dams arranged in series or in complex. *Natural Hazards, 56*(3), 917–939.
8. ICOLD. (1998). *Dam break flood analysis—review and recommendations*. Bulletins, ed. I.C. o.L. Dams (Vol. 111). Paris, France.
9. Dewals, B., Erpicum, S., Pirotton, M., & Archambeau, P. (2012). *Dam Break Flow Modelling With Uncertainty Analysis*. In *SimHydro 2012: New Trends in Simulation, Hydroinformatics and 3D Modeling*. Nice (France).
10. Sethian, J. A. (1999). *Level set methods and fast marching methods: evolving interfaces in computational geometry, fluid mechanics, computer vision, and materials science.* (p. 378). Cambridge: Cambridge University Press.
11. Ernst, J., Dewals, B., Detrembleur, S., Archambeau, P., Erpicum, S., & Pirotton, M. (2010). Micro-scale flood risk analysis based on detailed 2D hydraulic modelling and high resolution geographic data. *Natural Hazards, 55*(2), 181–209.

2D Modelling of the Rhone River Between Arles and the Sea in the Frame of the Flood Prevention Plan

Fabienne Scerri, Christophe Lescoulier, Camille Boudong and Caroline Hémain

1 Introduction

After the flooding on the Rhône on 3–4 December 2003 that affected more than 12,000 people over the entire river delta and caused more than €700 million of damage, the public authorities in France undertook a far-reaching flood prevention programme known as the "Rhône Plan".

The SYMADREM (interregional management authority for embankments in the Rhône delta) has been engaged in hydraulic modelling enabling sizing design for embankment projects on the Rhône and Petit Rhône rivers since 2007. The initial studies entrusted to the Compagnie National de Rhône (CNR) enabled accurate adjustment of design of the embankments between the Rhône from Beaucaire to the sea. In 2009, SYMADREM entrusted EGIS-EAU with the hydraulic studies for embankment engineering on the Petit Rhône, and for improved drainage on the left bank of the Grand Rhône between Tarascon and Arles [1, 2].

Hydraulic studies on the Petit Rhône allowed sizing design of embankments, so as to avoid breach, and management of the system for high water levels between the protection design discharge and exceptional flood levels, i.e. to organise the management of excess flows without the risk of embankment breach and ensure rapid drainage of flooded areas. For the left bank of the Grand Rhône, the aim is to

F. Scerri (✉) · C. Lescoulier · C. Boudong · C. Hémain
EGIS, 78 Allée John Napier, 34965, Montpellier Cedex 2, France
e-mail: montpellier.egis-eau@egis.fr; fabienne.scerri@egis.fr

C. Lescoulier
e-mail: Christophe.lescoulier@egis.fr

C. Boudong
e-mail: Camille.boudong@egis.fr

C. Hémain
e-mail: Caroline.hemain@egis.fr

P. Gourbesville et al. (eds.), *Advances in Hydroinformatics*,
Springer Water, DOI 10.1007/978-981-287-615-7_18

support the project for safetying of the embankments by engineering an overflow zone upstream of Arles and introducing measures to improve drainage in the downstream plain.

Several two-dimensional models were built for the purposes of these studies with the Télémac-2D and Infoworks RS 2D two-dimensional flow softwares, suited for the purposes and for the specific aspects of the areas were studied.

2 Hydraulic Modelling of the Petit Rhône

The hydraulic models of the Petit Rhône cover the perimeters of the embanked bed of the Petit Rhône from defluent to the sea (a length of 55 km), of the Camargue Gardoise protected riverbed (area 430 km^2) and of the Camargue Insulaire protected riverbed (area 730 km^2) (Figs. 1 and 2).

2.1 Aim of Modelling

The aim of the hydraulic study was to model the initial state, prior to works, and the final state after completion of works. More specifically, the aims were to:

- Model flows and determines the hazard in the embanked bed of the Petit Rhône and in the protected beds of the Camargue Gardoise and Camargue Insulaire, respectively, in initial state, for hydrological scenarios for the Rhône;
- Simulate the effect of a breach in the embankments on the Petit Rhône in the initial state and propagate into the protected plain and evaluate the behaviour of areas close to the embankment breaches (velocity, propagation time and depth); these results will be used for hazard studies;
- Determine the positioning in terms of height and layout of embankments on the right and left banks of the Petit Rhône, in line with the protection objectives established by the contracting authority;
- Model the final state for the hydrological scenarios and estimate the hydraulic impact of structures in the embanked and protected beds.

2.2 Choice of Software

Modelling of flows in embanked and protected beds was performed using the TELEMAC 2D bi-dimensional simulation software.

EGIS-EAU has been using the TELEMAC-2D bi-dimensional model developed by LNHE (Laboratoire National d'Hydraulique Environnement) of EDF (Electricité de France) since 1998.

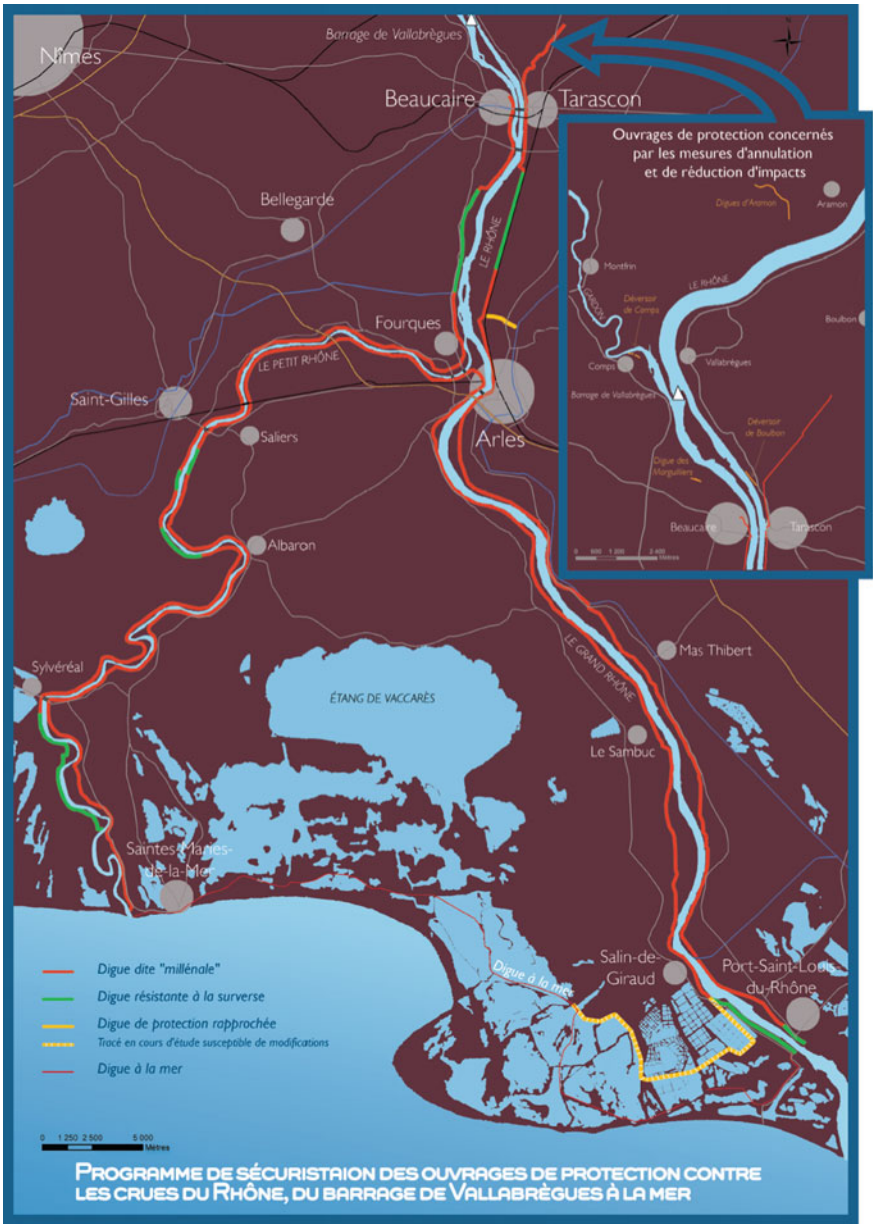

Fig. 1 Flood prevention structures on the Rhône

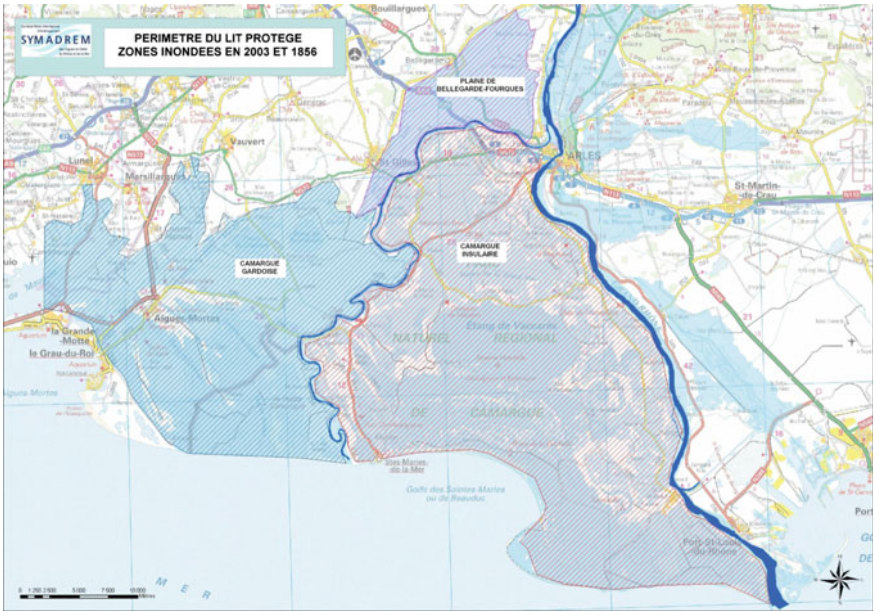

Fig. 2 Perimeter of protected riverbed (*Source* Symadrem)

This tool solves the Saint-Venant equations and is appropriate when it is necessary to model the effects of so-called turbulent friction, i.e. exchanges of quantity of movement between masses of water. It is useful whenever fine knowledge of current fields (e.g. embankment breach) is sought. Applied to rivers, this model enables local and very fine calculation of current fields in localised sectors of channels. The Telemac-2D model allows clear distinction between flows in the channel and in the plain between the river and its embankment. Flood levels can therefore be different in the channel and floodplain at a same kilometric reference point. Telemac-2D uses finite element numerical methods based on triangular elements, for which the mesh size can vary and be suited to topographical constraints.

2.3 Topographical and Bathymetric Data

Bathymetric and topographical data are essential for correct modelling and must be suited to the requirements of 2D modelling. The difficulty lies in obtaining sufficiently accurate altimetric data and sufficiently dense data in X, Y.

For example, for construction of the channel of the Petit Rhône, cross-sections are not sufficient, as would be the case for linear models. Therefore, for modelling of the channel, clusters of bathymetric points in the navigable channel were

supplemented by four long profiles between the navigable channel and the banks over the 55 km modelled.

For floodplain topography, the aim is to obtain a cluster of regular points but also of "break lines" that structure flows (embankments, roads, dikes, ditches, etc.). The topography of embankments and of natural terrain behind them is from specific LIDAR surveys (set of points on a mesh and dimensioned break lines for embankment feet and crests).

Similarly, for modelling of the protected beds of the Camargue Gardoise and Camargue Insulaire, LIDAR topographical data were used from the BDT (topographical database) of the IGN (National Geographical Institute), supplemented for the water bodies part (canals and ponds) by sets of bathymetric points. The IGN-BDT provides points on a regular mesh with a density of points every 2 m, altimetric accuracy of ±20 cm and break lines for singularities (embankments, dikes, ditches, etc.). These data were used in the form of a numerical model of the terrain for building of the mathematical model (Figs. 3 and 4).

2.4 Building of the Models

Three 2D models were built: embanked river, protected bed right bank (Camargue gardoise) and protected bed left bank (Camargue Insulaire). The model mesh was suited to the study area. Mesh density results from the constraints for representation of flows and bathymetry.

The modelled areas are represented by a mesh of triangular elements for which the extremities are both calculation points and topographical data points. The aim is

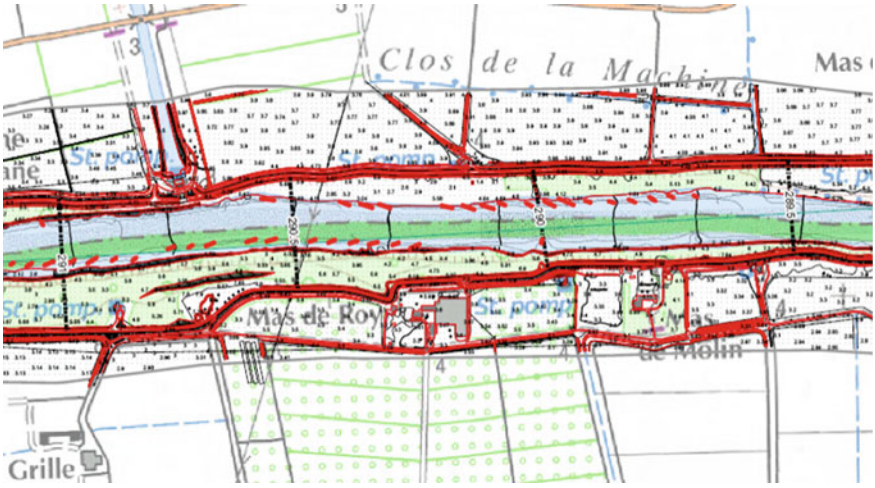

Fig. 3 Example of topographic and bathymetric data

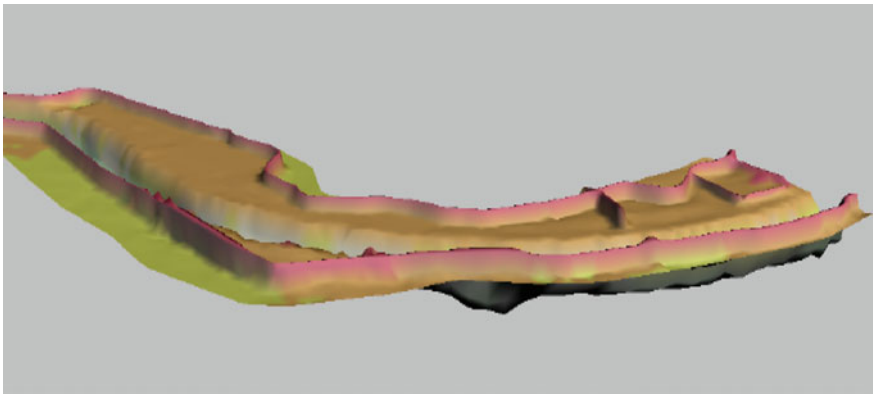

Fig. 4 Example of numerical terrain model

to take account of the topography with a sufficient degree of accuracy whilst ensuring "reasonable" computation times.

2.4.1 The Embanked Bed Model

The embanked bed model includes the entire embanked bed and a strip of around 200 m behind the embankment. The mesh is therefore based on the following principles:

- Use of "lines of constraint", i.e. topographical lines used in the mesh: embankments, banks of channel, embankments in floodplain (roads, etc.). Embankment overflows are represented by the topography of embankments, using lines for top of embankments, aligned embankment crests and embankment feet.
- Use of "regular mesh" for channel, i.e. lengthwise distorted mesh (the channel is represented by a minimum of 10 points over the width, that is to say element sizes may be less than 10 m in width and 50 m lengthwise).

The mesh used comprises 140,000 elements of between a few metres (at the embankments) and 50 m in the floodplain, without constraints.

2.4.2 The Camargue Gardoise and Camargue Insulaire Protected Bed Models

These models cover the protected bed of the right bank of the Petit Rhône, from St Gilles to the sea, for the Camargue Gardoise (area 430 km^2), and the protected bed on the left bank between the embankments of the Petit Rhône and Grand Rhône to the sea for the Camargue Insulaire (area 730 km^2).

The mesh, as previously, is based on the principles of use of "lines of constraint" (embankments, roads, canal banks, etc.) and use of the "regular mesh" for canal channels. Excluding the singularities, a mesh size criterion is given in accordance with the desired degree of accuracy (refined with elements of 10 m at embankment edges up to around 100 m for the rest of the territory).

Ultimately, the mesh adopted for the Camargue Gardoise has 300,000 elements, that for the Camargue Insulaire 200,000 elements, with sizes of between a few metres (at canals and dikes) and 100 m, in floodplain without constraint (Figs. 5 and 6).

2.5 Boundary Conditions

The boundary conditions for the embanked model are made up of hydrographs for the upstream Petit Rhône and representative maregraphe sea water level records downstream. They are obtained from the previous hydraulic study for adjustment of works on the Rhône conducted by SYMADREM and CNR with the same Télémac software. This study modelled the Rhône and Petit Rhône and included all of the engineering works in the Rhône Plan, as works on the Rhône affecting the distribution of defluent flows.

The embanked bed model includes an area behind the embankment allowing simulation of embankment overflow in free-flow regime, i.e. without influence of the level behind the dike. A lateral boundary is imposed on the model allowing drainage of overflows outside of the modelled area (of "free outflow" type for the upstream part, or of imposed level type for downstream part influenced by sea water level).

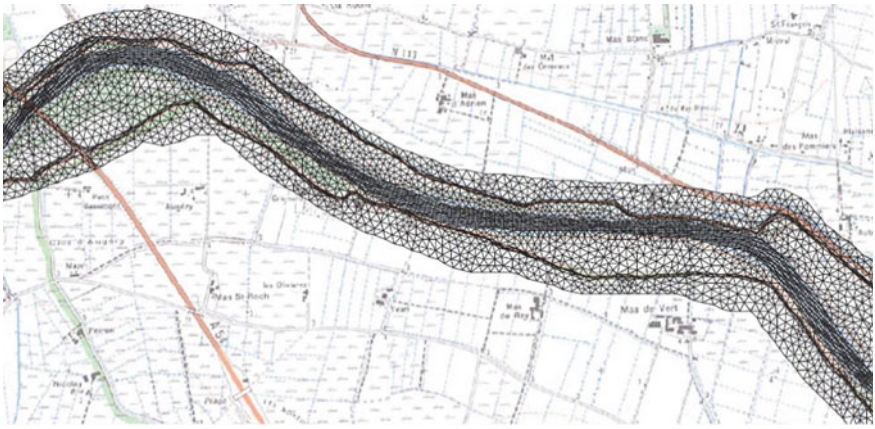

Fig. 5 Zoom on embanked bed mesh

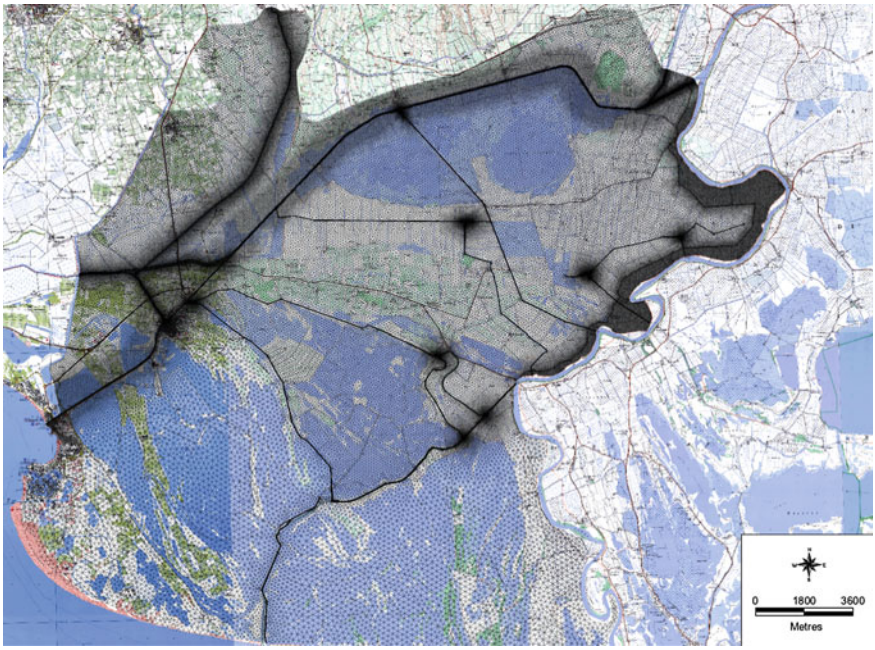

Fig. 6 Camargue Gardoise mesh

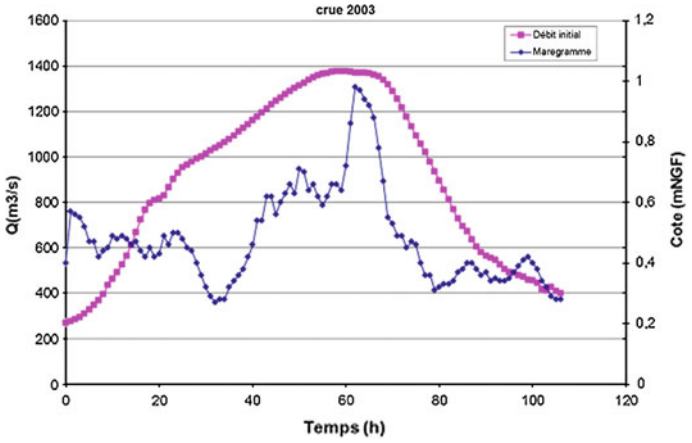

Fig. 7 Boundary conditions for floods of December 2003

The boundary conditions in the protected beds are made up of the breach and/or overflow hydrographs calculated by the embanked bed model, the overflow hydrographs for the Rhône embankments calculated by the adjustment study model and maregraphe records representative of sea water level downstream (Fig. 7).

2.6 Calibration and Sensitivity Testing

Calibration consists in adjusting the roughness (Strickler) coefficients so that the water levels calculated by the model coincide with levels observed for actual floods. These coefficients are established initially on the basis of size distribution of bed materials and of land use (vegetation, etc.). They are generally higher for 2D models than those normally used in linear models, because 2D modelling calculates local velocities better and represents individual head losses resulting from variations in velocity (bend, varying topography, etc.). They are then refined by adjusting the model to available flood observations.

2.6.1 Calibration of the Embanked Bed

The model is calibrated in relation to the flood of 3 December 2003, the highest flood in recent history for which calibration data are available (boundary conditions and limnigraph at measuring stations and highwater marks).

However, calibration on this flood is a delicate operation as two large breaches of widths of over 100 m occurred (at Argence and Claire Farine) and are greatly affected water lines. These breaches had a fundamental influence on the flooding downstream. Calibration of the Strickler coefficients was performed initially with the water line prior to breach. The values retained varied from 35 to 48 in the channel and 15–20 on the banks. The breaches were then reproduced iteratively in the model so as to return to the depth graphs observed at the measuring stations (Fig. 8).

2.6.2 Sensitivity Tests for the Embanked Bed

Given the difficulties of calibration to the 2003 flood, greatly influenced by breaches, sensitivity tests were performed on the Strickler coefficient and boundary conditions.

A relatively large change in the Strickler coefficients (±5 points in relation to values adopted) in the channel and floodway (between embankments) has an impact of ±40 cm on the water level upstream of the model, reducing in the direction of flow to less than 10 cm downstream. This effect decreases downstream as a result of overflowing of the embankment and of the influence of the sea water level.

Similarly, sensitivity to sea level tests was performed varying the sea water levels between 0 m NGF and 1.5 m NGF. The effect of sea water level, sensitive over a stretch of 15 km, is limited by the effects of overflows in the downstream part.

In addition, the study conducted on the Rhône and Petit Rhône also considered the effect of variations in discharge at the inlet to the Petit Rhône. The effect is relatively pronounced upstream of the model with a variation of ±5 % in the

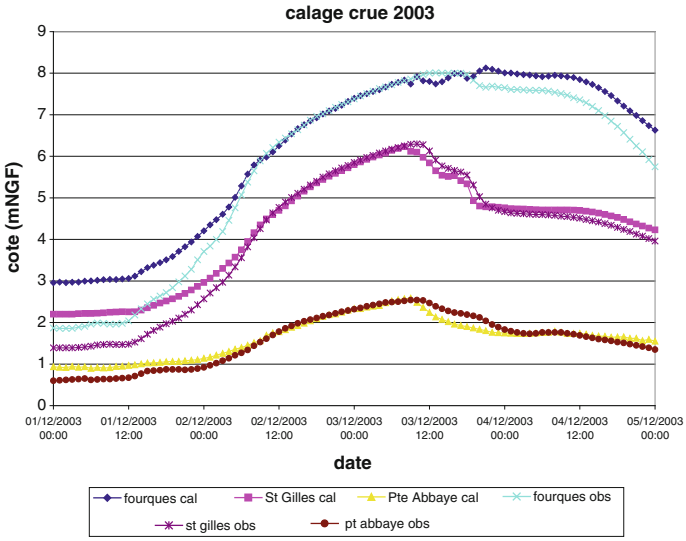

Fig. 8 Calibration using December 2003

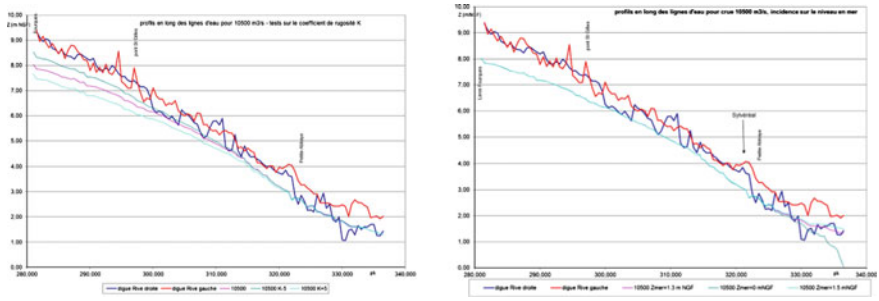

Fig. 9 Sensitivity tests on Strickler and downstream level

discharge of the Petit Rhône before the breach of 3 December 2003 leading to a variation of ±60 cm in water levels in the Petit Rhône upstream and of ±10 cm downstream (Fig. 9).

2.6.3 Calibration and Sensitivity Tests for Protected Beds

Calibration of the Camargue Gardoise was based on the December 2003 flood for which the hydrographs of the two breaches could be reconstituted from modelling of the embanked beds and 15 highwater marks taken from the study conducted by the Syndicat Mixte pour la Gestion et la Protection de la Camargue Gardoise

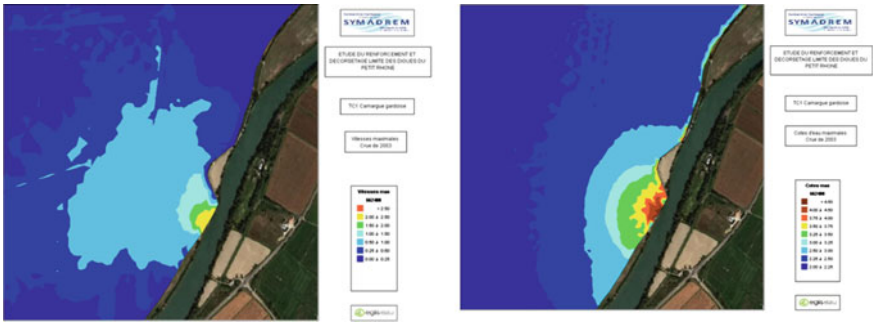

Fig. 10 Map of maximum water velocities (m/s) and water level (mNGF) for the 2003 December flood at the Claire Farine breach—Zoom on the Claire Farine sector

(Camargue Gardoise management and flood protection authority; study conducted by BCEOM consultants in 2006). For the Camargue Insulaire, the most recent floods were in 1993 and 1994; these occasioned breaches on the left bank but the hydrographs for the flows across the breaches are not known as there is no accurate flood marker to allow calibration of the model.

The Strickler coefficients adopted after calibration are 30 for canals and ponds and 10 for the floodplain. Sensitivity tests were conducted on the Strickler coefficients and on the model's boundary conditions.

Given the types of protected beds (gentle topographic slope and low velocity), the model exhibits low overall sensitivity to roughness coefficients since a variation of 10–15 in the coefficient induces a drop in water level of less than 10 cm over the entire area. Greater differences can be calculated at isolated points for particular hydraulic phenomena, for instance in the area behind a breach (Fig. 10).

2.7 The Scenarios Simulated

Several scenarios for flooding of the Rhône at Beaucaire were simulated: 10,500 m^3/s Rhône flood (January 1994, return period 50 years), December 2003 type (11,500 m^3/s, return period 100 years), reference flood of May 1856 (12,500 m^3/s, return period 250 years), exceptional 1,000 year flood (14,160 m^3/s, return period 1,000 years). These scenarios are combined with different hypotheses for the water level (variable or constant level limnigraph). For these scenarios, the Petit Rhône hydrographs were estimated in the overall modelling of the Rhône calibration study, in initial and final state of works on the Rhône (Table 1).

To limit computation time, the model was initialised over 24 h with a low discharge at the start of the flood hydrograph and for the initial sea water level from sea limnigraphs. The complete flood hydrographs, over 3–5 days, were simulated on the embanked bed model. For the protected bed models, duration of simulations

Table 1 discharges for modelled scenarios

Rhône flood scenario	Peak discharge on Petit Rhône (m^3/s)	
	Initial state	Future state
10,500 m^3/s	1,177	1,191
Dec 2003	1,378	1,384
May 1856	1,520	1,493
1,000 yrs	1,606	1,554

was about 20 days longer, so as to represent full propagation in the modelled area. The simulations require about 24 h, running on machines using 10 processors, thanks to the software's parallel processing capacity.

For the initial state, the hydrological scenarios were first simulated without a breach, to establish current functioning of overflows on the banks of the Petit Rhône. However, as the initial state corresponded to the condition of the unreinforced embankments, the risk of a breach is present and several scenarios for breaches in the Petit Rhône's embankments were simulated for the embanked bed, in order to calculate the hydrograph for failure and propagation of the embankment failure wave in the protected beds.

The breach scenarios in initial state were established from diagnostic studies of embankments that provided the location and characteristics of breaches. The widths of breaches modelled for the Petit Rhône vary between 60 and 130 m. The beginning of opening of the breach is concomitant with the flood peak at the breach point. This configuration is the one that gives the highest discharges in the breach and therefore the maximum depths and velocities immediately behind the breach. The breach opens in two stages: first, progressive opening of the embankment over 2–5 h over the width of the breach down to the level of the natural terrain, then creation of 5–10 m ditch, behind the breach, over 2 h. This operation is represented by FORTRAN programming of modification of the mesh points.

For the final state, which corresponds to the engineered state of the embankments on the Rhône and Petit Rhône, simulations were run without breach to allow adjustment of the embankment works on the Petit Rhône (pulled back position of embankments and adjustment of sections resisting overflow). The works were optimised by modelling so as to limit the hydraulic impact on both the embanked bed and, subsequently, on the protected beds (Figs. 11 and 12).

2.8 Simulation Results

Embanked bed model simulations enabled, initially, optimising of the works contained in the Rhône Plan in accordance with the sizing design principles adopted: reinforcement of embankments with increased height and pulling back if necessary, as well as sizing of sections resisting overflow calibrated in relation to the protection design flood ensuring, for higher flood levels, overflow without failure and

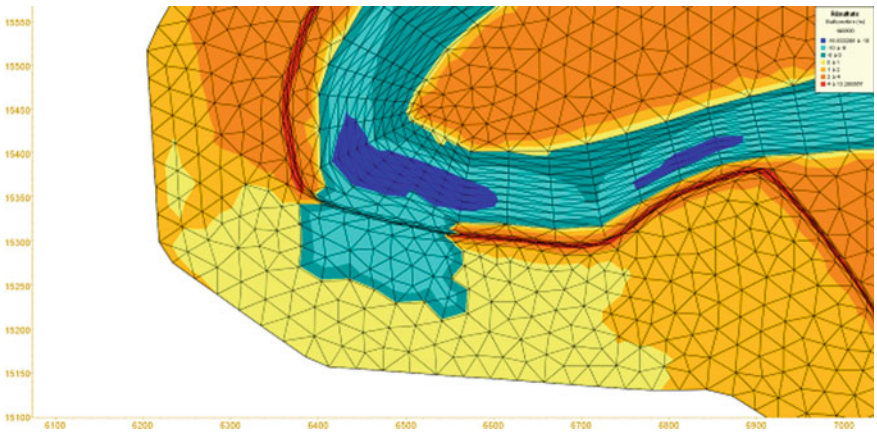

Fig. 11 Formation of a breach (topography)

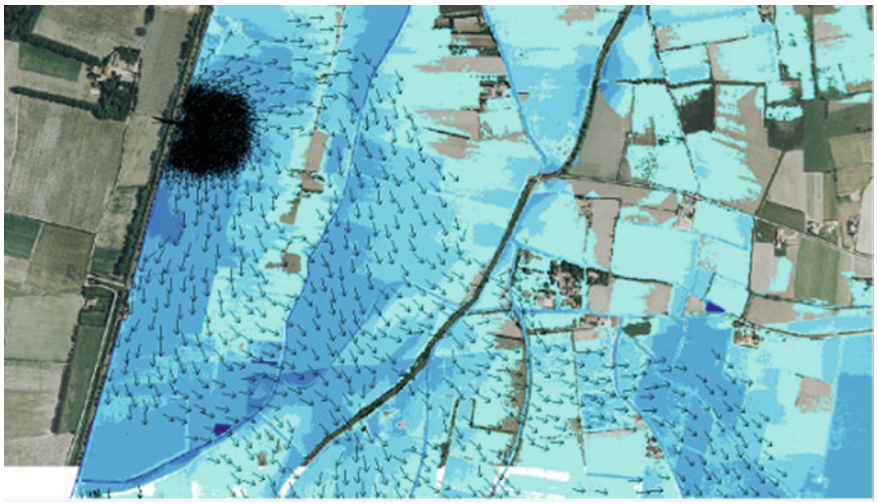

Fig. 12 Results of velocity in a breach

slow and controlled filling of the space protected by the embankments, with equal distribution of the overflowing volumes between the right and left banks.

Modelling for adjustment of the structures required incorporation in the model of the alignment of the pulled back embankments and of sections resisting overflow. It is to be noted that the criteria for the mesh within the current position of the embankments are the same in the initial and engineered states (same lines of constraint, same element size criteria). The meshes in the areas common to the two models (initial and engineered states) are therefore the same, allowing accurate quantifying of the impacts of the project.

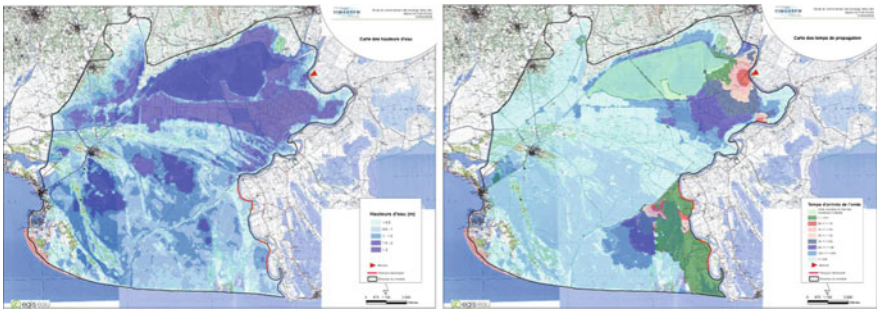

Fig. 13 Example of water level and propagation time map Camargue Gardoise (breach)

Sizing of the overflow areas for levels above the protection level was conducted iteratively so that the rates of overflow at the resistant sections compensate for overspills in the initial state, so that there is no aggravation of discharge downstream in relation to the current state and that discharges and volumes are distributed equally between the left and right banks.

Embankment overflows are modelled in 2D, with the Strickler coefficient as the sole calibration parameter. Roughness coefficient sensitivity tests were performed (variation of 1–2 % in maximum overflow rate for change in Strickler coefficient from 40 to 50), and coherence with the free-flow weir formulas used conventionally for this type of overspill was verified. It was thus possible to verify the value of the lateral weir coefficient (Hager, Dominguez laws) of around 0.2–0.25 for low hydraulic heads (depth 0.2 m).

The results for water levels, depths and speeds in each of the protected bed elements were mapped with a GIS, together with time of propagation and duration of submersion. These maps are used for risk and hazard studies (for breach scenarios) and are then cross-referenced with vulnerability; they allow conducting of the Cost-Benefit Analysis of the embankment safetying programme (Fig. 13).

3 Modelling of the Left Bank of the Rhone

3.1 Aim of Modelling

This modelling exercise was carried out for a study of drainage and management of overflowing water on the left bank of the Rhône, a measure accompanying an operation entitled: creation of an embankment to the west of the Tarascon/Arles railway line and hydraulic transparency of the railway embankment.

The perimeter of modelling is the entire left bank of the Rhône between the city of Tarascon and the sea (area 370 km^2).

The hydraulic modelling tool was proposed to meet the following aims: modelling of hydraulic functioning prior to engineering work (initial state and with-project state without drainage measures) and hydraulic impact of drainage works.

The results of modelling enabled, in addition to designing of measures to improve drainage in the plain, simulation of breaches in the railway embankment, as part of the hazard study by RFF (Réseau Ferré de France) (Fig. 14).

3.2 Choice of Mathematical Model

The software chosen was INFOWORK RS 2D. This appears to be the most suitable software for modelling of the left bank of the Rhône with inclusion of the singularities of the terrain (numerous canals, embankments, etc.) and of structures and plant to be modelled (siphons, closed conduit flow systems, etc.). The software benefits from the latest developments in cartography, (integration of GIS tools), is easier to use for building of a model and provides graphic results. Its characteristics, therefore, allow better consideration of singular structures such as siphons and of hydraulic transparency of the RFF embankment and optimisation of computation time for long-duration simulations, such as those necessary for analysis of drainage phenomena.

The 2D module uses the principle of discretisation of the floodable area in the form of a mesh of triangular elements and solves the Saint-Venant equations for depth and velocity in two dimensions. The software is developed by INNOVYZE and is commercially available in France from the GEOMOD company.

A 2D module has been developed to enable modelling of complex surface flows in flood prone areas using a bi-dimensional mesh. The floodable area is represented by triangular elements. Water levels and velocities are calculated locally at the centre of each triangular element. Solving uses the finite element method, based on the Gudunov programme and Riemann solver. The solving model is semi-implicit. The area to be modelled is discretised by a mesh of triangular elements. The Numerical Terrain Model must be used to create the mesh. Voids, lines of constraint and walls can be included in the mesh. Discharges can be calculated from a 2D line and from the limits of the polygon.

1D/2D coupling allows conventional 1D representation of the channel (enabling good bathymetric representation of hydraulic sections of small canals and in-river structures) and 2D representation of floodable areas to enable accurate modelling of obstacles to flow (dikes, embankments, buildings, etc.) from a numerical terrain model. The flood plain is represented by a mesh of triangular elements with sizes suited to the natural terrain and land use.

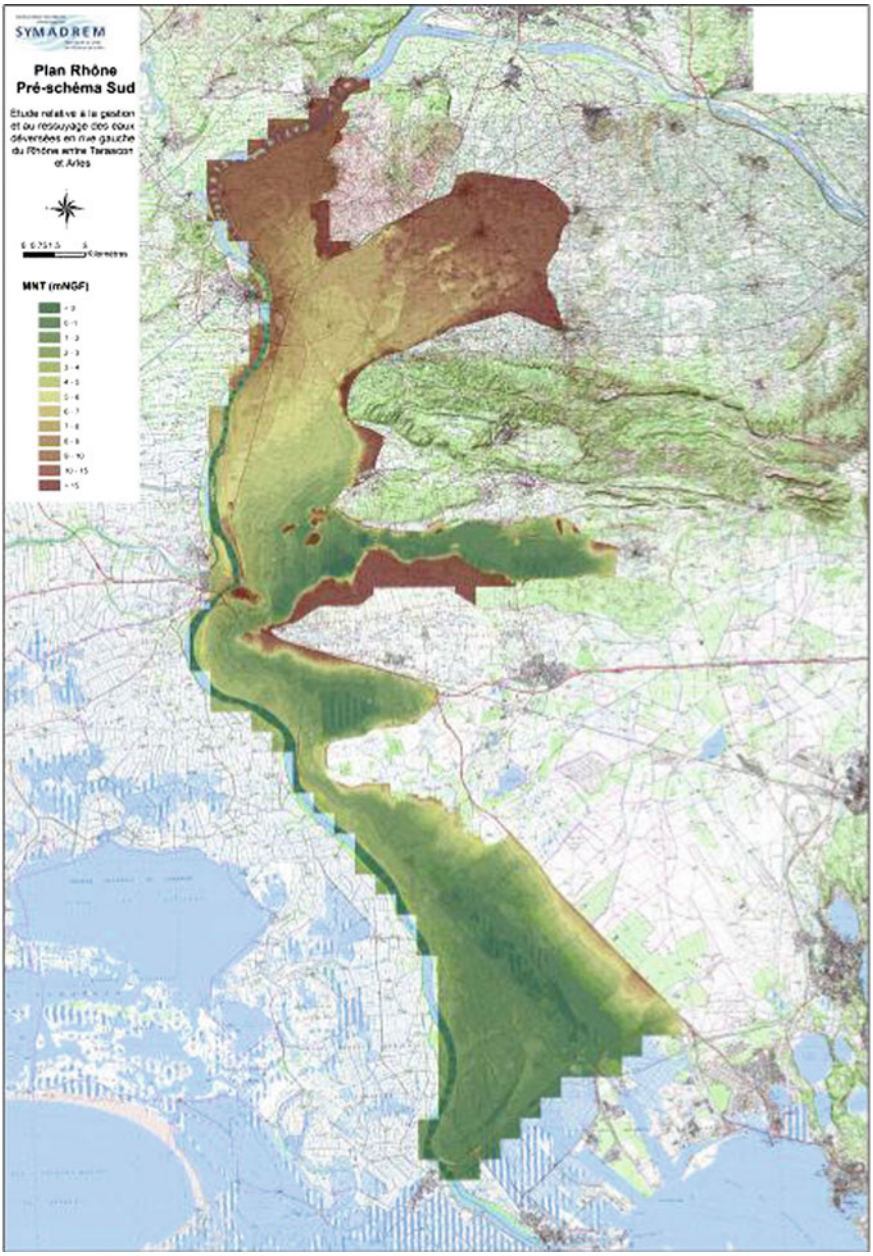

Fig. 14 Area modelled

3.3 Building the Mathematical Model

The model was applied to the left bank of the Rhône between the Boulbon plain and Fos sur Mer; the area to be modelled is extensive (370 km^2).

The model was built initially to be calibrated in relation to the flood of December 2003. Once calibrated, the works carried out north of the city of Arles and the projected embankment between Tarascon and Arles, as well as hydraulic transparency of the RFF embankment, were incorporated into the model.

The model mesh is suited to the configuration of the study area. The mesh density results from the constraints on representation of flows and the bathymetry while maintaining reasonable computation times for future simulations. A specific aspect of the study area is the large number of canals to be modelled, mostly with embankments and running above the natural terrain level, as well as a large number of structures: bridges but also siphons running under the embanked canals.

The channels are modelled with a one-dimensional simulation, avoiding degradation of the channel bathymetric information (the bathymetric description of the water course is not limited by the number of calculation points as in 2D models) and allowing modelling of the numerous closed conduit systems.

All of the structures on the canals are modelled with the conventional laws for structures (BRADLEY laws, to represent head losses at bridges, "orifice" type for closed conduit structures or "weir" and "valve" for fixed and moving weirs, or "siphon" type). Beyond the water courses described above, the 2D modelling areas are represented as meshes of triangles of which the apexes are topographical points (unlike Telemac, the calculation point is at the centre of the element with an average topographical level at triangle apex).

The intention is to obtain sufficiently accurate representation of the topography while maintaining "reasonable" computation times. The mesh is therefore based on use of "lines of constraint", that is to say topographical lines that must be used in making the mesh: this is the case for ditches, dikes and embankments in floodplains (roads, etc.). The "constraint" lines are lines that force the mesh so that required topographical data (in the case of embankment or ditch) are used in the mesh. It should be borne in mind that a 2D model only uses topographical data at mesh calculation points (unlike one-dimensional models for which the density of topographical points entered is far greater than the number of calculation points). Lastly, an element size criterion is given per area: between 10 and 200 m (Fig. 15).

3.4 Bathymetric and Topographical Data

The data required are of the same type as those for the preceding model, i.e. a topographical cluster in the floodplain (from the IGN database, altimetric accuracy

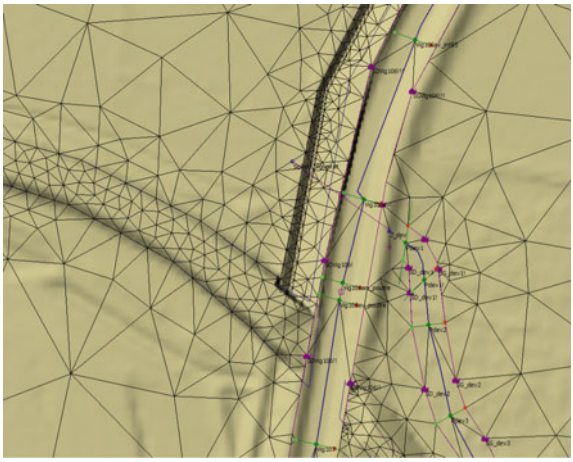

Fig. 15 Example of mesh (1D/2D)

of 20 cm; NTM pitch 2 m) completed by break lines (banks, canals, dike crests, embankments, walls, ditches, etc.) and bathymetric data in the form of cross-sections of canals and structures (from topographic ground surveys).

3.5 Boundary Conditions

The boundary conditions are constituted by the hydrographs and limnigraphs imposed at model boundaries: hydrographs of Rhône inflows in breaches and embankment overflows (source SYMADREM, CNR), the hydrographs of all of the drainage basins flowing into the canals in the study area, limnigraph measured downstream in the docks at Fos sur mer.

3.6 Calibration and Sensitivity Tests

The calibration information (boundary conditions and highwater marks) is available for the December 2003 flood. However, calibration in relation to the flood is delicate since it gave rise to several breaches that greatly influenced the water levels. The Rhône inflow hydrographs also come from formation of breaches in the railway embankment underpasses. The comparison of twenty flood markers and the areas inundated in 2003 allowed adoption of Strickler coefficients (20–30 for linear modelled canals, 15 for 2D modelled plain). Tests were performed using coefficients of 10 (instead of 15) in the 2D area, and of 25 (instead of 30 in the main canals), inducing a slight rise in water levels (5–10 cm).

3.7 Modelling of Engineering Projects

Since the flood of December 2003, which caused severe damage in the city of Arles, Protection work has been carried out to the north of the city. The initial state corresponds to inclusion of these works in the model. The works consist of a protection embankment to the north of Arles, a regulating structure (control structure in the bed and lateral weir) on the Vigueirat, limiting flows in the canal as it runs through Arles, and transfer siphon under the Vigueirat, allowing draining away of the Rhône waters impounded by the embankments of the Vigueirat.

The Project State without drainage measures comprises, in addition, safetying of the embankments of the Rhône between Beaucaire and Arles, which consists in building an overflowing embankment over 5 km at around 20 m west of the Tarascon-Arles railway embankment and structures ensuring hydraulic transparency of the railway embankment.

Building of the model for the project state required an accurate representation of the new Rhône embankment, of the inter-embankment space, of the railway embankment and of the structures under the railway embankment. The mesh was based on embankment foot and crest lines and on a fine mesh size. The structures under the railway embankment (10 structures for future hydraulic transparency and the 3 existing underpasses) are modelled by 1D/2D connections representing the conventional laws of hydraulics (for free-flow and submerged weirs and orifices, depending on the upstream and downstream levels). The full mesh has more than 150,000 triangular elements and 2,000 linear elements (profiles, bridges, other structures, siphons, weirs, etc.) (Fig. 16).

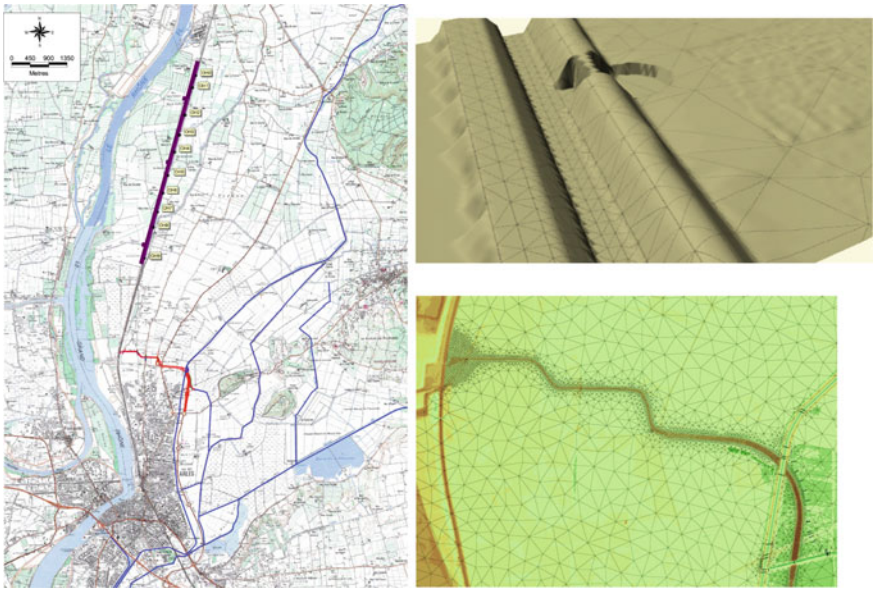

Fig. 16 Modelling of projects (RFF embankment, northern dike)

3.8 Scenarios Modelled

The simulations in initial state concern 10 scenarios for breaches in the railway embankment, for which the hydrographs were provided by SNCF (service provider to RFF for the hazard study). Propagation of flow from breaches was simulated in the study area and the results in terms of depth, velocity and propagation time were used for the railway embankment hazard study.

In the project state, with the Rhône embankments made safe, the inflows into the plain are from the Rhône overflowing the embankment for floods higher than the 100-year flood and flows from the drainage basins flowing into the study area (Vigueirat, Vallée des Baux).

Numerous tests allowed optimisation by modelling of the measures to improve drainage in the plain; these measures concern lowering of the embankment in the plain, passage through a siphon of an embanked irrigation channel, digging of new ditches, creation of new siphons under super-structure canals, etc. The results of the drainage improvement works are compared with the project state without improvement measures, in terms of gains in water levels and duration of submersion.

As the duration of floods to be simulated is long (around 20 days), in order to be able to calculate the time for drainage over the entire area, and the optimisation of works having required numerous tests, the issue of machine time for simulation was crucial and required the use of powerful computers. Simulation time nonetheless remains very long as the software does not allow parallel processing although, henceforward, this is a possible option after recent development of the Infoworks ICM software (Fig. 17).

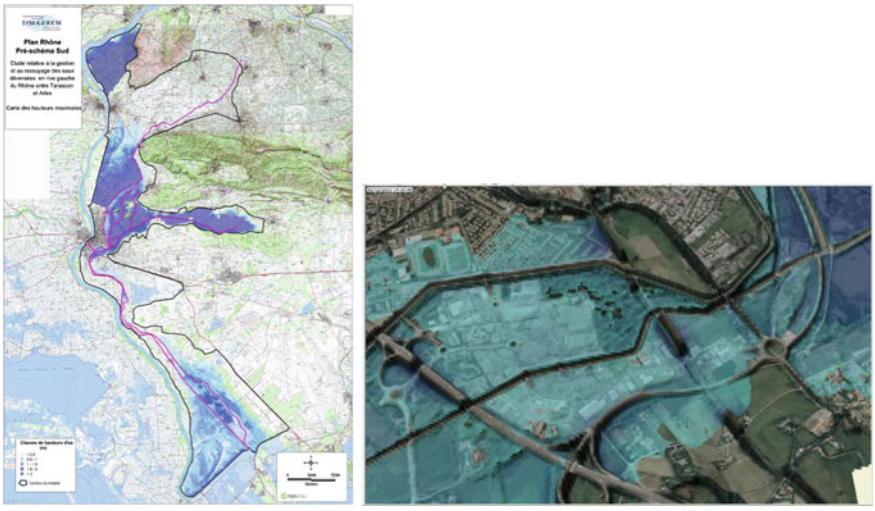

Fig. 17 Water level map, 3D view of free surface

4 Conclusions

Although 2D models are frequently used today, since some software packages are freely available and computers have become more powerful, the problem remains of maintaining reasonable computation times when accurately modelling large areas, such as those of the Petit Rhône and Grand Rhône, for enduring floods. As topographical data is only present in exclusively 2D models at the calculation points of triangular elements, it is necessary, in order to model topographical singularities accurately, to build fine meshes (sometimes of 1 m), which induce very long simulation times. It is therefore detrimental to degrade the topographical data which, today, is accurate thanks to LIDAR data (1 m space) by making a 2D mesh with elements of several tens of metres. A way round this is to use software enabling simultaneous modelling of one-dimensional elements and areas with a 2D mesh. This technique enables optimum use of topographical data correctly representing cross-sections of small streams (conventionally represented by linear models) or of topographical singularities, such as embankments or walls by linear elements of the weir type, that can be described by as many topographical points as are necessary. This type of 1D/2D coupling also allows representation of all specific types of closed conduit flow structures (bridges, siphons, valves, non-return valves, etc.). Modelling of the left bank of the Rhône would not have been possible with exclusively 2D modelling. Conversely, 1D/2D coupling requires, as for 2D models with small elements, very small time steps to limit instability of calculations. Parallelisation of calculation, possible after recent developments of Infoworks RS in ICM, allows significant reductions in simulation time. For instance, for 2D model with 800,000 elements, a one day flood is modelled in 3 h on a machine with ten processors and GPU card.

References

1. Etude hydraulique du renforcement des digues du Petit Rhône, SYMADREM, EGIS, 2013.
2. Etude relative à la gestion et au ressuyage des eaux déversées en rive gauche du Rhône entre Tarascon et Arles, SYMADREM, EGIS, 2014.

The Beijing Case Study of Risk-Based Resilience Planning for Urban Local Flooding Management

Yuwen Zhou, Zilong Liu, ShanShan Liu, Chan Liu, Ying Tang and Hongli Wang

1 Introduction

The term resilience was introduced by the science and environmental communities in the 1970s with the explanation of the ability of an organism or area to recover from (or to resist being affected by) some shock, insult, or disturbance. However, today, the application of the term resilience expands to relevant broader domains, such as engineering, physics, networks systems, ecology, and so on. For urban local flooding management, the resilience is defined as the ability of systems to anticipate, absorb, adapt to, and/or rapidly recover from a disruptive event. It comprises four principal strategic components which are named as resistance, reliability, redundancy, and response and recovery [1].

The resistance element of resilience emphasizes providing protection, and the reliability component is concerned with ensuring that the infrastructure components are inherently designed to operate under a range of conditions and hence mitigate damage or loss from an event. As for redundancy, it underlines the design and capacity of the network or system, whereas the response and recovery element aims to enable instant and effective response to and recovery from disruptive events.

Service Risk Framework (SRF) is a summary of current water industry practice of UK for evaluating system resilience to flooding hazards and proposes an approach that encourages best practice risk management strategies and addresses issues such as investment risks, hazard assessment, and climate change. Guidance is

Y. Zhou (✉) · Z. Liu · S. Liu · C. Liu · Y. Tang · H. Wang
Civil Engineering College of Beijing University of Technology, 100 Pingleyuan Chaoyangqu, Beijing 100124, China
e-mail: zhouyw68@bjut.edu.cn

Z. Liu
e-mail: liu360313@emails.bjut.edu.cn

P. Gourbesville et al. (eds.), *Advances in Hydroinformatics*,
Springer Water, DOI 10.1007/978-981-287-615-7_19

given on assessment of flood hazards, asset vulnerability, and consequences of project failure analysis. Ultimately, flood hazard-specific methodologies for the application of cost benefit analysis for justifying potential intervention investments is provided.

2 Methodology

The methodologies of SRF are composed of three main implementation stages which are Risk screening, Risk assessment, and Risk management. For the urban local flooding management, the three stages can be demonstrated as follows: [1] the screening of risk areas; [2] risk assessment based on smart modeling; and [3] intervention approaches to enhance the resilience of the urban local flooding management and the cost benefit analysis.

(1) Sometimes, it is possible for all the areas of the city to have a quantitative risk analysis, but it will take a long time and spend high costs. The risk screening enables prioritization of areas exposed to flood hazards that present a potential risk to service. Available knowledge of the historical flood hazards and topographic features are initially used to identify the most vulnerable areas exposed to potential flood disasters.
(2) The process of risk screening prioritizes a number of areas, where more detailed risk analysis will be implemented, aimed at providing a more quantitative and qualitative understanding of the specific risk exposed at the selected priority sites. In the process of risk analysis, the application of smart model is essential.
(3) Risk management involves selection of interventions and appraisal of intervention implementation where it is cost beneficial to do so. Typical interventions include two categories which are disaster recovery and disaster-resistant measures. The recovery measures, which are aimed to reduce the impact of flooding and restore normal function from disasters, include improving the system reliability, enhancing the operational management, and emergency response. The resistant measures which are used to prevent or minimize the impact of flooding before the arrival of the disaster or ongoing typically include the engineering and non-engineering approaches, such as raising standards of engineering structures, construction of new projects, pre-disaster warning response, and so on.

The process of Service Risk Framework (SRF) can be described in the following Fig. 1.

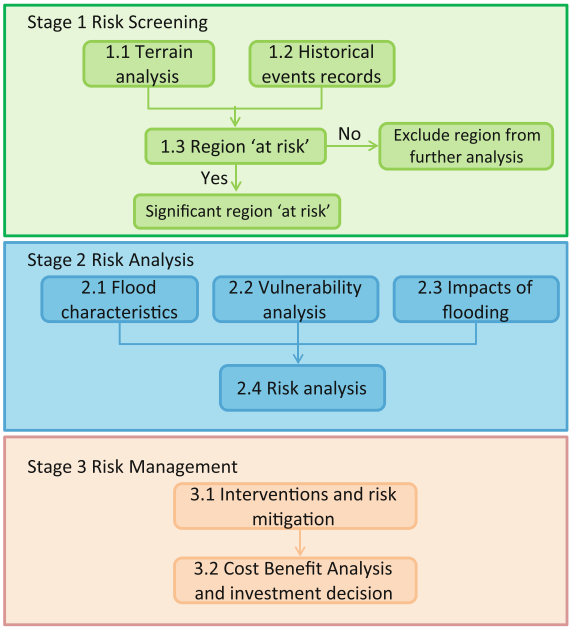

Fig. 1 SRF operation procedure

3 Case Study of Beijing

3.1 Risk Screening

The initial risk screening enables prioritization of drainage systems exposed to flood hazards that present a potential risk to service. Risk map of urban local flooding and historical affected areas are initially used to identify the most vulnerable ones exposed to potential flood disasters. On the one hand, flooding risk maps provided by Environmental Agency are a critical and valuable source for probability analysis.

Based on the local conditions and combined with the corresponding characteristics of geographic information and climate change, risk maps have provided prediction of potential hazards and showed clear boundaries of affected areas. As a result, a single separate drainage system is mapped to a potential disaster-risk areas have provided the best way to risk visualization. Additionally, it is noted that this process may overestimate the degree of risk and strongly affected by the specific terrain, but at this stage, it is more important that no high-risk ones have been omitted (Fig. 2).

On the other hand, a more straightforward screening approach is possible to identify the most consequentially significant areas by historical hazard information. Taking the statistics of flooding event on July 21, 2012 for instance, a total of 91 locations have been affected in the center city of Beijing, and among this, 20 areas have the maximum water depth of more than 2 m and affected time more than 6 h,

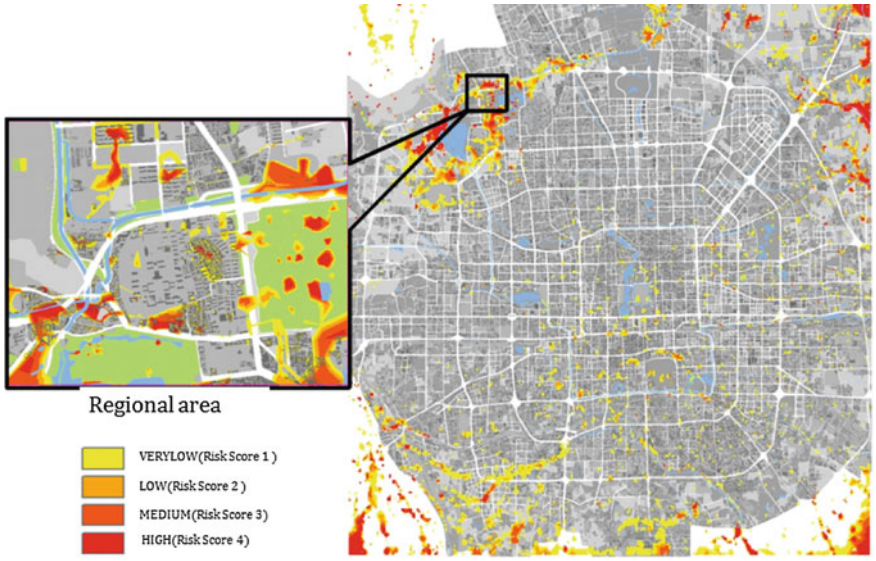

Fig. 2 Risk map of urban local flooding of Beijing

resulting in great economic losses and even casualties. Therefore, the statistics of historic disasters can be taken as a typical factor of intuitive judgement for drainage system importance (Fig 3).

3.2 Risk Analysis

Flood risk is defined as the potential loss resulted from hazard analysis, exposure analysis, and vulnerability analysis. More specifically, the extent of loss depends on the intensity and probability of hazard occurrence, exposure spatial distribution of bearing body, and fragility expression, which is termed as the integration outcomes of these three factors.

Hazard and bearing body are two primary elements taken into account for loss quantification process. Typically, hydraulic model is adopted to capture hazard properties, which possibly contains submerged depth, scope, duration, and discharge, together with bearing body, raster file, and vulnerability information to realize flood loss evaluation under various hazard conditions. This paper introduces the approach of deriving building content damage in urban local flooding events and demonstrates its feasibility through GIS spatial-based analysis tool to carry out Beijing Zuoan case study.

Flood damage is commonly classified as tangible and intangible [5]. The former could be quantified as specific numerical values which mainly involve the loss of infrastructure, building, and engineering structures, while the latter one focuses the

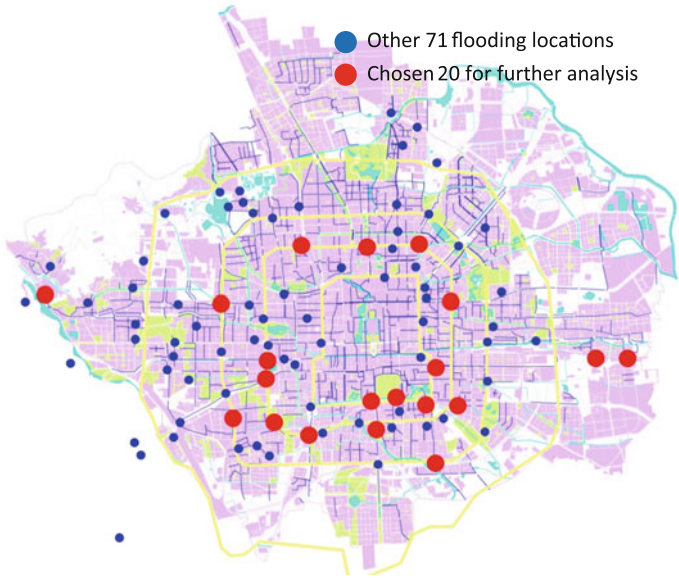

Fig. 3 Flooding location of central city on July 21, 2012

impacts on residence health, environment, and public psychology without regular indicators for analysis. According to the contacting pattern between bearing body and flood, the tangible damage is further categorized as direct and indirect losses. Direct loss, which is caused by physical contact between these two elements, is expressed as the loss of residential building, indoor properties, and commercial and industrial stock, while indirect loss refers to influence due to delay of production, delivery of industry, commerce, and tertiary industry owning to economic activity termination [4]. The core content of this research emphasizes the direct loss from tangible classification.

Flood damage evaluation typically encompasses four steps: hazard analysis, bearing body exposure assessment, vulnerability analysis, and loss quantification. Firstly, hazard analysis that acquires information such as indictor intensity, frequency, and scope for hydraulic modeling of scenarios has become the mainstream approach [2]. Secondly, through socio-economic survey and statistics and geo-spatial information database, the exposure assessment takes advantage of area-weighting method to derive spatial attributes of socio-economic condition, thereby reflecting spatial distribution difference in the economic indicator of bearing body. Lastly, vulnerability analysis, usually represented by depth–damage curve, relies on the typical sampling survey to establish statistical relationship between hazard and economic loss factors [7]. In view of above statement, the flood damage assessment procedure is demonstrated in Fig. 4.

The vulnerability expression could be identified as relationships between hazard and loss rate or absolute loss value. The depth–absolute loss vulnerability curves of

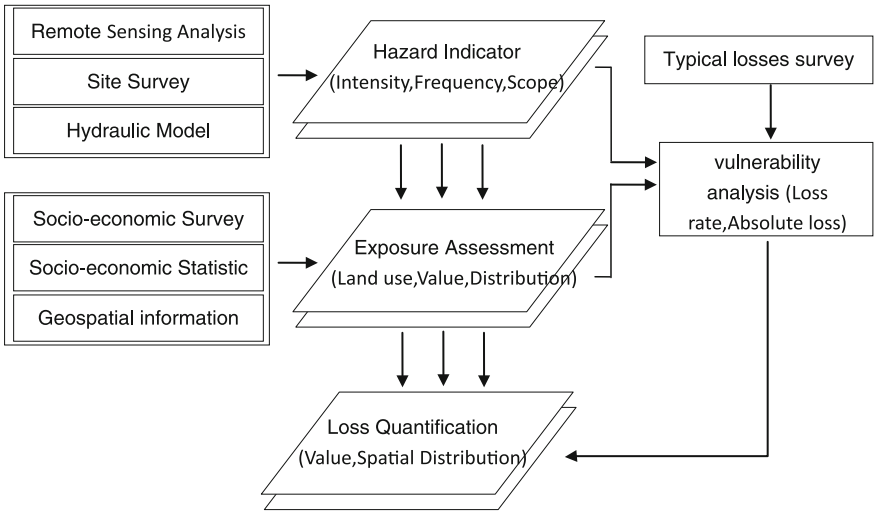

Fig. 4 Flood damage assessment procedure

various types of assets have been setup in large amount of developed countries [6], but the loss rate is more preferred in China. In fact, these two approaches just differ slightly in expression manner but with same essence. Due to the association between the building land use type and loss rate, the following formula is generated to calculate flood damage:

$$L = \sum_{i} \sum_{j} L_{ij} \sigma(i,j), \tag{1}$$

where L is the total flood loss, L_{ij} is the loss value of property category i at depth j, and $\sigma(i,j)$ is the loss rate of property category i at depth j.

Flooding risk is the possible losses, which means that risk is not only the value of flood damage, but also related with the probability of hazards occurrence. Kaplan and Garrick [3] proposed a risk calculation expression which is shown as follows:

$$R = \{S(ei), p(ei), L(ei)\} i \in N. \tag{2}$$

In the above formulation, R is the flood risk, $S(ei)$ represents the disaster scenarios, $p(ei)$ is the probability, and $L(ei)$ means the flood damage. Based on their research, risk is quantified by an expected value in this paper, and the modified calculation expression is as follows:

$$\mathrm{EAD} = \int_0^1 D_P dp \approx \sum_{i=1}^{N} (D_{i+1} + D_i) \bullet \left(p_{i+1} - p_i\right)/2, \tag{3}$$

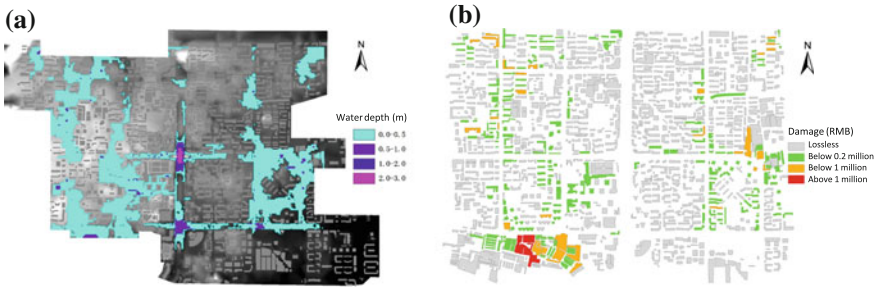

Fig. 5 Hydraulic model results and damage distribution for 100-year return period rainfall

where EAD is the expected annual damage, D_P is the damage of probability, and p is the probability of scenario occurrence. In practical application, p is desirable for 0.005, 0.01, 0.02, 0.05, 0.1, 0.2, 0.3, and 1.

We developed a flood damage assessment tool using Python scripts and the Geo-processing functions within the ESRI ArcGIS software to evaluate the damage directly from the hydraulic modeling results (Fig. 5a). This tool is capable of exerting flood damage calculation and risk analysis with spatial properties at single building scale (Fig. 5b). The flood damage statistics is summarized in Table 1.

The relationship of flood damage versus design storm frequency is shown in Fig. 6:

Table 1 Flood damage and rainfall statistics for different return periods (RMB means Chinese currency)

Return period (year)	1	3	5	10	50	100	200
Rainfall (mm)	90	129	147	172	229	254	279
Total loss (million RMB)	5	44	67	103	209	242	251

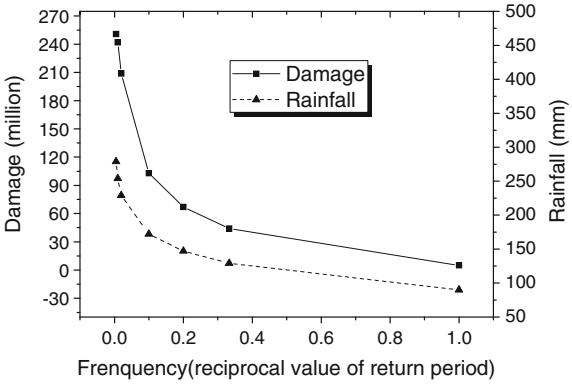

Fig. 6 Relationship of flood damage versus design storm frequency

The flooding risk can be calculated as described below:

$$\mathrm{EAD} = \sum_{i=1}^{N} (D_{i+1} + D_i) \bullet (p_{i+1} - p_i)/2 = 48.2 \ (\mathrm{millionRMB}). \tag{4}$$

3.3 Risk Management

Risk management involves selection of interventions and appraisal of intervention implementation where it is cost beneficial to do so. What is emphasized in this paper mainly refers to the engineering defense measures which can be used to enhance the resilience of urban drainage system.

The choice of engineering solutions is largely depends on "how to deal with the relationship of security and economy," and the engineering benefits have been used to reflect this relationship. Engineering benefit is defined as the ratio of disaster mitigation to investment. TLR represents the value of disaster mitigation, ARC is the sum of annual investment and annual operating costs, and the benefits of urban local flooding defense engineering (BLR) can be calculated as follows:

$$\mathrm{BLR} = \frac{\mathrm{TLR}}{\mathrm{ARC}}, \tag{5}$$

where TLR is the difference between the expected annual damage with and without corresponding engineering solutions. The value of disaster mitigation (TLR) is calculated by risk analysis process which has been mentioned above. In addition, annual investment and annual operating costs generally depend on the selection of engineering design standard (return period). If we take the total investment of planning projects as I, time limit for the normal operation as n (usually taken as 30–50 years in China), interest rate is i (6–9 % in China), and the annual fee of operation and management as 1–2 % of total investment (I), ARC can be expressed as follows:

$$\mathrm{ARC} = I \times \left(i + \frac{i}{(1+i)^n - 1} \right) + (0.01 \sim 0.02) \times I. \tag{6}$$

Taking the Zuoan drainage system for instance, the values of TLR, ARC, and BLR for different engineering design standards (return period) are shown in Table 2.

Table 2 TLR, ARC, and BLR for different design standards (return period)

Design standards (year)	1	3	5	10	50	80	100
TLR (million RMB)	12.91	25.35	32.51	39.81	45.97	46.67	47.22
ARC (million RMB)	2.39	2.84	3.83	4.15	4.79	6.13	7.43
BLR	5.39	8.91	8.48	9.58	9.61	7.61	6.36

As can be seen from Table 2, when the design standards of engineering solutions taken as 50-year return period, BLR will have its maximum value, which means that in this case, the investment will have the greatest income returns.

4 Conclusion

This paper is aimed at supporting and tailoring the derivation of a common framework of risk-based resilience planning for the urban local flooding management in China, thereby promoting economic development, social progress, and cultural prosperity.

This article, along with specific case study of flood resilience strategy—Service Risk Framework of Beijing—demonstrates the main contents and methods for three implementation stages, namely risk screening, risk analysis, and risk management, which provide valuable reference for proposing the idea of resilience and formulating relevant industry regulation standards.

Undoubtedly, considerable achievements have been realized; meanwhile, there are still a lot of areas where improvement is needed. Firstly, there is still no "one-suits-all" definition and assessment approaches for current resilience status. Therefore, the concepts and the evaluation method are a critical premise for deriving corresponding resilience adaptation guidelines and dominating the forward directions.

Secondly, although the conventional process of risk-based resilience planning has been finished through the Service Risk Framework (SRF), certain assumptions and neglections have been made at various stages. For example, in the stage of risk analysis, only the method of damage assessment for the buildings was proposed. For some more important indirect losses, such as the loss of urban traffic systems, the damage of water supply or electricity infrastructures, and follow-up continued economic losses, we still experience a lack of appropriate evaluation methods for quantification.

Lastly, it has been realized for a long time that the flooding management is not an isolated field, especially with the development of cross-industry interdependencies. Yet, the patterns or legislations for multi-industry operation have not been specified. Thence, the issue of joining the effort of related industry, sharing the responsibility, and enjoying benefits becomes extremely difficult for guaranteeing economic viability and social advancement. Determination of the boundaries of the resilience planning scope facilitates resources conservation, investment optimization, and manpower allocation, thereby realizing achievement across whole industries.

Acknowledgments Research on the CORFU (Collaborative research on flood resilience in urban areas) project was funded by the European Commission through Framework Programme 7, Grant Number 244047. Research on the "Resilience Planning for Urban Local Flooding Management" project was funded by the National Natural Science Foundation of China, Grant Number 51478016.

References

1. Cabinet Office (2011). Keeping the Country Running: Natural Hazards and Infrastructure.
2. Gambolati, G., & Teatini, P. (2002). GIS Simulations of the inundation risk in the coastal lowlands of the Northern Adriatic Sea. *Mathematical and Computer Modeling, 35*, 963–972.
3. Kaplan, S., & Garrick, B. J. (1981). On the quantitative definition of risk. *Risk Analysis, 1*, 11–27.
4. Li, H.Y. (2007). *Flood damage loss assessment based on GIS* (pp. 1–30). Xi'an: XIAN University of Technology.
5. Merz, B., Kreibich, H., Schwarze, R., & Thieken, A. (2010). Assessment of economic flood damage. *Natural Hazards and Earth System Sciences, 10*, 1697–1724.
6. Penning Rowsell, E., Viavattene, C., & Pardoe, J. (2010). *The benefits of Flood and Coastal risk management: A handbook of assessment techniques*. London: Flood Hazard Research Centre.
7. Smith, D. I. (1994). Flood damage estimation-a review of urban stage-damage curves and loss functions. *Water SA, 20*, 231–238.

A Statistical Approach to Downscaling of Daily Rainfall Process at an Ungauged Site

Myeong-Ho Yeo and Van-Thanh-Van Nguyen

1 Introduction

Information on the variability of rainfalls in time and space is critical for the planning, design, and management of a large number of water-resource projects. However, in most practical applications, rainfall records at the location of interest are often limited (a partially-gauged site) or unavailable (an ungauged site). Regionalization methods are hence frequently used to estimate rainfall information using the other locations where the data are available and sufficient or to improve the accuracy of the rainfall estimates where available records are too short [3]. Nevertheless, traditional regionalization techniques are often criticized for the obvious subjectivity, in the definition of hydrologically similar sites, and the lack of physical justifications [8]. In addition, according to the IPCC Synthesis Report [5], the annual precipitations in many different regions in the world, especially in America, northern Europe, and northern and central Asia, show an increasing trend. Global Climate Models (GCMs) have been extensively used in many studies for assessing this impact. However, outputs from these models are usually at resolutions that are too coarse (generally greater than 200 km) and not suitable for the hydrological impact assessment at a regional or local scale. Hence, downscaling methods have been proposed for linking GCM predictions of climate change to the historical observations of the precipitation processes at a local site or over a given watershed [9]. Moreover, the prediction of ungauged basin (PUB) under climate change conditions remains still a crucial challenge in the research and engineering practice [13].

M.-H. Yeo · V.-T.-V. Nguyen (✉)
Department of Civil Engineering and Applied Mechanics, McGill University, 817 Sherbrooke Street West, Montreal, QC H3A 0C3, Canada
e-mail: van.tv.nguyen@mcgill.ca

M.-H. Yeo
e-mail: myeong-ho.yeo@mail.mcgill.ca

P. Gourbesville et al. (eds.), *Advances in Hydroinformatics*,
Springer Water, DOI 10.1007/978-981-287-615-7_20

More specifically, in the context of regional impact study, regionalization methods have been developed and employed according to two main objectives: *considering spatial dependency* (homogeneity) and *reducing uncertainty*. Hence, these techniques are frequently used to transfer hydrologic information from one location to the other site where the data are needed but not available or to improve the accuracy of the hydrologic variable estimates at locations where available records are too short [3, 8]. Consequently, for rainfall estimation at an ungauged site, the homogeneity of precipitation processes at different sites is a necessity condition to obtain an accurate rainfall estimate with less uncertainty. Nevertheless, traditional regionalization techniques are often criticized for the obvious subjectivity, in particular in the definition of hydrologically similar sites (or hydrologically homogeneous regions), and the lack of physical justifications [1, 2, 4, 7, 12]. Hence, in the present study an improved regionalization technique will be proposed based on the similarity of rainfall occurrences at different locations using the Ordinal Factor Analysis (OFA) [6].

As mentioned above, with observations of climate change and its impacts on water resources systems, a number of studies have been conducted to establish the linkages between the large-scale climate variables given by GCMs and the observed characteristics of the daily precipitation process at a local site using different downscaling methods [9, 15]. These downscaling methods, however, are not suitable for dealing with cases where precipitation data at the location of interest are limited or not available. Hence, the estimation and prediction of hydrological variables such as precipitation and flow with climate change conditions for these ungauged or partially-gauged sites remains a crucial challenge for managing and planning water resources [13]. Therefore, this study proposes a statistical downscaling (SD) procedure for describing accurately the linkages between the large-scale climate variables given by GCM simulation outputs and the "estimated" daily precipitation characteristics at a location of interest where the precipitation data are limited or unavailable.

In brief, the suggested SD procedure is based on a combination of three components: (i) first, a regionalization approach was proposed to identify the homogeneous groups of observed daily precipitation series available at different raingauges based on the similarity of rainfall occurrences at different locations determined by the Ordinal Factor Analysis (OFA); (ii) second, a stochastic model was developed for constructing daily rainfall events at an ungauged site within a homogeneous group based on the application of the eigen-decomposition technique to data available at those raingauges within the same homogeneous group; and (iii) third, a statistical downscaling model (SDRain) was developed to describe the linkage between the constructed daily precipitation series and the large-scale climatic predictors given by GCM simulation outputs. The feasibility of the proposed stochastic approach has been assessed using the available daily precipitation data for the period 1973–2001 from a network of 62 raingauge stations in South Korea and the NCEP reanalysis climate predictors data over this study area. The jackknife

method was used to simulate the ungauged condition. Results of the numerical application have indicated that it is feasible to estimate the missing precipitation data at an ungauged site based on the data available at other sites within the same homogeneous region. Furthermore, it was found that the OFA could provide more physically meaningful homogeneous rainfall groups than those given by the commonly used Principal Component Analysis (PCA). Finally, the proposed SDRain downscaling model was able to generate daily precipitation sequences for an ungauged site with comparable statistical characteristics as those given by the application of the statistical downscaling for a gauged site with available observed precipitation data.

2 A Statistical Downscaling Approach for Ungauged Sites

As mentioned in the previous section, the proposed SD approach consists of three components as described in the following:

2.1 A Regionalization Analysis of Rainfall Occurrences

Factor analysis (FA) is a well-known statistical method for describing the variability among correlated observed variables using a lower number of latent (unobserved) variables called "factors". Although the number of latent variables (factors) is smaller than the number of original observed variables, they can account for the same information as the original data set. In this study, to identify the hydrologically homogeneous rainfall regions, the OFA was employed to describe the similarity of rainfall occurrences at different raingauges. The use of the OFA is appropriate in this case since the daily precipitation occurrence series are made up of values 0 and 1 only (i.e., binary variables). Detailed description of the OFA can be found in the publication by Jöreskog and Moustaki [6].

2.2 A Stochastic Rainfall Model for Estimating Precipitation Series at an Ungauged Site

The stochastic modeling of the precipitation process is based on the combination of two different components: the modeling of the rainfall occurrences and the modeling of the precipitation amounts. As mentioned above, the modeling of the rainfall occurrences is based on the homogeneous grouping given by the application of the

OFA to rainfall occurrences. Let F_j be the factor score for a given day j as defined in the following:

$$\begin{aligned} F_j &= \sum_{i=1}^{s} \left[\alpha'\left(x_{i,j} - \mu_i\right)\right] \\ &\text{if } r_j \geq F_j, \text{ then wet at day j} \\ &\text{if } r_j \leq F_j, \text{ then dry at day j} \end{aligned} \tag{1}$$

where α_i is the factor loading associated with the raingauge station i in a homogeneous region of s stations, $x_{i,j}$ is the precipitation occurrence at a station i for day j, and μ_j is the average vector for day j. With the homogeneous region identified by OFA, the factor score F_j represents hence at how many stations in a given region rainfalls occur for the given day j. A uniform random number r_j ($0 \leq r_j \leq 1$) was then used to determine the wet- or dry-day based on the value of F_j.

Regarding the modeling of rainfall amounts, since the distribution of precipitations on wet days is strongly skewed, a log-transformation technique could be used to reduce this strong skewness:

$$\ln P_{ij} = Y_{ij} \tag{2}$$

where P_{ij} denotes the precipitation amount at a station i for a given day j and Y_{ij} represents the corresponding log-transformed precipitation amount. Thus, Y becomes more closely to normally distributed variable. Hence, the relationship between the mean ($\bar{P}$) of P_{ij} and the mean (μ_Y) and variance (σ_Y^2) of Y_{ij} can be written as follows:

$$E(P) = \bar{P} = \exp\left(\mu_Y + {}^{\sigma_Y^2}/_{2}\right) \tag{3}$$

Thus, the regional expected value of the daily precipitation amount can be estimated by the following equation:

$$E\left(P_R^j\right) = \bar{P}_R^j = W_j \times \exp\left(\mu_{RY}^j\right) \tag{4}$$

in which $\bar{P}_R^j$ is the regional mean of the daily precipitations for a given day j; μ_{RY}^j is the regional mean of the log-transformed daily precipitations for the day j; and $W_j = \exp\left(\sigma_{RY}^2/2\right)$ is the correction factor for matching the expected values of the original and the log-transformed daily precipitations (σ_{RY}^2 is the regional variance of the log-transformed daily precipitation). Equations (1) and (4) can be used to generate missing rainfall series at a given site within a homogenous region.

Using Eqs. (1) and (4), a set of 100 daily precipitation occurrences and amounts was generated for each site. Only one representative daily precipitation series at the location of interest is necessary because the statistical downscaling model for a single raingauge station requires only one data sequence. Hence, from the 100 ensembles of generated precipitation occurrences by Eq. (1), the daily percentages of wet days are computed. Then, a representative wet/dry series for an ungauged station are decided by a critical point 0.5 (to obtain a median value) as follows:

$$PO_j = \frac{1}{m}\sum_{j=1}^{m} Occ_j \tag{5}$$

where PO_j is a daily percentage of wet day at a given day j, m is the number of generated ensembles, and Occ_j is the generated precipitation occurrence series. Moreover, the representative daily precipitation amount at an ungauged station can be expressed as follows:

$$\overline{\overline{Amo_R^j}} = W_j \times \exp\left(\mu_Y^j\right) \tag{6}$$

where Amo_R^j is the representative daily precipitation amount for a given day j, and W_j is a daily weight, and μ_Y^j is the mean of log-transformed precipitation amount in a homogeneous region delineated by the OFA regionalization method.

2.3 Statistical Downscaling Model for Estimated Ungauged Daily Precipitation

The proposed Statistical Downscaling for Rainfall process (SDRain) was developed to describe the linkage between the constructed daily precipitation series and the large-scale climatic predictors given by GCM simulation outputs. The SDRain models can be expressed as follows [10]:

$$\text{Prob}(\text{wet at } j \text{ day}) = \hat{\pi}_j = \frac{e^{a_0+a_1X_1+a_2X_2+K+a_mX_m}}{1+e^{a_0+a_1X_1+a_2X_2+K+a_mX_m}} \tag{7}$$

$$R_j = f \times \exp(b_0 + b_1X_1 + b_2X_2 + K + b_mX_m + \xi_j) \tag{8}$$

in which $\hat{\pi}_j$ is the probability of wet day at day j, X_i's are the large-scale atmospheric predictors given by GCM simulations, a's and b's are regression parameters, f is a bias correction coefficient, and R_j is the modeled daily precipitation amount.

3 Numerical Application

To test the feasibility of the proposed approach, the available daily precipitation data for the period 1973–2001 from a network of 63 raingauges in South Korea were used (see Fig. 1). South Korea is located in the lower portion of the Korean Peninsula and lies between latitudes 33° and 39° N and longitude 124° and 130 °E. The total area of South Korea is around 100,032 km^2 and consists of mostly mountainous area (70 % of the total area) as shown in Fig. 1. The two main mountainous systems are Taebaek (length of about 500 km and the highest peak, Seorak mountain, of 1,708 m above sea level) located in the eastern edge of the Korean Peninsula, and Sobaek (average height of over 1000 m above sea level) stretched from Taebeak to the southwest mountainous systems. These mountainous systems and the effect by the East Asian Monsoon bring out very complex and diverse climatic characteristics of South Korea. To indicate these diverse climatic conditions, Fig. 1 shows the distinct patterns of monthly normal average temperatures (°C) and precipitations (mm/day) for two representative stations that are located in two different regions separated by the two mountainous systems (Seoul station in the northwest and Busan station in the southeast). The topographic and East Asian Monsoon conditions play an important role in the identification of homogeneous rainfall regimes.

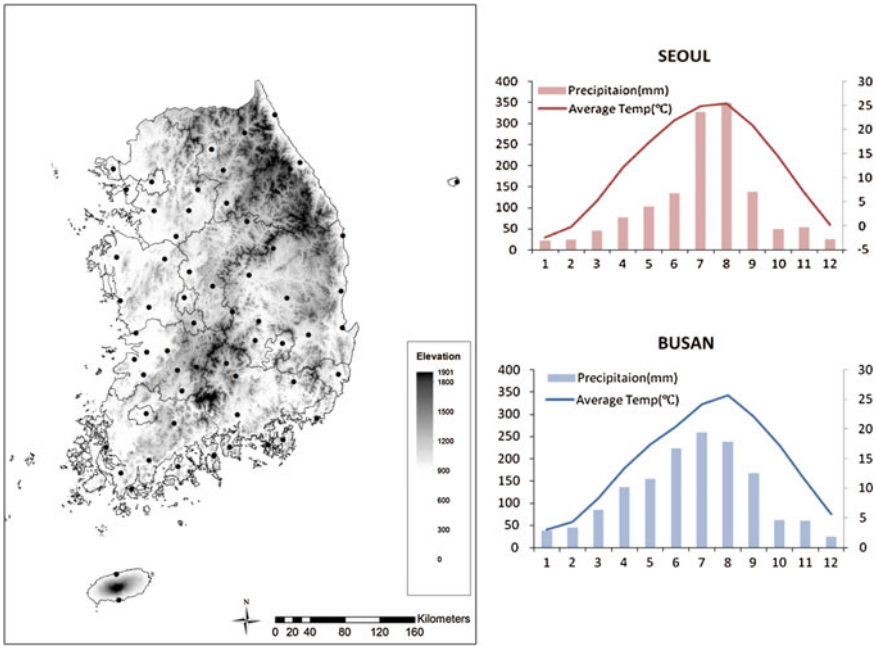

Fig. 1 Topographic map of South Korea including raingauge stations (*black points*) and normal average temperatures (°C) and precipitations (mm/day) for two representative stations divided by two main mountainous systems. Seoul is located in the northwest region, and Busan is in the southeast region

As mentioned above, the proposed statistical downscaling approach consists of three steps: (i) first, the OFA statistical regionalization was carried out for defining the hydrologically homogenous regions of daily precipitations; (ii) second, the stochastic precipitation model was used to generate the occurrences and amounts of the daily precipitation time series for an ungauged station; and (iii) third, the proposed SD for daily rainfall process based on SDRain was applied to the estimated daily precipitation series for the ungauged condition, and the results were compared to those obtained by the SDRain for the gauged condition at the same location.

For comparison purposes, Fig. 2 shows the hydrologically homogeneous rainfall regions delineated by the common Principal Component Analysis (PCA) technique and the proposed OFA. It can be seen that the OFA could provide more physically meaningful homogeneous regions than those given by the PCA since the identified regions correspond more closely to the particular topographic features of the study area. Furthermore, a sensitivity test was carried out to assess the robustness of the PCA and OFA in the regional analysis using the precipitation data for different time scales from 1 to 4 days. Results of this test have indicated that the PCA was quite sensitive to the time scale of the data used since the region of homogeneous raingauges became larger with the increase of the time scale; while the OFA was not sensitive to the time scales of the data [16]. Therefore, the homogeneous regions determined by the OFA were found to be more robust and more suitable for generating the rainfall series at an ungauged location.

In this application, to simulate the ungauged condition the jackknife method was used; that is, one station is removed from a group of homogeneous stations and the

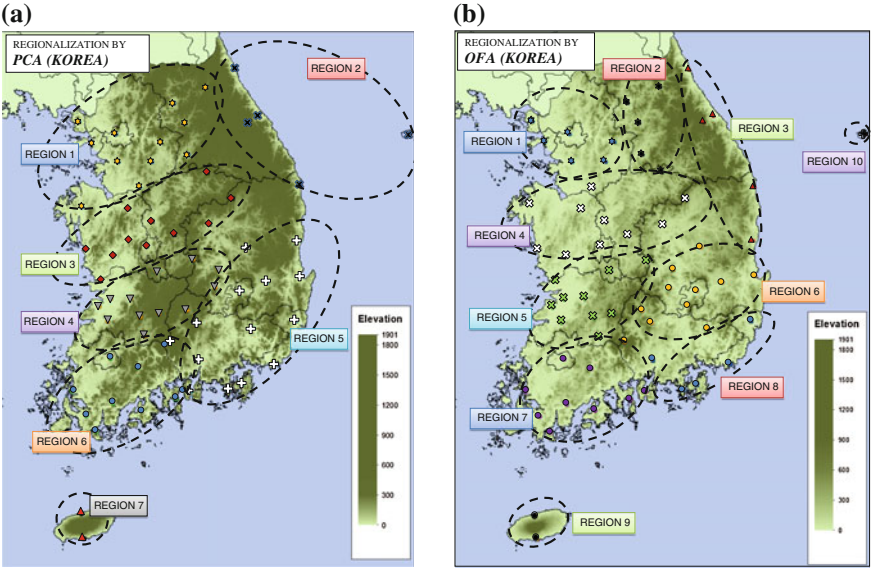

Fig. 2 Homogeneous regions delineated by PCA. **a** and by OFA. **b** Using precipitation data available from a network of 63 raingauge stations in South Korea

daily precipitation series was estimated based on the data available at the remaining raingauge stations in the group. This process was repeated until each station was removed once and the rainfall series were generated at each removed location [11]. The produced rainfall series at ungauged sites were then statistically analyzed and compared to the observed data for evaluating the performance of the proposed approach using the Proportion Correct (PC) index and the Success of Critical Index (SCI) as shown in the following equation [14]:

		Simulated		
		Wet	Dry	
Observed	Wet	a	b	a+b
	Dry	c	d	c+d
		a+c	b+d	N

$$PC = \frac{a+b}{N} \qquad SCI = \frac{a+d}{a+b+c} \tag{9}$$

The computation procedure for estimating the daily precipitation series at an ungauged site can be summarized as follows:

(a) Separate the daily precipitation process into two components (amount and occurrence). Apply the OFA regionalization approach to the daily precipitation occurrence series to identify the homogeneous groups of raingauges;
(b) Assume one raingauge station in a homogeneous group is an ungauged site. Calculate the tetrachoric correlation coefficients matrix using the daily precipitation occurrence data from the remaining raingauge stations in the group;
(c) Generate 100 daily precipitation occurrence series for an ungauged station based on the computed factor scores ($F_{i,j}$) (Eq. 1) and the generated uniform random number r_j;
(d) Generate 100 daily precipitation amount series using the regional average of rainfall amount and the calculated weights (Eq. 4);
(e) Multiply the occurrence series and the amount series.

For remaining stations, repeat from (b) to (e) based on the jackknife procedure for ungauged station.

For purposes of illustration, Fig. 3 shows the evaluation results for the annual number of wet days (NWD), PC, and SCI indices for Seoul station (K1) located in Region 1 and for Pusan station (K7) in Region 8 (see Fig. 2). It was found that the suggested approach was able to provide an accurate description of the rainfall occurrences for these two stations as indicated by the good agreement of the NWD index and the high values of the PC and SCI. Figures 4 and 5 present the comparison between the observed and estimated annual means of precipitation amounts and the annual number of wet days at four representative stations (K1-Seoul, K7-Pusan, K10-Jeonju, and K32-Jecheon). The ranges shown in this figure denote the maximum and minimum values of these two parameters, and the red and blue circles represent the observed values. It can be seen that the proposed stochastic rainfall generator can provide accurate annual and monthly statistics of the observed daily rainfall series at these stations.

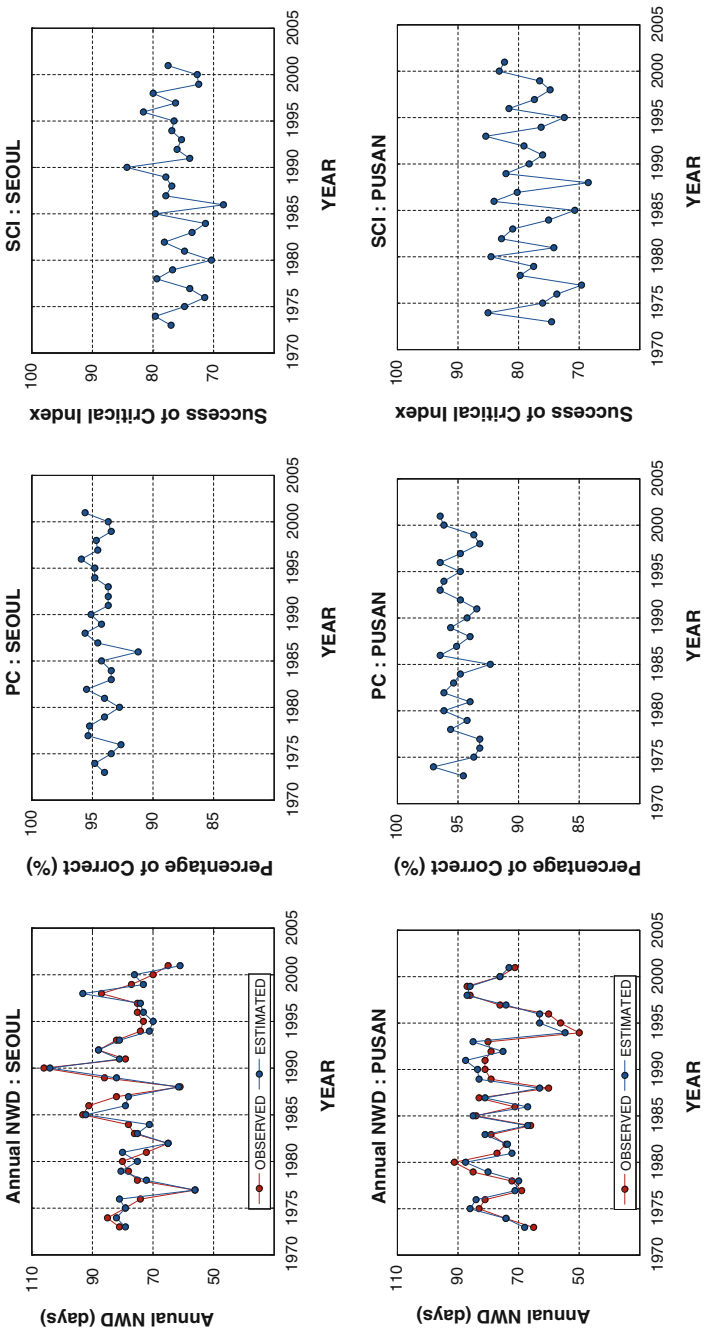

Fig. 3 Accuracy of the rainfall occurrence model for Seoul and Pusan stations based on the annual NWD, percentage of correct (PC), and success of critical index (SCI)

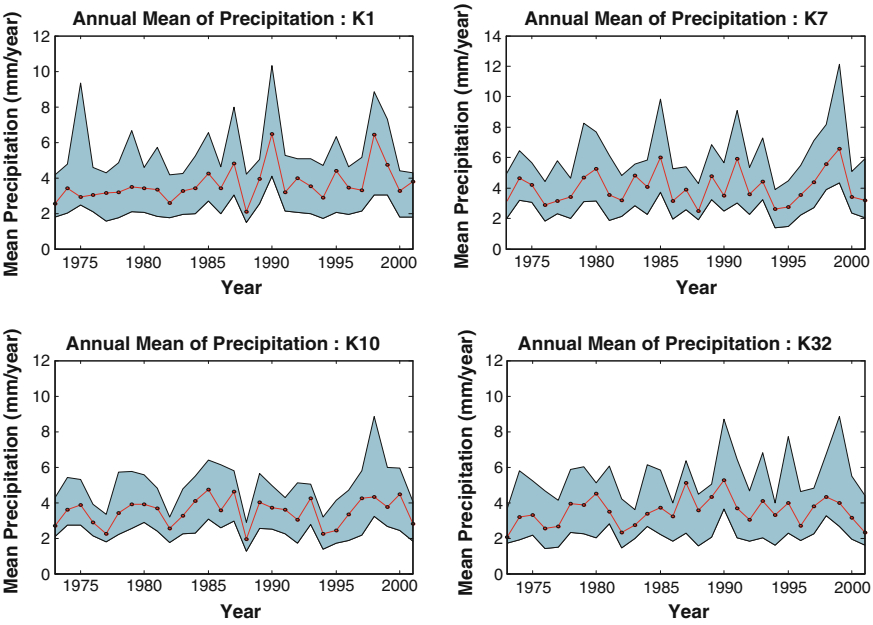

Fig. 4 Observed and estimated annual means of precipitations for four selected stations: K1, K7, K10 and K32. The range denotes the maximum and minimum values of these two parameters, and the *red* and *blue circles* represent the observed values

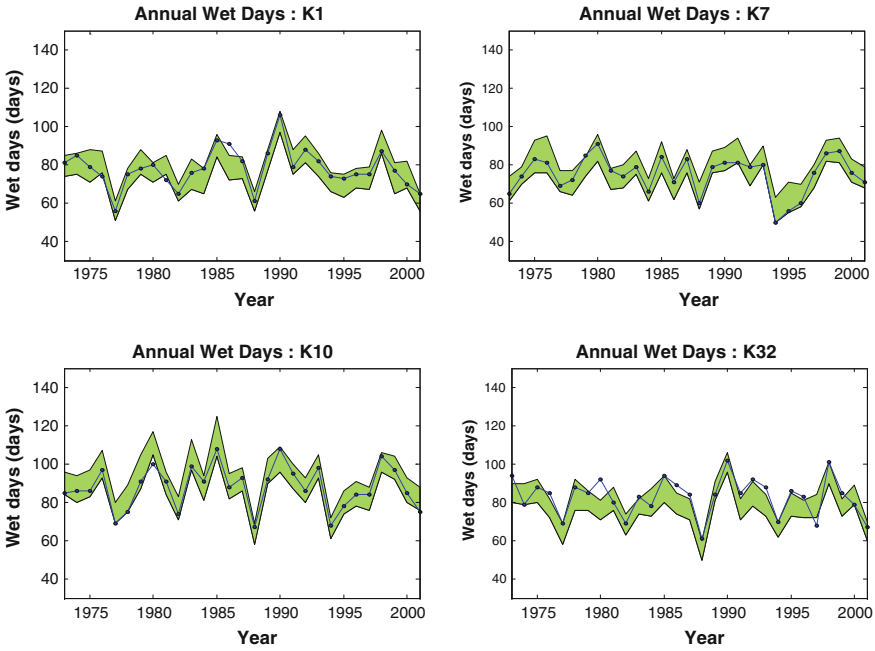

Fig. 5 Observed and estimated annual number of wet days for four selected stations: K1, K7, K10, and K32. The range denotes the maximum and minimum values of these two parameters, and the *red* and *blue circles* represent the observed values

To assess the accuracy of the proposed OFA regionalization method on the estimation of daily precipitation series at ungauged sites, a sensitivity study was carried out using the representative Seoul station (K1) and the four different homogeneous groups. The OFA procedure has assigned station K1 to region OR1 only. Hence, in this sensitivity analysis, the estimation of the daily precipitation series at station K1 was carried out using the raingauges from four different groupings of homogeneous regions: (i) OR1, (ii) OR1 and OR2, (iii) OR1, OR2, and OR3, and (iii) OR3 only. Figures 6 shows the comparison between observed and estimated NWDs at Seoul raingauge station (K1). It can be seen that the estimation of the precipitation series at this station using the corresponding homogeneous region OR1 as identified by the OFA procedure is the most accurate as compared to those given by the other grouping of raingauges. Hence, it can be concluded that the correct identification of homogeneous groups of raingauges is an essential step to obtain an accurate estimation of daily precipitation series at a location without data. Furthermore, it can be noted that the combination of regions OR1 and OR2 into one homogeneous group as suggested by the PCA procedure gave inaccurate results (see Fig. 2). The proposed OFA regional approach was therefore more accurate than the PCA in this case.

Figures 7 and 8 present the range plots of annual and monthly downscaled averages of precipitation amounts and number of wet days for the two selected stations, respectively. The range indicates simulated maximum and minimum

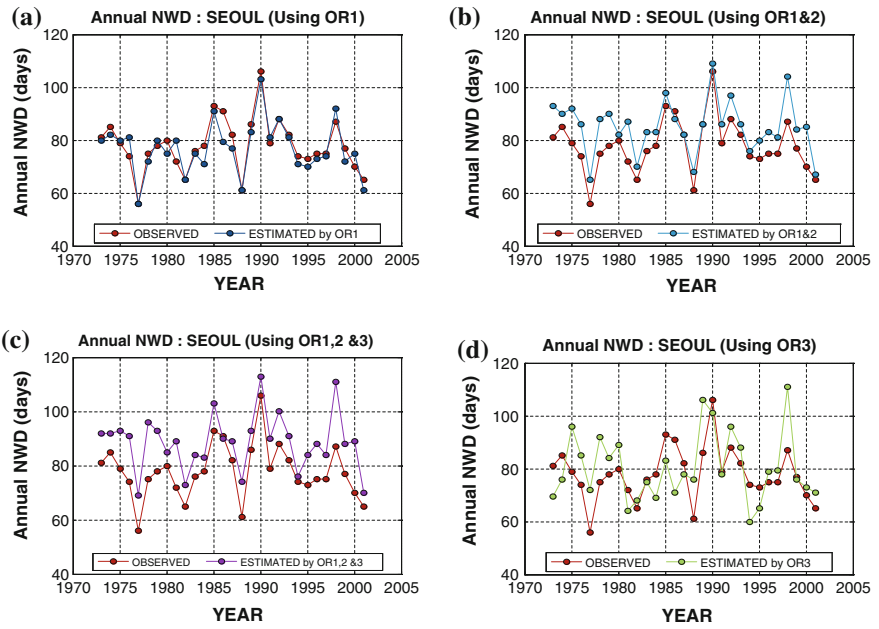

Fig. 6 Comparison of annual number of wet days (NWDs) at Seoul (K1) generated by the proposed stochastic rainfall model using different homogeneous groups in order to identify the effect due to the selection of a nonhomogeneous group

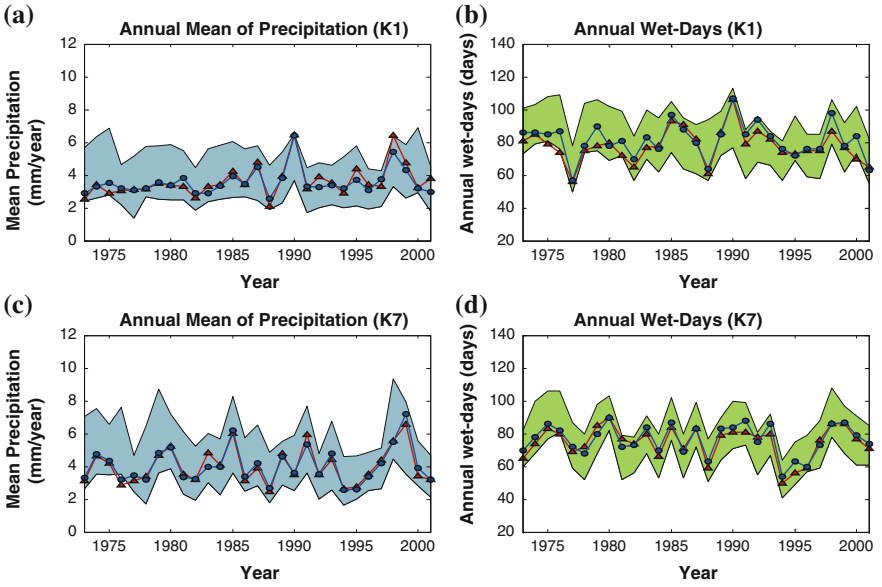

Fig. 7 Observed and estimated annual means of precipitation and the number of wet days (NWD) for Seoul (K1) and Busan (K7). *Blue/green* ranges denote maximum and minimum values of estimated means and NWD, and *red/blue circles* represent the observed and summarized annual values. Four representative stations (K1 and K7) in regions delineated by OFA were selected

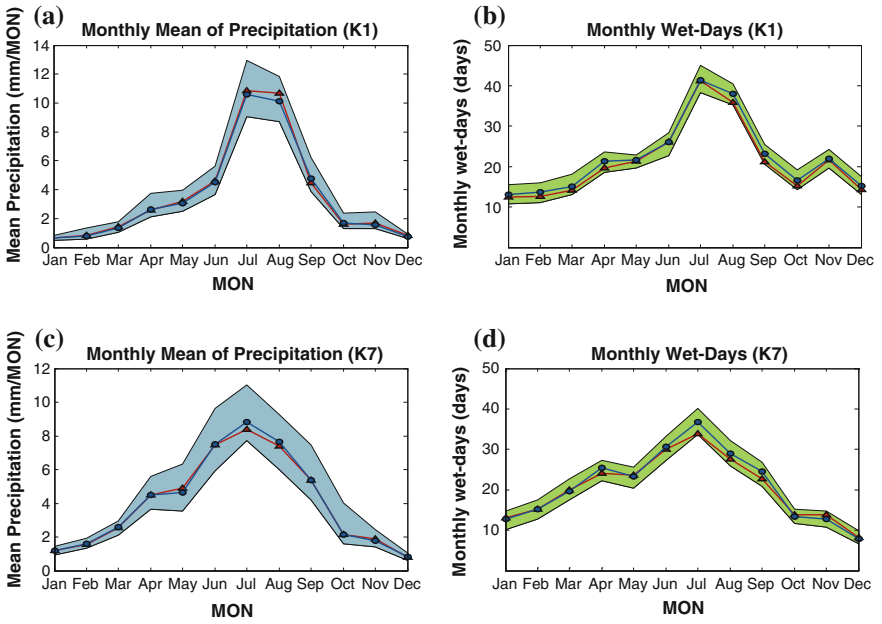

Fig. 8 Observed and estimated monthly means of precipitation and the number of wet days (NWD) for Seoul (K1) and Busan (K7). *Blue/green* ranges denote maximum and minimum values of estimated means and NWD, and *red/blue circles* denote the observed and summarized annual values

values of the simulated precipitation sequences, and the red/blue circles represent the statistics computed from observed data and from estimated precipitation series for an ungauged station, respectively. These graphical results show that the proposed SD procedure for ungauged sites was able to describe accurately the annual and monthly statistics of observed precipitation events.

4 Summary and Conclusions

In this study, a statistical downscaling procedure was proposed for downscaling the daily precipitation process at a location without data. More specifically, the suggested approach consists of three basic steps: (i) identifying hydrologically homogeneous regions based on the similarity of daily precipitation occurrences; (ii) constructing the daily precipitation series at an ungauged site using a stochastic precipitation model; and (iii) establishing the linkage between the large-scale climate predictors given by GCMs and the constructed precipitation series at the ungauged location using the SDRain downscaling model.

Results of an illustrative application using data from a network of 63 raingauge stations in South Korea have indicated the feasibility and accuracy of the proposed method. In addition, it was found that the OFA could identify more physically meaningful homogeneous rainfall regions than those given by the commonly used PCA. Furthermore, the very good agreement between the observed and the estimated statistical properties of the generated daily rainfall series using the jackknife procedure has indicated the accuracy of the suggested approach.

In summary, the results of this illustrative application have indicated that the proposed SD procedure for an ungauged site could provide comparable results as those given by the downscaling method for a gauged location with the available real-observed precipitation data.

References

1. Bárdossy, A. (2007). Calibration of hydrological model parameters for ungauged catchments. *Hydrology and Earth System Sciences, 11*(2), 703–710. doi:10.5194/hess-11-703-2007.
2. Besaw, L. E., Rizzo, D. M., Bierman, P. R., & Hackett, W. R. (2010). Advances in ungauged streamflow prediction using artificial neural networks. *Journal of Hydrology, 386*(1–4), 27–37.
3. González, J., & Valdés, J. (2008). A regional monthly precipitation simulation model based on an L-moment smoothed statistical regionalization approach. *Journal of Hydrology, 348*, 27–39.
4. Goswami, M., O'Connor, K. M., & Bhattarai, K. P. (2007). Development of regionalisation procedures using a multi-model approach for flow simulation in an ungauged catchment. *Journal of Hydrology, 333*(2–4), 517–531.
5. IPCC Synthesis Report (2007). *Climate Change 2007 : An Assessment of the Intergovernmental Panel on Climate Change* (pp. 12–17).

6. Jöreskog, K., & Moustaki, I. (2001). Factor analysis of ordinal variables: A comparison of three approaches. *Multivariate Behavioral Research, 36*(3), 347–387.
7. Li, M., Shao, Q., Zhang, L., & Chiew, F. H. S. (2010). A new regionalization approach and its application to predict flow duration curve in ungauged basins. *Journal of Hydrology, 389* (1–2), 137–145.
8. Nguyen, V.-T.-V. (2007). On regional estimation of floods for ungaged sites. In N. Park et al. (Eds.), *Advances in geosciences: Hydrological science* (Vol. 6, pp. 55–66). New Jersey: World Scientific Publishing Company.
9. Nguyen, V.-T.-V., Nguyen, T-D., & Gachon, P. (2006). On the linkage of large-scale climate variability with local characteristics of daily precipitation and temperature extremes: an evaluation of statistical downscaling methods. In: N. Park et al. (Ed.), *Advances in geosciences: hydrological science* (Vol. 4, pp. 1–9). New Jersey: World Scientific Publishing Company.
10. Nguyen, V.-T.-V., & Yeo, M.-H. (2011). *Statistical Downscaling of Daily Rainfall Processes for Climate-Related Impact Assessment Studies*. World Environmental and Water Resources Congress 2011, Palm Spring, USA, American Society of Civil Engineers, pp. 4477–4482.
11. Pandey, G.R., & Nguyen, V.-T.-V. (1999). A comparative study of regression based methods in regional flood frequency analysis. *Journal of Hydrology, 225*(1–2), 92–101.
12. Samuel, J., Coulibaly, P., & Metcalfe, R. (2011). Estimation of continuous streamflow in Ontario ungauged basins: comparison of regionalization methods. *Journal of Hydrologic Engineering, 16*(5), 447–459.
13. Sivapalan, M. (2003). Prediction in ungauged basins: a grand challenge for theoretical hydrology. *Hydrological Processes, 17*(15), 3163–3170.
14. Wilks, D. S. (2006). *Statistical methods in the atmospheric sciences* (2nd ed., p. 627). Burlington, MA ; London: Academic Press.
15. Yarnal, B., Comrie, A. C., Frakes, B., & Brown, D. P. (2001). Review developments and prospects in synoptic climatology. *International Journal of Climatology, 21*, 1923–1950.
16. Yeo, M.-H. (2014). *Statistical modeling of precipitation processes for gaged and ungaged sites in the context of climate change*. PhD Thesis, Department of Civil Engineering and Applied Mechanics, McGill University, Montreal, Quebec, Canada, 221 p.

Part II
Uncertainties, 3D Modelling, Models Coupling

Global Sensitivity Analysis with 2D Hydraulic Codes: Application on Uncertainties Related to High-Resolution Topographic Data

Morgan Abily, Olivier Delestre, Philippe Gourbesville, Nathalie Bertrand, Claire-Marie Duluc and Yann Richet

1 Introduction

To understand or predict surface flow properties during an extreme food event, models based on 2D Shallow Water Equations (SWEs) using high-resolution description of the environment are commonly used in practical engineering applications. In that case, the main role of hydraulic models is to finely describe overland flow maximal water depth reaching at some specific points or area of interest. In complex urban environment, above-ground surface features have a major influence on overland flow path, their implementations (buildings, walls, sidewalks) in hydraulic model are therefore required as shown in [1, 2]. The representation of

M. Abily (✉) · O. Delestre · P. Gourbesville
University of Nice-Sophia Antipolis/Polytech'Nice-Sophia/URE 005 I-City,
930 Route Des Colles, 06903 Sophia Antipolis Cedex, France
e-mail: abily@polytech.unice.fr

O. Delestre
e-mail: delestre@polytech.unice.fr

P. Gourbesville
e-mail: Philippe.Gourbesville@unice.fr

N. Bertrand · C.-M. Duluc
Institut de Radioprotection et de Sûreté Nucléaire (IRSN), PRP-DGE, SCAN,
BEHRIG, BP17, 92262 Fontenay-Aux-Roses Cedex, France
e-mail: nathalie.bertrand@irsn.fr

C.-M. Duluc
e-mail: claire-marie.duluc@irsn.fr

Y. Richet
Institut de Radioprotection et de Sûreté Nucléaire (IRSN), PSN-EXP, SNC,
BP17, 92262 Fontenay-Aux-Roses Cedex, France
e-mail: yann.richet@irsn.fr

P. Gourbesville et al. (eds.), *Advances in Hydroinformatics*,
Springer Water, DOI 10.1007/978-981-287-615-7_21

detailed surface features within models can be achieved through the use of high-resolution digital elevation models (HR DEMs).

Geomatics community intensively uses urban reconstruction relying on airborne topographic data gathering technologies such as imagery and Light Detection and Ranging (LiDAR) scans to produce HR DEM [3]. These technologies allow producing DEM with a high accuracy level [4–6]. Moreover, modern technologies, such as Unmanned Aerial Vehicle (UVA) use, make high-resolution LiDAR or imagery born data easily affordable in terms of time and financial investments [7, 8]. Consequently, hydraulic numerical modeling community increasingly uses HR DEM information from airborne technologies to model urban flood [9]. Among HR topographic data, photogrammetry technology allows the production of 3D classified topographic data [10]. This type of data is useful for surface hydraulic modeling community as it provides classified information on complex environments. It gives the possibility to select useful information for a DEM creation specifically adapted for flood modeling purposes [2].

Even though HR classified data have high horizontal and vertical accuracy levels (in a range of few centimeters), this dataset is assorted of errors and uncertainties. Moreover, in order to optimize model creation and numerical computation, hydraulic modelers make choices regarding procedure for this type of dataset use. These sources of uncertainties might produce variability in hydraulic flood models outputs. Addressing models output variability related to model input parameters uncertainty is an active topic, which is one of the main concern for practitioners and decision makers involved in assessment and development of flood mitigation strategies [11]. To tackle a part of the uncertainty in modeling approaches, practitioners are developing methods which enable to understand and reduce results variability related to input parameters uncertainty such as Global Sensitivity Analysis (GSA) [12, 13]. A GSA aims to quantify the output uncertainty in the input factors, given by their uncertainty range and distribution [14]. To do so, the deterministic code (2D hydraulic code in our case) is considered as a black box model as described in [13]:

$$\begin{aligned} f &: R^p \rightarrow R \\ X &\mapsto Y = f(X) \end{aligned} \tag{1}$$

where f is the model function, $X = (X_1; \ldots; X_p)$ are p independent input random variables with known distribution, and Y is the output random variable. The principle of GSA method relies on the estimation of input variables variance contribution to output variance. A unique functional analysis of variance (ANOVA) decomposition of any integral function into a sum of elementary functions allows to define the sensitivity indices as explained in [13]. Sobol's indices are defined as follow:

$$S_i = \mathrm{Var}[\mathrm{E}(Y|X_i)]/\mathrm{Var}(Y) \quad (2)$$

First-order Sobol index indicates the contribution to the output variance of the main effect of each input parameters. The production of Sobol index spatial distribution map is promising. Moreover, such maps have been done in other application fields such as hydrology, hydrogeology, and flood risk cost estimation [15]. GSA process most generally goes through uncertain parameters definition, uncertainty propagation, and results variability study. Such type of approach has been applied at an operational level in 1D hydraulic modeling studies by public institutions and consulting companies [14]. For 2D free surface modeling, GSA approach is still at an exploratory level. Indeed, GSA requires application of a specific protocol and development of adapted tools. Moreover, it requires important computational resources.

The purpose of this study is to investigate on uncertainties related to HR topographic data use for hydraulic modeling. Two categories of uncertain parameters are considered in our approach: the first category is inherent to HR topographic data internal errors (measurement errors) and the second category is related to operator choices for this type of data inclusion in 2D hydraulic codes.

This paper presents the results of an applied GSA approach performed over a 2D flood river event modeling case. The aim of our study is to rank the impact of uncertainties related to HR topographic use. To achieve this aim, a protocol and a tool for GSA application to 2D hydraulic codes have been developed. Input parameters considered as introducing uncertainty are chosen and a probability distribution is attributed to each uncertain input parameter. A Monte-Carlo uncertainty propagation is then carried out, uncertainties are quantified, and the influence of selected input parameters is ranked by the computation of the Sobol indices. Section 2 introduces the data and methodology used and followed. Then, Sect. 3 presents the first results, main outcomes, and perspectives.

2 Materials and Methods

2.1 Flood Event Scenario

On November 5, 1994, an intense rainfall event occurred in the Var catchment (France), leading to serious flooding in the low Var river valley [16]. For our study, hydraulic conditions of this historical event were used as a framework for a test scenario. The study area was restricted to the last 5 km of the low Var valley. Since 1994, the urban area has changed a lot, as levees, dikes, and urban structures have been intensively constructed and it has to be reminded that the objective here was not to reproduce the flood event itself. For the GSA approach, the hydraulic parameters of the model are set identically for the simulations (as described below),

only the input DEM changes from one simulation to another, following the strategy defined in the next section.

The 2D hydraulic code is FullSWOF_2D [17, 18]. FullSWOF_2D relies on 2D SWEs and uses a finite volume approach over a regular Cartesian grid. An estimated hydrograph of the November 5, 1994 flood event as described in [19] is used as the upstream boundary condition of the low Var river valley. To shorten the simulation length, we chose to run a constant 1,500 $m^3 \cdot s^{-1}$ discharge for 3 h, to reach a steady state with a water level in the riverbed just half a meter below the elevation of the flood plain. The reached steady state is used as an initial condition (or hot start) for the other simulations. For the GSA simulations, the unit hydrograph is then run until the estimated peak discharge (3,700 $m^3 \cdot s^{-1}$) and decreases until a significant diminution of the overland flow water depth is observed. The Manning's friction coefficient n is spatially uniform on overland flow areas with a standard value of 0.015 which corresponds to a concrete surfacing. No energy loss properties have been included in the 2D hydraulic model to represent the bridges, piers, or weirs. Downstream boundary condition is an open sea level with a Neumann boundary condition.

For our application, the 3D classified data of the low Var river valley is used to generate specific DEM adapted to surface hydraulic modeling.

2.2 *Photo-Interpreted High-Resolution Topographic Data of the Low Var Valley*

Aerial photogrammetry technology allows to measure 3D coordinates of a surface and its features, using 2D pictures taken from different positions. The overlapping between pictures allows calculating through an aerotriangulation calculation step, 3D properties of space and features based on stereoscopy principle [20–22]. Photo interpretation allows creation of vectorial information based on photogrammetric dataset. The 3D classification of features based on photo interpretation allows getting 3D high-resolution topographic data over a territory offering large and adaptable perspectives for its exploitation for different purposes [10]. A photo-interpreted dataset is composed of classes of points, polylines, and polygons digitalized based on photogrammetric data. Important aspects in the photo interpretation process are classes' definition, dataset quality, and techniques used for photo interpretation. Both will impact the design of the output classified dataset [22].

An HR photogrammetric 3D classified data gathering campaign was held in 2010–2011 covering 400 km^2 of Nice municipality [10]. Aerial pictures have a pixel resolution of 0.1 m at ground level. Features were photo interpreted by human operators under vectorial form in 50 different classes. These classes of elements include large above-ground features such as building, roads, bridges, sidewalks, etc. Thin above-ground features (like concrete walls, road-gutters, stairs, etc.) are

included in classes. An important number of georeferencing markers were used (about 200). Globally, over the whole spatial extent of the data gathering campaign, mean accuracy of the classified data is 0.3 and 0.25 m, respectively, in horizontal and vertical dimensions. For the low Var river valley area, a low flight elevation combined with a high level of overlapping among aerial pictures (80 %) was conducted to a higher level of accuracy. In the low Var river valley sector, classified data mean horizontal and vertical mean accuracy is 0.2 m. This mean error value encompasses errors, due to material accuracy limits, bias and nuggets, which occur within the photogrammetric data. For this dataset, errors in photo interpretation are estimated to represent 5 % of the total number of elements. This percentage of accuracy represents errors in photo interpretation, which results from feature misinterpretation, addition, or omission. To control and ensure both average level of accuracy and level of errors in photo interpretation, the municipality has carried out a terrestrial control of data accuracy over 10 % of the domain covered by the photogrammetric campaign.

2.3 Global Sensitivity Analysis

A GSA method quantifies the influence of uncertain input variables on the variability in numeric model outputs. To implement a GSA approach, it is necessary (i) to identify inputs and assess their probability distribution, (ii) to propagate uncertainty within the model (e.g., using a Monte-Carlo approach), and (iii) to rank the effects of input variability on the output variability through functional variance decomposition method such as calculation of Sobol indices (Eq. 1).

2.3.1 Uncertain Input Parameters

To encompass uncertainty related to measurement error in HR topographic dataset, Var. E is considered. Two other uncertain parameters are also considered as modeler choices: the level of details of above-ground elements included in DEM (Var. S), and the spatial discretization resolution (Var. R). Parameters Var. S, E, and R are independent parameters considered as described below.

Var. E: measurement errors of HR topographic dataset

In each cell of the DEM having the finest resolution (1 m), this parameter introduces a random error. For our study, only the altimetry errors are taken into account as the planimetric dimension of the error is assumed to be relatively less significant for hydraulic study purpose compared to altimetry error. This altimetry measurement error follows a Gaussian probability density function N (0; 0.2), where the standard deviation is equal to the mean global error value (0.2 m). This error introduction is spatially homogeneous. This approach is a first approximation: mean error could be spatialized in different subareas having physical properties,

which would impact spatial patterns of error value. Moreover, errors in photo interpretation (classification) are not considered in our study. One hundred grids of random errors are generated and named E1 to E100.

Var. S: modeler choices for DEM creation

This parameter represents modeler choices for DEM creation, taking advantage of selection possibilities offered by the above described classified topographic data. Four discrete schemes are considered: (i) S1, is the DTM of the study case, (ii) S2, the elevation information of buildings added to S1, (iii) S3, the elevation information of walls added to S2, and (iv) S4, elevation information of concrete features in streets added to S3. Var. S parameter is included in the SA as a categorical ordinal parameter. These discrete modeler choices are considered as having the same probability. Four DEMs are generated at resolution of 1 m, S1–S4.

Var. R: modeler choices for mesh spatial resolution

When included in 2D models, HR DEM information is spatially and temporally discretized. FullSWOF is based on structured mesh, therefore the DEM grid can be directly included as a computational grid without effort for mesh creation. Nevertheless, for practical application, optimization of computational time/accuracy ratio often goes through a mesh degradation process when an HR DEM is used. Var. R represents modeler choices, when decreasing regular mesh resolution. Var. R parameter takes five discrete values: 1, 2, 3, 4, or 5 m.

2.3.2 Applied Protocol for Uncertainty Propagation

To create the HR DEMs, the following approach has been carried out. A HR DTM using multiple ground level information sources (points, polygons and polylines) is created and provided at a 0.5 m resolution by The GIS Department of Nice Côte d'Azur Metropolis (DIGNCA). The HR DEM resolution is degraded to 1 m resolution. At this resolution, the number of mesh cells is above 17.8 million. Then, a selection procedure among classified data is performed. This selection is achieved by considering concrete elements which can influence overland flow drainage path only. It includes dikes, buildings, walls, and "concrete" above-ground elements (such as sidewalks, road-gutters, roundabout, doors steps, etc.). 12 classes are selected among the 50 classes of the 3D photo-interpreted dataset. During this step, polylines giving information on elevated roads and bridges, which might block overland flow paths, are removed. The remaining total number of polylines is 52,600. Selected above-ground features are aggregated in three groups of features (buildings, walls, and concrete street features). Extruding elevation information of selected polylines groups on the DTM (S1), four 1 m resolution DEMs, S1–S4, are produced. The previously described method has allowed inclusion of thin elements impacting flow behavior of inframetric dimension, oversized to metric size, in the 1 m resolution regular mesh. Then, 100 grids of var. E are produced and added to var. S1, S2, S3, and S4 at resolution 1 m. These 400 DEMs are used to create 2,000

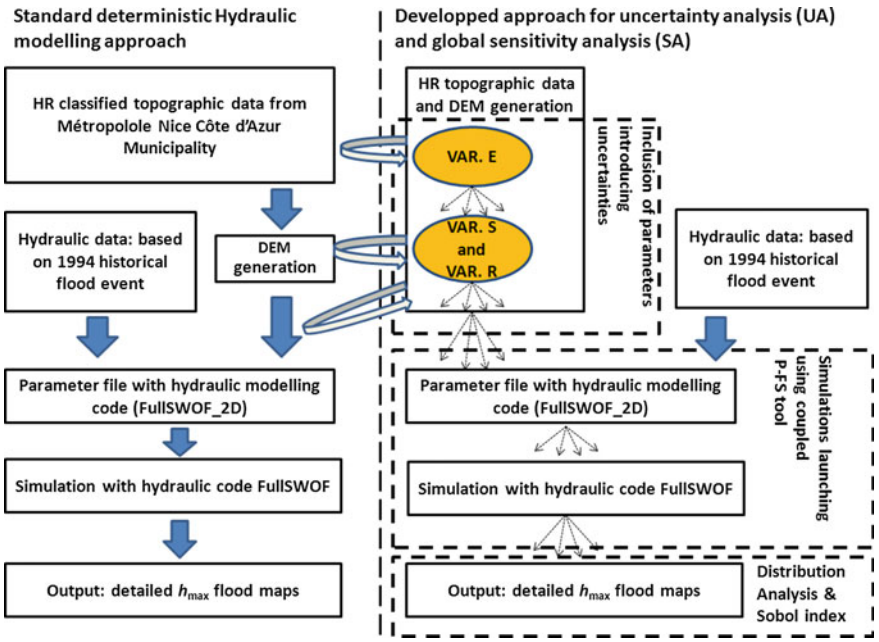

Fig. 1 Implemented GSA approach

DEMs with a resolution from 1 to 5 m. DEMs are named $S_mR_nE_x$, with the parameters m between [1, 4], n between [1, 5] and x between [1; 100]. These DEMs are used in the coupled parametric environment (Prométée)—2Dhydraulic code (FullSWOF_2D) through parameterization of the input files, and integrated in whole GSA as summed up in Fig. 1. Promethée-FullSWOF (P-FS) is presented in more detail in the next section.

2.3.3 Operational Tool and Setup Developed for Uncertainty Analysis and Sobol Index Mapping

To apply a GSA with 2D hydraulic models, a coupling between Prométhée, a code allowing a parametric environment of other codes, has been performed with FullSWOF_2D, a 2D SWE-based hydraulic code. The coupling procedure has taken advantage of the previous coupling experience of Promethée with 1D SWE-based hydraulic code [14]. The coupled code Prométhée-FullSWOF (P-FS) has been performed on a HPC computation structure. The aim was to use tool for a proof of concept of protocol application requiring extensive computational resources.

- FullSWOF_2D

FullSWOF_2D (Full Shallow Water equation for Overland Flow in 2D) is a code developer as a free software based on 2D SWE [16, 17]. In FullSWOF_2D, the 2D SWE are solved thanks to a well-balanced finite volume scheme based on the hydrostatic reconstruction. The finite volume scheme, which is suited for a system of conservation low, is applied on a structured spatial discretization, using regular Cartesian mesh. For the temporal discretization, a variable time step is used based on the CFL criterion. The hydrostatic reconstruction (which is a well-balanced numerical strategy) allows to ensure that the numerical treatment of the system preserves water depth positivity and does not create numerical oscillation in case of a steady state, where pressures in the flux are balanced with the source term here (topography). Different solvers can be used such as HLL, Rusanov, Kinetic, and VFROE combined with first-order or second-order (MUSCL or ENO) reconstruction. FullSWOF_2D is a object-oriented software developed in C++. Two parallel versions of the code have been developed allowing to run calculations under HPC structures [23].

- Promethée-FullSWOF

Prométhée software is coupled with FullSWOF_2D. Prométhée is an environment for parametric computation, allowing to carry out uncertainties propagation study, when coupled to a code. This software is an open source environment developed by IRSN (http://promethee.irsn.org/doku.php). The main interest of Prométhée is the fact that it allows the parameterization of any numerical code. Also, it is optimized for intensive computing resources use. Moreover, statistical posttreatment can be performed using Prométhée as it integrates R statistical computing environment [24]. The coupled code Prométhée/FullSWOF (P-FS) is used to automatically launch parameterized computation through R interface under Linux OS. A graphic user interface is available under Windows OS, but in case of large number of simulation launching, the use of this OS has shown limitations as described in [14]. A maximum of 30 calculations can be run simultaneously, with the use of 30 “daemons”.

Once simulations were completed with P-FS, GSA analysis has been carried out. First, the convergence of the results, in other word it has been checked that the number of simulations is large enough to generate a representative sample of the uncertainties associated to the studied source. Then uncertainties analysis was conducted, followed by the calculation of Sobol indices. The selected output of interest is the overland flow water surface elevation ($h_{\max} + z$).

3 Results and Discussion

3.1 Operational Achievement of the Approach

A performed version of P-FS couple allows to run simulations with selected set of input parameters (Var. E, S, and R). The coupled tool is operational on the Mésocentre HPC computation center and P-FS would be transposable over any common high-performance computation cluster, requiring only slight changes in the coupling part of the codes. Through the use of R commands, it is possible to launch several calculations. Using "Daemons", up to 30 simulations can be launched at a time. The calculations running time of our simulation is significant. Indeed, this computation time is highly dependent of mesh resolution as the dx will directly impact the CFL dependent dt. Over a 12 cores node of the Mésocentre HPC, the computation time is 2, 6, 12, 24, 80 h, respectively, for 5, 4, 3, 2, 1 m resolution grids. Using about 400,000 CPU hours, it has been possible to run 1,500 simulations. Out of these 1,500 simulations, few runs (about 30) have shown numerical errors leading to computational crash. These simulations have been removed from our set of simulations used to carry out the GSA. This will be clarified in future work, but errors are possibly due to numerical instabilities generated by important topographic gradient change at the boundary condition. This first data set of output allows us to carry out the first UA and GSA. The remaining 500 simulations are mainly for R1 and R2 resolutions, which are the most resource-demanding simulations, and will run in a close future, using more than one HPC node per each run to decrease running time.

The variable of interest is the maximal water surface elevation ($h_{max} + z$) reached during a given simulation at different locations, with h_{max} as the maximal water depth reached at the point of interest and z the DEM surface elevation at this point. The Fig. 2 illustrates the difference of $h_{max} + z$ obtained between two simulations when Var. S varies. At different points of interest (see next section), difference in $h_{max} + z$ value can be significant. The analyses carried out over 40 points of interests, highlights the influence of the selected variables. For example, for a given scenario when only Var. E varies, an up to 0.5 m difference in $h_{max} + z$ can be observed. Between all the 1,500 scenarios, a maximal difference of 1.26 m in $h_{max} + z$ estimation at one of the point of interest is observed.

3.2 Local Results for a Point of Interest

In the first place, a local analysis of the influence of topographic parameters has been achieved; 40 points of interest have been selected and used for the analyses.

The convergence for Var. E has been analyzed for the different points. As illustrated by Fig. 3a, it appears that the distribution and the standard deviations of $h_{max} + z$, becomes stable with a sample size (N) of Var. E is around 40–50.

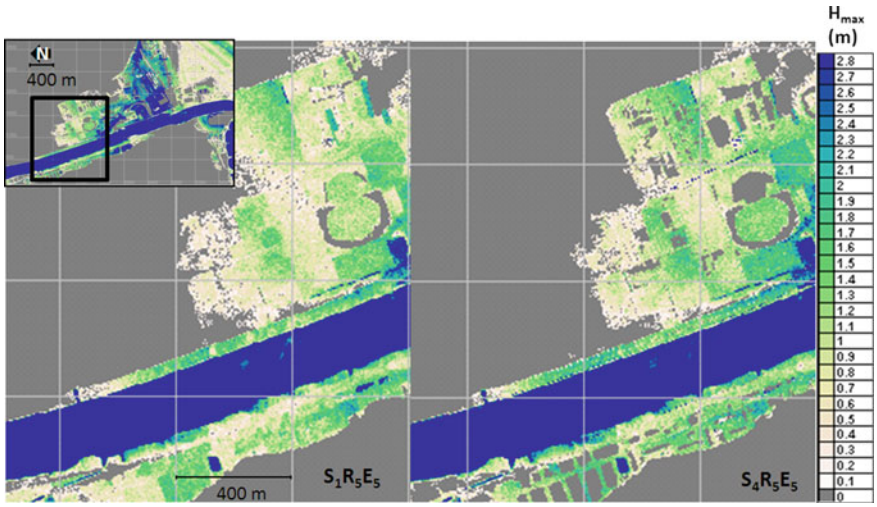

Fig. 2 Illustration of h_{max} value for two given simulations where Var. S changes

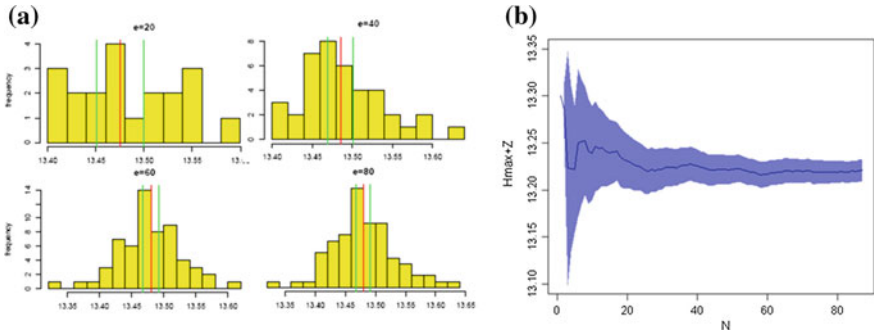

Fig. 3 **a** Illustration of $h_{max} + z$ distribution and **b** convergence of mean and CI with fixed Var. S and Var. R when increasing sample of size of Var. E

This gives qualitatively a first idea of what should be the minimum size of sample N of Var. E to allow performing reliable statistical analysis with an acceptable level of convergence.

To strengthen these findings, tests of convergence have been performed observing the evolution of mean $h_{max} + z$ value and the 95 % confidence interval (CI) when N size increases. Figure 3b shows this result for a given point of interest. The analysis shows the sample size to be above 30, the mean and the CI become stable. It has to be noticed that similar results are obtained with the other selected points of interest, 30–40 realizations are sufficient to generate a representative sample of the uncertainties associated to the Var. E.

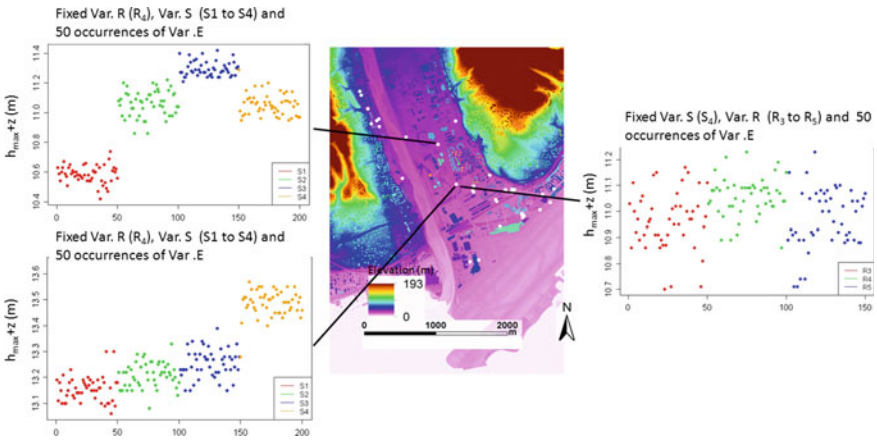

Fig. 4 Output ($h_{max} + z$) distribution plots at two points of interest with one fixed value (either Var. S or Var. R)

When looking at the output variable of interest $h_{max} + z$, it is relevant to check its distribution behavior for a fixed value of one of the two discrete input parameters (Var. R or Var. S). This has been done with a subset of sample $N_{Var.\ E}$ equal to 50 for each discrete value of nonfixed variables Var. R and Var. S (Fig. 4). This approach helps to make a qualitative description of the output distribution behavior relatively to the nonfixed parameters. This test has been carried out for 40 different points of interest. Figure 4 illustrates the main observations which can be effectuated using different distribution plots for fixed Var. R or for fixed value of Var. S. Results show that for a given value of Var. R, Var. E impact over variability of $h_{max} + z$ is relatively less significant than the impact of Var. S (discrete choices). It has also been observed that increasing level of geometric details included in DEM (Var. S) will not involve linear variations in $h_{max} + z$ values. Indeed, detailed above-ground feature implementation leads to more local effects in terms of overland flow path modification and consequently, highly impact local $h_{max} + z$ values. When focusing on $h_{max} + z$ distribution for varying discrete meshes resolution (Var. R) for a given fixed Var. S value (Fig. 4), it is observed that, comparatively to effect of Var. E in output distribution, the influence generated by Var. R on $h_{max} + z$ values is negligible. This finding does not consider the finest Var. R (1 m) as less than 50 realizations of Var. E were available so far with these resolutions.

The final step of the GSA approach calculates the Sobol indices (Fig. 5). As mentioned previously Var. R1 has not been considered for the calculation. The parameter which influences the most $h_{max} + z$ is Var. S. Concerning the Sobol indices, it has to be mentioned that the sum of Sobol indices should be one, in our

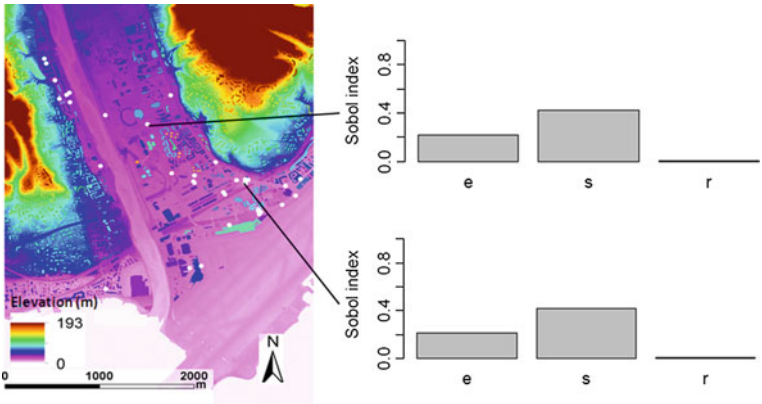

Fig. 5 First-order Sobol indices for two selected points

case the sum is smaller than one. Similar results have been highlighted by [13]. This finding is due to the parameters cross variation. Moreover, the inclusion of results at the highest resolution (1 m) might increase the cross variation effects. These promising results for analysis are already useful and further analysis to observe cross variation effects as well as spatial variation of Sobol index are in progress. So far it can be observed that 32 of the 40 points of interest have Var. S with the highest Sobol index and 8 points have Var. R with the highest Sobol index. These two parameters are modeler choices. In the 32 cases where Var. S has the highest Sobol Index, 50 % of the points have Var. R in the second rank and 50 % Var. E.

3.3 Perspectives and Analyze for Further Work

One of the main advantages of 2D hydraulic models is their spatial distribution over the area modeled. Therefore, uncertainties related to topography variability can be spatially represented for the Var river valley. Sobol index maps are presented in Fig. 6 over a subarea in a near future and integrating cross variation effect.

Nevertheless, as it has been mentioned, our representation of Var. E, using a spatially uniform distribution function of average measurement error is a first simple approximation. Indeed, the average error is a spatially varying function of physical properties (slope notably). Assigning different spatially varying parameters of Var. E distribution function would be a more sophisticated approach. Moreover, errors in photo interpretation, which will spatially impact Var. S, deserve to be investigated as well.

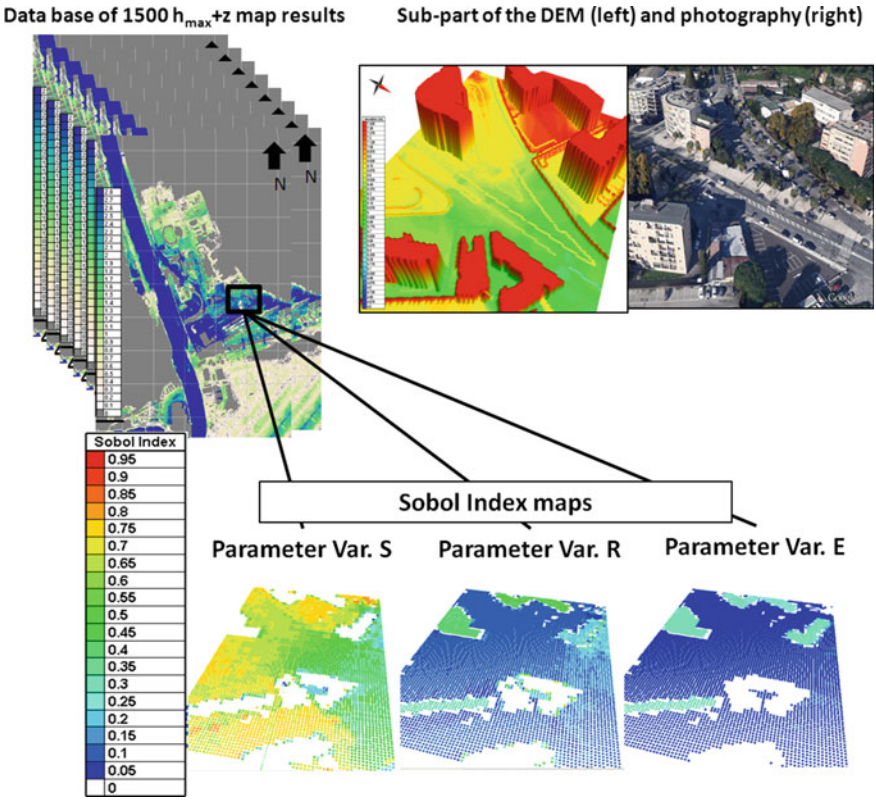

Fig. 6 Sobol index maps over 150 m long per 200 m large part of the domain

4 Conclusions

In this study, a GSA is performed based on Sobol sensitivity analysis to quantify the uncertainties related to high-resolution topography data inclusion in two-dimensional hydraulic model. Input parameters considered in the study encompass both measurement errors, and modeler choices for high-resolution topographic data used in models. The applied GSA method relies (i) on the use of a specific tool coupling a parametric environment with a 2D hydraulic modeling tool Prométhée-FullSWOF_2D, and (ii) on the use of high-performance computation resources. The implemented approach is able to highlight the uncertainties generated by topography parameters and operator choices when including high-resolution data in hydraulic models.

Thousand five hundred simulations have been effectuated at this stage of the study. Convergence of the approach is checked and output distribution analyzed for qualitative apprehension of input parameters local effects on maximal computed

overland flow ($h_{max} + z$). The major source of uncertainty related to water elevation $h_{max} + z$ is the modeler choice Var. S, which is the choice of operator regarding above-ground features, included in DEM used for hydraulic simulation. Errors related to measurement Var. E significantly impacts variability of $h_{max} + z$ model outputs, but in a relatively smaller extend. Regarding Var. R, further investigations will be undertaken when more realizations will be available. Overall, these results confirm the relative importance of the uncertainty in topography input data. The main limits of the approach are concerning the way Var. E and Var. S are integrated in the analysis. Future work will be focussed on the design of Sobol map index over the whole flood extend.

Acknowledgments Photogrammetric and photo-interpreted dataset used for this study have been kindly provided by Nice Côte d'Azur Metropolis for research purpose. Technical expertise on DIGNCA dataset has been provided by G. Tacet and F. Largeron. This work was granted access to the HPC resources of Aix-Marseille Université financed by the project Equip@Meso (ANR-10-EQPX-29-01) of the program "Investissements d'Avenir" supervised by the Agence Nationale pour la Recherche. Technical support for codes adaptation on high-performance computation centers has been provided by T. Nguyen, J. Brou, F. Lebas, H. Coullon and P. Navarro.

References

1. Abily, M., Duluc, C.-M., Faes, J. B., & Gourbesville, P. (2013). Performance assessment of modelling tools for high resolution runoff simulation over an industrial site. *Journal of Hydroinformatics, 15*(4), 1296–1311.
2. Abily, M., Gourbesville, P., Andres, L., & Duluc, C.-M. (2013). Photogrammetric and LiDAR data for high resolution runoff modeling over industrial and urban sites. In W. Zhaoyin, J. H.-W. Lee, G. Jizhang & C. Shuyou (Eds.), *Proceedings of the 35th IAHR world congress*, Chengdu, Beijing, China: Tsinghua University Press. Sept. 8–13, 2013.
3. Musialski, P., Wonka, P., Aliaga, D. G., Wimmer, M., van Gool, L., & Purgathofer, W. (2013). A survey of urban reconstruction. *Computer Graphics Forum, 32*(6), 146–177.
4. Lafarge, F., Descombes, X., Zerubia, J., & Pierrot Deseilligny, M. (2010). Structural approach for building reconstruction from a single DSM. *Transaction on Pattern Analysis and Machine Intelligence, 32*(1), 135–147.
5. Lafarge, F., & Mallet, C. (2011). Building large urban environments from unstructured point data. In *2011 IEEE international conference* on *computer vision (ICCV)* (pp. 1068–1075). Los Alamitos, CA, USA: IEEE Computer Society.
6. Mastin, A., Kepner, J., & Fisher, J. (2009). Automatic registration of LIDAR and optical images of urban scenes. In *2009 IEEE conference on computer vision and pattern recognition* (pp. 2639–2646). Miami, FL: IEEE. June 2009.
7. Remondino, F., Barazzetti, L., Nex, F., Scaioni, M., & Sarazzi, D. (2011). UAV photogrammetry for mapping and 3D modeling—current status and future perspectives. In *Archives of photogrammetry, remote sensing and spatial information sciences*, Vol. 38 (1/C22). ISPRS Conference UAV-g, Zurich, Switzerland.
8. Nex, F., & Remondino, F. (2013). UAV for 3D mapping applications: A review. *Applied Geomatics*, *6*, 1–15.
9. Tsubaki, R., & Fujita, I. (2010). Unstructured grid generation using LiDAR data for urban flood inundation modelling. *Hydrological Processes, 24*, 1404–1420.

10. Andres, L. (2012). L'apport de la donnée topographique pour la modélisation 3D fine et classifiée d'un territoire. Revue XYZ, 133—4e trimester (pp. 24–30).
11. ASN (2013). Protection of basic nuclear installations against external flooding—guide no. 13—version of 08/01/2013. Technical report, Autorité de Sûreté Nucléaire.
12. Herman, J. D., Kollat, J. B., Reed, P. M., & Wagener, T. (2013). Technical note: Method of Morris effectively reduces the computational demands of global sensitivity analysis for distributed watershed models Hydrol. *Earth System Science Discussion, 10*, 4275–4299.
13. Iooss, B. (2011). Revue sur l'analyse de sensibilité globale de modèles numériques. *Journal de la Société Française de Statistique, 152*(1), 1–23.
14. Nguyen, T., Richet, Y., Balayn, P., & Bardet, L. (2013). Propagation d'incertitudes dans les modèles hydrauliques 1D Proceeding of congress SHF—Evènements extrêmes d'inondation 2013, Lyon, France. Nov. 13–14, 2013.
15. Saint-Geours, N. (2012). Analyse de sensibilité de modèles spatialisés—Application à l'analyse coût-bénéfice de projets de prévention des inondations. Ph.D. thesis, Université Montpellier II—Sciences et Techniques du Languedoc.
16. Lavabre, J., Mériaux, P., Nicoletis, E., & Cardelli, B. (1996). Catastrophic Var river flood of 5 November 1994. Convegno internazionale la prevenzione delle catastrofi idrogeologichi il contributo della ricerca scientifica (pp. 375–380) Alba, ITA.
17. Delestre, O., Cordier, S., Darboux, F., Du, M., James, F., Laguerre, C., Lucas, C., & Planchon, O. (2014). FullSWOF: A software for overland flow simulation. In P. Gourbesville, J. Cunge, & G. Caignaert (Eds.), *Advances in hydroinformatics, springer hydrogeology* (pp. 221–231). Singapore: Springer.
18. Delestre, O., Darboux, F., James, F., Lucas, C., Laguerre, C., & Cordier, S. (submitted). FullSWOF: A free software package for the simulation of shallow water flows. http://hal.archives-ouvertes.fr/hal-00932234.
19. Guinot, V., & Gourbesville, P. (2003). Calibration of physically based models: back to basics? *Journal of Hydroinformatics, 5*(4), 233–244.
20. Egels, Y., & Kasser, M. (2004). *Digital photogrammetry*. London: Taylor & Francis.
21. Linder, W. (2006). *Digital photogrammetry: A practical course*. Berlin: Springer.
22. Lu, D., & Weng, Q. (2007). A survey of image classification methods and techniques for improving classification performance. *International Journal of Remote Sensing, 28*(5), 823–870.
23. Cordier, S., Coullon, H., Delestre, O., Laguerre, C., Le, M. H., Pierre, D., & Sadaka, G. (2013). FullSWOF paral: Comparison of two parallelization strategies (MPI and SKELGIS) on a software designed for hydrology applications. *ESAIM: Proceedings, 43*, 59–79.
24. Ihaka, R. (1998). R: Past and Future History. Interface 98 (Technical report). Statistics Department, The University of Auckland, Auckland, New Zealand.

Modeling of a Navigation Canal with Unknown Inputs: The Cuinchy-Fontinettes Case Study

Klaudia Horváth, Eric Duviella, Lala Rajaoarisoa and Karine Chuquet

1 Introduction

Canals for navigation are artificial waterways used for the transport of commodities and persons by means of maneuverable waterborne craft [11]. The interest for inland navigation has increased in the past decade, the environmental and economic affects have been studied [7, 14, 20, 22]. The effect of climate change on navigation is also studied [15]. There are European [5] and national projects [9] on this topic.

Studies are published on the main waterways of Europe, analyzing the waterways from the ecologic and economical point of view. Mihic et al. [19] focus on analysis of the amount of transported goods and the number of transported people. Other recent study by Jonkeren et al. [16] focuses on the River Rhine. It addresses qualitative measures for the adaptation of climate change. These studies mainly model the transport of goods over a heavily modified water body, in large scale. In this study we focus on a smaller scale completely artificial water body. A generic model hydro-environmental model is developed in [8] modeling not only lock operations, weir flow, but also algae growth.

The goal of this work is to obtain a large-scale hydraulic model of a navigation canal that is able to approximate and characterize (quantity, seasonality, etc.) the

K. Horváth (✉) · E. Duviella · L. Rajaoarisoa
Mines-Telecom Institute, Mines Douai, 764 Boulevard Lahure, 59500 Douai, France
e-mail: hklau85@gmail.com

E. Duviella
e-mail: eric.duviella@mines-douai.fr

L. Rajaoarisoa
e-mail: lala.rajaoarisoa@mines-douai.fr

K. Chuquet
Voies Navigables de France, Service de la navigation du nord, Lille, France
e-mail: karine.chuquet@developpement-durable.gouv.fr

P. Gourbesville et al. (eds.), *Advances in Hydroinformatics*,
Springer Water, DOI 10.1007/978-981-287-615-7_22

unknown flows into the reach in the past using past measurement data. A further objective of the same model, if there are no unknown inputs, it could model the water level changes. It should be able to predict the response of the system (the water levels) for different future inputs (inflows).

The model uses only water level measurement data and data about the position of the hydraulic structures to predict discharges. This is very often the case, since the measurement of water levels is less expensive and complicated than the measurement of discharge and they are needed to be known for navigation or for flood protection [23]. The discharge of the hydraulic structures is calculated using the measurement of their position and the water level. This work is an improvement of the pervious study by Le Pocher [18]. While in the previous work data mining was excessively used, in this work we try to restrict the use of the data to validation of the hydraulic description, and we also assign uncertainties. The modeling approach is implemented in the case study of the Cuinchy-Fontinettes Reach (CFR).

2 Methodology

The volumetric models are commonly used for hydrological modeling [17, 25]. Similar mass balance models can be applied to model a canal reach with controlled inputs [20] and outputs.

The mass balance for a canal reach can be written as

$$\frac{dV}{dt} = q_{in}(t) - q_{out}(t) - q_{evap}(t) + q_{runoff}(t) + q_{pre}(t) + q_{gw}(t) + q_{ant}(t) \tag{1}$$

where V is the volume of the reach, q_{in} is the known input discharge, q_{out} is the known output discharge, q_{evap} is the evaporation, q_{runoff} is the runoff, q_{pre} is the rainfall and q_{gw} is the groundwater flow and q_{ant} is discharge of anthropomorphic origin. If all the hydrological processes are unknown, the latter five terms of (1) can be gathered into one term q_u, unknown input.

$$\frac{dV}{dt} = q_{in}(t) - q_{out}(t) + q_u(t) \tag{2}$$

where

$$q_u(t) = -q_{evap}(t) + q_{runoff}(t) + q_{pre}(t) + q_{gw}(t) + q_{ant}(t). \tag{3}$$

Discretizing and rearranging (3) the unknown discharge can be expressed as

$$q_u(k) = \frac{V(k) - V(k-1)}{\Delta T_m} - \sum_{l=1}^{\Delta T_m/\Delta T} q_{in}(l) + \sum_{l=1}^{\Delta T_m/\Delta T} q_{out}(l) \tag{4}$$

where ΔT_m and ΔT are the sampling time of the model and the measured data respectively. The uncertainties are treated as standard deviation. In order to express the uncertainty of the unknown inputs it is supposed that all discharges: the right side of (3) carries normally distributed errors, with zero covariance. The standard deviation of the unknown discharge can be obtained in the following way [12]:

$$\sigma_{\Delta qu}(k) = \sqrt{\sigma^2_{\Delta V}(k) + \sigma^2_{qin}(k) + \sigma^2_{qout}(k)} \tag{5}$$

where $\Delta V = V(k) - V(k-1)$. In order to obtain the standard deviation of the terms different methods are used. In case of the ΔV the standard deviation is calculated directly, in the other cases a relative standard deviation is associated to each sub-model. The model is presented through the Cuinchy-Fontinettes study case.

3 The Cuincy-Fontinettes Case

The CFR belongs to the navigation network of the north of France that ensures the connection between the capital and the major ports of the north such as Calais or Dunkerque (Fig. 1). It is managed by the Navigable Waterways of France (VNF: Voies Navigables de France). The main management objective is to ensure navigation, to keep the water level within a certain range around the normal navigation level (NNN = 19.52 m). The water level is influenced by the lock operations upstream and downstream of the reach: upstream the lock of Cuinchy empties its

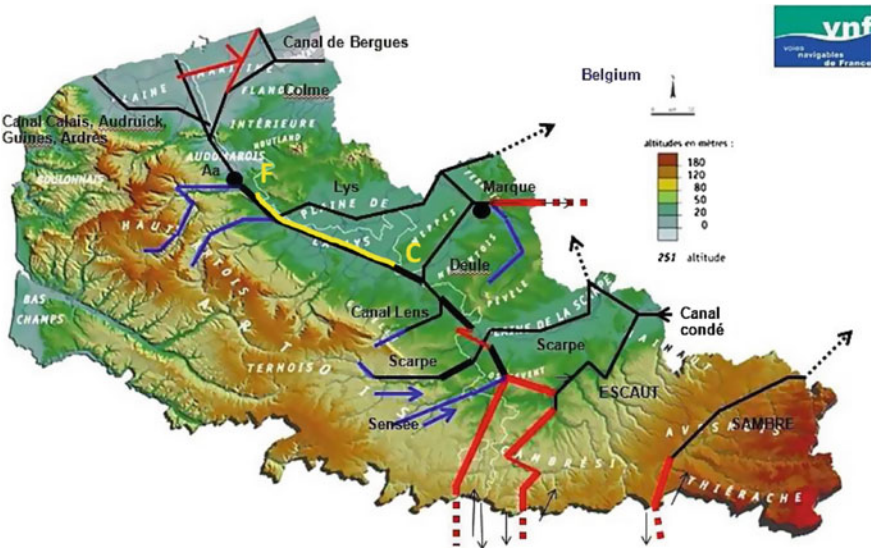

Fig. 1 The location of the Cuinchy-Fontinettes Reach

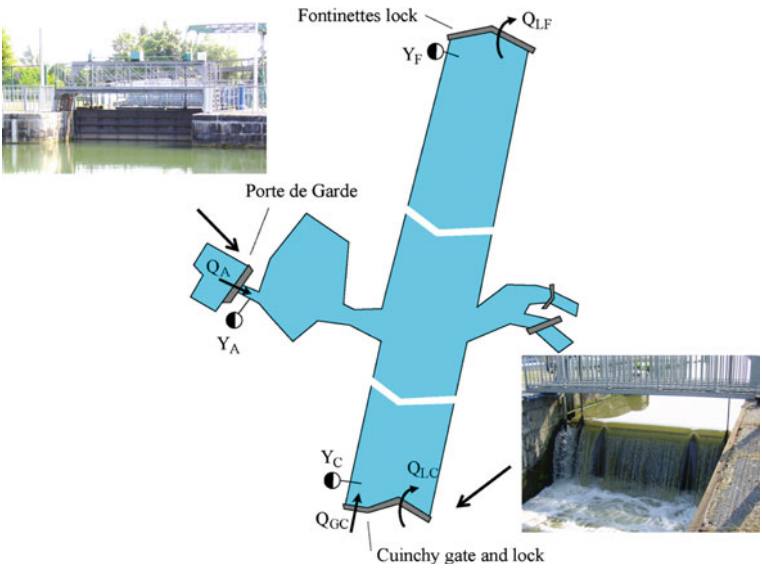

Fig. 2 The Cuinchy-Fontinettes Reach

chamber to the CFR and downstream the lock of Fontinettes fills its chamber from the reach (Fig. 2). The latter has much bigger volume and hence it causes a huge effect—at about 15 cm drop in the water level. This operation generates waves that can travel up and down in the reach for several hours before their attenuate. The behavior and control of this kind of water systems is studied in [24, 13].

The water level can be controlled by some controllable inflows through hydraulic structures. Anthropogenic and non-anthropogenic (rain, evaporation) sources also affect the water level. The quantity of these inputs and their influence is not defined yet. The rain influences through direct runoff and infiltration, while it does not cause unmeasured effect from the confluences, because the inflow is controlled. There are several anthropogenic sources located throughout the CFR and their quantity is unknown. In order to characterize or identify these sources, past water level (and gate opening) measurement data can be used. By characterizing these unknown sources their localization might be easier and also it can be seen if they are negligible for future approximations.

4 Application to the the Cuinchy-Fontinettes Case

4.1 General Description of the Model

The CFR is modeled using the volume model expressed in (1–4). The CFR has five discharge inflows and outflows (Fig. 2): two at the upstream end (i) Gate of

Cuinchy, Q_C (ii) Lock of Cuinchy Q_{LC}, one in the middle of the reach (iii) Gate of Aire Q_A (this can be input or output) and (iv) unknown sources located all along the reach Q_U and the outflow is the (v) operation of the lock of Fontinettes Q_{LF}, located downstream. Hence the terms in (3) can be expressed as

$$q_{in}(k) = Q_{GC}(k) + Q_{LC}(k) + Q_A(k). \tag{6}$$

$$q_{out}(k) = Q_{LF}(k). \tag{7}$$

$$\sigma^2_{qin}(k) = \sigma^2_{GC}(k) + \sigma^2_{LC}(k) + \sigma^2_A(k). \tag{8}$$

$$\sigma_{qout}(k) = \sigma_{LF}(k). \tag{9}$$

The input variables are the measured values at every 15 min (ΔT = 900 s): water levels and openings of structures. Currently there is no available data about discharge measurement. All the incoming and outflowing discharges are modeled separately using a submodel. The output of these submodels are discharges. Combining all these submodels, the change in volume can be calculated (the right-hand side of (2)), and it can be compared to the volume change obtained from the change in the water levels (left-hand side of (2)). Using (6–7) the unknonwn inputs and by (8–9) their uncertainty can be obtained.

In some of the submodels the relative standard deviation is given, σ_R. From this the absolute standard deviation for each data point can be calculated as

$$\sigma(k) = \sigma_R Q(k) \tag{10}$$

where $\sigma(k)$ is the absolute standard deviation, $Q(k)$ is the discharge calculated by any model, σ_R is the relative standard deviation obtained previously for each submodel.

4.2 Model of the Gate Cuinchy

The overshot gate of Cuinchy is modeled with the submerged weir Eq. [4]:

$$Q_{ws}(t) = \frac{3\sqrt{3}}{2} C_{dw} B_w \sqrt{2g} \frac{2}{3} \sqrt{H_1(t) - H_2(t)} H_e(t), \tag{11}$$

where Q_{ws} is the weir discharge, C_{dw} is the free flow weir discharge coefficient, B_w is the width of the weir, H_1 is the upstream water depth, H_2 is the downstream water depth, and H_e is the head over the weir and it is equal to $H_e(t) = H_1(t) - W(t)$ where $W(t)$ is the weir height. See the notation in Fig. 3.

There is no available measurement data about the discharge to verify (11). Therefore, the formula is used without calibration with the classical 0.61 discharge

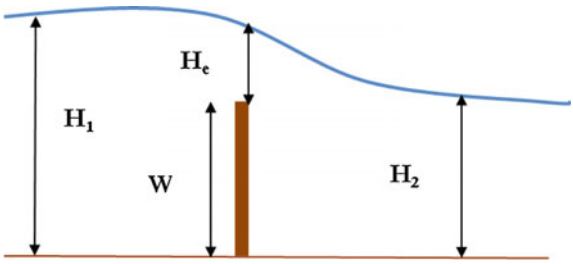

Fig. 3 Schematics of the overshot gate

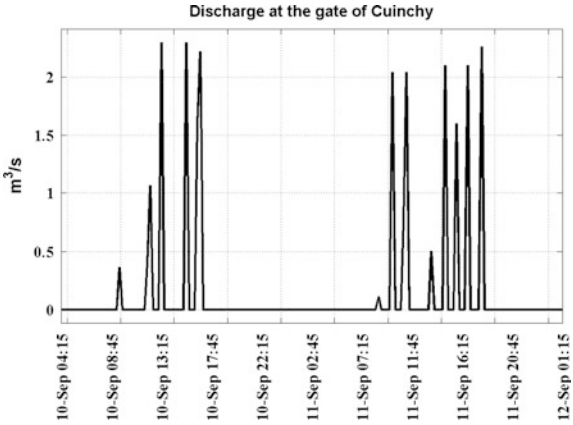

Fig. 4 Discharge at the gate of Cuinchy

coefficient that proved to be a good approximation [21]. The resulting discharge ($Q_{GC}(l)$) calculated from the water level and gate opening data using (11) is shown in Fig. 4. It can be seen that the gate is usually closed during the night, and operated with different discharge values during daytime. The purpose of these operations is to compensate the water level disturbances caused by the lock operations.

In order to develop a global model with uncertainty a standard deviation value should be assigned to model. Standard deviation values can be found in the literature. The discharge measurement error for overflow gates is about 5 % in free flow conditions [10] and 10 % in submerged conditions [7]. Since in this case both operation points are present, 10 % is relative standard deviation (σ_{RGC}) used in the case of Cuinchy. From the relative standard deviation the absolute standard deviation of each measurement is obtained using (10) (Fig. 5).

4.3 Model of the Gate of Aire

The gate of Aire is an undershoot gate with a sill (see Fig. 6). Depending on the upstream (H_1) and downstream (H_2) water levels and the opening (L) it can behave as a free or submerged weir, or as a free or submerged sluice gate. There are five

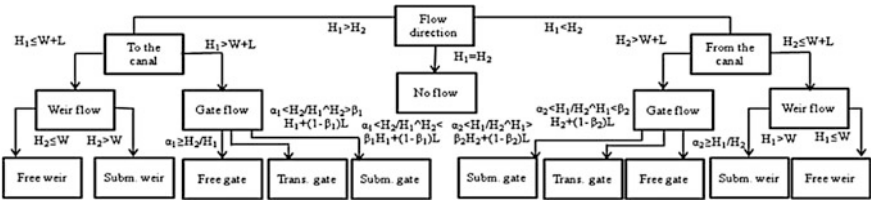

Fig. 5 The different operations of the gate of Aire, based on [1]

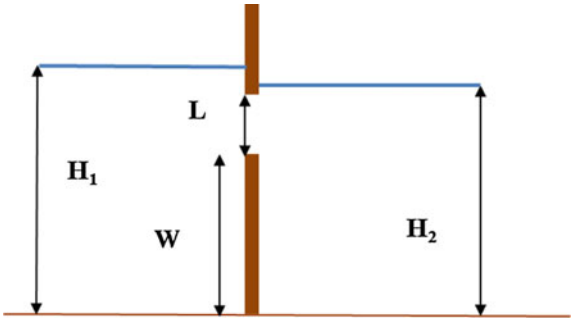

Fig. 6 Schematics of the undershot gate

possible flow types through the structure: (i) free weir flow (see 15), (ii) submerged weir flow (see 11), free gate flow (12), partially submerged gate flow (13) or submerged gate flow (14).

In case of gate flow the following equation is used [1] for free flow:

$$Q_g(t) = B_g\sqrt{2g}\left(\mu H_1(t)^{3/2} - \mu_1(H_1(t) - L(t))^{3/2}\right), \tag{12}$$

partially submerged flow:

$$Q_g(t) = B_g\sqrt{2g}\left(k_F\mu H_1(t)^{3/2} - \mu_1(H_1(t) - L(t))^{3/2}\right), \tag{13}$$

submerged flow:

$$Q_g(t) = B_g\sqrt{2g}\left(k_F\mu H_1(t)^{3/2} - k_{F1}\mu_1(H_1(t) - L(t))^{3/2}\right), \tag{14}$$

where B_g is the width of the gate, L is the gate opening, and μ, μ_1, k_F and k_{F1} are coefficients whose value can be obtained based on [12]. Finally, the free flow over the weir is

$$Q_{wf}(t) = C_{dw}B_w\sqrt{2g}\frac{2}{3}\sqrt{H_1(t) - H_e(t)}, \tag{15}$$

where Q_{wf} is the free weir discharge, C_{dw} is the free flow weir discharge coefficient, B_w is the width of the weir, H_1 is the upstream water depth, and H_e is the head over the weir and is equal to $H_e(t) = H_1(t) - W(t)$ where $W(t)$ is the weir height, see also Fig. 3.

The five different modes can occur in both directions, so altogether there are 10 different operating modes. These are summarized by Fig. 5, where

$$\alpha_i = 1 - 0.14\frac{H_j(t)}{W(t)}, \beta_i = \alpha_i\big(H_j(t) - W(t)\big), \tag{16}$$

where $i = 1, j = 2$ if $H_1 > H_2$ and $i = 2, j = 1$ if $H_1 < H_2$. In this structure the water can flow in two directions. If the flow is in the other direction, the computation is similar and negative sign is considered. Depending on the water levels the discharge at the gate of Aire ($Q_A(l)$) is computed using (11–15).

Just as in case of the gate of Cuinchy there is no available data to validate the equation. A measurement error of 10 % is reported for standard submerged sluice gates [6]. In this case the structure has five possible operating modes for each flow direction. Taking into account that the discharge coefficient is not calibrated, it is possible to make an error in determining the flow regimes. In [2] the importance of the errors coming from the wrong determination of the operation mode is emphasized, and solution for discharge calculation in all regimes with smooth changes is proposed in [3]. Hence, finally, a relative standard deviation of 30 % is considered (σ_{RA}).

4.4 Lock Operations of Cuinchy and Fontinettes

In order to know the total discharge entering through the locks the total number of daily lock operations should be known. Unfortunately, they are only registered for a very short period, and for the rest of the years they can only be approximated from the water level measurements. The approximation uses the following criteria: (i) There are at least three data point differences between two lock operations; a lock operation occurs either (ii) if the difference between two consecutive data points exceeds a threshold or (iii) the difference of three consecutive data points exceeds a bigger threshold and one of the two neighboring points have a difference exceeding another threshold. Figure 7 illustrates (ii) at points located at 7–8: the difference between the values of points 7 and 8 exceeds a threshold (Th_2). (iii) is illustrated at points located at 2–4: the difference between the values of points 2 and 3 and between 3 and 4 both exceed a certain threshold (Th_1). The thresholds are chosen such that $Th_2 < 2Th_1$.

The purpose of this model is to detect the number of daily lock operations from the water level measurements, because normally they are not registered. However,

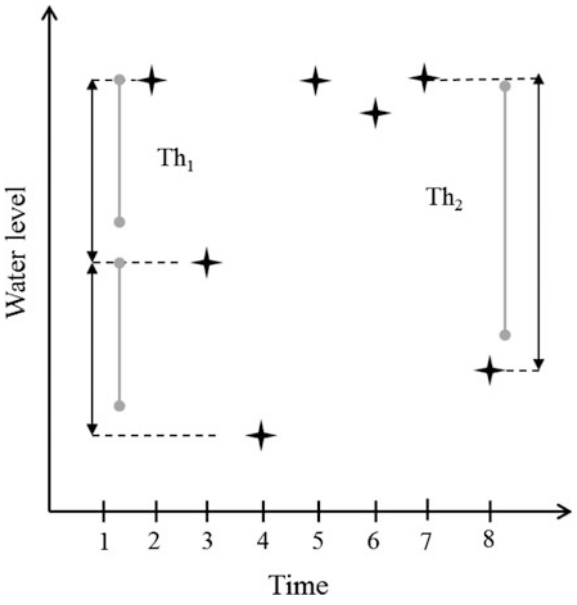

Fig. 7 Lock operation detection example: the measured water levels are noted with stars, and the thresholds by *gray lines*

for a short period of time, there is available measurement. This period can be used to calibrate the lock operation detection model. The thresholds (Th_1 and Th_2) were adjusted in order to minimize the error between the modeled and the measured number of daily lock operations. The data period for calibration was chosen based on its availability: for the lock of Fontinettes 4 months of data were analyzed, between September and December of 2007, while for the lock of Cuinchy only the last two months of this period could be analyzed. The error measured at Cuinchy does not reject the zero mean hypotheses within a 5 % and Fontinettes with 2 % significance level. In other words, the (daily discharge) error between the measured and detected lock operations can be considered having standard normal distribution. The relative standard deviation is 34 % for Cuinchy (σ_{RLC}) and 25 % for Fontinettes (σ_{RLF}). Note that these values are rather big. However, this is the error that the lock operations could be deduced from the water levels.

Figures 8 and 9 show the approximation of the lock operations for December 2007. The approximated number of daily lock operations is plotted compared to the available measured data. It can be seen that the approximations are quite close to the real number of lock operations for lock Fontinettes (Fig. 9), while for lock Cuinchy the difference is bigger. The reason is that a lock operation at Cuinchy causes smaller disturbance in the water level, therefore, it is more complicated to detect the occurrence of the operation from water level measurement data.

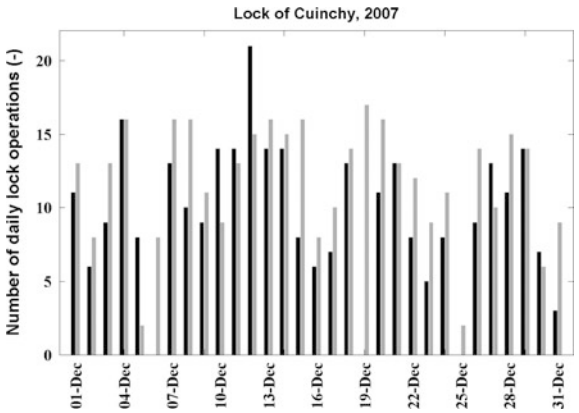

Fig. 8 In *black* are the measured number of lock operations, in *gray* is the approximation for lock Cuinchy

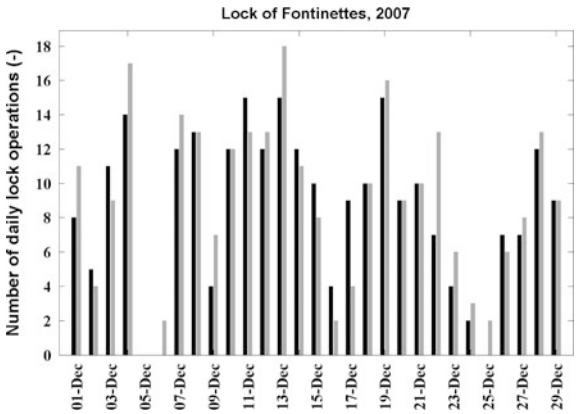

Fig. 9 In *black* are the measured number of lock operations, in *gray* is the approximation for lock Fontinettes

4.5 Model of the Volume Change

The canal reach is considered as a tank, the wave phenomenon is neglected. This assumption can be valid only if the discretization time ΔT_m is large enough. This assumption might be weak during the day when there are high waves caused by the lock operations, but for the night when there is no lock operation it might be more acceptable. (The balance is taken before and after the period of lock operations.) ΔT_m is chosen to be 12 h.

The volume can be obtained, for example, by modeling the height volume relationships like in [20]. Here, the change in volume is approximated using the three measurement points along the canal with the volume of two trapezoidal prisms (Fig. 10). The change in the volume during ΔT_m is calculated from the measured data in the beginning (at sample $k - 1$) and end (at sample k) of the ΔT_m period. This volume change is approximated as the product of the surface of the trapezoid created by the two measurement points at the two sampling instants

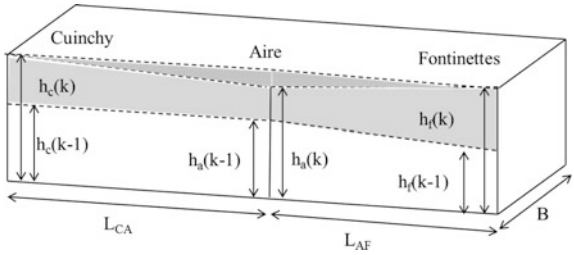

Fig. 10 The calculated volume change in the CFR is gray is the calculated volume, in *dark gray* is the calculated error

(k – *1* and k) and the distance between these two measurement points and the average width (Fig. 10). As there are three level measurement points the two calculated volumes are added up:

$$\Delta V(k) = [h_c(k) - h_c(k-1) + h_a(k) - h_a(k-1)]\frac{BL_{CA}}{2} + [h_a(k) - h_a(k-1) + h_f(k) - h_f(k-1)]\frac{BL_{AF}}{2} \quad (17)$$

where $\Delta V\,(k)$ is the water volume change within a period of ΔT_m, $h_c(k)$ is the water level at Cuinchy at the *kth* step (the difference between k and k – *1* is 12 h), $h_a(k)$ is the water level at Aire at the *kth* step, $h_f(k)$ is the water level at Fontinettes at the *kth* step, L_{CA} is the distance between Cuinchy and Aire, L_{AF} is the distance between Aire and Fontinettes and B is the average width of the reach (see also Fig. 10). An error was associated to the volume approximation, shown in Fig. 10 as the volume belonging to the dark gray area. This might not be the actual error of the measurement but can represent the order of magnitude of the error. It is calculated as

$$\Delta V_{err}(k) = [h_c(k) - h_c(k-1) - h_a(k) + h_a(k-1)]\frac{BL_{CA}}{2} + [h_a(k) - h_a(k-1) - h_f(k) + h_f(k-1)]\frac{BL_{AF}}{2} \quad (18)$$

where $\Delta V_{err}(k)$ is the approximated error on the water volume change within a period of ΔT_m. The standard deviation is approximated as

$$\sigma_{\Delta V} = \frac{\Delta V_{err}}{\Delta V}. \quad (19)$$

Finally, using (4)–(9) the unknown discharge and its standard deviation can be computed.

5 Results

A volume model was used to approximate the unknown discharges to the CFR. According to the management company these unknown discharge sources are of anthropogenic origin, it is not possible to predict them, or model them any way for the future, because their source and nature is unknown. Therefore, it should be emphasized again that the unknown discharges can be approximated only for the past. Nevertheless, these approximations can be helpful to locate their origin, study their evolution, and see their contribution to the final state. The results of the approximation of unknown discharges are shown in Figs. 11, 12, 13 and 14.

Figure 11 shows the unknown discharges for February: each point corresponds to a 12 h period, one for the daytime and one for the nighttime within each day. A peak during the first days can be observed. In the second half of the month a fluctuation can be seen between daytime and nighttime values. Note also the changes in the range of uncertainty. In order to have a better comparison between day and night the two values are plotted separately in Fig. 12. It can be seen that in

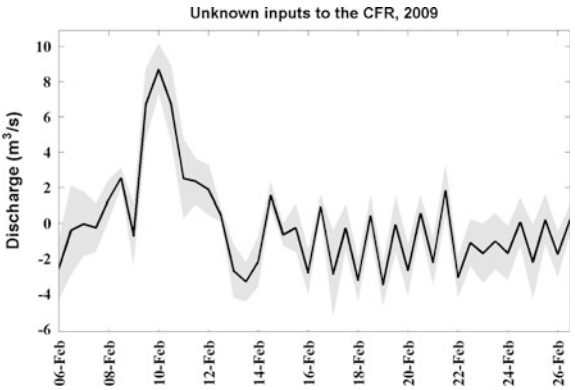

Fig. 11 In *black* is the modeled unknown input, in *gray* the uncertainty

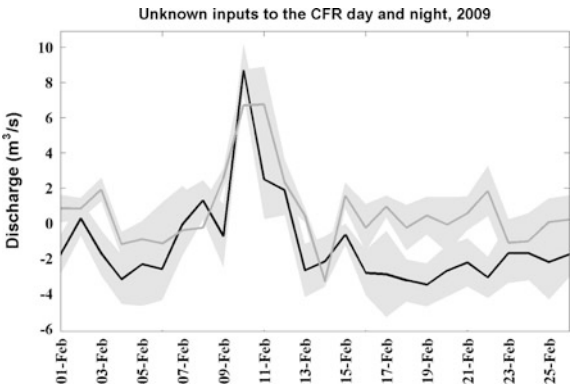

Fig. 12 In *black* is the discharge during day, in *gray* is the discharge during night

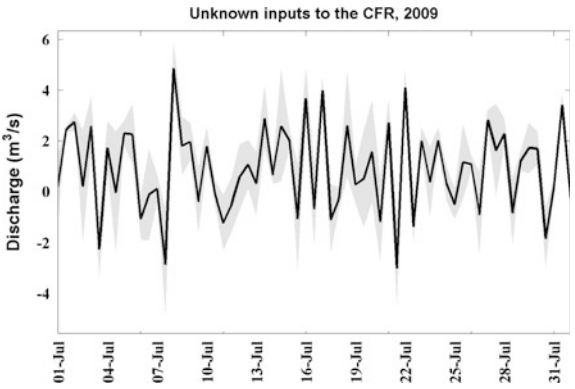

Fig. 13 In *black* is the modeled unknown input, in *gray* is the uncertainty

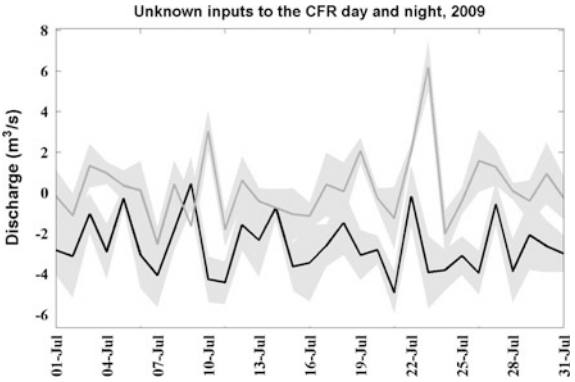

Fig. 14 In*black* is the discharge during day, in *gray* is the discharge during night

general the mean value is greater during night, however, very often the uncertainty ranges overlap. In these places we cannot say if the discharge is greater during night or not. It is also seen that in some cases the uncertainty is smaller in the night values. The reason is that during the night the locks do not operate, so they do not contribute to the error. The range depends on the operation of the gates of Cuinchy and Aire and the volume measurement. In Figs. 13 and 14 a summer month, July is plotted. Similar conclusions can be drawn, the quantity of the unknown discharge does not differ considerably between summer and winter. In summer time there is a bigger separation between day and night, the unknown inputs are smaller in night.

The effect of rain and evaporation is taken into account indirectly with the water level measurements. The input values are anthropogenic, that is, the lock operations and gate movements are adjusted and to these adjustments the effect of the rain was also taken into account. The unknown inputs satisfy the zero mean normal distribution test. It can be said that on average these unknown inputs balance, and in a yearly scale calculation they might be negligible.

There is a small difference between day and night behavior. The mean of all the unknown input is –0.08 m^3/s, the mean of only the night data is 0.95 m^3/s, and

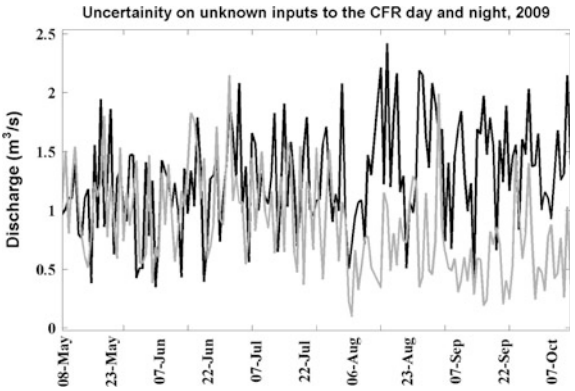

Fig. 15 In *black* is the discharge during day, in *gray* is the discharge during night

during the day it is –1.17 m^3/s. It is also possible that some anthropogenic activities released water during night and took water during the day. However, these values are only the mean values. Figure 15 shows the evolution of the uncertainty in time, separated for night and day. It can be seen that in the second time of the year the night discharge has less uncertainty. In general, the values range between 1 m^3/s and 2 m^3/s. The average day and night uncertainty is 1.3 m^3/s and 1.0 m^3/s respectively. When this uncertainty is concerned, the average unknown inputs are within the uncertainty bar around zero. Therefore, this procedure cannot confirm the strong effect of these unknown inputs.

There is a slight seasonal difference between the calculated input discharges. The mean unknown discharge is –0.5 m^3/s in summer and 1.2 m^3/s during winter. However, the mean uncertainty is 1 m^3/s in summer and 1.2 m^3/s in winter. While the mean shows clear increase in winter time, it is still in the uncertainty bound, therefore, this increase cannot be firmly confirmed.

It should also be mentioned that all the results given by the model are based on using all the measurements and trusting them within the uncertainty bound. In other words, if there is a bigger error than the uncertainty in any of the measurements, the model assigns this to the unknown inputs.

6 Conclusions

A navigation reach was modeled based on the mass balance using water level measurement data. The goal of the modeling work was to approximate the unknown inputs to the reach in using data measured in 2009. The unknown inputs were approximated with a range of uncertainty. They show some slight fluctuation between day and night (less during day) and also a greater seasonal fluctuation: there are more unknown inputs during winter. These fluctuations are within the limits of the uncertainty bounds. Within the uncertainty limits, the presence of considerable unknown inflows cannot be confirmed.

It is also possible to use the model for prediction. In this case either constant or zero unknown inputs are assumed. Then the effect of, for example, change in the number of lock operations to the water level can be modeled.

The perspective of this model can be to study the evolution of the unknown inputs during the past years. From this evolution it might help to identify the main anthropogenic sources. Also, the correlation with the rain can be verified. The past evolution can be used to advise the management company about the nature of these unknown inflows.

Acknowledgments This work is a contribution to the GEPET'Eau project which is granted by the French ministry MEDDE–GICC, the French institution ORNERC, and the DGITM. More information about the GEPETEau project can be found at: http://gepeteau.wordpress.com/enversion/.

References

1. Baume, J.-P., Malaterre, P.-O., Vion, P.-Y., & Litrico, X. (2003). *Simulation of irrigation Canals*. Theoretical Concepts Modeling Approach, Vol. II. France: CEMAGREF.
2. Bijankhan, M., & Kouchakzadeh, S. (2014). Discussion of "Revisiting the energy-momentum method for rating vertical sluice gates under submerged flow conditions" by Oscar Castro-Orgaz, Luciano Mateos, and Subhasish Dey. *Journal of Irrigation and Drainage Engineering, 140*(1), 07013003.
3. Bijankhan, M., Kouchakzadeh, S., & Bayat, E. (2011). Distinguishing condition curve for radial gates. *Flow Measurement and Instrumentation, 22*(6), 500–506.
4. Bos, M. (1976). Discharge measurement structures. Wageningen: International Institute for Land Reclamation and Improvement.
5. Breemersch, T., & Heyndrickx, C. (2012). Effects of climate change on inland waterway transport networks. In Second Nordic International Conference on Climate change adaptation, Helsinki, Finland.
6. Castro-Orgaz, O., Mateos, L., & Dey, S. (2013). Revisiting the energy-momentum method for rating vertical sluice gates under submerged ow conditions. *Journal of Irrigation and Drainage Engineering, 139*(4), 325–335.
7. de Vries, C. J. (2011). The power of inland navigation. Technical report, Dutch Inland shipping Information agency (BVB).
8. Dongfang, L., Zeckoski, R. W., & Wang, X. (2013). *Development of a hydro-environmental model for inland navigational canals*.
9. Duviella, E. (2014). The GEPET-Eau project. http://gepeteau.wordpress.com/enversion/.
10. El-Ansary, M., Awad, M., Nassar, A., & Farag, A. (2010). Calibration of three common flow measurement devices for open channels. *Misr Journal Agricultural Engineering, 27*(1), 151–169.
11. European Conference of Ministers of Transport (2006). *Inland waterways and environmental protection*. Paris: OECD Publishing.
12. Feller, W. (1971). *An introduction to probability theory and its applications*. Wiley series in probability and mathematical statistics: Probability and mathematical statistics. New York: Wiley.
13. Horváth, K. (2013). Model predictive control of resonance sensitive irrigation canals. PhD thesis, Technical University of Catalonia, Barcelona, Spain.

14. International Navigation Association and International Navigation Association. Environmental Commission. Working Group 6 (2003). *Guidelines for sustainable Inland waterways and navigation*. International Navigation Association.
15. Jan Brooke Environmental Consultant Ltd and Ian White Associates (Navigation) Ltd (2009). *Climate change mitigation and adaptation: Implications for inland waterways in England and Wales*. Technical report, Inland Waterways Advisory Council.
16. Jonkeren, O., Rietveld, P., van Ommeren, J., & Te Linde, A. (2013). *Climate change and economic consequences for inland waterway transport in Europe*. Regional Environmental Change.
17. Karpouzos, D. K., Baltas, E. A., Kavalieratou, S., & Babajimopoulos, C. (2011). A hydrological investigation using a lumped water balance model: the Aison River Basin case (Greece). *Water and Environment Journal, 25*(3), 297–307.
18. Le Pocher, O. (2011). Modélisation des réseaux hydrographiques et détection de défauts : Application au bief Cuinchy-Fontinettes. Masters Thesis, École des Mines de Douai, Douai, France.
19. Mihic, S., Golusin, M., & Mihajlovic, M. (2011). Policy and promotion of sustainable inland waterway transport in Europe—Danube River. *Renewable and Sustainable Energy Reviews, 15*(4), 1801–1809.
20. Rabelo, L., Petros Xanthopoulos, M. M., Lennox, C., Coiduras, P., & Andrade, L. (2012). Expansion of the Panama canal: Simulation modeling and artificial intelligence. In *Proceedings of the IIE Annual Conference (Institute of Industrial Engineers)*.
21. Sepúlveda, C., Gómez, M., & Rodellar, J. (2009). Benchmark of discharge calibration methods for submerged sluice gates. *Journal of Irrigation and Drainage Engineering, 135*(5), 676–682.
22. Stern, C. V. (2013). Inland waterways: Recent proposals and issues for congress. Technical report, Congressional Research Service.
23. The Ministry of Ecology, Sustainable Development and Energy, France (1999). Vigicrues: Information sur la vigilance “crues”.
24. van Overloop, P.-J., Miltenburg, I. J., Bombois, X., Clemmens, A. J., Strand, R., & van de Giesen, N. (2010). Identification of resonance waves in open water channels. *Control Engineering Practice, 18*(8), 863–872.
25. Zhang, L., Potter, N., Hickel, K., Zhang, Y., & Shao, Q. (2008). Water balance modeling over variable time scales based on the Budyko framework—Model development and testing. *Journal of Hydrology, 360*(1–4), 117–131.

Real-Time Reservoir Operation for Flood Management Considering Ensemble Streamflow Prediction and Its Uncertainty

Daisuke Nohara, Yuya Nishioka, Tomoharu Hori and Yoshinobu Sato

1 Introduction

It is concerned that water resources management will become more challenging in the future as a result of climate change which may bring increased contrast of precipitation between dry and wet seasons as global temperatures increase [1]. Thus, efficient operation of existing water infrastructures is considered important for effective water resources management. A multi-purpose reservoir, which controls river water for both water use and flood control, can play a significant role to establish effective management of water resources.

In order to make reservoir operation more efficient, forecast information on hydrological condition in the target river basin plays an important role. Better foreseeing the future situation of the target river basin with consideration of forecast information may provide a better decision making for water release strategy from the target reservoir. Such hydrological forecasts, however, essentially contain uncertainty as it is technically difficult to perfectly predict future situations. Consideration of uncertainty in forecasts is therefore important for decision making in reservoir operations using hydrological forecasts.

On the other hand, various operational ensemble hydro-meteorological predictions have been provided by meteorological or hydrological authorities in many regions. The ensemble prediction technique, which conducts multiple numerical forecasts with different initial conditions, is expected to enable to estimate not only

D. Nohara (✉) · T. Hori
Disaster Prevention Research Institute, Kyoto University, Gokasho, Uji 611-0011, Japan
e-mail: nohara.daisuke.2v@kyoto-u.ac.jp

Y. Nishioka
Graduate School of Engineering, Kyoto University, Kyoto University Katsura Campus, Nishikyo, Kyoto 615-8540, Japan

Y. Sato
Faculty of Agriculture, Ehime University, 3-5-7 Tarumi, Matsuyama 790-8566, Japan

P. Gourbesville et al. (eds.), *Advances in Hydroinformatics*,
Springer Water, DOI 10.1007/978-981-287-615-7_23

future conditions but also uncertainty contained in the prediction by seeing variance in the situations, respectively, predicted by the numerical forecasts. Such information on uncertainty of prediction can be important for more robust decision making in the real-time reservoir operation.

From the viewpoint that considering ensemble hydrological prediction may improve real-time reservoir operation, various studies have been conducted in recent years. Faber and Stedinger (2001) proposed an optimization method of an existing reservoir system for drought management considering operational ensemble streamflow prediction [2]. They combined three dynamic programming (DP) models for optimization with weekly updated forecast information derived from ensemble streamflow prediction (ESP) of the United States National Weather Service. Kim et al. [3] developed an optimization model for operational policies of Korean multi-reservoir system by using DP models with monthly updated ESP, and confirmed that reservoir operations optimized by stochastic dynamic programming (SDP) models with ESP showed better performance than those without ESP [3]. Nohara et al. [4] investigated optimizing process of reservoir operation by DP models including SDP and sampling stochastic dynamic programming (SSDP) models with operational one-month ensemble forecast of precipitation provided by Japan Meteorological Agency (JMA) for more effective drought management by a reservoir [4]. On the other hand, Alemu et al. [5] developed a decision support system for reservoir operation for power generation considering ESPs to help reservoir managers with planning operation strategy by showing expected condition of streamflow and the target reservoir [5].

These studies mainly focus on long-term reservoir operation for water utilization, as the ensemble predicting technique has been mainly introduced into operational forecasts on long-term hydro-meteorological conditions which is difficult to be estimated deterministically. It is, however, considered that real-time reservoir operation for flood management can also be enhanced by considering ensemble hydrological predictions especially with medium temporal ranges, from several days to a week. Although some studies such as Masuda and Oishi [6] have introduced ensemble hydrological predictions into real-time reservoir operation for flood management, number of such studies has been small, compared with those considering drought management by reservoirs.

In this study, a real-time operation method of a single multi-purpose reservoir for flood management considering medium-term ensemble hydrological prediction is discussed. Preliminary release operation, which releases storage water from a reservoir in advance of arrival of flood waters so as to prepare empty storage volume much enough to control the flood, is considered. Ensemble streamflow prediction is calculated from One-week Ensemble Forecast of precipitation provided by JMA by using Hydrological River Basin Environment Assessment Model (Hydro-BEAM). Ensemble estimation of expected states of the target reservoir is then conducted by simulating reservoir operation according to its operation rules considering each member of the ensemble streamflow prediction, in order to consider possible situations and uncertainty derived from the prediction. A method to provide information on possible situations and their uncertainty to support preliminary release

operation of a single multi-purpose reservoir considering the ensemble streamflow prediction is investigated through a case study with a Japanese existing reservoir.

2 Outline

2.1 Operational Ensemble Forecast of Precipitation in Japan

Ensemble prediction technique is introduced into medium-term and long-term operational ensemble meteorological forecasts in Japan. They include one-week forecast, one-month forecast, and seasonal forecasts such as three-month and six-month forecasts. Because this study focuses on reservoir's flood management for which hydrological prediction for the coming several days is generally important in Japan, One-week Ensemble Forecast of precipitation provided by One-week Ensemble Prediction System (EPSW) of JMA is considered in this study.

Specs of One-week Ensemble Forecast employed in this study are summarized as shown in Table 1. The forecast provides predicted precipitations accumulated for every six hours for the coming 192 h (eight days), as grid point values (GPVs) by 1.25 with 51 ensemble members.

2.2 Preliminary Release Operation of Reservoirs in Japan

Securing more empty storage capacity enlarges the ability of a reservoir to control flood waters. Many reservoirs in Japan therefore have restriction of storing water to decrease their water level during the flood season so that they can control flood waters in the river by storing water with the secured empty capacity in case of a flood event. However, keeping low water level may cause adverse impacts for water utilization such as water supply or power generation, especially when demands for such utilization of water are large in the flood season. In order to meet the needs for both flood management and water utilization, preliminary release operation has

Table 1 Specs of One-week Ensemble Forecast of JMA considered in this study

Spatial range	Spatial resolution	Temporal range	Temporal resolution	Update frequency	Number of members
22.5°N–71.25°N 90°E–180°E (Japan Area)	1.25° grid	192 h	6 h	1 day	51

As of February in 2013, the temporal range has been extended to 264 h since March in 2013. Update frequency and number of members have also been changed since February 2014

been introduced into multi-purpose reservoirs in the regions where both the floods and water scarcity are issues in Japan.

In the preliminary release operation, the reservoir keeps high water level for water utilization under non-flood situation. When a flood is expected in the river basin where the reservoir is located, water level is decreased by releasing water from the reservoir in advance of the arrival of flood so as to secure empty storage enough to control the flood water. Water level is then recovered by storing the flood water at the end of the flood event. By this operation, reservoir storage can always be maintained as much as possible for water utilization without interfering flood control by the reservoir in case of floods.

Because reservoir managers need to estimate future hydrological condition in the target river basin in order to conduct preliminary release effectively, real-time hydrological predictions play a significant role in the operation. Hydrological predictions for the coming several hours to several days are important for the estimation of timing and scale of a flood event, as rain waters received by the basin generally runoffs within several hours due to steep river conditions and a flood event lasts for several days. It is also important to take prediction's uncertainty into account when they make a decision for the operation, as wrong estimation of the future condition can lead to inappropriate operation that may push the reservoir into a dangerous situation. Thus, it is considered that one-week ensemble hydrological prediction, from which uncertainty contained in the prediction can be estimated, can enhance preliminary release operation of reservoirs.

2.3 Framework of Preliminary Release Operation Considering Ensemble Streamflow Prediction

The framework of the proposed method of reservoir's preliminary release operation for flood management considering JMA's One-week Ensemble Forecast is summarized as follows. Firstly, ensemble prediction of basin precipitation for the coming eight days is estimated from GPVs of One-week Ensemble Forecast of precipitation provided by JMA. Ensemble prediction of streamflow of the target river basin for the coming eight days is then calculated from the ensemble prediction of basin precipitation by use of Hydro-BEAM. Expected states of the reservoir for the coming eight days on the occurrence of each member of the ensemble streamflow prediction are subsequently estimated, and decision of preliminary release operation is made considering the estimated states of the reservoir. The flow described above is shown in Fig. 1.

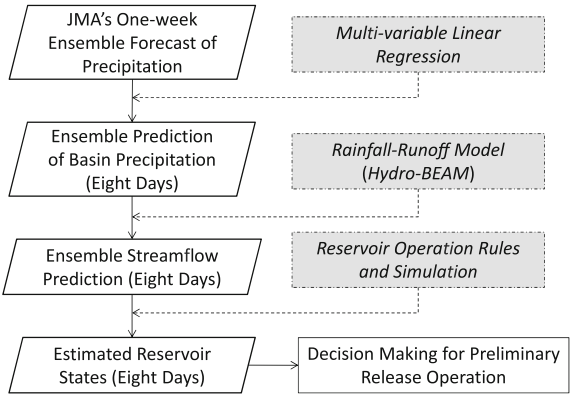

Fig. 1 Flow of the preliminary release operation of a reservoir considered in this study

3 Methodology

3.1 Calculation of Ensemble Basin Precipitation Prediction

Ensemble hourly streamflow prediction for the coming eight days is calculated from JMA's One-week Ensemble Forecast of precipitation. Firstly, hourly precipitations for the coming eight days are calculated from GPVs of six-hourly precipitations forecasted by JMA's One-week Ensemble Forecast. Forecasted GPVs of precipitations at grid points around the target river basin are considered here, and hourly precipitation sequence for the coming eight days at each considered grid point is respectively calculated from the six-hourly precipitation sequence forecasted by JMA's One-week Ensemble Forecast for that grid point. This calculation is respectively conducted for each member of JMA's One-week Ensemble Forecast, and 51 hourly precipitation predictions are respectively calculated for each considered grid point. Prediction of hourly basin precipitations for the coming eight days is then calculated from the hourly precipitation prediction sequence estimated for the considered grid points of JMA's One-week Ensemble Forecast Model. A multi-variable regression model is developed to estimate statistical relationships between forecasted GPVs of hourly precipitation at the considered grid points and hourly basin precipitation by use of historical data of observation and the forecast. Prediction of hourly basin precipitation for the coming eight days is calculated from the forecasted GPVs by using the estimated regression equation. The regression equation is described as the following equation:

$$p(t, m, l) = a_0 + \sum_{i=1}^{I} a_i x_i(t, m, l), \tag{1}$$

where $p(t, m, l)$ denotes hourly basin precipitation of member m predicted at period (h) t for l hours ahead, a_0 is intercept, a_i denotes regression coefficient for explaining variable i, I is total number of considered grid points, and $x_i(t, m, l)$ is the forecasted GPV of hourly precipitation predicted by member m at period t for

l hours ahead at grid point i as explaining variable i. The estimation is respectively conducted from each ensemble member of forecasted GPVs to generate ensemble prediction of basin precipitation with 51 members.

3.2 Calculation of Ensemble Streamflow Prediction

Hourly ensemble streamflow prediction is subsequently calculated for the coming eight days from the prediction of hourly basin precipitation estimated through the previous process. The Hydro-BEAM, which is a cell concentrated type distributed rainfall-runoff model developed by Kojiri et al. [7], is used to calculate streamflow prediction from the predicted basin precipitations. Hydro-BEAM divides each square-shaped grid cell into a pair of rectangular hill slopes and one river channel. The soil condition of each grid cell is represented as multi-layers, including the upper soil (layer A), where runoff flow is assumed to be surface flow, and the two lower soil layers (layers B and C) where a multi-layer linear storage function model is assumed to calculate base flows. Surface flow and sub surface flow are calculated by a kinematic wave model. The spatial resolution (grid size) is 1 km, and deeper infiltration as well as long-term ground water storage is not considered in this study. Five land uses (namely, field, forest, urban area, paddy field, and water body) are considered for land surface and the upper layer (layer A) of a non-river grid cell, and different parameters for soil and flow are respectively employed based on the land use. On the other hand, river streamflow is calculated by a kinematic wave model for a river grid cell. Flow directions are estimated by considering digital elevation data within a grid cell as well as between adjacent grid cells.

The basic equations of Hydro-BEAM are summarized as below. (For further details, see Kojiri [8] or Sato et al. [9].) Runoff processes on land surface and in layer A of a grid cell which is not river channel are calculated by a kinematic wave model. Runoff water amount is calculated assuming that surface flow follows Manning's equation, and that sub-surface flow follows Darcy's law. Both the runoff water amounts are calculated by the following equations:

$$\frac{\partial h}{\partial t} + \frac{\partial q}{\partial x} = f\gamma, \tag{2}$$

$$q = \begin{bmatrix} \alpha(h-d)^m + ah \\ ah \end{bmatrix}, \quad \text{when} \quad \begin{bmatrix} h \geq d \\ h < d \end{bmatrix}, \tag{3}$$

$$d = D\lambda, \quad \alpha = \frac{\sqrt{\sin\theta}}{n}, \quad a = \frac{k\sin\theta}{\lambda}, \quad m = \frac{5}{3}, \tag{4}$$

where h is the water level (depth) (m), q denotes the discharge per unit depth (m^3s^{-1}), f is the direct runoff rate, γ represents effective rainfall intensity (ms^{-1}), d is the saturated storage level (m), D denotes the depth of the layer A, $\sin\theta$ is the slope

gradient (radian), n denotes the Manning's roughness coefficient ($m^{-1/3}s$), a is a constant for Darcy's flow, k is the saturated hydraulic conductivity and λ denotes the effective porosity, respectively. The values for direct runoff rate f and Manning's roughness coefficient n are respectively decided for each land use pattern of the surface.

On the other hand, water flows in the layers B and C are calculated by use of a storage function model described as the following equations:

$$\frac{\partial S_B}{\partial t} = I_B - O_B, \quad O_B = (k_{BH} + k_{BV})S_B, \tag{5}$$

$$I_B = (1 - f)\gamma, \tag{6}$$

$$\frac{\partial S_C}{\partial t} = I_C - O_C, \quad O_C = k_{CH}S_C, \tag{7}$$

$$I_C = k_{BH}S_B, \tag{8}$$

where S_B and S_C are, respectively, storage depths (m) in the layer B and the layer C, I_B and I_C are, respectively, runoff inputs (m^3s^{-1}) to the layer B and the layer C, O_B and O_C are, respectively, runoff outputs (m^3s^{-1}) to the river channel in the grid cell from the layer B and the layer C, k_{BH} and k_{BV} are, respectively, the horizontal and vertical runoff coefficients (s^{-1}) of the layer B, and k_{CH} is the horizontal runoff coefficient (s^{-1}) in the layer C. Vertical infiltration from the layer C is not considered in this study with the assumption that layer C has the impermeable bed.

In regard to a grid cell of a river grid cell, water flow is calculated by a kinematic wave model for open channel. Assuming that cross-sectional shape of a river is triangle, runoff process in a river grid cell is represented by the following equations:

$$\frac{\partial E}{\partial t} + \frac{\partial Q}{\partial x} = q_{in}, \tag{9}$$

$$Q = \alpha_M A^{\frac{4}{3}}, \tag{10}$$

$$\alpha_M = \frac{\sqrt{I_r}}{n}\left[\tau \Big/ \left(2\sqrt{1+\tau^2}\right)^2\right]^{1/3}, \tag{11}$$

$$\tau = \frac{B}{H}, \tag{12}$$

where E denotes the section area of water flow (m^2), Q denotes the flow discharge (m^3s^{-1}), q_{in} is the lateral inflow discharge per unit length (m^3s^{-1}), α_M is the constant of Manning's equation, I_r represents the channel slope, n denotes the Manning's friction coefficient of equivalent roughness ($m^{-1/3}s$), τ is the river bank slope, B is the channel width (m) and H is the water depth (m) at maximal flood level which is assumed to be design flood level.

Streamflow prediction is calculated by use of Hydro-BEAM from each member of ensemble precipitation prediction estimated in the previous process. Ensemble streamflow prediction can be obtained by aggregating the streamflow predictions calculated from every ensemble precipitation prediction.

3.3 Estimation of Reservoir States for Decision Making of Preliminary Release Operation

The target reservoir's future states are then estimated from the ensemble streamflow prediction calculated in the previous process. Reservoir's storages and water releases at every time step (h) for the coming eight days are estimated from each member of ensemble streamflow prediction through a simulation of reservoir operation based on the actual operation rules of the target reservoir for flood control including preliminary release. Ensemble estimation of reservoir states is obtained by considering all the reservoir operation trajectories estimated for every member of ensemble streamflow prediction. Decision making of preliminary release operation is conducted considering the ensemble estimation of reservoir states and the trajectory of each member in the estimation.

4 Case Study

4.1 Study Area

Proposed method was applied to Nagayasuguchi Reservoir in the Naka River basin in Japan. Nagayasuguchi Reservoir is a multi-purpose reservoir which is operated by Japan Ministry of Land, Infrastructure, Transport and Tourism for flood control, power generation and water supply. Operational characteristics of Nagayasuguchi Reservoir are summarized as shown in Table 2. Nagayasuguchi Reservoir does not have restriction for its storage water level for preparation of flood control during the wet season, which is often seen in the other reservoirs in Japan. Instead, preliminary release operation is employed to secure empty storage volume in advance of the arrival of flood waters as a preparatory operation for flood control. The preliminary release operation of Nagayasuguchi Reservoir consists of two steps: the storage volume is decreased to the height of 222.7 m above the sea level (38,100,000 m^3 in storage volume) by releasing water of 5,397,000 m^3 as the first step of the preliminary release operation if rainfall is predicted after inflow to the reservoir exceeds 70 m^3/s; and the storage volume is decreased to the height of 219.7 m above the sea level (32,537,000 m^3 in storage volume) by releasing water as the second step of the preliminary release operation if inflow to the reservoir exceeds 500 m^3/s. By the two steps of the preliminary release operation, storage water of

Table 2 Operational characteristics of Nagayasuguchi Reservoir

Active storage capacity (m^3)	43,497,000
Water use capacity (for power generation and water supply) (m^3)	43,497,000
Flood control capacity (m^3)	10,960,000
Storage volume to be released by the first stage of preliminary release operation (m^3)	5,397,000
Storage volume to be released by the second stage of preliminary release operation (m^3)	10,960,000
Designed inflow to start flood control operation (m^3/s)	2,500
Designed flood inflow (m^3/s)	6,400
Designed release discharge for flood control (m^3/s)	5,400
Maximal release discharge in case of non-flood situation (m^3/s)	500

10,960,000 m^3 is released in order to secure empty volume as much as the flood control capacity. On the other hand, water release amount calculated by the following equation is conducted during the flood control operation after inflow exceeds 2,500 m^3/s:

$$r_t = 0.774(i_t - 2500) + 2500, \tag{13}$$

where r_t and i_t are, respectively, water release (m^3s^{-1}) and inflow (m^3s^{-1}) at time step t.

4.2 Development of Models for Prediction of Basin Precipitation and Inflow

Linear regression models to estimate precipitation in the target river basin from forecasted GPVs of JMA's One-week Ensemble Forecast were developed by use of historical data during the wet season (from May to October) since 2006 to 2009. Seven precipitation gauges in the catchment of Nagayasuguchi Reservoir were considered as objective variables, and a linear regression model was developed to estimate precipitations at every precipitation gauge. Ensemble mean predictions of precipitation forecasted by JMA's One-week Ensemble Forecast for the six grid points around the catchment of Nagayasuguchi Reservoir were considered to be candidates of explaining variables of the regression model. As a result of comparison in deterministic coefficient, the forecasted precipitation for the grid point (33.75°N, 133.75°E) which is nearest to the target catchment was chosen as the explaining variable of the linear regression model for prediction of precipitation at every precipitation gauge. The basin precipitation was calculated by simply averaging the predicted precipitations at the seven gauges. On the other hand, as for the rainfall-runoff process, parameters of Hydro-BEAM were adjusted so as to maximize reproducibility in streamflows in 12 flood events observed in four years from

2009 to 2012. Only inflow to Nagayasuguchi Reservoir was predicted in this study, by assuming that streamflow condition is assessed at the point just downstream the reservoir to exclude effects of runoffs downstream the reservoir in analyzes of the results for simplification.

4.3 Results

4.3.1 Ensemble Inflow Prediction

Results of the ensemble inflow prediction calculated by Hydro-BEAM from the ensemble precipitation prediction are shown in Figs. 2 and 3. The results of ensemble mean prediction of precipitation in these flood events are also shown in these figures for reference. It can be seen in Fig. 2 (the forecast on Sep. 13th, 2012) that precipitation predicted by the ensemble mean prediction was underestimated through the predicted period. Reflecting the tendency of underestimation in the precipitation prediction, all members of ensemble inflow prediction also underestimated the flood inflow in terms of both the peak flow amount and total inflow volume. On the other hand, it can be seen in Fig. 3 (the forecast on Sep. 28th, 2012) that precipitation prediction showed different patterns in time series from observed precipitation. Precipitation was longer but more moderate in the prediction (ensemble mean prediction) while shorter and intensive precipitation was observed actually. However, some members of the ensemble inflow prediction foresaw the peak of inflow well, and some of them were even greater than actual. It can be considered important from these results to consider each member of a real-time ensemble hydrological prediction in order not to overlook a possibility that a flood event to be controlled by the reservoir would occur.

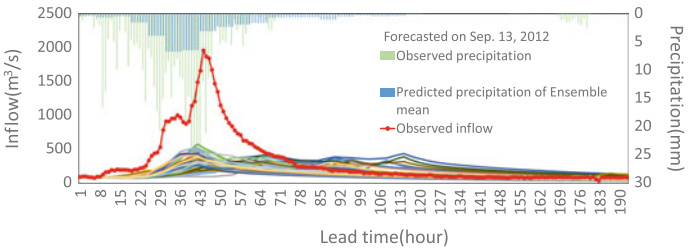

Fig. 2 The result of ensemble inflow prediction based on JMA's One-week Ensemble Forecast of precipitation provided on September 13th, 2012. (Observed peak inflow and total inflow volume during the period were, respectively, 1870.5 m^3/s and 220,953,960 m^3.) All the ensemble members underestimated the peak and total amounts of inflow due to the underestimation in predicted precipitation

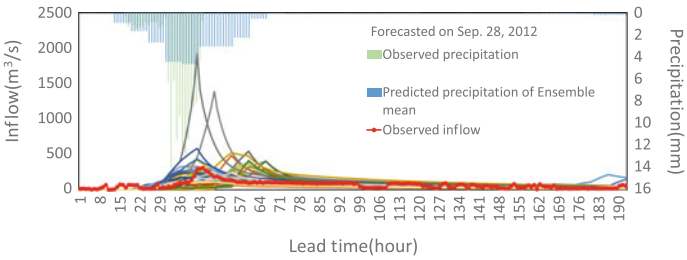

Fig. 3 The result of ensemble inflow prediction based on JMA's One-week Ensemble Forecast of precipitation provided on September 28th, 2012. (Observed peak inflow and total inflow volume during the period were, respectively, 310.8 m^3/s and 47,868,120 m^3.) Observed inflow fell within the range predicted by members of the ensemble inflow prediction although longer but less intensive precipitation was predicted in the ensemble mean precipitation prediction

4.3.2 Estimation of Reservoir States

Considering the calculated ensemble inflow predictions, states of Nagayasuguchi Reservoir for the coming eight days (192 h) were estimated as ensemble predictions of reservoir states. The results of the estimated storage volumes using the forecast provided on September 13th in 2012 are shown in Fig. 4. It can be seen in Fig. 4 that trajectories of reservoir storage in the early part of the forecasted period can be classified roughly into two groups: one conducted only the first step of the preliminary release operation, and the other group conducted both of the two steps of the preliminary release operation. This is because the preliminary release operation at Nagayasuguchi Reservoir consists of binary decisions that is to decide whether

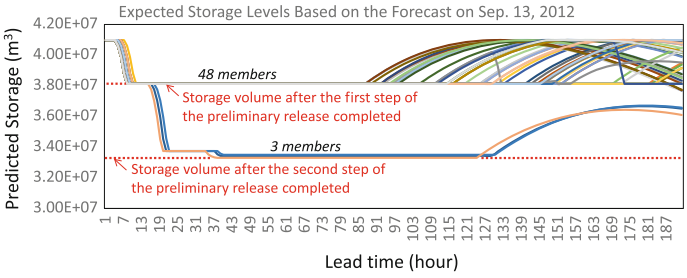

Fig. 4 The result of ensemble estimation of expected storage volumes for the coming 192 h from Sep. 13th, 2012, if Nagayasuguchi Reservoir is operated according to its operation rules for flood control including preliminary release assuming that each ensemble member of the inflow prediction becomes reality. Preliminary release was conducted to the second step in three ensemble members (scenarios) while it was conducted only to the first step in 48 members (scenarios). A variety can be seen in the amount of storage recovery in the latter part of the forecasted period according to the predicted situation of each member of the ensemble inflow prediction, which would give information on possible reservoir states and their uncertainty associated with decisions for preliminary release operation

preliminary release to be conducted or not at each step. With such operation rules, expected reservoir states for the ensemble members may aggregate into a limited number of states even if there is a variety among members in the ensemble inflow prediction. Moreover, most ensemble members (48 out of 51 members) were classified into the first group which conducted only the first step of the preliminary release operation, and only the three member prepared empty volume as much as designed (10,960,000 m^3). As it can be seen in Fig. 2, the peak flow of the flood event was near 1,961 m^3/s) which is greater than the designed flow rate to start flood control operation (500 m^3/s). Thus, the three members which lowered the water storage to the designed storage volume by conducting the second preliminary release operation was the correct operation as a result. This indicates that number of ensemble members which are likely to present the similar trajectory do not always foresee the true condition, hence ensemble members presenting minority trajectories also need to be paid attention in order to avoid failing in flood control.

4.3.3 Analysis for Decision Making of Preliminary Release Operation

Effect of preliminary release operation based on a specific member of the ensemble inflow prediction was analyzed considering four flood events observed in 2012. The reservoir operation was evaluated from the two points of view here: whether it conducted preliminary release operation correctly or not, and whether water storage was recovered to the designated storage (43,497,000 m^3) after the flood event ended. The peak inflow rate and the total inflow volume of a member of an ensemble inflow prediction were considered for the decision making of preliminary release operation. Reservoir operation based on members of ensemble inflow prediction at four rank orders (1st greatest, 12th greatest, 39th greatest and 1st smallest), respectively, from the two point-of-view in the predicted inflow (peak inflow rate and total inflow volume) are evaluated for comparison. The results can be summarized as shown in Table 3. It can be seen here that only the reservoir operation based on the first greatest member in terms of peak inflow rate in the ensemble inflow prediction conducted preliminary release correctly in all the flood events considered. Reservoir operation based on the other members failed to conduct preliminary release in some flood events. This can be considered because ensemble inflow prediction derived from JMA's One-week Ensemble Forecast's GPVs had a tendency to underestimate flood scale in terms of both the peak inflow rate and total inflow volume in this case study and could not foresee the necessity of preliminary release. On the other hand, reservoir operations based on the first greatest member in terms of the peak inflow rate and the total inflow volume failed in a flood event to recover water storage as much as the designated storage volume after the flood event due to conducting unnecessary preliminary release based on the overestimated prediction, while the other operations could recover water storage. As long as we give priority to flood management by the reservoir as it is often seen in Japan, preliminary release operation of the Nagayasuguchi Reservoir should be conducted considering the first greatest member of ensemble inflow prediction

Table 3 Analysis of the effect of preliminary release operation based on a member of ensemble inflow prediction for four flood events observed in 2012

Order in terms of	Order of an ensemble member considered out of 51 members	Number of events in which the preliminary release conducted (rate to the number of events (%))	Number of events in which water storage recovered to the designed storage after flood event (rate to the number of events (%))
Peak inflow rate	1st greatest	4 (100)	3 (75)
	12th greatest (25 % upper)	2 (50)	4 (100)
	39th greatest (75 % upper)	2 (50)	4 (100)
	51st greatest (1st smallest)	2 (50)	4 (100)
Total inflow volume	1st greatest	2 (50)	3 (75)
	12th greatest (25 % upper)	2 (50)	4 (100)
	39th greatest (75 % upper)	2 (50)	4 (100)
	51st greatest (1st smallest)	2 (50)	4 (100)

from these results if we consider a specific ensemble member, while there would be a possibility as much as 25 % to fail in recovering water storage after the floods' end. Although the number of analyzed flood events was small and it should not be concluded with this case study, this kind of analysis on effect and uncertainty of ensemble inflow prediction may provide an important idea on effects and risks to reservoir operation when the ensemble prediction is considered in real-time reservoir operation.

5 Conclusions

Reservoir's real-time preliminary operation method for flood management considering JMA's One-week Ensemble Prediction of precipitation was investigated in this study. Ensemble inflow prediction for the coming eight days was calculated from the predicted precipitation by JMA's One-week Ensemble Forecast by use of Hydro-BEAM. Ensemble estimation of expected states of the target reservoir for the coming eight days was conducted by simulating reservoir operation according to its operation rules considering each member of the ensemble inflow prediction, in order to consider possible situations and uncertainty derived from the prediction. Through the case study on Nagayasuguchi Reservoir, it was demonstrated that expected reservoir states may be aggregated into a small pattern when decision for

reservoir operation consists of a combination of binary decisions, even if a large variety is seen in the ensemble inflow prediction. It was also presented that analysis on the expected future states of the target reservoir based on each member of the ensemble inflow prediction could effectively show potential effects and risks in preliminary release and water recovery after flood events. Such information can be considered useful for decision making in preliminary release operation for more robust operation of reservoirs. However, the number of flood events and reservoirs was small in this study. Further investigations with a larger set of dataset and flood events are therefore considered necessary to develop a more effective way of decision making for preliminary release operation, considering operational ensemble hydrological predictions. A more flexible method of decision making for preliminary release operation could also be sought by considering relationships between storage capacity and total inflow volume derived from ensemble hydrological predictions while existing fixed decision making criteria were considered in this case study.

Acknowledgements This work was supported by JSPS KAKENHI Grant Number 25420523. Data of One-week Ensemble Forecast of JMA, which has been collected in Kyoto University Active Geosphere Investigations for the 21st Century COE Program and been offered on the web site of GFD Dennou Club, was used in this study. The authors would like to express sincere appreciation to all of them.

References

1. IPCC. (2013). *Climate Change 2013: The Physical Science Basis* (1535 pp). Cambridge, United Kingdom and New York, NY, USA: Cambridge University Press (Stocker, T. F., D. Qin, G. -K. Plattner, M. Tignor, S. K. Allen, J. Boschung, A. Nauels, Y. Xia, V. Bex & P.M. Midgley (eds.) Contribution of Working Group I to the Fifth Assessment Report of the Intergovernmental Panel on Climate Change).
2. Faber, B. A., & Stedinger, J. (2001). Reservoir optimization using sampling SDP with ensemble streamflow prediction (ESP) forecasts. *Journal of Hydrology, 249*, 113–133.
3. Kim, Y. O., Eum, H. I., Lee, E. G., & Ko, I. H. (2007). Optimizing operational policies of a Korean multireservoir system using sampling stochastic dynamic programming with ensemble streamflow prediction. *Journal of Water Resources Planning and Management, 133*(1), 4–14.
4. Nohara, D., Tsuboi, A., & Hori, T. (2009). Long-term reservoir operation optimized by DP models with one-month ensemble forecast of precipitation. *IAHS Publications, 331*, 284–295.
5. Alemu, E. T., Palmer, R. N., Polebitski, A., & Meaker, B. (2011). Decision support system for optimizing reservoir operation using ensemble streamflow predictions. *Journal of Water Resources Planning and Management, 137*(1), 72–82.
6. Masuda, H. & Oishi, S. (2013). Study on optimization of the integrated operation using ensemble prediction in the upper reaches of the Nabari river. In *Proceedings of the 35th IAHR World Congress*, S10065.
7. Kojiri, T., Tokai, A., & Kinai, Y. (1998). Assessment of river basin environment through simulation with water quality and quantity. *Annuals of Disaster Prevention Research Institute, Kyoto University, 41*(2), 119–134.

8. Kojiri, T. (2006). Hydrological river basin assessment model (Hydro-BEAM). In V. P. Singh & D. K. Frevent (Eds.), *Watershed models* (pp. 613–626). Boca Raton, FL, USA: Taylor & Francis, CRC Press.
9. Sato, Y., Kojiri, T., Michihiro, Y., Suzuki, Y., & Nakakita, E. (2013). Assessment of climate change impacts on river discharge in Japan using the super-high-resolution MRI-AGCM. *Hydrological Processes, 27*, 3264–3279.

Building of a Simulator to Study Low-Head Hydropower Plants Performance

Olivier Bertrand, Fabrice Loiseau, Emmanuelle Lopez, Claude Rebattet, Pierre Roumieu and Bertram Velichorpillai

1 Introduction

Low-head hydropower schemes are those that operate on rivers with a high discharge and head of less than 20 m. Because they operate on a run-of-river basis, the turbines (which are generally of the bulb type) are vulnerable to flow disturbances, especially upstream. Any loss of uniformity caused by disturbance at the intake is immediately felt at the turbine and results in production losses that can quickly become significant.

The goal of the project known as PENELOP2 (Performance ENergétiques, Economiques, et environnementaLes des Ouvrages de Production hydroélectrique de basse-chute—Energy, economic and environmental performance of low-head hydro production structures) is to understand and study the influence of different factors contributing to the flow disturbance through low-head plant. PENELOP2 is

O. Bertrand (✉)
ARTELIA, 6 Rue de Lorraine, 38130 Echirolles, France
e-mail: olivier.bertrand@arteliagroup.com

F. Loiseau
ALSTOM, 82 Avenue Léon Blum, 38041 Grenoble Cedex 9, France

E. Lopez
JKL, 30 Chemin Du Vieux Chêne, 38240 Meylan, France

C. Rebattet
INPG CREMHYG 101 Rue de La Passerelle, Domaine Universitaire, 38402 Saint-Martin D'Hères Cedex, France

P. Roumieu
CNR Laboratoire Hydraulique et Mesures, 4 Rue de Chalon-Sur-Saône, 69007 Lyon, France

B. Velichorpillai
ACTOLL, 30 Chemin Du Vieux Chêne, 38240 Meylan, France

P. Gourbesville et al. (eds.), *Advances in Hydroinformatics*,
Springer Water, DOI 10.1007/978-981-287-615-7_24

a collaborative research project involving major players in the area of hydraulics in France (Compagnie Nationale du Rhône (CNR), Alstom Hydro France, Artelia Eau and Environnement, In Vivo Environnement, Actoll, JKL Consultants and Grenoble INP (CREMHYG laboratory)). PENELOP2 is approved by the Tenerrdis competitiveness cluster, with funding granted in the framework of the 9th Fonds Unique Interministériel (FUI) programme.

2 The Pilot Site: Vaugris Hydropower Plant

The pilot site of the project is the Vaugris hydropower plant, owned by CNR and located on the Rhône river about fifty kilometers downstream of Lyon. It is equipped with four ALSTOM bulb turbines of 6.25 m runner diameter each delivering 18 MW under 6.70 m head. The maximum discharge of each unit is about 350 m^3/s. Unit 4 of the Vaugris site was chosen because the pier situated between the plant and the dam generates transversal asymmetries in the flows, upstream of this unit. This "upstream influence," which can generate performance losses, is an integral part of the parameters to be studied in the context of the PENELOP2 project [3].

The dam is equipped with six spillway gates. The maximum discharge of each gate is about 1 250 m^3/s (Q1000 = 7 500 m^3/s).

3 Different Studies

In order to study the entire hydraulic path and go back to the energy production of the plant, different studies have been conducted during the project. These studies were based on measurements on the Vaugris site, physical models at different scales, and numerical models.

3.1 Measurement on the Site

Three absolute methods were used to do the on-site measurements: Current Meter (CM), Acoustic Scintillation Flow Meter (ASFM), and Acoustic Doppler Current Profiler (ADCP). In addition, the Winter-Kennedy relative method was used to verify the stability of the discharge during the comparative tests and also to compare the relative discharge value with the absolute ones.

The measurement required the fabrication of two steel frames. The first one (18 m high and 12 m wide), supporting the ASFM sensors (thirty acoustic paths) and the ADCP sensors (fourteen sensors), was fitted into the stop-log slot. The

second one, supporting the CM propellers (twenty-two propellers), was inserted vertically into the first one.

Each method was applied without knowledge of the results obtained from the other methods (blind test). Comparisons made on eight selected tests show that the flow rate measurements were much closed (less than 3 % between ADCP, ASFM, and CM methods). This on-site measurement gives a lot of data used, concerning the axial velocity distribution upstream from the turbine. These data were used to validate/calibrate the other tools (numerical and physical models).

3.2 The Physical Models

As measurements are realized on the operational plant, we have used physical models to investigate and analyze the impacts of some new configurations or modifications of the Vaugris run-of-river development.

3.2.1 The Physical Model of the Vaugris Hydropower Plant

A physical model (scale 1/30th) reproducing the Vaugris scheme was achieved by CNR. This model reproduces 500 m section of the entire width of the Rhône River including the hydropower plant and the dam.

The reproduction of the open-channel flows is guaranteed by observing the Froude similarity. These dimensions allow the distribution of velocities upstream of the work and the current patterns downstream to be well modeled. In order to test the influence of the operation of the dam on the velocity fields upstream of the units and more particularly of G4, all six gates are considered.

For the plant, all the four units are modeled. This allows the influence of the operating configuration of units on the current pattern upstream and downstream to be studied.

The turbine in unit 4 is faithfully represented: the body of the bulb, the guide vanes, and the runner with moving blades is modeled. The unit's rotational speed is provided by an electric motor coupled to a velocity controller. In order to reproduce the influence of the rotation of the unit's runner on the flows, the specific velocity similarity is conserved.

For the other units, the representation is simplified: the bulb is not represented in the hydraulic channel. A system of adjustable-opening racks is put in place to reproduce the head loss linked to the unit. An UlatraSon flow-meter placed on each of the draft tubes allows the flows transiting via the units to be measured.

These dimensions allow the distribution of velocities upstream of the works and the current patterns downstream of the works to be reproduced correctly.

Velocity measurements were carried out by micro current-meter and by PIV immediately upstream the turbine (Figs. 1 and 2).

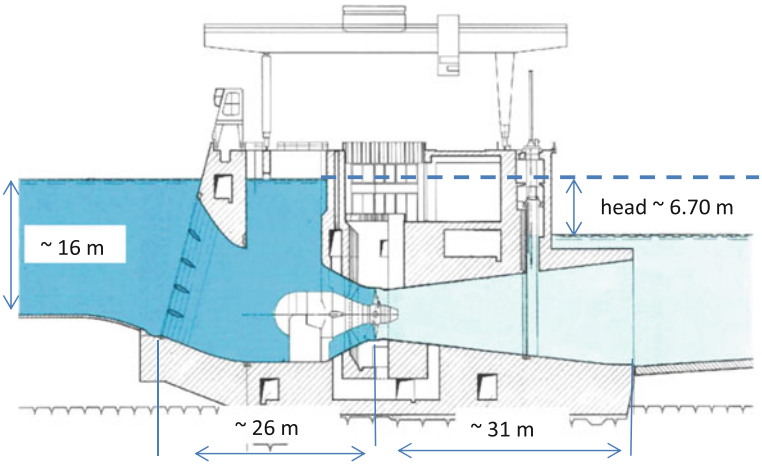

Fig. 1 Cross section of Vaugris hydropower plant

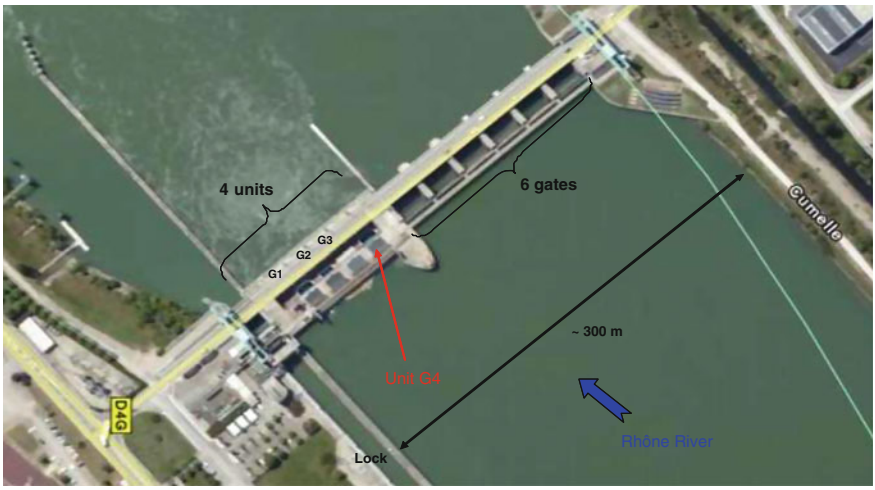

Fig. 2 Plan view of Vaugris hydropower plant

In order to feed the study's mathematical model of the turbine performance and to validate the measurements recorded in situ at the Vaugris site, five vertical and five horizontal planes were put in place at the entry of the unit (see Fig. 3: vertical planes).

This physical model is able to study the impact of modification of the Vaugris run-of-river development on the flow disturbance, but cannot study the performance of the unit according to a large expected operating range in flow and net head. So, in order to obtain this performance in a perturbed situation, another physical model has been built.

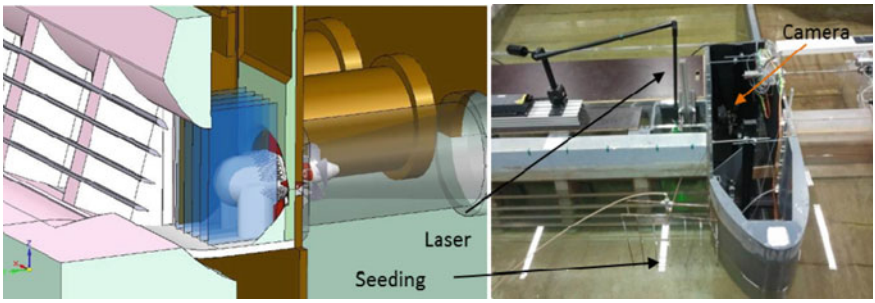

Fig. 3 Vertical PIV measurements on bulb unit G4

3.2.2 An Hydraulic Bench

To investigate perturbations caused by asymmetry of inlet flow stream, the CREMHYG laboratory achieves a tunnel simulating the flow deviation; the main focus is to reproduce the velocity profiles measured on Vaugris plant. For that purpose, deviations are produced by three NACA horizontal profiles located upstream in the bulb of the turbine. Runner effect is not reproduced considering our approach, with the shape of the turbine but without the vanes and the runner. The flowrate is 350 l/s, total length of the tunnel is around 7 m, the measured section is squared with 0.5 m each side. Measurements are plotted in the same section than the vaugris site measurements (the stop-log grooves). By different inclinations of the NACA profiles, it may be possible to intensify the vertical gradient. At the end, these informations may be used to reproduce the deviation during future testings of the reduced scale turbine at ALSTOM laboratory. The ALSTOM test rig will be then able to quantify with a high level of accuracy the effect of this disturbance on the global performance of the bulb turbine.

LDV dualbeam from Dantec measures two components: horizontal Vz along the axis of turbine bulb and vertical Vy from the bottom to the top of tunnel.

3.3 The Numerical Models

All the physical models are focused on the Vaugris hydropower plant. We have then investigated the ability of numerical models to reproduce physical results in order to study in the future, a new plant in another site. For doing that, we have firstly built numerical models applied on Vaugris to validate the methodology.

3.3.1 The Vaugris Reservoir and Unit G4 Models

To meet the objectives of the project, and study hydraulic losses, a numerical model of the currents through the Vaugris reservoir was constructed by ARTELIA by coupling the two softwares Telemac 3D and OpenFOAM [2]. The Telemac 3D model footprint covers the entire low water bed of the Rhône over a distance of about 2 km upstream of the dam [1]. The size of the horizontal mesh segments varies from 1 m, in the immediate vicinity of the water intakes for the four bulb units, to 50 m upstream of the model. The OpenFOAM model [4] runs from 70 m upstream of the inlet to unit G4 (on which instrumentation was placed during the PENELOP2 project), to the outlet from the draft tube downstream of the plant. The grid consists mainly of cubic meshes, the size of which varies from 10 cm to 1 m depending on the area modeled. The grid is refined near the walls and in potentially highly turbulent areas (Fig. 4).

Figure 5 shows comparison between on-site measurements, numerical and physical models. Shapes of the average profiles are very similar for the higher part of the inlet; the discrepancy is greater for the lower part close to the wall.

With these two models, we are now able to study future flow disturbances at the inlet of any unit of a low-head hydropower plant. We are also capable to couple these models with the ALSTOM one which is focused on the bulb turbine and its performance.

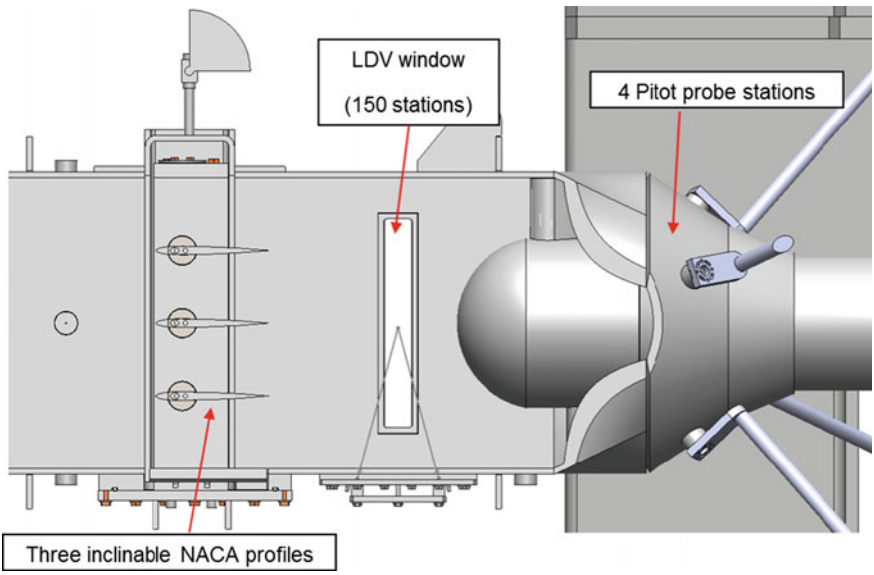

Fig. 4 Water tunnel experimented in the CREMHYG laboratory to simulate flow disturbance

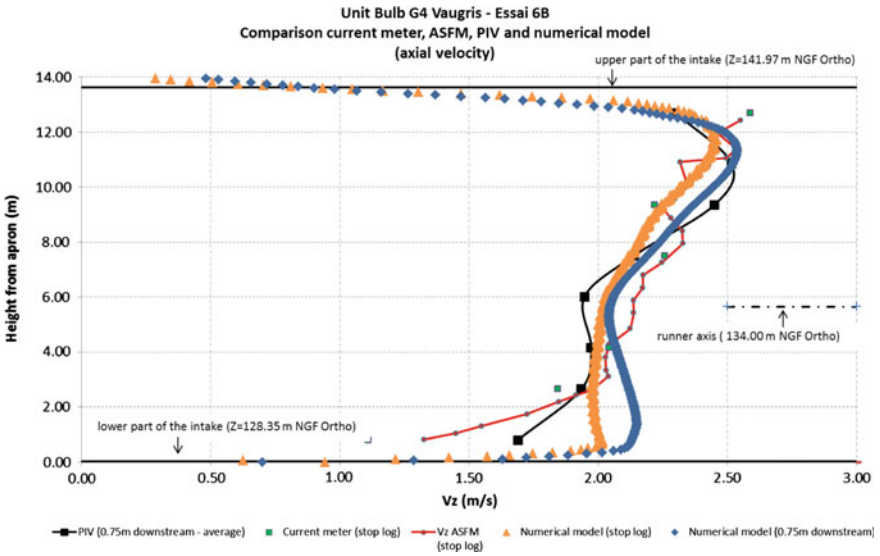

Fig. 5 Comparison of axial velocities measured on-site, by PIV on the CNR physical model and obtained through the model (velocities averaged over the width of the *inlet*)

3.3.2 The Bulb Unit Model

ALSTOM has studied for many years, with numerical models, the unit performance under perfect inflow and outflow hydraulic conditions. Before testing the coupling between this model (built under CFX) with the other ones, and due to schedule requirements, the model has been used to study the impact of an upstream floor slope (Fig. 6).

With such simulations, it is thus possible to monitor the evolution of the head losses along the turbine flow passages and consequently to correct the head losses due to the bottom slope upstream to the turbine intake (Fig. 7).

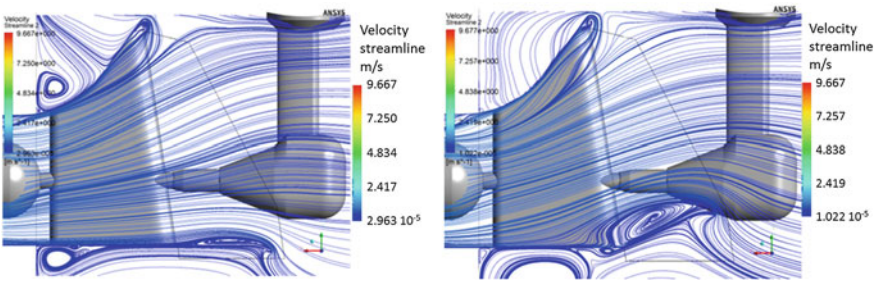

Fig. 6 Comparison of axial velocities measured on-site, hydraulic flow through the turbine intake according to a floor slope (bulbe on the *left*)—(flat floor on the *left* and floor slope on the *right*)

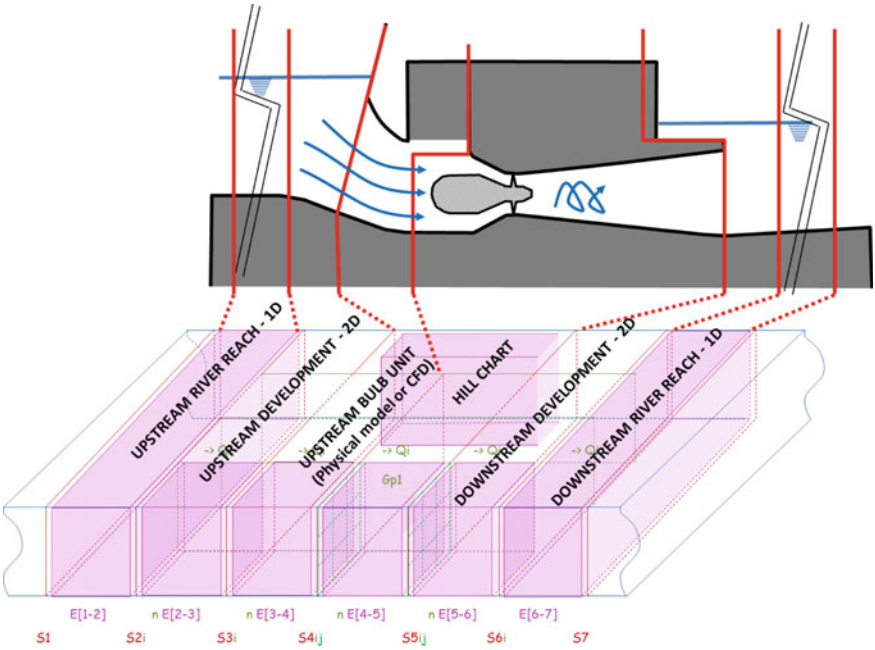

Fig. 7 Conceptual scheme of the simulator applied to the Vaugris plant

4 Simulator of the Energy Performance

At the beginning of the project, we have imagined to build a simulator of the energy performance which will be capable to easily study a project at the feasibility stage. This simulator is now under construction and integrates a large part of the project results.

4.1 Conceptual Model

The simulator of energy performance consists of connectable blocs that represent the different elements from upstream to downstream the low-head hydropower plant. It is based on all the previous results obtained by measurements or the different models.

A building environment has been developed for assembling the different blocs in order to define a specific topology and allocate sets of boundary conditions for calculations.

The simulation is static. Batch of simulations, i.e. scenario can be launched to get the results for sets flow rates and boundary conditions representing a whole year and allows to obtain the corresponding produced energy.

Bloc calculations are based on knowing how and studies realized by the different stakeholders during the project.

4.2 Upstream and Downstream the Plant

In upstream and downstream of the production site, hydraulic variables (flowrate and free surface) are solved by gradually varied flow equations. The simulator considers firstly a single section of the catchment studied (equation of the water line involving the Strickler coefficient) and after a transverse discretization (equations of the water line with lateral exchanges). On the immediate approach of the plant, only numerical and/or physical models can feed the simulator with asymmetries of vertical or transverse flow. All these calculations allow to know the impact, of the river geometry or different elements of civil engineering management (dam, sluice gate, unit entrance, apron …), on the flow that will feed each unit of the power plant.

4.3 Inside the Plant (the Hill Chart)

With ALSTOM models, it is now possible to monitor the evolution of the head losses along the turbine flow passages and consequently to correct the head losses due to any disturbance. Such comparison allows finally to define one head losses law according to the disturbance scale (in the figure below the bottom slope upstream the bulb). The next step is to reproduce other representative disturbances corresponding to hydraulic perturbations we can observe on some power dams. A part of these disturbances will be replicated by the CREMHYG model providing complementary setting of the 3 NACA profiles.

All this procedure allows to measure with accuracy the impact and the modification of the reference turbine hill chart.

We will then put the modified hill charts in the simulator which can model performance of a hydropower plant under different hydrological conditions and by taking interaction between upstream and downstream gross head.

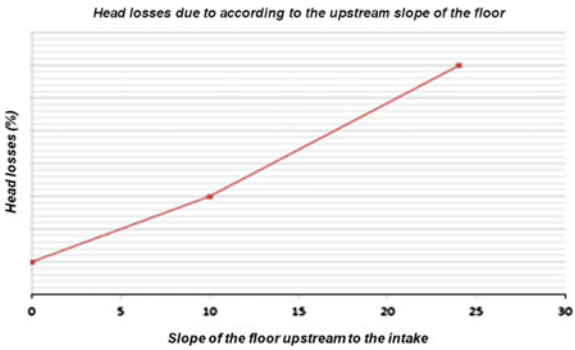

Fig. 8 Head losses law according to the bottom slope upstream the bulb

5 Conclusions

The major aim of the PENELOP project is to understand, qualify, and quantify inadequate performance of hydropower plants. The partners have devised new systems for representing in detail what is observed on-site and have studied the origins and consequences of disturbances in flows. All the studies have defined new ways of monitoring disturbances and have proposed innovative processes and technologies for controlling and correcting them.

During this approach, the pilot site of the Vaugris plant is used to validate physical and numerical models by comparing their results with measurements taken on-site. Indeed, the study of the entire hydraulic path requires different testing methods which are necessary to validate and interlock with each other.

We are now developing a simulator to quantify the impact of current patterns on the performance of the power plant. All the collected data are integrated into this performance software. The advantage to the simulator is that it makes it possible to study new layout configurations easily (Fig. 8).

This tool is still under development, even though many blocks are now built and under test (Fig. 9). The convergence of the simulator remains a key point that will be certainly improved after the project. First, studies should be now performed and an application will be presented at the conference.

In the future, the performance simulator will be used to analyze different configurations for schemes that are going to be built or redeveloped in order to optimize their profitability.

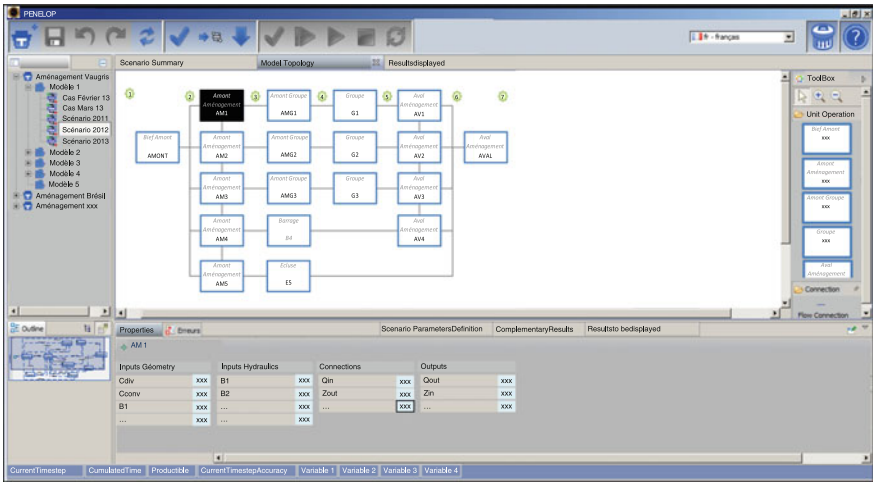

Fig. 9 Graphical user interface of the simulator for energy performance calculations

Acknowledgments This work was carried as part of the PENELOP2 project approved by the Tenerrdis competitiveness cluster, with funding granted in the framework of the 9th Fonds Unique Interministériel (FUI) programme.

References

1. Bertrand, O., Lavedrine, A., Rebai, A., David, E., Pierrefeu, G. & Roumieu, P. (2011). Numerical modelling of the Vaugris reservoir on the Rhône with Telemac 3D. In P*roceeding of the XVIIIth telemac and mascaret user club*, Chatou, France, Oct. 19–21, 2011.
2. Girard, C., Schaguene, J. & Masson A. (2013). Sécurisation de la rive gauche du Rhône and transparence hydraulique du remblai ferroviaire—phase 3, report 8410049-TF3-V5, unpublished, 2013.
3. Roumieu, P., Tomas, L., Cornut, X., Pobanz, K., Chaize, C., Billenness, D. & Bertrand, O. (2012). Assessement of a CNR Bulb turbine flow: Comparison of acoustic scintillation, ADCP, Winter-Kennedy tests with the current meters method (PENELOP2 project). Hydro 2012, Bilbao Spain, Oct. 29–31, 2012.
4. Schaguene, J., Bertrand, O., David, E., Roumieu, P., Pierrefeu, G., Pobanz, K., Cornut, X. & Tomas, L. (2012) The use of numerical modelling to optimize the placement of data gathering equipment in low-head hydro production structures. In *Proceeding of the SimHydro 2012*, Sophia Antipolis—Nice, Sept. 12–14, 2012.

3D Computational Modeling of the Galaube Dam Spillway

Adrien Gellibert, Jérémy Savatier, Nicolas Pépin and Olivier Fully

1 Introduction

The Galaube dam is located in the sector of Montagne Noire, France. It is a rockfill dam of 33 m height. The reservoir volume is 7.7 hm^3. The studies and the project management of the Galaube dam have been done by ISL during the 90s. In 2012 and to complete the dam safety report, a new hydrological study was made by ISL in order to update the information concerning inflow design flood for the dam [1]. It appears that the inflow design flood (10,000 year return period) has increased of about 30 %. In that condition, the evacuation of the design flow by the spillway must be reconsidered.

The spillway is located on the right bank of the Galaube dam. It includes a 28 m reinforced concrete weir with a nappe-shaped crest profile and a concrete spillway channel. Downstream from the spillway channel, there are a bucket and a rockfill reception area (Fig. 1).

Olivier Fully—Institutions des Eaux de la Montagne Noire (IEMN) is the owner of the dam.

A. Gellibert (✉) · J. Savatier · N. Pépin
ISL Ingénierie, Etablissement Sud Ouest, 15 rue du Maréchal Harispe,
64500 St Jean de Luz, France
e-mail: gellibert@isl.fr

J. Savatier
e-mail: savatier@isl.fr

N. Pépin
e-mail: pepin@isl.fr

O. Fully
Institution des Eaux de la Montagne, 102 rue du Lac, Immeuble Les Erables, France
e-mail: o.fully@i-emn.fr

P. Gourbesville et al. (eds.), *Advances in Hydroinformatics*,
Springer Water, DOI 10.1007/978-981-287-615-7_25

Fig. 1 The Galaube dam and the *spillway*

2 Presentation of the Galaube Dam Spillway

The spillway includes the following elements:

- A nappe-shaped free weir, with a developed length of approximately 28 m. This weir is made of reinforced concrete and leveled at the height of 720.5 m NGF,
- A counter sill downstream from the weir reception area,

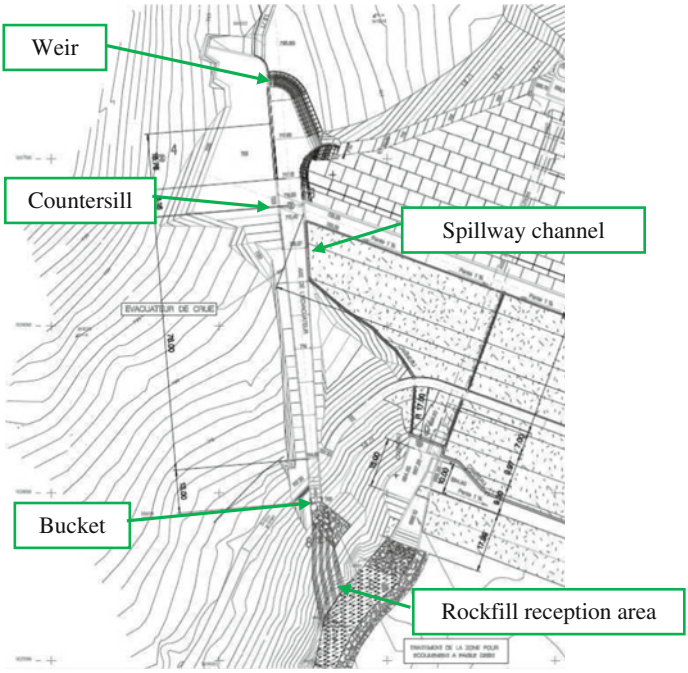

Fig. 2 Drawning of the Galaube dam spillway

Fig. 3 Pictures of the spillway

- A concrete spillway channel, of approximatively 100 m, with a slope of about 8 % in the upper part and a slope of about 33 % in the lower part,
- A concrete spillway bucket, leveled at the height of 701.0 m NGF,
- A rock fill reception area, downstream the bucket, which permits to protect the riverbed.

The following figures present the Galaube dam spillway and all its components (Figs. 2 and 3).

3 3D Computational Fluid Dynamics (CFD) Model Construction and Validation, Spillway Rating Curve

3.1 Presentation of the 3D CFD Model

3.1.1 Geometry

The three-dimensional free surface hydraulic model is performed with ANSYS CFX software. The model area is located between:

- An upstream boundary located approximately 25 m upstream from the dam,
- A downstream boundary located downstream from the rock fill reception area.

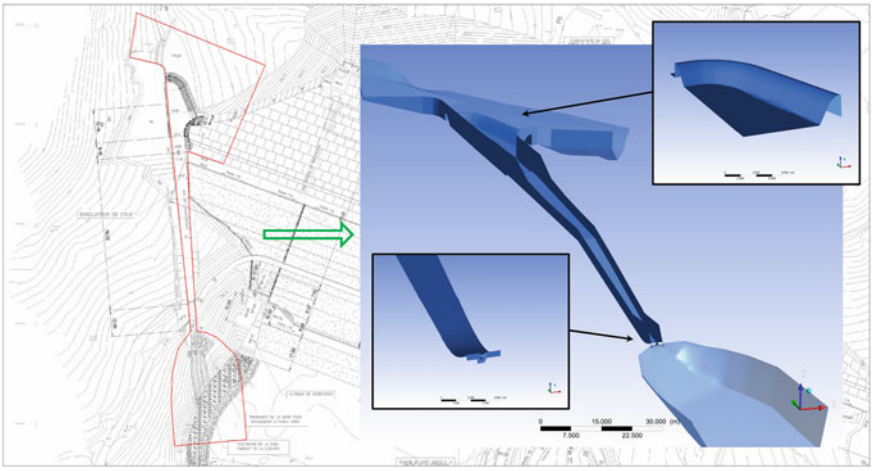

Fig. 4 Localisation and geometry of the 3D CFD model

Geometry is built according to the drawings of the reservoir, dam, and spillway. The figures below present the localization and the geometry of the 3D CFD model (Fig. 4).

3.1.2 Mesh

A tetrahedral mesh is made and setup of about 1.1 million cells. Recommendations in 3D hydraulics modeling require a fine mesh over the spillway weir, with cell size of about 6–7 % of the water height in order to get satisfactory accuracy without excessive duration of computation [2]. Considering the reservoir level at the maximum (721.76 m NGF), the water height on the spillway weir is 1.26 m, and the chosen cell size must be about 8 cm on the spillway weir. However, considering the new inflow design flood for the dam, the new maximum reservoir level is about 722.39 m NGF. Thus, the water height on the spillway weir is 1.89 m, and the chosen cell size must be about 11–13 cm on the spillway weir.

The chosen dimensions of the cells range from 10 to 12 cm at the weir vicinity to 2–3 m for the largest cells in the reservoir. On the spillway and the training wall, the cell sizes are between 50 and 75 cm. The mesh size of 8 cm on the spillway weir is not conserved because it increases the computation time of about 40 %. So, in that case, we just take into consideration the relation above for the reservoir maximum water level. Nevertheless, a sensitivity test on the mesh size is made in order to check if this mesh is enough to give a good representation of the flow into the spillway (Fig. 5).

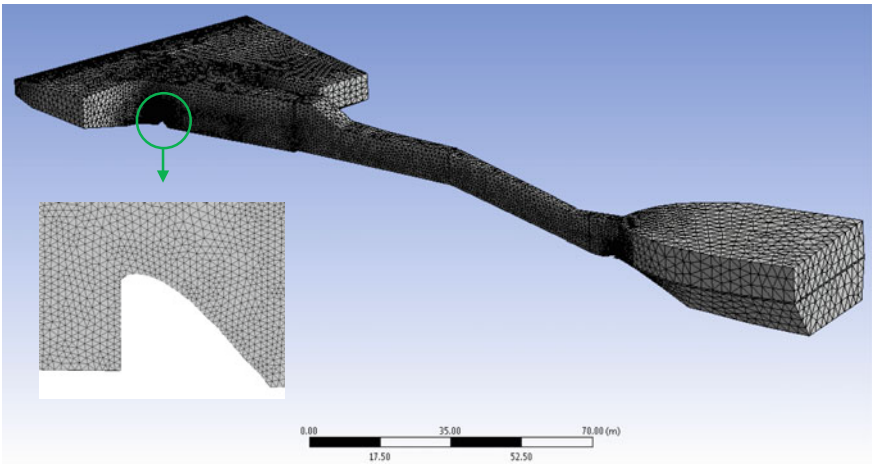

Fig. 5 Tetrahedral mesh

3.1.3 Roughness

The roughness coefficients are introduced on the different faces according to the materials. The 3D CFD model is cut into three sections. In these different sections, the chosen roughnesses are (Figs. 6 and 7):

- For concrete sections (upper part of the spillway channel, training wall …): 5 mm,

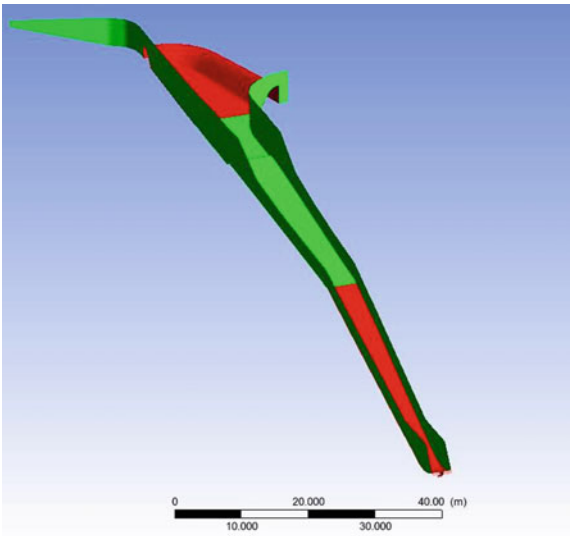

Fig. 6 Localisation of the different concrete roughness coefficients for the spillway—*green*: concrete section, *red*: concrete with materials abraded section

Weir – concrete is abraded

Lower part of the spillway – concrete is abraded and steel is visible

Fig. 7 Pictures of concrete in the weir and the lower part of the spillway

- For concrete sections where the materials are abraded (weir and lower part of the spillway channel are concerned and presented on the following pictures): 10 mm,
- For natural ground: 50 cm.

3.1.4 Turbulence Model

The turbulence model chosen for these simulations is the model $\kappa - \varepsilon$. It is the best turbulence model which allowed convergence of results with acceptable computation time, with the standard parameters of computation.

3.2 *Results of the Model and Sensitivity Tests*

3.2.1 Main Results

First of all, the model is run for two reservoir levels which are close to the maximum reservoir level of water. The aim of these simulations is to check if the flow into the spillway in the 3D CFD model is close to the flow determined in the study of the dam, namely, 80 m^3/s at the height of 721.76 m NGF [3]. The results of the 3D CFD model are:

- For a reservoir level of 721.72 m NGF, the flow into the spillway is 82.2 m^3/s,
- For a reservoir level of 721.80 m NGF, the flow into the spillway is 89.8 m^3/s.

A 7.5 % difference appears between the CFD model and the flow rate obtained during the dam studies. In the CFD model, the flow rate is higher. Nevertheless, the water level in the spillway was determined with a 1D hydraulics model in the 90s. This approach is different and may explain the gap between the results.

The figures bellow present the results of the 3D CFD model: water level and flow velocity (Figs. 8 and 9).

The following figure represents the water level into the spillway for the 3D CFD model. The water level in the spillway channel is close to the water level estimated in the studies of the dam in 1996. Nonetheless, this is just a comparison of the water level and not a setting of the 3D CFD model. Indeed, a setting is only possible on a real measure of the water level, which is not the case here. This comparison highlights the fact that the 3D CFD model is consistent and, even if the rating curve seems to be more important than the initial rating curve, the model allows a good representation of the phenomenon on the spillway. The precision is satisfactory according to the uncertainty on the hydraulics models (Fig. 10).

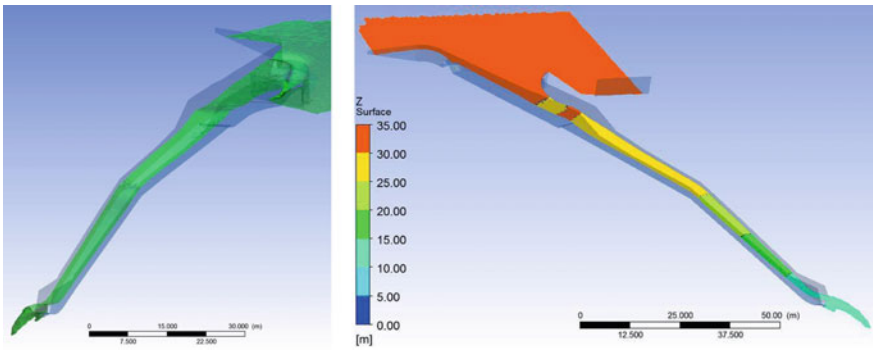

Fig. 8 Free surface and elevation of water

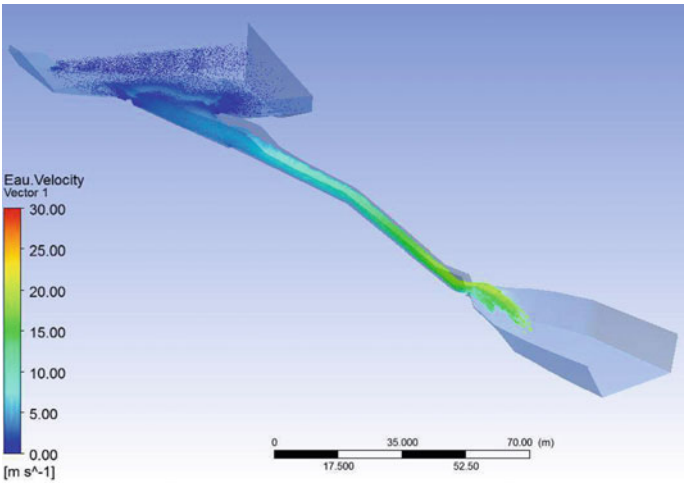

Fig. 9 Water velocity

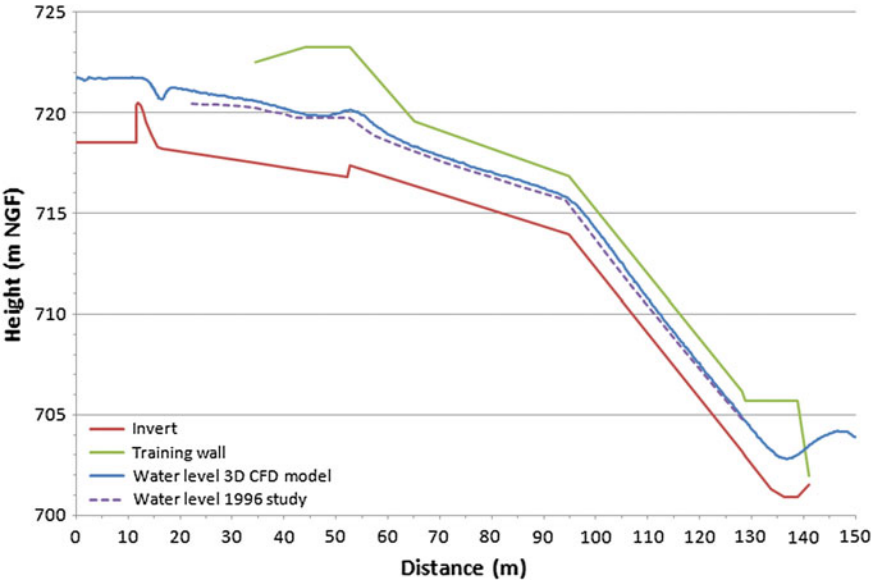

Fig. 10 Water level in the spillway—reservoir water level: 721.72 m NGF, flow rate: 82.2 m^3/s

3.2.2 Sensitivity Tests

Sensitivity tests are lead on the roughness coefficients and the mesh size of the model.

Roughness coefficients
For the simulations, two roughness coefficients were used for the concrete, according to the quality of the concrete. New simulations are made with different roughness coefficients for the concrete surfaces:

- A roughness of 5 mm in every concrete surface,
- A roughness of 10 mm in every concrete surface.

The results are given in the Table 1.

The difference between flow rates into the spillway is very small. Indeed, there is only a 0.2 % difference between the three situations. The influence of the roughness coefficient is considered insignificant.

Mesh size
The initial mesh size is modified to examine the influence of the mesh onto the 3D CFD model. Mesh size is reduced to 20 % on the entire domain. Both models run for the new design flow condition, with a reservoir level of 722.39 m NGF. The following table shows the flow rate into the spillway for the two configurations (Table 2).

For a same reservoir level, the difference between the flow rates into the spillway is small (less than 1 %). Moreover, it is important to point out the fact that:

- The flow rate estimated with the initial mesh size is less than the flow rate calculated with the smaller mesh size. Therefore, the initial mesh seems to give a smaller rating curve for the spillway,
- The computation times are doubled for the mesh size 20 % smaller. The new computation time is about 28 h, when it was 12 h for the initial mesh size (on a standard desk computer).

Similar studies have been made by EDF [2], which came to the same conclusion: in a certain state, reducing mesh size do not lead to an important advantage in terms

Table 1 Flow rate into the spillway for the same water level and different roughness coefficients

Initial simulation: roughness coefficients of 5 and 10 mm (according to the section of the spillway)	Roughness coefficient of 5 mm on every section	Roughness coefficient of 10 mm on every section
64.4 m^3/s	64.5 m^3/s	64.3 m^3/s

Table 2 Flow rate into the spillway for the two meshes configurations

Initial mesh size	Initial mesh size reduced of 20 %
121.4 m^3/s	122.3 m^3/s

of precision, but increase considerably the computation time. For instance, two meshes were compared: the first one presents a mesh size near 6 % of the height of water on the spillway weir; the second one, proposes a mesh size of about 4 % of the height of water. The results show that reducing the mesh size leads to an increase of the model precision of about 0.4 %, but the computation time increase twofold.

Finally, reducing the size of the mesh does not have an important influence on the results of the 3D CFD model, but has an influence on the computation time. The water level difference into the spillway is about ±5 cm between both mesh sizes. The main modifications appear on the counter sill and on the downstream part of the spillway channel.

3.3 Rating Curve of the Galaube Dam Spillway

3.3.1 Rating Curve

The 3D CFD model is used for different reservoir levels, which permits to draw the rating curve of the Galaube dam spillway. The figure bellow presents the rating curve (Fig. 11).

The rating curve obtained by the CFD model is different than the rating curve presented into the dam information file. For small flow rates (less than 60 m^3/s), the

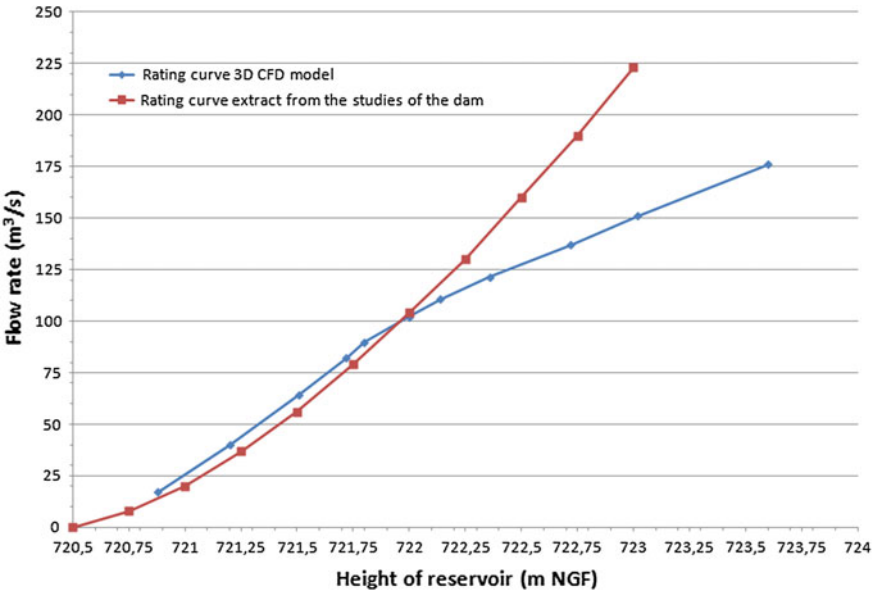

Fig. 11 Rating curve of the Galaube dam spillway

gap between the two curves is near 15 %. For flow rates included between 60 and 90 m^3/s, the gap is reduced to 8–9 %.

For important flow rates (more than 90 m^3/s), a reduction of the rating curve obtained by the 3D CFD model appears. This phenomenon is due to the drowning of the weir.

3.3.2 The Drowning of the Spillway Weir

In order to verify the consistency of the 3D CFD model, the drowning of the spillway weir is studied. In the book "Design of Small Dams" [4] the reduction of a weir discharge coefficient according to the downstream level of water is presented. Thus, the water level upstream and downstream of the weir, obtained thanks to the 3D CFD model, and the information extracted from "Design of Small Dams" allows to estimate the reduction of the weir discharge coefficient.

The following figure presents the discharge coefficient obtained with the 3D CFD model and the application of the Design of Small Dams relation (Fig. 12).

In both cases, for a flow rate higher than 90 m^3/s over the weir, there is a reduction of the discharge coefficient due to the drowning of the weir. Nevertheless, a difference between the two curves appears. The relation taken from the Design of Small Dams is made for a weir placed perpendicularly in a straight channel, which is not the case for the Galaube dam spillway weir. That difference may explain the gap between the two curves. Indeed, according to the Galaube spillway geometry

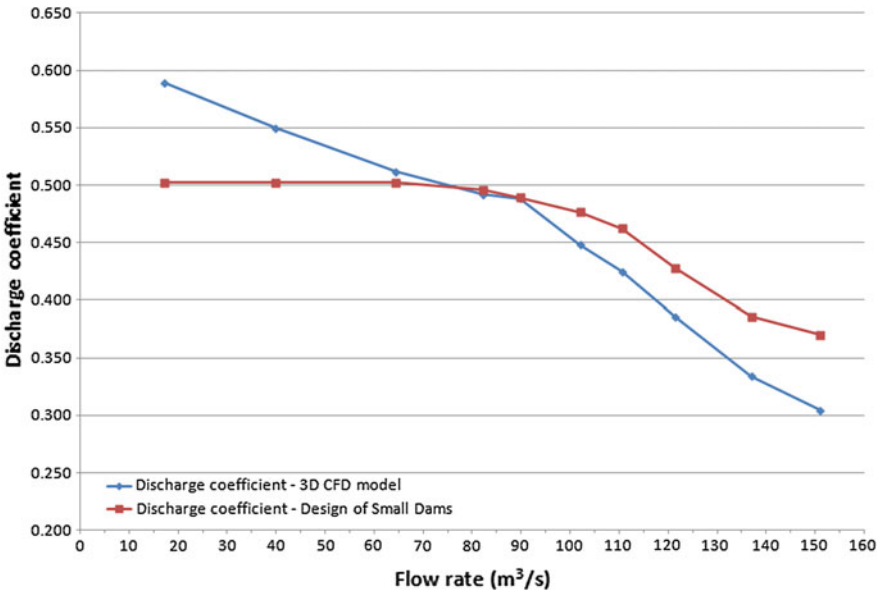

Fig. 12 Evolution of the weir discharge coefficient

(converging area downstream the weir), the reduction of the flow rate must be more important for this spillway.

The following figures present the water level on the spillway weir for different situations: before and after the drowning of the weir, and during the transition. The drowning of the weir can be seen on the third figure (Fig. 13).

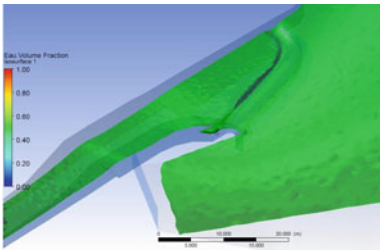

Reservoir level: 721.7 m NGF – Flow rate: 82 m^3/s

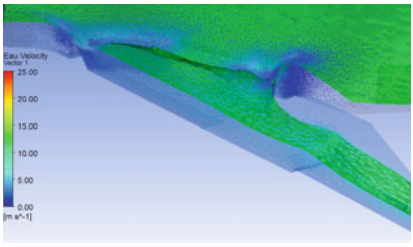

Reservoir level: 721.7 m NGF – Flow rate: 82 m^3/s

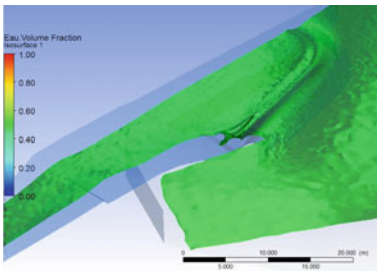

Reservoir level: 721.8 m NGF – Flow rate: 90 m^3/s

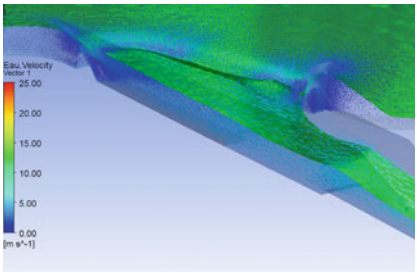

Reservoir level: 721.8 m NGF – Flow rate: 90 m^3/s

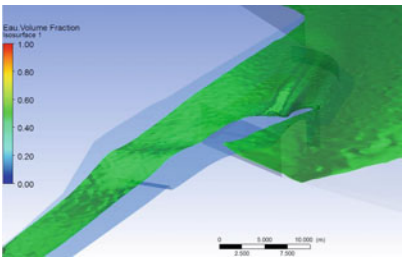

Reservoir level: 722.0 m NGF – Flow rate: 102 m^3/s

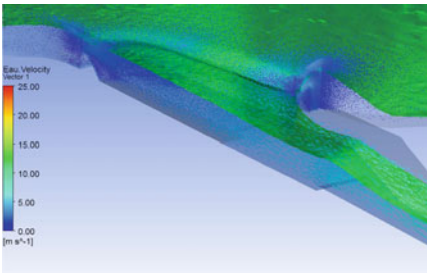

Reservoir level: 722.0 m NGF – Flow rate: 102 m^3/s

Fig. 13 Drowning of the weir

4 Consequences of Flood on the Reservoir and Dam Safety Works

4.1 Reservoir Water Level

The Galaube dam spillway rating curve permits to determine, for different floods entering the reservoir, the level of water in the reservoir and the flow rate evacuated

Table 3 Evacuation of flood (without the outlet conduit)

	1,000 year period of return flood	5,000 year period of return flood	10,000 year period of return flood (design flood)	100,000 year period of return flood (security flood) (1.3 × 10,000 year flow rate)
Flow rate entering the reservoir (m^3/s)	107	153	178	231
Flow rate evacuated by the spillway (m^3/s)	87.7	112.4	122.7	150.6
Reservoir level of water (m NGF)	721.78	722.18	722.39	723.02

by the spillway. That was possible, thanks to a hydrological model representing the reservoir, the spillway rating curve and the flood entering the reservoir. These results are presented in the following table. According to the CFBR (Comité Français des Barrages et Réservoirs) [5], the flood design for a rockfill dam is the 10,000 year return period flood (Table 3).

The new reservoir's maximum level is 722.39 m NGF, which correlates with an increase of 63 cm of the current reservoir's maximum level. The dam freeboard is 86 cm.

4.2 Safety Works

The increase of the reservoir water level and of the flow rate evacuated by the spillway leads to define works to insure the security of the dam.

First of all, it is necessary to check the dam freeboard (vertical distance between maximum reservoir level and elevation of dam crest) and the wave wall stability. It appears that, currently, the Galaube dam can manage the wave action, even for the new reservoir's maximum level of water. Moreover, the wave wall is stable.

Second, the freeboard of the spillway channel training walls has to be reconsidered. Indeed, the new flow rate for the design flood has increased about 50 % compared to the initial flow rate. Currently, the freeboard is not satisfactory to safely insure the evacuation of the design flood, according to the recommendation given by the Design of Small Dams. Moreover, an overflowing over the training wall could be possible for the security flood. In that case, it is necessary to increase the training wall height so as to respect both criteria: on the one hand, the minimum freeboard presented in the Design of Small Dams for the design flood and on the other hand, the safe evacuations of the security flood without overflowing.

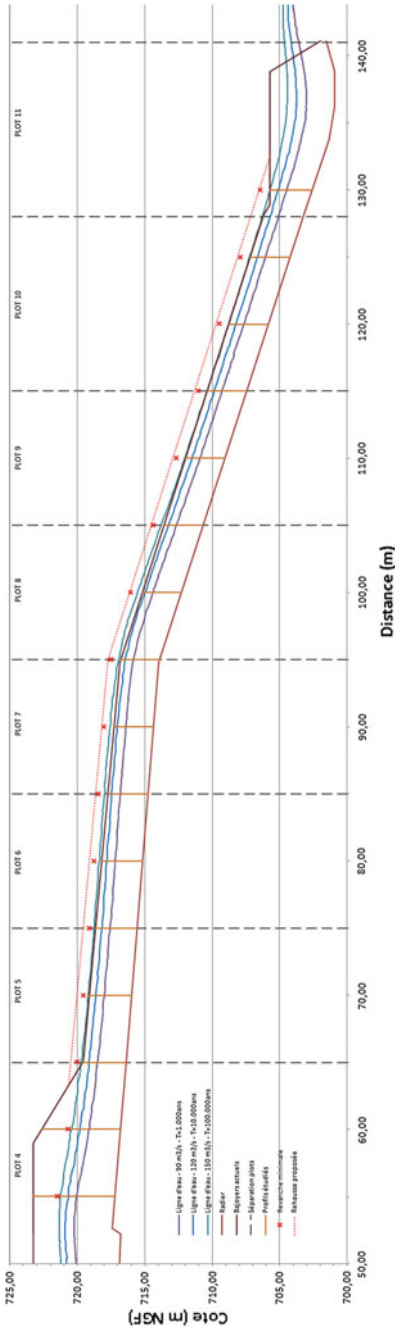

Fig. 14 Minimum freeboard and increase of the training wall height proposed

The following figure presents the new minimum freeboard on the training wall of the Galaube dam spillway. The height is increased to 90 cm (Fig. 14).

Finally, for the new design flood, the gate chamber could be filled of water and thus unattainable. Moreover, the elevation of the access shaft to the intake tower has to be increased in order to avoid overflows from the reservoir to the gate chamber.

5 Conclusion

A 3D CFD model has been developed in order to estimate:

- The Galaube dam spillway rating curve, and thus, determine the maximum reservoir level for new hydrological conditions (10,000 year return period condition),
- The flow characteristics into the spillway.

This model was validated on two points:

- The results of the 3D model were compared to the results of the initial studies,
- The model sensitivity has been tested on the following parameters: roughness coefficients and thinner model mesh size.

Three simulations for a same level storage were made with different roughness coefficients for concrete surfaces. The gap in terms of flow in the spillway is insignificant (of about 0.2 %). As far as the mesh is concerned, in the initial computational model, the mesh size in the area of the weir has been defined with the following relation: one mesh size represents 6–7 % of the water level on the weir. The new mesh size was reduced by 20 % and the gap between the flows on the spillway for a same level storage is less than 1 %.

The spillway rating curve was calculated with the 3D computational model and compared to the rating curve, which was determined during the studies of the Galaube dam. For small flow values, the difference between the two rating curves was not important (about 10 % in certain range of flow). But for important flow values on the spillway (more than 90 m^3/s), the rating curve calculated with the 3D computational model was reduced. This phenomenon appeared as a result of the drowning of the weir and thus reduces the capacity of the spillway for a certain level of storage. The limit-flow rate was estimated at 90 m^3/s. Beyond this value, the weir discharge coefficient decreases because of the drowning.

This new rating curve was introduced in a hydrological model of the Galaube dam reservoir, which allowed obtaining the reservoir water level and the flow rate evacuated for different flood conditions entering the reservoir. This hydrological model gives the new reservoir maximum level for the design flood.

Finally, all these results permit to define safety works to insure the safety of the dam. Additional studies, focusing on the dam and the spillway, were lead. For the dam, the freeboard and the wave wall stability were checked. It appears that the current wave wall can manage the new reservoir's maximum level. As far as the

spillway is concerned, the current freeboard is not sufficient for the design flood. The heights of the training walls have to be increased (of about 90 cm at most). Moreover, the elevation of the access shaft to the intake tower has to be increased in order to avoid overflows from the reservoir to the gate chamber. We can observe that technique with this level of accuracy is used today by ISL to make the initial design of a dam spillway. It permits to verify the behavior of water into the spillway, and thus to control if everything is good or if a modification of the spillway geometry has to be done.

References

1. ISL. (2014). *Etude de dangers du barrage de la Galaube*.
2. Laugier, F., Guyot, G., Valette, E., Blancher, B., Oguic, A., & Lincker, L. (2009). *Utilisation industrielle de la modélisation hydrodynamique 3D pour l'évaluation de la débitance d'un évacuateur*. Colloque CFBR-SHF "Dimensionnement et fonctionnement des évacuateurs de crues".
3. ISL & BRLi. (1996). *Barrage de la Galaube sur l'Alzeau. Dossier définitif. Dossier Annexe: détails des calculs.*
4. United States Department of the Interior, Bureau of Reclamation. (1987). *Design of Small Dams*.
5. Groupe de travail "Dimensionnement des évacuateurs de crues de barrages" du Comité Français des Barrages et Réservoirs. (2012). *Recommandations pour le dimensionnement des évacuateurs de crues de barrages*.

3-D Numerical Simulation of a Real Dam Reservoir: Thermal Stratified Flow

Fatih Üneş, Mustafa Demirci and Hakan Varçin

1 Introduction

Inflow river water may have different temperatures, concentration of dissolved or suspended substances from the ambient water in a dam reservoir. Therefore, density of inflow river water is generally different from the ambient freshwater in the reservoir. The differences may lead to baroclinic forces affecting the flow structure. If river flow enters an ambient dam reservoir waters, then three basic types of currents may occur. These are called the overflow, interflow, and plunging flow. If density of incoming flow is smaller than the ambient water body in the reservoir, this type of flow will move along the free surface and is called overflow. If reservoir ambient water is stratified due to temperature or other effects, incoming flow will go forward an intermediate layer that density of this layer is equal to inflow density. This flow is named interflow. If a river water flowing density is denser due to lower temperature, dissolved solids, or suspended sediments than quiescent water density, then this type of flow will plunge below the ambient water, and the flow will move along the reservoir bottom. This flow is called as underflow, density negatively buoyant flow, stratified or plunging flow.

Real reservoirs do not have typical geometry. The geometry of the dam reservoir inlet plays an important role in process of plunge, divergence flow, and underflow. But in generally, it has a narrow valley, and river inflow may have little divergence and more slope effect, or it has a wide valley, of course, river inflow may affect

F. Üneş (✉) · M. Demirci · H. Varçin
Engineering Faculty Civil Engineering Department, Hydraulics Division,
Mustafa Kemal University, 31200 İskenderun, Hatay—Turkey
e-mail: funes@mku.edu.tr

M. Demirci
e-mail: mdemirci@mku.edu.tr

H. Varçin
e-mail: hvarcin@mku.edu.tr

P. Gourbesville et al. (eds.), *Advances in Hydroinformatics*,
Springer Water, DOI 10.1007/978-981-287-615-7_26

divergence. Such features may lead to incomplete lateral mixing of the inflow. Therefore, the geometry of dam reservoir at the point of discharge entrance also plays an important role in the formation of the plunge and the subsequent evolution of the underflow. Contaminants are often transported and diffused as density divergence flows into dam reservoir. Therefore, the analysis of such currents is very important in order to predict the distribution of contaminants. The analysis of this flow is of importance from the point of view of reservoir sedimentation studies, water quality modeling and management, effluent mixing analyses and dam reservoir flow characteristic parameters, such as circulation flows in ambient waters, and habitat in dam reservoirs. It is also essential to study inflows transport suspended solids, variation of temperature and velocity of stratified reservoirs, and the formation of separated flows, such as wall-jet and free-jet flows.

River flows entering into the dam reservoir can have different temperatures due to variation in temperatures over the year and therefore, density differences exist. These variations may lead to lateral mixing of the inflow and uncertain currents in dam reservoir. Moreover, real dam reservoirs can have very variable cross-section geometry, shape, and volume. Therefore, the geometry of reservoir and seasonal temperatures variation can play an important role in the formation of flow into the reservoir such as buoyancy flow, density flow, and divergence flows.

Many researchers have treated the stratified reservoir, density plunging, and divergence flow released on a sloping bottom in laboratory conditions [1–6]. Although most of the data available are from flume tests in laboratory, laboratory experimental works are not sufficient to understand the longitudinal developments of the hydraulic characteristics of density flows over a long distance. However, mathematical model studies can give more information about density flow characteristics over the entire dam reservoir. Therefore, a few authors have also considered the problem by solving it using mathematical models and numerical solution to investigate the plunging and underflow [1, 3, 7–10]. Farrell and Stefan [3] studied negatively buoyancy flow in diverging channel with experimental and mathematical model. Singh and Shah [1] made an experimental study and mathematical model for plunging flow in a dam reservoir. As a result of the researches, different plunging flow model criteria are suggested. Unes [9, 10], one of the researchers, investigated density flow in dam reservoirs using a three-dimensional mathematical model including Coriolis effect. These solutions provided useful results for further realistic reservoir model studies.

In the present paper, a simulation model of a real reservoir of medium size is investigated using a previously developed numerical model for the dynamics of a dam reservoir in three dimensions (3-D) by Üneş [9–12]. Since these types of studies require accurate descriptions of the dynamics of inflow rivers and dam properties, the dominant physical processes, initial and boundary conditions in the long run variation, such as seasonal temperatures, inlet discharge, and reservoir level are incorporated in the simulation model. The main aim of this research is to create a dam reservoir model as accurate as possible to define realistic dam reservoir flow parameters. In this way, the effect of the wall divergence angle in reservoir

inlet, channel bottom slope variation of flow types and parameters through the dam reservoir can be investigated.

2 The Mathematical Model Description

In this paper, 3-D mathematical model is used to better understand the real dam reservoir flow. The present model equations are solved using FLUENT software program based on the initial and boundary conditions of the field measurement reservoir flow parameters. Model equations are solved using control-volume-based technique. If dam reservoir with large volume and long dimensions is considered as a whole, the Coriolis force effect should be added in the model. The length and width on the surface of Egrekkaya dam reservoir are, respectively, 2360 and 7800 m in the month of August. In this respect, if real reservoir conditions want to be obtained, the dam reservoir is investigated using the mathematical model including Coriolis force. But the software does not incorporate Coriolis effect. Therefore, a user defined function is written in C language to take into account this effect in the software program.

The model results are calibrated field measurement data. In the model simulations, it is assumed that density flows occur only due to differences in temperatures of ambient water and inflow water. These flow types are modeled for different seasonal conditions. The model can simulate the entire very long-dimension reservoir, and additionally, plunging region and other parts of dam reservoir need not be separated from entire reservoir flow. Stratified flows such as plunging, overflow, and seasonal variation are examined using temperature variation through three dimensions in a real dam reservoir. The flow parameters are evaluated from temperature contour and desired velocity vector profiles in reservoir.

Since density flows in dam reservoir have circulation flow properties, eddy viscosities are used to describe vertical transport due to velocity at the interface on stratified flow in the mathematical model. To calculate eddy viscosities, k-ε turbulence model approach is used [2, 3, 9, 10]. This method is very useful for complex reservoirs that have inner circulation and temperature stratified flows. Since the density difference occurs due to varying water temperatures, the present mathematical model includes an energy equation for the heat transport in the reservoir.

Three-dimensional mathematical model is applied to the actual size of the Egrekkaya dam and reservoir. Model Simulations and results were compared with previously measured dam reservoir flow for August. There is a good agreement between the previously measured and field measurements data sets.

2.1 The Mathematical Model

The reservoir shape (Fig. 1) is located in 3-D, x, y, and z, Cartesian coordinates. A dam reservoir is a complicated phenomenon and hard to solve. Therefore, some simplification process has to be made before presenting the governing equations. One of them, the free surface phenomenon such as wind or wave effect is not considered in reservoir surface, and the free surface of the reservoir is modeled as rigid lid in the present model simulation. Furthermore, suspended or dissolved substances effects are neglected on density differences. Another simplification is that the temperature difference is taken to be the source of the stratified and buoyancy flow. Inflow river properties, such as temperature variations and turbidity currents, exhibit different models of density currents. It is a fact that turbidity current occurring due to sediment laden reduces dam storage capacity. Since, at present, a new master project includes consecutive dam construction and one dam outflow creates inflow in another dam, the most effective parameter is taken as temperature change of density reservoir flow. Therefore, extra temperature gradients are consisted in the reservoirs. The important issue in these types of projects is to construct an accurately thermal stratification flow.

Small temperature differences are enough to produce density flow in the reservoir. Therefore, the density term in the momentum equation can be linearized using the following approximation [2, 3]:

$$\rho = \Delta\rho + \rho_0 = \beta\rho_0[T_0 - T], \tag{1}$$

where ρ is the water density, ρ_0 is reference density taken in the present case as reservoir water density, T is the water temperature, and β is the coefficient of thermal expansion and is calculated as $\beta = -(\Delta\rho/\rho_0)(1/\Delta T)$, where ΔT is the temperature difference between ambient and inflow river waters, ρ_0 and T_0 refer to the

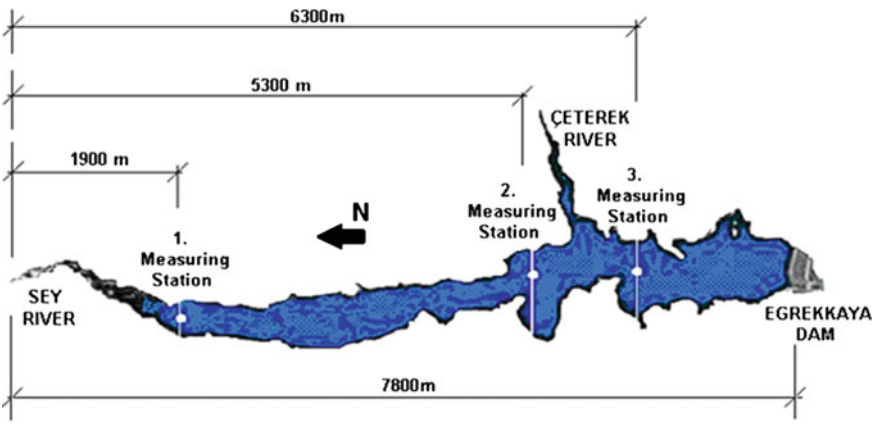

Fig. 1 Egrekkaya reservoir (Google Earth) and measuring stations

reservoir conditions. Equation (1) will be substituted into the momentum equation. If density variation is not large, "$(\Delta\rho/\rho_0)$" is the neglected part of multiplier in temporal and convective terms in the momentum equations, this process is called as "Boussinesq approximation". Reduced pressure, $P' = P - \rho_0 gy$, approach is also considered as another simplification in this work. This relationship is meaningful only when the rigid lid assumption is used. The occurred deflection along dam reservoir flow due to Coriolis effects is considered in mathematical model for the northern hemisphere. The amount of deflection of flow particles is directly related to both its speed and latitude. So, Coriolis effect is only applied in the x and y components of the momentum equations and energy equation.

If all the previous processes are applied, the mathematical model consists of the following equations: the continuity equation, momentum equations, energy equation, and the turbulence model equations. When momentum equations are examined, it can be seen that reduced pressure and buoyancy terms, $\beta\rho_0[T_0 - T]$ is directly related to the gravitation effect.

Continuity equation

$$\frac{\partial \rho}{\partial t} + \frac{\partial(\rho\overline{u})}{\partial x} + \frac{\partial(\rho\overline{v})}{\partial y} + \frac{\partial(\rho\overline{w})}{\partial z} = 0 \tag{2}$$

Momentum equations

For the x axis,

$$\frac{\partial \overline{u}}{\partial t} + \overline{u}\frac{\partial \overline{u}}{\partial x} + \overline{v}\frac{\partial \overline{u}}{\partial y} - \overline{w}\frac{\partial \overline{u}}{\partial z} - f\overline{v} = -\frac{1}{\rho_o}\frac{\partial \overline{\overline{P}}}{\partial x} + v_{\text{eff}}\left(\left(\frac{\partial^2 \overline{u}}{\partial x^2} + \frac{\partial^2 \overline{u}}{\partial y^2} + \frac{\partial^2 \overline{u}}{\partial z^2}\right) + \left(\frac{\partial^2 \overline{u}}{\partial x^2} + \frac{\partial^2 \overline{v}}{\partial x \partial y} + \frac{\partial^2 \overline{w}}{\partial x \partial z}\right)\right) \tag{3}$$

for the y axis,

$$\frac{\partial \overline{v}}{\partial t} + \overline{u}\frac{\partial \overline{v}}{\partial x} + \overline{v}\frac{\partial \overline{v}}{\partial y} + \overline{w}\frac{\partial \overline{v}}{\partial z} + f\overline{u} = -\frac{1}{\rho_o}\frac{\partial \overline{\overline{P}}}{\partial y} + v_{\text{eff}}\left(\left(\frac{\partial^2 \overline{v}}{\partial x^2} + \frac{\partial^2 \overline{v}}{\partial y^2} + \frac{\partial^2 \overline{v}}{\partial z^2}\right) + \left(\frac{\partial^2 \overline{u}}{\partial y \partial x} + \frac{\partial^2 \overline{v}}{\partial y^2} + \frac{\partial^2 \overline{w}}{\partial y \partial z}\right)\right) \tag{4}$$

and for the z axis,

$$\begin{aligned}\frac{\partial \overline{w}}{\partial t} + \overline{u}\frac{\partial \overline{w}}{\partial x} + \overline{v}\frac{\partial \overline{w}}{\partial y} + \overline{w}\frac{\partial \overline{w}}{\partial z} &= -\frac{1}{\rho_o}\frac{\partial \overline{\overline{P}}}{\partial y} \\ &+ v_{\text{eff}}\left(\left(\frac{\partial^2 \overline{w}}{\partial x^2} + \frac{\partial^2 \overline{w}}{\partial y^2} + \frac{\partial^2 \overline{w}}{\partial z^2}\right) + \left(\frac{\partial^2 \overline{u}}{\partial z \partial y} + \frac{\partial^2 \overline{v}}{\partial z \partial y} + \frac{\partial^2 \overline{w}}{\partial z^2}\right)\right) + g\beta(T_o - \overline{T})\end{aligned} \tag{5}$$

Energy equation

Temperature field is defined by solving the following Energy equation

$$\frac{\partial \overline{T}}{\partial t} + \overline{u}\frac{\partial \overline{T}}{\partial x} + \overline{v}\frac{\partial \overline{T}}{\partial y} + \overline{w}\frac{\partial \overline{T}}{\partial z} = \alpha_{\text{eff}}\left(\frac{\partial^2 \overline{T}}{\partial x^2} + \frac{\partial^2 \overline{T}}{\partial y^2} + \frac{\partial^2 \overline{T}}{\partial z^2}\right) \tag{6}$$

where $\overline{u}$, $\overline{v}$ and $\overline{w}$ are the mean velocities in the x, y, and z directions, respectively, ρ is the water density, $\overline{\overline{P}} = \overline{P'} + \rho k(2/3)$, $\overline{P'}$ is the mean pressure adjusted to absorb the hydrostatic portion of the gravity terms, k is turbulent kinetic energy and $\overline{T}$ is the mean temperature, v_{eff} is effective kinematics viscosity, $v_{\text{eff}} = v + v_{\text{t}}$, where v is the kinematics viscosity and v_{t} is the kinematics eddy (turbulence) viscosity; and $\alpha_{\text{eff}} = (v/P_r) + (v_{\text{t}}/\sigma_{\text{t}})$ is effective thermal diffusivity coefficient; where P_{r} and σ_{t} are the Prandtl and turbulent Prandtl numbers, respectively.

k-ε turbulence model equations

The *k-ε* turbulence model is used for the turbulence closure. The method is useful for complex reservoirs that have inner circulation and temperature stratified flows. Since *k-ε* turbulence model for density and stratified flow was used many times in previous studies and successful results were monitored, the *k-ε* turbulence model closure is used in the current study. The effect of turbulence is simulated using the modified standard *k-ε* turbulence model including the suitable buoyancy terms. Therefore, Standard *k-ε* model is a semiempirical model of Launder and Spalding [13] based on model transport equations for turbulent kinetic energy (k) and its dissipation rate (ε). *k-ε* transport model equations have been implemented by Rodi [14]. For a three-dimensional unsteady flow at the sloping bottom reservoir, the eddy viscosity v_{t} is computed from the following equation:

$$v_t = C_\mu \frac{k^2}{\varepsilon}, \tag{9}$$

where k is the turbulent kinetic energy and ε is the turbulent energy dissipation rate per unit mass. k and ε are obtained from the solution of the following equations in three-dimensional flow.

Equation of k

$$\frac{\partial k}{\partial t} + \bar{u}_j \frac{\partial k}{\partial x_j} = \frac{\partial}{\partial x_j}\left[\left(v + \frac{v_t}{\sigma_k}\right)\frac{\partial k}{\partial x_j}\right] + \text{Prod} + G - \varepsilon \tag{10}$$

and equation of ε,

$$\frac{\partial \varepsilon}{\partial t} + \bar{u}_j \frac{\partial \varepsilon}{\partial x_j} = \frac{\partial}{\partial x_j}\left[\left(v + \frac{v_t}{\sigma_\varepsilon}\right)\frac{\partial \varepsilon}{\partial x_j}\right] + C_{1\varepsilon}\frac{\varepsilon}{k}\text{Prod} - C_{2\varepsilon}\frac{\varepsilon^2}{k} + C_{1\varepsilon}C_3\frac{\varepsilon}{k}G, \tag{11}$$

where Prod is the production of turbulent kinetic energy from the mean flow and is given as

$$\text{Prod} = v_t\left(\frac{\partial \bar{u}_i}{\partial x_j} + \frac{\partial \bar{u}_j}{\partial x_i}\right)\frac{\partial \bar{u}_i}{\partial x_j} \tag{12}$$

In these equations, G is the production or destruction of turbulent kinetic energy by buoyancy forces and is given as

$$G = g_i\beta\frac{v_t}{\sigma_t}\frac{\partial \bar{T}}{\partial x_i}, \tag{13}$$

where β is thermal expansion coefficient. In addition, the values of the coefficients C_μ, $C_{1\varepsilon}$, $C_{2\varepsilon}$, C_3, σ_k, σ_3, and σ_t appearing in the k-ε turbulence model equations used herein were given the standard values recommended by Launder and Spalding [15]. For the standard k-ε model, these constants are taken as $C_\mu = 0.09$, $C_{1\varepsilon} = 1.44$, $C_{2\varepsilon} = 1.92$, $\sigma_k = 1.00$, $\sigma_\varepsilon = 1.3$, and $\sigma_t = 0.9$. C_3 is not part of the standard k-ε model but enters through the buoyancy terms and the constant C_3 is not a stable value. In FLUENT, C_3 is not specified, but is instead calculated according to $C_3 = \tanh|w/u|$, where w is the component of the flow velocity parallel to the gravitational vector and u is the component of the flow velocity perpendicular to the gravitational vector. Further details and solution procedure can be found in the FLUENT user's guide [16].

2.2 Boundary and Initial Conditions

Since flows of reservoir are unsteady and turbulence flow, boundary conditions in flow field must be specified individually on the reservoir inlet and outlet planes, at the walls, and at the free surface. Moreover, initial fields for each variable must also be specified. So for each variable, boundary and initial conditions must be chosen individually.

Velocity is given a symmetry condition at the free surface. At the reservoir bottom and dam face, velocities are determined using the standard wall function that is based on the proposal of Launder and Spalding [15]. This function assumes a log-law velocity profile near the wall and is provided in FLUENT as follows:

$$\frac{u_p}{u_*} = \frac{1}{K}\ln\left(E\frac{u_* y_p}{v}\right) - \Delta B, \tag{14}$$

where u_p is the mean flow velocity at point p; u^* is the friction velocity; K is the von Karman constant; E is the empirical constant having a value of 9.81; y_p is the distance from point p to the wall; and ΔB is the roughness function that depends, in general, on the wall roughness height, K_s. At the inflow boundary, the horizontal velocity component in the x direction, u, is given uniform velocity distribution. The vertical velocity component in the y direction, v, is set to zero. At the outflow point of the reservoir, the horizontal velocity component is allocated a value in order to exactly balance inflow and the vertical velocity component is taken as zero. The

initial velocity field into the reservoir consists of a forward horizontal velocity, u, and zero vertical velocity, v, at all points except close to the dam.

The bottom and the free surface of the reservoir's temperatures are taken as adiabatic. The initial temperature field consists of a constant temperature throughout the reservoir. The dam face temperature is taken equal to the initial temperature of the reservoir water. The inflow river water temperature is set at a constant value with no variation over river depth. Reservoir temperature conditions will be changed later during the simulation run time. Therefore, initial temperature values are not of importance.

The k and ε are given a symmetry condition at the free surface, the same as the velocity condition in the turbulence model. So a zero gradient condition for k is valid at the reservoir bottom and on the dam face. k and ε in the inflow river, and near the wall grid points are given a linear profile related to the river shear velocity, u^* is proposed by Launder and Spalding [13, 15]. At the outflow point, k and ε conditions are the same as the velocity conditions. That is, the zero gradient condition is imposed at the outflow point for k and ε.

2.3 Application Details

The governing equations are solved using the computational fluid dynamics solver FLUENT. In the study, the program solves the governing integral equations for the conservation of mass and momentum, energy, and turbulence equations using pressure-based solver numerical method. In this approach, the pressure field is extracted by solving a pressure or pressure correction equation which is obtained from continuity and momentum equations. In the solution control-volume-based technique is used. This technique contains the following steps; first, division of the domain into discrete control volumes using a computational grid, second, integration of the governing equations on the individual control volumes to construct algebraic equations for the discrete dependent variables such as velocities, pressure, temperature, and turbulence parameters, finally, linearization of the discretized equations and solution of the resultant linear equation system to yield updated values of the dependent variables.

When the velocity fields into the dam reservoir have complex currents such as density flow or circulation flow, two types of problems arise because the density reservoir flows are nonlinear and velocity–pressure field interdependent. These problems are solved using the SIMPLE procedure approach. This procedure is the iteration method and is based on the predictor–corrector approach. FLUENT provides the option to choose SIMPLE pressure–velocity coupling algorithms. Since the density flow is unsteady and the run time is too large due to reservoir dimension, the fully implicit scheme is used for converting the discrete equations in the present model to give a stable and realistic solution at the large time steps.

3 Field of Study

Field data gathered from the Egrekkaya dam reservoir is used to obtain flows that may occur through a real dam reservoir. Egrekkaya Dam in Ankara region (capital of Turkey) was selected for this study. This dam which is 70 km away from Ankara was constructed for the purpose of drinking water supply for Ankara. Egrekkaya dam is an earth-fill dam; crest length is 340 m, height from the river bed is 67 m, drainage basin area is about 780 km^2, and maximum volume of reservoir is almost 1130 hm^3. Generally, the highest inflow to Eğrekkaya dam reservoir was observed in March and April. Moreover, the most water consumption in reservoir occurred in April and August. In addition to, the most evaporation was observed in July and August. It was defined 4.447 hm^3 in reservoir volume during the year 1999 (DSI, 2001).

The data for Egrekkaya dam (used in this study) were obtained from Turkish General Directorate of State Hydraulic Works (DSI). The observed (monitored) data comprises the time period between February 1999 and October 2000 on a monthly average basis [17, 18]. Three measurement stations are established by DSI for water quality modeling through the dam reservoir. Egrekkaya reservoir map has an intricate configuration due to narrow and variable cross-section (Fig. 1). The centerline length and width of the largest place of dam reservoir in August are 7.8 and 2.36 km, respectively. The Sey and Çeterek River flow into the reservoir. Three measuring stations on the dam reservoir are located in reservoir centerline approximately 1.9, 5.3, and 6.3 km, respectively, from reservoir inlet. Location of measuring station in Fig. 1 was determined according to DSI field measuring stations presented in the same figure.

Inflow discharges from two inlet and monthly mean temperature variation data measured at inlet gauging station are presented in Table 1. In the table, T_s °C), the water temperature of entering Sey River; T_c °C), the water temperature of entering Çeterek River; T_o °C), reservoir ambient water temperature; Q_s ve Q_c (m^3/s), monthly mean inflow discharges of Sey and Çeterek River. Temperature variations for months measured at three gauging stations are given in Fig. 2. The measurement comparison data for temperature variation in reservoir were the major components of density difference between the inflow and dam reservoir during August.

The measurement records data for temperature variations throughout both reservoir and the depth of the reservoir were obtained from DSI; meanwhile, measurements were provided for three gauge stations along the reservoir for a time period covering one year. Temperature variations within August and also at the end of summer season are shown in Fig. 2.

Table 1 Two river inflow data entering Egrekkaya dam reservoir [11, 18]

	Sey river			Çeterek river		
	T_s (°C)	T_o (°C)	Q_s (m^3/s)	T_c (°C)	T_o (°C)	Q_c (m^3/s)
August	10.3	24.2	2.0	6.1	24.2	0.2

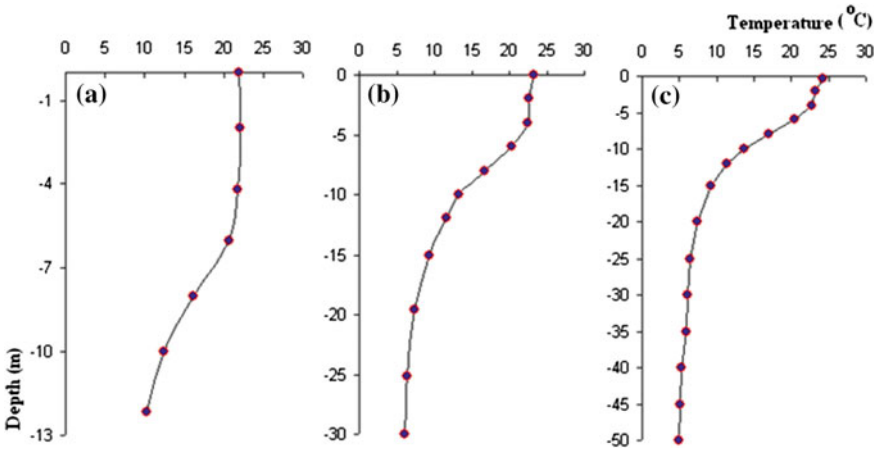

Fig. 2 Observed temperature variations in August for Egrekkaya dam at three gauging stations. **a** Sampling station 1; **b** sampling station 2; **c** sampling station 3 [18]

The reservoir flows are stratified during the warm season due to temperature variations as seen in Fig. 2. These stratified flows occur as densities or plunging flow during spring and summer due to temperature variation between inflow and ambient water. Figure 2 shows that water temperatures in Egrekkaya reservoir were in the range of 4.99–24.18 °C in August. Table 1 shows that the Sey and Çeterek River flows entering the reservoir are averaged at 2.0 and 0.2 m^3/s discharge, respectively, with a temperature of 24.2 °C in August.

Flow parameters (temperature, velocity, pressure, etc.) are defined at every point of the reservoir in the simulation model. For representing spring and summer seasons, temperature stratified flow and plunging (density, negatively) flow are clearly obtained from the model in August. The field measurements were compared with the model results at gauging stations in the Egrekkaya reservoir. The model showed a good agreement with the field values for these stations. Then, the stratified flow, density, speed, and temperature variation in the reservoir body can be obtained for whole dam reservoir. The results obtained simulations that provide confirmation of the model's ability for real dam reservoir flow.

4 Application of the Model

Before preparing the mathematical model in FLUENT of Egrekkaya dam, a drawing software program, GAMBIT, is used to draw the experimental reservoir configuration. After the reservoir shape is sketched with the drawing software by taking a cross-section of each 50–100 m along the reservoir (67 m in depth, 2360 m in width, 7800 m in length for warm season), as given in Fig. 3. The proposed

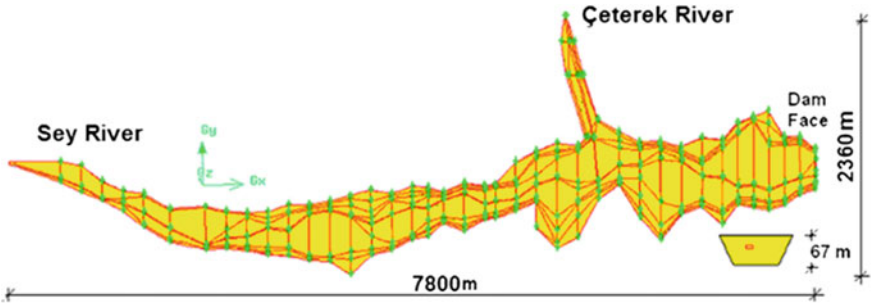

Fig. 3 Cross-section points at each 50–100 m layout and dam face section in August

mathematical model is implemented into FLUENT with the appropriate boundary and initial conditions.

Numerical diffusion is one of the serious problems in computational fluid dynamics. Generally, numerical diffusion arises because of the inability of a discrete grid in space and time to perfectly simulate continuous process [2]. In the literature, there are many kinds of numerical diffusion, but in this study, especially skewness error which is part of numerical diffusion is taken into account. If flows such as recirculation flow, plunging flow, and underflow in a dam reservoir take place at an angle to the numerical scheme grid lines, it is well known that the occurrence of skewness error is inevitable.

Skewness and other problems are solved getting smaller mesh dimension grid line. Since the real shape of reservoir is considered in the model, the skewness error is increased due to the intricate shape of the reservoir. These errors are defined and are corrected by increasing the numbers of mesh with GAMBIT. However, when the mesh gets smaller, the numbers of mesh are increased. Obviously, this requires more computer capacity and time. Furthermore, the computational domains for all cases are approximately divided into 1070,000–1010,000 tetrahedral mesh volumes to obtain acceptable skewness coefficients. This represents approximately 2500,000 nodes. In the model cases, the convergence criterion of flow parameters is taken as 0.001 for all runs. High capacity parallel computer system, which has 16 processes were used in typical model runs where each process has 1 GB ram and high data store capacity. Since Egrekkaya dam reservoir has big dimension and volume, iteration and solution time of simulation model took about two months for each model run. The calculation and iterations were run until insignificant changes are observed in the flow field. The time included the development of underflow through the dam reservoir and until it reached the steady state in the flow characteristic. In order to have the desired converged solution, a time step size of 50–100 s and maximum iteration per time step of 10 were chosen after the preliminary trials.

4.1 Model Results

Seasonal simulations yielded realistic flows measured in fields in all models. Ambient reservoir water and inflow river water temperature vary during the year. This change creates different types of density flow in the reservoir. Since incoming flow temperature is generally smaller than the ambient water body in the reservoir during the hot season, incoming flow as underflow moves along the bottom of the dam ambient water (density negatively flow or plunging flow). However, unlike the summer season, incoming river flow temperature is generally equal to or sometimes greater than the ambient water body in the reservoir during the winter. Therefore, incoming river flow as overflow will move along the free surface.

In this study, reservoir flows are modeled for August representing summer seasons. Presented mathematical model is applied to Egrekkaya dam reservoir. The data for Egrekkaya dam were obtained from measurements at three gauging stations. Table 1 and Fig. 2 show the independent variables governing the density flow for the two season models in dam reservoir and temperature variations throughout both reservoir and the depth of the reservoir.

In the model simulations, the reservoir is first filled with warm water in accordance with the measured reservoir surface water temperature and air temperature, and then the cold water in accordance with the measured inflow rivers water temperatures and discharges are released at the upstream end of the inflow rivers channel at a specified rate. The current proceeds forward until it reaches the downstream boundary. The present model is the first step in the real dam reservoir simulation model. The entire reservoir flow can be simulated with the presented model approach. Therefore, plunging region need not be separated from entire reservoir flow as in the previous study. Moreover, flow current parameters of all the points in the reservoir such as temperature, velocity, density, turbulence kinetic energy, etc., can be defined in the real dam reservoir using the present simulation models.

Model results for August

In order to examine the real dimension reservoir flow, the mathematical model governing equations are solved and analyzed for August with the computational fluid dynamics solver, FLUENT. The model results were also examined and compared with the observed field data. The measurements for August showed that inflow water temperatures for Sey and Çeterek Rivers, T_s and T_c ^oC, are defined at 10.3 and 6.1 ^oC), respectively. In addition to river inflow temperature, the ambient water temperature is measured as 23.4 ^oC. Therefore, the density stratified flows are formed due to the difference in warmth between stable water and inflow river water. The run simulations in August show that, initially the inflow cold river water advanced into the dam reservoir, and pushed forward under the ambient warm water. Then the warm water is displaced forward and the flows are in the downstream direction at all points. The warm water is initially displaced forward. When the denser cold water pushed slightly forward under the warm water, a recirculation region appeared on both the section and the ambient water surface. Then, plunging

flow starts and consequently the river inflow cold water flows downstream under the ambient warm water as underflow current. Together with these formations, since inflow river water plunges, ambient water is entrained in the downstream direction and underflow water is diluted due to entrainment from the circulating warm water.

Temperature variations along the reservoir depth obtained from these simulations and the measurements of DSI [18] are compared and the percentages of errors are shown in Fig. 4 and Table 2. The percentage of errors at the first, second and third gauging stations are determined as 3.1, 5.7, and 4.3 %, respectively. It can be seen from the data and results in Table 2 and Fig. 4 that the mathematical model and simulation results are found to be of the same magnitude as the field measurements in the respective stations. These results indicate that the mathematical model can be effectively used for reservoir flow estimation.

Isodilution contours, lines of constant temperature, are found in August. Temperature variations of the model are consistent with the reservoir measurements. These cases are investigated at three field station cross-sections where observations are made, namely 1.9, 5.3, and 6.3 km, respectively, along the reservoir.

The contours at the surface and the longitudinal sections (1.2, 1.4, 1.6, 1.8, and 2.0 km respectively) are also investigated and evaluated. Figures 5 and 6 show contours of temperature fields of real dam reservoir for three measuring station cross-sections and different longitudinal sections in 3-D. Thermocline variations in the reservoir are defined through the dam face, cross and longitudinal sections. Figure 5 represents the 3-D plot of the thermocline variation obtained from the model for Station 1 and six sections along the Egrekkaya dam reservoir.

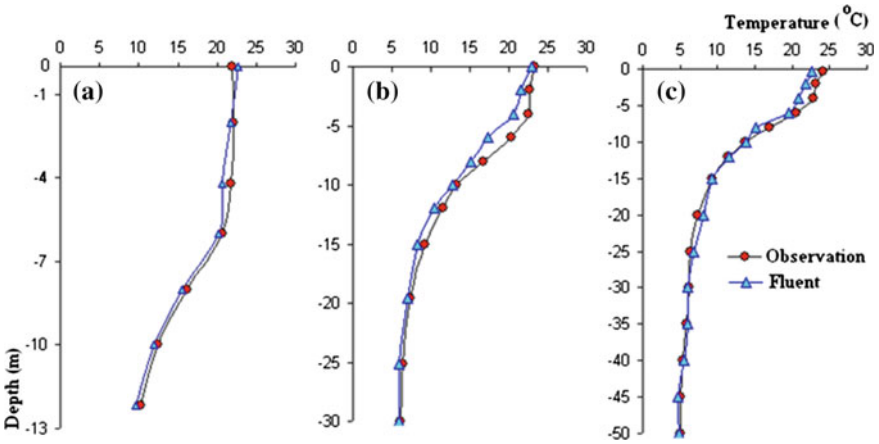

Fig. 4 Comparison of observed and present numerical model temperatures in August. **a** 1st station, **b** 2nd station, **c** 3rd station

Table 2 Temperature-depth values in August at 1st, 2nd, and 3rd stations for measured and obtained results

Depth (m)	1st station			2nd station			3rd station		
	Measured (° C)	Model (° C)	Error (%)	Measured (° C)	Model (° C)	Error (%)	Measured (° C)	Model (° C)	Error (%)
0	21.99	22.7	3.2	23.3	22.9	1.7	24.18	22.6	6.5
−2	22.13	21.8	1.5	22.68	21.6	4.8	23.21	21.8	6.1
−4	21.74	20.7	4.8	22.52	20.7	8.1	22.82	20.9	8.4
−6	20.61	20.2	2.0	20.26	17.4	14.1	20.52	19.5	5.0
−8	16.19	15.6	3.6	16.79	15.1	10.1	16.98	15.1	11.1
−10	12.4	11.9	4.0	13.3	12.8	3.8	13.68	13.9	1.6
−12	10.27	9.7	5.6	11.64	10.5	9.8	11.44	11.6	1.4
−15	–	–	–	9.28	8.3	10.6	9.22	9.3	0.9
−20	–	–	–	7.38	7.1	3.8	7.35	8.1	10.2
−25	–	–	–	6.42	6	6.5	6.35	6.9	8.7
−30	–	–	–	6.09	6	1.5	6.13	6.1	0.5
−35	–	–	–	–	–	–	5.86	6	2.4
−40	–	–	–	–	–	–	5.3	5.5	3.8
−45	–	–	–	–	–	–	5.07	4.8	5.3
−50	–	–	–	–	–	–	4.99	4.9	1.8
Mean error percentage			3.1			5.7			4.3

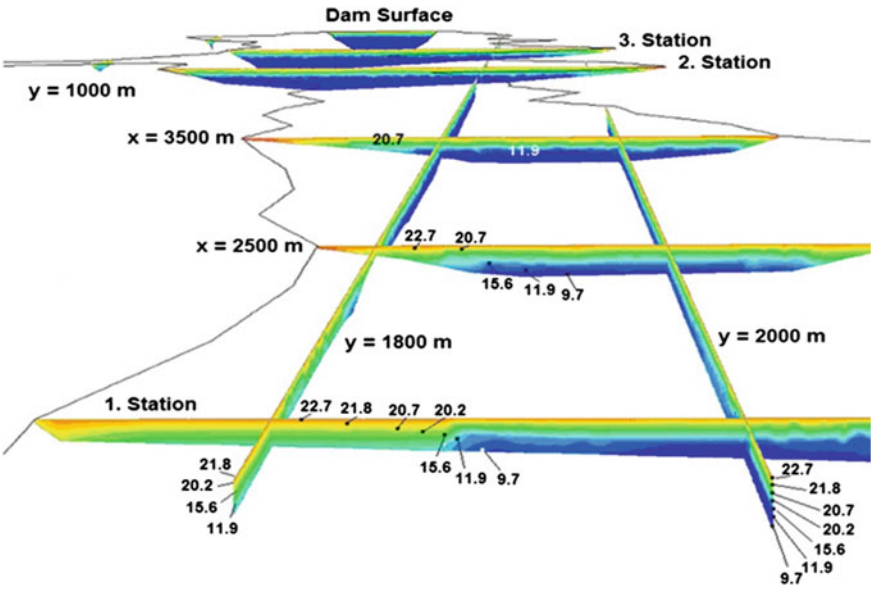

Fig. 5 Cross-sectional view of thermocline variations at different water depths at station 1 and various cross-sections along the Egrekkaya reservoir, and longitudinal section variations of thermocline at 1600, 1800, and 2000 m in August

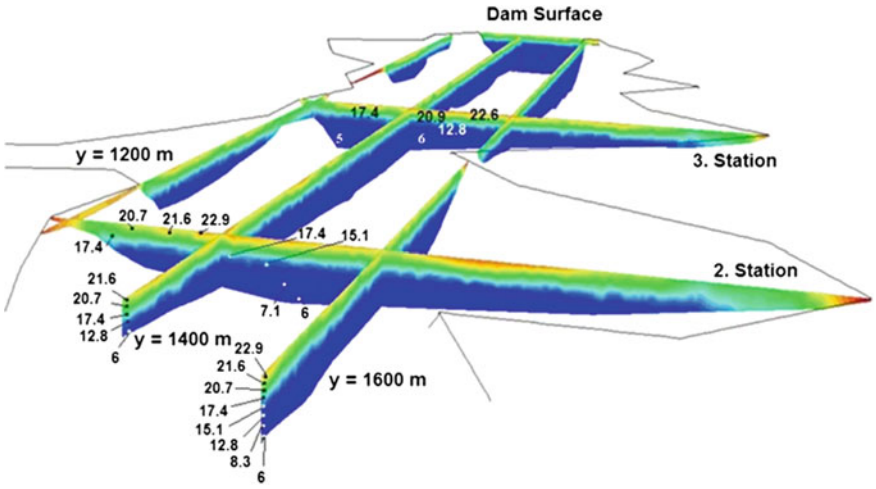

Fig. 6 Cross-sectional view of thermocline variations at different water depths at stations 2, 3, and on the dam face, and longitudinal cross-sections at 1200, 1400, and 1600 m in August

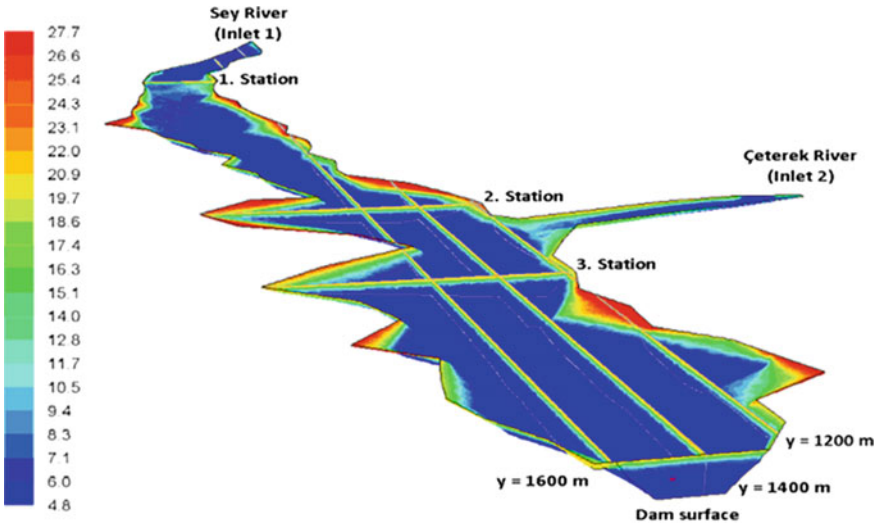

Fig. 7 Temperature variation of side surfaces of the reservoir and cross-sections in August (dam model perspective view from downstream)

Figure 6 shows the results of the thermocline variation obtained from the model for Stations 2 and 3, and also along the reservoir. Moreover, temperature variation along the reservoir is stratified, and the development of underflow can be clearly seen for August in Fig. 6.

Figure 7 shows the plot of the thermocline contour sections, and variations on the side surface along the reservoir in August. As seen in these figures, temperature variations change as the depths increase. Since Egrekkaya reservoir has an intricate configuration, the water temperature of the reservoir increases along the reservoir shoreline and in secluded places due to shallow water at littoral zone. As expected, the water temperatures in shallow water along the shoreline are much higher than deep-water parts of the reservoir as seen in Fig. 7. The determination of the temperature variations in a dam reservoir is of importance, particularly in terms of environmental pollution and water quality modeling.

It can be seen from the figures that since inflow Çeterek River temperature is smaller than ambient water, plunging and stratification are observed in the reservoir after the junction of Çeterek River. Even if the temperature difference between the inflow and ambient reservoir water is approximately 1 $^{\circ}$C, nevertheless, stratified flow and temperature variations are clearly seen. Flow in borders of river is shallower and slower than the flow in these areas is a variety. Also, affecting the surface temperature conditions in the border regions reveals that this difference is more pronounced.

5 Conclusion

In this study, the inflow behavior of a real dam reservoir is determined for August. The simulation analysis offers a useful insight into the development, variation of ambient reservoir flow, and the impacts of the temperature variations on the reservoir flow. If cross-sections of the river valley under the reservoir, the mean temperature of the ambient reservoir water, the discharge and the temperature of incoming river flow are known, then the dam reservoir flows occurring during the year and other important reservoir parameters can be estimated from the mathematical model simulation results.

Flows consisting of the real dam reservoir are greatly affected by the reservoir cross-sections and shapes, seasonal changes, and variations in the river inflow conditions. Overflow, plunging, and density flow and recirculation zone development into the reservoir can be well defined in the temperature, velocity, pressure, and turbulence fields in the model simulation results.

The model results are compared with the field measurements. The agreement between the model results and the observed field data is found to be promising. The developed mathematical model can also successfully simulate the turbulent density flow under realistic reservoir conditions.

Clear and freshwater sources are dwindling and becoming contaminated throughout the world due to growing population and environmental problems. In this sense, the present model and results can also be utilized for the water quality modeling, pollution problems of reservoir water, and management in real dam reservoirs.

Acknowledgements This study was supported by The Scientific and Technological Research Council of Turkey (TÜBİTAK) under Grant No: 106Y294.

References

1. Singh, B., & Shah, C. R. (1971). Plunging phenomenon of density currents in reservoirs. *La Houille Blanche, 26*, 59–64.
2. Farrell, G. J., & Stefan H. G., (1986). Buoyancy induced plunging flow intoreservoirs and coastal regions. *Project Report, No. 241*. St. Anthony falls Hydr. Lab., University of Minnesota.
3. Farrell, G. J., & Stefan, H. G. (1988). Mathematical modeling of plunging reservoir flows. *Journal of Hydraulics Research, 26*, 525–537.
4. Johnson, T. R., Farrell, G. J., Ellis, C. R., & Stefan, H. G. (1987). Negatively buoyant flow in diverge channel: Part I: Flow regimes. *Journal of Hydraulic Engineering, ASCE, 113*, 716–730.
5. Johnson, T. R., Ellis, C. R., & Stefan, H. G. (1987). Negatively buoyant flow in diverging channel: Part II: 3-D Flow field regimes. *Journal of Hydraulic Engineering, ASCE, 113*, 731–742.
6. Dallimore, C. J., Imberger, J., & Hodges, B. R. (2004). Modeling a plunging underflow. *Journal of Hydraulic Engineering, 130*(11), 1068–1076.

7. Uneş, F., (2004). Investigation of effects of coriolis forces and outlet levels on reservoir flow using mathematical model. *Istanbul Technical University,* Ph.D. Dissertation, Institute of Science and Technology, Istanbul.
8. Uneş, F., (2005). Investigation of temporary variation of plunging point caused by density plunging reservoir flow using mathematical modeling. Digest 2005, *Turkish Chamber of Civil Engineers*, *Technical Journal*.
9. Uneş, F. (2008). Analysis of plunging phenomenon in dam reservoirs using three dimensional density flow simulations. *Canadian Journal of Civil Engineering, 35*, 1138–1151.
10. Uneş, F. (2008). Investigation of density flow in dam reservoirs using a three-dimensional mathematical model including carioles effect. *Computers and Fluids, 37*, 1170–1192.
11. Uneş F., (2009). Investigation of flows into a real dam reservoir using three dimensional mathematical model. *Project Report*, No. 106Y294.
12. Uneş, F. (2010). Prediction of density flow plunging depth in dam reservoirs: an artificial neural network approach. *Clean—Soil, Air, Water, 38*(3), 296–308.
13. Launder, B. E., & Spalding, D. B. (1972). *Mathematical Models of Turbulence*. New York: Academic Press.
14. Rodi, W. (1987). Example of calculation methods for flow and mixing in stratified fluids. *Journal of Geophysical Research, 92*, 5305–5328.
15. Launder, B. E., & Spalding, D. B. (1974). The numerical computation of turbulent flows. *Computer Methods in Applied Mechanics and Engineering, 3*, 269–289.
16. FLUENT 6.3 users Guide, (2008). FLUENT incorporated.
17. Uneş, F., & Varcin, H. (2012). Investigation of plunging depth and density currents in Egrekkaya dam reservoir. *Turkish Chamber of Civil Engineers, Technical Journal, 367*, 5725–5750.
18. DSI (Turkish General Directorate of State Hydraulic Works). (2001). *Egrekkaya dam reservoir and basin pollution research report*. Turkey: Ankara.

Comparison and Validation of Two Parallelization Approaches of FullSWOF_2D Software on a Real Case

Olivier Delestre, Morgan Abily, Florian Cordier, Philippe Gourbesville and Hélène Coullon

1 Introduction

Bi-dimensional (2D) hydraulic modeling is widely used in model flows in various contexts, such as: rainfall overland flow [1–4], rivers [5], flooding [6], and dam breaks [7, 8], sea dynamics [9]. 2D simulations are more and more used with (i) fine meshes in case of high-resolution data [10, 11], (ii) big domains of simulation such as big watersheds or long rivers [11] and (iii) long or multiple scenarios to study uncertainties [11]. These modern applications imply high computational costs.

One solution to overcome this problem consists in parallelizing computation codes. Parallelization is a coding method which allows many calculations to be carried out simultaneously. This is based on the principle that a large problem can often be divided into smaller ones and then, can be solved in parallel. Parallel

Olivier Delestre is also affiliated to Lab. J.A. Dieudonné UMR 7351 CNRS

O. Delestre (✉) · M. Abily · F. Cordier · P. Gourbesville
University of Nice Sophia Antipolis/Polytech'Nice-Sophia/URE 005 I-CiTy,
930 Route des Colles, 06903 Sophia Antipolis Cedex, France
e-mail: delestre@polytech.unice.fr

M. Abily
e-mail: abily@polytech.unice.fr

F. Cordier
e-mail: cordier@polytech.unice.fr

P. Gourbesville
e-mail: philippe.gourbesville@unice.fr

H. Coullon
LIFO, University of Orléans and Géo-Hyd, bâtiment IIIA, 6 rue Léonard de Vinci,
BP 6759, 45067 Orléans Cedex 2, France
e-mail: helene.coullon@univ-orleans.fr

P. Gourbesville et al. (eds.), *Advances in Hydroinformatics*,
Springer Water, DOI 10.1007/978-981-287-615-7_27

architectures have become dominant for all computers since the beginning of the 2000s. In fact, with the processing speed, which is related to the increase in the frequency of processors, may face some technological limits. The creation of multi-core processors, processing multiple instructions at the same time within the same component, solves this dilemma for office machines since the mid 2000s. To be effective, the methods used for programming the different tasks that constitute a parallel program, should be made with this aspect in mind. These methods were initially developed theoretically and on supercomputers, which were at one time the only computers having many processors. Nowadays, the parallelization is widely used by software developers because of the pervasiveness of such architectures. Alternative options used by scientific software developers to speed-up computation rely on the use of GPU resources [12, 13].

Certain types of calculations are particularly well suited to parallelization, such as 2D flow modeling and simulation of problems of large dimensions (for which domain decomposition is possible). Thus more and more commercial softwares, such as MIKE 21, MIKE 21 FM [14, 15], and TELEMAC 2D [16–19], are developed with these parallel strategies. This allows modelers to use the resources of powerful computing structures and thus decreases the cost of computing time.

In this work we are interested in FullSWOF_2D (Full Shallow Water equations for Overland Flow) [1, 2, 20]. It is an object-oriented code devoted to hydraulic free surface modeling applications, which requires important computation time. This software is free and open-source software under the CeCILL-V2 (GPL compatible) license which allows us to use the software without any limitation. The sources in C ++ are available from the website https://sourcesup.renater.fr/projects/fullswof-2d/ and the structure of the source code is designed to make future evolutions easy for new developers. This software has been first designed to simulate rainfall overland flow on agricultural fields [1, 2]. As this software is based on the resolution of the 2D shallow water equations (2D SWE), it is possible to use this software on other kind of flows (river flows, dam-break, etc.). Also, two parallel versions, FullSWOF_Paral of FullSWOF_2D have been developed [21]. The first one is based on a master-slave architecture using MPI library (Message Passing Interface [22, 23]) and the second one uses the implicit parallel library SkelGIS (Skeletons for Geographical Information Systems [21, 24, 25]). These parallel versions have been done in order to run calculations on large domains and on fine meshes as what has already been done for the downstream part of the Var river [11, 26, 27]. The non parallel version of FullSWOF_2D has already been validated on analytical solutions which are integrated in SWASHES library [28, 29] and on real events simulations [1, 2, 20]. As far as they are concerned, up to now, the parallel versions have not been validated so extensively. We aim at validating and comparing the performance of these two versions on real cases such as Malpasset dam break [7, 8, 17] or the Toce valley flooding [30, 31]. At present time, the validation is not achieved yet and work is still in progress in that direction. Thus, we have chosen to present here the protocol we will use to achieve our purpose. This will be illustrated with Malpasset test case. In the first part, we will present the material and the method which will allows us to make this validation. We will describe the test

case and present 2D Shallow Water Equations-based softwares (MIKE21, MIKE21 FM, and TELEMAC) especially FullSWOF_2D and its parallel versions. In the second part, we will present the numerical results obtained up to now with the MPI version. In the final section, discussion and perspectives are then given.

2 Materials and Methods

To achieve our performance comparison between the two parallel versions of FullSWOF_2D code, a well-documented dam-break case is used (Malpasset dam break). Several 2D SWE-based models have successfully reproduced arrival time and flood wave elevation estimation on several control points in the valley. It has to be reminded that a dam-break event modeling can be done using different strategies, depending on the purpose of a model. For a long distance dam-break wave propagation study, 1D SWE-based codes are often used [17]. If purposes of a dam-break model are to focus on local effects and/or short time after dam break then 3D SWE or Navier-Stokes-based models are used to include the non-negligible vertical velocity component which is highly present at this scale. 2D SWE-based codes are used to model dam break when the objective is to assess flood extent and water elevation of a dam-break wave, not without standing the omission of local vertical effects and inevitable hypothesis on dam collapsing.

2.1 Malpasset Dam Break

Malpasset dam break is a real life application widely used as a benchmark test for numerical methods and hydraulics softwares [7, 8, 13, 17, 32–35]. The Malpasset dam was a 60 m high double curvature arch dam with a variable thickness between 1.5 and 6.77 m. The upper crest was 223 m long. It has been built because of lack of water for irrigation and drinking needs, combined with the wish to stop regular inundations by the river. This dam was located 14 km upstream of the river mouth of the Reyran in Southern France (Fig. 1). In december 1959, Malpasset dam broke due to heavy rain and discharged 49×10^6 m^3 of water into the lower Reyran valley at a velocity estimated to be up to 20 $m.s^{-1}$. This catastrophic event caused more than 400 casualties, mainly located in the city of Fréjus (Var). Due to its structure, the failure was assumed to be very rapid. The flood wave swept across the downstream part of Reyran valley modifying its morphology [36] and destroying constructions (such as bridges and freeway). A map (1/20000 IGN map of Saint-Tropez N°3, dated 1931) providing information on the valley topography before the dam construction had been used to generate the Digital Terrain Model (DTM) of the area [18, 19].

The French rules concerning dam safety have been revised and expanded following the disaster caused by Malpasset dam failure [18, 37]. In May 1968, a

Fig. 1 Malpasset test domain with location of the transformers, the 9 gages along the Reyran valley and the dam

decree made compulsory to provide emergency plans for all the large French dams. As a dealer of most of the big French dams, Electricité de France (EDF) was primarily concerned by this new regulation. Since that time, this French electricity producer has developed means of study of dam-break waves to furnish emergency plans. The main tools to achieve this type of study are constituted by scale-models (physical models) and by numerical models using computer codes. Th tools allow us to provide others maps of potential flooded areas. In 1964, a 1/400 scale model of Malpasset event was built and has been calibrated against observations (shut-down of three electricity transformers A, B and C located on Fig. 1 and maximum flood levels at some 100 locations along the valley banks) by the Laboratoire National d'Hydraulique (LNH), a division of EDF, in order to study dam-break flows. The maximum water levels and wave arrival times were recorded at 9 points in the scaled model (named from 6 to 14 on Fig. 1). This test has already been used in the framework of CADAM (Concerted Action of Dam-break Modeling) [7, 38]. In this context, the valley bathymetry was distributed by EDF to all participants, as a non-structured grid of some 13,000 points and calibration has been performed. From this grid, we have generated a structured regular grid [21], that we are using here and we have beneficiated from the calibration already done.

The dimensions of the domain are 16,500 m along x-axis with 1,100 cells and 6,600 m along y-axis with 440 cells, the total time of simulation is 3,000 s and we consider the Manning friction law with a spatially uniform friction coefficient value $n = 0.033\ \mathrm{m}^{1/3}.\mathrm{s}^{-1}$. According to the information given by EDF, the dam was considered as a straight line as illustrated on Fig. 2. As initial condition, water level upstream of the dam was set to 100 m and the rest of the valley was considered dry (illustrated in Fig. 2). Here, an open boundary conditions is used to represent a constant sea level whereas other dry boundary conditions are considered as closed boundary conditions.

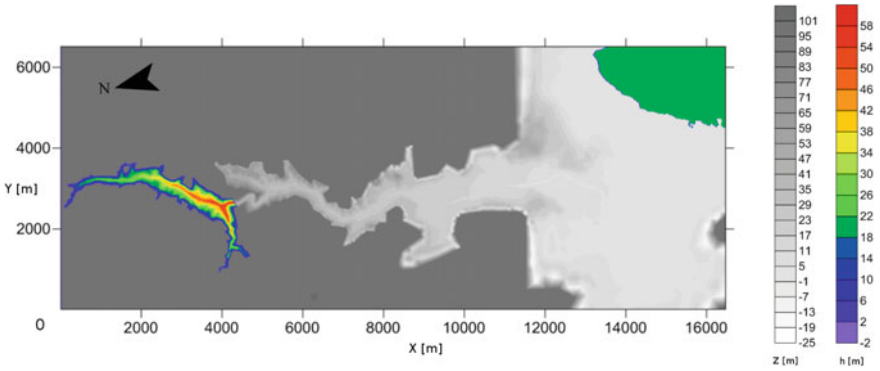

Fig. 2 Initial water height conditions, non zero water heights are considered upstream the dam and in the sea

2.2 2D SWE-Based Numerical Codes

FullSWOF_2D is a free and open-source software based on the 2D SWE under conservative form. This set of conservation laws is resolved thanks to a finite volume scheme, where the topography source term is treated thanks to the hydrostatic reconstruction [39]. This numerical method is conservative, positive water height preserving, and moreover well balanced (i.e., at least able to preserve steady state at rest). Two strategies have been chosen to parallelize it. The first one is a classical one. It is based on domain decomposition and MPI library. Domain decomposition method consists in dividing the data into many independent domains. On each domain, the code is executed by one anonymous process and when it is necessary, the processes communicate between each others via calls to MPI communication functions [22, 23]. The second one uses an implicit parallelism library called SkelGIS [25]. An implicit parallelism library is a library which proposes tools and interfaces to write a program, while hiding technical details of the parallelization of codes. SkelGIS is a C++ header-only library (only composed of C++ header files) to solve mesh-based partial differential equations in parallel, while preserving a sequential programming style. SkelGIS is composed of four components to hide parallelization of codes and to preserve a sequential programming style. First, to hide the distribution of the mesh among available processors, a distributed mesh is available, and called DM. Then, a way to map data onto the DM is proposed and called the DPMap component. Furthermore, a set of appliers, to apply user sequential functions (called operations) to a set of DPMaps, is the third component of SkelGIS. Finally, the last component is a programming interface to manipulate DPMaps almost as the containers of the C++ Standard Template Library (using iterators and specific algorithms). Up to now, SkelGIS has been implemented for Cartesian two-dimensional regular meshes and for the specific case of network simulations, where two different kinds of discretization are

composed in a same simulation [40]. The parallelization of FullSWOF_2D using SkelGIS has been detailed by Coullon et al. [24]. SkelGIS can be compared to OP2 [41] and Liszt [42], both created to handle parallel simulations-based on unstructured meshes discretization. OP2 is a complete implicit parallelism framework in C++ with a specific compilation process. Liszt, on the other hand, is denoted as a Domain Specific Language (DSL). Actually, the new language proposed by Liszt is specifically compiled and transformed to a parallel program. SkelGIS is a light header-only implicit parallelism library. Moreover, SkelGIS does not exactly propose the same level of abstraction than OP2 and Liszt.

To strengthen our comparison between the two parallel versions of FullSWOF_2D, standard commercial codes solving 2D SWE are used to simulate Malpasset dam-break case. Aim here is not to benchmark codes, but rather to check FullSWOF_2D results within a control group of codes which relies on different numerical schemes, and parallelization strategies. Numerical schemes of tested standard codes used for our controls use different approach, either based on Finite Differences (Mike 21), on Finite elements (TELEMAC 2D), or on Finite volumes (Mike 21 FM and TELEMAC 2D). Moreover, the spatial discretization is different among codes which rely either on structured mesh (Mike 21) or on non-structured mesh (TELEMAC 2D, Mike 21 FM).

Mike 21 and Mike 21 FM hydrodynamic modules solve the 2D SWE. The codes version used in this study are from the DHI 2012 release of the codes. Mike 21 uses finite differences scheme, with an Alternate Direction Implicit (ADI) method which implements an upwind treatment of the 2D SWE momentum equations convective term [43]. This approach allows code to handle supercritical flow occurrence, introducing numerical diffusion for computational stability sake [14, 44]. Mike 21 code solves ADI method using sequential CPU solution algorithm (Thomas algorithm). Development is in progress at DHI and in latest version of the code to include GPU-accelerated solvers for Mike 21 [45].

Mike 21 FM uses a spatially centered finite volume scheme. Roe solver is used to calculate convective fluxes at each cell interface. The code allows to use first order or second order method (Van Leer TVD slope limiter for second order in space and a second order Runge-Kutta method in time) [14]. Mike 21 FM uses shared memory (open MP) and distributed memory (MPI) architecture. These parallelization methods use METIS domain decomposition algorithm [46, 47] where computational domain is divided in sub-domains and where each CPU will compute solution for a given sub-domain. The exchange between sub-domains is computed using “halo-cells” [46].

TELEMAC 2D solves the 2D SWE, either using finite element or finite volume schemes. The version of TELEMAC code used here is the release V.6.2. TELEMAC 2D finite element method relies on a Stream Upwind Petrov-Galerkin (SUPG) solver to solve the hydrodynamic equations [48]. TELEMAC is parallelized using MPI. PARTEL is the utility used to proceed to mesh partitioning. Partel relies on METIS utility [48].

3 Results

3.1 Codes Results at Gaging Points and Transformers

Figures 3, 4, 5 and 6 illustrate results within the group of tested codes. FullSWOF_2D results are all computed using the MPI version. The time arrival at gauging points (Fig. 3), as well as elevation estimation of flood wave at these different gauging points (Fig. 4) are comparable among the softwares. When checking time arrival of the flood wave at the transformers (Fig. 5), it has to be noticed that beside for the first transformer, where FullSWOF_2D time arrival error is relatively more important compared to the other softwares, the results are comparable among numerical codes.

On Fig. 6, results show a comparison of the dam-break flood waves spatial extend at a given time. Comparable results are observable among the different softwares.

3.2 Parallel Experiments

To handle a complete comparison of both parallel implementations of FullSWOF_2D, the last important point to deal with, and thus the last point of our methodology, is to compare the obtained performance results. The most common way to evaluate the performance of a parallel program is to compute the speedup of the program. The speedup of a parallel programming represents the ratio between

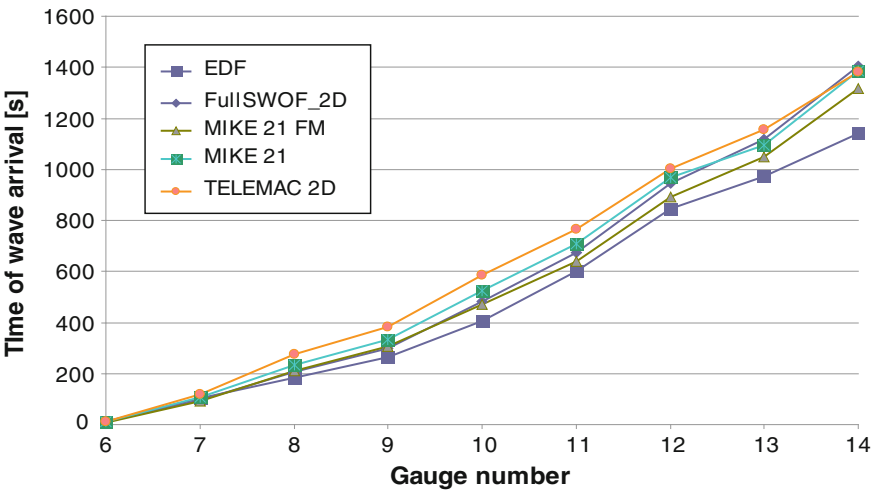

Fig. 3 Time arrival of Malpasset wave front at different gaging points with the different simulations relying on the group of tested codes

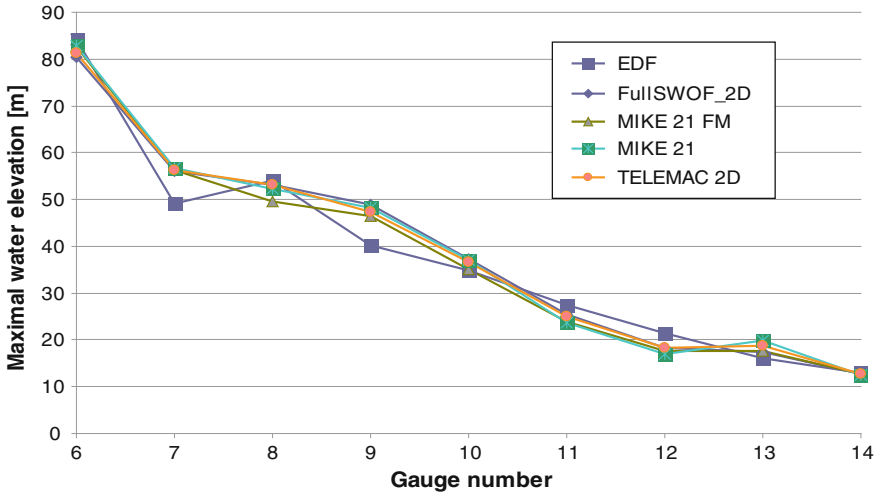

Fig. 4 Elevation estimated at the different gaging points with the different simulations relying on the group of tested codes

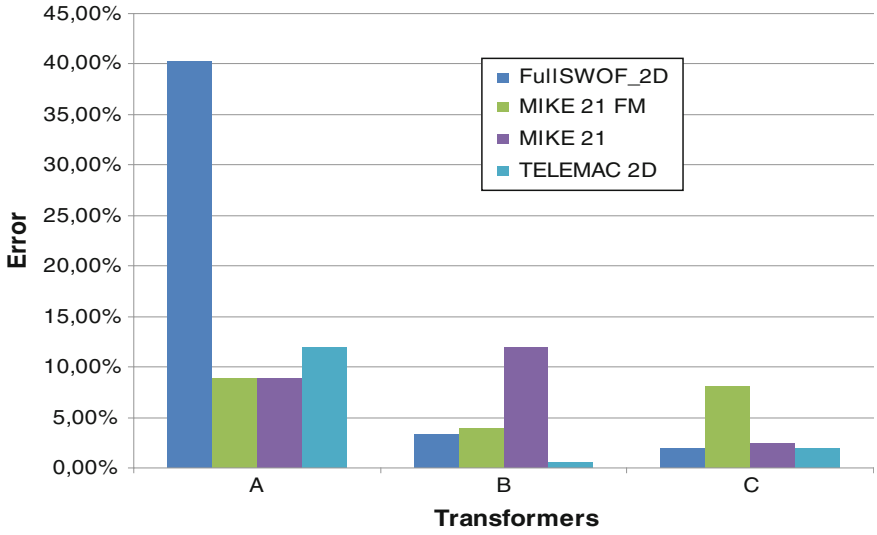

Fig. 5 Errors in time arrival of Malpasset wave front at different transformers relatively to real time of transformers shut down

the sequential execution time of the program, and the parallel execution time of the program. If we denote by p the number of processors (or cores) used by the parallel program, the ideal speedup is p. It means that, theoretically, it is not possible to obtain a better ratio than the number of processors used. To represent the speedup

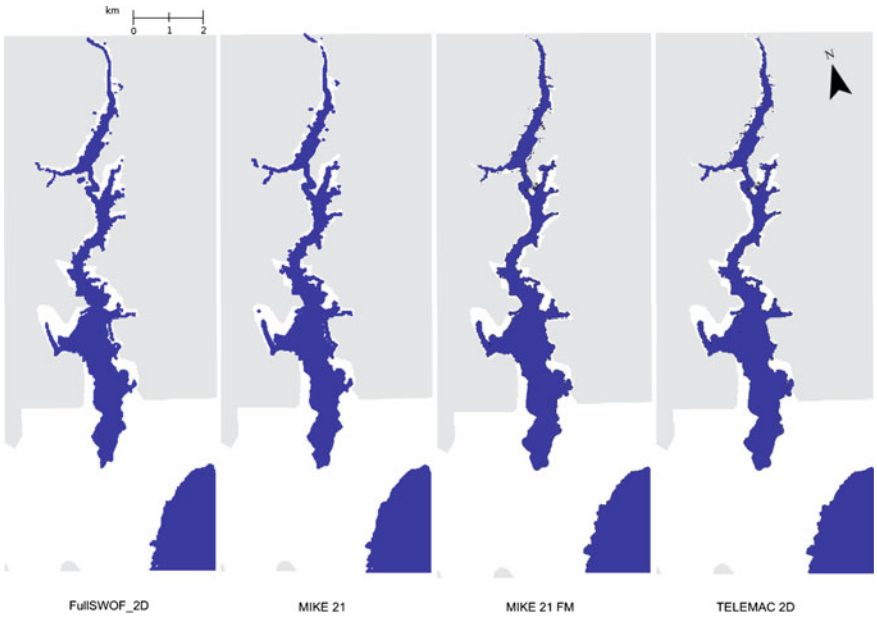

Fig. 6 Location of the front wave after 1500 s for the 4 considered codes

of a program, it is common to preserve the same inputs of the program, while modifying the number of processors (or cores) for each run. Thus, the speedup of a parallel program is drawn as a function of the number of processors. If the speedup is linear, the parallel program has a regular performance and it does not suffer from an increase of the number of processors. Thus, the load-balancing of work on the different processors is good and the communication cost between processors does not grow exponentially. The ideal speedup, as already explained, is represented by the line $f(x) = x$. The more the speedup is close to the ideal line, the more the performance of the program is interesting.

Figure 7 illustrates the first experiments carried out to evaluate the performance of the MPI parallel implementation of FullSWOF_2D. To carry out those experiments, the TGCC-Curie cluster (the 20th cluster of the top 500 list of November 2013) has been used. More precisely, a single "Curie super fat node" has been used. It contains sixty eight-cores CPU Nehalem-EX clocked at 2.27 GHz with 512 GB of memory. Thus, the speedup of the MPI implementation of FullSWOF_2D has been evaluated from 1 to 128 cores.

On Fig. 7, one can note that the speedup of the MPI implementation of FullSWOF_2D (drawn in red) is linear and close to the ideal speedup drawn in blue. Thus, this speedup shows that a very good performance could be expected from the MPI implementation of FullSWOF_2D. In the proposed methodology, speedups of both implementations will be compared.

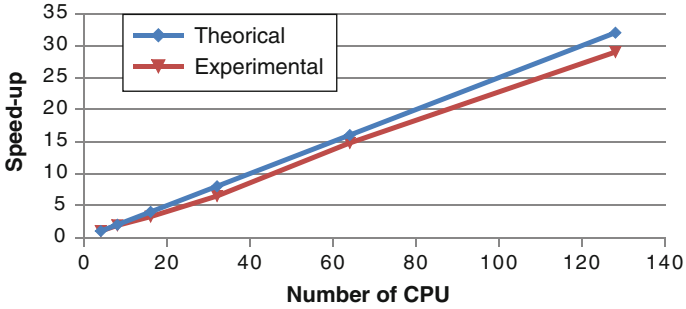

Fig. 7 Speedup observed with MPI version of FullSWOF_2D

4 Conclusions and Perspectives

On the Malpasset dam-break test case, FullSWOF_2D version results are compared to the results from other commercial softwares (Mike 21, Mike 21 FM, and TELEMAC 2D) which relies on different numerical schemes and parallelization strategies. FullSWOF_2D MPI version results in terms of hydrodynamic of the dam-break event simulation are comparable to the range of results obtained by other tested codes. The speedup of the MPI version of FullSWOF_2D code is promising. The framework of the dam break will be used to compare the MPI version with the SKELGIS version of FullSWOF_2D. Moreover, other applications are planed to be used to strengthen the comparison such as the Toce Valley flooding case [30, 31] and other real cases.

Acknowledgments This work was granted access to the HPC resources of Aix-Marseille Université financed by the project Equip@Meso (ANR-10-EQPX-29-01) of the program "Investissements d'Avenir" supervised by the Agence Nationale pour la Recherche.

References

1. Delestre, O. (2010). *Simulation du ruissellement d'eau de pluie sur des surfaces agricoles*. PhD thesis University of Orléans, in french. http://tel.archives-ouvertes.fr/INSMI/tel-00531377/fr.
2. Delestre, O., Cordier, S., Darboux, F., Du, M., James, F., Laguerre, C., et al. (2014). FullSWOF: A software for overland flow simulation. In P. Gourbesville, J. Cunge, & G. Caignaert (Eds.), *Advances in Hydroinformatics* (pp. 221–231). Springer Hydrogeology.
3. Esteves, M., Faucher, X., Galle, S., & Vauclin, M. (2000). Overland flow and infiltration modelling for small plots during unsteady rain: Numerical results versus observed values. *Journal of Hydrology, 228*, 265–282.
4. Tatard, L., Planchon, O., Wainwright, J., Nord, G., Favis-Mortlock, D., Silvera, N., et al. (2008). Measurement and modelling of high-resolution flow-velocity data under simulated rainfall on a low-slope sandy soil. *Journal of Hydrology, 348*(1–2), 1–12.

5. Goutal, N., & Maurel, F. (2002). A finite volume solver for 1D shallow-water equations applied to an actual river. *International Journal for Numerical Methods in Fluids, 38*, 1–19.
6. Caleffi, V., Valiani, A., & Zanni, A. (2003). Finite volume method for simulating extreme flood events in natural flood events in natural channels. *Journal of Hydraulic Research, 41*(2), 167–177.
7. Alcrudo, F., & Gil, E. (1999). The Malpasset dam break case study. In *The 4th CADAM Workshop, Zaragoza* (pp. 95–109).
8. Valiani, A., Caleffi, V., & Zanni, A. (2002). Case study: Malpasset dam-break simulation using a two-dimensional finite volume methods. *Journal of Hydraulic Engineering, 128*(5), 460–472.
9. Popinet, S. (2011). Quadtree-adaptive tsunami modelling. *Ocean Dynamics, 61*(9), 1261–1285.
10. Andres, L. (2012). L'apport de la donnée topographique pour la modélisation 3D fine et classifiée d'un territoire, in french, Revue XYZ (Vol. 133, 4th trimester, pp. 24–30).
11. Abily, M., Bertrand, N., Delestre, O., Richet, Y., Duluc, C.-M., & Gourbesville, P. (2014). Global sensitivity analysis with 2D hydraulic codes: Application on uncertainties related to high resolution topographic data. In *Proceeding of SimHydro 2014: Modelling of rapid transitory flows*. Sophia Antipolis, France, June 11–13, 2014.
12. Aackermann, P., Pedersen, P., Engsig-Karup, A., Clausen, T., & Grooss, J. (2013). Development of a GPU-accelerated mike 21 solver for water wave dynamics. In R. Keller, D. Kramer, & J.P. Weiss (Eds.), *Facing the Multicore-Challenge III, Springer Berlin Heidelberg* (Vol. 7686, pp. 129–130).
13. Brodtkorb, A. R., Saetra, M. L., & Altinakar, M. (2012). Efficient shallow water simulations on GPUs: Implementation, visualization, verification, and validation. *Computers and Fluids, 55*, 1–12.
14. DHI. (2007). MIKE 21 FLOW MODEL (p. 58). Hydrodynamic module: Scientific documentation. Danish Hydraulics Institute.
15. DHI. (2007). MIKE 21 and MIKE 3 FLOW MODEL FM (p. 50). Hydrodynamic and transport module: Scientific documentation. Danish Hydraulics Institute.
16. Hervouet, J.-M. (1999). TELEMAC, a hydroinformatic system/Télémac, un système hydroinformatique. *La Houille Blanche, 3–4*, 21–28.
17. Hervouet, J.-M., & Petitjean, A. (1999). Malpasset dam-break revisited with two-dimensional computations. *Journal of Hydraulic Research, 37*(6), 777–788.
18. Hervouet, J.-M. (2000). A high resolution 2-D dam-break model using parallelization. *Hydrological Processes, 14*, 2211–2230.
19. Hervouet, J.-M. (2007). *Hydrodynamics of free surface flows: Modelling with the finite element*. West Sussex: Wiley.
20. Delestre, O., Darboux, F., James, F., Lucas, C., Laguerre, C. & Cordier, S. (submitted). FullSWOF: A free software package for the simulation of shallow water flows. arxiv.org/abs/1401.4125.
21. Cordier, S., Coullon, H., Delestre, O., Laguerre, C., Le, M. H., Pierre, D., et al. (2013). FullSWOF_Paral: Comparison of two parallelization strategies (MPI and SKELGIS) on a software designed for hydrology applications, *ESAIM: Proc.*, **43**, 59–79.
22. Brugeas, L. (1996). Utilisation de MPI en décomposition de domaine. CNRS-IDRIS. http://www.idris.fr/data/publication/mpi.ps, p. 27.
23. EM Karniadakis, G., & Kirby II, R. M. (2003). *Parallel scientific computing in C++ and MPI*. Cambridge: Cambridge University Press.
24. Coullon, H., Le, M. -H., & Limet, S. (2013). Parallelization of shallow-water equations with the algorithmic skeleton library skelgis. International Conference of Computational Science. Barcelona Spain. Elsevier Procedia Computer Science, **18**, 591–600.
25. Coullon, H., Limet, S. (2013). Algorithmic skeleton library for scientific simulations: SkelGIS. International Conference on High Performance Computing and Simulation. Helsinki Finland. IEEE HPCS 2013 (pp. 429–436).

26. Abily, M., Delestre, O., Amossé, L., Bertrand, N., Richet, Y., Duluc, C.-M., et al. (submitted). Uncertainty related to high resolution classified topographic data use for flood event modeling over urban areas: a sensitivity analysis based approach.
27. Abily, M., Delestre, O., Amosse, L., Bertrand, N., Laguerre, C., Duluc, C.-M. et al. (2014). *Use of 3D classified topographic data with FullSWOF for High Resolution simulations of river flood event over a dense urban area*. 3rd IAHR Europe Congress, Book of Proceedings, 2014, Porto, Portugal.
28. Delestre, O., Lucas, C., Ksinant, P.-A., Darboux, F., Laguerre, C., Vo, T. N. T., et al. (2013). SWASHES: a compilation of Shallow-Water analytic solutions for hydraulic and environmental studies. *International Journal for Numerical Methods in Fluids, 72*, 269–300. doi:10.1002/fld.3741.
29. Delestre, O., Lucas, C., Ksinant, P.-A., Darboux, F., Laguerre, C., James, F., et al. (2014). SWASHES: A library for benchmarking in hydraulic. In Gourbesville, P., Cunge, J., & Caignaert, G., (Eds.), *Advances in Hydroinformatics*, Springer Hydrogeology (pp. 233–243).
30. Caleffi, V., Valiani, A., & Zanni, A. (2003). Finite volume method for simulating extreme flood events in natural channels. *Journal of Hydraulic Research, 41*, 167–177.
31. Valiani, A., Caleffi, V., & Zanni, A. (1999) Finite volume scheme for 2D Shallow-Water equations: Application to a flood event in the Toce river. *The 4th CADAM Workshop*, Zaragoza, Spain (pp. 185–206).
32. Berger, M. J., George, D. L., LeVeque, R. J., & Mandli, K. T. (2011). The GeoClaw software for depth-averaged flows with adaptive refinement. *Advances in Water Resources, 34*, 1195–1206.
33. Duran, A., Liang, Q., & Marche, F. (2013). On the well-balanced numerical discretization of shallow water equations on unstructured meshes. *Journal of Computational Physics, 235*, 565–586.
34. Malleron, N., Zaoui, F., Goutal, N., & Morel, T. (2011). On the use of a high-performance framework for efficient model coupling in hydroinformatics. *Environmental Modelling and Software, 26*, 1747–1758.
35. Singh, J., Altinakar, M. S., & Ding, Y. (2011). Two-dimensional modeling of dam-break flows over natural terrain using a central explicit scheme. *Advances in Water Resources, 34*, 1366–1375.
36. Mulder, T., Zaragosi, S., Jouanneau, J.-M., Bellaiche, G., Guérinaud, S., & Querneau, J. (2009). Deposits related to the failure of the Malpasset Dam in 1959 An analogue for hyperpycnal deposits from jokulhlaups. *Marine Geology, 260*, 81–89.
37. Benoist, G. (1989). Les études d'ondes de submersion des grands barrages d'EDF. *La Houille Blanche, 1*, 43–54.
38. Valiani, A., Caleffi, V., & Zanni, A. (1999). Finite volume scheme for 2D shallow-water equations. Application to Malpasset dam-break. In *The 4th CADAM Workshop, Zaragoza* (pp. 63–94).
39. Audusse, E., Bouchut, F., Bristeau, M.-O., Klein, R., & Perthame, B. (2004). A fast and stable well-balanced scheme with hydrostatic reconstruction for shallow water flows. *SIAM Journal on Scientific Computing, 25*(6), 2050–2065.
40. Coullon, H., Fullana, J.-M., Lagrée, P.-Y., Limet, S., & Wang, X. (2014). blood flow arterial network simulation with the implicit parallelism library SkelGIS. International Conference of Computational Science. Cairns Australia (On press).
41. Mudalige, G. R., Giles, M. B., Reguly, I., Bertolli, C., & Kelly, P. H. J. (2012). Op2: An active library framework for solving unstructured mesh-based applications on multi-core and many-core architectures. IEEE innovative Parallel Computing (InPar) (pp. 1–12).
42. de Vito, Z., Joubert, N., Palacios, F., Oakley, S., Medina, M., Barrientos, M., Elsen, F. H., Aiken, A., Duraisamy, K., Darve, E., Alonso, J., & Hanrahan, P. (2011). Liszt: A domain specific language for building portable mesh-based PDE solvers. In *Proceedings of 2011 International Conference for High Performance Computing, Networking, Storage and Analysis*, SC'11, pp. 1–12. ACM.

43. McCowan, A. D., Rasmussen, E. B., & Berg, P. (2001). Improving the performance of a two-dimensional hydraulic model for floodplain applications, In *Hydraulics in Civil Engineering*, (p. 11) T.I.o. Engineers (Ed.), Hobart, Australia.
44. DHI. (2007). *mike 21 and mike 3 flow model fm* (p. 50). Hydrodynamic and transport module: Scientific documentation. Danish Hydraulics Institute.
45. Aackermann, P., Pedersen, P., Engsig-Karup, A., Clausen, T. & Grooss, J. (2013). Development of a GPU-accelerated mike 21 solver for water wave dynamics. In R. Keller, D. Kramer, & J.-P. Weiss (Eds.), *Facing the Multicore-Challenge III, Springer Berlin Heidelberg* (Vol. 7686, pp. 129–130).
46. Sørensen, O. R., Sørensen, L. S., & Carlson, J. (2010). Parallelization of the flexible mesh modeling systems with MPI. In *International MIKE by DHI Conference 2010* (pp. 30.1–30.8). Copenhagen, Denmark,
47. Karypis, G. & Kumar, V. (1998). METIS: family of multilevel partitioning algorithm. http://glaros.dtc.umn.edu/gkhome/views/metis.
48. Audouin, Y., Moulinec, C., Barber, R. W., Sunderland, A. G., Gu, X. -J. & Emerson, D. R. (2011). Preparing TELEMAC-2D for extremely large simulations. In *Proceedings of the XVIIIth Telemac and Mascaret User Club 19–21 October 2011*. Chatou (France): EDF R&D.

Numerical Simulation of Hydrodynamics and Residence Time in Alpine Lake with Three-Dimensional Model

Wen-Cheng Liu, Ming-Hsi Hsu and Wei-Bo Chen

1 Introduction

In aquatic environment such as shallow lakes, can stratify and destratify in a day, and may even remain persistently stratified over a couple of days. The entire water column in a shallow lake can behave as a diurnal mixed layer. The diurnal physical dynamics and the dynamics of phytoplankton [7], dissolved oxygen [1, 2], phosphorus [8], water color [12], methane [6], and other biogeochemical processes have been investigated.

Typhoon-induced inflow in Taiwan is an important factor to affect the mixing in the water column. Vertical mixing by turbulence in the mixed layer and circulation due to meteorological conditions have been numerically studied using one-dimensional mixed layer and two-dimensional, three-dimensional circulations models. Most of the existing numerical models are based on solving the shallow water equations, together with diffusion equations for the transport and dispersion of constituents and pollutants. Many two-dimensional models [3–5, 9] have been developed, but the deployment of two-dimensional models to simulate vertical

W.-C. Liu (✉) · M.-H. Hsu
Department of Civil and Disaster Prevention Engineering,
National United University, Miaoli 36003, Taiwan
e-mail: wcliu@nuu.edu.tw

W.-C. Liu
Taiwan Typhoon and Flood Research Institute, National Applied Research Laboratories,
Taipei 10093, Taiwan

M.-H. Hsu
Department of Bioenvironmental Systems Engineering,
National Taiwan University, Taipei 10617, Taiwan

W.-B. Chen
National Science and Technology Center for Disaster Reduction, New Taipei City 23143,
Taiwan

P. Gourbesville et al. (eds.), *Advances in Hydroinformatics*,
Springer Water, DOI 10.1007/978-981-287-615-7_28

mixing, circulation, and wind-induced currents is not appropriate because the three-dimensional characteristics exist in the lakes. In recent years, a variety of three-dimensional models have been developed to simulate the hydrodynamics and wind-induced circulation, enabling to predict the substantial variation and reversal of the current along the bed induced by the wind action.

In the present study, a real-time three-dimensional hydrodynamic and hydrothermal model is adopted to simulate water temperature and circulation in the stratified lake. Model simulation was validated against water level, current, time-series water temperature, and vertical profiles of water temperature in 2008. The validated model was then applied to investigate the wind-driven current and mean circulation in the Yuan-Yang Lake (YYL). The lake's residence time was also calculated and discussed using the validated model.

2 Description of Study Site

Yuan-Yang Lake (YYL) is in the northeastern region of Taiwan (24°35′N, 121°24′E) (Fig. 1a). YYL is a small (3.6 ha), shallow (4.5 m maximum depth) lake in a mountainous catchment 1,730 m above sea level. Figure 1b shows the bathymetry of YYL. The lake and surrounding catchment (374 ha) were designated as a long-term ecological study site by the Taiwan National Science Council in 1992 and joined the Global Lake Ecological Observatory Network (GLEON) in 2004. The steep watersheds are dominated by pristine Taiwan false cypress [*Chamaecyparis obtusa* Sieb. & Zucc. var. *formosana* (Hayata) Rehder] forest. YYL is slightly stained, with an average DOC concentration of 6.1 mg L^{-1} and mean pH of 5.9. The average annual temperature is approximately 13 °C (monthly average ranges from −5 to 15 °C) and the annual precipitation is more than 4,000 mm. YYL is subject to three to seven typhoons in summer and autumn each year, during which more than 1,700 mm of precipitation may fall on the lake [11].

An instrumented buoy was deployed at the deepest spot in YYL (Fig. 1b) to record surface dissolved oxygen (DO), water temperature, and wind speed every 10 min. Surface DO concentrations were measured at 0.25 m depth by a sonde (600-XLM, YSI, Inc. Yellow Springs, OH, U.S.A.) fitted with a rapid-pulse oxygen–temperature electrode (YSI, model 6562). Water temperatures were measured through the water column at 0.5 m increments by a thermistor chain (Templine, Apprise Technologies, Inc. Duluth, MN, U.S.A.). Wind speed was measured 1 m above the lake by an anemometer (model 03001, R.M. Young, Traverse, MI, U.S.A.). Precipitation, air temperature, and downwelling photosynthetically active radiation (PAR) were measured at a land-based meteorological station approximately 1 km away from the lake. Variation in water level was measured using a submersible pressure transmitter (PS 9800(1), Instrumentation Northwest, Kirkland, WA, U.S.A.) deployed at the lake shore (Fig. 1b).

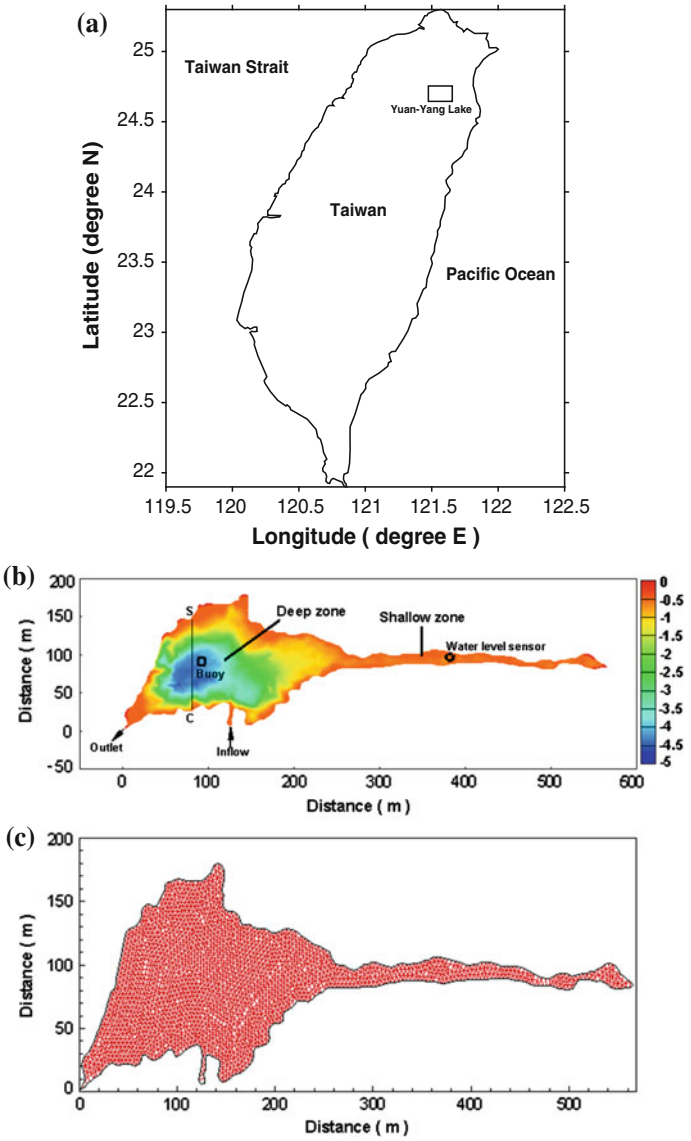

Fig. 1 **a** Location of Yuan-Yang lake in Taiwan, **b** bathymetry, buoy, and water level locations, and **c** unstructured horizontal grid of Yuan-Yang Lake

3 Numerical Model

In this paper, a three-dimensional semi-implicit Eulerian–Lagrangian finite element model [17] was implemented to the YYL. SELFE solves the Reynolds-stress averaged Navier–Stokes equations consisting of conservation laws for mass, momentum, and temperature, under the hydrostatic and the Boussinesq approximations, to yield the free surface elevation, three-dimensional water velocity and water temperature.

$$\nabla \cdot \overrightarrow{u} + \frac{\partial w}{\partial z} = 0 \tag{1}$$

$$\frac{\partial \eta}{\partial t} + \nabla \cdot \int_{-h}^{\eta} \overrightarrow{u} dz = 0 \tag{2}$$

$$\begin{aligned} \frac{D\overrightarrow{u}}{Dt} &= \mathbb{F} - g\nabla\eta + \frac{\partial}{\partial z}\left(v\frac{\partial \overrightarrow{u}}{\partial z}\right) \\ \mathbb{F} &= -f\overrightarrow{k} \times \overrightarrow{u} + \alpha g \nabla \hat{\psi} - \frac{1}{\rho_0}\nabla P_A - \frac{g}{\rho_0}\int_z^{\eta} \nabla\rho d\zeta + \nabla \cdot (\mu \nabla \overrightarrow{u}) \end{aligned} \tag{3}$$

$$\frac{DT}{Dt} = \frac{\partial}{\partial z}\left(K_{sv}\frac{\partial T}{\partial z}\right) + \frac{\dot{Q}}{\rho_0 C_p} + F_h \tag{4}$$

$$\rho = \rho_0(p, T) \tag{5}$$

where (x, y): horizontal Cartesian coordinates; z: vertical coordinate, positive upward; $\nabla: \left(\frac{\partial}{\partial x}, \frac{\partial}{\partial y}\right)$; t: time; $\eta(x, y, t)$: free surface elevation; $h(x, y)$: bathymetric depth; $\overrightarrow{u}(x, y, z, t)$: horizontal velocity, with Cartesian components (u, v); w: vertical velocity; f: Coriolis factor; g: acceleration of gravity; $\hat{\psi}(\phi, \lambda)$: earth tidal potential; α: effective Earth elasticity factor; $\rho(x, t)$: water density; by default, reference value ρ_0 is set as 1025 kg/m^3; $P_A(x, y, t)$: atmospheric pressure at the free surface; p: pressure; T: water temperature; v: vertical eddy viscosity; μ: horizontal eddy viscosity; K_{sv}: vertical eddy diffusivity for water temperature, F_h: horizontal diffusion for transport equation; $\dot{Q}$: rate of absorption of solar radiation; and C_p: specific heat of water.

SELFE model is based on a finite element scheme. Unlike most three-dimensional models, no mode splitting is allowed. Semi-implicit schemes are applied to all equations to enhance stability and to maximize efficiency. An Eulerian–Lagrangian method (ELM) is used to treat the advection, thus allowing large time step to be used without compromising stability. The entire domain is discretized in the horizontal and vertical directions. Unstructured triangular grids are used in the horizontal direction.

In the vertical, models based on terrain-following coordinated suffer, to some degree, from the hydrostatic inconsistencies. This follows from the fact that terrain-following coordinates do not conform to the geopotential, and the pressure gradient is evaluated as the difference between two large components that tend to cancel each other, thus being to large discretization errors. It can also be viewed as result of evaluating pressure at a grid point efficiently using extrapolation when steep bathymetric slopes are presented [16]. Many remedies have been used to prevent this, including evaluating the gradient in the Z-coordinate [16] or applying high-order schemes [14]. In the present model, the use of a hybrid coordinate system in the vertical effectively wards off the hydrostatic inconsistency because the Z-coordinates used in the deeper part of the vertical serves to "stabilize", while S-coordinates used at the upper part of the water column.

SELFE uses the Generic Length Scale (GLS) turbulence closure of Umlauf and Burchard [15] which has the advantage of encompassing most of the 2.5-equation closure model. The detailed description of turbulence closure model, vertical boundary conditions for the momentum equation, the numerical solution methods, and numerical stability can be found in [17].

In this study, the bottom topography data in the YYL which were measured in August, 2007, were obtained from the Academia Sinica, Taiwan. The deepest depth within the study area is 4.5 m near the buoy station (Fig. 1b). The model mesh for the YYL consists of 4,148 polygons in horizontal direction (Fig. 1c). High solution grids which include the mesh size ranged from 3.2 to 6.6 m are used in the YYL. The terrain-following "pure S" layers were adopted in vertical direction and 20 evenly spaced S-levels were used. The "pure S" representation of SELFE was chosen to avoid the staircase representation of the bottom and surface, and thus loss of accuracy. For this model grid, a large time step ($\Delta t = 120$ s) was used in simulations with no sign of numerical instability. It means that 263520 time steps for 1 year simulation. One year of simulation takes about 2.5 days on an Intel Core I5 PC.

4 Model Validation

The SELFE has been successfully applied to several estuaries and coastal oceans [10, 17], but little used to lakes. To ascertain the model accuracy for practical application, a large set of observational data is used to validate the model and to verify its capability to predict water surface elevation, residual current, and water temperature in this study.

4.1 Water Surface Elevation and Velocity

The model validation of water surface elevation was conducted with daily discharge at the inflow and outlet in the lake (shown in Fig. 1b). Figure 2a presents the

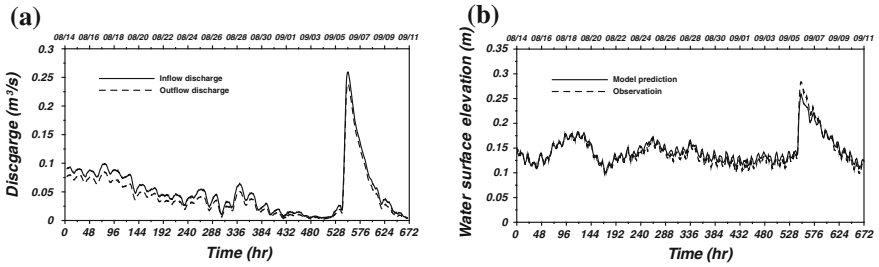

Fig. 2 **a** Time-series inflow and outflow discharges and **b** Comparison of water surface elevation between model prediction and observation from August 14 to September 10, 2008

time-series inflow and outflow discharges. It reveals that the peak discharge occurred on September 6 due to the typhoon event. The observed water surface elevations in the YYL from August 14 to September 10, 2008 were used to compare with model predictions shown in Fig. 2b.

Good model performance is indicated by the calculated absolute mean error (AME) and root-mean-square error (RMSE) statistic values. AME is the average of the absolute values of differences between observed data and simulated values. RMSE basically specifies the overall difference in the sum of squares normalized to the number of observations. Both AME and RMSE provide an indication of the magnitude of the model's prediction uncertainty for a type data point. RMSE is similar to a standard error of the mean for the model's uncertainty. The AME and RMSE between computed and observed water surface elevation are 0.65 and 0.79 cm, respectively. It reveals that the simulated results mimic the observed water surface elevations.

Figure 3 presents the comparison of model simulated and measured velocity profiles at the buoy station on September 16, 2008. It shows that the return current occurred in the velocity profiles at u and v components. The simulated results closely match the measured velocity profiles and indicate that the model has the capability to predict the current patterns in the lake.

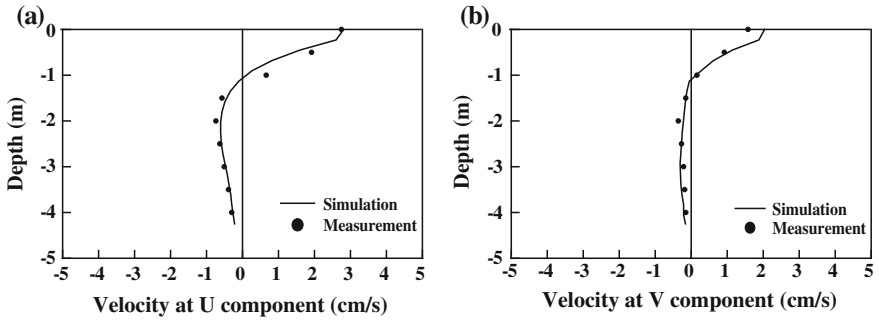

Fig. 3 Comparison of model simulated and measured velocities on September 16, 2008 at the **a** *u* component, and **b** *v* component

4.2 Water Temperature

To validate the water temperature, the time-series data collected from July to September 2008 was used to compare with simulated results. Figure 4a presents the comparison of model predicted and measured water temperature at depths 0.25 and 3.5 m from July 6 to September 4, 2008. Two typhoon events hit Taiwan during July 16–18 and July 26–29 and resulted in well mixing conditions because the high precipitation and inflow occurred during these periods. The AME and RMSE between computed and observed water temperature at 0.25 m depth are 0.96 °C and 1.47 °C, respectively, while AME and RMSE at 2.0 m depth are 0.50 °C and 0.97 °C, respectively. Figure 4b–d illustrate the observed and calculated water temperature profiles at three time periods.

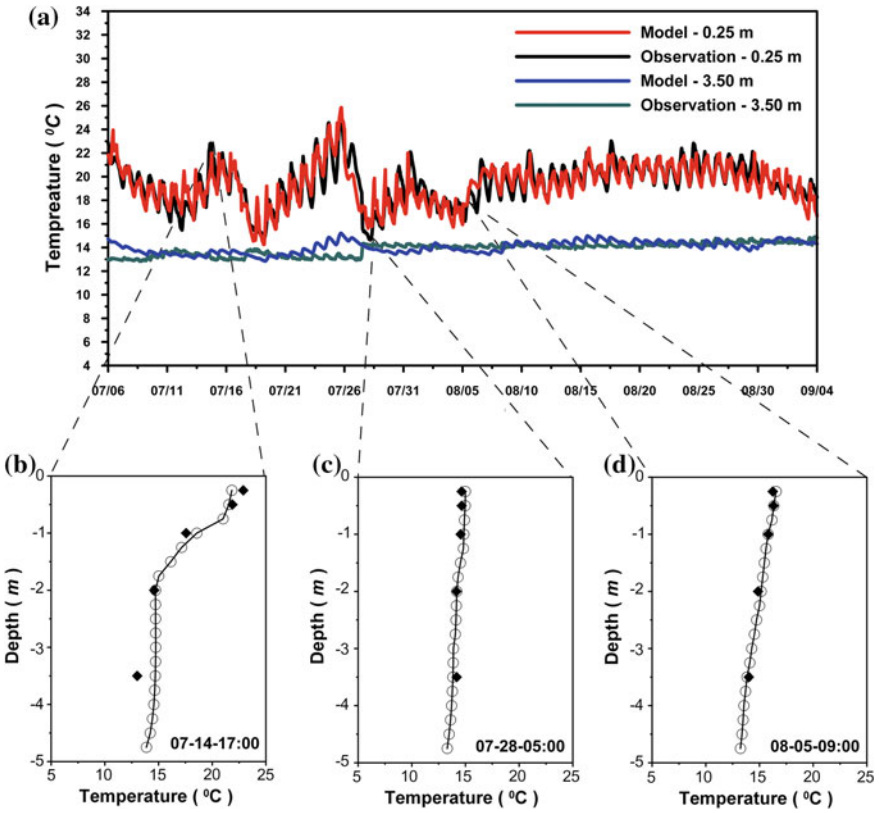

Fig. 4 **a** The comparison of model predicted (*open circles line*) and measured (*diamond*) water temperature in the YYL from July to September 2008. Vertical temperature profile at different time spans **b** 17:00 July 14, **c** 5:00 July 28, and **d** 9:00 August 5

5 Mean Circulation and Residence Time

5.1 Mean Circulation

The mean circulation in the YYL is one of the important factors responsible for the transport and distribution of nutrients within the lake. In order to examine how the nutrients could be distributed in the YYL, the mean circulation of the model that runs for the period of May 1 to June 30, 2008 was yielded (Fig. 5). The large-scale patterns of the mean surface circulation produced by the model follows the general wind pattern over the area. The surface currents, in general flow toward the southwest direction and forms a clockwise rotation. The bottom currents are in opposite direction as surface currents due to return flows. The near-bottom currents are smaller than surface currents. The mean surface currents were between 1.1 and 3.6 cm/s. The mean surface temperature during this whole period was around 22 °C at the shallow area and 19 °C at the deep region. The mean temperature difference between the surface and bottom was around 5 °C in the deeper region. No remarkable cyclonic and anticyclonic circular gyres were found in the lake through the simulated mean currents.

5.2 Residence Time

The evaluation of the mean residence time of water in a lake is a problem of fundamental importance for theoretical and applied limnology. It can lead to the knowledge of the proportions and dynamics of the chemical substances dissolved in the water, or the rate at which the processes of concentration, dilution, and permanence of substances within the lake occur, with resulting implications for the water quality.

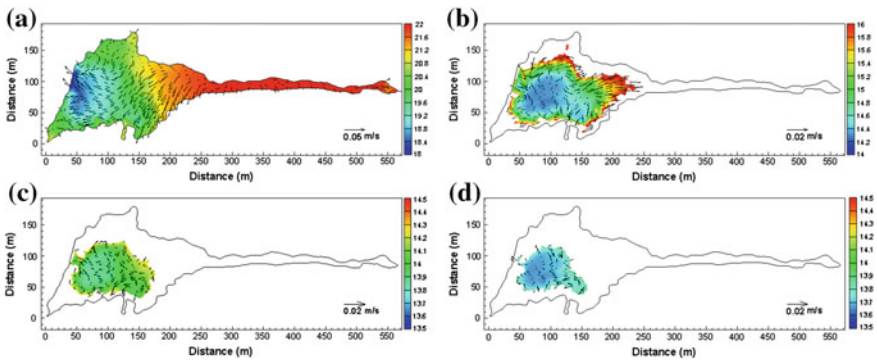

Fig. 5 Mean circulation and average temperature during May and June 2008 at **a** surface **b** 1 m below surface, **c** 2 m below surface, and **d** 3 m below water surface

A first-order description of transport is expressed as "residence time" or "flushing time", a measure of water mass retention within defined boundaries. Aquatic scientists often estimate retention time to compare to time scales of input or biogeochemical processes to calculate mass balances or understand dynamics of population and chemical properties [13].

The residence time is preferred in this study to investigate the possibility of physical transport mechanisms. The experiment was conducted with a certain amount of mass, m_0, of a conservative tracer injected at time t_0 and at certain location. The time varying tracer mass, $m(t)$, remaining in the water body is then measured. The quantity $m(t)$ is found from the spatial integration of the measured concentration field within the water body, and its decline over time reflects the net rate at which tracer leaves the water body. The rate of mass loss as a function of time $r(t)$ provides residence time distribution, $\varphi(t)$,

$$r(t) = \varphi(t) = -\frac{1}{m_0}\frac{dm}{dt} \tag{6}$$

Equation (1) represents the residence time distribution of unit, $[T]^{-1}$. The mean residence time, based on the first moment of $r(t)$, can be calculated as

$$T_r = \int_0^\infty r(t)tdt = -\frac{1}{m_0}\int_0^\infty t[\frac{dm}{dt}]dt \tag{7}$$

where t is time and T_r is the mean residence time.

One issue remains in the application of Eq. (7) is the upper limit of the integration. Theoretically, the integration should be processed to the time when the residual mass reaches zero. In most circumstances, it may take infinitely long time. In this study, we adopt 1 % of residual mass which is designed to be the upper limit of the integration in Eq. (7).

The validated three-dimensional hydrodynamic and hydrothermal model was used to calculate the residence time in response to different inflow discharges with and without wind effects in the YYL. Tracer concentration of 10 was occupied in the lake and then the model was run with different discharges from inflow boundaries. To investigate the wind effects on the residence time, the model was forced with northeast wind, southwest wind, and without wind stress. The wind speed was specified with 1.4 m/s when wind stress was included.

Figure 6 plots the residence time versus the inflow discharge with and without wind effects. In all three scenario runs, data obtained from hydrodynamic and hydrothermal model simulations indicate that residence time reduce in response to inflows in a similar pattern. Least square regression analysis was conducted. Empirical best-fitting equations were obtained in forms of power law. The power law empirical equations fit well with the residence time resulted from the hydrodynamic and hydrothermal model simulations, with correlation R^2 values above 0.97. Empirical regression equations of residence time (T_r) versus inflows (Q) are given below:

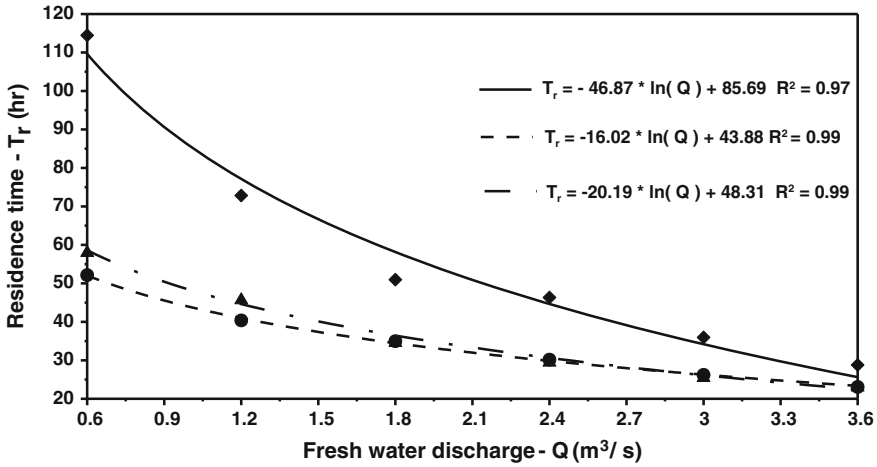

Fig. 6 Residence time (T_r) corresponding to the different discharges (Q), which include without wind effect (*solid line* and *diamonds*), with northeast wind (*dashed line* and *circles*), and with southwest wind (*dotted-dashed line* and *triangles*)

(a) Without wind stress:

$$T_r = -46.87 \cdot \ln(Q) + 85.69, R^2 = 0.97 \tag{8}$$

(b) With northeast wind effect:

$$T_r = -16.02 \cdot \ln(Q) + 43.88, R^2 = 0.99 \tag{9}$$

(c) With southwest wind effect:

$$T_r = -20.19 \cdot \ln(Q) + 48.31, R^2 = 0.99 \tag{10}$$

where R^2 is coefficient of determination.

The simulated results reveal that the residence time without wind stress is higher than that with wind stress, indicating that wind plays a significant role in mixing in the lake. The residence time with southwest wind is slightly higher that with northeast wind. A shorter residence time is beneficial to pollutant removal.

When the inflow is 0.6 m^3/s, the distribution of tracer concentration at cross-section C–S (see Fig. 1b) at 48th h with and without wind effects is presented in Fig. 7. It reveals that the obvious stratification in trace concentration and the concentration at the bottom layer is higher than that at the surface layer. The bottom concentration without wind effect is higher than that with wind effect. The bottom concentration with southwest wind is also higher than that with northeast wind. It means that the residence time is higher without wind effect because it takes longer time to reach 1 % of residual mass presented in Eq. (7).

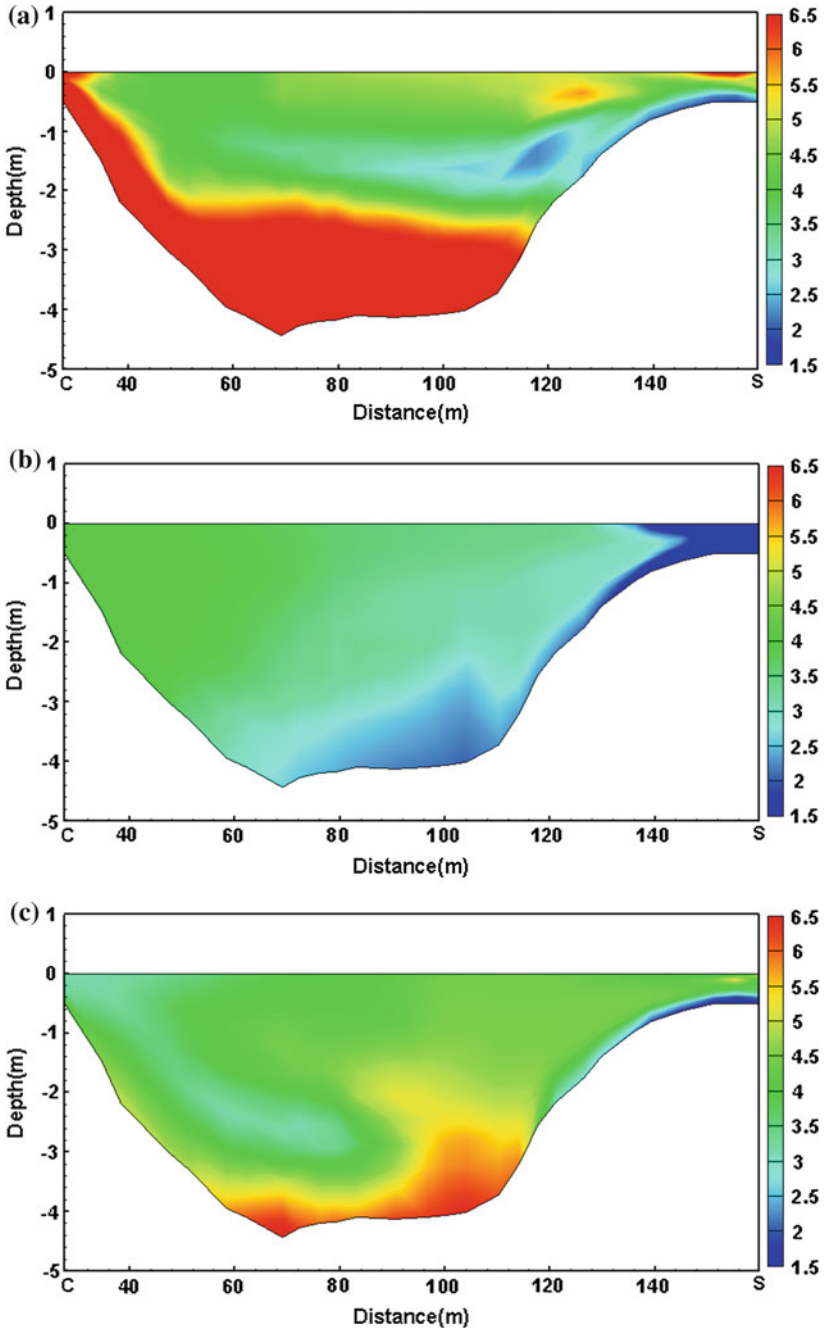

Fig. 7 Tracer distribution at cross-section C–S under the 0.6 m^3/s discharge condition at 48th h **a** without wind effect, **b** with northeast wind, and **c** with southwest wind

6 Conclusions

A three-dimensional hydrodynamic and hydrothermal model was implemented and applied to the subtropical alpine Yuan-Yang Lake (YYL) in the northeastern region of Taiwan. The model was verified with measured water surface elevation, current, and water temperature in 2008. Overall the model simulation results are in reasonable agreements with observations. Through the verification results, we also found that water temperature exhibited more mixing condition during the high rainfall event, while more stratification occurred during the normal condition.

The validated model was also used to calculate the mean residence time in response to different inflows with and without wind effects. Regression analysis of model results reveals that an exponential equation can be used to correlate the residence time to change of inflow discharges. The calculated system residence time is strongly dependent on the inflows and wind effects. The residence time decreases as the inflow discharge increases. The residence time without wind stress is higher than that with wind effect, indicating that wind plays an important role in lake mixing. The simulated results reveal that residence time is approximately 2–2.5 days under low inflow with wind effect. Because the residence time is an important indicator for lake water quality and ecosystem assessments, results from this study are helpful for environmental management of the YYL.

Acknowledgments This study was supported by the National Science Council and Academia Sinica, Taiwan, under the grant number NSC-96-2628-E-239-012-MY3 and AS-98-TP-B06, respectively. The financial support is highly appreciated.

References

1. Branco, B. (2007). *Coupled physical and biogeochemical dynamics in shallow aquatic systems: Observation, theory and models*. The University of Connecticut, 223 p.
2. Branco, B., & Torgersen, T. (2009). Predicting the onset of thermal stratification in shallow inland waterbodies. *Aquatic Sciences, 71*(1), 65–79.
3. Cole, T. M., & Wells, S. A. (2000). *Hydrodynamic modeling with application to CE-QUAL-W2*. Portland, OR: Workshop Notes, Portland State University.
4. Edinger, J. E., & Buchak, E. M. (1983). *Development in LARM2: A longitudinal-vertical, time-varying, time-varying hydrodynamic reservoir model*. US Army Corps of Engineers Waterways Experiment Station Technical Report.
5. Falconer, R. A. (1986). Water quality simulation study of a natural harbor. *Journal of Waterway, Port, Coastal, and Ocean Engineering ASCE, 112*(1), 15–34.
6. Ford, P. W., Boon, P. I., & Lee, K. (2001). Mathane and oxygen dynamics in a shallow floodplain lake: the significance of periodic stratification. *Hydrobiologia, 485*(1–3), 97–110.
7. Ganf, G. G. (1974). Diurnal mixing and the vertical distribution of phytoplankton in a shallow equatorial lake (Lake George, Uganda). *Journal of Ecology, 62*(2), 611–629.
8. Havens, K. E., Jin, K. R., Nenad, I., & Thomas, J. R. (2007). Phosphorus dynamics at multiple time scales in the pelagic zone of a large shallow lake in Florida, USA. *Hydrobiologia, 581*(1), 25–42.

9. Lap, B. Q., & Mori, K. (2007). A two-dimensional numerical model of wind-induced flow and water quality in closed water bodies. *Paddy and Water Environment, 5*(1), 29–40.
10. Liu, W.C., Chen, W.B., & Wu, C.H. (2008). Modelling effects of realignment of Keelung River, Taiwan. *Proceedings of the Institution of Civil Engineers-maritime Engineering*, *161* (2), 73–87.
11. Kimura, N., Liu, W. C., Chiu, C. Y., Kratz, T. K., & Chen, W. B. (2012). Real-time observation and prediction of physical processes in a typhoon-affected lake. *Paddy and Water Environment, 10*(1), 17–30.
12. Persson, I., & Jones, I. D. (2008). The effect of water color on lake hydrodynamics: a modeling study. *Freshwater Biology, 53*(12), 2345–2355.
13. Rueda, F., Moreno-Ostos, E., & Armengol, J. (2006). The residence time of river water in reservoirs. *Ecological Modelling, 191*(2), 260–274.
14. Shchepetkin, A. F., & McWilliams, J. C. (2003). A method for computing horizontal pressure-gradient force in an oceanic model with a nonaligned vertical coordinate. *Journal Geophysical Research, 108*(C3), 3090.
15. Umlauf, L., & Buchard, H. (2003). A generic length-scale equation for geophysical turbulence models. *Journal of Marine Research, 61*(2), 235–265.
16. Yuan, H. L., & Wu, C. H. (2004). An implicit three-dimensional fully non-hydrostatic model for free-surface flows. *International Journal for Numerical Methods in Fluids, 46*(7), 709–733.
17. Zhang, Y. L., & Baptista, A. M. (2008). SELFE: A semi-implicit Eulerian-Lagrangian finite-element model for cross-scale ocean circulation. *Ocean Modelling, 21*(3–4), 71–96.

1D, 2D, and 3D Modeling of a PAC-UPC Laboratory Canal Bend

Manuel Gómez and Eduardo Martínez-Gomariz

1 Introduction and Scope of the Study

The free surface flow is a type of flow widely studied in hydraulics, particularly related with canals and fluvial dynamics. Their study can be made through 1D, 2D, or 3D numerical modeling, the most common being the 1D modeling to carry out the hydraulic analysis of rivers or channels. More and more is implemented on the 2D analysis, even assuming a higher computational cost, but the 3D analysis is not considered too often yet. The 2D analysis is carried out in areas where the velocity components in two directions dominate over the third (deltaic areas for example) and 3D analysis is performed in localized areas, where clearly 3D effects (eddies and complex phenomena) occur needing a higher computational cost.

Currently, in Campus Nord hydraulic lab in Barcelona, a canal is located to test control algorithms, canal PAC-UPC. This canal tries to reproduce aspects of real irrigation canals with gates and offtakes. It was built in 2003 and since then several PhD and MSc theses related to irrigation canals were presented, and specifically with the development of canal control algorithms. These algorithms aim at the automation of the canal sluice gates, so that in every canal reach flow, water levels can be prescribed at selected points, and sluice gates can be moved to ensure desired water flows and water levels at those selected points (offtakes).

From the beginning it was observed the local over-elevation on the bend zone. Because the canal aims to reproduce a real irrigation canal and the real irrigation canal control problems, these over-elevations had to be studied and the consequences over the canal facility have to be verified.

M. Gómez · E. Martínez-Gomariz (✉)
FLUMEN Research Institute, Technical University of Catalonia, Jordi Girona, 1-3, 08034 Barcelona, Spain
e-mail: eduardo.martinez-gomariz@upc.edu

M. Gómez
e-mail: manuel.gomez@upc.edu

P. Gourbesville et al. (eds.), *Advances in Hydroinformatics*,
Springer Water, DOI 10.1007/978-981-287-615-7_29

Such flow behavior is clearly observable visually, which suggests that hydraulic phenomenon occurs even with low velocities. Flow trajectories with abrupt changes along the bend in the horizontal plane, and 90° turns off the streamlines in the vertical plane are produced, before the pass is under the sluice gate. These paths indicate that the velocity components are significant in all three directions and not only prevalent in one (1D) or two directions (2D).

Figure 1 shows the irregularities that occur on the free surface, mostly next to the bend and with the influences from the downstream sluice gate and the weir.

Numerical methods applied to hydraulic problems increasingly offer more computing power and the market has a variety of softwares, including many open-sources. A powerful tool for the modeling and simulation of 3D problems is the Flow-3D program. This tool has been used for the studies reported in this work and the analysis has been supplemented by open-source softwares such as Hec-Ras and Iber [6]. So it has been performed a detailed flow analysis, through 1D-, 2D-, and 3D codes.

The main objective of this study is to understand in detail the flow patterns in this canal, when the flow encounters a bend, a weir, and a downstream sluice gate. Obviously, this flow behavior knowledge may lead to secondary but no less important goals, such as relocation of the measuring instrument if necessary or even the rehabilitation of the bend shape if the flow behavior requires it.

The use of 1D, 2D, and 3D numerical modeling tools offers the possibility to compare the results of these tools and study the pros and cons of each of these types of approach. So the aims of this study can be summarized as:

- To understand in detail the hydraulic behavior of the flow that occurs in the PAC-UPC laboratory canal curved reach.
- Comparison of 1D, 2D, and 3D modeling, and analysis of their suitability as needed.
- Analyse, after the hydraulic behavior of the flow, the possibility of relocating the canal instrumentation, and modify the shape of the canal's structure.

Fig. 1 PAC-UPC laboratory canal bend in operation

2 Canal Description

Canal PAC-UPC is the acronym of "Canal de Pruebas de Algoritmos de Control (Test Canal Algorithms Control)—Universitat Politècnica de Catalunya (Technical University of Catalonia)". As its name suggests, it is a specially designed laboratory canal for basic and applied research in the area of irrigation canal control, canal instrumentation, canal modeling, water measurements, etc. It is implemented in the Laboratory of Physical Models, Campus Nord UPC.

Its construction was intended to reproduce the characteristics of real irrigation canals and thus control problems that may appear. For this reason, a canal with maximum possible length and zero slope to produce the maximum time delay was built. Limited space in the laboratory became necessary to construct the current snake shape that optimizes the area occupied. This is a 220 m long canal, with a rectangular cross-section of 44 cm wide and 1 m high, occupying a total floor area of 22.5 m × 5.4 m approx.

As shown in Fig. 2, the elements of installation are as follows:

- A header reservoir
- Three vertical sluice gates (G1, G3, and G5)

Fig. 2 Detailed scheme of the whole PAC-UPC canal

- Four rectangular weirs (W1, W2, W3, and W4)
- Nine level sensors (LS1 to LS9)
- A control room

Items marked as transparent are not in operation, such as gates 2 and 4, and sensors 4 and 8, but it is possible to use if needed for future experiments. Sluice gates and weirs allow different work operations.

3 General Approach to the Problem

3.1 Introduction

This study is on PAC-UPC canal and more specifically on the canal bend where weir (W1) and sluice gate (G3) are located, according to Fig. 2.

Instrumentation needs, in particular the placement of the level sensors, took a special interest in the study of these canal bends. With this canal design it is possible to foresee how the streamlines, the more the higher the flow of velocity, will perform a complex path through the canal-curved reach and also water levels will be locally increased, difficult to control, and determine with some accuracy unless detailed studies are made.

Based on the uncertain behavior of the flow in these bends of the PAC-UPC canal and the study of the best placement of the level sensors as accurately as possible, an experimental campaign of data collection was carried out. This consisted the measurement of depths in 10 points throughout the canal bend for 10 different combinations (discharge, sluice gate openings, and height of the weir). These experimental data are basic and essential to calibrate, and validate the models presented in this study.

1D, 2D, and 3D numerical modeling proposed in with the dual purpose of: (1) to study in detail this bend zone being able to determine accurately the placement of instrumentation throughout the canal; and (2) allow the comparative analysis of 1D, 2D, and 3D models results in order to determine which one offers the most and best information to this case study.

3.2 Study Zone Description

Four bends, three of them including a rectangular weir (W1, W2, and W3) are located in one side of the canal. Bends showing a weir are those that generate a complex flow pattern (if the weir is operating) and so a detailed study is interesting. In this case, the bend, where W1 weir is located, was selected. It should be mentioned that the results of this study will be extrapolated to the different bends.

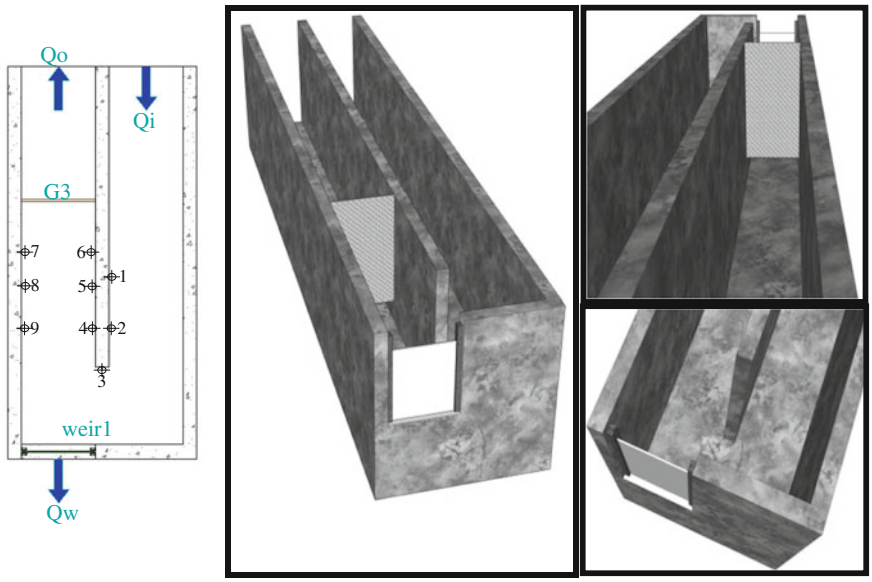

Fig. 3 Study zone. Measurement points in 2D drawing (*left*) and 3D drawing (*right*)

Figure 2 shows highlighted the study area, with water level measurements and hydraulic and instrumentation elements found there. Also note that there is not a soft curve but it is a sudden change of direction at 90º, without rounded corners. Study area has been reproduced in 2D and 3D model drawing, which has been exported to Iber and Flow-3D program, respectively. Figure 3 shows a 2D plan map with the location of the measurement points and a detailed 3D drawing.

3.3 Case Studies

The data used in the present study was acquired during 10 experiments performed in the canal in steady flow conditions. Different discharges, sluice gate openings, and weir heights were combined such as the Table 1 indicates. The variables taken into account are described below:

Q_i [m^3/s] Inflow to the study area, measured with a V-notch weir

w [m] W1 weir height. It is the sum of the wall concrete height (35 cm) and the added plates, less 7 mm of embedded plate in the concrete wall

a [m] G3 sluice gate opening

Table 1 Case studies. Data obtained on the PAC-UPC laboratory canal

					Depth at each point [m]								
Case study	Inflow Q_i [m^3/s]	Weir height w [m]	Sluice gate opening a [m]	Measured sensor depth LS6 [m]	1	2	3	4	5	6	7	8	9
1	0.0940	0.843	0.170	0.640	0.804	0.801	0.790	0.790	0.796	0.800	0.805	0.791	0.795
2	0.0940	0.643	0.170	0.600	0.740	0.737	0.727	0.729	0.735	0.740	0.742	0.730	0.735
3	0.0983	0.443	0.170	0.545	0.620	0.621	0.608	0.609	0.623	0.620	0.615	0.613	0.608
4	0.0983	0.443	0.117	0.520	0.644	0.639	0.630	0.644	0.640	0.637	0.638	0.640	0.634
5	0.0983	0.443	0.700	0.570	0.590	0.588	0.571	0.568	0.575	0.578	0.586	0.578	0.583
6	0.0607	0.643	0.037	0.455	0.807	0.806	0.807	0.809	0.807	0.807	0.808	0.805	0.806
7	0.0660	0.643	0.073	0.510	0.767	0.763	0.762	0.765	0.769	0.765	0.766	0.768	0.765
8	0.0740	0.443	0.073	0.470	0.625	0.624	0.620	0.623	0.623	0.624	0.619	0.628	0.623
9	0.0604	0.443	0.073	0.470	0.592	0.590	0.581	0.592	0.589	0.589	0.590	0.590	0.587
10	0.0768	0.443	0.073	0.480	0.638	0.641	0.635	0.632	0.640	0.645	0.637	0.631	0.640

Moreover, depth measurements were acquired at nine locations (Fig. 3), strategically distributed over the study area. Depths were measured at each of the measuring points with a ruler. Additionally, LS6 level sensor readings provide the downstream boundary condition of the study area.

The singularities of case 1 and 5 should be pointed out with respect to others. As Table 1 shows for case 1, the weir height "w" exceeds values obtained in all points. This indicates that W1 weir was inoperative. On the other hand, in case 5, the sluice gate opening "a" is greater than any water depth for this case, so the gate has no influence. These two cases are necessary to further calibrate the models, since the cases in which both of the hydraulic elements (weir and sluice gate) substantially influence the flow complicating the calibration/validation of the models.

3.4 Presence of a Weir and a Sluice Gate in the Canal Bend

Sluice gates and weirs are hydraulic elements studied by many different authors [2, 3] but significantly, different results have been obtained. It is possible to find in the literature different formulas to estimate the discharge under a sluice gate [4] or over a weir [7].

This is a clear experimental topic, since analytical studies have proposed various simplifications, eventually included in the discharge coefficient. Some comments are set out below:

- The discharge coefficient assumes the velocity and contraction sluice gate coefficient uncertainties.
- The discharge coefficient is very sensitive to the sharpness degree of the sluice gate lip, and also to the different developments of the boundary layer next to the gate.
- The C_d both sluice gates as weirs, include localized energy losses.
- It is assumed that over the weir, velocities have horizontal direction. The discharge coefficient assumes the error integrating the velocity distribution between 0 and depth over the weir.
- The discharge coefficient depends generally on the weir geometry and energy head over the weir crest (h) or discharge (Q). In experimental tests in sharp-crested weirs of various geometries, approximate values of $C_d = 0.60$ have been obtained.

While individually, the hydraulic calculation of these structures has large uncertainties, the implementation of these two comes close to each other, and the weir in the bend zone (no perpendicular inflow to the plane of the weir) adds even more unknowns, if possible, than the traditional study. That is why a detailed study was set out in this paper.

4 Numerical Modeling

4.1 Introduction

The experimental tests were simulated numerically using three different types of software: Hec-Ras, Iber, and Flow 3D, through a 1D, 2D, and 3D approach, respectively. Different results are presented by each one of these, in line with their calculus limitations due to the simplifications of government equations of the problem that they do. Obviously, Flow 3D software solves the full RANS equations directly, so it offers complete information required for this detailed analysis.

Many numerical modeling studies in 1D, 2D, and 3D can be found in the hydraulic engineering literature [6]. Some of them combine the use of 1D and 3D models, the 1D analysis providing a first approximation to the problem and the 3D analysis performing a more detailed analysis. However, few comparative studies among these three approaches have been found. This can be due to the fact that they are tools designed to solve different type of problems. But performance comparison undertaken in this study is still of interest, since it can highlight the limitations and benefits of each one.

4.2 Model Calibration

1D and 2D models have been calibrated by adjusting the discharge sluice gates and weir coefficients. In the case of the 3D model, calibration was accomplished by means of the surface roughness and the adequate turbulence model. Manning's coefficient was calibrated experimentally, obtaining a value of 0.016. This value accounts for the whole dissipation energy and therefore, has been included in the 1D and 2D computation. However, it is not possible to use it for the 3D computation, because of the need to input the surface roughness and turbulence instead of Manning's coefficient.

The target of the calibration is to minimize the error between experimental and numerical depths at each measuring point. The final results assure minimum achievable errors and guarantee the validity of the model, without saying that this model is the only correct one for this study.

4.3 One-Dimensional Numerical Modeling

The 1D approach has been done with the public domain code Hec-Ras. It has three types of hydraulic calculation: steady flow, variable, and estimate sediment transport in moving beds. The one-dimensional Saint Venant equations are calculated

only in the case of unsteady flow, directly solving the Bernoulli equation for the case of steady flow.

$$z_1 + y_1 + \alpha_1 \cdot \frac{v_1^2}{2g} = z_2 + y_2 + \alpha_2 \cdot \frac{v_2^2}{2g} + \Delta H \tag{1}$$

Where:

- z_1 and z_2: Elevation of sections upstream and downstream, respectively, compared to an arbitrary reference plane.
- y_1 and y_2: Depths in each section considered.
- v_1 and v_2: Average velocity in each section. Steady flow is simply the quotient between the discharge and the flow area.
- α_1 and α_2: Coriolis coefficients that correct the velocity distribution in each section away from the uniform.
- ΔH: Energy dissipation between Sects. 1 and 2. This term considers the continuing losses and is localized as follows:

$$\Delta H = I \cdot L_{12} + \Delta H_{\mathrm{LOCAL}} \tag{2}$$

Being I, the energy gradient slope, L_{12} the distance between the two sections, and $\Delta H_{\mathrm{LOCAL}}$ the localized energy losses.

This is a steady flow study. Thus Hec-Ras solves the energy balance equation using the by-step method and the canal bend has been discretized using different sections. The Hec-Ras program is intended to assume 1D flow, considering negligible the other two velocity components. Also slopes are considered to be very small, less than 1v: 10 h. In this study the canal is horizontal.

As seen in this 1D analysis, the concept of turbulence does not appear. All energy dissipation is imposed on the continuous and localized losses. As said before, the Manning's coefficient was calibrated experimentally and a value of 0.016 was obtained, thus assuming that all the energy dissipation was due to the energy gradient slope without considering a turbulence model. The boundary conditions for a subcritical flow are two: the discharge for upstream boundary condition and a fixed water depth (LS6 reading) for downstream boundary condition.

4.4 Two-Dimensional Numerical Modeling

The 2D numerical modeling approach has been developed with the public domain code Iber [5]. It is a modeling system that uses high-resolution schemes (FVM with TVD schemes), with a user friendly interface, compatible with GIS system. Iber modeling system has the following features:

- Simulation of free surface flow in natural and artificial channels.
- Resolution of the full Saint Venant Equations 1D and 2D.
- Explicit finite volume TVD schemes.
- Wetting and Drying front with an exact conservation of water volume.
- Graphical User Interface (pre and post processing) with GiD (CIMNE.www.gidhome.com).
- GIS integration.
- Verified with different laboratory and field data.

Iber solves 2D depth averaged equation, also known as 2D Shallow Water Equations (2D-SWE) or 2D St. Venant equations. These equations assume a hydrostatic pressure distribution and a uniform vertical velocity distribution. It solves mass and momentum conservation equations in two horizontal directions:

$$\frac{\partial h}{\partial t} + \frac{\partial (hu)}{\partial x} + \frac{\partial (hv)}{\partial y} = 0 \tag{3}$$

$$\frac{\partial u}{\partial t} + u\frac{\partial u}{\partial x} + v\frac{\partial u}{\partial y} = -g\frac{\partial Z}{\partial x} + \frac{1}{\rho h}\frac{\partial h\tau_{xx}}{\partial x} + \frac{1}{\rho h}\frac{\partial h\tau_{xy}}{\partial x} - \frac{\tau_{bx}}{\rho h} \tag{4}$$

$$\frac{\partial v}{\partial t} + u\frac{\partial v}{\partial x} + v\frac{\partial v}{\partial y} = -g\frac{\partial Z}{\partial y} + \frac{1}{\rho h}\frac{\partial h\tau_{yx}}{\partial x} + \frac{1}{\rho h}\frac{\partial h\tau_{yy}}{\partial x} - \frac{\tau_{by}}{\rho h} \tag{5}$$

Being h the depth, u and v are the velocity components in the horizontal x and y coordinate directions, g is the gravity acceleration, z is the water surface elevation, τ_{xx} and τ_{yy} are the normal turbulent stresses in the x and y directions, τ_{xy} and τ_{yx}, are the lateral turbulent shear stresses, τ_{bx} and τ_{by} are the bed shear stresses in the x and y directions, and ρ is the water density.

Iber computes the bed shear stresses by the following expressions: $\tau_{bx} = \rho C_f u|V|$ and $\tau_{bx} = \rho C_f v|V|$ being $|V|$ the modulus of the velocity vector, C_f the friction bed coefficient computed by $C_f = gn^2/h^{1/3}$ with n = Manning's roughness coefficient. And the turbulent normal and shear stresses can be formulated with different types of turbulent models: (a) Constant turbulent viscosity; (b) Parabolic model; (c) Mixing length model turbulence; and (d) k- ε model.

These are different models increasing in complexity to obtain the turbulent viscosity and it is possible to choose the most adequate for each study. All these models are based on the formulation according to the Boussinesq's assumption to evaluate the turbulent or Reynolds stresses. In this case, as said before, energy dissipation is considered through the Manning's coefficient, so no turbulent model has been taken into account. The dominium has been discretized with a cell size mesh of 1 cm. On the other hand, the boundary conditions, introduced to the

program, that fix the hydraulic behavior of the canal in subcritical regime are (the case study):

- Upstream (input). Inflow (Q_i) uniformly distributed.
- Downstream (output). Fixed water depth (LS6 reading) at the end of the canal bend and a weir in the bend area.

4.5 Three-Dimensional Numerical Modeling

The three-dimensional numerical modeling has been developed through Flow-3D code [1]. It is used for numerous applications by incorporating a "multiphysics" environment and especially emphasize its behavior for simulation of free surface flows. The numerically solved equations by Flow-3D for hydraulic studies are mass and momentum conservation equations with some additional terms:

$$\frac{\partial}{\partial x}(uA_x) + R\frac{\partial}{\partial x}(vA_y) + \frac{\partial}{\partial z}(wA_z) + \xi\frac{uA_y}{x} = \frac{R_{\mathrm{SOR}}}{\rho} \tag{6}$$

$$\begin{aligned}\frac{\partial u}{\partial t} + \frac{1}{V_F}\left\{uA_x\frac{\partial u}{\partial x} + vA_yR\frac{\partial u}{\partial y} + wA_z\frac{\partial u}{\partial z}\right\} - \xi\frac{A_yv^2}{xV_F} \\ = -\frac{1}{\rho}\frac{\partial p}{\partial x} + G_x + f_x - b_x - \frac{R_{\mathrm{sor}}}{\rho V_F}(u - u_w - \delta u_s)\end{aligned} \tag{7}$$

$$\begin{aligned}\frac{\partial v}{\partial t} + \frac{1}{V_F}\left\{uA_x\frac{\partial v}{\partial x} + vA_yR\frac{\partial v}{\partial y} + wA_z\frac{\partial v}{\partial z}\right\} + \xi\frac{A_yuv}{xV_F} \\ = -\frac{1}{\rho}\left(R\frac{\partial p}{\partial x}\right) + G_x + f_x - b_x - \frac{R_{\mathrm{sor}}}{\rho V_F}(u - u_w - \delta u_s)\end{aligned} \tag{8}$$

$$\begin{aligned}\frac{\partial w}{\partial t} + \frac{1}{V_F}\left\{uA_x\frac{\partial w}{\partial x} + vA_yR\frac{\partial w}{\partial y} + wA_z\frac{\partial w}{\partial z}\right\} \\ = -\frac{1}{\rho}\frac{\partial p}{\partial z} + G_z + f_z - b_z - \frac{R_{\mathrm{sor}}}{\rho V_F}(w - w_w - \delta w_s)\end{aligned} \tag{9}$$

Where (6) is the continuity equation and (7)–(9) are the Navier–Stokes equations. In addition, Flow-3D adds some components to the equations:

A_i	Fractional area open to flow in the i direction
R	Coefficient used to change Cartesian to cylindrical coordinates
ξ	For Cartesian coordinates has a value of 0
R_{SOR}	Mass source. You can add flow entries for example
V_F	Fraction volume of fluid
u_w; δu_s	Components of relative velocities related to the mass source. For this study are not taken into account
G_i	Part of the gravity acceleration in the i direction

f_i Component of the viscous forces in the i direction
b_i Abbreviation that only is taken into account when there are porous media. It will be 0 in calculations of this study.

Flow-3D Model calibration was made for tuning parameters of energy dissipation. Such dissipation is due to surface roughness, and the effects of turbulence. Since the experimental calibration assumed that all the energy dissipation was due to the surface roughness, Manning number was calibrated, obtaining a value of 0.016. In this way, the value of Manning cannot be taken into account as Flow-3D considers power dissipation by surface roughness and turbulence. In Figs. 4 and 5 are shown the calibration results for roughness surface and turbulence model choice.

Finally, a value of 0.003 has been chosen for surface roughness and a RNG dynamic calculation as turbulence model for all the cases. It has been used three mesh blocks of cells of 1, 2 and 4 cm, respectively. The smallest cell size (1 cm) has been used exactly in the most interesting zone, from the weir to 0.5 m sluice gate downstream. Beside this has been constructed the 2 cm cell block and finally, the biggest one with 4 cm cell size, close to both boundary conditions.

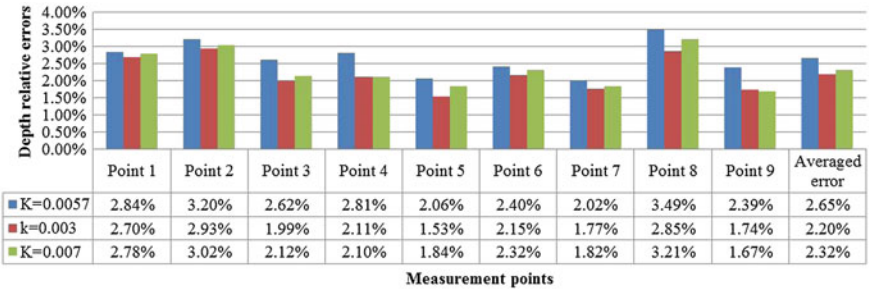

	Point 1	Point 2	Point 3	Point 4	Point 5	Point 6	Point 7	Point 8	Point 9	Averaged error
K=0.0057	2.84%	3.20%	2.62%	2.81%	2.06%	2.40%	2.02%	3.49%	2.39%	2.65%
k=0.003	2.70%	2.93%	1.99%	2.11%	1.53%	2.15%	1.77%	2.85%	1.74%	2.20%
K=0.007	2.78%	3.02%	2.12%	2.10%	1.84%	2.32%	1.82%	3.21%	1.67%	2.32%

Fig. 4 Roughness surface calibration in Flow 3D. Case 2 analysis

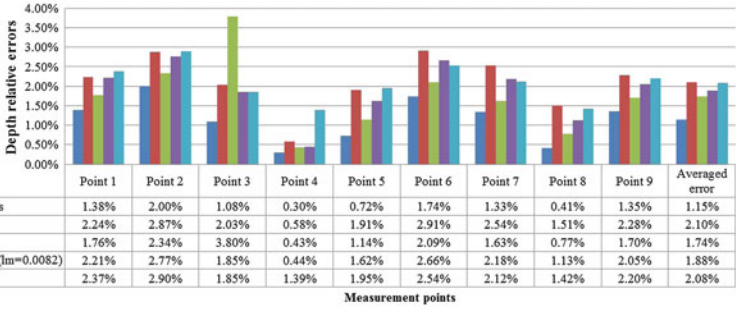

	Point 1	Point 2	Point 3	Point 4	Point 5	Point 6	Point 7	Point 8	Point 9	Averaged error
RNG dynamic calculus	1.38%	2.00%	1.08%	0.30%	0.72%	1.74%	1.33%	0.41%	1.35%	1.15%
RNG (lm=0.013)	2.24%	2.87%	2.03%	0.58%	1.91%	2.91%	2.54%	1.51%	2.28%	2.10%
RNG (lm=0.0082)	1.76%	2.34%	3.80%	0.43%	1.14%	2.09%	1.63%	0.77%	1.70%	1.74%
Two equations (K-e) (lm=0.0082)	2.21%	2.77%	1.85%	0.44%	1.62%	2.66%	2.18%	1.13%	2.05%	1.88%
Large eddy simulation	2.37%	2.90%	1.85%	1.39%	1.95%	2.54%	2.12%	1.42%	2.20%	2.08%

Fig. 5 Model turbulence calibration in Flow 3D. Case 4 analysis

Concerning the boundary conditions, three types are taken into account: (1) Outflow: located in the weir; (2) Specified pressure (equivalent to fixed water level): downstream of the study zone, using the Level Sensor 6 reading; and (3) Mass source: located in the entrance of the study zone, with the corresponding discharge as the case study. The initial condition has been considered close to the real depth (experimental data) in each case.

4.6 *Comparing Results Between 1D, 2D and 3D Numerical Modeling*

Once all the results are obtained, according to the three modeling approaches (1D, 2D, and 3D), a benchmark exercise had been done. Each program offers the results in different formats, but it is possible to compare the obtained depths at the measurement points. A comparative analysis of the differences was performed using a histogram for each case study, obtaining a total of 10 histograms. In each of them is represented, for each measurement point, the experimental depth and numerical depths obtained with Hec-Ras, Iber, and Flow- 3D (Fig. 6).

It should be mentioned that the main target of the comparison between the results of different computer codes is not to determine which program or calculation methodology is the most appropriate. Getting closer numerical depths to experiment is not indicative of a more appropriated model. In each case, it is possible to compare the difference of the obtained numerical depths for each program with respect to experimental depths.

There is no defined general trend attending to the results of the histograms, but each case is independent. The obtained results by Hec-Ras in all cases are very close to experimental, but bear in mind that, in almost all points, these are average data in each section since, only one depth was obtained for each couple of measurement points, and 1D approach cannot describe different water levels at the same section. So, this results that in some cases differences are negative or positive depending if we are in the internal or external part of the bend. So there is no better

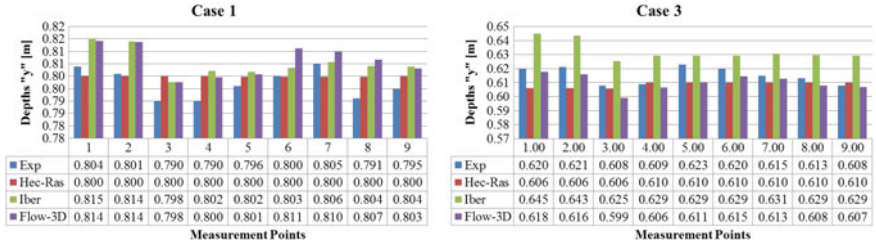

Fig. 6 Comparative of the depths. Case 1 and 3

code than another, but results lead to the use of each one. Of course it should be mentioned that if the study requires only the determination of averaged water level, the use of Hec-Ras program offers an excellent results in general terms.

5 General Results and Discussion

The obtained results using Hec-Ras does not provide information on the local hydraulic behavior of the study area, although the expressions of weirs and sluice gate used are well suited for 1D calculation. Iber gives more details about the flow patterns in different cases, but neglects the vertical velocity changes, considering just average values in vertical. The study area corresponds to a clear 3D behavior, where the three velocity components are important. Therefore, a 3D calculation tool such as Flow-3D is extremely useful for a comprehensive analysis of the PAC-UPC canal bend.

By using a 3D calculation code, it has been able to obtain the following information:

- Details of the recirculation zones, analyzing various cross-sections, and observing the variation of the flow patterns. We can observe recirculation zones before the gate, next to the corners near the walls, and recirculation zones involving the three components of velocity.
- A simulation of weirs and sluice gates, without appeal to experimental expressions of different authors, most of them 1D formula, and without a discharge coefficient which summarized the whole uncertainty of the process.
- Detailed analysis of the streamlines and observing the different paths in the three spatial directions. Further measurements with a Vectrino side-looking device (Acoustic Doppler Velocimeter) will be used to confirm velocity results found with the 3D model.

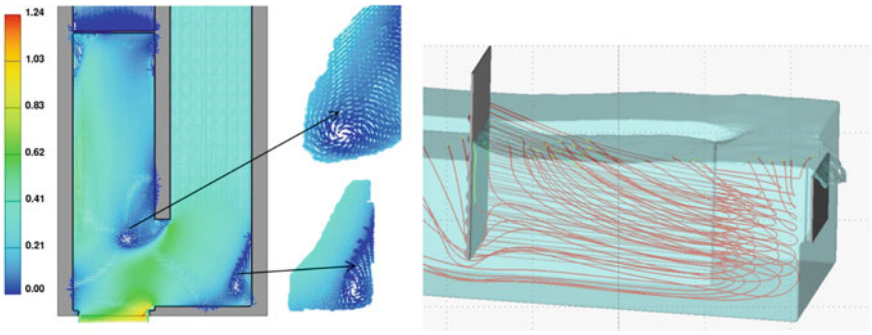

Fig. 7 Velocity vector in a plant cross-section, in a half depth approximately in case 3 (*left*) and analysis of streamlines (*right*) in vertical planes

Possibility to propose and check changes in the existing structure, as well as new locations of instrumentation items if required (Fig. 7).

6 Conclusions

This study was focused in the PAC-UPC lab canal bend, with 10 experimental case studies, varying flow, sluice gate opening, weir height, and measuring water depths at 9 measurement points strategically located in the canal.

This zone has been modeled through 1D (Hec-Ras), 2D (Iber), and 3D (Flow-3D) approaches and determining the water depth error in the different measurement points, compared with experimental data. Calibration of the 1D and 2D models has been performed based on the weir and sluice gate discharge coefficients, and using the experimentally calibrated Manning coefficient. 3D models required the calibration of turbulence model used and the surface roughness value, both being the key concepts of the energy dissipation problem.

For 1D and 2D models, there is great uncertainty regarding the weir and sluice gate discharge coefficients. These coefficients require a laborious calibration process based on reliable measures. Also Iber uses 1D expressions (weir and sluice gates discharge formula), the 2D calculations already performed. Flow-3D solves numerically RANS equations, which responds to a more general hydraulic case, and therefore no empirical or theoretical expressions associated with elements such as sluice gates or weirs are required.

A new proposed geometry of the bend was studied, with more rounded edges in order to a soft incorporation into the bend. It was also suggested to change the weir location, since during the canal construction there was no occasion to analyze different alternatives at the time. The different flow behaviors in the bend after the change in geometry are also studied. The weir behavior is also studied in terms of changes in flow discharge, depending on new location, obtaining a 26 % more

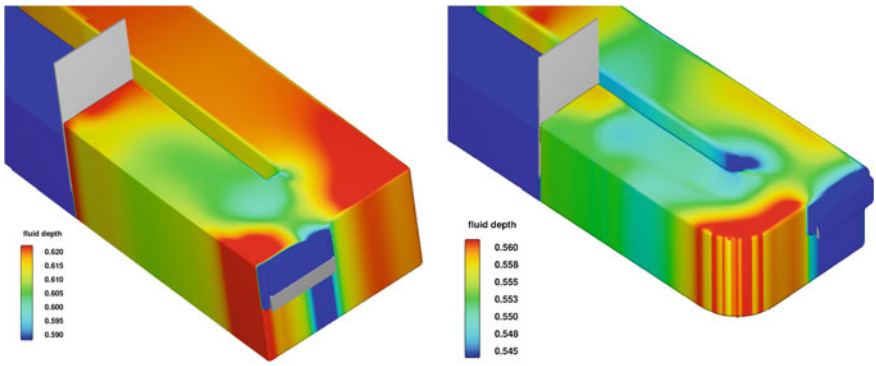

Fig. 8 3D view of fluid depth ranges. Original structure (*left*) and proposed structure (*right*)

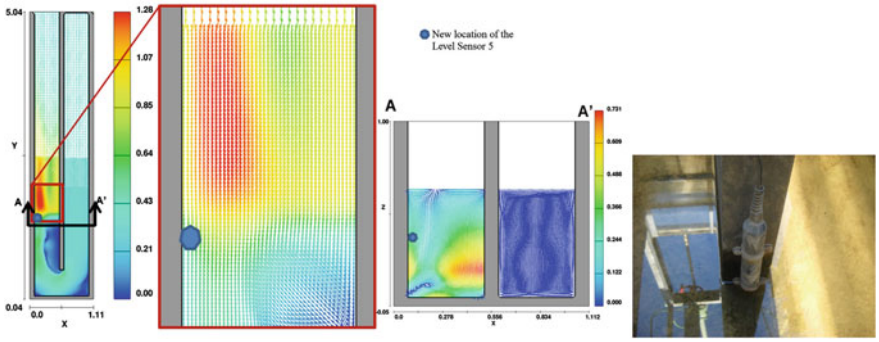

Fig. 9 New location of the level sensor 5

discharge with the proposal location. New location is more oriented in front of the incoming flow and rounded corners minimize the energy losses due to recirculation zones (Fig. 8).

The current level sensor 5 located at the measuring point 3 was placed there, the center wall, to protect the sensor against local disturbance velocities that could distort the measurement. From the results, we can conclude that the high complexity of the flow produces a great local depression of the free surface, precisely in that area, which gives lower levels than other points in the nearby area. It is proposed to relocate the sensor, closer to the gate above the gate opening, ensuring lower velocities, as shown in Fig. 9.

References

1. Flow Science lnc, Flow3D. http://www.flow3d.com/.
2. Henderson, F.M. (1996). *Open channel flow*. New York, USA.
3. Henry, H.R., Albertson, M.L., Dai, Y.B., Jensen, R.A. (1950). *Discussion of 'Diffusion of Submerged Jets,' ASCE* (Vol. 115, pp. 87–694). Transactions.
4. Rajaratnam, N., & Subramanya, K. (1967). Flow equation for the sluice gate. *Journal of Irrigation and Drainage Engineering, 93*(3), 167–186.
5. de Ros, M. (2012). *Modelación del flujo en un cruce de calles mediante un código de cálculo 3D* (p. 80). Barcelona, Spain.
6. Technical University of Catalonia and Flumen Institute, Modelo Bidimensional Iber. http://www.iberaula.es/web/index.php.
7. U.S. Department of the Interior. (1997). *Bureau of Reclamation (USBR)*, Water Measurement Manual. Washington, DC, Chap. 7.

Limitation of High Water Levels in Bays and Estuaries During Storm Flood Events

Benoit Waeles, Xavier Bertin, Damien Chevaillier, Jean-François Breilh, Kai Li and Baptiste Le Mauff Dorn

1 Introduction, First Headings

Many questions have been raised after some major coastal floods induced by extreme storms as Xynthia (February 2010) that occurred on the West Coast of France and resulted in extensive damage. Several research projects aimed at analyzing the physical processes responsible for the very large observed storm surge during Xynthia, compared to the wind that was not exceptionally strong. These researches revealed that, this exceptional storm surge resulted mainly from an Ekman transport related to the SW wind, strongly enhanced by the presence of young and steep waves. This particular sea-state was explained by the unusual track of Xynthia from SW to NE, which restricted the fetch to a few hundred km in the Bay of Biscay [1]. In addition to the wind and sea level pressure effects, an important contribution of the storm surge resonance on the continental shelf has been highlighted [1, 11]. Statistical analysis was carried out to define the return

B. Waeles (✉) · X. Bertin · D. Chevaillier · J.-F. Breilh · K. Li · B.L. Mauff Dorn
Plouzané, france
e-mail: benoit.waeles@gmail.com

X. Bertin
e-mail: xbertin@univ-lr.fr

D. Chevaillier
e-mail: chevaillier@creocean.fr

J.-F. Breilh
e-mail: jbreil01@univ-lr.fr

K. Li
e-mail: kai.li.jx@gmail.com

B.L. Mauff Dorn
e-mail: baptiste.le-mauff@univ-nantes.fr

P. Gourbesville et al. (eds.), *Advances in Hydroinformatics*,
Springer Water, DOI 10.1007/978-981-287-615-7_30

periods of such events and to foresee the water levels that had been reached during even more rare events (e.g. Pineau Guillou et al. [8]; Duluc et al. [5]).

However, flows through the coastline during submersion events are not well described. Tide gauge measurements are only carried out occasionally in some harbours, and there is limited information available on the water levels reached in the bays or estuaries.

In the fluvial domain, flood phenomena are generally well understood either in its forcing factors (rainfall, watersheds…), in the determination of the return periods associated to the exceptional occurrences, or in the characterization of the flows through the riverbanks. The design of the banks already benefits from this knowledge. Land development strategies integrate generally expanding flood areas behind the banks: the flows, through structures like spillways are oriented towards non-urbanized areas or at least areas without any major issues. The water volumes, by filling the expanding flood areas, help to limit the water levels reached on more sensitives areas (urbanized areas, industrial sites…), as defined by eaudefrance.fr (in Degoutte et al. [6]): "an expanding flood area is a natural or developed area where the waters flow during the river flooding. The momentary storage of the waters clips the flood by increasing its duration."

By contrast, in the coastal domain, water volumes are often considered as infinites with regards to the water volumes flooding the lands behind the coastline during extreme storms. At mid-latitudes, storm surges are usually moderate and therefore the water levels that may exceed the top of the protection works or natural barrier beaches are generally induced by the concomitance of spring tides and a storm surge associated with a low pressure and strong winds. The high variability of the water levels induced, both in time (with vertical variation in the range of 1 m/h) and in space (tide and storm surge may be amplified at the coastline), makes the understanding of these mechanisms complex. In particular, the role played by the terrestrial expanding areas is difficult to understand and quantify.

This study, which involves process-based numerical models validated with reference to tide gauge measurements, tends to specify in what extent the flooding behind the coastline may limit the water levels reached during exceptional events.

2 Contexts: Description of Areas and Extreme Events

Processes for both embayed and estuarine environments are analyzed within Eastern Channel (Authie Bay and Dives Estuary) and along French Atlantic coast (Aiguillon Bay) (Fig. 1).

Fig. 1 Location of studied coastal areas

2.1 Pertuis Charentais Sea, Aiguillon Bay and Lay Estuary

Pertuis Charentais Sea is located in the central part of the Bay of the Biscay, characterized by a continental shelf with width locally exceeding 150 km. Tide regime is meso- to macro-tidal (spring tidal range >6 m in the inner Pertuis Charentais Sea) and semi-diurnal. Offshore wave regime is characterized by median significant wave heights (Hs) in the order of 1.5 m and winter storms can episodically induce Hs exceeding 8 m (e.g. Bertin et al. [2]). Aiguillon Bay is a tidal bay mainly consisting of kilometric tidal mudflats and Lay Estuary to the North of the bay entrance. The bay coastline corresponds to several kilometres of dykes. These dykes isolate the Poitevin marshland, whose hundreds of square kilometres are under typical high sea levels. During Xynthia storm, more than 150 km^2 of the Poitevin marshland were flooded [3], causing extensive loss of human lifes and material damage.

2.2 Authie Bay

Morphology of Authie Bay, in the North-East of eastern Channel, is mainly characterized by very shallow areas including an extensive sandy spit in the southern part of the bay entrance and large mudflats with broadly developed schorre.

Low-lying areas south of the bay are parts of the Marquenterre territory that is framed by two bays (Authie and Somme). These areas are former salt marshes, with reclamation starting in the twelfth century. The coastline at the South of Authie Bay consists of an earth embankment; the so-called Mollières dyke, that has already experienced overflows. In 1984 and 1985 several storm events occurred and extreme levels induced rather large submersion with water penetration at several kilometres inland. Top level and general state of the Mollières dyke is questionable with regards to extreme storm events and to sea level rise related to global warming. Low-lying areas behind the dyke are globally 1–2 m lower than assessed high water levels for a centennial event.

Hydrodynamic features are first characterized by a macro-tidal environment with tidal ranges upto 9 m. Waves are very low due to, among others, drastic damping over the sand banks at the bay entrance. During storm events, strong winds usually blow from SW to W and the southern part of the bay are then sheltered. Authie River flood conditions, even for strong floods (1/1 year or more) were shown to induce an almost negligible contribution to extreme water levels.

2.3 Dives Estuary

Dives estuary is a narrow estuary in the SE of the Bay of Seine. There is a macro-tidal regime with tidal range up to 8 m or more. Estuary banks are mostly artificial and footprints of inter-tidal areas are small. Low-lying areas behind the estuary banks are largely urbanized.

3 Numerical Modelling Set-up

3.1 Pertuis Charentais Sea: Aiguillon Bay and Lay Estuary

LIENSs laboratory performed a hindcast of the storm surge and flooding associated with Xynthia, based on a numerical modelling system that couples a 2DH hydrodynamic circulation model (SELFE [14]) and a spectral wave model (WWMII [9]). The two models share the same decomposition domain and unstructured grid. The grid consists of more than 1.5 million triangular elements and encompasses the whole NE Atlantic, with a resolution ranging from 30 km offshore, far from the study area to less than 5 m along the coastline. Such a spatial resolution is necessary to correctly represent the wave-breaking zones and the dykes and natural barriers, as usual obstacles to flooding. Comparisons with available data (tide gauge in La Rochelle harbour and wave buoy offshore Oléron Island) show that the numerical modelling system is able to reproduce water levels and wave conditions during

Xynthia with normalized errors in the order of 5 and 10 %, respectively. The extension of marine submersion induced by Xynthia is also satisfactorily reproduced, particularly over the Poitevin marshland.

3.2 Authie Bay

The model system is based on MIKE21 (DHI) software.

Within the framework of risk mapping studies, 1/1–1/100 years extreme levels have been assessed. Evaluation is based on statistical analysis of Dieppe tide gauge data [10] and dedicated simulations (carried out by [4]) of specific events with a model set-up on the whole Eastern Channel and refined in the bay of Authie, and in its surroundings. Surge contribution to extreme levels is in the 1–1.5 m range.

Tide and storm surge induced levels in the bay are shown to be lowly spatialized. Sensitivity tests have been carried out for various wind conditions. For the simulated extreme events, there is low variability of high water levels in the bay: increase between bay entrance and end remains globally lower than 0.2 m.

For simulations with flooding, the flexible mesh grid is adapted to reproduce correctly the smaller structures, like dykes and roads that are obstacles to flows; mesh dimensions there are metric. Characteristic bottom roughness values have been specified for the bay and for the low-lying areas.

Validation of the model system, including for submersion process, has been carried out for historical 1984 and 1985 events for which the model show consistent agreement with partial observations [4].

Simulations have been run for schematic extreme events in the future, including a centennial event with a hypothesis of 0.6 m sea level rise related to global warming.

3.3 Dives Estuary

On behalf of Dives-sur-Mer city council, for a risk mapping study, a MIKE 21 numerical model has been set up to simulate marine submersion. Boundary conditions were specified schematically, at several kilometres off the mouth of the estuary, combining spring tide water level variations with a uniform offset to represent storm surge and sea level rise related to global warming. Mesh dimensions on the dykes are metric.

Different scenarios of flooding were run: no marine submersion at all, submersion on right bank (Dives-sur-Mer side) and submersion on both sides.

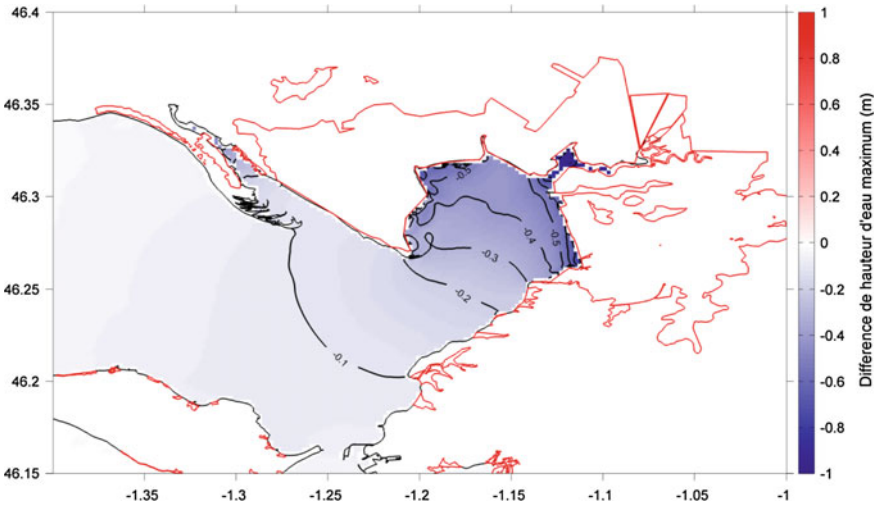

Fig. 2 Differences of maximum sea level between a simulation allowing flooding and a simulation not allowing flooding in the LIENSs numerical model. Xynthia event. *Red lines* indicate the inland limits of flooded areas. Axes in geographical coordinates

4 Results

4.1 Pertuis Charentais Sea: Aiguillon Bay and Lay Estuary

Comparisons of reached high water sea levels, with and without flooding, simulated by the model set-up by LIENSs [7] show that the levels are significantly higher when the flooding is disabled in the simulations. Flooding occurs over the whole Poitevin marshland, with high water level differences increasing progressively from 0.2 m at the bay entrance to almost 1.0 m in the Sèvre Niortaise estuary (Fig. 2).

4.2 Authie Bay

Results of simulations, with and without flooding areas behind the coastline, have been compared for the same extreme schematic events (as described in the previous chapter). The comparison is related to the simulated high water levels over the whole bay and the coastal water surroundings.

Limitation of high water level starts at the entrance of the bay: high water levels are 0.1 m lower than high water levels, if the dykes on the bay coastline were assumed to be high enough to avoid submersion. Then, limitation is increased within the bay: a mean value of 0.3–0.4 m is obtained and a maximum of 1 m is reached

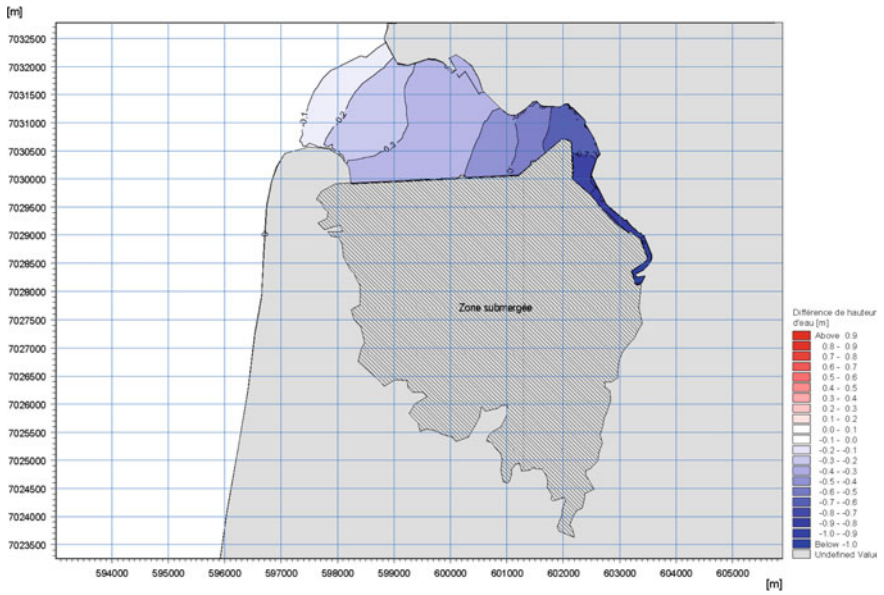

Fig. 3 Differences of maximum sea level between a simulation allowing flooding and a simulation not allowing flooding. Assessed centennial event in 2100. *Gray stripes* show flooded area

upstream. However, submersion of low-lying areas is simulated in the South of the bay; tide damping has almost the same intensity on both sides of the bay (Fig. 3).

4.3 Dives Estuary

Results are mapped in order to represent impacts of flooding on right bank (Dives-sur-Mer side) only and on both sides (Dives-sur-Mer and Cabourg).

Tide clipping is much more consequent, in case both sides of the estuary are flooded. There is an increase of tide clipping from mouth to upstream: a mean value of 0.5 m is obtained on the study area whereas the difference exceeds 2 m upstream (not shown on map) (Figs. 4 and 5).

4.4 Synthesis of Results for Limitation of High Water Levels

For the different sites and set up numerical models, the following table summarizes hydrodynamic (tidal ranges and storm surge) characteristics, information on flooded areas with regard to bay or estuary areas, and then orders of magnitude of high tide limitations.

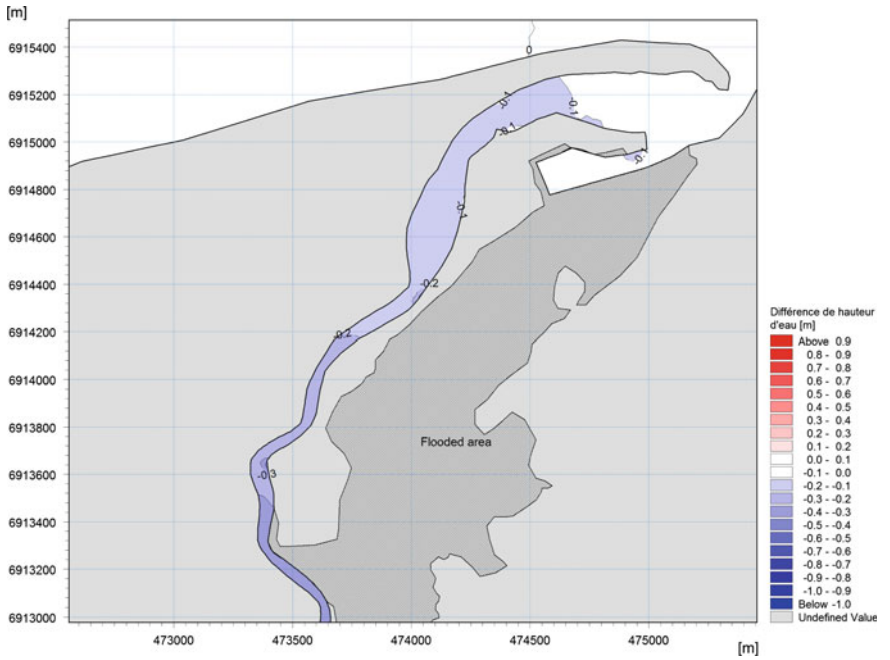

Fig. 4 Differences of maximum sea level between a simulation allowing flooding (on *right* bank) and a simulation not allowing flooding. Assessed centennial event in 2100

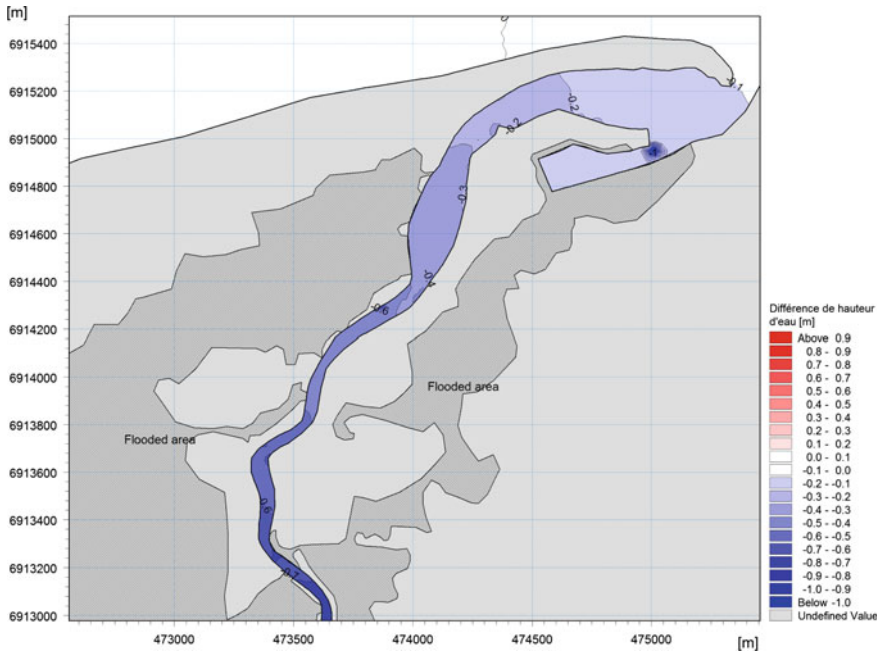

Fig. 5 Differences of maximum sea level between a simulation allowing flooding (on both *right* and *left* banks) and a simulation not allowing flooding. Assessed centennial event in 2100

Sites	Model	Extreme event				Results	
		Type	Tidal range[a] (m)	Storm surge[a] (m)	Sea level rise[b] (m)	Flooded area[c]	Limitation of high tide levels
Aiguillon Bay, Lay Estuary and Sèvre Niortaise Estuary	SELFE (LIENSs)	Xynthia storm	6	1.5	no	6–7 (ref.: Aiguillon Bay)	0.2–0.5 m in the bay, and upto 1 m in the Sèvre Niortaise Estuary
Authie Bay	MIKE21 (Creocean)	schematic 1/100 years event	9	1	0.6	7	0.1–0.8 m in the bay
Dives Estuary: Dives-sur-Mer flooding	MIKE21 (Creocean)	schematic 1/100 years event	7.5	1	0.6	1	0.2–0.3 m along the section where flooding occurs
Dives Estuary: Dives-sur-Mer and Cabourg flooding	MIKE21 (Creocean)	schematic 1/100 years event	7.5	1	0.6	10	0.4–0.6 m along the section where flooding occurs, up to more than 2 m upstream

[a]Order of magnitude on the study area for the simulated event; [b]Hypothesis related to global warming; [c]Ratio: flooded surface/bay (or estuary) surface

5 Discussion on High Tide Limitation Process

In estuaries, effect of lateral tidal storage (local inundation of tidal flats or flood plains), on tidal range is already well described for classic conditions (e.g. Van Rijn [13]) or extreme events [12]. Van Rijn carried out computations, on the Scheldt Estuary, reducing or increasing the surface areas. Among others, results showed that an increase of about 20 % (relative to the total 450 km^2 between the mouth and the end of the estuary) of the surface areas led to lower tidal range values of about 0.3–0.4 m (i.e. almost 10 % of the 4 m tidal range). Research undertaken by Townend and Pethick on the Humber Estuary highlighted the capacity of inter-tidal areas to dissipate major flood events. Sensitivity tests, with flood in plains area representing up to four times the current estuary area, suggested that high water levels could be lowered to approximately 0.5 m in the inner estuary and to more than 2 m upstream (where the respective contributions of tide, surge and river flood on high water levels are about 5, 1–1.5 and 0.5 m).

Roughly speaking, increasing lateral surface areas along estuaries deviates the system, from a funnel-shaped morphology that is known for favouring tidal

amplification. During submersion, events related to extreme sea level conditions, the low-lying areas behind the coastline make the estuary less funnel-shaped with regard to the tide propagation during flood. The role of low-lying areas is the same as lateral tidal flats in tidal damping.

Another way to describe the processes that induce tidal signal clipping is to compare the tidal prisms with the water volumes that flood the low-lying areas behind the coastline. During the Xynthia storm, the volumes that flooded Charente-Maritime and Vendée departments corresponded to a non-negligible fraction of the tidal prisms of the Pertuis Charentais Sea (area between Ré and Oléron Islands and the continent): the order of magnitude is assessed to be 10 %.

Hypsometry curves (i.e. variation of potential wet area with water level) of such coastal domains can also be analyzed to understand the general trend of tidal clipping process. For both bays and estuaries, flooded areas behind the coastline tend to modify the shape of the hypsometry curve. When the crests of the dykes along the coastline are exceeded, broad low-lying areas modify consequently the hypsometry towards convexity (assuming wet area on the X-axis and water level on Y-axis). That is to say, the system (bay or estuary and low-lying areas) is related to a more convex hypsometry than the bay or the estuary itself. For the upper part of the tide, flows experience more frictional losses due to bed shear stress if low-lying areas are submerged.

6 Conclusions

The results from the different models applied in both bay and estuary environments showed that flooding of low-lying areas behind the coastline tends to limit high water levels. This limitation is rather significant as it may exceed 0.5 m. Therefore, it has to be taken into account in numerical modelling methodology for submersion phenomena and a unique model including both coastal waters and low-lying areas is relevant to simulate the limitation process. In case of a nesting approach with the land model open boundary along the coastline, the models need to be run together in two-way nesting; one-way nesting from sea to land largely overestimates the water volumes towards the low-lying areas and then the extent of the submerged areas.

Planning strategies for coastal defense and risk mapping are of course closely linked; reflections and studies have to be carried out on the global scale of coastal systems (bays, estuaries, inlets…). Historically, borders between administrative areas were defined at the location of bays and estuaries. Then, defense strategies and risk mapping are often managed at local scales. The consequences are unrealistic risk mapping and unsuitable coastal defense strategies. Furthermore, the setup of unsinkable dykes along the coastline may increase high tide levels on other parts of the bay or the estuary which are managed by other authorities, and then increase pressure on existing defenses.

With regard to the strategy for coastal defense against flood risk, the results highlight the necessity to include flood plains that provides storage volumes behind the coastline; managed retreat is already planned in coastal systems such as the Humber estuary in the UK [12]. Complementary guideline/elements for reflection include the location of coastal defenses. If possible, it would be preferable not to locate dykes directly along the coastline, but further inland. Such a strategy induces lower high tide levels at the dyke location and dykes do not require to be designed to resist to the wave action. Moreover, it allows minimizing the risk elsewhere or at least not to worsen it.

Acknowledgments We acknowledge the help of Creocean's colleagues, Alain Juif and Jehane Ouriqua, for their technical support.

References

1. Bertin, X., Bruneau, N., Breilh, J. F., Fortunato, A. B., & Karpytchev, M. (2012). Importance of wave age and resonance in storm surges: The case Xynthia Bay of Biscay. *Ocean Modelling, 42* (2012), 16–30.
2. Bertin, X., Castelle, B., Chaumillon, E., Butel, R., & Quique, R. (2008). Estimation and inter-annual variability of the longshore transport at a high-energy dissipative beach: The St. Trojan beach, SW Oléron Island, France. *Continental Shelf Research, 28*, 1316–1332.
3. Breilh, J. F., Chaumillon, E., Bertin, X., & Gravelle, M. (2013). Assessment of static flood modeling techniques: application to contrasting marshes flooded during Xynthia (western France). *Natural Hazards and Earth System Science, 13*, 1595–1612.
4. CREOCEAN. (2014). Analyse et caractérisation des aléas. *In: Elaboration du plan de prévention des risques naturels du Marquenterre.*
5. Duluc C.M., Deville Y. & Bardet L. (2014). Extreme sea level assessment: application of the joint probability method at Brest and La Rochelle and uncertainties analysis. La Houille Blanche, n°1, 2014, p. 11–17
6. Degoutte et al. (2012). Les déversoirs sur digues fluviales. *Editions Quae*.
7. Li, K., Bertin, X., Roland, A.., Zhang, Y. J., & Breilh, J. F. (2013). A high-resolution hindcast of the flooding during Xynthia storm, central bay of Biscay. *Proceedings of Coastal Dynamics 2013*.
8. Pineau-Guillou et al. (2010). Caractérisation des niveaux marins et modélisation des surcotes pendant la tempête Xynthia. *Proceedings of the XIth Journées Nationales Génie Côtier-Génie Civil, Paralia Ed., Les Sables d'Olonne, 22–25th of June 2010*. pp. 625–634.
9. Roland, A.., Zhang, Y. J., Wang, H. V., Meng, Y., Teng, Y.-C., Maderich, et al. (2012). A fully coupled 3D wave-current interaction model on unstructured grids. *Journal of Geophysical Research* 117.
10. SHOM and CETMEF. (2012). Statistiques des niveaux marins extrêmes des côtes de France (Manche et Atlantique).
11. Thiebaut, S., & Vennell, R. (2011). Resonance of long waves generated by storms obliquely crossing shelf topography in a rotating ocean. *Journal of Fluid Mechanics, 682*, 261–288.
12. Townend, I., & Pethick, J. (2002). Estuarine flooding and managed retreat. *In: Proceedings of "Flood risk in a changing climate". Royal Society of London Philosophical Transactions A.* Vol. 360. Issue 1796, p. 1477.
13. Van Rijn, L. (2010). Tidal phenomena in the Scheldt Estuary. *Deltares*, 99 p.
14. Zhang, Y., & Baptista, A. M. (2008). SELFE: A semi-implicit Eulerian-Lagrangian finite-element model for cross-scale ocean circulation. *Ocean Modelling, 21*(3–4), 71–96.

A Stochastic Model for Particle Deposition in Turbulent Flows and Clogging Effects

Céline Caruyer, Jean-Pierre Minier, Mathieu Guingo and Christophe Henry

1 Introduction

Particle deposition in turbulent flows is a phenomenon met in various applications which can lead to fouling and affect normal operating conditions of key components of industrial processes. Particle deposition is due to several thermohydraulic or chemical processes. Fouling can be divided into different stages: with first deposition of single particles on a clean surface, and then formation of a multilayer deposit, up to a possible complete blocking of the fluid cross section.

In our modeling approach, the complete fouling phenomenon is separated into four elementary phenomena (Fig. 1) which are as follows:

- Deposition: governed by particle–fluid interactions and particle–surface interactions.
- Resuspension: a particle initially deposited on a wall loses contact with it. This phenomenon depends on the balance between the hydrodynamic efforts exerted on a deposited particle by the flow and the adhesion forces between the particle and the wall. These adhesion forces can be of different natures (van der Waals, electrostatic forces) and depends on parameters that can be difficult to know precisely, such as the characteristics of surface roughness.

C. Caruyer (✉) · J.-P. Minier · M. Guingo
EDF R&D, 6 Quai Watier, 78401 Chatou, France
e-mail: celine.caruyer@edf.fr

J.-P. Minier
e-mail: jean-pierre.minier@edf.fr

M. Guingo
e-mail: mathieu.guingo@edf.fr

C. Henry
Institute of Fluid Flow Machinery, 80-231 Gdańsk, Poland
e-mail: christophe.henry@mines-paris.org

P. Gourbesville et al. (eds.), *Advances in Hydroinformatics*,
Springer Water, DOI 10.1007/978-981-287-615-7_31

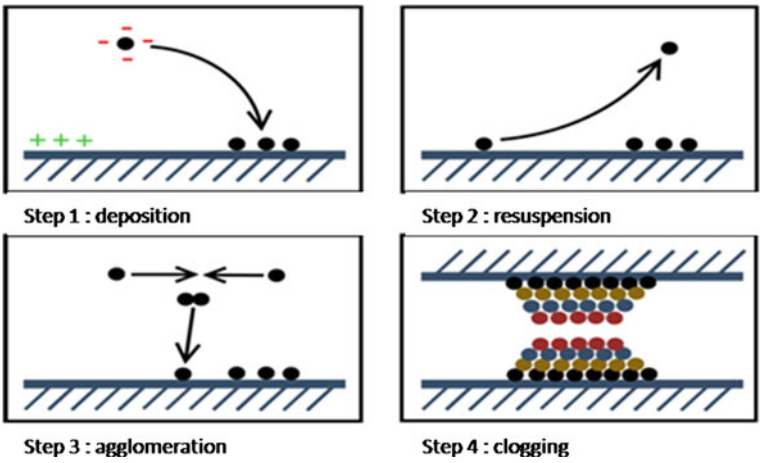

Fig. 1 Elementary phenomena of fouling

- Agglomeration: for a high concentration of particles in the flow, particle–particle interaction must be taken into account. For instance, the formation of aggregates can modify the particle mass flowrate toward the wall (since particle aggregates have a different inertia compared to "elementary" particles, their response to near-wall turbulence is also different, and thus their probability to reach the wall).
- Clogging: several layers of particle can accumulate on the surface, forming a multilayer deposit. Particle–particle interactions are important in this phenomenon. For a sufficiently significant particle deposit, the influence of the deposit morphology on the local flow structure must be modeled; an example of this influence being the acceleration of the local flow velocity during its passage through a cross section reduced by fouling.

In this model, the interactions between particles and near-wall coherent structures are explicitly simulated [7]. The modeling approach is not limited to particle–turbulence interactions, and particle–surface interactions are accounted for using an energy balance method: particles impacting the wall (or particle already deposited) deposit if their wall-normal kinetic energy is high enough to overcome the energy barrier, otherwise they rebound on the surface [8, 9].

The model accounts accurately for two major fundamental mechanisms: first, the hydrodynamic transport of particles (which describes particle–fluid interactions such as particle–turbulence interactions) and, second, the attachment mechanism (where physico-chemical interactions between two bodies occur). Roughness is also specifically included in the stochastic description of the surface since it plays an important role, in particular in repulsive cases where the energy barrier can be lowered [9].

The present article deals with the clogging issue and, more precisely, with the influence of multilayer deposits on the flow. The first part describes the multilayer deposition model, while the second part is dedicated to the influence of a deposit on the fluid flow. Different approaches able to perform this coupling are briefly described. Then a calculation which brings out the impact of a deposit on the flow is performed, using a porous medium approach.

2 Multilayer Deposition

Recent developments [8] have shown that the model is not only able to reproduce single-particle deposition and resuspension but can also be applied to simulate the formation and the growth of multilayer deposits. Such deposits result from the competition between particle–fluid, particle–surface, and particle–particle interactions. According to the chemical properties of the surfaces involved (both particles and walls), different morphologies of the deposit can exist (monolayer, dendrite, multilayer) and this is well captured qualitatively by the present model. For the cases considered in the present paper, we neglect particle–particle interactions in the bulk of the fluid and particle detachment is also not taken into account.

2.1 Modeling Approach

When modeling the formation of multilayer deposits, the transport step is not modified and only the attachment step is extended to account for particles interacting with fouled surfaces.

The deposition of a particle on a fouled surface is given by an energy balance approach in the wall-normal direction. The wall-normal kinetic energy of incoming particles is the result of the transport step, while the wall-normal energy barrier between a particle and a fouled surface is determined according to the attachment model. This means that the interaction between a particle and a fouled surface is similar to the interaction between a particle and a rough substrate (covered by hemispherical asperities).

Then, various cases can appear: if the particle interacts with a clean surface, the energy barrier is given by the model developed previously, whereas if deposited particles are present inside the contact area, the energy barrier is determined using the DLVO theory [12], named after Derjaguin–Landau [2] and Verwey–Overbeek [15], assuming interaction energies to be additive:

$$U_{\text{part}-\text{surf}} = U^{DLVO}_{\text{part}-\text{plate}}(1 - S_{\text{cov}}) + \sum U^{DLVO}_{\text{part}-\text{part}},$$

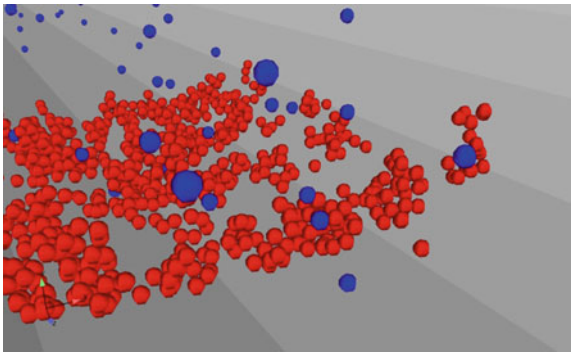

Fig. 2 Multilayer deposition of particles on the wall. Calculation with a low jamming limit and particle–particle attraction

where S_{cov} is the surface coverage, $U_{part\text{-}plate}$ is the interaction between a particle and the plane, and $U_{part\text{-}part}$ is the interaction between particles.

The contact surface S_{cont} defining the contact area is

$$S_{cont} = \pi \left(2\sqrt{R_{part}R_{dep}} + R_{dep}\right)^2,$$

where R_{part} is the particle radius and R_{dep} is the deposited particle radius.

If deposited particles are present inside the contact area, a particle is chosen randomly among them and the incoming particle is deposited on this one with a random angle.

Two parameters have been introduced in the simulation of fouling: the jamming limit and the minimal porosity. The jamming limit corresponds to the maximum attainable surface coverage of deposited particles. This parameter has been introduced since the use of a probabilistic approach allows single-particle deposition to occur until a surface coverage of 100 % whereas, in reality, the packing of spheres on a surface cannot be higher than a jamming limit (equal to 90 % for a 2-D hexagonal close packing of spheres). Once the surface coverage reaches that limit value, incoming particles are always considered to deposit on adhering particles (Fig. 2). The minimal porosity of a cell is equal to 0.366 for a structure obtained by random deposition of monodispersed particles.

2.2 Numerical Results

2.2.1 Effect of the Ionic Strength

Bacchin et al. [1] studied the deposition of 4.9 μm latex particles under Brownian motion on polymer substrates (PDMS). In this experiment, multilayer deposition was observed with an ionic force of I = 100 mM, but no multilayer deposition occurred at I = 10 mM or lower (Fig. 3). Particle–particle interactions have been calculated using a zeta potential of −52 mV at pH 7 for the two ionic strengths

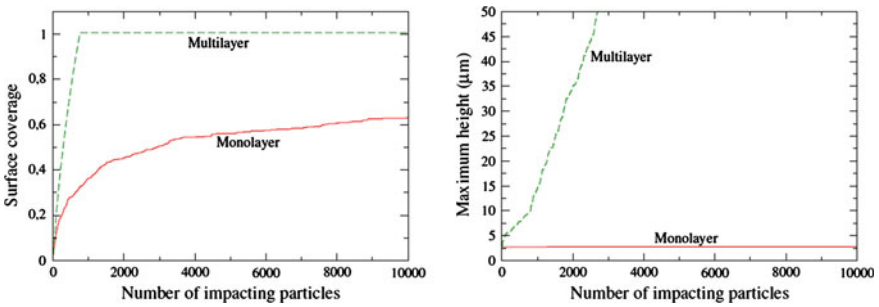

Fig. 3 Clogging behavior of polymer substrates by 4.9 µm latex particles at various solution conditions: *red line* I = 10 mM, *green line* I = 100 mM

considered and a Hamaker constant of 4.10^{-20} J. Particle–substrate interactions were not considered. Numerical results confirm that the model is able to predict the formation of multilayers: multilayer deposition occurs at an ionic strength of 100 mM, while only monolayers can be formed at an ionic strength lower than 60 mM.

2.2.2 Effect of the PH

Perry et al. [14] studied the deposition of 250 nm alumina particles on silicon substrates. The study was performed for different pHs and showed that the first layer is determined by particle–surface interactions, while next layers are piloted by particle–particle interactions. For a pH of 3, a monolayer deposit was obtained because particle–surface interactions are attractive but particle–particle interactions are repulsive. At pH = 9, a multilayer deposit develops due to particle–particle attraction (close to the point of zero charge of alumina particles). At a pH of 10, there is no deposit on the substrate due to high particle–surface repulsion. These qualitative results have been confirmed numerically (Fig. 4).

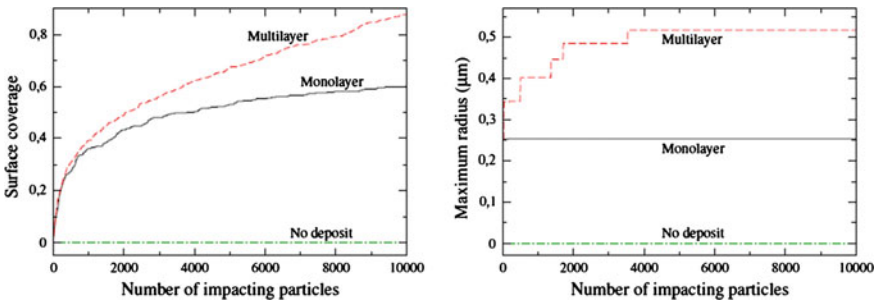

Fig. 4 Clogging behavior of silicon substrates by 250 nm alumina particles at various solution conditions: pH = 3 (*black*), pH = 9 (*red*), pH = 10 (*green*)

3 Influence of the Multilayer Deposit on the Fluid Flow

When the size of multilayer deposit becomes significant which means that the fluid section is reduced, it is important to account for the influence of the deposit on the fluid flow in order to obtain more realistic evolutions, both of the fluid flow and of the deposit formation.

3.1 Possible Approaches

Different methods can be applied to address this issue, such as Arbitrary Lagrangien Eulerien (ALE) methods [3, 11], porous medium approaches, hybrid methods, or Smoothed Particle Hydrodynamics (SPH) approach [6, 13].

The choice of a modeling approach is based on two criteria: first, it needs to be consistent with models already developed within the framework of statistical or stochastic models; second, it must be sufficiently open to allow future developments (in particular, the deposit cohesion and multilayer resuspension) to be introduced. According to these criteria, we have retained the porous medium approach.

3.2 Chosen Modeling Approach: Porous Medium Approach

The impact of the deposit on the flow can be taken into account at the mesh size by the use of a porous media approach (Fig. 5). Indeed, the number of deposited particles is known at the end of each time step, and each wall-bounded cell can then be described by its porosity which represents the volume fraction not occupied by the deposited particles. As particle deposition goes on and the resulting deposit grows in size, the cell porosity is decreased (from one down to zero when the cell if completely clogged or blocked). A head loss coefficient is added in the equation of momentum for concerned cells in order to represent the pressure variation induced by the passage of fluid through a porous medium. This method has the advantage of being rather simple to implement since it does not require important numerical

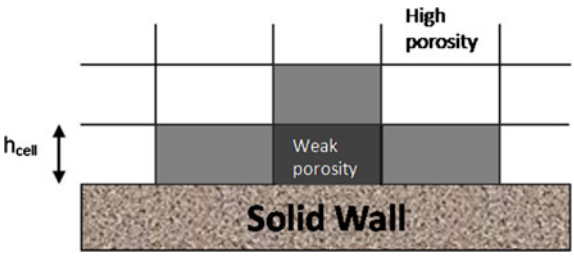

Fig. 5 Mesh and cell porosity

developments. However, the use of a single head loss coefficient in every cell implies that the deposit formed is properly described by the porosity only. This may appear as a restrictive assumption since the deposit morphology (dendrite or compact clusters) can change. Yet, it is believed that in simple geometry (such as in a parallel-plate channel), the interactions at play in fouling are not highly dependent on the cell position and the resulting deposit morphology is rather homogeneous and thus properly described by its porosity. It should be borne in mind that this assumption may become unrealistic in complex geometries (such as impacting jet or sudden reduction of the fluid cross section) due to specific hydrodynamic conditions (this remains to be studied both numerically and experimentally though).

A fluid flow in a porous medium is modeled using the Darcy law:

$$\underline{u} = -\frac{k}{\mu}\underline{\nabla} P,$$

where $\underline{u}$ is the velocity (m/s), p is the pressure (Pa), μ is the dynamic viscosity (Pa.s), and k is the permeability (which depends only on the porous medium, in m^2). The hydraulic conductivity or the permeability coefficient of the porous medium (m/s) is written as

$$K = \frac{k\rho g}{\mu}.$$

The momentum equation with the head loss term K_{pdc} is

$$\rho\frac{\partial \underline{u_{\text{i}}}}{\partial t} + \rho\underline{u_{\text{i}}}\frac{\partial \underline{u_{\text{i}}}}{\partial x_j} = -\frac{\partial P}{\partial x_i} + \mu\frac{\partial^2 \underline{u_{\text{i}}}}{\partial x_j^2} - \rho K_{\text{pdc}}.\underline{u_{\text{i}}}.$$

The head loss coefficient is given by correlations according to different configurations, such as a flow through a pile of spheres or in cylinders with a section restriction. Laws have a phenomenological origin and are obtained from experiments realized in a macroscopic scale.

This method remains simple enough to be implemented in a straightforward manner and does not require extensive numerical developments. However, as mentioned previously, it should be borne in mind that the underlying assumption is that the deposit is homogeneous in space so as to describe it using only its porosity.

According to the literature, the regular head loss in a duct is

$$\Delta P = \lambda\frac{l}{D}\rho\frac{\overline{U^2}}{2},$$

where λ is a head loss coefficient (m^{-1}) dependent of the flow nature, l is the duct length, D is the hydraulic diameter, ρ is the fluid density, and U is the velocity.

The head loss coefficient K_{pdc} is defined such as

$$\Delta P = K_{\text{pdc}} \rho \overline{U},$$

where $K_{\text{pdc}} = \lambda \frac{l}{D} \frac{\overline{U}}{2}$.

The cell porosity ε can be defined by

$$\varepsilon = \frac{V_{\text{cel}} - V_{\text{part}}}{V_{\text{cell}}},$$

where V_{cel} corresponds to the volume of the cell, V_{part} is the particle volume given by $V_{\text{part}} = N_{\text{dep}} \frac{4}{3} \pi r_p^3$ with r_p the particle radius, and N_{dep} is the number of deposited particles in the cell (considering a monodispersed case, i.e., all particles have the same diameter).

The head loss, according to the porosity, for a pile of spheres of the same diameter, is given by the Ergun formula [5]:

$$\begin{aligned} \frac{\Delta P}{H} &= \left[\frac{150 \mu_f}{\rho_f d_p^2} \frac{(1-\varepsilon)^2}{\varepsilon^3} + 1.75 \frac{1-\varepsilon}{\varepsilon} \frac{1}{d_p} |U| \right] \rho_f U \\ \Delta P &= K_{\text{pdc}} \rho_f U \\ K_{\text{pdc}} &= \frac{150 \mu_f H}{\rho_f d_p^2} \frac{(1-\varepsilon)^2}{\varepsilon^3} + 1.75 * \frac{1-\varepsilon}{\varepsilon^3} \frac{H}{d_p} |U| \end{aligned} \quad , \qquad (1)$$

where H is a characteristic length of the granular medium, μ_f is the fluid dynamic viscosity, and ρ_f is the fluid density.

The head loss is the sum of two terms representing, respectively, the losses of viscous and kinetic energy of the fluid. This law is valid for fluid flows through porous media formed by pile of homogeneous, fixed, and spherical particles from laminar to turbulent flows.

The necessary data to calculate the head loss coefficient are

- the porosity (determined from the number of deposited particles in each cell),
- the characteristic length H, and
- the diameter of the particles d_p.

Initially, the cells of the fluid domain have a porosity of 1, and thus a head loss coefficient equals 0. The cell porosity decreases according to the number of deposited particles in this cell. The head loss term is calculated with the Ergun law (1) according to the cell porosity at each time step.

The maximal compactness of sphere pile with a same diameter is c = 0.74, thus a minimal porosity of ε_p = 1 − c = 0.26. For a random deposit, the compactness is between 0.591 and 0.634 [8].

Other formulae exist to take into account the polydispersion by a mean diameter and the standard deviation [4] or the mean Sauter diameter [10]. The non-sphericity of particles can be also considered using appropriate formulae. Some improvements have still to be provided to have a head loss coefficient more representative of

general cases. The porosity is homogeneous in the cell, and it is calculated from the number of deposited particles and does not depend on the deposit morphology. At the moment, developments are performed for monodispersed particles.

4 Results and Discussion

4.1 Particle Injection in a Cylindrical Duct

This test case is performed with the deposition and clogging models, while no resuspension is considered. The flow is calculated at each time step in order to take into account the impact of the deposit on the fluid flow. The geometry is a cylindrical duct with a diameter of 1.27 cm and a length of 1.22 m. The mesh is composed of 159,040 hexahedra, and a radial cut of the mesh is represented in Fig. 6. Ten particles are injected onto the flow at each time step ($\Delta t = 10^{-4}$ s) from the center of the inlet with an initial velocity directed toward the wall (Fig. 8). Large particles with a diameter of 8.10^{-5} m (monodispersed) are injected in order to obtain a multilayer deposit more rapidly and observe the effect on the flow. Only, a part of the wall between 0.025 and 0.03 m is considered favorable for deposit growth, somewhere else particles impacting the wall are removed.

The head loss coefficient is calculated by the Ergun formula (1) according to the cell porosity (Fig. 7).

In Figs. 8, 9 and 10, we can see the injection of particles and the growth of a deposit as a function of time. The flow is perturbed by the multilayer deposit, and the bulk velocity increases with time since a part of the section is blocked by the deposit.

Fig. 6 Radial cut of the mesh

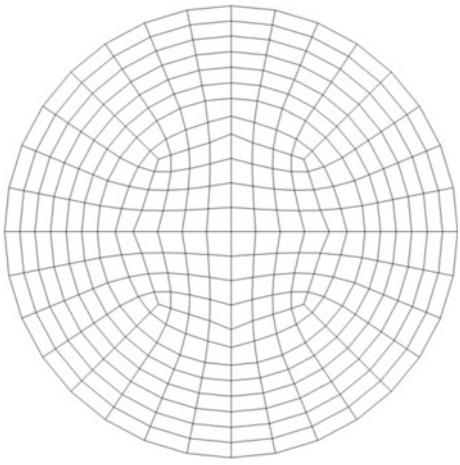

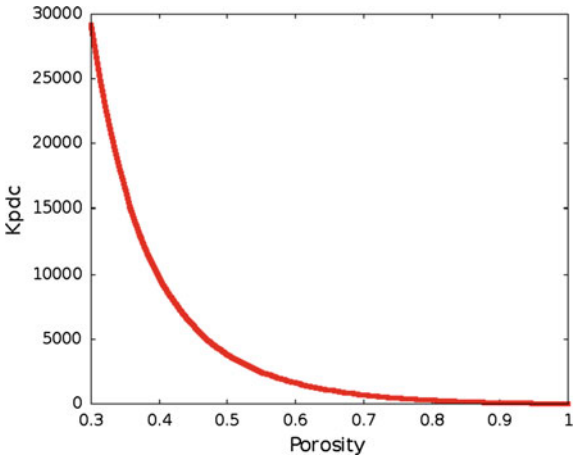

Fig. 7 Head loss coefficient according to the cell porosity

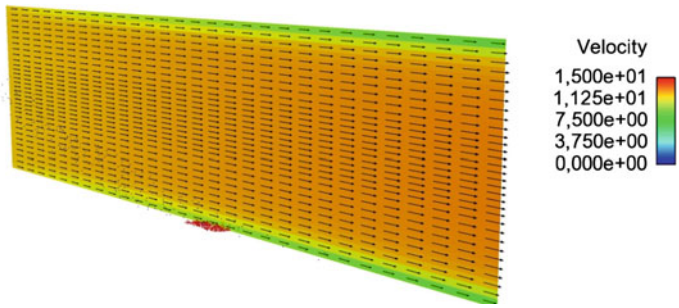

Fig. 8 Deposit of particles and velocity at t = 0.1 s

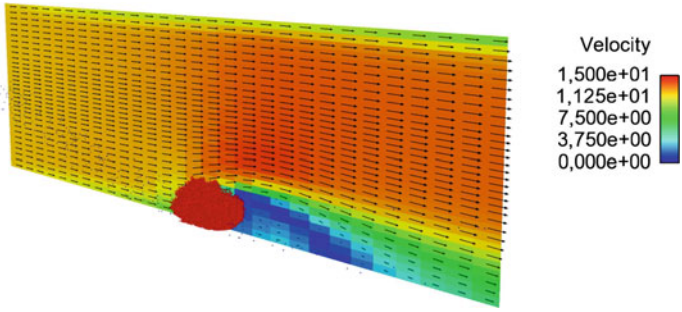

Fig. 9 Deposit of particles and velocity a t = 10 s

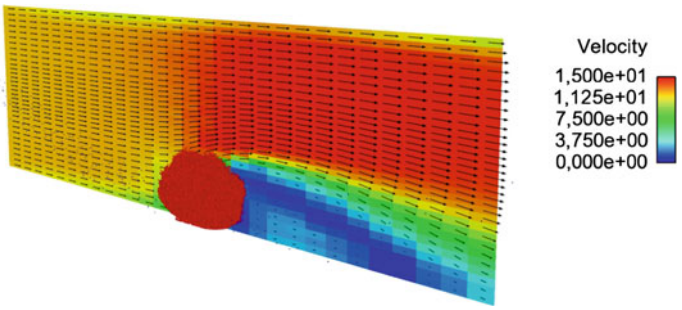

Fig. 10 Deposit of particles and velocity a t = 30 s

4.2 Evolution of Fluid Velocity and Pressure with Time

Figure 11 displays the fluid velocity along the duct at different times, at the center of the flow and near the wall. At the initial moment, the flow velocity at the center of the flow increases along the duct because the flow is still in a transition state. The velocity at the center of the flow increases from 12.5 to 15 m/s when the deposit grows (between 0 and 30 s). The multilayer deposit reduces indeed the pipe cross section resulting in an increased fluid velocity (for a constant flow rate). On the contrary, the velocity near the wall decreases inside the deposit and also downstream. The velocity just downstream the deposit is very low and increases again further away (4 m/s at the exit of the domain). A zone of recirculation is observed downstream from the deposit around z = 0.025–0.03 m (Fig. 12).

Figure 13 shows pressure profiles along the duct at different times at the center of the flow and near the wall. Near the wall, there is a small pressure rise upstream from the deposit and a depression downstream. The pressure gap through the deposit is about 106 Pa. At the center of the flow, the pressure is also perturbed by the deposit.

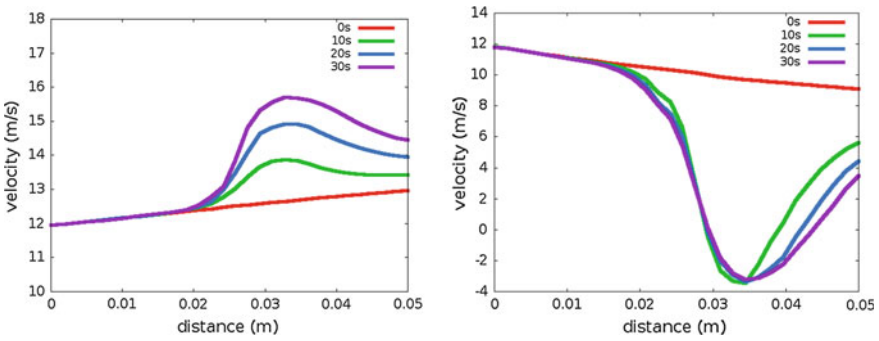

Fig. 11 Velocity along the cylindrical duct for four different times t = 0, 10, 20, and 30 s (*left* at the middle of the flow, *right* near the wall)

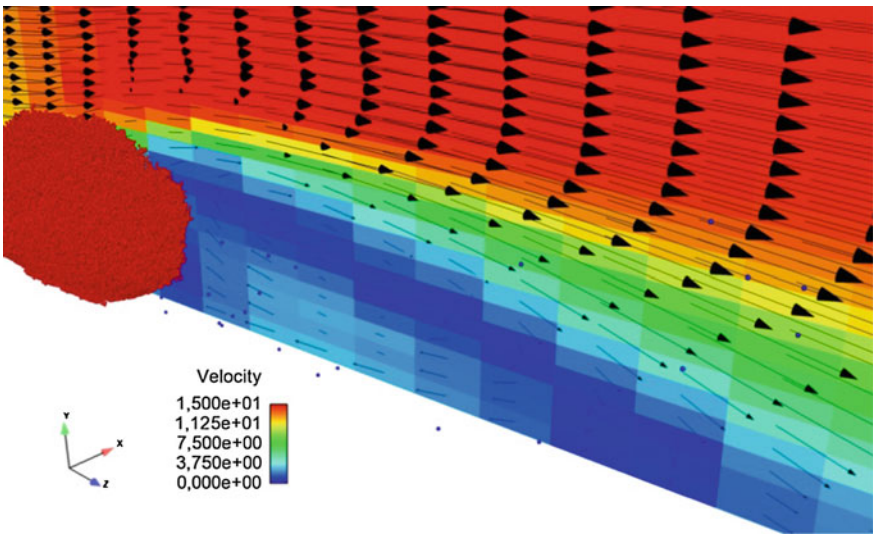

Fig. 12 Zone of recirculation downstream of the multilayer deposit

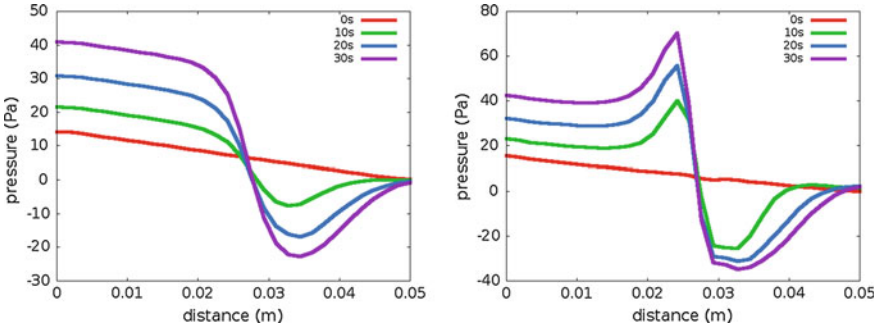

Fig. 13 Pressure along the cylindrical duct for four different times (*left* at the middle of the flow, *right* near the wall)

The cell porosity is determined from the number of deposited particles in a cell. If the cell porosity becomes inferior to a limit value (equal to 0.366 for a structure obtained by random deposition of monodispersed particles), we prevent particles from depositing in this cell and a rebound condition is applied (Fig. 14).

4.3 Sensitivity Study

To test the influence of the head loss coefficient on the flow velocity, different parameters such as the particle diameter or the fluid velocity are modified in the

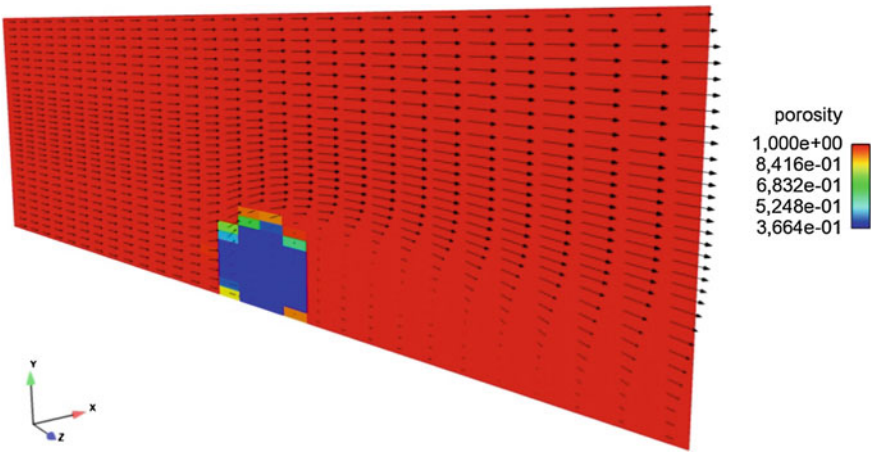

Fig. 14 Cell porosity at t = 30 s

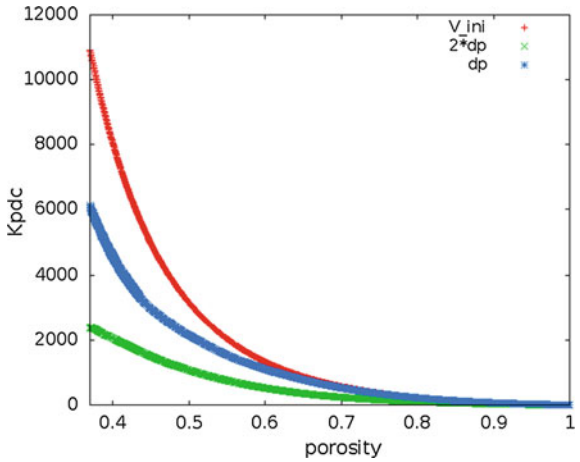

Fig. 15 Head loss coefficient according to the porosity for different parameters

Ergun formula (1). The head loss coefficient is represented in three cases according to three porosities (Fig. 15). The red curve corresponds to a head loss coefficient calculated with the initial velocity, the blue one to the previous case, and the green one to a particle cluster.

A ratio of almost five is obtained for the maximal value of the head loss coefficient.

A difference of about 2 % is observed on velocities at the center of the flow for the various head loss coefficients (Fig. 16 left). An increase about 10 % exists between the initial velocity and the velocity at t = 10 s. In Fig. 16 (right), we

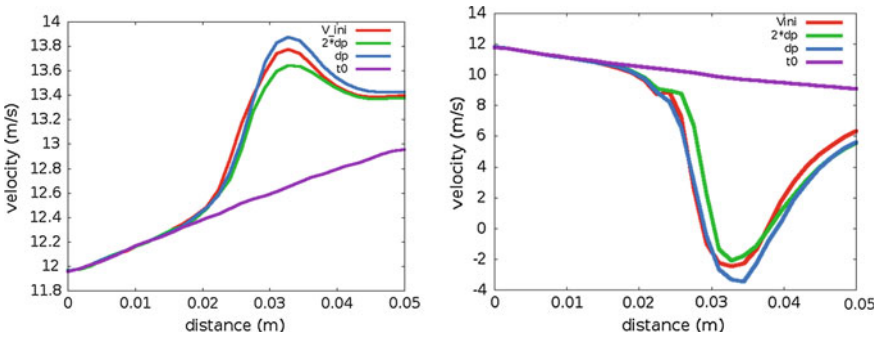

Fig. 16 Velocity along the cylindrical duct at t = 10 s for different head loss coefficients (*left* at the middle of the flow, *right* near the wall)

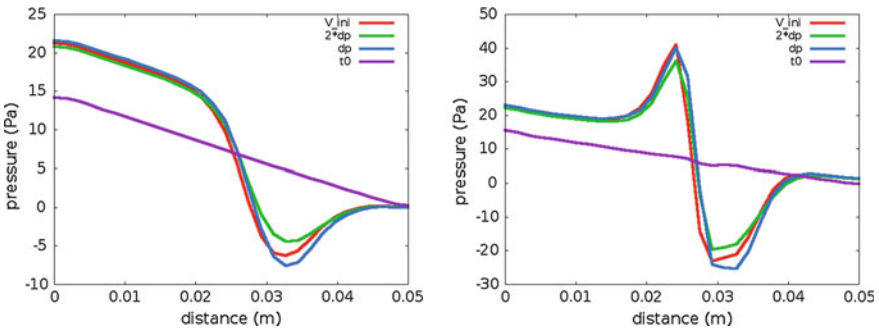

Fig. 17 Pressure along the cylindrical duct at t = 10 s for different head loss coefficients (*left* at the middle of the flow, *right* near the wall)

observe a reduction of the velocity in the zone corresponding to the deposit (around z = 0.025–0.03 m). According to the value of the head loss coefficient applied, the velocity which is obtained in the deposit is in the range within −2 and −3.5 m/s against approximately 10 m/s upstream of the deposit formation. For pressure, differences of about 24 % are found near the wall downstream of the deposit (Fig. 17).

For the three conditions, the evolution of the multilayer deposit is slightly different because of the velocity difference.

The deposit morphology has an influence on the prediction of the head loss coefficient applied in the momentum equation and thus on the fluid flow calculations.

5 Conclusion and Perspectives

The present work has presented new coupled approaches to address the influence of a particle deposit on the carrier-fluid motion. Among the methods presented here, the porous medium approach seems well adapted to capture the coupled effects between the fluid flow and the particle deposits. In this approach, fluid velocities modified by multilayer deposits are predicted using a head loss coefficient in the momentum equation. However, there are some limitations due to the uncertainty on some parameters and even to the formulation of a physically relevant law for the head loss coefficient. At the moment, an Ergun law has been retained but additional developments are needed to come up with accurate expressions. Furthermore, it is difficult to have experimental data to validate the results. On the other hand, our understanding of particulate fouling remains incomplete. Significant efforts are still required to comprehend resuspension in multilayer deposits and to explore the influence of the deposit morphology on inter-particle cohesion. To put forward one example, the deposit morphology plays also an important role and must be correctly included in the modeling picture. Thus, this is clearly a subject which is currently evolving, with some uncharted aspects, and, in that sense, it appears justified to select an approach (such as the porous medium one) which allows first developments to be made without too many complications. It is believed that with new insights provided by experimental studies and feedbacks from additional numerical works, a proper framework will be outlined. Finally, it is worth recalling that particle resuspension must also be accounted for and, in turn, this represents an additional challenge as particle re-entrainment from multilayer deposits is more intricate than single-particle re-entrainment.

References

1. Bacchin, P., Aimar, P., & Sanchez, V. (1995). Model for colloidal fouling of membranes. *AICHE, 41*, 368–376.
2. Derjaguin, B., & Landau, L. (1941). Acta physicochim. *URSS, 14*, 633–662.
3. Donea, J. (1983). *Arbitrary Lagrangian-Eulerian finite element methods. Computational methods for transient analysis.* (pp. 473–516). Amsterdam: North-Holland.
4. Endo, Y., Chen, D.-R., & Pui, D. Y. H. (1998). Effects of particle polydispersity and shape factor during dust cake loading on air filters. *Powder Technology, 98*, 241–249.
5. Ergun, S. (1952). Fluid flow through packed columns. *Chemical Engineering Progress, 48*(2), 89–94.
6. Gingold, R. A., & Monaghan, J. J. (1977). Smoothed particle hydrodynamics: Theory and application to non-spherical stars. *Monthly Notices of the Royal Astronomical Society, 181*, 375–389.
7. Guingo, M., & Minier, J. P. (2008). A stochastic model of coherent structures for particle deposition in turbulent flows. *Physics of Fluids, 20*, 053303.
8. Henry, C., Minier, J. P., & Lefebvre, G. (2012). Towards a description of particulate fouling: From single particle deposition to clogging. *Advances in Colloid and Interface Science, 185–186*, 34–76.

9. Henry, C., Minier, J. P., & Lefebvre, G. (2012). Numerical study of the adhesion and reentrainment of nondeformable particles on surfaces: the role of surface roughness and electrostatic forces. *Langmuir, 28*, 438–452.
10. Holdich, R. G. (2002). *Fundamentals of particle technology*. U.K: Department of Chemical Engineering, Loughborough University.
11. Hughes, T. J. R., Liu, W. K., & Zimmermann, T. K. (1981). Lagrangian-Eulerian finite element formulation for incompressible viscous flows. In Interdisciplinary Finite Element Analysis (p. 179). College of Engineering and School of Civil and Environmental Engineering of Cornell University.
12. Israelachvili, J. N. (2011). *Intermolecular and surface forces*, 3rd Edition. London: Academic Press.
13. Lucy, L. B. (1977). A numerical approach to the testing of the fission hypothesis. *Astronomical Journal, 82*, 1013–1024.
14. Perry, J. L., & Kandlikar, S. G. (2008). Fouling and its mitigation in silicon microchannels used for IC chip cooling. *Microfluidics and Nanofluidics, 5*, 357–371.
15. Vervey, E., & Overbeek, J. T. G. (1948). *Theory of stability of lyophobic colloids*. Amsterdam: Elsevier.

Part III
Two-phase Flows and Cavitation

Presentation of the Multi-Phase CFD Solver NEPTUNE_CFD

Namane Mechitoua, Mathieu Guingo and Philippe Montarnal

Nomenclature

g Gravitational acceleration ($m.s^{-2}$)
I′ Interfacial momentum transfer ($kg.m.s^{-2}$)
P Pressure (Pascal)
U Mean velocity ($m.s^{-2}$)
T Temperature (Kelvin)
α Volume fraction (m^3/m^3)
μ Dynamic viscosity ($kg.m^{-1}.s^{-1}$)
Σ Turbulent constraint tensor
Γ Mass transfer term ($kg.m^{-3}.s^{-1}$)
Π Heat transfer term ($J.m^{-3}.s^{-1}$)

1 Introduction

Further to a thorough analysis of the industrial needs and of the limitations of current simulation tools, EDF (Electricite de France) and CEA (Commissariat `a l'Energie Atomique) launched in 2001 a long-term joint development program for the next generation of nuclear reactor simulation tools. The NEPTUNE Project [1], which represents the thermal-hydraulics part of this comprehensive program, aims at building a new software platform for advanced two-phase flow

N. Mechitoua (✉) · M. Guingo
Electricite de France R&D, 6 Quai Watier, 78400 Chatou Cedex, France
e-mail: namane.mechitoua@edf.fr

M. Guingo
e-mail: mathieu.guingo@edf.fr

P. Montarnal
CEA, Centre de Saclay, 91191 Gif Sur Yvette, France
e-mail: philippe.montarnal@cea.fr

P. Gourbesville et al. (eds.), *Advances in Hydroinformatics*,
Springer Water, DOI 10.1007/978-981-287-615-7_32

thermal-hydraulics allowing easy multi-scale and multi-disciplinary computations meeting the industrial needs. The different modeling strategies can be taken into account through four different simulation scales: direct numerical simulation (DNS), computational fluid dynamics (local CFD), component (subchannel-type analysis), and system (reactor modeling) scales. New physical models and numerical methods are being developed for each scale as well as for their coupling.

This paper consists of a general presentation of the model implemented in NEPTUNE_CFD code, originally designed for CFD scale simulations. Applications of this code are illustrated through the detailed presentation of two examples; the first one borrowed to hydraulic domain and the second one to nuclear domain.

2 Multi-Fluid Volume Averaged Models

2.1 General Equations

Multi-fluid volume averaged models play a central role for numerically handling multi-phase flows having complex and rapidly changing topology of the interface separating two immiscible fluids. In order to avoid description of the small scales that may appear in multi-phase flows, a volume (or time) averaging of the Navier-Stokes equations leads to a set of separate mean balance equations for each phase [2, 3] which looks like to the single-phase conservation equations of mass, momentum, energy, and turbulent quantities. The averaging procedure in time and/or space introduces additional coupling inter-phase transfer terms between phases, which have to be modeled.

NEPTUNE_CFD code solves the general compressible or incompressible multi-field balance equations, which is an extension of the "two fluid-one pressure" model to the case of m phases (up to 20 envisaged). The mass and momentum balances for each phase k are written as follows:

$$\frac{\partial \alpha_k \rho_k}{\partial t} + \mathrm{div}(\alpha_k \rho_k \vec{U}_k) = \Gamma_k \tag{1}$$

$$\frac{\partial \alpha_k \rho_k \vec{U}_k}{\partial t} + \mathrm{div}\vec{}(\vec{U}_k \otimes \alpha_k \rho_k \vec{U}_k) = \mathrm{div}\vec{}(\alpha_k \vec{\bar{\tau}}_k + \vec{\bar{\Sigma}}_k) - \alpha_k \vec{\nabla} P + \overrightarrow{I}'_k + \alpha_k \rho_k \vec{g} + \alpha_k \vec{S}_k + \Gamma_k U_k^I, \tag{2}$$

where α_k and U_k represent, respectively, the volume fraction and the velocity of phase k at the same given spatial point.

The global volume, momentum, and mass conservations imply

$$\sum_{k=1}^{N\text{phase}} \alpha_k = 1 \quad \sum_{k=1}^{N\text{phase}} \vec{I}'_k = 0 \quad \sum_{k=1}^{N\text{phase}} \Gamma_k = 0. \tag{3}$$

Notice that
$\vec{\vec{\tau}}_k$ is the laminar viscous constraint tensor:

$$\vec{\vec{\tau}}_k = \mu_k(\vec{\vec{\nabla}}\vec{U}_k + {}^t\vec{\vec{\nabla}}\vec{U}_k) - 2/3\vec{\vec{1}}\text{div}\vec{U}_k \tag{4}$$

$\vec{\vec{\Sigma}}_k$ is the turbulent constraint tensor:

$$\vec{\vec{\Sigma}}_k = -\left\langle \alpha_k \rho_k \vec{U}''_k \otimes \vec{U}''_k \right\rangle \tag{5}$$

$\vec{I}'_k$ represents the momentum interfacial transfer of all phases p onto the phase k (drag, added mass, turbulent contributions to drag and added mass, …):

$$\vec{I}'_k = \sum_{p \neq k} \vec{I}'_{p \to k}\,. \tag{6}$$

Additive equations for each field can be used in order to model physics, such as turbulence, phase separation, diameter of the inclusion, nucleate boiling near walls, and radiation heat transfer. The influence of turbulence between phases is taken into account through correlations which modify the turbulent viscosity. The correlations depend on turbulence quantities of each phase, such as turbulent kinetic energy and turbulent dissipation, the covariance of the fluctuating velocities and the turbulent characteristic time scale of the droplet and bubbles.

For the important particular case of two-phase steam/ liquid flows involved in nuclear safety problems, with mass transfer due to heat transfer, the source and sink terms appearing in enthalpy balance equations can be written with the following general form:

$$\begin{array}{l} \Pi_k = \Gamma_k H_k + \Pi'_k,\ \Pi'_k = \xi_k(T_{sat} - T_k) \\ \text{With:} \\ \sum_k \Pi_k = 0,\ \sum_k \Gamma_k = 0 \end{array} \tag{7}$$

Several models are available in NEPTUNE_CFD for evaporation and condensation physics, taken into account through the heat transfer coefficient ξ_k. The simplest form, proposed in terms of characteristic time scales, can be written as

Evaporation of liquid fluid:

$$\Pi'_L = \alpha_L \rho_L Cp_L(T_{sat} - T_L)/\tau_F,\ \Pi'_V = 0 \text{ if } T_L \succ T_{sat}. \tag{8}$$

This is the mass transfer of liquid into steam which limits in upper bound the averaged liquid temperature to the saturation temperature.

Condensation of steam fluid:

$$\Pi'_V = \alpha_V \rho_V Cp_v (T_{sat} - T_V)/\tau_C,\ \Pi'_L = 0\, if\ T_V \leq T_{sat}. \tag{9}$$

This is the mass transfer of steam into liquid which limits in lower bound the averaged steam temperature to the saturation temperature.

For obtaining realizable models preserving the boundedness of the volume fractions, the rate of creation/destruction of steam should be respectively proportional to a nth power of the depleted phase.

2.2 Numerical Procedure

A segregated procedure is used for advancing in time [4]. The first step consists of predicting velocity for each phase from the momentum equations. This step solves an implicit equation for velocity, all other variables as pressure and volume fractions being frozen. Then, a reduced form of the momentum equations containing the predicted velocity, the implicit part of the pressure, and volume fractions gradients is coupled with the mass equations. This system is solved using sub-cycles, combining mass predictions and pressure corrections. The convergence of the non-linear system is assessed if the predicted volume fractions obey to the volume conservation. This criterion is very strong since it applies to the maximum volume conservation constraint over the computation domain. The elliptic feature of the overall algorithm is due to the elliptic form of the pressure correction equation. Taking into account of the non-linear coupling between pressure and volume fractions within the sub-cycles and the symmetric treatment of all fields, it makes this algorithm tractable for the whole range of void fraction, without any artificial numerical need.

Spatial discretization follows a 3D full unstructured finite volume approach, with a collocated arrangement for all variables. A face-based data structure allows the use of arbitrary-shaped cells (tetrahedron, hexahedron, prisms, pyramids, …), including non-matching meshes. Numerical consistency and precision for diffusive and convective fluxes for non-orthogonal and irregular cells are taken into account through a gradient reconstruction technique. A careful treatment of gradient terms of momentum equations, similar to a Rhie and Chow interpolation, is needed in order to avoid spurious oscillations of pressure, velocity components, and volume fractions.

2.3 Focus on Interfacial Drag Modeling

Among the different forces including in the momentum interfacial terms, the interfacial drag between immiscible phases has a key role in the modeling of momentum transfer. Considering the example of two phases, this term can be written in the following form:

$$I_1^{'} = \alpha_1\alpha_2 F_{12}(\vec{U}_2 - \vec{U}_1) \equiv k\alpha_1\alpha_2 \frac{\mu}{D^2}(\vec{U}_2 - \vec{U}_1). \quad (10)$$

It depends on the relative velocity and a coefficient F_{12} homogeneous to a dynamic viscosity divided by the square of a length D characteristic of the two-phase flow.

In dispersed flows modeling, physical considerations show that this length scale is proportional to the diameter of the inclusion. Formulas and correlations corresponding to the drag of a non-deformable sphere by a continuous fluid surrounding it are generally used (bubble and droplet laws).

For liquid/gas flow covering all the range of void (0 up to 1), the translation of the volume fraction values in terms of drag modeling is not unique. Figure 1 shows an example of choice of models for a volume fraction close to 0.5. We can consider a stratified flow with two continuous phases and two types of dispersed flows (dispersed droplets in a continuous gas or dispersed bubbles in a continuous liquid). The simplest form provided in NEPTUNE_CFD is the SIMMER flow chart [5], for which dispersed droplets in a continuous gas are considered for a void fraction greater than 0.7, dispersed bubbles in a continuous liquid are considered for a void fraction smaller than 0.3. For intermediate values taken between 0.3 and 0.7, the drag law is continuously interpolated between a bubble and droplet drag law. This quite simple model gives acceptable results for a quite wide range of applications, as it can be shown in [5, 6, 4].

Nevertheless, for pure stratified flows, the model described above may lead to a significant over-evaluation or under-evaluation of the friction between the gas and the liquid. Indeed, the drag model based on the friction between a dispersed and a continuous phase is sensitive to the diameter value. Interfacial area modeling, which gives information about the dimensions of the inclusions, still remains a challenging task for two-phase flows simulation.

Instead, the recognition of large interfaces within a volume averaged model represents a viable alternative for improving the modeling of the friction. A three layers model, named Large Interface Model or LIM, has been implemented in NEPTUNE_CFD [7, 8]. If the void fraction varies between 0 and 1 on three contiguous cells, a specific friction law is applied in the intermediate cell in which the void fraction is far from 0 and 1. Figure 4 shows a scheme of such a

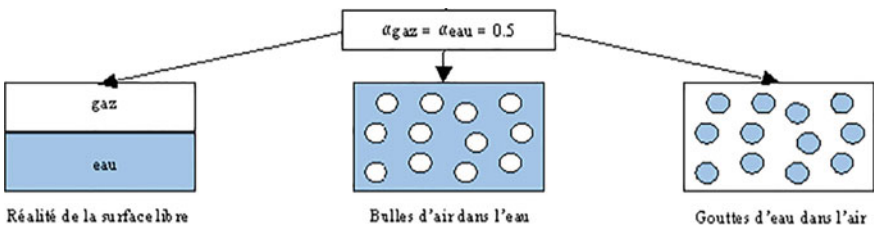

Fig. 1 Example of flow chart choices for a volume fraction ~ 0.5

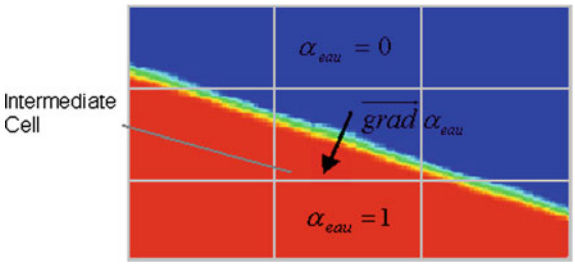

Fig. 2 Recognition of a surface of separation between two stratified flows (*red* and *blue*)

configuration of flows. The dispersed/continuous drag law (10) projected on the recognized separation surface is replaced by a continuous/continuous friction law, taking into account the laminar and turbulent contributions on both sides of the interface. The other part of the dispersed/continuous drag law acting along the strongest gradient of the volume fraction is conserved, even if it has no longer physical signification. It links the residual phase velocity to the most present phase velocity and hence avoids the apparition of too large relative velocities, which may induce numerical difficulties.

Multifluid approaches concerning the simulation of large bubbles are under development [9]. These techniques can be used for simulating free surfaces, as large bubbles can degenerate into large interfaces (Fig. 2).

3 Free Surface Flow Over a 3D Gated Creager Spillway

The first example concerning the flow upon a Creager spillway equipped with three segment gates has been investigated by the use of a reduced scale experiment at EDF R&D [10]. The experimental tests performed in a current channel allowed

- To measure the discharge for different geometrical configurations (number of the gates in service, position of the gates with respect to the highest level of the spillway, opening, …) and two types of pile; and
- To show hysteresis phenomenon due to the transition between a free surface flow and a partially confined flow controlled by the gate.

This case is particularly interesting for the evaluation of CFD codes [11], since non-linear phenomena drive the transition when the water level touches the gate. Moreover, a predictive evaluation of the free surface level is capital, since it determines if there is or not air entrainment under the gate.

The configuration contains three Creager weirs separated by two piles and three fixed gates, opened of 15 mm. Half of the geometry is simulated, provided that the flow remains symmetric in average according to a vertical plane located at the middle of the intermediate bump. Figure 3 shows the experimental setup viewed of front and behind and the unstructured mesh composed of hexahedra and prisms.

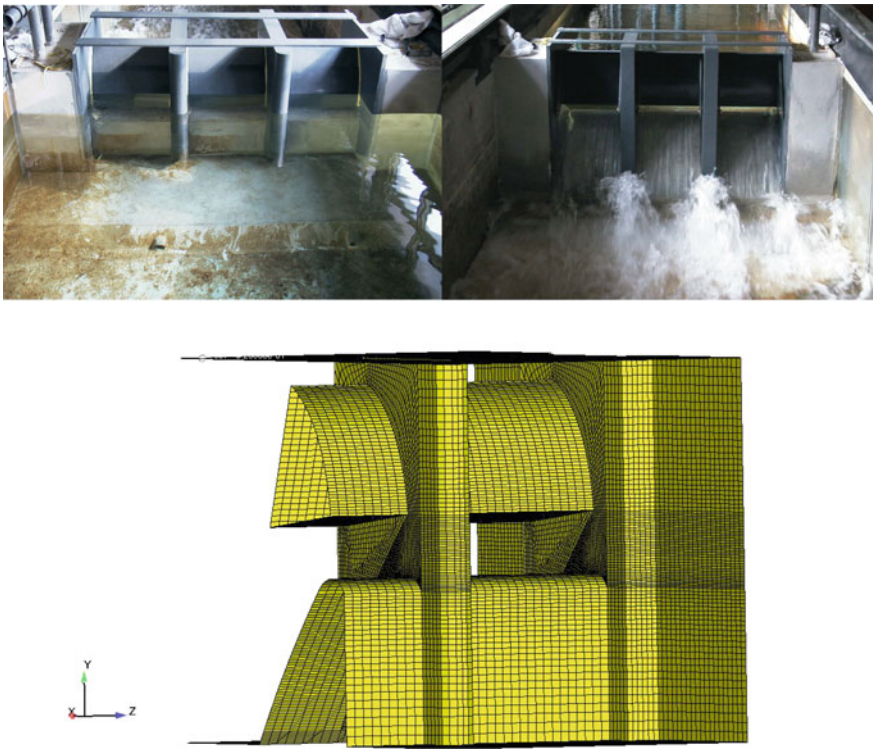

Fig. 3 Reduced scale model of the Creager spillway equipped with 3 sector gates. Corresponding mesh of the configuration

The hysteresis phenomenon has been reproduced by imposing an inlet flow-rate corresponding to the hysteresis zone and two initial different water levels, respectively, slightly lower and higher than the level of the gate. The numerical simulations then give two steady water levels, corresponding to a free surface flow and to a mixed flow controlled by the gate. Figure 4 shows on the coarsest mesh the initial

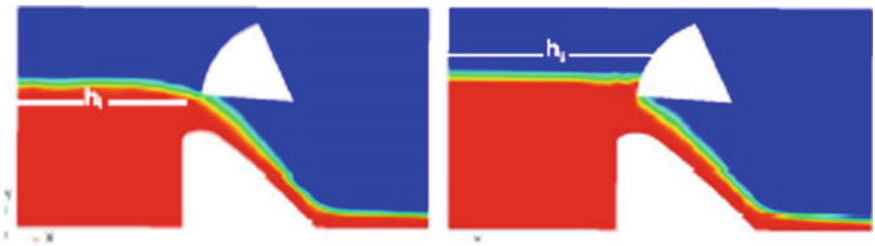

Fig. 4 Reproduction of the hysteresis phenomena at 80 l/s. *White* and *green lines* represent initial and final levels

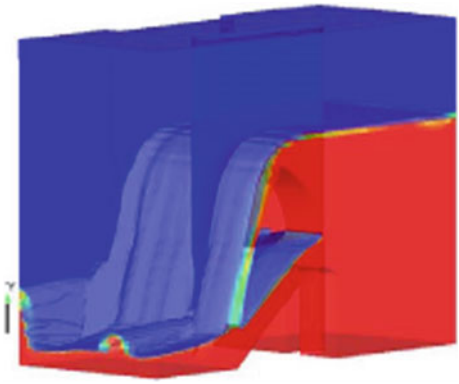

Fig. 5 3D flow with sector gate submerged with water ($H/H_d = 2$). Liquid volume fraction field (*red* = liquid and *blue* = air)

water levels (white line) and the final water levels (green) corresponding to a discharge for which a hysteresis phenomenon can be observed.

Figure 5 shows a mixed flow (free surface and partially confined) obtained for a charge of H/Hd = 2, for which the sector gate is submerged.

Figure 6 shows the relation of the computed discharges by passes with the imposed upstream charge. The computations have been performed with the following boundary conditions: the charge (corresponding to the stagnation pressure) and the level of liquid and air (through volume fractions of the two phases) at the inlet, a pressure condition at outlet; the computed pressure is prolonged to the boundary faces and rescaled in order to remain close to the atmospheric pressure far from the liquid flow.

The computed discharges are in good agreement with the experimental data, only available for non-dimensional charges ranging from 0.6 up to 1. The first slope corresponds to a free surface flow passing under the sector gate, the second slope to a flow controlled by the sector gate, and the third slope to a flow submerging the sector gate. The Large Interface Model (LIM) model gives here much better results than the dispersed drag model.

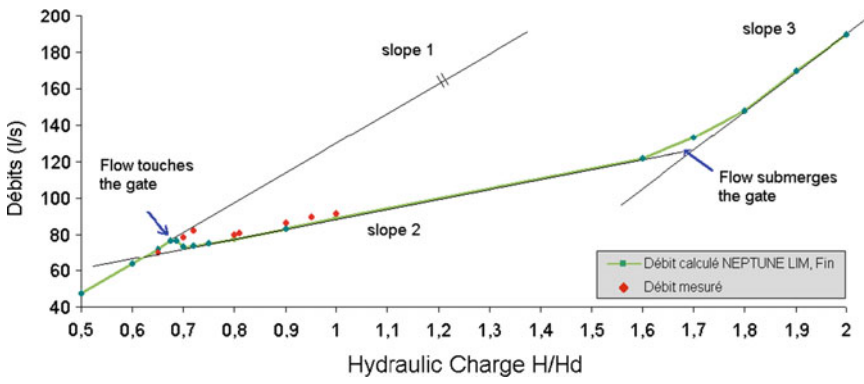

Fig. 6 Flow-rate by passes with respect to the imposed charge

4 Heated Tube Bundle Modeled at a Component Scale

The study presented here is an evaluation of NEPTUNE_CFD used at a component scale, for which the structures are homogenized with the fluid. The test-case VATICAN performed at EDF R&D [12] represents a full scale tube bundle representing a part of fuel assemblies of cores of french PWR reactors. Figure 7 shows the geometry of the tube bundle at a horizontal dilated scale with its tube support plates at 4 locations (left) and the used mesh with the porosity distribution represented the fluid volume fraction (right). Freon fluid flows vertically upward, heated by a 10 × 4 tubes of 9.5 mm diameter. There are three independent heating zones, delivering a maximum heat flux of 15 w/cm^2. The experimental steam fractions are obtained with Gamma radiography: attenuation of Gamma rays on both sides of the model gives the density of the traversed medium, and hence the void fractions.

The heating power dissipated in the homogenized volume containing the fluid and the heating tube increases the average temperature of the liquid. This latter can be smaller than saturation temperature, while close to the tube bundle, temperature may exceed saturation temperature, involving evaporation of the liquid. This phenomenon, filtered par the spatial scale, is taken into account by the sub-saturated model of THYC code [13], implemented in NEPTUNE_CFD [14].

Figure 8 shows the axial profile of the pressure along the vertical axis z to two horizontal ribs corresponding to the left and right branches. The difference between the experimental data and the computed pressure is low. The axial head losses more important in the center of the configuration do not involve transverse pressure gradient. As the head loss coefficients are very large according to the radial

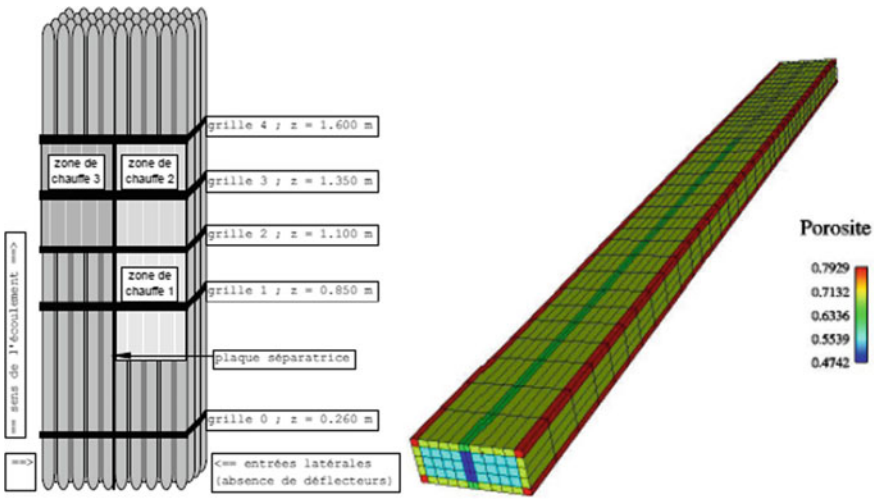

Fig. 7 Geometry of the heated tube bundle at dilated scale (*left*). Mesh and porosity distribution at right scale (*right*)

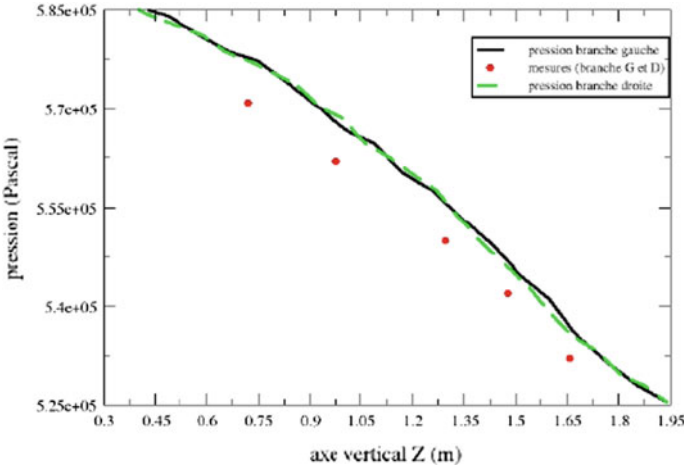

Fig. 8 Experimental and numerical pressure vertical profile

direction, the flow is adjusted axially. The axial velocity of the mixture is of the order of 2–6 m/s as shown in Fig. 9, much larger than the transverse velocity.

The computational results compare fairly well with experiment. The relative difference between the measurements and the calculation is less than 1 %. On the absolute point of view, the simulations overestimate the pressure of 5000 pascals.

Figure 9 shows the results obtained by two multi-phase flow models upon the VATICAN test-case. THYC, the EDF reference code for thermal-hydraulics core simulations, uses a "4 equations" model corresponding to two mass balances, a mixture momentum balance, and a mixture enthalpy balance. NEPTUNE_CFD uses a "6 equations" model, corresponding to two mass balances, two momentum balances, and two energy balances. For the VATICAN test-case, the sub-saturated heat transfer model of THYC is implemented in NEPTUNE_CFD.

NEPTUNE_CFD and THYC reproduce correctly the main characteristics of the two-phase flow in the tube bundle. The maximum evaporation is in the central zone, because the friction of the flow on the separating plate significantly lowers the velocity of the coolant. The used model overestimates the steam in the central area of the flow behind the separator plate. The model reproduces properly the flow and heat transfer and mass transfer in the intermediate zones and board.

The relative velocity computed by NEPTUNE_CFD between steam and liquid is small compared to the velocity of the mixture, confirming the validity of the homogeneous model used for this type of configuration.

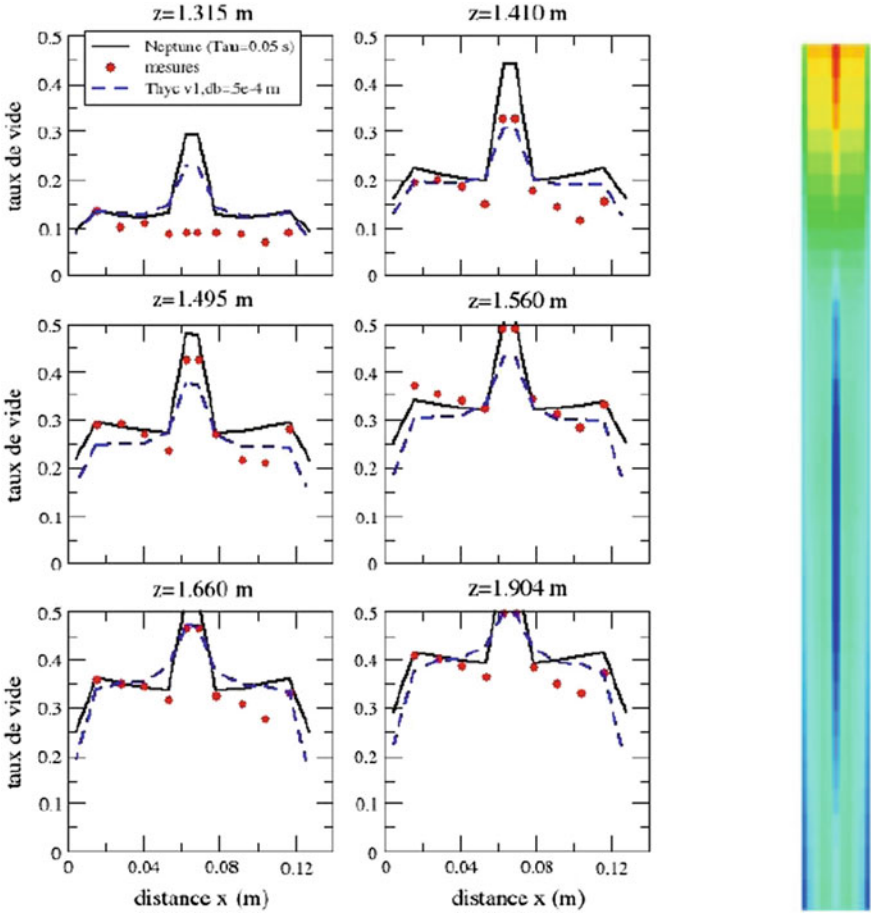

Fig. 9 Experimental and computed radial profiles of steam volume fraction for several heights (*left*). Axial velocity of the steam-liquid mixture (*right*)

5 Conclusion

The paper deals with a short presentation of the model implemented in NEPTUNE_CFD code, originally designed for CFD scale simulations. Applications of this code are illustrated through the detailed presentation of two examples; the first one borrowed to hydraulic domain and the second one to nuclear engineering.

The numerical results obtained by NEPTUNE_CFD upon the 3D gated creager spillway compare fairly well with experimental data and with numerical results obtained with methods widely used for free surface flows simulation. A predictive simulation of such flows, characterized by the presence of dispersed and separated

fluids in the same computational domain, still remains a challenging task for which multi-fluid approach coupled with accurate interface locating method still under development can be promising.

The second presented study concerns computations of flows within a heated tube bundle at a component scale, for which fluid and structures are homogenized. The obtained computational results upon the axial pressure profiles and radial steam volume fractions are reasonably comparable with experimental data. The model overestimates evaporation in the central zone just behind the separated plate and correctly reproduces the flow and mass/heat transfer in the intermediate zones.

Acknowledgments The presented computations have been performed in the framework of EDF R&D projects, with the financial support of EDF (Electricite de France).

The authors are grateful to the NEPTUNE_CFD development team for their support to the use of the code and help for implementing specific models.

In the frame of the NEPTUNE project, NEPTUNE_CFD code is jointly developed by EDF (Electricite de France) and CEA (Commissariat à l'Energie Atomique). The project is also funded by AREVA-NP and IRSN (Intstitut de Radioprotection et de Sûreté Nucléaire).

References

1. Guelfi, A., Bestion, D., Boucker, M., Boudier, P., Fillion, P., Grandotto, M., et al. (2007). NEPTUNE—A new software platform for advanced nuclear thermal-hydraulics. *Nuclear Engineering and Design, 156*, 281–324.
2. Ishii, M., & Hibiki, T. (2006). *Thermo-fluid dynamics of two phase flows*. New York: Springer Science Business Media.
3. Simonin, O. (2000). Statistical and continuum modelling of turbulent reactive particulate flows. Theoretical and Experimental Modelling of Particulate Flows. Lecture Series 2000–06, Von Karman Institute for Fluid Dynamics, Rhode Saint Genèse, Belgium.
4. Méchitoua, N., Boucker., M., Lavieville, J., Hérard, J.M., Pigny, S., & Serre, G. (2003). An unstructured FV solver for two phase water/vapor flows modelling based on an elliptic oriented fractional step method, NURETH'10, Seoul, October 5–9, 2003.
5. Tobita, Y., Kondo, S., Yamano, K., Morita, W., Maschek, P., Coste, P., & Cadiou, T. (2006). The development of SIMMER-III, an advanced computer program for LMFR safety analysis, and its application to sodium experiments. *Nuclear Technology, 153*, 245–255.
6. Pigny, S., Boucker, M., Laviéville, J., & Méchitoua, N. (2004). Benchmarks for the NEPTUNE 3D code. In *Proceedings International Conference on Multiphase Flows*, *Yokohama, Japan*, May 31–June 03, 2004.
7. Coste, P., Pouvreau, J., Morel, C., Laviéville, J., Boucker, M., & Martin, A. (2007) Modeling turbulence and friction around a large interface in a three dimensional-two velocity Eulerian code. NURETH'12, Pittsburgh, Pennsylvania, USA, September 30–October 4 (2007).
8. Lavieville, J., & Coste, P. (2008). Numerical modeling of liquid-gas stratified flows using two phase Eulerian approach. In *Proceeding of 5th International Symposium on Finite Volumes for Complex Applications*, *Aussois, France*, June 08–13, 2008.
9. Mimouni, S., Denèfle, R., Fléau, S., & Vincent, S. (2014). Multifield Approach and Interface Locating Method for Two Phase Flows in Nuclear Power Plant. SIMHYDRO2014, Sophia Antipolis, France, June 11–13, 2014.

10. Cicéro, G. M., Boursiquot, D., Brémont, O., & Menon, J. M. (2014). Projet Maîtrise de la Débitance des Ouvrages—Synthèse des essais sur modèle réduit de vannes segment sur seuil Creager. Internal Report EDF R&D LNHE HP-75/04/014/A.
11. Mechitoua, N., Jennesson, B., Schneider, J. P., Luck, M., & Valette, E. (2010). Assessment of NEPTUNE_CFD code for some free surface flows interesting fluvial hydraulic. ICMF 2010, Tampa, Florida, May 30–June 4, 2010.
12. Guichard, J., & Thomas, B. (1992). Compte rendu des Essais Diphasiques VATICAN-1. Note EDF R&D HT-33/92.09.A.
13. Guelfi, A., & Pitot, S. NPR : Note de principe THYC Version 4.1, Partie 1 : Modélisation. Note EDF R&D HI-84/03/020/A.
14. Mechitoua, N. (2006). Vit Evaluation de NEPTUNE_CFD sur une configuration d'écoulements en faisceau de tubes. Note EDF R&D H-I81-2006-04525-FR.

Multifield Approach and Interface Locating Method for Two-Phase Flows in Nuclear Power Plant

Stéphane Mimouni, Romain Denèfle, Solène Fleau and Stéphane Vincent

Nomenclature

c Color function
d Diameter (m)
g Gravitational constant ($m.s^{-2}$)
n Interfacial normal vector ($m.s^{-1}$)
F Volume force (N)
I Interfacial momentum transfer ($kg.m^{-2}.s^{-2}$)
P Pressure ($N.m^{-2}$)
S Rate-of-strain tensor (s^{-1})
T Total stress tensor ($kg.m^{-1}.s^{-2}$)
U Mean velocity ($m.s^{-1}$)

Greek letters

α Volume fraction
ε Diffusivity of artificial compression step ($m^2.s^{-1}$)
κ Curvature (m^{-1})
ν Viscosity ($m^2.s^{-1}$)
ρ Density ($kg.m^{-3}$)
σ Surface tension (m^{-1})

S. Mimouni (✉) · R. Denèfle · S. Fleau
Electricité de France, R&D Division, 6 Quai Watier, 78401 Chatou, France
e-mail: stephane.mimouni@edf.fr

R. Denèfle
e-mail: romain.denefle@edf.fr

S. Fleau
e-mail: solene.fleau@edf.fr

S. Vincent
I2M Université de Bordeaux, UMR 5295, 33607 Pessac, France
e-mail: stephane.vincent@enscbp.fr

P. Gourbesville et al. (eds.), *Advances in Hydroinformatics*,
Springer Water, DOI 10.1007/978-981-287-615-7_33

τ Relaxation time (s)
Δ Filter width (turbulence model) (m)
Γ Mass transfer ($kg.m^{-3}.s^{-1}$)

Subscripts

i,j Space directions
k,p Field index
cg Continuous gas field
dg Dispersed gas field
cl Continuous liquid field

1 Introduction

Many situations in nuclear power plant are characterized by liquid vapor interfaces as the dewatering step of the cold leg of the reactor pressure vessel, boiling crisis, and flows occurring in a steam generator. Let describe the industrial context in a few words.

During a loss-of-coolant accident, a relevant safety issue in the context of PWR life extension study is the possibility of a cold shock, the so-called Pressurized Thermal Shock (PTS), when subcooled water flows from Emergency Core Cooling (ECC) system through the cold leg (a horizontal pipe) toward the reactor pressure vessel. The thermal hydraulics problem is to evaluate the heat-up of water between the ECC injection and the vessel. A two-phase stratified flow may take place in a part of the cold leg, as well as more complex turbulent two-phase flow configurations in the cold leg region close to the ECC injection and in the downcomer region below the junction with the cold leg. In the situations of interest, the cold leg is thought to be a liquid–vapor stratified flow; the ECC jet is thought not to break-up and to plunge into the free surface; direct contact condensation takes place with a maximum in the ECC region of the cold leg; the free surfaces are thought to be mostly wavy or rough; the water and gas are turbulent.

In this context, the interface locating method is of relevant interest to deal with mass, momentum, and energy exchanges through the interface. In cells where the interface is not captured, the interfacial area, mass, momentum, and energy transfer terms correspond to that of bubbles, droplets, or other intermediate states. The paper aims at improving the interface locating method without changing the models already validated against experiments.

Moreover, in two-phase CFD involving large interfaces, the liquid or gas volume fractions cover the whole range from 0 to 1 and the great majority of cells are of course out of large interfaces. There can be bubbles entrained below the jet or droplets ejected. These phenomena could require a multifield approach to be taken into account.

When a liquid is flowing onto a heated wall, the heat transferred by the wall to the liquid causes the liquid to partly evaporate, therefore giving a two-phase bubbly along the wall. This kind of situation, called nucleate boiling regime, is an efficient manner to evacuate the heat produced into the wall, for example by Joule effect or by a nuclear reaction. Unfortunately, in nucleate boiling, heat flux increases and reaches a maximum value with increasing surface temperature. Further increase in the surface temperature results in decreasing heat flux because the transition from nucleate boiling to film boiling takes place. The maximum heat flux that can be obtained by nucleate boiling is referred to as critical heat flux (CHF). In the case of controlled heat flux, a slight increase of heat flux beyond the CHF can cause the surface temperature to rise to a value exceeding the surface material's maximum allowable temperature. This in turn can cause severe damage or meltdown of the surface.

As a consequence, CHF has been extensively studied in the last five decades, as a major limiting phenomenon for nuclear power plant capabilities, as well as in other industries.

Two-phase flows are featuring many other industrial applications such heat exchangers and chemical reactors. Based on the interface structures, several flow regimes can be identified and commonly separated into three main groups; separated flows, dispersed flows, and the last group would contain the flows such as bubbly annular, churn turbulent, or slug flow. Although this classification has been experimentally confirmed since a few decades, the numerical simulation of complex two-phase flow regimes is still challenging and a universal model remains to be established.

There are several approaches for two-phase flow modeling, describing the interfaces either with a dispersed or a located point of view. Bubbly flows are often modeled with an Eulerian-dispersed description, within the two-fluid model of Ishii [1]. The averaged momentum balance equation is in this case closed with a set of interfacial forces such as drag, lift, virtual mass, and turbulent dispersion. These forces rely on empirical or statistical correlations making assumptions on the bubbles mean diameter and shape, generally considered as spherical or slightly ellipsoidal. To treat accurately problems where these assumptions are not verified, an interface tracking model is preferred to follow the distortions of the bubbles.

On the other hand, large interface flows such as slugs or free surfaces are mostly simulated through located approaches such as front tracking [2], Level-set [3, 4], or Volume of Fluid [5] with an Eulerian point of view or Lagrangian grid methods [6] with a Lagrangian point of view. All these methods aim at calculating the local characteristics of the interface, such as the curvature and the normal vector, to model the interfacial transfer in the momentum equation.

New approaches are explored to simulate more accurately the transition regime between bubbly and separated flows. The concept of a four-field and two-fluid model has been presented and studied over the last decade [7, 8].

Each phase is decomposed into a continuous and a dispersed field, resulting in a four-field system of mass, momentum, and energy equations. This kind of approach requires the set of mass transfer terms between the continuous and the dispersed

fields of the same physicochemical phase. A spatial cutting length is dividing a phase between unresolved structures that are modeled and the larger ones that are simulated. This concept allows the simulation of a wide range of two-phase flow regimes with both a good accuracy on the behavior of the most distorted interfacial structures, and less CPU consuming than the direct simulation of every two-phase scale. If the dispersed fields are commonly dealt with an Eulerian point of view, several methods can be used to locate the interface between the liquid and gas continuous fields.

We present a hybrid multifield approach based on this four-field concept. It consists in modeling the two-phase flow with an Eulerian approach, the gas phase being split into two fields. The small bubbles, assumed to be spherical, are modeled with a dispersed approach, whereas the larger bubbles, considered as too distorted to be accurately described by correlations, are simulated through an interface locating method. As a first step toward this new approach, we simplify the general concept by considering the liquid phase as continuous in our simulations. The principle of this three-field approach is summarized in Fig. 1. This approach is generalized to simulate free surfaces (large bubbles considered as continuous gas phase degenerate into large interfaces) and heat and mass transfer.

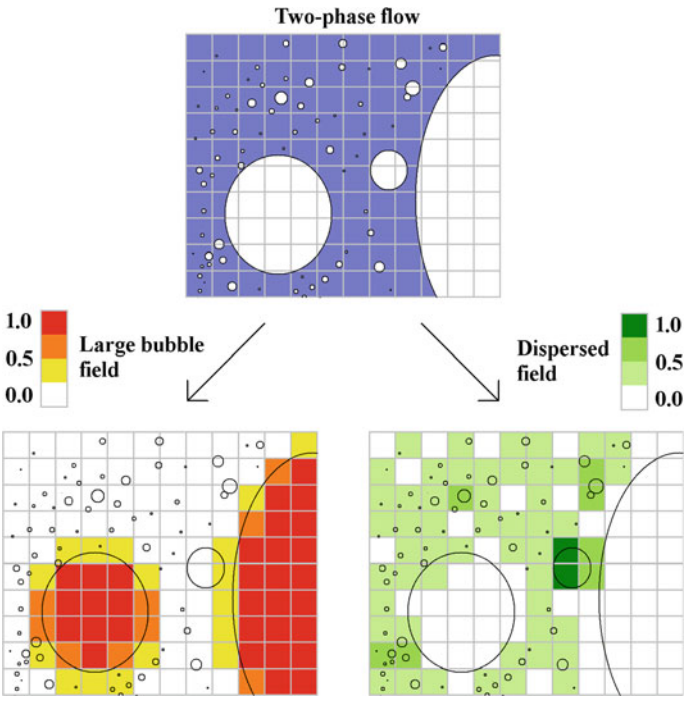

Fig. 1 Scheme of the principle of the multifield hybrid approach. The gas phase is split into two fields, one being dealt with a dispersed approach (*green*) and the other one having its interface located

2 Two-Field Model

These models have been implemented in the CFMD code NEPTUNE CFD [9]. The flow motion is followed using the two-fluid model of Ishii [1] extended to n-phase. With the assumption of a common pressure for all fields, the system consists in three balance equations per field, describing the conservation of the mass, the momentum, and the energy. The solver SIMPLE [10] is based on a finite volume discretization, together with a collocated arrangement for all variables. An iterative coupling of the equations is used to ensure both mass and energy conservation. The data structure is totally face based, which allows the use of arbitrary-shaped cells including nonconforming meshes.

Following the strategy of the code, the choice is made to keep an Eulerian point of view for every field. In this section, we restrict our study to adiabatic cases, simplifying the system to the mass and momentum.

2.1 Governing Equations

The overall method is based on the Eulerian multifluid formalism. The closure laws for the dispersed field have already been validated. It has given reasonable agreement with experimental data in cases where spherical shape assumption is valid.

The two-fluid model is based on Eulerian multifield balance equations, described by Ishii [1]. These balance equations can be written as a mass (Eq. (1)) and a momentum (Eq. (2)) equation per field in case of isothermal simulations:

$$\partial_t(\alpha_k \rho_k) + \partial_{xi}\left(\alpha_k \rho_k U_{k,i}\right) = \Gamma_k \tag{1}$$

$$\partial_t\left(\alpha_k \rho_k U_{x,i}\right) + \partial_{x_j}\left(\alpha_k \rho_k U_{k,i} U_{k,j}\right) = \partial_{x_j}\left(\alpha_k T_{k,ij}\right) - \alpha_k \partial_{x_i} P + \alpha_k \rho_k g_i + I_{k,i}. \tag{2}$$

2.2 Dispersed Gas Field

The Eulerian-dispersed approach for small interfaces that can be considered as spherical has already been validated [11, 12]. It has given reasonable agreement with experimental data, using the multifield CFD code NEPTUNE_CFD.

I_k is the sum of all interfacial forces acting between the dispersed field and the liquid, such as drag force, lift force, wall lubrification, virtual mass, and turbulent dispersion force. The closure laws used here and more details of the dispersed modeling of bubbly flows can be found in Mimouni et al. [11, 12].

2.3 Continuous Gas Field

The continuous gas field is mostly described by the position of its interface. As the modeling is done in an Eulerian point of view, this interface is localized by a volume color function c. The closure laws for the continuous field are here a drag force (Eq. (3)) representing an inner wall friction law and the surface tension force (Eq. (4)). This latter is expressed in a volume discretization, allowed by the Continuum Surface Force (CSF) method of Brackbill [13].

$$\vec{F}_{\text{drag}}^{1\to 2} = \frac{\alpha_1\alpha_2(U_1 - U_2)(\alpha_1\rho_1 + \alpha_2\rho_2)}{\tau_{\text{drag}}} \cdot d\Omega \tag{3}$$

$$\vec{F}_{st}^{k} = \alpha_k\sigma\left[\nabla \cdot \left(\frac{\nabla c}{\|\nabla c\|}\right)\right]\nabla c \cdot d\Omega \tag{4}$$

$d\Omega$ is the cell volume. An artificial compression step was coupled to a level-set method by Olsson and Kreiss [14] (Eq. (5)), resulting in a conservative level-set. This model controls the interface thickness, allowing a constant accuracy on the interface properties calculation such as the local curvature and the interfacial vector.

$$\partial_\tau\alpha_k + \nabla(\alpha_k(1 - \alpha_k)\vec{n}) = \varepsilon\Delta\alpha_k, \tag{5}$$

where $\varepsilon = \Delta x/2$ and $\Delta\tau = \Delta x/32$, which correspond to a interface thickness spread over five cells [19].

In a first approach, τ_{drag} was taken equal to 10^{-7}. Nevertheless, we do not take into account the variation of viscosity with this expression. Therefore, by considering the standard drag coefficient formulation, we derive the new following expression:

$$\begin{aligned}
&\alpha_2 < 0.3: && F_{\text{bubble}} = \alpha_1\alpha_2\frac{18\mu_1}{\alpha_1 d_p^2}(U_2 - U_1)\\
&\alpha_2 > 0.7: && F_{\text{droplet}} = \alpha_1\alpha_2\frac{18\mu_2}{\alpha_2 d_p^2}(U_1 - U_1)\\
&0.3 \le \alpha_2 \le 0.7: && F_{\text{mix}} = \frac{0.7-\alpha_2}{0.7-0.3}F_{\text{bubble}} + \frac{\alpha_2-0.3}{0.7-0.3}F_{\text{droplet}}
\end{aligned} \quad . \tag{5}$$

To allow continuous evolutions between bubbles and droplets, we implement the drag force as presented. For the definition of the characteristic distance d_p, we separate two domains: the domain close to the interface and far from the interface. Moreover, we introduce the possibility to deal with a third dispersed phase flow with a continuity between the drag force applied to large interfaces and to the dispersed field. Then, we consider that d_p is equal to the diameter of the dispersed bubbles/droplets far from the free surface and equal to $d_p = \frac{\alpha_2}{\|\nabla\alpha_2\|}$ close to the interface. A smooth transition between both domains is explained in Fig. 2.

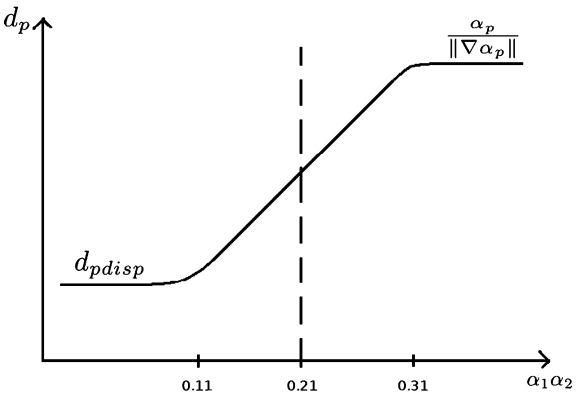

Fig. 2 Clipping method, d_{pdisp} corresponds to the diameter of the dispersed bubbles/droplets

2.4 Validation Cases

These approaches for the simulation of either dispersed or located bubble interfaces have already been validated against experimental measurements in previous work [15, 16] with the drag force given by (3). As examples, the numerical predictions for the experiments of Bhaga and Weber [17] and of Brereton and Korotney [18] are presented in Fig. 3.

As already discussed above, we do not take into account the variation of viscosity with the formulation given by (3). In case of lower liquid viscosity, the superimposition of the Bhaga's experimental data and the results of the simulation (Fig. 4) show a real benefit with the new drag force. The fact that we take the viscosity into account in the force seems to improve the simulation.

In the following, we show that the interface locating method developed can be applied to calculate free surfaces. The method is assessed on Rayleigh–Taylor instability and Kelvin–Helmholtz instability.

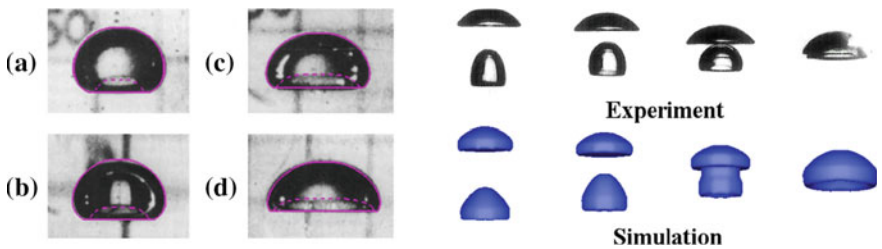

Fig. 3 The picture on the *left* presents the comparison between experimental captures from Bhaga and Weber [17] and numerical prediction of the final shape of a rising bubble (*red line*) for four viscosities of the liquid phase. The picture on the *right* shows the in-line coalescence phenomena of two bubbles. The *upper* pictures are experimental captures, and the *lower* are numerical calculations, the time interval being the same for both series (dt = 30 ms)

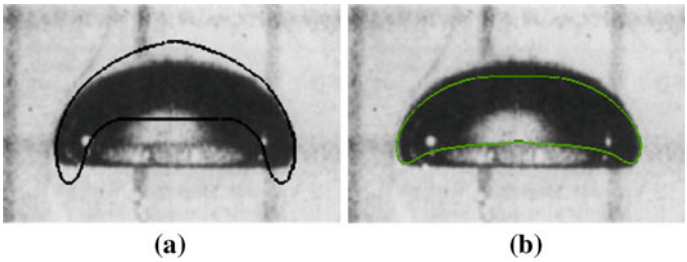

Fig. 4 The picture presents the comparison between experimental captures from Bhaga and Weber [17] and numerical prediction of the final shape of a rising bubble (*blue* and *green lines*) for lower viscosity of the liquid phase. *Left* $\tau_{drag} = 10^{-7}$. *Right* New drag force

The Rayleigh–Taylor instability occurs in a system with two immiscible fluids of different densities in the presence of gravity fields such as $\nabla P \wedge \nabla \rho \neq 0$. The fluid with higher density ($\rho_1 = 3$ kg/m^3, $\mu_1 = 0.03$ Pa.s), is initially located above the fluid with lower density ($\rho_2 = 1$ kg/m^3, $\mu_2 = 0.01$ Pa.s). The simulation was performed in a closed box (H = 5 m, L = 1 m) [19]. A wall boundary condition was imposed at the top and the bottom of the mesh and symmetry boundary planes everywhere else. The interface between the two fluids was initialized as a small cosine wave with an amplitude equal to 1 mm. Figure 5 represents the amplitude instability plotted against time and shows that CFD calculations are in good agreement with theoretical results (Fig. 6).

The Kelvin–Helmholtz instability deals with a system with two immiscible fluids, which move with different velocities (Thorpe's experiment, see [19]). The Kelvin–Helmholtz instability is observed when the relative velocity between the two fluids exceeds a critical velocity. This experiment was performed in practice and also simulated, which allows a comparison with theoretical and experimental data. The two fluids are contained in a rectangular tube, which is tilted for a small

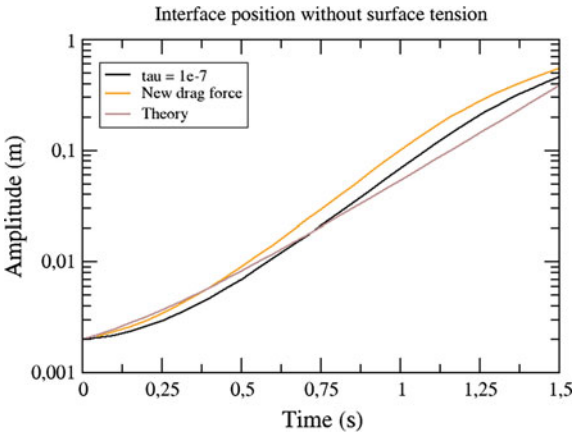

Fig. 5 Comparison of the simulation with the different drag forces, without surface tension, adaptive time step, mesh with 46,080 cells

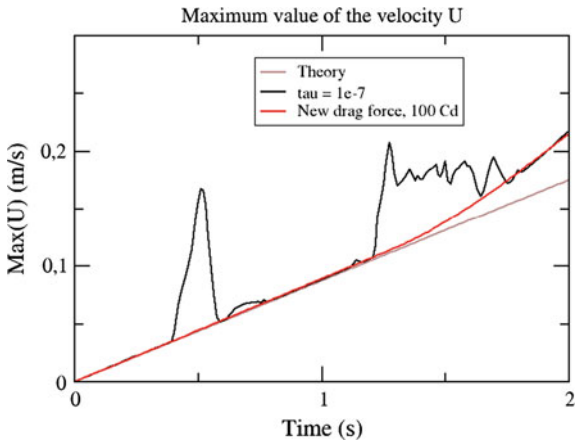

Fig. 6 The velocity U corresponds to the expression defined in Eq. (6)

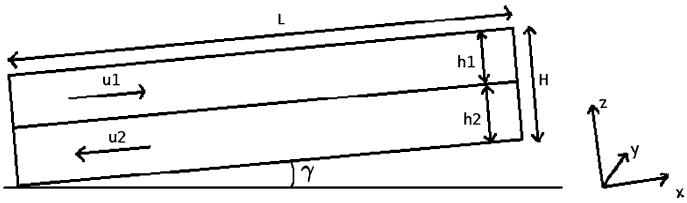

Fig. 7 Thorpe's experiment

angle (sin(γ) = 0.072). The dimensions of the tube are L = 1.83 m and H = 3 cm (see Fig. 7). The mesh contains 80 × 4880 cells. Both fluid layers have the same initial height h1 = h2 = 1.5 cm.

The properties of the two fluids are $\rho_1 = 780$ kg/m^3, $\mu_1 = 0.0015$ Pa.s and $\rho_2 = 1000$ kg/m^3, $\mu_2 = 0.001$ Pa.s. The surface tension is equal to 0.04 N.m.

A wall boundary condition was imposed everywhere except in front and behind planes, where symmetry conditions are imposed. We compare the previous drag force with the new one, in terms of interface shape, critical wave number, evolution of the maximum value of the average velocity of the interface U at the beginning of the simulation, and the velocity profile, where

$$U = \frac{\alpha_1 \rho_1 U_1 + \alpha_2 \rho_2 U_2}{\alpha_1 \rho_1 + \alpha_2 \rho_2}. \tag{6}$$

In Fig. 8, we can notice that the instability appears later in our simulations than in Štrubelj's ones (see p. 62, [19]). Nevertheless, the evolution is slower with the new drag force. The waves are also more regular with this force, which is better. The wave numbers obtained with the FFT are equal to 149.5 m^{-1} for the previous drag force and 194.6 m^{-1} for the new one. The results are closer to the experimental data with the new drag force (Fig. 9).

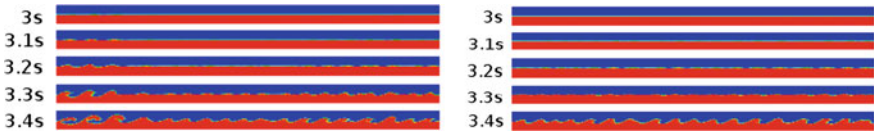

Fig. 8 Influence of the drag force expression in terms of interface shape, *Left* previous drag force with: new drag force, only the *middle* 0.6 m long section of the channel is shown

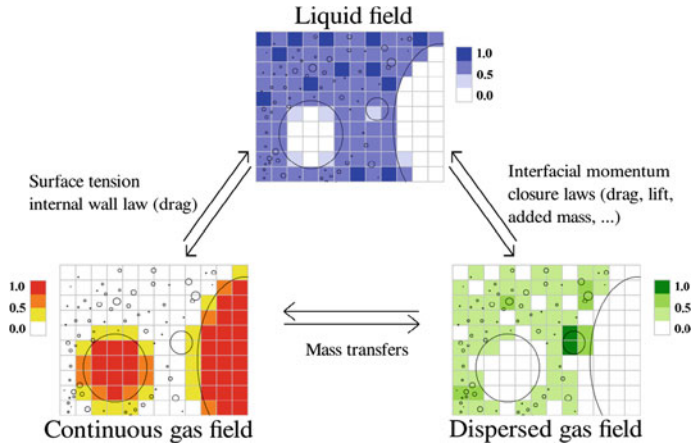

Fig. 9 Scheme of the principle of the field coupling in the multifield hybrid approach. The gas phase is split into two fields. Each one exchange momentum with the continuous liquid phase through specific closure laws. The exchange between the two gas fields is modeled by mass transfer terms (inducing momentum exchange, cf. Eq. (3))

In Fig. 6, we see that the new drag force is in better agreement with the theory because the curve with the new drag force does not have discontinuities. Therefore, we improve the simulation results with this drag force. In fact, the new drag force has a more physical expression, which reduces the numerical instabilities. Finally, the velocity profiles are equivalent with the two drag forces (not represented in the paper).

3 Three-Field Model

3.1 Computational Model

As explained previously, the three-field model consists in a multifield approach where the gas phase is split into two separated fields. To build this approach, mass transfers have to be implemented between these two gas fields. Three contributions of this mass transfer term between the gas fields have been identified. The first one

is the initiation of a located large bubble by accumulation and coalescence of the dispersed field. A criterion based on the dispersed phase void fraction and its gradient is settling the coefficient of this dispersed to continuous mass transfer, as presented in Eq. (7). The second is the creation of dispersed field when the located interface becomes unresolved. Pigny [20] proposed to consider a located bubble as unresolved if its diameter is lower than 8 Δx. As it can be seen in Fig. 10, a bubble with a diameter inferior to 8 Δx will present, because of the CSF scheme for the curvature calculation, an overlap of the information used to calculate the curvature at two opposite points of the interface. The resolution criterion for a local interface is evaluated by the comparison of the local curvature and the local void fraction gradient of the continuous gas void fraction to the space scale of the grid. Knowing the thickness and the curvature of a resolved interface, it results in a first numerical criterion for the dispersed gas creation of Δx/20, presented in Eq. (7). Finally, the interaction between dispersed field and a located interface has to be modeled. Only coalescence is modeled here, and the dispersed field is merged into the continuous gas field when it comes across the interface:

$$\begin{aligned} \Gamma_{cg\,\text{creation}} &= C_{dg\to cg} H(\alpha_{dg} - \alpha_{crit}) H(\nabla\alpha_{dg} - \nabla\alpha_{\text{crit}}) \\ \Gamma_{dg\,\text{creation}} &= C_{cg\to dg} H\left(\kappa\nabla\alpha_{cg} d\Omega - \frac{\Delta x}{20}\right) \end{aligned} \quad , \tag{7}$$

where H is the Heaviside function. The two coefficients $C_{dg\to cg}$ and $C_{cg\to dg}$ are relaxation times modeling the time scale of the two creation transfers. These creation terms of the continuous (Eq. 8) and the dispersed (Eq. 9) gas fields are gathered in the mass transfer term Eq. (10):

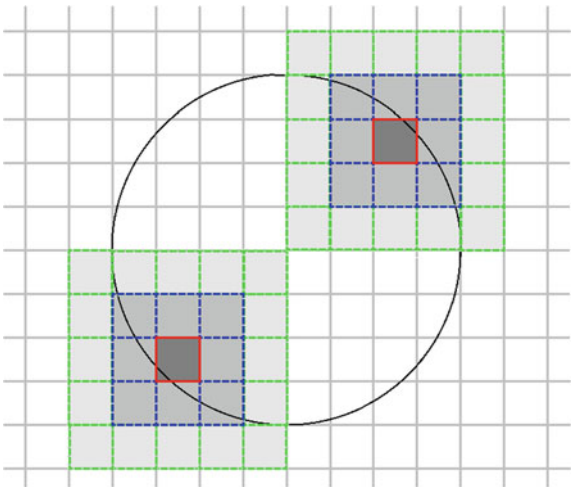

Fig. 10 Illustration of the limit of the resolution of a bubble with the calculation of the curvature with the CSF method from Brackbill. The two layers of neighbor needed for the calculation of the gradient and then the divergence of the gradient are represented, respectively, in *blue* and *green*

$$\Gamma_{dg\to cg} = \alpha_{dg}\alpha_{cg}\frac{\rho_g}{\Delta t} = \left(\Gamma_{cg\,\text{creation}} - \Gamma_{dg\,\text{creation}}\right). \tag{8}$$

The coefficient α_{dg} α_{cg} is directly derived from the two-fluid formalism. The resulting coupled approach is illustrated in Fig. 9. We use a simple Heaviside function activating the transfer between the two gas fields when the volume fraction of the dispersed field is over a critical value ($\alpha_{dg} > \alpha_{\text{crit}} = 0.3$) and when $\nabla\alpha_{dg} > \nabla\alpha_{\text{crit}} = {}^{1}/_{20}\,\Delta x$.

Although this first demonstrating test case has physical modeling for each field, the threshold $C_{dg\to cg}$ is just an example to show the capability of the method.

3.2 Experimental Comparisons

The bubble plume case chosen here is the experiment of Castillejos [21]. As illustrated in Fig. 11, air is injected at the center of the bottom of a cylindrical water tank of diameter 50 cm. The initial water height is 40 cm, and the air mass flow is 876 $cm^3\ s^{-1}$, the inlet being a 6.35 mm diameter nozzle. This experiment presents a range of bubble sizes from about 6 cm to smaller than 1 mm. That makes it very difficult to model with classical two-phase two-field models such as the Euler–Euler dispersed two-phase approach because of the difficulty to set up correlation for the closure laws when the ranges of bubble size and shapes are so wide.

A full resolution of every interface scales would be in this case very CPU consuming. Considering a local interface as fully resolved when the curvature radius is 15 times the grid scale [15, 16], it would require a mesh containing several millions of cells to follow correctly bubbles with a diameter of 1 mm. The experiment is simulated with the two-field and two-phase and with the three-field and two-phase approach. The mesh contains about 5.8 million of cells, which allows a calculation during a week on 768 processors. The filtering scale at the center of the domain is 5 mm for the located gas structure in the flow. The dispersed

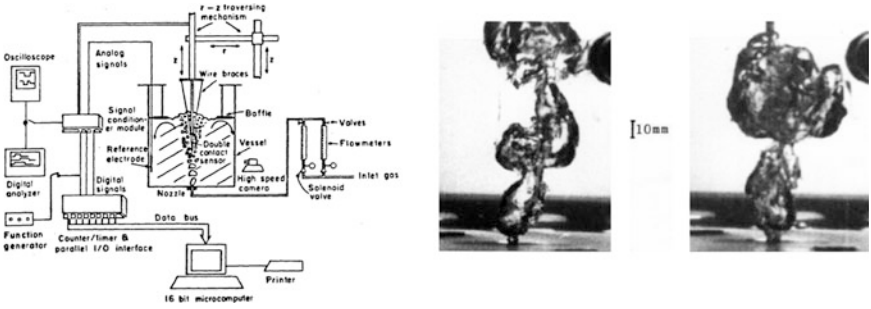

Fig. 11 Castillejos's experimental apparatus sketch (on the *left side*). The pictures on the *right* are experimental captures of the plume few centimeters above the *inlet*

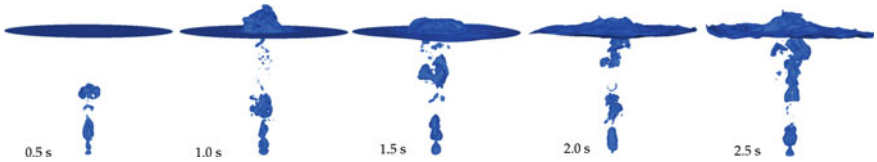

Fig. 12 The picture is a view of the gas plume after 2 s of injection for the case of a two-field and two-phase simulation. The iso surface of the volume fraction of the continuous field ($\alpha_{cg} = 0.5$) is colored in *blue*

field of the three-field and two-phase approach is modeled through a simplified mono-dispersed approach with a constant bubble diameter set to 1 mm.

Figure 12 presents snapshots of the simulated plume at different times (0.5, 1.0, 1.5, 2.0, and 2.5 s) with the two-field and two-phase approach. Two phenomena can be observed on this picture: the air flow after the inlet is puffing, creating the large bubbles of about 6 cm length, and the high fragmentation rate of the plume.

As it can be seen for example on the second plume snapshot at t = 1.0 s, the smallest bubble simulated at the top of the plume is far from being correctly resolved on the spatial grid that we used here. This is exactly what is expected from the hybrid three-field and two-phase approach. Instead of refining the mesh size, which is known to be currently impossible for the aimed application (Re numbers too high for DNS Simulation), the idea is to model the small two-phase scales that can be considered as spherical or ellipsoidal. Figure 13 presents the snapshots of the simulated plume at the same times as in Fig. 12, but using the three-field and two-phase approach. The isosurface of the volume fraction of the dispersed field ($\alpha_{cg} = 0.15$) has been superposed in red to identify the areas where the interfaces are located, and where they are modeled.

A first result is hereafter that our coupled hybrid approach is numerically effective. In addition, it can be observed in Fig. 13 that the aimed areas (i.e., the under-resolved interfaces of the two-field and two-phase approach) have been detected and modeled with a dispersed approach in the three-field and two-phase model. More quantitatively results are available in [16] where a reasonable agreement between calculations and experimental data is reached, but the higher averaged void fraction at the center of the plume suggests that additional efforts

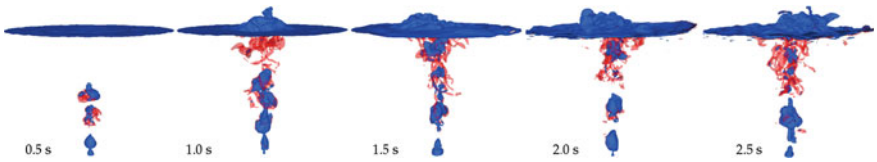

Fig. 13 The picture is a view of the gas plume after 2 s of injection for the case of a three-field and two-phase simulation. The isosurface of the volume fraction of the continuous field ($\alpha_{cg} = 0.5$) is colored in *blue*, and the isosurface of the volume fraction of the dispersed field ($\alpha_{cg} = 0.15$) is in *red*

should be made on the transfer terms that have numerically be set here. In other words, Eqs. (7) and (8) and particularly the two relaxation times $C_{dg\rightarrow cg}$ and $C_{cg\rightarrow dg}$ deal with a computational model, and additional efforts should be provided to describe more accurately the physical phenomena involved.

4 Heat and Mass Transfer

4.1 Physical Model

Two total enthalpy balance equations are solved in supplementary for each field:

$$\begin{aligned}\frac{\partial}{\partial t}\left[\alpha_k\rho_k\left(h_k+\frac{V_k^2}{2}\right)\right]+\nabla\cdot\left(\alpha_k\rho_k\left(h_k+\frac{V_k^2}{2}\right)\underline{V}_k\right)\\ =\alpha_k\frac{\partial p}{\partial t}+\alpha_k\rho_k\underline{g}\cdot\underline{V}_k+\Gamma_k\left(h_{ki}+\frac{V_k^2}{2}\right)\\ +\Pi_k' A_i+q_{wk}'''-\nabla.\left[\alpha_k\left(\underline{q}_k+\underline{q}_k^T\right)\right]\qquad k=l,v\end{aligned}\quad,\tag{9}$$

where h_k is the phase-averaged enthalpy for phase k and h_{ki} is the interfacial-averaged enthalpy. The term $\Pi_k' A_i$ denotes the interfacial transfer term of heat, the quantity A_i being the interfacial area concentration. The term q_{wk}''' denotes the wall-to-fluid heat transfer per unit volume and unit time for each phase. The two terms $\underline{q}_k$ and $\underline{q}_k^T$ denote the molecular and turbulent heat fluxes inside phase k.

The interface sharpening equation given by (5) is generalized by the new formulation (10) in order to ensure the mass conservation in case of heat and mass transfer:

$$\partial_\tau\alpha_2\rho_1\rho_2+\nabla(\alpha_1\alpha_2\rho_1\rho_2\vec{n})=\varepsilon\Delta(\alpha_2\rho_1\rho_2).\tag{10}$$

For the cases we are going to deal with in this section, the interfacial mass transfer rate is defined as

$$\Gamma=\frac{q_2+q_1}{L},\tag{11}$$

where q_1 and q_2 are the heat fluxes coming from the liquid and vapor sides of the interface, respectively, and L is the latent heat. In the NEPTUNE_CFD code, the sum of the heat fluxes is divided by the difference between the vapor and the liquid enthalpy (which is close to the latent heat).

Then, the heat fluxes are defined as

$$q_k = \lambda_k \left(\partial_{xi} T_k\right)\, n_i, \tag{12}$$

where n is the normal vector to the interface pointing from vapor to liquid and λ is the thermal conductivity. In the first approximation, we use the following expression for the heat flux in the stratified cell for the liquid phase (phase 1):

$q_1 = h_1 (T_{sat} - T_1)$, with $h_1 = \lambda_1 / y_1$, where y_1 is the evaluated thanks to the liquid volume fraction in the stratified cell: α_S.

Therefore, we define T_1 and y_1 (replaced by X_1 in the following expression) and T_{sat} by

$$X_1 = \alpha_S X_1^S + (1 - \alpha_S) X_1^1 \text{ and } T_{sat} = \alpha_S T_{sat}^2 + (1 - \alpha_S) T_{sat}^S. \tag{13}$$

The notations and the configuration of the three cells in the "LI3C method" [22] are given in Fig. 14. Then, for the vapor phase (phase 2), the same expressions are used to calculate T_1, y_1, and q_2 with α_S, the volume fraction of vapor in the stratified cell. For T_{sat}, we take also into account its value in the liquid cell:

$$T_{sat} = 0.5(T_{sat}^S + \alpha_S T_{sat}^2 + (1 - \alpha_S) T_{sat}^1). \tag{14}$$

Moreover, in this part, we also deal with the possible presence of vapor in the liquid as a residual phase. In this case, we add an interfacial transfer term to relax the vapor temperature toward the saturation temperature:

$$\Pi' = \alpha_1 \alpha_2 \rho_2 C_{pv} \frac{T_v - T_{sat}}{\tau}. \tag{15}$$

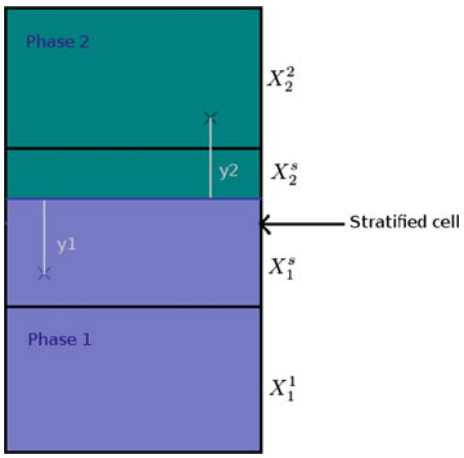

Fig. 14 Diagram of the three cells in the LI3C method and notations for the heat flux

4.2 Validation Case

The Stefan problem deals with a 1D heat and mass transfer between water and steam. Vapor and liquid are contained in a tube with a heated wall [23]. In this case, vapor is superheated and the liquid temperature is equal to the saturation temperature: T_{sat} = 373.15 K. The wall temperature keeps a constant value during the simulation: T_{wall} = 398.15 K. As a consequence, there is a temperature gradient in the vapor phase (Fig. 16). The pressure of the system was equal to 1013 hPa, the surface tension to 0.059 N/m, and the latent heat to 2.26 10^6 J/kg. For the initialization of the volume fractions, we defined four cells, which contain only vapor, a cell with 50 % of each phase and the rest with liquid only. We also initialized the vapor temperature with an affine function. Therefore, we see in Fig. 15 that the results are in good agreement with the analytical expression of the interface position for all the mesh refinements. For all these simulations, the average mass balance error was equal to 10^{-5} % and the average energy balance error to 10^{-7} %.

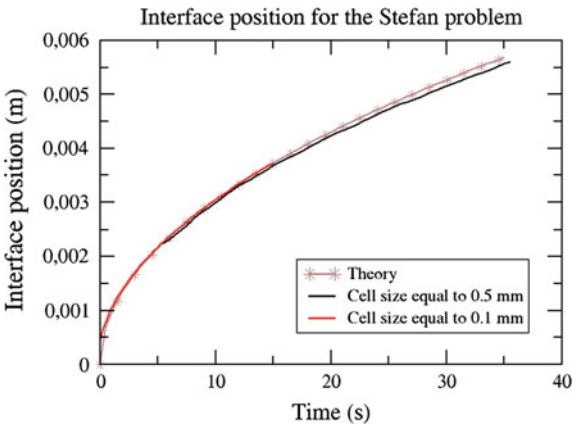

Fig. 15 Stefan case: interface position

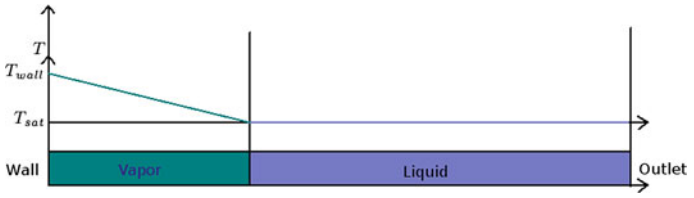

Fig. 16 Conditions of simulation at a given time for the Stefan problem, the liquid boils and the interface moves to the right side due to volume expansion of the liquid–vapor phase change

5 Conclusions

A multifield numerical model, coupling the dispersed two-phase and interface located approach, has been established. Every field is followed with an Eulerian point of view. The dispersed field is modeled through the Euler–Euler two-fluid model, and the interface of the continuous gas field is located with a tracking method, extending a level-set method to the two-fluid Eulerian formalism. The approach has proved to be numerically robust, even used on a nonconforming mesh. A first comparison with experimental observations has been presented and showed a qualitatively good accordance. The quantitative comparison now shows tendencies and points out the effort that has to be made on the modeling of the transfer terms between the two gas fields.

This type of coupled models is of relevant interest for complex and industrial two-phase simulations. The coupling terms presented here should be improved by the further comparison with experimental measurements. In particular, the creation term for the continuous gas field should rely on the dispersed bubble diameter, which is calculated through coalescence and break-up models. This means that a polydispersed approach for the dispersed gas field should be used to improve the physical modeling. Another difficulty is the modeling of the two-phase turbulence of such two-phase structures. The LES modeling of two-phase turbulence terms is still a major issue in the literature [24]. In the present work, the turbulence was not modeled.

In this context, heat and mass transfer are also challenging because of numerical instabilities for large time step.

Acknowledgements The calculations have been performed with NEPTUNE_CFD code which is being developed in the framework of the NEPTUNE project financially supported by EDF (Electricité de France), CEA (Commissariat à l'Energie Atomique et aux Energies Alternatives), IRSN (Institut de Radioprotection et de Sûreté Nucléaire), and AREVA-NP.

References

1. Ishii, M. (1975). *Thermo-fluid dynamic, theory of two-phase*. Paris: Eyrolles press.
2. Unverdi, S. O., & Tryggvason, G. (1992). A front-tracking method for viscous, incompressible, multi-fluid flows. *Journal of Computational Physics, 100*, 25–37.
3. Sussman, M., Smereka, P., & Osher, S. (1994). A level set approach for computing solutions in incompressible two-phase flow. *Journal of Computational Physics, 114*, 146–159.
4. Sussman, M., & Puckett, E. (2000). A coupled level set and volume-of-fluid method for computing 3D ands axisymmetric incompressible two-phase flows. *Journal of Computational Physics, 162*, 301–337.
5. Hirt, C. W., & Nichols, B. D. (1981). Volume of fluid (VOF) method for the dynamics of free boundaries. *Journal of Computational Physics, 39*, 201–225.
6. Hyman, J. M. (1984). Numerical methods for tracking interfaces. *Physica D: Nonlinear Phenomena, 12*, 396–407.

7. Lahey, R. T., & Drew, D. A. (2001). The analysis of two-phase flow and heat transfer using a multidimensional, four field, two-fluid model. *Nuclear Engineering and Design, 204*, 29–44.
8. Bestion, D. Applicability of two-phase CFD to nuclear reactor thermal hydraulics and elaboration of best practice guidelines. *Nuclear Engineering and Design*, 253.
9. Douce, A., Mimouni, S., Guingo, M., Morel, C., Laviéville, J., & Baudry, C. (2010). Validation of NEPTUNE CFD 1.0.8 for adiabatic bubbly flow and boiling flow. CFD4NRS-3, Washington DC, USA.
10. Patankar, S., & Spalding, D. (1972). A calculation procedure for heat, mass and momentum transfer in three-dimensional parabolic flows. *International Journal of Heat and Mass Transfer, 15*(10), 1787–1806.
11. Mimouni, S., Archambeau, F., Boucker, M., Laviéville, J., & Morel, C. (2010). A second order turbulence model based on a reynolds stress approach for two-phase boiling flow and application to fuel assembly analysis. *Nuclear Engineering and Design, 240*, 2225–2232.
12. Mimouni, S., Laviéville, J., Seiler, N., & Ruyer, P. (2011). Combined evaluation of second order turbulence model and polydispersion model for two-phase boiling flow and application to fuel assembly analysis. *Nuclear Engineering and Design*, *241*(11), 4523–4536.
13. Brackbill, J. U., Kothe, D. B., & Zemach, C. (1992). A continuum method for modeling surface tension. *Journal of Computational Physics, 100*, 335–354.
14. Olsson, E., & Kreiss, G. (2005). A conservative level set method for two phase flow. *Journal of Computational Physics, 210*, 225–246.
15. Denèfle, R., Mimouni, S., Caltagirone, J.-P., & Vincent, S. (2013). Hybrid multifield method applied to bubble rising and coalescence. International Journal of Computational Methods and Experimental Measurements (accepted in 2013).
16. Denèfle, R., Mimouni, S., Caltagirone, J.-P., & Vincent, S. (2013) Multifield hybrid approach for two-phase flow modeling—Part 1: Adiabatic flow, Submitted to Computers and Fluids in December 2013.
17. Bhaga, D., & Weber, M. E. (1981). Bubbles in viscous liquids: shape, wakes and velocities. *Journal of Fluid Mechanics, 105*, 61–85.
18. Brereton, G., & Korotney, D. (1991). Coaxial and oblique coalescence of two rising bubbles. In *Proceedings of AMD-Vol0 119: The ASME Applied Mechanics Conference*, Columbus, Ohio, USA.
19. Štrubelj, L. (2009). Numerical simulations of stratified two-phase flows with two-fluid model and interface sharpening. PhD Thesis at University of Ljublana directed by Mavkov B. and Tiselj I.
20. Pigny, S. (2011). Intermediate scales between simulation and modeling of two-phase flows. *Nuclear Engineering and Design, 241*(2011), 874–887.
21. Castillejos, A. H. (1986). A study of the fluid-dynamic characteristics of turbulent gas-liquid bubble plumes, PhD Thesis, University of British Columbia.
22. Welch, S. W. J., & Wilson, J. A. (2000). Volume of fluid based method for fluid flows with phase change. *Journal of Computational Physics, 160*, 662–682.
23. Coste, P. (2012). A large interface model for two-phase CFD. *Nuclear Engineering and Design*. doi:10.1016/j.nucengdes.2012.10.008.
24. Larocque, J., Vincent, S., Lacanette, D., Lubin, P., & Caltagirone, J. P. (2010). Parametric study of LES subgrid terms in a turbulent phase separation flow. *International Journal of Heat and Fluid Flow, 31*(2010), 536–544.

Large Eddy Simulation of Cavitating Throttle Flow

Wilfried Edelbauer, Jure Strucl and Alexander Morozov

Nomenclature

a, C_1, C_2	Closure coefficient in turbulence model (-)
C_L, C_{T*}, $C_{\varepsilon 1}$	Closure coefficient in turbulence model (-)
$C_{\varepsilon 2}$, C_η, C_μ	Closure coefficient in turbulence model (-)
D	Interphase exchange term of ε-equ. (W/m^{3}s)
E	Magnitude of velocity gradient tensor (s^{-1})
f	Elliptic relaxation term (s^{-1})
g	Gravitational acceleration (m/s^2)
k	Turbulence kinetic energy (m^2/s^2)
K	Inter-phase exchange term of k-equ. (W/m^3)
L	Length scale (m)
M	Inter-phase exchange term of U-equ. (N/m^3)
n_{ph}	Number of phases (-)
N'''	Number density of bubbles (1/m^3)
p	Pressure (Pa)
P	Shear production term (m^2/s^3)
Q	Second invariant of velocity gradient tensor (s^{-1})
S	Velocity strain tensor (s^{-1})
t	Time (s)
T^*	Turbulent time scale (s)
U	Velocity (m/s)
v^2	Reynolds stress normal to wall (m^2/s^2)
V	Volume (m^3)

W. Edelbauer (✉) · A. Morozov
AVL List GmbH, Hans List Platz 1, 8020 Graz, Austria
e-mail: wilfried.edelbauer@avl.com

A. Morozov
e-mail: alexander.morozov@avl.com

J. Strucl
AVL-AST d.o.o, Ulica kneza Koclja 22, 2000 Maribor, Slovenia
e-mail: jure.strucl@avl.com

P. Gourbesville et al. (eds.), *Advances in Hydroinformatics*,
Springer Water, DOI 10.1007/978-981-287-615-7_34

W	Vorticity tensor (s^{-1})
x, y, z	Space coordinate directions (m)
$\bar{z}$	Z-coordinate divided by channel depth (-)
α	Volume fraction (-)
Γ	Mass transfer rate (kg/m^3s)
ε	Turbulence dissipation rate (m^2/s^3)
μ	Dynamic viscosity (Ns/m^2)
ν	Kinematic viscosity (m^2/s)
ρ	Density (kg/m^3)
$\sigma_k, \sigma_\varepsilon, \sigma_\zeta$	Closure coefficient in turbulence model (-)

1 Introduction

There are various approaches for the numerical simulation of cavitating two-phase flow, i.e., injector flows. They can be roughly subdivided by the treatment of the conservation equations, Euler or Lagrangian, by the cavitation model, and by the method for the turbulence closure. The Euler-Eulerian multi-fluid approach is widely used for cavitating injector flows, as discussed by Alajbegovic et al. [1] and several others. There the liquid and gaseous phase(s) are treated as inter-penetrating continua, and for every phase the complete set of transport equation is solved. This is different to the Euler-Lagrangian approach which applies the Eulerian approach for the continuous phase, and the Lagrangian treatment for the dispersed phase. For injector flows, the Euler-Lagrangian approach has benefits in the description of single-bubble effects, i.e., bubble oscillations and implosions, but suffers from attenuated validity in regions with dominating vapor phase. Explicit interface tracking with volume-of-fluid (VOF) or similar methods for surface capturing are nowadays applied for detailed investigations of single-bubble flows; for most of the industrial applications the computational effort is too high.

Many cavitation models are based on the Rayleigh-Plesset equation, and either solve it fully for individual parcels, as discussed by Giannadakis et al. [2], or they neglect viscous and surface tension term to obtain correlation for the mass transfer and solve it within the Euler-Eulerian framework, as discussed by Alajbegovic et al. [3]. Other cavitation models are based on the thermodynamic equilibrium assumption and focus on compressibility effects, as presented by Schmidt et al. [4].

For the turbulence treatment, Reynolds averaged Navier-Stokes equations in combination with different kinds of eddy viscosity models for the turbulence closure is state of the art for many years. The most famous model is the two-equation k-ε model of Launder and Spalding [5]. In the meantime, there exist many improvements of this model. Most of them focus on better near wall treatment, extension of the Reynolds number range, and the predictability of separation effects. For multi-fluid flows, the turbulent transport equations are solved either for

every phase separately, as mixture, or only for the dominating continuous phase. In recent years, Large Eddy Simulation has become a very popular method for simulating turbulent flows. This method is certainly superior to RANS methods in strongly separated flows, since it simulates directly the large turbulent structures and models only the influence of the sub-grid scales on the resolved ones. Through low-pass filtering of the Navier-Stokes equations, the small scales are eliminated and a turbulence closure is necessary. In many cases, this is done by the eddy viscosity assumption, as proposed by the well-known Smagorinsky model [6].

The aim of the present study is to perform unsteady RANS as well as LES simulations of a cavitating throttle flow within the Euler-Eulerian multi-fluid approach, and to compare the vapor distributions and velocity profiles with measurements performed in the previous publication presented by Morozov and Iben [7]. These experiments analyze the cavitating flow in micro-geometries which are close to real-life Diesel injection systems. Although a rectangular channel is used, and the pressure is lower than in a state-of-the-art common rail system, the optical measurement technique provides an understanding of the cavitation inception, and clearly shows shear flow cavitation effects in combination with laminar separation.

The paper is organized as follows. The second section discusses the modeling approach, containing a brief summary of the Euler-Eulerian multi-fluid model, the cavitation model, and the turbulence modeling. The third section deals with the experimental set-up, and the fourth section discusses the numerical set-up including geometry, solution procedure, and shows the comparison between simulations and experiments.

2 Theoretical Background

2.1 Multi-Fluid Model

The Euler-Eulerian multi-fluid approach has been applied for the throttle flow simulations in the present study. Based on the work of Drew and Passman [8], the complete set of conservation equations is solved for an arbitrary number of inter-penetrating phases, n_{ph}. The governing equations are obtained from an ensemble-averaging procedure of the conservation equations. Each phase is characterized by its volume fraction α. The governing equation for conservation of mass is described by the equation

$$\frac{\partial \alpha_k \rho_k}{\partial t} + \frac{\partial}{\partial x_j}\left(\alpha_k \rho_k U_{k,j}\right) = \sum_{l=1, l\neq k}^{n_{ph}} \Gamma_{kl}, \tag{1}$$

where ρ_k is the density, U_k is the velocity vector, and Γ_{kl} represents the mass transfer rate per unit volume between phases k and l. Here and in all the other

transport equations the Einstein summation convention is implied. The *i*th component of the momentum conservation equation for phase k is given as

$$\frac{\partial \alpha_k \rho_k U_{k,i}}{\partial t} + \frac{\partial}{\partial x_j}\left(\alpha_k \rho_k U_{k,j} U_{k,i}\right) = -\alpha_k \frac{\partial p}{\partial x_i} + \frac{\partial}{\partial x_j}\left(\alpha_k \rho_k \left(\tau_{k,ij} + \tau^t_{k,ij}\right)\right) + \alpha_k \rho_k g_i + \sum_{l=1, l\neq k}^{n_{ph}} \mathrm{M}_{kl,i} + \sum_{l=1, l\neq k}^{n_{ph}} U_{kl,i} \Gamma_{kl}. \tag{2}$$

$\tau_{k,ij}$ denotes shear stress tensor (divided by the density), g is the gravitational acceleration vector, and the term M_{kl} represents the interfacial forces between the phases, such as drag and turbulent dispersion. Uniform pressure, $p_k = p$, for all phases is assumed, and the sum of the volume fractions of all phases must equal one to fulfill the compatibility condition.

2.2 Cavitation and Erosion Model

The CFD code AVL FIRE® offers several cavitation models, linear or non-linear, and also poly-dispersed cavitation model. All models are based on the simplified Rayleigh-Plesset equation for single-bubble growth to obtain a correlation for the mass transfer and solve it within the Euler-Eulerian framework, as discussed by Alajbegovic et al. [3]. The viscous and surface tension terms of the Rayleigh-Plesset equation are neglected. The linear cavitation model assumes balance between pressure term and quadratic term only, while the non-linear cavitation model additionally considers the bubble radius acceleration term. The poly-dispersed cavitation model solves additional transport equations for bubble number density and interfacial area and takes into account bubble break-up and collisions. Details about this model are discussed by Wang et al. [9].

The focus of the current study is on the turbulence model. Thus, the most simple cavitation model, the linear cavitation model, was applied for the simulations. There the mass transfer between dispersed vapor phase d and continuous liquid phase c is described by the equation

$$\Gamma_{dc} = 3.95 \frac{\Delta p}{|\Delta p|} \frac{\rho_d}{\sqrt{\rho_c}} N'''^{\frac{1}{3}} \alpha_d^{\frac{2}{3}} |\Delta p|^{\frac{1}{2}} = -\Gamma_{cd}, \tag{3}$$

where N''' is the bubble number density, and Δp denotes the difference between static and saturation pressure.

The erosion model used in the present analysis follows the work of Berchiche et al. [10], and Franc and Riondet [11]. The driving force for the erosion mechanism is the bubble collapse on the material surface. If the collapses occur repeatedly at

the same location, the material yields after a certain time, and material removal is started. After removal of the hardened layer, the erosion process accelerates until steady material removal rate is reached. The applied model estimates the so-called Mean Depth of Penetration Rate (*MDPR*) under steady material removal conditions. Thus, the *MDPR* represents the rate of the solid material removal in meter per second. The essential point of the cavitation erosion model is to quantify the flow aggressiveness, or the mean amplitude of impact loads. Regions of collapsing bubbles are identified by negative mass transfer term, $\Gamma_{dc} < 0$. If these regions are located near the wall surface within a critical distance, the cavitation erosion model is evaluated. Details about the model and implementation can be found in the publication of Greif and Wang [12].

2.3 Turbulence Model

The nature of the flow through fuel injectors is turbulent. The Reynolds numbers of the experiments are in the range of 20,000 and above. The aim of this study is to compare different turbulence models in cavitating throttle flows with respect to velocity fields and vapor distribution. Therefore, simulations with the four-equation k-ε-ζ-f model, which is an unsteady RANS model, are compared with Large Eddy Simulations.

2.3.1 RANS Model

Following the same ensemble-averaging procedure as that used for deriving the multi-fluid transport equations, one obtains turbulent transport equations for each phase. The four-equation k-ε-ζ-f model proposed by Hanjalic et al. [13] and enhanced by Basara [14] is particularly suitable for predicting near wall turbulence. The authors propose a version of the eddy viscosity model based on Durbin's elliptic relaxation concept [15]. The aim is to improve numerical stability of the original $\bar{v}^2 - f$ model by solving a transport equation for the velocity scale ratio $\zeta = \bar{v}^2/k$ instead of the wall normal velocity scale $\bar{v}^2$. This model has been adopted for multi-fluid applications, and it is fully available in the CFD code FIRE®. The k-ε-ζ-f model solves transport equations for every phase for the turbulence kinetic energy k, the turbulence dissipation rate ε, and the velocity scale ζ which determines the ratio of wall normal velocity scale and k. Additionally, elliptic relaxation equations for f, which is a parameter closely related to the pressure-strain redistribution term, are solved for each phase k. The full model is given below:

The eddy viscosity is obtained from the equation

$$\mu_k^t = C_\mu \zeta_k k_k T_k^*, \tag{4}$$

where T_k^* is the turbulent time scale. The transport equations for the turbulent kinetic energy k_k and the turbulence dissipation rate ε_k of phase k yield

$$\frac{\partial \alpha_k \rho_k k_k}{\partial t} + \frac{\partial}{\partial x_j}\left(\alpha_k \rho_k U_{k,j} k_k\right) = \frac{\partial}{\partial x_j}\left(\alpha_k\left(\mu_k + \frac{\mu_k^t}{\sigma_k}\right)\frac{\partial k_k}{\partial x_j}\right) + \alpha_k P_k - \alpha_k \rho_k \varepsilon_k + \sum_{l=1,l\neq k}^{n_{ph}} \mathrm{K}_{kl} + \sum_{l=1,l\neq k}^{n_{ph}} k_{kl}\Gamma_{kl} \tag{5}$$

$$\frac{\partial \alpha_k \rho_k \varepsilon_k}{\partial t} + \frac{\partial}{\partial x_j}\left(\alpha_k \rho_k U_{k,j} \varepsilon_k\right) = \frac{\partial}{\partial x_j}\left(\alpha_k\left(\mu_k + \frac{\mu_k^t}{\sigma_\varepsilon}\right)\frac{\partial \varepsilon_k}{\partial x_j}\right) + \alpha_k \rho_k \frac{C_{\varepsilon 1}^* P_k - C_{\varepsilon 2}\varepsilon_k}{T_k^*} + \sum_{l=1,l\neq k}^{n_{ph}} \mathrm{D}_{kl} + \sum_{l=1,l\neq k}^{n_{ph}} \varepsilon_{kl}\Gamma_{kl}. \tag{6}$$

The production term due to shear is given by $P_k = \tau_{k,ij}^t \partial U_{k,i}/\partial x_j$. The terms K_{kl} and D_{kl} represent the exchange terms for turbulence between phases k and l. According to the closure assumptions for multiphase turbulence of Lee et al. [16], it is assumed that the turbulence level of the dispersed phase is equal to the continuous phase, and the interaction between these phases is neglected. In the equations for k_k and ε_k, the differences to the standard k-ε model of Launder and Spalding [5] are the limitation of the time scales T_k, the omitted compressible correction term, and adapted closure coefficients. The transport equations for the velocity scale ratio are described by the equation

$$\frac{\partial \alpha_k \rho_k \zeta_k}{\partial t} + \frac{\partial}{\partial x_j}\left(\alpha_k \rho_k U_{k,j} \zeta_k\right) = \frac{\partial}{\partial x_j}\left(\alpha_k\left(\mu_k + \frac{\mu_k^t}{\sigma_\zeta}\right)\frac{\partial \zeta_k}{\partial x_j}\right) + \alpha_k \rho_k f_k - \alpha_k \rho_k \frac{\zeta_k}{k_k} P_k + \sum_{l=1,l\neq k}^{n_{ph}} \zeta_{kl}\Gamma_{kl}, \tag{7}$$

and the elliptic relaxation equation for f_k yields

$$f_k - L_k^2 \frac{\partial^2 f_k}{\partial x_j \partial x_j} = \left(C_1 + C_2 \frac{P_k}{\zeta_k}\right)\frac{\frac{2}{3} - \zeta_k}{T_k}. \tag{8}$$

The turbulent time and length scales, T_k^* and L_k, are given by

$$T_k^* = \max\left(\min\left(\frac{k_k}{\varepsilon_k}, \frac{a}{\sqrt{6} C_\mu \zeta_k \sqrt{S_{ij} S_{ij}}}\right), C_{T^*}\sqrt{\frac{\nu_k}{\varepsilon_k}}\right) \tag{9}$$

Table 1 Closure coefficients of the four-equation *k-ε-ζ-f* model

$C_\mu = 0.22$	$\sigma_k = 1.0$	$\sigma_\varepsilon = 1.3$	$C_{\varepsilon 1} = 1.4$	$C_{\varepsilon 2} = 1.9$	$\sigma_\zeta = 1.2$
$C_1 = 0.4$	$C_2 = 0.65$	$a = 0.6$	$C_{T^*} = 6.0$	$C_L = 0.36$	$C_\eta = 85.0$

$$L_k = C_L \cdot \max\left(\min\left(\frac{k_k^{3/2}}{\varepsilon_k}, \frac{\sqrt{k_k}}{\sqrt{6}C_\mu \zeta_k \sqrt{S_{ij}S_{ij}}}\right), C_\eta \left(\frac{v_k^3}{\varepsilon_k}\right)^{\frac{1}{4}}\right). \tag{10}$$

The constant $C_{\varepsilon 1}^*$ in the turbulence dissipation equation is damped close to the wall according to

$$C_{\varepsilon 1}^* = C_{\varepsilon 1}\left(1 + 0.045\sqrt{1/\zeta}\right). \tag{11}$$

The closure coefficients of all equations in the *k-ε-ζ-f* model are summarized in Table 1.

2.3.2 LES Model

The idea of the current study is to apply the governing LES equations for every phase of the Euler-Eulerian transport equations separately. This means that the turbulence of every phase is independent from the other phases, the coupling in between, and therefore the effect on turbulence takes place through the interfacial mass and momentum exchange terms. This is different to other approaches where the LES governing equations are either taken into account only for the dominating liquid phase, as applied by Niĉeno et al. [17], or where only one mixture velocity field for all phases is calculated. The benefit of the applied approach is that all phases, liquid and vapor, have same relevance, and the turbulent structures are well represented in zones where one phase dominates. In zones of coexisting phases, the effect of turbulence is weighted by the phase volume fraction.

Alajbegovic [18] has shown that sub-grid scales (SGS) filtered balance equations of mass and momentum have the same form as those obtained from the ensemble-averaging. Thus, the SGS filtered momentum balance equation based on Eq. (2), and applied for incompressible flows, can be written as

$$\frac{\partial \alpha_k \bar{U}_{k,i}}{\partial t} + \frac{\partial}{\partial x_j}\left(\alpha_k \bar{U}_{k,j}\bar{U}_{k,i}\right) = -\frac{\alpha_k}{\rho_k}\frac{\partial \bar{p}}{\partial x_i} + \frac{\partial}{\partial x_j}\left(\alpha_k\left(\nu_k \frac{\partial \bar{U}_{k,i}}{\partial x_j} \underbrace{-\left(\overline{U_{k,i}U_{k,j}} - \bar{U}_{k,i}\bar{U}_{k,j}\right)}_{\tau^r_{k,ij}}\right)\right) + \alpha_k g_i + \frac{1}{\rho_k}\sum_{l=1, l\neq k}^{n_{ph}} \left(\mathrm{M}_{kl,i} + \bar{U}_{kl,i}\Gamma_{kl}\right). \tag{12}$$

The overbar indicates filtered properties, and the term $\tau^r_{k,ij}$ denotes the residual or SGS stress tensor which is often modeled by the Smagorinsky model [6]. This is an eddy viscosity model, and for phase k the relation between SGS stress tensor and the filtered strain rate tensor $\bar{S}_{k,ij}$ can be written as

$$\tau^r_{k,ij} - \frac{1}{3}\tau_{k,ii}\delta_{ij} = \nu_{k,T}\underbrace{\left(\frac{\partial \bar{U}_{k,i}}{\partial x_j} + \frac{\partial \bar{U}_{k,j}}{\partial x_i}\right)}_{2\bar{S}_{k,ij}} = 2\nu_{k,T}\bar{S}_{k,ij}, \tag{13}$$

where $\nu_{k,T}$ denotes the eddy viscosity. In the Smagorinksy model, $\nu_{k,T}$ is modeled by $\nu_{k,T} = (C_s\Delta)^2|\bar{S}_k|$, where C_s is the Smagorinsky coefficient depending on the flow regime, Δ is the length scale depending on the cell volume, $\Delta = V^{1/3}$, and the resolved strain rate tensor is $|\bar{S}_k| = \left(2\bar{S}_{k,ij}\bar{S}_{k,ij}\right)^{1/2}$. Alternatively to the Smagorinsky model, the Coherent Structure Model (CSM) proposed by Kobayashi [19, 20] uses a local coefficient C_{CSM} for the calculation of the eddy viscosity, as described by $\nu_{k,T} = C_{CSM}\Delta^2|\bar{S}_k|$. There the eddy viscosity is modeled by a coherent structure function F_{CS} with a fixed model parameter. F_{CS} is defined as the second invariant Q_k normalized by the magnitude of the velocity gradient tensor E_k, $F_{CS} = Q_k/E_k$, and it plays a role of wall damping. Q_k and E_k are defined by the equations

$$\begin{aligned} Q_k &= \frac{1}{2}\left(\bar{W}_{k,ij}\bar{W}_{k,ij} - \bar{S}_{k,ij}\bar{S}_{k,ij}\right) = \frac{1}{2}\frac{\partial \bar{U}_{k,j}}{\partial x_i}\frac{\partial \bar{U}_{k,i}}{\partial x_j} \\ E_k &= \frac{1}{2}\left(\bar{W}_{k,ij}\bar{W}_{k,ij} + \bar{S}_{k,ij}\bar{S}_{k,ij}\right) = \frac{1}{2}\left(\frac{\partial \bar{U}_{k,j}}{\partial x_i}\right)^2 \\ \bar{W}_k &= \frac{\partial \bar{U}_{k,i}}{\partial x_j} - \frac{\partial \bar{U}_{k,j}}{\partial x_i}, \end{aligned} \tag{14}$$

where $\bar{W}_{k,ij}$ is the grid scale vorticity tensor. C_{CSM} is then calculated by the equation

$$C_{CSM} = \frac{1}{22}|F_{CS}|^{3/2}F_\Omega, \tag{15}$$

where $F_\Omega = 1 - F_{CS}$ is the energy decay suppression function. Since $\bar{S}_{k,ij}\bar{S}_{k,ij}$ and $\bar{W}_{k,ij}\bar{W}_{k,ij}$ are always positive, F_{CS} and F_Ω have definite upper and lower limits of $-1 \le F_{CS} \le 1$ and $0 \le F_\Omega \le 2$, respectively. Consequently, C_{CSM} is always positive, and its range is narrow as described by

$$0 \le C_{CSM} \le 0.05 \quad \text{and} \quad 0 \le C_s = \sqrt{C_{CSM}} \le 0.22. \tag{16}$$

The strong advantages of the CSM model are that no damping function near the wall and no additional transport equations are needed; it is applicable for laminar flows, and the model implementation uses no time-averaged values which make it easily applicable for fully transient flow problems.

3 Experimental Facilities and Optical Measurement Technique

The experiments used for this study have been already published in the previous publication of Morozov and Iben [7]. A brief summary of the experimental facility and the optical measurements techniques is given here. Details about continuative work are described by Iben et al. [21].

A complete hydraulic system consisting of a fluid tank, a high pressure pump, a metal throttle, and a cooling system for fluid was installed. The metal throttle is sandwiched between two sapphire glass windows. The optical access allows visualization of the fluid flow with high pressure differences up to 1000 bar. The tested geometry, a throttle with a sharp inlet called I-channel, is included in a steel plate with a thickness of 300 μm. The test facility, the geometrical dimensions of the throttle, and the location of the measuring planes are illustrated in Fig. 1. The flow enters and leaves the domain perpendicular to the steel plate plane with low fluid velocity due to the large entrance and exit diameters. The flow path is marked with a light blue line. The inlet and outlet pressures are measured by Kistler pressure sensors with a sampling rate of 50 kHz. Working fluid is commercially available Diesel fuel. The experimental results were not influenced by small variations of Diesel fuel properties such as component composition, viscosity, and density from one manufacturer to another. Additionally, measurements of pressure and temperature field distributions as well as variations of the channel geometries have been performed, but they are not considered in this study.

The distribution of liquid and vapor regions was determined by using light transmission measurements. The local velocity profiles and local velocity fluctuations were measured through Laser-Induced Fluorescence (LIF). The optical part consisted of the imaging System with ≈10 times optical magnification in combination with digital cameras PCO SensiCam and DiCAM and a set of light sources, i.e., flash lamp, continuous wave He–Ne (633 nm), and pulsed KrF (248 nm) excimer lasers. The system supported an image size 1280 × 1024 pix with resolution up to 0.8 μm/pix and image recording times of 10 ns (KrF-laser and

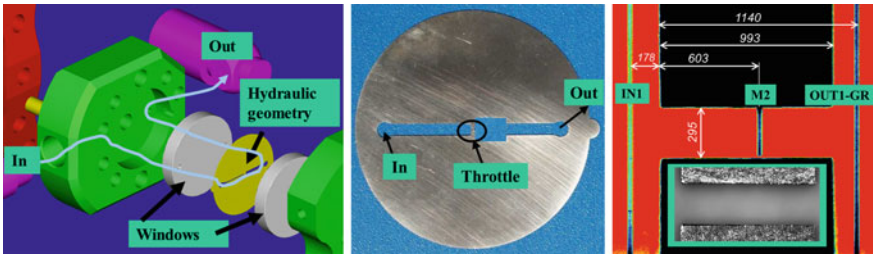

Fig. 1 Test facility and throttle with optical access (*left*), plate with throttle (*middle*), throttle geometry with positions of the three measurement planes IN1, M2, and OUT1-GR (*right*). Geometrical dimension are presented in μm

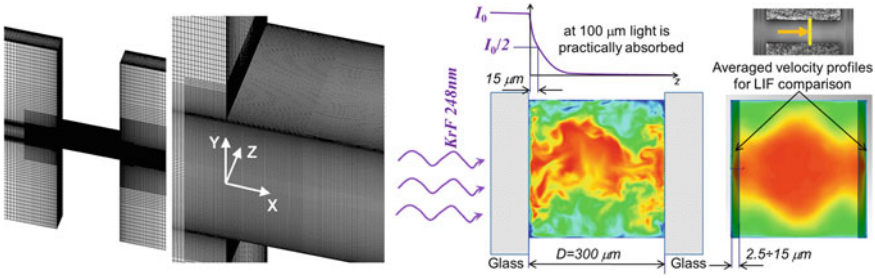

Fig. 2 Computational mesh for LES (*left*); measured region to be compared with averaged velocity profiles (*right*)

DiCAM-camera for velocity measurements) and 100 ns (flash lamp and SensiCam-camera for cavitation and turbulence visualization).

The LIF method for the velocity measurements has an estimated error of 3 % inside the velocity range of 50–500 m/s. It is essential to consider that Diesel fuel has strong absorption at 248 nm, and practically 100 % of light is absorbed within a 100-μm layer of Diesel fuel. Additional measurements of the spatial decays of LIF-signal in the direction perpendicular to the pumping direction were made. These measurements show that LIF-intensity has an exponential decay with intensity maximum at the glass wall and a penetration half width of about 15 μm. This means that the measured velocity profiles show the flow conditions in a relative thin layer close to the sapphire glass wall, as illustrated in Fig. 2 right. In [7], calibration coefficients have been used to realize a proper fit between mass flow data and direct velocity data. In this study, an arithmetic mean value of the simulated velocity profiles in 15-μm layer near the wall is compared with the direct velocity data from the measurements. Thus, no calibration coefficient is applied, and this explains the different scales of the experimental data between our study and the velocity profiles published in [7].

4 Numerical Simulations

4.1 Geometrical Model and Simulation Set-up

Four simulations with changing outlet pressure and different turbulence models have been performed. For simplicity, compressibility and thermal effects are neglected. This means that all simulations are performed incompressible and energy equation is not solved assuming iso-thermal behavior. Fluid properties of Diesel have been applied. For the liquid phase, the density is set to 830 kg/m^3, the saturation pressure is 4500 Pa, and the dynamic viscosity is 0.0021 Pa·s which corresponds to a temperature of approximately 48 °C. The operation conditions are summarized in Table 2. The computational mesh of the LES simulations is

Table 2 Operation conditions of the simulation cases

Case	RANS 300-120	RANS 300-165	LES 300-120	LES 300-165
Turbulence model	RANS k-ε-ζ-f		LES-CSM	
Inlet–Outlet pressure [bar]	300-120	300-165	300-120	300-165
Simulation time step [s]	5×10^{-7}		5×10^{-9}	
Simulation time/averaging time [s]	10^{-3}		10^{-4}	
Total number of cells	1,854,258		17 097 570	
Mesh resolution in channel ($N_x \times N_y \times N_z$)	$73 \times 43 \times 42$		$292 \times 172 \times 168$	

illustrated in two different zoomed views in Fig. 2 left. The channel height L_y is 295 μm, channel depth L_z is 300 μm, and the length L_x is almost 1 mm. Note, the coordinate axis x points into flow direction, y into the channel height direction where the point of origin is in the channel center, and z points in direction perpendicular to the glass wall where the origin is located at the frontal glass wall.

In the channel region, the computational mesh of the LES simulations is four times finer than the mesh of the RANS simulations. Static pressure of 300 bar is applied on the boundary faces on the left-hand side, and total pressure of 120 or 165 bar on the right-hand side. For the LES simulations, the time integration is done with the fully implicit second-order three time level scheme; the spatial discretization is performed with the second-order accurate central differencing scheme for the momentum and pressure equations, and the MINMOD scheme [22] as differencing scheme for the volume fraction equation. A very small blending with the first-order convection scheme in the momentum equation avoids numerical oscillations in the velocity field. The RANS simulations are performed with first-order implicit Euler method for time integration. The pressure correction equation is solved with standard SIMPLE algorithm. The linear cavitation model with fixed nuclei number density is applied for all four cases.

The RANS simulations have been initialized with zero velocity and pure liquid in the whole computational domain. After approximately 0.5 ms, the flow field, and especially the local vapor distribution, has reached a quasi-steady state. Then the simulation is continued to reach at least 1 ms for the evaluation of the results. In order to reduce the computational effort for the LES simulations, they have been started with the final flow field of the RANS simulations, and a few time steps are calculated on the coarse mesh. Then the flow field is mapped onto the finer mesh and the simulation is continued for further 0.1–0.2 ms until the local velocity, pressure, and vapor fluctuations are fully developed. Finally, the averaging period is started for at least 0.1 ms to produce the results for comparison with the RANS simulations and the measurements.

4.2 Simulation Results

This section presents the comparison of the simulated and measured vapor distributions and velocity profiles, and shows the predicted regions of cavitation erosion. The light transmission measurements provide images of the vapor distribution. Since an image is always two-dimensional, but the vapor distribution is highly three-dimensional, it was decided to compare the transmission images with iso-surface plots of the vapor volume faction at $\alpha_d = 0.5$ as shown in Fig. 3. There, single-shot transmission images are compared with instantaneous LES and the RANS simulations, and they show a good agreement. It is interesting to observe that the vapor field from the LES 300-120 simulation is not stable. The more or less homogenous vapor cloud from sheet cavitation formed at the channel entrance periodically alternates with the fully scattered vapor field formed from the growing flow instabilities at the shear layer. The LES 300-165 case is operated with lower pressure difference. There, only small vapor pockets are formed in the vortex centers along the shear layer in which the local pressure is significantly lower than in the surrounding bulk flow. Since the RANS simulation cannot resolve this effect, case RANS 300-165 does not show any vapor.

Figure 4 shows the vapor distribution from the statistical evaluation of 50 transmission images, and the averaged volume fraction in two plane cuts parallel to the glass wall of case LES 300-120, at $z = 50$ µm ($\bar{z} = 0.166$) and at the mid-plane of the channel at $z = 150$ µm ($\bar{z} = 0.5$). Dark blue represents presence of vapor and red

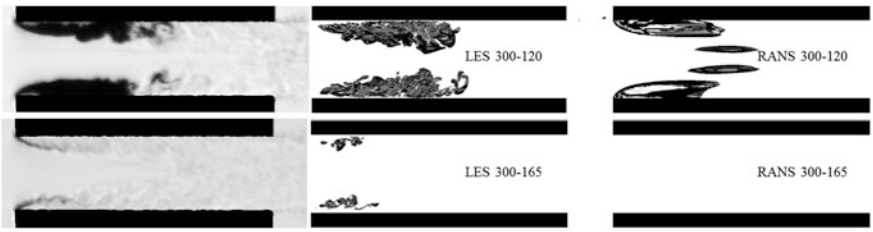

Fig. 3 Vapor distribution of the experiment (*left*), instantaneous iso-surfaces of the vapor volume fraction at $\alpha = 0.5$ of the LES simulations (*middle*), and iso-surfaces of the vapor volume fraction at $\alpha = 0.5$ of the RANS simulations (*right*) for the pressure difference 300-120 bar (*top*) and 300-165 bar (*bottom*)

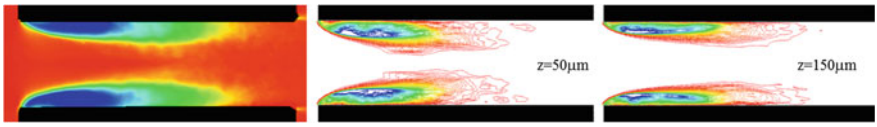

Fig. 4 Statistical evaluation of the experimental vapor distribution from $N = 50$ images (*left*), averaged vapor volume fraction at a distance of $z = 50$ µm from the glass wall (*middle*), and at $z = 150$ µm (*right*) for case LES 300-120

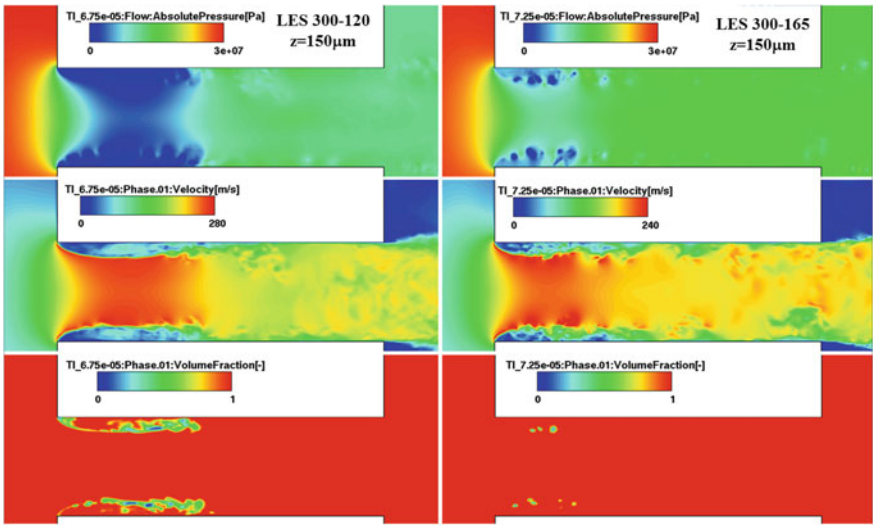

Fig. 5 Instantaneous pressure (*top*), velocity (*middle*), and volume fraction (*bottom*) of cases LES 300-120 (*left*) and LES 300-165 (*right*) in the central cuts at z = 150 µm ($\bar{z}$ = 0.5)

stands for liquid. These images cannot be compared directly, since plane cuts should not be compared with the transmission images. Nevertheless, an overall agreement of the vapor cloud contour is visible, although the experiment shows slightly more vapor than the simulation.

Figure 5 presents flow field snap-shots of the cases LES 300-120 and LES 300-165 in the channel center cut at $\bar{z} = 0.5$. The pressure fluctuations from the flow instabilities in the shear layer are clearly visible. The low pressure in the vortex center is the origin for the vapor pockets. In the plots of the velocity field, one can observe that the longer the cavitation zone, the later the transition from laminar to turbulent flow takes place. Case LES 300-120 has a more distinct vapor cloud, and therefore the bulk flow stays longer laminar. The transition to turbulent flow in case LES 300-165 takes place earlier. The experiments show similar behavior. One can conclude that a distinct cavitation zone damps the flow instabilities in the shear layer, and the bulk flow is longer laminar.

Next the simulated velocity fields are compared with the LIF measurements performed in three planes called IN1, M2, and OUT1-GR. Locations of these planes are sketched in Fig. 1. The simulations have shown that the shape of the velocity profiles strongly depends on the distance to the glass wall boundary. While at the channel center plane, at z = 150 µm, the bulk flow is fully developed; the velocity profiles closer to the wall show different shapes and magnitudes. Exemplarily, Fig. 6 shows the profiles at different z-positions for LES 300-165 in M2 and OUT1-GR, and for RANS 300-165 in M2. Owing to the high light absorption of Diesel fuel, the LIF method provides velocity profiles close to the glass wall, as illustrated in Fig. 2 right. Thus, the measured LIF profiles are compared with the

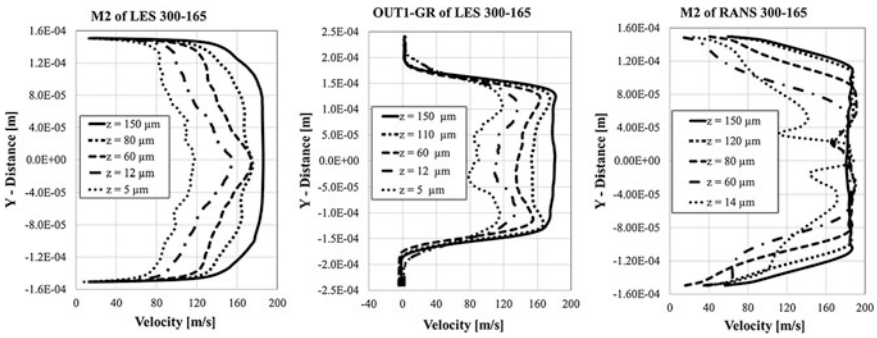

Fig. 6 Simulated velocity profiles at different distances from the sapphire glass wall (z-position) for M2 in case LES 300-165 (*left*), OUT1-GR in LES 300-165 (*middle*), and M2 in RANS 300-165

arithmetic mean of the simulated velocity profiles at different z-positions between approximately 2.5 and 15 µm ($\bar{z} = 0.00833$ and $\bar{z} = 0.05$) where the laser sheet has its highest intensity. For the LES simulations in planes M2 and OUT1-GR, the mean value is composed from thirteen velocity profiles, for the RANS simulations, due to the coarser mesh, only from three profiles.

The full comparison of all velocity profiles in the three measurement planes is shown in Fig. 7. Only x-components of the velocity in main flow direction are measured. Hence, negative velocities may occur. Note, different scales in y-axis are used for the three measurement planes. The LES simulations show very good agreement with the measurements. Especially, the curves in plane M2, shown in Fig. 7 middle, match very well. Only case LES 300-165 in plane OUT1-GR, shown in Fig. 7 top-bottom, overestimates the velocity and shows double peaks. At higher distance from the glass wall this double peaks vanish. The results of the RANS cases are acceptable but do not have the same quality as the LES cases. It is assumed that one reason is the relative coarse grid. As listed in Table 2, the mesh resolution of the RANS simulations is four times coarser (in every coordinate direction) than that of the LES. Especially close to the glass wall where the velocity profiles were measured, the coarser mesh has higher impact on the result quality. In the channel center plane, the difference between LES and RANS is significantly smaller. This can be observed, if one compares the velocity profiles of plane M2 at $\bar{z} = 0.5$ in Fig. 6 left and right, for cases LES 300-165 and RANS 300-165, respectively. Both curves show comparable plateau and shape.

Finally, the erosion rate results of case LES 300-120 are presented in Fig. 8. The cavitation erosion model calculates the distribution of the mean depth of penetration rate MDPR which represents the rate of the solid material removal. Currently, the simulation allows qualitative prediction of the erosion damage. For quantitative prediction, micro-hardness surface measurements to obtain the thickness of the hardened layer and the metallurgical shape factor are mandatory. Since these data were not available for the current study, only qualitative erosion damage is shown.

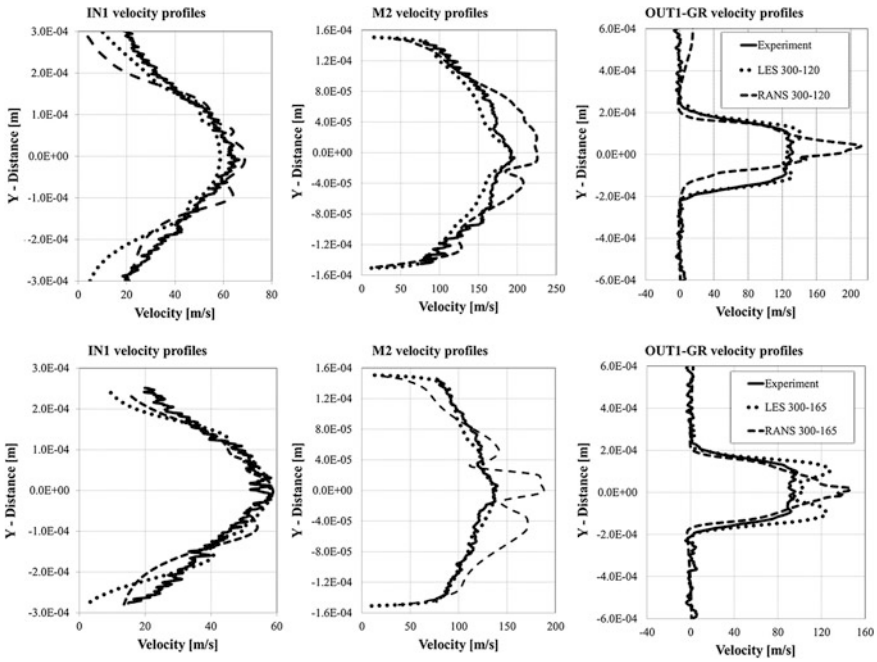

Fig. 7 Velocity profile of LES 300-120 and RANS 300-120 (*top*), and LES 300-165 and RANS 300-165 (*bottom*) compared with the measurements at the measurement planes IN1 (*left*), M2 (*middle*), and OUT1-GR (*right*)

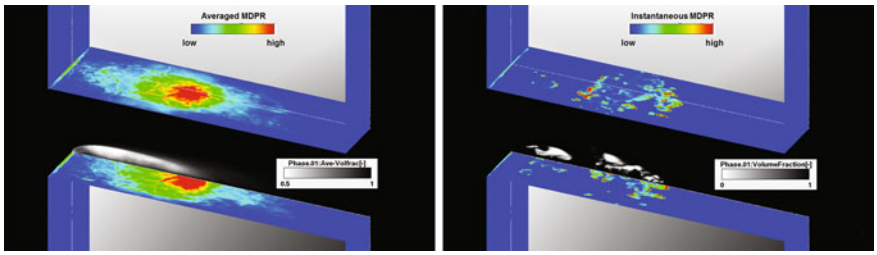

Fig. 8 Qualitative prediction of the mean depth of penetration rate (MDPR) of case LES 300-120. *Left* Averaged MDPR and averaged liquid volume fraction. *Right* instantaneous MDPR and instantaneous liquid volume fraction

The left-hand side of Fig. 8 shows the averaged MDPR distribution on the channel wall, and the averaged vapor distribution in black-white style in the cut at $\bar{z} = 0.583$. The averaged MDPR is obtained through time-averaging of the instantaneous MDPR over the entire simulation time. The highest erosion damage will take place near the tail of the vapor cloud. There the bubble collapse rate has its maximum, and consequently erosion damage will start there. This behavior can be also

observed in Fig. 8 right where the instantaneous MDPR and vapor distribution are shown. If bubble collapse, indicated by negative mass transfer rate Γ_{dc} in Eq. (3), takes place near the wall, the instantaneous MDPR is evaluated. The higher the bubble impact rate, which is related to the mass transfer rate Γ_{dc}, the higher is the MDPR. The other operation point, calculated at case LES 300-165 has much lower vapor, and consequently no remarkable erosion damage is predicted.

5 Summary and Conclusions

LES simulations with the coherent structure model have been performed on cavitating throttle flow for two operation points with different pressure conditions. The simulated vapor distributions and velocity profiles have been compared with measurements and RANS simulations. There is a good agreement between simulation and experiment. Furthermore, the LES gives deeper inside into the flow phenomena. Beside of the transition of the bulk flow from laminar to turbulent, the LES resolves the flow instability in the shear layer at the channel entrance. The consequential pressure fluctuations are the cause of vortex cavitation on small scales which cannot be resolved by RANS simulations in general. Moreover, the simulations have shown that the bulk flow in the throttle channel is inhomogeneous, and that the comparison of simulated velocity profiles or vapor distribution at single cuts with experiments is not reasonable. The applied erosion model allows qualitative prediction of the erosion damage. Simulations with even finer computational meshes in order to resolve more details of the shear layer instability, taking into account liquid compressibility and thermal effects, and qualitative prediction of the erosion damage are part of further research.

References

1. Alajbegovic, A., Grogger, H., & Phillip, H. (1999). Calculation of transient cavitation in nozzle using two-fluid method. *International Conference on Liquid Atomization and Spray Systems*, Indianapolis, USA.
2. Giannadakis, E., Gavaises, M., & Arcoumanis, C. (2008). Modeling of cavitation in diesel injector nozzles. *Journal of Fluid Mechanics, 616*, 153–193.
3. Alajbegovic, A., Greif, D., Basara, B., & Iben, U. (2003). Cavitation calculation with the two-fluid model, *3rd European-Japanese Two-Phase Flow Group Meeting*, Certosa di Pontignano, Italy.
4. Schmidt, S. J., Mihatsch, M., Thalhamer, M., & Adams, N. A. (2011). Assessment of the prediction capability of a thermodynamic cavitation model for the collapse characteristics of a vapor-bubble cloud, *WIMRC 3rd International Cavitation Forum 2011*, UK.
5. Launder, B. E., & Spalding, D. B. (1974). The numerical computation of turbulent flows. *Computer Methods in Applied Mechanics and Engineering, 3*, 269–289.
6. Smagroinsky, J. (1963). General circulation experiments with the primitive equations, 1. *The Basic Experiment. Monthly Weather Review, 91*, 99–164.

7. Morozov, A., & Iben, U. (2008). Experimental analysis and simulation of cavitating throttle flow. *6th International Conference on Heat Transfer, Fluid Mechanics and Thermodynamics HEFAT 200*8, Pretoria, South Africa.
8. Drew, D. A., & Passman, S. L. (1998). *Theory of multicomponent fluids*. New York: Springer.
9. Wang, D.M., Han, J., Greif, D., Zun, I., & Perpar, M. (2005). Interfacial area and number density transport equations for modeling multiphase flows with cavitation. *9th International Symposium on Gas-Liquid Two-Phase Flow ASME FEDSM'05*, Houston, Texas, USA.
10. Berchiche, N., Franc, J. P., & Michel, J. M. (2002). A cavitation erosion model for ductile materials. *Journal of Fluids Engineering, 124*, 601–606.
11. Franc, J. P., & Riondet, M. (2006). Incubation time and cavitation erosion rate of work-hardening materials. *6th International Symposium on Cavitation CAV2006*, Wageningen, The Netherlands.
12. Greif, D., & Wang, D. M. (2007). Modeling of cavitation erosion within diesel injector and its effect on spray propagation. *International Conference Towards Clean Diesel Engines*, Ischia, Italy.
13. Hanjalic, K., Popovac, M., & Hadziabodic, M. (2004). A robust near-wall elliptic-relaxation eddy-viscosity turbulence model for CFD. *International Journal of Heat and Fluid Flow, 25*, 1047–1051.
14. Basara, B. (2006). An eddy viscosity transport model based on elliptic relaxation approach. *AIAA Journal, 44*, 1686–1690.
15. Durbin, P. A. (1991). Near-wall turbulence closure modelling without damping functions. *Theoretical and Computational Fluid Dynamics, 3*, 1–13.
16. Lee, S. J., Lahey, R. T, Jr, & Jones, O. C, Jr. (1989). The prediction of two-phase turbulence and phase distribution phenomena using a k-e model. *Japanese Journal of Multiphase Flow, 3*, 335–368.
17. Niĉeno, B., Boucker, M., & Smith, B. L. (2009). Euler-Euler large eddy simulation of a square cross-sectional bubble column using the Neptune CFD code. *Science and Technology of Nuclear Installations, 2009*, 1–8.
18. Alajbegovic, A. (2001). Large eddy simulation formalism applied to multiphase flows, *ASME 2001 Fluids Engineering Division Summer Meeting*, New Orleans, Louisiana, USA.
19. Kobayashi, H. (2005). The subgrid-scale models based on coherent structures for rotating homogeneous turbulence and turbulent channel flow. *Physics of Fluids, 17*, 045104.
20. Kobayashi, H., Hama, F., & Wu, X. (2008). Application of a local SGS model based on coherent structures to complex geometries. *International Journal of Heat and Fluid Flow, 29*, 640–653.
21. Iben, U., Morozov, A., Winklhofer, E., & Wolf, F. (2011). Laser-pulse interferometry applied to high-pressure fluid flow in micro channels. *Experiments in Fluids, 40*, 597–611.
22. Sweby, P. K. (1984). High Resolution Schemes Using Flux Limiters for Hyperbolic Conservation Laws. *SIAM Journal on Numerical Analysis, 21*, 995–1011.

Rans Computations of a Cavitating Tip Vortex

Jean Decaix, Guillaume Balarac and Cécile Münch

Nomenclature

α_L	Liquid volume fraction
σ_v	Cavitation parameter
C	Chord length (m)
I	Angle of incidence (degree)
K	Turbulent kinetic energy (m^2/s^2)
P	Pressure field (Pa)
p_{vap}	Vaporisation pressure (Pa)
u_i	Velocity field (m/s)
v	Molecular kinematic viscosity (m^2/s)
v_t	Turbulent eddy viscosity (m^2/s)
ω	Turbulence frequency (1/s)
σ_{ij}	Viscous stress tensor ($kg/(m.s^2)$)
τ_{ij}	Reynolds stress tensor ($kg/(m.s^2)$)
τ	Gap width (m)

J. Decaix (✉) · C. Münch
Route Du Rawyl 47, 1950 Sion, Switzerland
e-mail: jean.decaix@hevs.ch

C. Münch
e-mail: cecile.muench@hevs.ch

G. Balarac
LEGI, Université Grenoble Alpes, F-38000 Grenoble, France
e-mail: guillaume.balarac@legi.grenoble-inp.fr

G. Balarac
LEGI, CNRS, F-38000 Grenoble, France

P. Gourbesville et al. (eds.), *Advances in Hydroinformatics*,
Springer Water, DOI 10.1007/978-981-287-615-7_35

1 Introduction

A tip vortex develops when an obstacle of finite span is immersed in a flow. Tip vortices can be encountered both in external and internal flows. External flows can be illustrated by the helicopter rotor blades or by aircraft wings, for which the tip vortex develops at the end of the wing close to the leading edge. For the external tip vortices, the researches focus on the vortex growth and decrease. Internal flows that involve tip vortices are encountered in aircraft engines or hydraulic turbines. In these cases, the influence of the gap between the blade and the stator is of the most importance. A large part of the studies are confined to one-phase flows due to the difficulties to perform measurements and numerical simulations for two-phase flows.

For one-phase flow, several experimental studies investigate the influence of the gap width on the tip vortex behaviour [1, 2]. One of the most documented studies was performed by Devenport [3, 4] in the case of a compressor cascade. Overall, these studies focus on the field downstream the blade by analysing the mean and turbulent flow and the influence of a moving end wall. The turbulent flow is not isotropic since the longitudinal fluctuations dominate. Moreover, the endwall motion does not affect the main features of the tip vortex. An attention is also devoted to the wandering motion of the tip vortex. This phenomenon is not well understood; particularly, it is not clear if the wandering depends on the experimental tunnel [5].

Numerically, the tip vortex was investigated using various models as vortex methods [6], Reynolds Averaged Navier Sokes (RANS) approach coupling with an eddy viscosity model [7] or second moment closure [8], or Large Eddy Simulation [9]. In [10], the author uses the Joseph criterion to determine the regions that can be affected by cavitation. Nevertheless, no cavitation simulations have been attempted.

Since several years, cavitating flows have been experimentally investigated in various configurations. Some studies focus on the tip vortex [11, 12]. The study of Miorini gives information of the velocity field inside the gap due to PIV measurements. However, the measurements are rarely available inside the vortex. Regarding the computations, only few attempts have been performed [13, 14] using RANS or ILES (Implicit LES) modelling. The validations are often restricted to flow vizualisations.

The present work consists in the computation of a truncated Naca 0009 profile mounted in a channel. The computations are carried out with the OpenFOAM solver release 2.1.0. Previous RANS and LES computations without cavitation have been already performed [15]. In the present study, a non-cavitating case is firstly computed and compared with experimental measurements provided by the Laboratory of Hydraulics Machines—Swiss Federal Institute of Technology Lausanne [16, 17]. Then, cavitation is introduced in the simulation. Results are discussed by comparisons between the cavitating and non-cavitating cases.

2 Flow Modelling

The OpenFOAM solver provides various turbulence and cavitation models. For the present computations, the two-phase flow is modelled using a homogeneous relaxation model. Therefore, the two phases are considered to share the same velocity, the same temperature and the same pressure. The mixture density is computed as

$$\rho = \alpha_L \rho_L + (1 - \alpha_L)\rho_V, \tag{1}$$

where α_L is the liquid volume fraction and ρ_L and ρ_V, respectively, are the liquid and the vapour density.

The RANS equations for the mixture read

$$\begin{aligned} \frac{\partial \rho}{\partial t} + \frac{\partial \rho \bar{u}_i}{\partial x_i} &= 0 \\ \frac{\partial \rho \bar{u}_i}{\partial t} + \frac{\partial \rho \overline{u_j u_i}}{\partial x_j} &= -\frac{\partial \bar{p}}{\partial x_i} + \frac{\partial \left(\sigma_{ij} + \tau_{ij}\right)}{\partial x_j} \end{aligned}, \tag{2}$$

where σ_{ij} is the viscous stress and τ_{ij} is the turbulent stress defined as

$$\begin{aligned} \sigma_{ij} &= \rho\nu\left(\frac{\partial \bar{u}_i}{\partial x_j} + \frac{\partial \bar{u}_j}{\partial x_i}\right) \\ \tau_{ij} &= -\rho\overline{u_i' u_j'} = \rho\nu_t\left(\frac{\partial \bar{u}_i}{\partial x_j} + \frac{\partial \bar{u}_j}{\partial x_i}\right) \end{aligned}, \tag{3}$$

where ν is the kinematic molecular viscosity and ν_t is the kinematic turbulent eddy viscosity. The overbar and the prime superscript denote, respectively, the mean and the turbulent parts.

The turbulent eddy viscosity ν_t is computed using the k-ω SST model [18]:

$$\nu_t = \frac{a_1 k}{\max\left(a_1 \omega, SF_2\right)}, \tag{4}$$

where k is the turbulent kinetic energy, ω is the turbulence frequency, S is the invariant measure of the strain rate, F_2 is a blending function and $a_1 = 0.31$.

The liquid volume fraction α_L is computed using a transport equation that reads

$$\frac{\partial \alpha_L}{\partial t} + \bar{u}_j \frac{\partial \alpha_L}{\partial x_j} = m_v + m_c, \tag{5}$$

where m_v and m_c are, respectively, the vaporisation and the condensation source terms. These two terms are estimated using a derivation of the Kunz's model [19]:

$$m_v = \frac{\rho}{\rho_L}\frac{C_v}{t_\infty}\frac{\min\left(p - p_{vap}, 0\right)}{0.5\rho_L U_\infty^2}$$
$$m_c = \frac{\rho}{\rho_L}\frac{C_c}{t_\infty}\alpha_L^2\frac{\max\left(p - p_{vap}, 0\right)}{\max\left(p - p_{vap}, 0.01p_{vap}\right)} \quad (6)$$

where p_{vap} is the vaporisation pressure, U_∞ is a velocity reference, t_∞ is a relaxation time and C_v and C_c are the two empirical parameters specified by the user.

3 Test Case

The test case consists in a Naca 0009 blade with a truncated trailing edge mounted in a channel. The chord blade length c is of 0.1 m, the angle of attack i is of 10° and the gap width τ divided by the chord length is of $\tau/c = 0.1$. The cross section is a square of length 1.5 c. The inlet velocity is set to $U_\infty = 10.2$ m/s.

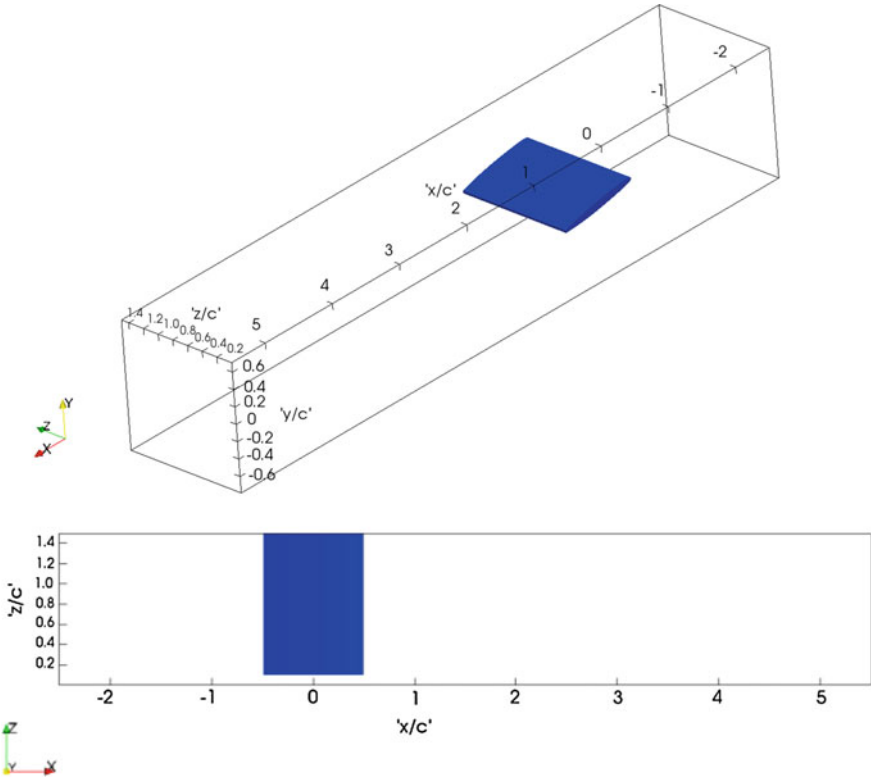

Fig. 1 Computational domain: 3D view (*top*) and top view (*bottom*)

The computational domain extends two chords upstream the leading edge and five chords downstream the trailing edge (Fig. 1). The equations are discretised on a structured mesh containing approximately 2 millions of nodes. The gap region is filled with 30 nodes. The boundary conditions are as follows:

- At the inlet: $u_x = 10.2$ m/s, $u_y = u_z = 0$ m/s.
- At the outlet: a convective condition is applied. Pressure reference is provided at a point located 1.3 c upstream the trailing edge.
- Walls: no slip condition with the use of an extended wall law.

The system of equations is solved using a mix of the SIMPLE and PISO algorithms called PIMPLE algorithm in the OpenFOAM framework. The time step is set to 10^{-5} s.

4 Results

4.1 Computation Without Cavitation

Figure 2 displays the tip vortex identified using the Q-criterion and the three planes where the experimental data are available. To assess the accuracy of the computation, the centre of the vortex is determined using the maximum of the axial vorticity. Table 1 gathers the position of the vortex both for the experiment and the computation. Overall, the discrepancy is lower than 15 %, excepted for the y-position at x/c = 0.15 m. Figure 3 shows the contour of the velocity components. The axial velocity acceleration on the left side of the vortex is captured by the computation even if the magnitude is slightly underestimated. The high magnitude of the crosswise components is also capture. It is noticeable that compared to the

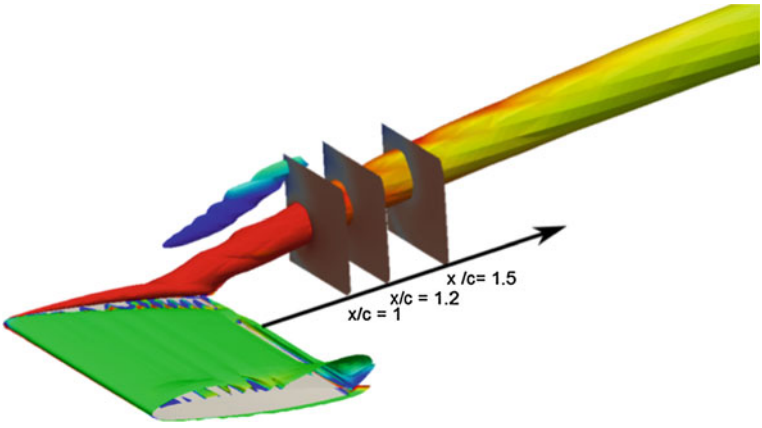

Fig. 2 Tip vortex determined with the Q-criterion and location of the experimental measurement planes

Table 1 Position of the centre of the tip vortex

x/c	y/c (Experiment)	y/c (RANS)	z/c (Experiment)	z/c (RANS)
1	0.14	0.13	0.12	0.1
1.2	0.18	0.18	0.13	0.12
1.5	0.3	0.22	0.16	0.15

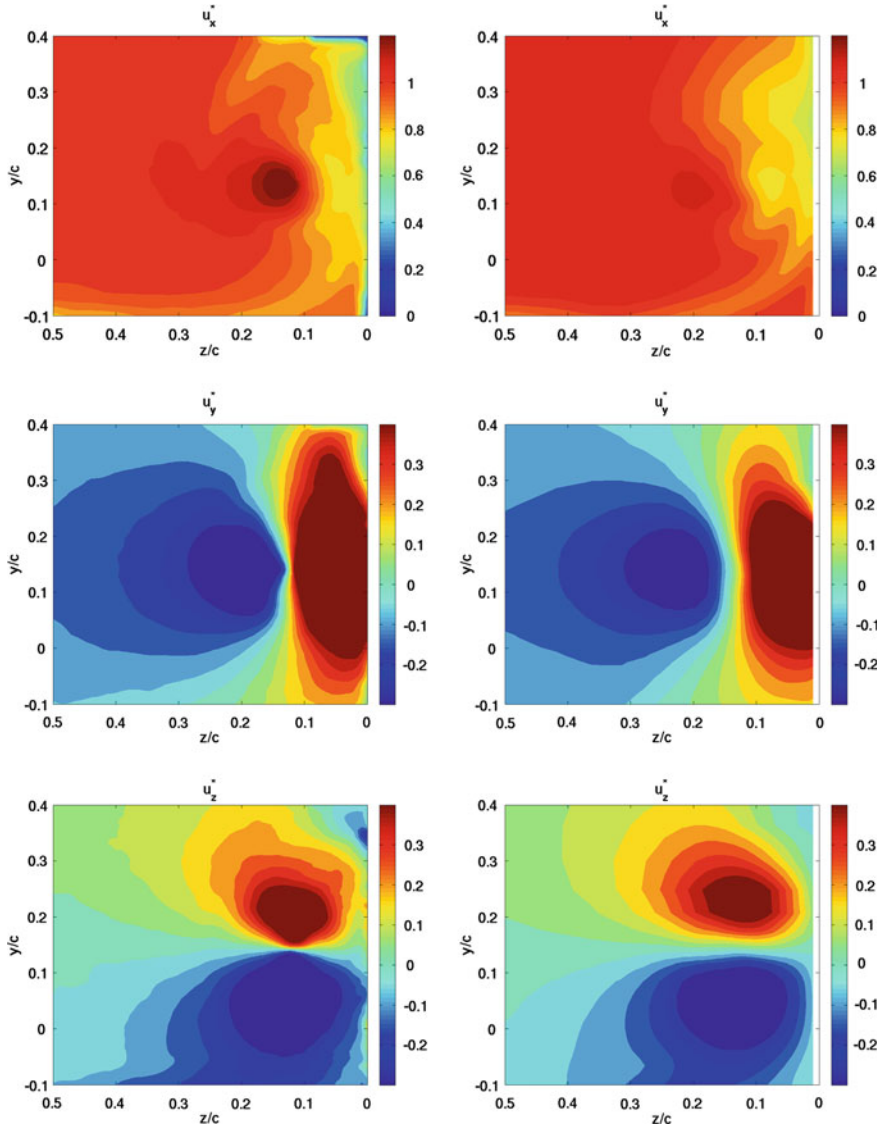

Fig. 3 Contour of the velocity components (downstream view). Experiment (*left*) and RANS (*right*)

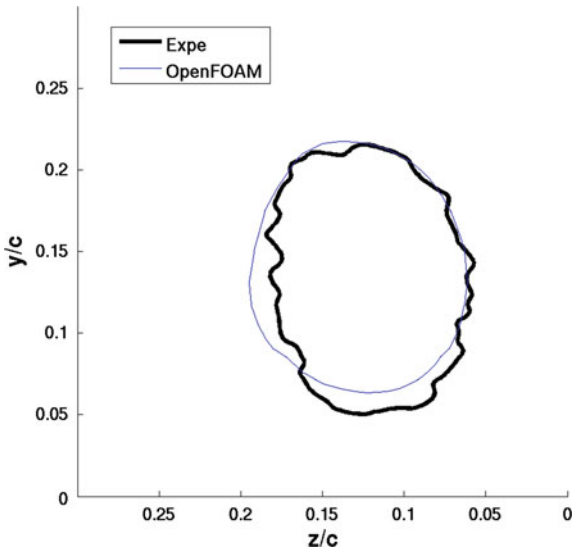

Fig. 4 Iso-line of the non-dimensional axial vorticity ($\Omega_x^* = 10$ at $x/c = 1$)

experiment, the computation diffuses the gradient of the crosswise components in the core of the vortex. Therefore, the value of the axial vorticity in the core of the vortex is underestimated. Nevertheless, focusing on the iso-contour of the axial vorticity near the vortex centre (Fig. 4), the vorticity is well resolved since the iso-line matches. It can be concluded that the RANS computation is able to provide results in accordance with the experiment.

4.2 Computation with Cavitation

For the cavitating computation, the parameters of the cavitation model are set to

- $t_\infty = 0.001$ s.
- $U_\infty = 10$ m/s.
- $p_{vap} = 255000$ Pa.
- $C_c = 500$ and $C_v = 3500$.

The value of p_{vap} can be explained by the fact that the vorticity inside the vortex core is underestimated. Indeed, such an underestimation leads to an overestimation of the pressure inside the vortex. Therefore, the expected low pressure inside the vortex (approximately $p_{vap} = 2330$ Pa at 293 K) cannot be reached. A first computation was performed at the same cavitation parameter $\sigma_v = 2.1$ in which the experiment was not able to provide a cavitating tip vortex. A second computation at $\sigma_v = 1.3$ provides a cavitating tip vortex that can be compared qualitatively with

Fig. 5 Iso-contour of the liquid volume fraction ($\alpha_L = 0.9$)

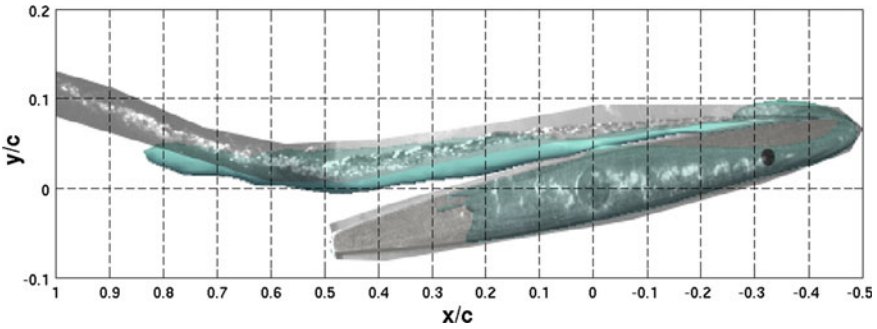

Fig. 6 Superposition of the tip vortex between the experiment (*in front*) and the RANS computation (*behind*)

the experiment. The iso-contour of the liquid volume fraction (Fig. 5) shows that cavitation appears mainly in the core of the vortex and in the gap. No cavitation is observed on the suction side, except a thin layer at the leading edge.

Experimental data are restricted to high-speed viewings. Figure 6 shows a superposition of an experimental view of the tip vortex and the iso-contour of the liquid volume fraction provided by the computation. The trajectory of the cavitating tip vortex is well predicted by the computation. The volume occupied by the tip vortex is slightly larger for the computation than the experiment.

The results are also compared with the computation without cavitation. The mean axial velocity field is strongly affected by the presence of cavitation (Fig. 7). Indeed, for the cavitating computation, the boundary layer separates on the suction side. This is caused by the presence of the thin film of cavitation at the leading edge. Moreover, the trajectory of the tip vortex downstream the trailing edge is modified. Figure 8 represents the tip vortex trajectory projected on an x-y plane and an x-z plane. The y-position is lower with cavitation than without cavitation. The z-position is closer to the sidewall in case of cavitation. These two features can be explained by the separation of the flow on the suction side. The separation decreases the pressure difference between the pressure side and suction side leading to a lower y value and involves a larger wake, which prevents the tip vortex from moving to the centre of the channel.

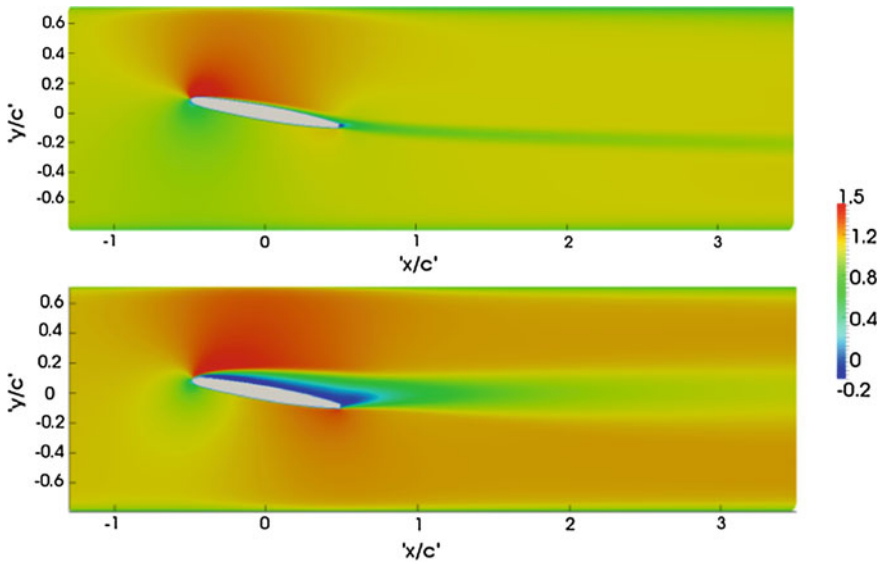

Fig. 7 Mean axial velocity field in the mid-span section. Computation without cavitation (*top*) and with cavitation (*bottom*)

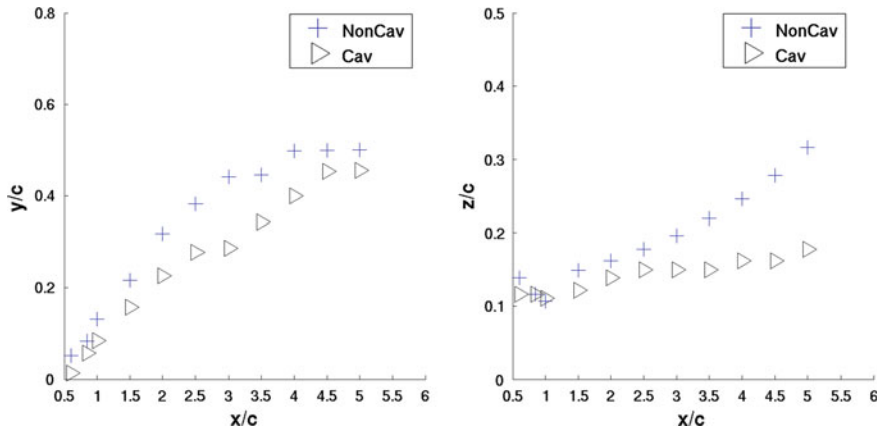

Fig. 8 Position of the centre of the vortex projected in an *x-y* plane (*left*) and *x-z* plane (*right*)

5 Conclusion

Computations of the tip vortex including the gap between the blade and the side wall are performed for cavitating and non-cavitating configurations. The non-cavitating computation is assessed compared with experimental data available downstream the trailing edge. Results based on the vortex trajectory and the

velocity field show few discrepancies between the experiment and the computations. However, an inability of the computation to resolve the vorticity in the core of the vortex is put in evidence even if the vorticity near the vortex core is well captured. This feature prevents the computation from predicting an accurate drop in pressure in the vortex core. Consequently, the computation with cavitation cannot be carried out for the same operating point than the experiment. Adjusting the operating point, a cavitating tip vortex can be obtained with a qualitative agreement with the experiment. The computation put in evidence that the development of cavitation involves a separation of the boundary layer on the suction side. Therefore, the tip vortex trajectory downstream the trailing edge is modified. Particularly, the vortex evolves closer to the sidewall, which can enhance erosion problems.

The results make appear that additional works are needed. For instance, the development of methods can allow resolving the vorticity inside the vortex core and performing cavitating computations at the same operating point than the experiment. Moreover, experimental data inside the cavitating vortex will be welcome in order to assess the relevance of the parameters used for the cavitation model.

Acknowledgments The authors are very grateful to the Competence Center in Energy and Mobility CCEM, Swisselectric Research, and the foundation The Ark through the programme The Ark Energy for their financial support.

References

1. Roussopoulos, K., & Monkewitz, P. A. (2000). Measurements of tip vortex characteristics and the effect of an anti-cavitation lip on a model kaplan turbine blade. *Flow, Turbulence and Combustion, 64*, 119–144.
2. Kang, S., & Hirsch, C. (1993). Experimental study on three dimensional flow within a compressor cascade with tip clearance: Part II: The tip leakage vortex. *ASME Journal of Turbomachinery, 115*, 444–452.
3. Muthanna, C., & Devenport, W. J. (2004). Wake of a compressor cascade with tip gap, part 1: Mean flow and turbulence structure. *AIAA Journal, 42*(11), 2320–2331.
4. Wang, Y., & Devenport, W. J. (2004). Wake of a compressor cascade with tip gap, part 2: Effects of endwall motion. *AIAA Journal, 42*(11), 2332–2340.
5. Devenport, W. J., & Rife, M. C. (1996). The structure and development of a wing-tip vortex. *Journal of Fluid Mechanics, 312*, 67–106.
6. Higashi, S., Yoshida, Y., & Tsujimoto, Y. (2002). Tip leakage vortex cavitation from the tip clearance of a single hydrofoil. *JSME International Journal*, 45(3), 662–671.
7. Kunz, R. F., & Lakshminarayana, B. (1992). Three-dimensional Navier Stokes computation of turbomachinery flows using an explicit numerical procedure and a coupled k-ε turbulence model. *ASME Journal of Turbomachinery, 114*, 627–642.
8. Borello, D., & Hanjalic, K. (2007). Computation of tip-leakage flow in a linear compressor cascade with a second-moment turbulence closure. *International Journal of Heat and Fluid Flow, 28*, 587–601.
9. You, D., Wang, M., Moin, P., & Mittal, R. (2007). Large-eddy simulation analysis of mechanisms for viscous losses in a turbomachinery tip-clearance flow. *Journal of Fluid Mechanics, 586*, 177–204.

10. You, D., Wang, M., Moin, P., & Mittal, R. (2006). Effects of tip-gap size on the tip-leakage flow in a turbomachinery cascade. *Physics* of *Fluids*, *18*(10), 1051.
11. Watanabe, S., Seki, H., Higashi, S., Yokota, K., & Tsujimoto, Y. (2001). Modeling of 2-D leakage jet cavitation as a basic study of tip leakage vortex cavitation. *Journal of Fluids Engineering, 123*, 50–56.
12. Miorini, R. L., & Katz, J. (2012). The internal structure of the tip leakage vortex within the rotor of an axial waterjet pump. *Journal of Turbomachinery*, *134*, 031018.
13. Ugajin, K., & Matsumoto, H. (2009). Numerical analysis of the influence of the tip clearance flows on the unsteady cavitating flows in a three-dimensional inducer. *Journal of Hydrodynamics, 21*(1), 34–40.
14. Cupillard, S. (2013). CFD Simulation of the tip vortex cavitation in a propeller turbine. *5th International Workshop on Cavitation and Dynamic Problems in Hydraulic Machinery*, Lausanne, Switzerland.
15. Decaix, J., Münch, C., & Balarac, G (2013). Numerical computations of a tip vortex including gap with RANS and LES turbulence models. *5th International Workshop on Cavitation and Dynamic Problems in Hydraulic Machinery*, Lausanne, Switzerland.
16. Dreyer, M., & Farhat, M. (2013). Experimental characteristics of tip leakage vortex dynamics. *5th International Workshop on Cavitation and Dynamic Problems in Hydraulic Machinery*, Lausanne, Switzerland.
17. Dreyer, M., Decaix, J., Münch, C., & Farhat, M. (2014). Mind the gap–tip leakage vortex in axial turbines. *27th IARH Symposium on Hydraulic Machinery and Systems*, Montréal, Canada.
18. Menter, F. R. (2009). Review of the shear-stress transport turbulence model experience from an industrial perspective. *International Journal of Computational Fluid Dynamics*, *23*(4), 305–316.
19. Kunz, R. F., Boger, D. A., Stinebring, D. R., Chyczewski, S., Lindau, J. W., Gibeling, H. J., et al. (2000). A preconditioned Navier–Stokes method for two-phase flows with application to cavitation prediction. *Computers and Fluids*, *29*, 849–875.

Numerical Modeling of Aerated Cavitation Using Compressible Homogeneous Equilibrium Model

Petar Tomov, Sofiane Khelladi, Christophe Sarraf and Farid Bakir

1 Introduction

The numerical modeling of cavitation phenomena is a challenging task taking into account the various aspects of physics modeling and the development of robust numerical approach. In the case of the cavitating flows, a high amount of different flow regimes coexist simultaneously. Moreover, coupling aeration in a cavitating flow is a recent technique to control the overall effect of the cavitation over the zone of interest [12, 28]. The aeration process is done by injecting spherical air bubbles into the fluid flow. Such type of flows is defined by large variations of the local Mach number, compressibility, and thermodynamical changes as a result of the phase change phenomena [4]. In addition to this, the turbulence modeling plays an important role in the unsteady flow behavior. [2, 14] studied such kind of a flow behavior in a venturi flow using a barotropic cavitation model. In the present paper, the differential equation system is composed of the Navier-Stokes equations, implemented with the Homogeneous Mixture Model [24]. The model takes into consideration the re-entrant jet at the cavity closure region. The same re-entrant liquid travels upstream on the surface of the venturi and "cuts" the vapor cloud. That latter process is repeated several times which results in a periodic vapor

P. Tomov (✉) · S. Khelladi · C. Sarraf · F. Bakir
DynFluid Laboratory, École Nationale Supérieure des Arts et Métiers,
151, Boulevard de l'Hôpital, 75013 Paris, France
e-mail: Petar.TOMOV@ensam.eu

S. Khelladi
e-mail: Sofiane.KHELLADI@ensam.eu

C. Sarraf
e-mail: Christophe.SARRAF@ensam.eu

F. Bakir
e-mail: Farid.BAKIR@ensam.eu

P. Gourbesville et al. (eds.), *Advances in Hydroinformatics*,
Springer Water, DOI 10.1007/978-981-287-615-7_36

shading. In the present work, an iLES was used to investigate the cavitation process and the interaction with injected air bubbles. The aim of the paper is to not only to present the aerated cavitating behavior of a flow in a venturi duct but also the contact handling algorithm behind the simulations. For the sake of the paper, a 2D venturi type duct has been used with the symmetrical $18^\circ - 8^\circ$ convergent/divergent angles, respectively, on the top and bottom walls.

2 Numerical Code

2.1 Homogeneous Mixture Model

The Navier–Stokes equations are coupled with the Homogeneous Mixture Model which was developed initially by [26]. The latter model accounts for the momentum, mass, and energy equations in the case of the homogeneous mixture flow. The liquid and vapor phases are separately described by equations of state in order to preserve the hyperbolicity of the system. In such a way, the each of the two phases keeps their proper thermodynamic behavior [16]. In the cavitation zone, the conservation equations lose their hyperbolic character and become elliptic. The use of this model suppose the presence of thermodynamic equilibrium at each point of the numerical domain, therefore the vapor phase pressure is considered as constant and is equal to the saturation vapor pressure. The model does not take into account the relative motion between the phases i.e., the slip velocity is equal to zero. The vapor volume fraction is defined by

$$\alpha = \frac{\rho - \rho_{l,sat}(T)}{\rho_{v,sat}(T) - \rho_{l,sat}(T)}, \tag{1}$$

where $\rho_{v,sat}(T), \rho_{l,sat}(T)$ are the saturation densities for the vapor, liquid state, respectively. For the Homogeneous Mixture Model the conservation equations are written as it follows:

Mass conservation:

$$\frac{\partial \rho}{\partial t} + \frac{\partial \rho U_i}{\partial x_i} = 0, \tag{2}$$

where U is the velocity since the slip velocity is zero, and ρ is the density for the mixture defined as it follows:

$$\rho = \sum \rho_K \alpha_K. \tag{3}$$

The Momentum Conservation:

$$\frac{\partial \rho U_i}{\partial t} + \frac{\partial}{\partial x_j}\left(\rho u_i u_j\right) = -\frac{\partial P}{\partial x_i}, \tag{4}$$

where P is the pressure defined in a similar manner as the density for the mixture phase:

$$p = \sum p_K \alpha_K. \tag{5}$$

The Conservation of Energy:

$$\frac{\partial \rho E}{\partial t} + \frac{\partial}{\partial x_i}(\rho E u_i) = -\frac{\partial P U_i}{\partial x_i}. \tag{6}$$

The specific energy of the mixture phase is defined as follows:

$$\rho e = \sum \rho_K \alpha_K e_K. \tag{7}$$

In all the formulas (3)–(7), k is the phase (liquid, gas or mixture).

2.2 Vapor Phase

As we have mentioned previously in the beginning of the paper, the vapor phase is described by its own equations of state, in order to prevent the loss of hyperbolicity. The code uses the equation of state of a perfect gas.

$$p_v = (\gamma - 1)(\rho_v e_v). \tag{8}$$

The temperature equation is written in terms of the latent heat of vaporization L_v for a $T = T_0 = 273.15\,\mathrm{K}$ as it follows:

$$T_v = \frac{e - e_{l0} - L_v(T_0)}{C_v} + T_0. \tag{9}$$

The Sutherland law [31] is used for the dynamic viscosity formulation.

$$\mu_v = \mu_{ref}\left(\frac{T}{T_{ref}}\right)^{3/2}\frac{T_{ref} + s}{T + s}, \tag{10}$$

where T_{ref}, μ_{ref} are the reference temperature and the viscosity at the given temperature, respectively. s is Sutherland's temperature for air $= 110.56\,\mathrm{K}$. The speed of sound is given perfect gas law formulation.

$$c_v^2 = \frac{\gamma p}{\rho} = \gamma r T. \tag{11}$$

2.3 Liquid Phase

The liquid phase equation of state is the modified Tait equation [26] written as follows:

$$p = K_o \left[\left(\frac{\rho}{\rho_{sat}(T)} \right)^N - 1 \right] + p_{sat}, \tag{12}$$

where K_0 and N are constants depending on the fluid and $\rho_{v,sat}(T), \rho_{l,sat}(T)$ are the saturation densities for the liquid. The Tait equation considers the pure state liquid as a saturated component in the multiphase flow. Further, [26] proposed a simplified formulation for the case of a water:

$$e(T) = c_v \left(T - T_{ref} \right) + e_0. \tag{13}$$

The previous equation gives the temperature dependence as

$$T = \frac{e - e_{lo}}{c_l} + T_0. \tag{14}$$

The liquid viscosity is given by the Vogel's equation:

$$\mu_l = e^{\left(A + \frac{B}{C+T} \right)}, \tag{15}$$

where A, B, and C are the empirical parameters. In the case of water they are as follows:

$$A = -3.7188, \quad B = 578.919, \quad C = -137.546. \tag{16}$$

The speed of sound for the liquid water is calculated as follows [5]:

$$c_l^2 = \frac{N(p - p_{sat}(T) + K_0)}{\rho} + \frac{p}{\rho^2 C_l(T)} \left(\frac{\partial p_{sat}(T)}{\partial T} - \frac{N(p - p_{sat}(T) + K_0)}{\rho_{sat}(T)} \frac{\partial \rho_{sat}(T)}{\partial T} \right). \tag{17}$$

2.4 Mixture Phase

The mixture phase considers the presence of both phases at thermodynamical equilibrium. The mixture phase pressure is equal to the saturation pressure.

$$p_l = p_v = p_{sat}(T) = p, \tag{18}$$

$$T_l = T_v. \tag{19}$$

The mixture dynamic viscosity is a function of the liquid and vapor viscosities of the two phases:

$$\mu_m = \alpha\mu_v + (1-\alpha)\mu_l. \tag{20}$$

The thermodynamic equilibrium of the homogeneous model allows the use of the Wallis relation [15] for the calculation of the speed of sound in the Liquid-Vapor mixture.

$$\frac{1}{\rho c_m} = \frac{\alpha}{\rho_{v,sat}(T)c_v^2} + \frac{1-\alpha}{\rho_{l,sat}(T)c_l^2}. \tag{21}$$

3 Finite Volume Approach

The numerical procedure of a Moving Least Squares (MLS) method is applied in order to compute the order of derivation in a Finite Volume (FV) framework [24]. A Taylor expansion series of variables have been used in the interior of each cell for the computations of the higher order of accuracy. The approximation of the higher order derivatives has been made possible by a MLS approach further described in the next subsection.

3.1 Moving Least Squares Reproducing Method

A variable $U(\cdot, X)$ can be written in Taylor expansion series:

$$U(\cdot,X) = \sum_{\alpha=0}^{+\infty}\sum_{\beta=0}^{\alpha}\frac{1}{\beta!(\alpha-\beta)!}(X-X_I)^{\alpha-\beta}(Y-Y_I)^{\beta}\left(\frac{\partial^{\alpha}U}{\partial X^{(\alpha-\beta)}\partial Y^{\beta}}\right)(\cdot,X_I). \tag{22}$$

The FV-MLS method is a point-wise method which calculates the values of the conserved variables in the cell centers. Let $\Phi(x)$ be a function which is approximated using MLS, then $\Phi(x)$ can be written as

$$\Phi(X) \approx \hat{\Phi}(X) = \sum_{i=1}^{m} P_i(X)\alpha_i(z)]_{z=x} = P^T(X)\alpha_i(z)]_{z=x} = N^T(X)\Phi_{\Omega_x}, \tag{23}$$

where $P^T(X)$ is a m dimensional functional basis, $N^T(X)$ is MLS shape vector and Ω_x is the support with the grid nodes. $\alpha_i(z)$ is the set of parameters as a result of the weighted least-square fitting of $\Phi(X)$ done in such a way that the following expression of the error has a minimum value.

$$J\big(\alpha(z)]_{z=x}\big) = \int W(z-y,h)]_{z=x}\big[\Phi(y) - P^T(y)\alpha(z)_{z=x}\big]^2 \mathrm{d}\Omega_x. \tag{24}$$

In order to implement the MLS approach, we have to define a number of neighboring points of each node. In this paper, a kernel function is used for the definition of the shape function. The following exponential formula has been used:

$$W(x,x^*,k_x) = \frac{e^{-\left(\frac{s}{c}\right)^2} - e^{-\left(\frac{d_m}{c}\right)^2}}{1 - e^{-\left(\frac{d_m}{c}\right)^2}}, \tag{25}$$

where $s = |x - x^*|$ and $d_m = 2\max(|x - x^*|)$, $c = \frac{d_m}{k_x}$ and x^* is the position of the cell center point of calculation, x is the position of any cell center point and k_x is the shape parameter. The 2D kernel is a multiplication of the two 1D kernel functions. The construction of a stencil is of crucial importance for the behavior of the numerical simulation over unstructured grids. For further and more profound description of the FV-MLS method, the reader is referred to read [7, 10]. Since cavitation is a very rapidly taking place phenomenon, our numerical approach needs to deal with shocks and strong gradients. For this reason, a slope limiters [3, 32] are coupled with the FV-MLS detector gradient [23].

3.2 Riemann Problem

In cavitating flows, one can find a large specter of different flow regimes. If in the liquid and vapor pure phases the flow is subsonic, it is not the case in the mixture phase. Very often, the speed of sound can be found varying by a factor of 100 which makes the numerical procedure quite delicate and it should be handled with care. In order to deal with that kind of a strong gradient at the grid interfaces, the code makes use of a Riemann solver. The latter is based on the modified low dissipative solver—SLAU [29]. One can find more details about its properties [18, 19, 20].

3.3 Time Stepping Mechanism

The time stepping numerical scheme used here is the second-order "leap-frog" algorithm [30].

3.4 Geometry and Boundary Conditions

The computational domain is a 2D venturi type duct with the symmetrical $18^\circ - 8^\circ$ convergent/divergent angles, respectively, on the top and bottom walls. The ratio of the inlet and nozzle sections is equal to 3. The total length of the duct is 45 cm. The boundary conditions on the top and bottom walls are set as a "wall." The velocity at the inlet is equal to 3 m/s and the pressure at the outlet is equal to 60 kPa. This implies the cavitation number σ to be equal to 5.5 defined as in [9].

Since one can observe shock waves as a result from the bubbles implosions/explosions, the code needs absorbing (non-reflecting)-type boundary conditions at the inlet and outlet of the computational domain. Constructing such kind of boundary conditions is a pretty delicate task due to the high sensitivity of the accuracy to the small spurious wave reflex ions at far field boundaries. The latter implementation means that the entire energy is dissipated at the boundaries. One is referred to [27] for further reading of the non-reflecting set of boundary conditions and their set-up.

4 Bubble Injection Approach and Contact Handling Procedure

In the present section, we expose the bubble injection approach and the contact handling technique between the bubbles. Each bubble is treated individually and the Navier–Stokes equations are solved for the moving fluid domain.

4.1 Contact Handling Procedure

The contact handling algorithm is based on the projection of the velocity field of the injected bubbles over the velocity field of the fluid flow. This is done in such a manner that at each time step the gradient of the distance between every two bubbles is kept non-negative as a guarantee of the non-overlapping. The latter numerical procedure is based on the work of Maury and Lefebvre [17, 22]. The collisions between the bubbles are considered as inelastic. The method consists of imposing a constraint on the velocity field of the bubbles. This imposition

guarantees that at each time step the calculated bubble velocity field belongs to an eligible velocity field of the fluid. The latter will be described further in the paper. Then, the position of a bubble's centers at each time step can be written as follows:

$$\boldsymbol{X}^{n+1} = \boldsymbol{X}^{n} + \Delta t \boldsymbol{V}^{n}. \tag{26}$$

The computation of the translation and angular velocities of the bubbles:

$$\boldsymbol{V}_i^n = \frac{\int \rho_i \boldsymbol{u}^n}{\int \rho_i} \quad \text{And} \quad \boldsymbol{W}_i^n = \frac{\int \rho_i \boldsymbol{u}^n (\boldsymbol{x} - \boldsymbol{x}_i)^T}{\int \rho_i |\boldsymbol{x} - \boldsymbol{x}_i^2|}. \tag{27}$$

The last step of the algorithm procedure consists of updating the position of the bubbles:

$$\theta_i^{n+1} = \theta_i^n + \theta t W_i^n, \tag{28}$$

where θ_i^{n+1} is the angle of rotation. Equation (26) may lead to a non-acceptable numerical overlapping. From a numerical point of view, it means that the particles may overlap when their positions are updated after the velocity field computation. In order to deal with it and to be sure of the non-overlapping of the bubbles, a velocity projection in the acceptable velocity filed has been done. The velocity projection procedure is presented hereafter. Let $K(\boldsymbol{X}^n)$ be the velocity field defined as

$$K(\boldsymbol{X}^n) = \left\{ V \in R^{2N}, D_{ij}(\boldsymbol{X}^n) + \Delta t G_{ij}(\boldsymbol{X}^n). \quad V \geq 0, \forall i < j \right\}, \tag{29}$$

where $D_{ij}(\boldsymbol{X}^n)$ is the distance between every two bubbles. It is defined in the following manner:

$$D_{ij}(\boldsymbol{X}^n) = x_i^n - x_j^n - (R_i - R_j), \tag{30}$$

where R_i, R_j are the radii of the particles i and j, respectively. In Eq. (29), $G_{ij}(\boldsymbol{X}^n)$ is the gradient of the distance $D_{ij}(\boldsymbol{X}^n)$ and is written as follows:

$$G_{ij}(\boldsymbol{X}^n) = \nabla D_{ij}(\boldsymbol{X}^n) = (\ldots, 0, -e_{ij}^n, 0, \ldots, 0, e_{ij}^n, 0, \ldots), \tag{31}$$

where e_{ij}^n is the normal vector:

$$e_{ij}^n = \frac{x_i^n - x_j^n}{x_i^n - x_j^n}. \tag{32}$$

For further clarity, the exposed calculation procedure is visualized on Fig. 1:

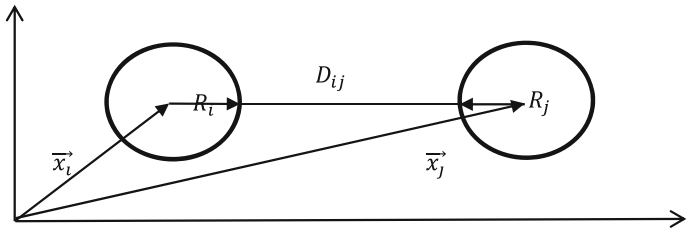

Fig. 1 Sketch diagram of the distance between two bubbles in the reference frame

In order to avoid overlapping, the following splitting procedure is proposed:

- First, we solve the variation problem without taking into account the possible overlapping of the particles
- Second, we compute the projection of this a priori velocity onto the set of admissible velocities defined by Eq. (29). The constrained problem is formulated as a saddle-point problem, by using the introduction of Lagrange multipliers.

The number of Lagrange multipliers corresponds to the probable number of shocks between the bubbles. For instance, if there is no contact between two bubbles, then $\Lambda_{ij} = 0$ and the multiplier is not activated. On the contrary, if there is a contact between the bubbles, then $\Lambda_{ij} > 0$ and the corresponding auxiliary field allows the velocity field to satisfy the non-overlapping constraint. The approximate reaction fields $\Lambda^n = \Lambda_{ij}^n$ are the dual component of a solution to the associated saddle-point problem. The interest of this procedure relies in the fact that one can use any suitable iterative solver. In our case, an Uzawa algorithm has been used.

As a result of the latter decomposition procedure, the algorithm procedure of paragraph 4.1 is updated as it follows.

- Computation of the *admissible translation velocities* by projection of the a priori translation velocities onto the set of *admissible translational velocities.*

$$V^n = argmin(\left|\boldsymbol{V} - \widehat{\boldsymbol{V}^n}\right|, \boldsymbol{V} \in K(\boldsymbol{X}^n)). \tag{33}$$

4.2 Bubble Inlet Injection

All the bubbles are initially injected using a Gaussian function. Their quantity can vary and can be adapted in respect with the necessities of the simulation. Since the duct is placed horizontally we impose only one directional velocity component. The bubbles' diameters range from 0.1 to 1 mm. For the sake of the simulation, we have

introduced 1500 bubbles, 3 bubbles per time step. As soon as all the bubbles are injected, the particles velocities are projected over the flow field velocity space. One should have enough particles in order to properly represent the dynamics of the fluid flow.

4.3 Drag, Lift, and Buoyancy Forces

The drag and lift forces are implicitly taken into account in the projected velocity space. The bubble *Reynolds number* (Re_b) is based on the admissible translation bubble velocity V_i^n and the diameter d_b.

The flow regimes described in terms of the Re_b is as follows: Stoke's flow for $Re_b \ll 1$, intermediate regime $1 < Re_b < 1000$, and fully developed turbulent flow for higher Re_b. In a fully turbulent regime, the drag coefficient (C_d) is independent of the bubble velocity and Reynolds number [25] and a good approximation equals $C_d \cong 0.44$. In our case, the Re_b is equal to 1000. For further bubble drag coefficient correlations readings, one is kindly referred to [6, 8, 11,13].

Some expressions have been obtained for the lift force in the limits of high and low Re_b. In the upper limit, [1] found that the lift coefficient is independent of the Reynolds number and is equal to $\frac{1}{2}$. In the case of a $Re_b \in [0.1;500]$, the lift coefficient can be expressed as a function of the shear rate and the Reynolds number [21]. The latter authors have considered some transient effects of the lift force. They have showed analytically that just after the introduction of the bubble in the flow, the lift coefficient equals to $\frac{3}{4}$ for any Re_b. It is interesting to note that in a 3D high Re_b case, the lift force reaches its steady value after the vorticity is advected past the bubble. In our 2D case, the lift force will immediately reach its constant value due to the lack of a vortex stretching.

The buoyancy force is not taken into account in this initial development of our numerical approach. Nevertheless, it takes part of its future expansion. Buoyancy force will play a major role in the physics behind the interactions of the injected bubbles. One can think of a preferred side of cavitation development since air bubbles will tend to go towards the upper wall due to buoyancy effects.

5 Results and Discussions

There are two purposes of the present paper. The first one is to show the cavitation phenomena in a symmetrical venturi duct. The second and main purpose of the paper is to display numerically the existence of trapped bubbles on either side of the divergent part of the venturi, as a result oft of the influence of the re-entrant jet which normally can be seen at the closure of the cavitation zone. In parallel with the main idea of the work, the authors tried to reveal the interaction between the

cavitation zones and the bubbles passing through them. In each one of the figures shown below, the corresponding iso-lines are presented, in order to facilitate the reading and distinguish easily the corresponding color zones.

5.1 Mesh

The mesh used for the simulation is a structured symmetrical mesh having 33,000 elements and 33,611 grid nodes, which gives a time step of 10^{-8} s.

5.2 Evolution of the Vapor Fraction and Velocity Vector Space During Cavitation

Hereafter, we show the development of the cavitation zones on the top and bottom sides of the venturi as well as the velocity vector field. The latter reveals the existence of recirculation zones at the closure of the vapor pockets and their diffusion by the fluid flow.

As can be seen from the images on Fig. 2, in the beginning, the growth of the vapor phase profile is symmetrical in respect to the x-axis, which is not the case at

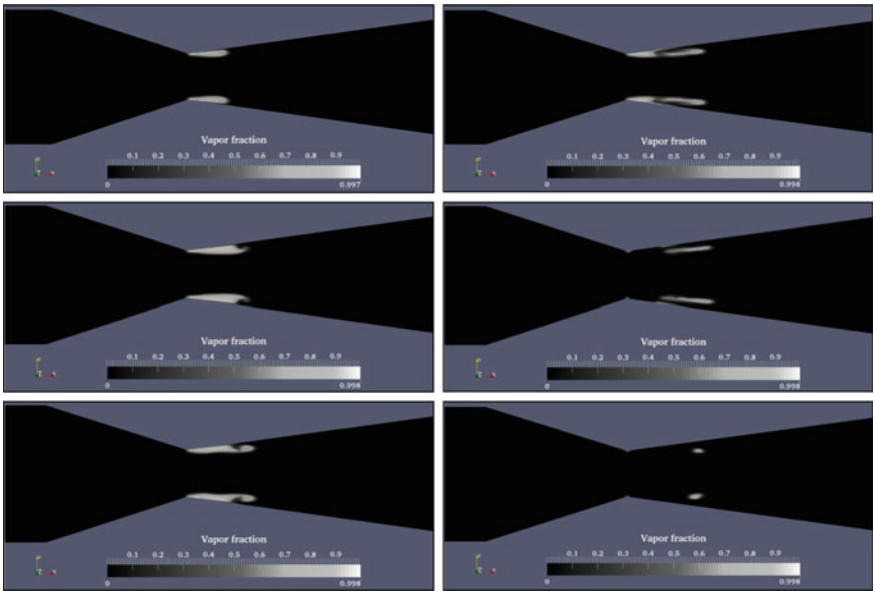

Fig. 2 Evolution of the vapor fraction

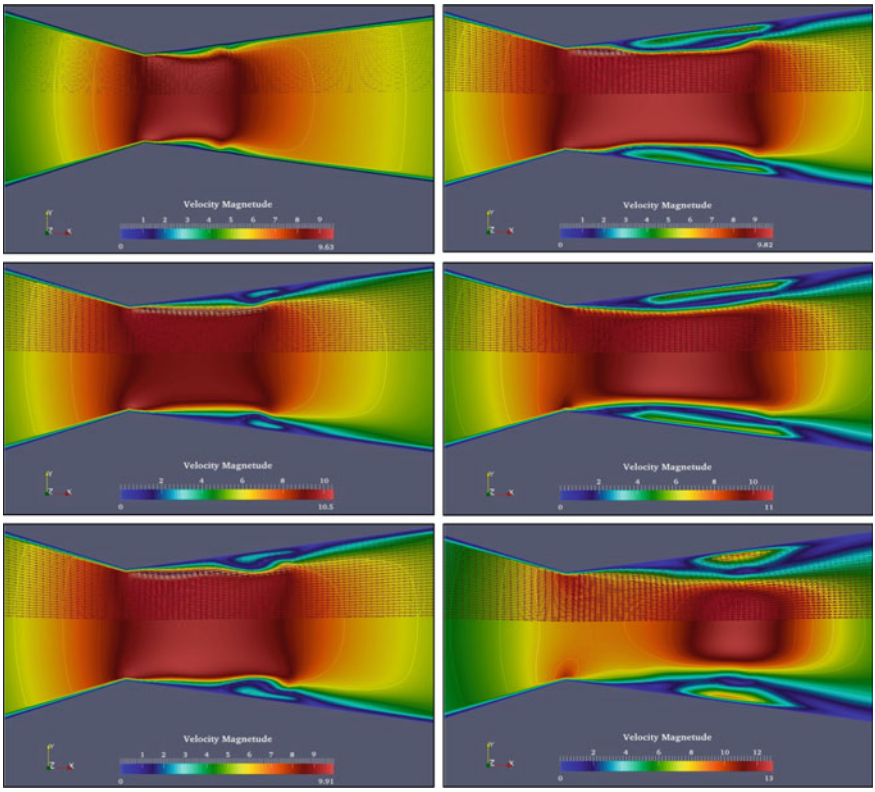

Fig. 3 Evolution of the velocity vectors

the end of the simulation. This is due to the instabilities formed at the divergent part of the tube. One can see the expansion of the vapor zone as well as the beginning of the forming of the re-entrant jet which continuously moves upwards the venturi profile until a pocket detachment is observed. Then, the reader can see that at the throat of the venturi, a very small amount of vapor is present, while the rest is being diffused by the fluid flow, forming two non-symmetrical vapor zones. What is left on the throat will give the beginning of a new cavitating region (Fig. 3).

5.3 Pressure Field

Hereafter, we present the pressure field at the two instances corresponding at each first and last of the above pictures at the vapor fraction and the velocity fields. We can clearly see the cavitation inception in the throat and the corresponding low pressure region and the position of the two detached vapor bubbles.

5.4 Aerated Cavitation Results

In the current paragraph, we present the results obtained once the bubble injection is done and the cavitation results are available. The injection position is of capital importance, in order to properly represent the dynamics of the fluid flow. What the authors have tried in the beginning is to introduce the bubbles at a section belonging to the divergent part of the duct. This is extremely important in two ways. The first one is that the bubbles are able to properly follow the fluid velocity and the second is that some computational time has been saved. The bubble boundary conditions are set that all the exiting particles are reinjected at the inlet which is in the convergent zone of the venturi duct. Once we have reached the maximum number of bubbles inside the fluid flow, the injection algorithm stops and the projecting velocity takes place. Since the time step of for the cavitation simulation is set to 10^{-8} s. We dispose with saved files every thousand iterations, the bubble time step is equal to 10^{-5} s.

First, we present the moment when the all the bubbles are randomly spread, just before the initialization of the interaction with the cavitation data. One can clearly see that the velocities at the walls are close to zero, which is in agreement with the velocity field shown on Fig. 4. Furthermore, one can see that the spread of the bubbles is very randomly and the identity can be clearly disguised. In blue can be seen those particles which are injected first and on blue the first ones. After 500 computational iterations, one can see the isotropic bubble dispersion. The authors were not interested in the evolution of the particles over the entire flow domain, due to the necessity of computational time and the lack of obvious cavitation after the divergent part of the duct (Fig. 5).

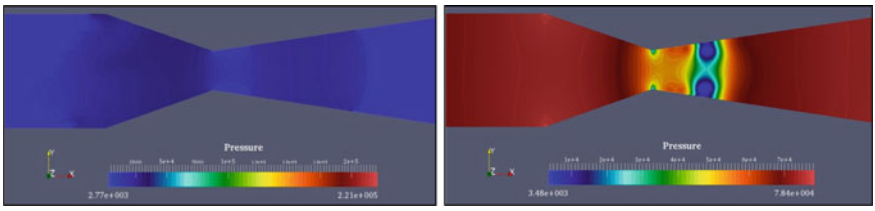

Fig. 4 Pressure field at initial and final stages

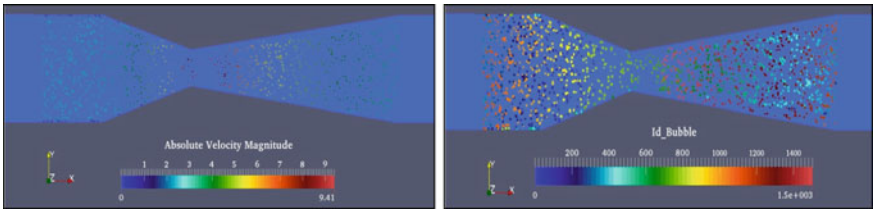

Fig. 5 Particle dispersion according to order of injection and velocity field

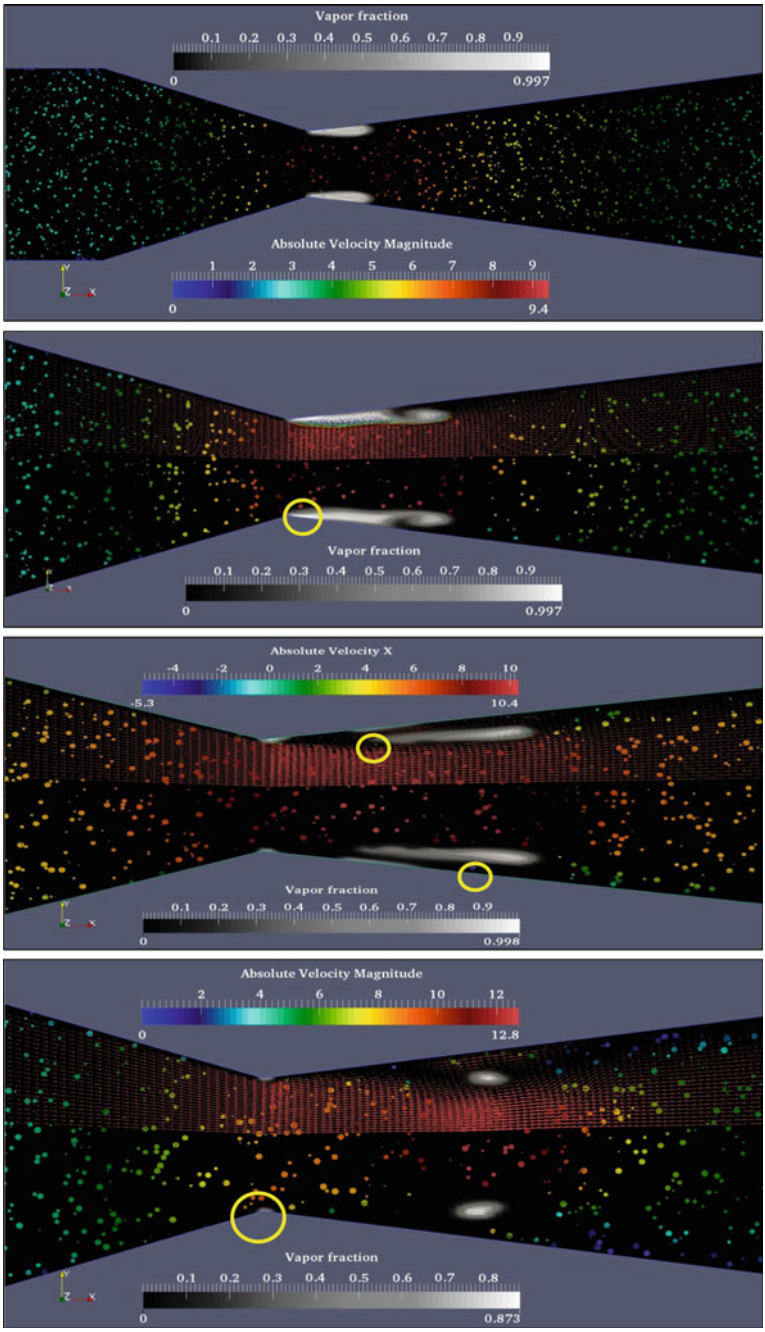

Fig. 6 Bubble–cavitation interactions

Second, we show the one-way aeration-cavitation coupling. Only four moments of the simulation have been chosen in order not to exceed the paper imposed length.

From the images of Fig. 6, the existence of certain particles (yellow circles) which follow the dynamics of the re-entrant jet can be clearly distinguished; hence their behavior in the recirculation zone cannot be neglected anymore. They will certainly influence the dynamics of the fluid flow and vice versa.

Another key finding is that certain bubbles actually touch the upper layer limit of both cavitating zones. It would be interesting to see whether those bubble particles can influence the vapor pocket shape as well as its thermodynamic behavior.

Furthermore, the injected gas is air which differs from the water vapor. The mixture of both may influence the sound velocity, which changes rapidly in the wake of cavitation zone. As a result, one should investigate the vapor boundary where the transformation from gas to liquid and vice versa takes place, since some passing bubble having different physics, might be able to change the cavitation separation frequency.

Lastly, we should further investigate the impact of particles on the cavitation inception on the venturi throat. Since we clearly see that some of the bubbles are flowing through the cavitation zone, the presented numerical model should take into account the interactions between the vapor-air phases and vapor-air-liquid.

Logically, the work done leads to the conclusion that this is a promising modeling method which should be further expanded. This implies the use of a penalization method with the homogeneous mixture model, which is a challenge on its own.

6 Future Development of the Code

The future works regarding the finite volume moving least squares (FV-MLS) in-house code is its extension into three-dimensional spaces. Indeed, the first 3D version is already under development. The two-way coupling between cavitation and aeration is considered as a major task at the later time add-on of the code. Other possible major development can be the shift into fluids which is different than water and air as a liquid and gas phase, respectively.

References

1. Auton, T. R. (1987). The lift force on a spherical body in a rotational flow. *Journal of Fluid Mechanics, 183*, 199–218.
2. Barre, S., Rolland, J., Boitel, G., Goncalves, E., & Patella, R. F. (2009). Experiments and modeling of cavitating flows in venturi: attached sheet cavitation. *European Journal of Mechanics—B/Fluids, 28*(3), 444–464. doi:10.1016/j.euromechflu.2008.09.001.

3. Barth, T., & Jespersen, D. (1989). The design and application of upwind schemes on unstructured meshes. *27th Aerospace Sciences Meeting*. American Institute of Aeronautics and Astronautics. doi:10.2514/6.1989-366.
4. Bergerat, L., Khelladi, S., & Bakir, F. (2012). Cavitation modeling of thermosensitive fluids using compressible phases approach. *Proceedings of the 8th International Symposium on Cavitation, Cav2012, no. 185*, pp. 1–6.
5. Brennen, C. (2005). Fundamentals of multiphase flow.
6. Brown, P., & Lawler, D. (2003). Sphere drag and settling velocity revisited. *Journal of Environmental Engineering, 129*(3), 222–231. doi:10.1061/(ASCE)0733-9372s.
7. Chenoweth, S. K. M., Soria, J., & Ooi, A. (2009). A singularity-avoiding moving least squares scheme for two-dimensional unstructured meshes. *Journal of Computational Physics, 228*(15), 5592–5619. doi:10.1016/j.jcp.2009.04.036.
8. Clift, R. (2005). *Bubbles, drops, and particles*. Mineola: Dover Publications.
9. Coutier-Delgosha, O. (2005). Test case number 30: Unsteady cavitation in a Venturi type section (PN), (30), pp. 1–11.
10. Cueto-Felgueroso, L., Colominas, I., Nogueira, X., Navarrina, F., & Casteleiro, M. (2007). Finite volume solvers and Moving Least-Squares approximations for the compressible Navier-Stokes equations on unstructured grids. *Computer Methods in Applied Mechanics and Engineering, 196*(45–48), 4712–4736. doi:10.1016/j.cma.2007.06.003.
11. Dijkhuizen, W., van Sint Annaland, M., & Kuipers, J. (2010). Numerical and experimental investigation of the lift force on single bubbles. *Chemical Engineering Science, 65*(3), 1274–1287. doi:10.1016/j.ces.2009.09.084.
12. Dong, Z., & Su, P. (2006). Cavitation control by aeration and its compressible characteristics. *Journal of Hydrodynamics, Series B, 18*(4), 499–504. doi:10.1016/S1001-6058(06)60126-1.
13. Flemmer, R. L. C., & Banks, C. L. (1986). On the drag coefficient of a sphere. *Powder Technology, 48*(3), 217–221. doi:10.1016/0032-5910(86)80044-4.
14. Goncalves, E., Decaix, J., & Patella, R. F. (2010). Unsteady simulation of cavitating flows in Venturi. *Journal of Hydrodynamics, Series B, 22*(5), 753–758. doi:10.1016/S1001-6058(10)60026-1.
15. Graham B. W. (1969). *One dimensional two phase flow*. New York: McGraw-Hill.
16. Le Métayer, O., Massoni, J., & Saurel, R. (2004). Elaboration des Lois d'Etat d'un liquide et de sa vapeur pour les modèles d'ecoulements diphasiques. *International Journal of Thermal Sciences, 43*(3), 265–276. doi:10.1016/j.ijthermalsci.2003.09.002.
17. Lefebvre, A., & Lefebvre-Lepot, A. (2007). Modélisation numérique d'écoulements fluide/particules.
18. Liou, M. (1993). On a new class of flux splittings. *Thirteenth International Conference on Numerical, 1*, 115–119.
19. Liou, M.-S. (1996). A sequel to AUSM: AUSM+. *Journal of Computational Physics, 129*(2), 364–382. doi:10.1006/jcph.1996.0256.
20. Liou, M.-S. (2006). A sequel to AUSM, Part II: AUSM + -up for all speeds. *Journal of Computational Physics, 214*(1), 137–170. doi:10.1016/j.jcp.2005.09.020.
21. Magnaudet, J., & Legendre, D. (1998). Some aspects of the lift force on a spherical bubble. *Fascination of Fluid Dynamics* (pp. 441–461).
22. Maury, B. (2006). A time-stepping scheme for inelastic collisions. *Numerische Mathematik, 102*(4), 649–679. doi:10.1007/s00211-005-0666-6.
23. Nogueira, X., Cueto-Felgueroso, L., Colominas, I., Navarrina, F., & Casteleiro, M. (2010). A new shock-capturing technique based on Moving Least Squares for higher-order numerical schemes on unstructured grids. *Computer Methods in Applied Mechanics and Engineering, 199*(37), 2544–2558.
24. Nogueira, X., Khelladit, S., Cueto-Felgueroso, L., Bakirt, F., Colominas, I., & Gómez, H. (2010). Implicit large-Eddy simulation with a moving least squares-based finite volume method. *IOP Conference Series: Materials Science and Engineering, 10*, 012235. doi:10.1088/1757-899X/10/1/012235.
25. Peker, S., & Helvaci, S. (2011). *Solid-liquid two phase flow*. London: Elsevier Science.

26. Saurel, R., Cocchi, J., & Butler, P. (1999). Numerical study of cavitation in the wake of a hypervelocity underwater projectile. *Journal of Propulsion and Power*, *15*(4), 513–522.
27. Schnerr, G. H., Sezal, I. H., & Schmidt, S. J. (2008). Numerical investigation of three-dimensional cloud cavitation with special emphasis on collapse induced shock dynamics. *Physics of Fluids, 20*(4), 040703. doi:10.1063/1.2911039.
28. Shamsborhan, H., Coutier-Delgosha, O., Caignaert, G., & Abdel Nour, F. (2010). Experimental determination of the speed of sound in cavitating flows. *Experiments in Fluids, 49*(6), 1359–1373. doi:10.1007/s00348-010-0880-6.
29. Shima, E., & Kitamura, K. (2009). On new simple low-dissipation scheme of AUSM-family for all speeds. *AIAA Paper*, (January), pp. 1–15.
30. Skeel, R. (1993). Variable step size destabilizes the Störmer/leapfrog/Verlet method. *BIT Numerical Mathematics*, *33*(September 1992).
31. Sutherland, W. (1893). LII. The viscosity of gases and molecular force. *Philosophical Magazine Series 5*, *36*(223), 507–531. doi:10.1080/14786449308620508.
32. Venkatakrishnan, V. (1993). On the accuracy of limiters and convergence to steady state solutions. *31st Aerospace Sciences Meeting*. American Institute of Aeronautics and Astronautics. doi:10.2514/6.1993-880.

Experimental and Numerical Modelling of Free-Surface Turbulent Flows in Full Air-Core Water Vortices

Sean Mulligan, John Casserly and Richard Sherlock

Nomenclature

ϕ_k	Volume fraction of phase k
f	Laser pulse frequency (Hz)
g	Gravitational acceleration (m s^{-2})
r	Radius (m)
r_c	Vortex core radius (m)
θ, r, z	Cylindrical coordinate system (rad, m, m)
x, y, z	Cartesian coordinate system (m, m, m)
t	Time (s)
v_θ	Tangential velocity (m s^{-1})
v_r	Radial velocity (m s^{-1})
v_z	Axial velocity (m s^{-1})
Γ	Vortex circulation (m^2 s^{-1})
P	Static pressure (Pa)
H_r	Vortex depth at r (m)
D	Effective diameter (m)
d	Orifice diameter (m)
d_p	Particle diameter (m)
B	Channel width (m)
B_{In}	Inlet width (m)

S. Mulligan (✉)
CERIS, Department of Civil Engineering and Construction,
Institute of Technology, Ash Lane, Sligo, Ireland
e-mail: sean.mulligan@mail.itsligo.ie

J. Casserly · R. Sherlock
Department of Civil Engineering and Construction, Institute of Technology,
Sligo School of Science, Institute of Technology, Sligo, Ireland
e-mail: casserly.john@itsligo.ie

R. Sherlock
e-mail: sherlock.richard@itsligo.ie

P. Gourbesville et al. (eds.), *Advances in Hydroinformatics*,
Springer Water, DOI 10.1007/978-981-287-615-7_37

ρ Fluid density (kg m^{-3})
μ Dynamic viscosity (N.s m^{-2})
T Fluid temperature (K)

1 Introduction

Concentrated, full air-core vortices are a commonly observed hydraulic phenomenon in both nature and industry. These fluid systems exhibit a range of effects which can be detrimental or profitable in various industrial applications. To date, free-surface water vortices have been primarily investigated in order to propose methods to suppress their formation in unfavourable situations such as that above vertical or horizontal pump and hydropower intakes. In such circumstances, excessive air ingestion significantly reduces efficiencies and can have catastrophic effects on turbine impellers and other downstream machinery. A summary of research carried out in this context is presented by Knauss [1]. On the other hand, the nature of free-surface vortex flow has been found to be valuable in new/emerging technologies. The annular discharge characteristics of vortex flow through a horizontal orifice render the flow system advantageous when used for energy dissipation in vortex drop shafts [2]. More recently, the water vortex hydropower plant system has utilised the strong full air-core vortex for generating hydroelectric power on rivers. Examples of such hydraulic structures are highlighted in Figs. 1 and 2. This increasing demand for the use of strong free vortex flows necessitates an improved understanding for the underlying hydrodynamic theory of this type of flow system. In this work, the techniques of analytical and numerical modelling are employed and validated using a scaled physical model.

Also known as bathtub vortex flow [3], this fluid system is characterised by an intense axial down flow at the discharge orifice in combination with a dominating tangential velocity field. It is well known that the strength of vortex flow and the nature of the free-surface are strongly dependent on the nature of the approach flow (e.g. Fig. 1) which originates a field circulation (Γ). The nature of the free vortex conserves angular momentum throughout the system which causes an inverse increase in tangential velocity radially in the majority of the flow field. Knowledge of the velocity fields and water surface profiles is of significant value to the hydraulic engineer for safe operation and quality control of hydraulic systems.

The simplest analytical solutions for the tangential velocities in a viscous vortex were proposed by Rankine [4], Scully [5] and Vatistas [6] which will be discussed in more detail in Sect. 2. Another analytical model was proposed by Burgers [7] in the statistical theory of turbulence and was later successfully applied on vortex flows by Rott [8], Miles [9] and Stepanyants and Yeoh [10]. Other work was carried out by Einstein and Li [11] and Lewellen [12] on theoretical derivations of three-dimensional vortex models based on a simplification of the Navier–Stokes equations.

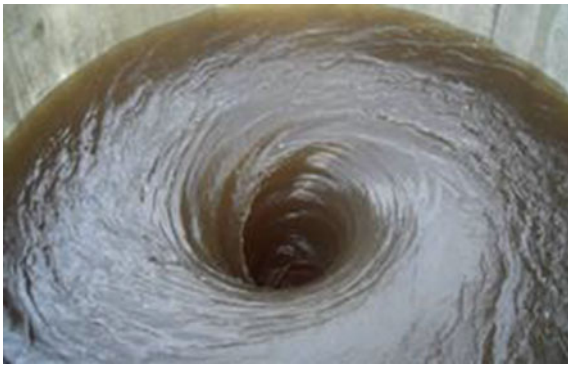

Fig. 1 Flow in an open channel vortex chamber

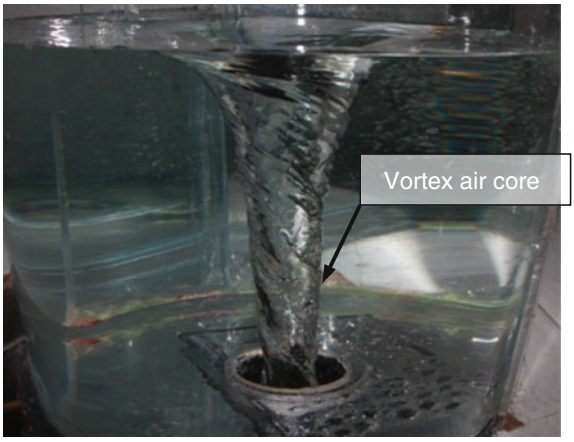

Fig. 2 Physical model of vortex chamber at the IT Sligo fluid mechanics laboratory

Efforts have been made to validate previous analytical models through experimental methods and physical modelling. Hite and Mih [13], Anwar [14] and Wang [15] all carried out analysis on physical models of vortices to determine non-dimensional parameters and to measure water surfaces and velocity profiles. In all cases, the investigations were carried out on weak air-core vortices above hydraulic intakes. Although the agreement between the theoretical and measured experimental velocity profiles was reported to be reasonable, the work does not conclude if the theoretical models apply to strong vortex behaviour. In general, analytical models have been derived for ideal two-dimensional fluid domains, and therefore the results obtained can have a high degree of uncertainty when compared to real, complex three-dimensional fluid domains. As stated by Trivellatto [16], no mathematical model capable of representing the flow field in free-surface vortex flows has yet obtained a general consensus, and therefore confusion arises when reviewing literature.

Recently, the approach of analytical modelling has been supplanted by numerical modelling in hydraulic engineering. However, from a review of current literature, there are very few investigations carried out on topics of free-surface vortices which adopt the finite volume method (FVM) of numerical modelling. Trivellato [16] performed FVM modelling of free-surface draining vortices in order to advance on his previous numerical investigation using the finite difference method. This work demonstrates that the numerical model is capable of predicting the whole steady flow field. With commercial CFD software becoming more readily available, numerous authors have presented benchmark work on intake vortices for various codes. Okamura et al. [17], Hai-Feng et al. [18] and Tanweer et al. [19] investigated free-surface vortex flows using a single-phase model assuming that the water surface boundary condition is a frictionless free-slip wall. This work was further advanced by Shukla [20] and Bayeul-Lainé et al. [21] who modelled the flow field as a multiphase system using two stratified fluid domains representing air and water independently. Chen et al. [22] carried out an investigation into numerical modelling of the vertical vortex at a hydraulic intake where different turbulence models were investigated and compared.

To date, as far as the author is aware, little to no work has been conducted on numerical modelling of strong free-surface water vortex flows. Furthermore, it is evident from previous literature on numerical modelling of weak vortex structures that the work fails to comment on methods of multiphase modelling, mesh sensitivity and turbulence modelling in great detail. The work presented here sets out to investigate the phenomenon of strong free-surface vortex flow by analytical and numerical simulation to be validated by data obtained in the physical experimental model of the flow system.

2 Flow Analysis

The type of flow under consideration is shown in Fig. 3. The subcritical approach flow enters the domain through a spiral inlet and discharges axially at some smaller radius through the outlet (or discharge orifice). The flow system is a three-dimensional system and is described using the cylindrical coordinate system for tangential velocity (v_θ), radial velocity (v_r) and axial velocity (v_z) where their distributions are expressed as a function of the radius $f(r)$. In the ideal, nonviscous vortex model, the flow is classified as fully irrotational and the tangential velocity profile takes the form of

$$v_\theta(r) \propto \frac{1}{r}. \tag{1}$$

However, in a real newtonian fluid, effects of viscosity limit the tendency of the fluid to achieve the infinite singularity as $r \to 0$. To take into account for the viscosity in the near field, a simple analytical model was proposed by Rankine [4]

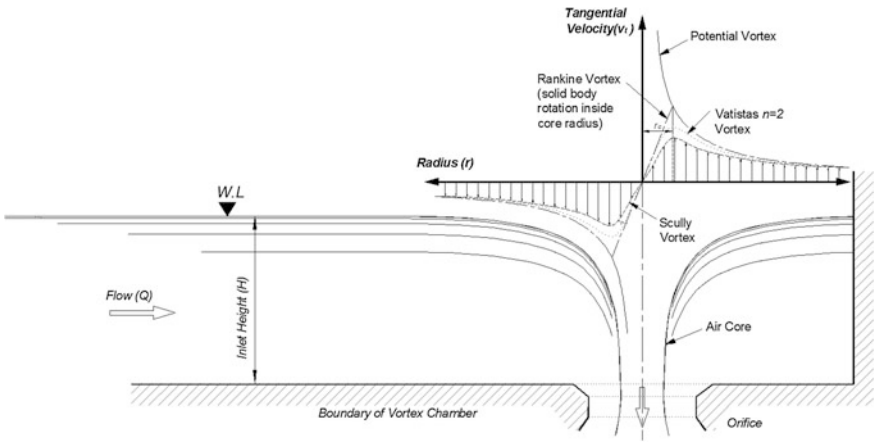

Fig. 3 Summary of tangential velocity profiles as determined from Eqs. (1) and (2) (produced by author)

which describes the velocity field by representing the viscous core region as a rotational fluid zone at $r < r_c$, where r_c is the core radius, and therefore limiting the tangential velocity. This was later improved by Vatistas [6] who devised a model that overcomes the discontinuity generated in Rankines model using an algebraic family (represented by n) of velocity profiles highlighted in Eq. (2).

$$v_\theta(r) = \frac{\Gamma}{2\pi}\left(\frac{r}{\left(r_c^{2n} + r^{2n}\right)^{\frac{1}{n}}}\right) \; when \; 0 \le r \le \infty. \tag{2}$$

As indicated in Fig. 3, these analytical models can be used to predict the tangential velocity when the core radius (r_c) and circulation (Γ) for the flow field are known.

To address the vortex pressure distribution, one model for the complete water surface profile can be derived from the radial momentum equation of the steady, Navier–Stokes equations of in cylindrical coordinates:

$$\rho\left(v_r\frac{\partial v_r}{\partial r} + \frac{v_\theta}{r}\frac{\partial v_r}{\partial \theta} - \frac{v_\theta^2}{r} + v_z\frac{\partial v_r}{\partial z}\right) = -\frac{\partial P}{\partial r} + \mu\left[\frac{1}{r}\frac{\partial}{\partial r}\left(r\frac{\partial v_r}{\partial r}\right) + \frac{1}{r^2}\frac{\partial^2 v_r}{\partial \theta^2} + \frac{\partial^2 v_r}{\partial z^2} - \frac{v_r}{r^2} - \frac{2}{r^2}\frac{\partial v_\theta}{\partial \theta}\right]. \tag{3}$$

Through an order of magnitude analysis, assuming that the system is axissymetric, free from external forces and neglecting the effects viscosity, Eq. 3 can be simplified to yield Eq. 4. By substituting Eq. 1 for the irrotational velocity field into (4) and integrating between two arbitrary points in the flow field (1) and (2), an expression for the water vortex surface profile can be derived (Eq. 5).

$$\frac{V_\theta^2}{r} = \frac{1}{\rho}\frac{\partial P}{\partial r} \tag{4}$$

$$h_1 - h_2 = \frac{1}{2g}\left(\frac{\Gamma}{2\pi}\right)^2\left(\frac{1}{r_2^2} - \frac{1}{r_1^2}\right). \tag{5}$$

3 Experimental Configuration and Description

Experiments are carried out in an open-tank test facility which is used specifically to model vortex flows of various degrees of circulation. The tank, shown in Fig. 4, contains a circular orifice located centrally and can be adapted with various geometric boundaries to develop a range of vortex flow structures. In this examination, scaled acrylic casings of the spiral vortex chamber are installed (See Fig. 5). The casings are secured in place via a water-tight seal during testing. The inlet comprises a 65-mm bell mouth pipe entrance and 140 mm flow straightening plates which homogenise the incoming velocity profile. Water is circulated through the system by a centrifugal pump which ranges in capacity from 0 to 3.5 l/s. A magnetic flow meter (accuracy ≈ 0.1 %) is used to monitor flowrate throughout testing.

The two-dimensional velocity-field data are obtained using a particle tracking velocimetry technique. Neutrally buoyant tracer particles ($d_p = 1$ mm) are injected and tracked at various horizontal planes (z/H_{in}) in the flow field to determine if the

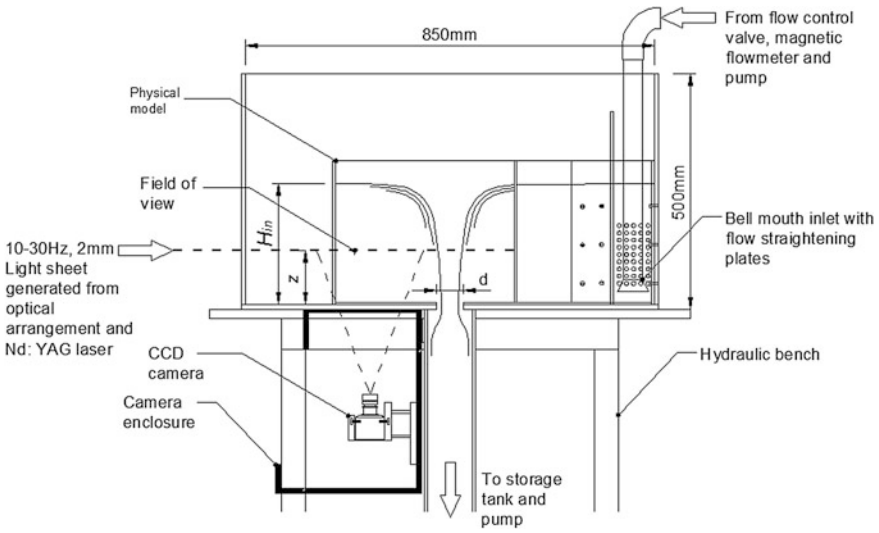

Fig. 4 Schematic of hydraulic test rig highlighting the tank, inlet, physical model and camera compartment

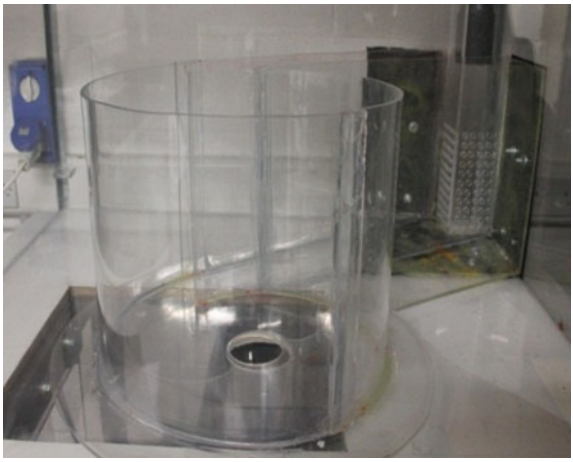

Fig. 5 Physical model installed in test rig

velocity fields are influenced by their position on the vertical z-axis. The planes are illuminated using a 2-mm-thick laser light sheet generated by a 532 nm Nd:YAG laser system. The light sheet is shaped by passing the laser emitting 6-mm-diameter circular beam profile through appropriate light sheet optics. This optical arrangement can be transposed at various collimations to probe the required z/H_{in} position in the flow field. Illumination is provided in pulses with frequencies (f) ranging between 10 and 30 Hz. Particle displacements within each pulse (time separation $\Delta t = 1/f$) are recorded by acquiring successive images of the light sheet using a CCD camera system (Mikrotron MiniCube). The camera is installed in a compartment which permits imaging of the light sheet through a view port on the underside of the tank. The lens used is a 16 mm fixed focal length objective with a maximum distortion/aberration of less than 0.1 %. The displacement vectors determined from the particle images are then used to calculate velocity vectors v_θ and v_r from the time separation between laser pulses.

4 Multiphase Modelling Using CFX

To accurately predict the location and shape of the free-surface and flow-field variables in an air-core vortex, both the liquid phase and the gaseous phase need be modelled. In order to simplify the computation, it will be assumed that the flow is steady and fully stratified with no interfacial mixing. It is also safe to assume that the gas phase is approximately at rest and therefore there is no interphase momentum transfer. Thus, the fluid domain is modelled using an Eulerian–Eulerian homogeneous multiphase flow model. In this approach, both phases are treated as interpenetrating continua and share a common velocity and turbulence field. However, because the system is fully separated, both phases are parted by a

well-defined resolvable interface (free-surface). The flow field is determined by numerically solving the modified Reynolds-Averaged Continuity and Navier-Stokes (RANS) multiphase flow equations. The interacting forces between faces (e.g. surface tension) are modelled as source terms in the equations.

The homogeneous Eulerian–Eulerian multiphase method relies on the fact that the air/water interface is distinct and well-defined throughout the fluid, and that there is no entrainment from one fluid into another. Therefore, cells that are located away from the interfacial zone will be representative of either air or water and cells in the vicinity of this zone will contain a mixture of both. Therefore, in this approach, the term volume fraction (ϕ_k) of phase k is introduced. In this investigation, the governing equations are solved for water (ϕ_w), and the volume fraction of air (ϕ_a) can be calculated by $\phi_a = 1 - \phi_w$ if required. The air–water interface is then determined by identifying the cells where $0 < \phi_w < 1$.

Since the flow system in question is highly turbulent, additional modelling must be considered. The Reynolds-Averaged Navier-Stokes (RANS) equations are derived from the general Navier-Stokes equations by substituting the main and fluctuating fluid dynamic mixture quantities into the momentum equations. The turbulent stresses in the momentum equations, represented by the Reynolds stress tensor, are unknown and have to be modelled using a particular turbulence model. CFX offers the following turbulence models; $k - \varepsilon$, $k - \omega$ and Shear Stress Transport (SST) eddy viscosity models and Reynolds Stress models which are used extensively. Since all computations are isothermal ($\Delta T = 0$) and the material properties are constant throughout, the models discussed previously are coupled to yield a closed system of governing equations which are solved numerically by ANSYS CFX 14.5.

5 CFX Modelling Process and Test Cases

In this study, flow in the vortex chamber is modelled using a steady-state, multiphase model comprising water as the primary fluid and air as the secondary fluid. Three test cases are investigated in this work for various flow rates (Q_{in}) and corresponding inlet depths (H_{in}). Details of the boundary conditions and test cases are highlighted in Table 1.

Sensitivity analysis is carried out on the A3 test case for mesh type and density. An unstructured tetrahedral mesh and a structured hexahedral mesh of various cell sizing are tested independently (see Table 2). Figures 6 and 7 highlight an example of the finely sized unstructured and structured mesh cases for the computational domain in the outlet region. Inflation is applied at chamber perimeters with a growth rate of 1.2 to refine the computation at the boundary layer. Furthermore, in order to capture a sharp prediction of the free-surface, mesh refinement is applied for a water.volume fraction of 0.5. Refinement of the mesh at the water surface also ensures enhancement of the computational domain at the air core where the near

Table 1 Boundary conditions and test cases

Boundary		Details			
A	Inlet	Boundary type: Mass flow normal to boundary			
		Test cases	A1	Q_{in} = 0.725 kg/s	H_{in}/d = 1 = 67 mm
			A2	Q_{in} = 1.677 kg/s	H_{in}/d = 2 = 134 mm
			A3	Q_{in} = 3.111 kg/s	H_{in}/d = 3.5 = 235 mm
B	Outlet	Boundary type: Opening with entrainment			
C	Walls	Boundary type: No-slip, smooth wall boundary			
D	Opening	Boundary type: Opening with pressure and direction			

Table 2 Summary of mesh characteristics

	Details	Density	No. of Nodes	No. of Elements	Sizing at outlet (mm)	Ratio of cell size to outlet diameter (%)
Unstructured	Tetrahedral mesh with inflation applied at boundaries	Fine	190,800	463,100	4.5	6.9
Structured	Predominantly hex mesh using a multi-domain with inflation applied at boundaries	Fine	491,000	461,600	1.25	1.8
		Medium	401,200	378,000	2.50	3.7
		Coarse	330,400	310,400	5.00	7.5

Fig. 6 Unstructured mesh

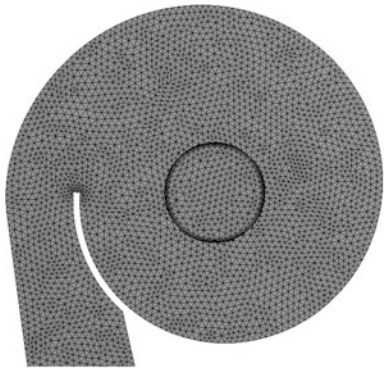

field high velocity gradients are expected. This refinement technique is carried out for 15 steps and a maximum of 50 iterations per step to reach a target residual of 0.001.

The mesh dependency analysis is implemented using the (a) shear stress transport (SST) $k-\omega$ model, because it is more robust and computationally inexpensive compared to that of the Reynolds stress model. Subsequent sensitivity analysis for

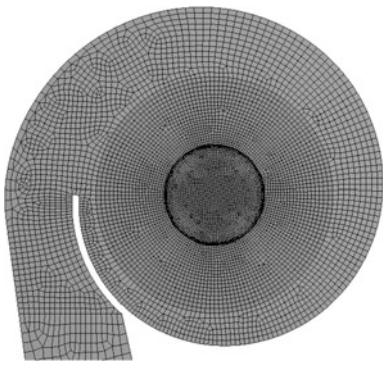

Fig. 7 Structured mesh

turbulence modelling is investigated using (b) SST $k-\omega$ with curvature correction and (c) the baseline Reynolds stress model (BSL RSM). In the curvature correction process of (b), modification of the production term has been derived which allows the sensitisation of the turbulence model to system rotation and streamline curvature based on the work of Spalart and Shur [23]. The specific limiter of 1.25 is used for the multiplier as generally suggested for this type of flow using the SST model. The eddy viscosity approaches of (a) and (b) are compared to the Reynolds stress model (c) which accounts for rotating flows of anisotropic turbulence.

Surface tension is also taken into account using a surface tension coefficient of 0.072 N/m and a continuum surface force. To obtain a converged solution, the target value for the normalised residual for each flow variable was set to 10^{-5} as generally suggested. Initial conditions for the domain are set for an air.volume fraction of 1 (domain empty of water), and the false transient method is applied to reach a steady state to best simulate the physical model.

6 Results and Discussion

6.1 Solution Sensitivity

Results are presented for water surface and velocity profile data across half of the vortex vertical cross section, spanning radially from the inlet to the orifice. Figures 8 and 9 present a summary of the solution sensitivity analysis for the mesh and turbulence model discussed previously. It is evident that the unstructured mesh approach is unsuitable for such an analysis. It is concluded that this is due to excessive numerical diffusion error generated from poor alignment of the grid with the general flow pattern. The structured mesh presents a substantially improved solution for the flow field. With regards mesh size dependency it can be seen that the solution tends to become grid independent when the fine mesh scenario is reached (mesh size/outlet size ratio = 1.8 %). The curvature correction of the SST model presents a significant improvement to the overall solution, particularly close

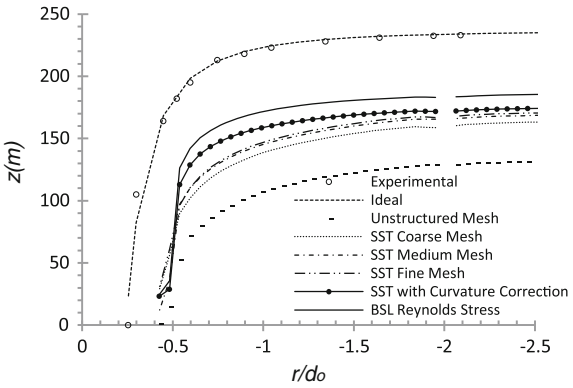

Fig. 8 Sensitivity analysis for water surface (A3)

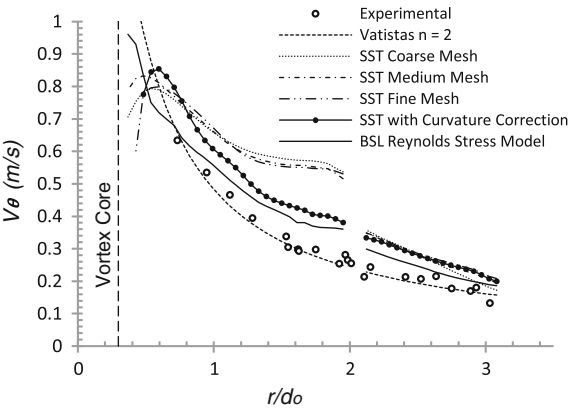

Fig. 9 Sensitivity analysis for tangential velocity (A3)

to the vortex core where high tangential velocity gradients are experienced. The BSL Reynolds stress model offers the most accurate solution for both the free-surface and tangential velocity field. However, discrepancies in the water level at the inlet and vortex core were found to be 22 and 29 %, respectively. The model also slightly over estimates the tangential velocity field at the inlet; however, it still maintains a greater accuracy when compared to results from the SST eddy viscosity models.

6.2 Free-Surface

Figure 10 presents a summary of the comparative analysis carried out on the numerical, analytical and the experimental model. The water surface is determined visually in CFX Post using an isosurface for a water.volume fraction of 0.5. In all three cases, the results reveal that the general predicted shape and appearance of the

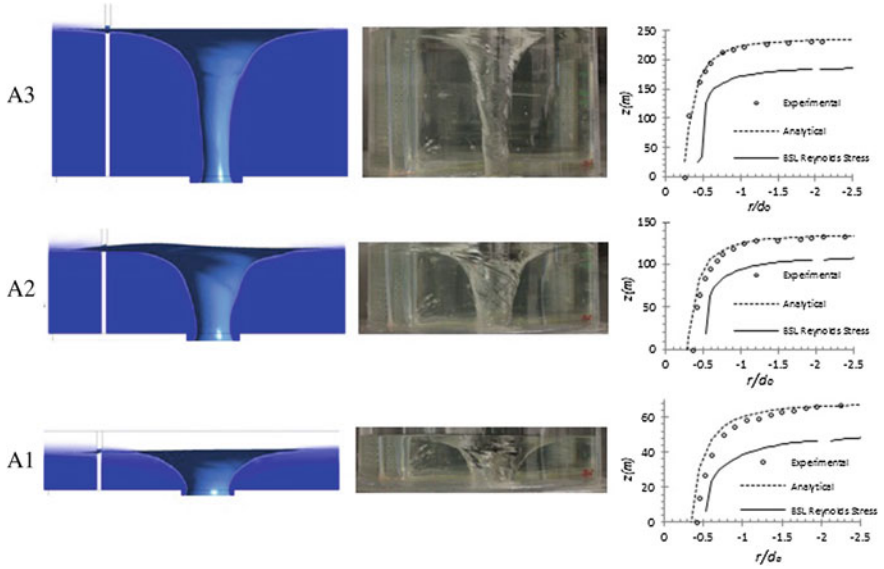

Fig. 10 Summary of comparison between numerical, experimental and analytical models, respectively, for test cases A1, A2 and A3

free-surface agrees well with the experimental observations. However, the location of the free water surface is under predicted in each test case (A3–A1) by approximately 22, 21 and 26 %, respectively.

6.3 *Velocity Distributions*

A comparison between the tangential and radial velocity profiles at various collimations (z/H_{in}) determined in the numerical, analytical and experimental models are presented in Figs. 11, 12, 13, 14, 15, and 16 for boundary condition A2. Similar relationships and agreements were found for boundary test cases A1 and A3. A visual representation of the water superficial velocity field is also highlighted for each case in Figs. 17, 18 and 19.

Considering the tangential velocity comparison in Figs. 11, 12 and 13, it is evident that the Vatistas n = 2 model is in good agreement with the experimental data. The numerical Reynolds stress model also agrees well with the tangential velocity field but tends to marginally overestimate the distribution in the far field and at the inlet. Figures 11, 12 and 13 as well as Figs. 17, 18 and 19 indicate that the tangential velocity distribution is generally independent of the depth (z/H_{in}). However, larger core velocities are experienced close to the vessel floor ($z/H_{in} \rightarrow 0$) where the air core diameter is at its minimum thus allowing the velocity profile to develop further in this region.

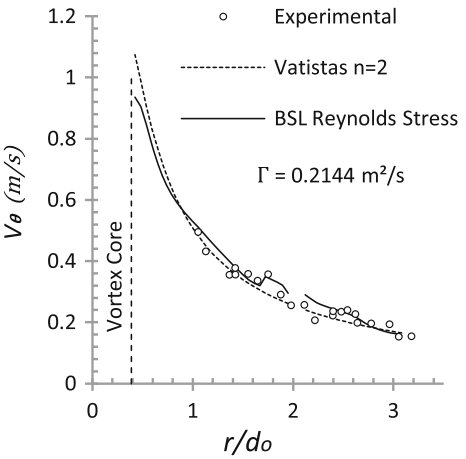

Fig. 11 Tangential velocity comparison for z/H_{in} = 0.26

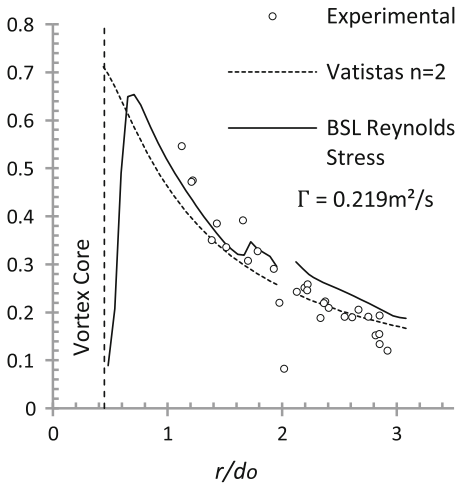

Fig. 12 Tangential velocity comparison for z/H_{in} = 0.56

Regarding the radial velocity, the experimental plot revealed a disorganised distribution of radial velocities with indications of an inverse trend with the radius. In some cases, negative velocities are experienced highlighting outward radial flow activity. This centrifugal flow characteristic is also apparent in the vector field representation of the vortex cross section (Fig. 20). The numerical simulation also presents similar trends for the radial velocity distribution, but the results tend to be generally underestimated when compared to the experimental data.

The relationship between inlet velocity and depth profile is investigated in the physical model to understand its potential effects on the velocity fields. Velocity data for the free-surface were determined by particle tracking using floating tracers. As is highlighted in Fig. 21, the velocity approaches zero near the no-slip boundary at the vessel floor but increases gradually to a free stream, relatively constant velocity

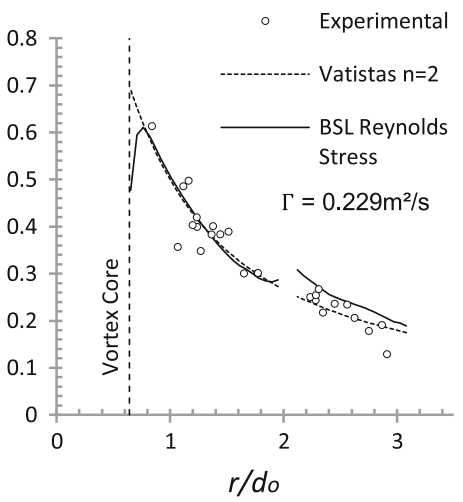

Fig. 13 Tangential velocity comparison for z/H_{in} = 0.75

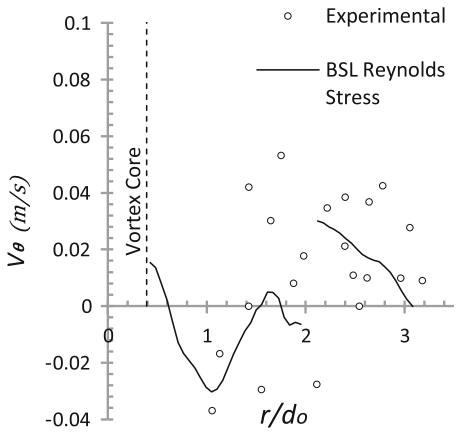

Fig. 14 Radial velocity comparison for z/H_{in} = 0.26

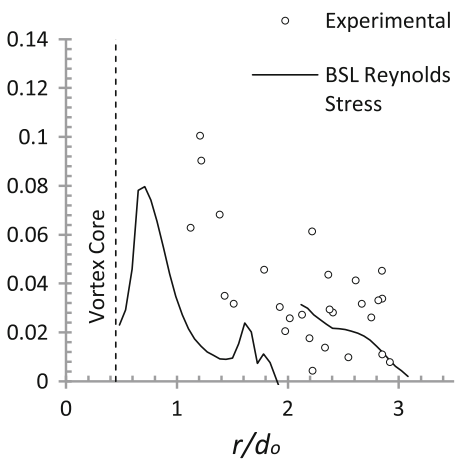

Fig. 15 Radial velocity comparison for z/H_{in} = 0.56

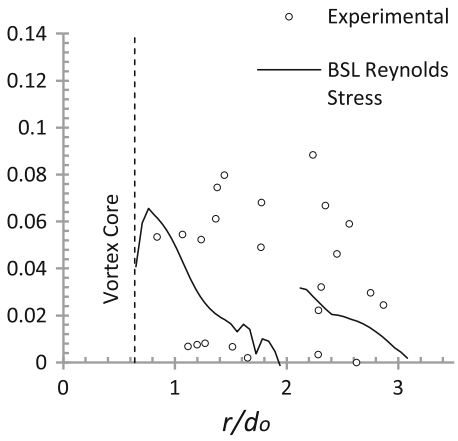

Fig. 16 Radial velocity comparison for z/H_{in} = 0.75

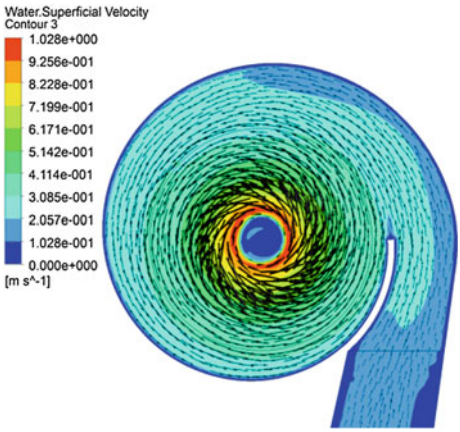

Fig. 17 Water superficial velocity for z/H_{in} = 0.26

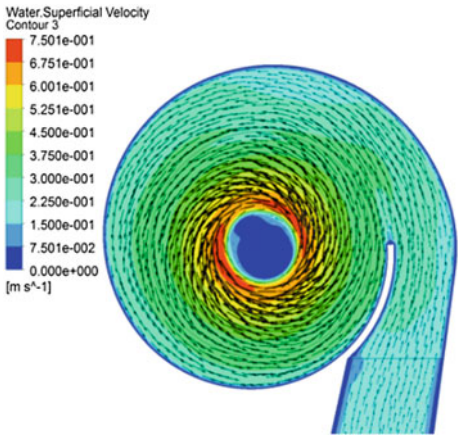

Fig. 18 Water superficial velocity for z/H_{in} = 0.56

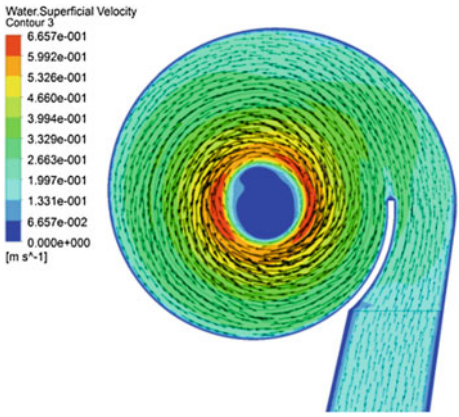

Fig. 19 Water superficial velocity z/H_{in} = 0.75

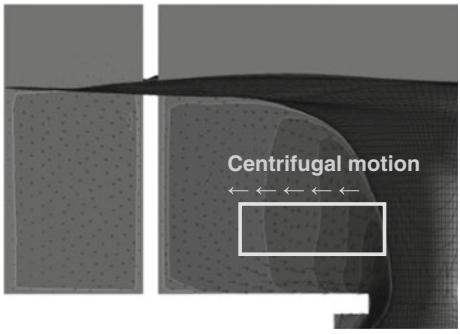

Fig. 20 Cross-sectional vector plot displaying a region of negative (outward) radial motion

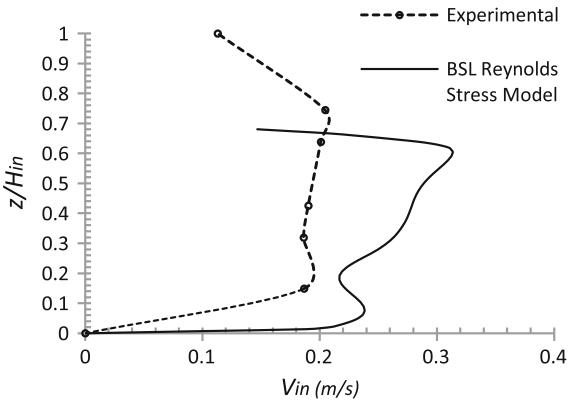

Fig. 21 Inlet water velocity comparison for test case A2

between z/H_{in} = 0.2 and 0.7 before reducing again at water surface. This depth-independent characteristic of the inlet velocity away from the tank boundaries and water surface agrees with results presented in Figs. 11, 12 and 13. Also highlighted in Fig. 21 is the computed depth velocity profile which overestimates the real

velocity profile quite significantly. This over estimation is expected because, for the same mass flowrate to exist in the simulation, water velocities must be larger to ensure continuity through the underpredicted inlet cross-sectional area equal to $(1 - 0.21)H_{in}B_{in}$ (determined in Sect. 6.2). Therefore, a better solution for the velocity fields can only be achieved when there is a corresponding improvement in predicting the water.volume fraction and air/water interface.

6.4 Uncertainty and Transient Features

Although steps were taken to ensure that all test and modelling processes were to be practically free from error, uncertainty is always going to be an unknown variable in such experimental/numerical comparative studies. Regarding the experimental model, it will be accepted that minimal error is integrated into the results of this paper from the head and discharge monitoring. The flow meter used has an accuracy rating of 0.1 %, and the head readings were obtained from a depth gauge on the physical water surface. The nature of particle tracking velocimetry is susceptible to significant uncertainty if sources of error are not accounted for. Errors in this context can originate from lens distortion, improper calibration of the field of view, out of plane displacement, poorly focused light sheet and pulse jitter all of which were reduced to a practically reasonable level during experimental setup and calibration. The particle velocity lag is a factor that could not be accounted for completely. The particles used are approximately 2 mm in size and possess a specific gravity (S.g. = 1.05) slightly greater than that of water. Therefore, the measured velocities would differ from the actual fluid velocities due to gravitational and other accelerating forces. This lagging/drifting characteristic is proportional to the particle diameter, relative density, fluid viscosity and local particle acceleration [24]. A check, using Eqs. 2.1 and 2.2 in Ref. [24], was carried out on this for both the gravitational lag and for large streamline drift near the vortex core, and its effect was found to be negligible. In short, the combined contribution of all these uncertainties would not have been large enough to justify for the poor agreement found in Sects. 6.1 and 6.3.

Numerical modelling using the Finite Volume Method poses a number of significant uncertainties. Systematic, physical errors arising from geometry approximation were considered. It is understood that the three-dimensional models generated cannot make an accurate representation of the geometry of the real, physical model due to variations of model quality during fabrication. This was investigated, and it was found that the computer-generated model and physical model differed on the periphery by an average of ± 4 %. This was concluded to be reasonable. Numerical error can also be introduced by round-off errors as a result of precision floating-point numbers which can only represent discrete points on the real number line. The double-precision method was employed to give 15 significant decimal digits precision to minimise such errors. To a greater degree, numerical error can be introduced by spatial discretization error by choosing a poor mesh to

capture large gradients in the flow field. From the solution sensitivity analysis (Sect. 6.1), a mesh independent solution can be obtained when the finely structured mesh case is used. Thus having exercised this mesh structure throughout testing, in addition to mesh adaptation at the water surface, it is assumed that spatial discretization error was reasonably diminished. It is also important to note here that a structured grid is of vital importance for accurate vortex flow analysis where routinely, large streamline curvature is experienced. Where the unstructured case is used in such circumstances, excessive numerical diffusion may arise from the grid not been adequately aligned with the general flow pattern. Truncation error, resulting from a difference in the partial differential equation and the algebraic equation, could contribute significant error in the computation; however, second-order schemes for both advection and turbulence modelling were used in all cases.

It is recognised that there is potentially a large degree of uncertainty related to uncountable, collective or accumulative error from the sources above which may at least partially explain the poor agreement found between the numerical and physical models in Sect. 6. However, an examination of the steady-state momentum, mass residuals and monitor point for tangential velocity at the vortex core reveals that the solution does not converge to the target residual of 10^{-5} in the

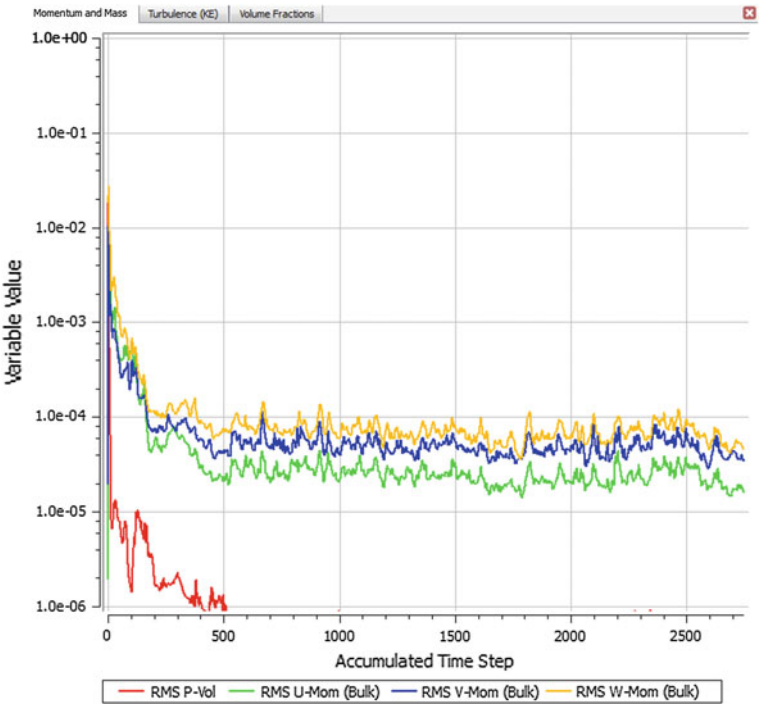

Fig. 22 Evidence of poor convergence and fluctuating residuals

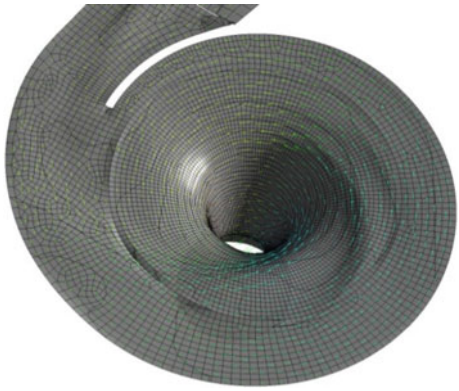

Fig. 23 Surface waves and instabilities evident in the numerical solution

majority of cases. The residuals also appear to be fluctuating vigorously (see Fig. 22). Furthermore, a screenshot of the free surface represented as an isosurface is shown in Fig. 23 for the steady-state solution. The evidence of instabilities and waves on the isosurface implies that the steady-state solution is struggling to be resolved. Similar surface waves and instabilities are also very distinct in the physical model. It may be concluded from this that there are heavy (local and/or global) transient features in the flow field, for example, surface and subsurface waves and instabilities, which cannot be resolved by the steady-state model. It would seem more probable that these transient features are the source of the disagreements found, particularly in resolving the water surface, and therefore further transient analysis is required in order to improve the accuracy of the solution.

7 Conclusion

An integrated experimental and CFD modelling investigation into turbulent free-surface vortex flows is implemented. The investigation concludes that the Reynolds stress model is the most suitable amongst those tested for analysing strong air-core water vortices in a multiphase flow model. This is due to the fact that the model accounts for streamline curvature and anisotropic turbulence. Although the shear stress transport with curvature correction offers an improved solution over the standard SST model, the Reynolds stress approach still renders better accuracies. Mesh sensitivity analysis indicates that an unstructured mesh is unsuitable for vortex flow due to excessive numerical diffusion (false diffusion), and a finely structured radial grid is required. The solution was found to be independent of the mesh when a fine case is used (1.8 % cell/outlet size ratio). Despite the superiority of the Reynolds stress model over the other turbulence closure methods, the model still presents a significant discrepancy in predicting the water surface (21–26 % under prediction). The computed tangential velocity agrees well with the experimental data except for a marginal over prediction at the inlet. The numerical model

also presents similar trends in simulating the radial velocity profile but tends to severely under predict the real solution.

Regarding the analytical analysis, the Vatistas n = 2 solution gives a good estimation for the water surface and tangential velocity profiles. However, because the model is one-dimensional and assumes axisymmetric properties, the solution may exhibit uncertainty in complex three-dimensional domains. Furthermore, the validity of the model would begin to break down close to the free-surface and vessel walls where boundary layer properties prevail.

From an overview of the uncertainty analysis, it is concluded that the disagreements between numerical and actual data may owe to a degree of uncountable, accumulative numerical error. However, considering the poor convergence of the steady-state solution, residual fluctuations and local transient features in the flow field, it is more probable that the poor agreement is due to local or global transient features in the flow field which cannot be resolved by the steady-state approach. Therefore, further transient analysis is required in order to improve the numerical solution.

Acknowledgments The authors would like to express their gratitude to the Irish Research Council for the financial support of this work. In addition, the authors would like to thank the School of Engineering and Design and Estates Management at IT Sligo for facilitating the fluid dynamics research laboratory.

References

1. Knauss, J. (1987). *Swirling flow problems at intakes*. Balkema/Rotterdam: IAHR Hydraulic Structures Design Manual. Taylor & Francis.
2. Echavez, G., & Ruiz, G. (2008). High head drop shaft structure for small and large discharges. *11th International Conference on Urban Drainage*. Edinburgh, Scotland, UK.
3. Ogawa, A. (1993). *Vortex Flow*. Boca Raton: CRC Press, Inc.
4. Rankine, W. J. M. (1858). *Manual of Applied Mechanics*. London: C. Griffen Co.
5. Scully, M. P. (1975). Computation of Helicopter Rotor Wake Geometry and its influence on Rotor Harmonic Airloads. Massachusetts Institute of Technology. Report No. ASRL TR, 178–1.
6. Vatistas, G. H. (1986). Theoretical and experimental studies of vortex chamber flow. *American Institute of Aeronautics and Astronautics (AIAA) Journal, 24*(4), 635–642.
7. Burgers, J. M. (1948). A mathematical model illustrating the theory of turbulence. *Advances in Applied Mechanics, 1*(1), 171–199.
8. Rott, N. (1958). On the viscous core of a line vortex. *Zeitschrift fur Angewandte Mathematik und Physik, 9b*(5–6), 543–553.
9. Miles, J. (1998). A note on the Burgers-Rott vortex with a free surface. *Journal of Mathematical Physics, 49*, 162–165.
10. Stepanyants, Y. A., & Yeoh, G. H. (2008). Stationary bathtub vortices and a critical regime of liquid discharge. *Journal of Fluid Mechanics, 604*, 77–98.
11. Einstein, H. A., & Li, H. (1955). Steady vortex flow in a real fluid. *La Houille Blanche, 10*(4), 483–496.
12. Lewellen, W. S. (1962). A solution for three-dimensional vortex flows with strong circulation. *Journal of Fluid Mechanics, 14*, 420–432.

13. Hite, J. E., & Mih, W. C. (1994). Velocity of air-core vortices at hydraulic intakes. *Journal of Hydraulic Engineering, 120*(3), 284–297.
14. Anwar, H. O. (1965). Flow in a free vortex. *Water Power, 17*(4), 153–161.
15. Wang, Y. K., Jiang, C. B., & Liang, D. F. (2011). Comparison between empirical formulae of intake vortices. *Journal of Hydraulic Research, 49*(1), 113–116.
16. Trivellato, F. (1995). On the near field representation in a free surface vortex. *12th Australasian Fluid Mechanics Conference*, Australia: The University of Sydney.
17. Okamura, T., Kamemoto, K., & Matsui, J. (2007). CFD prediction and model experiment on suction vortices in pump sump. *Proceedings of the 9th Asian International Conference on Fluid Machinery*.
18. Hai-feng, L., Hong-xun, C., & Zheng, M. A. (2008). Experimental and numerical investigation of free surface vortex. *Journal of Hydrodynamics, 20*(4), 485.
19. Tanweer, S., Desmukh., & Gahlot, V.K. (2010). Simulation of flow through a pump sump and its validation. *IJRRAS 4* (1). Civil Engineering Department. M.A.N.I.T, Bhopal.
20. Shukla, S.N. Numerical prediction of air entrainment in pump Intakes. Pune, India.
21. Bayeul-Lainé, A.C., Simonet, S., Bois, G., & Issa, A. (2012). Two-phase numerical study of the flow field formed in water pump sump: influence of air entrainment. *26th IAHR Symposium on Hydraulic Machinery and Systems*. August 19–23, Beijing.
22. Chen, Y. I., Wu, C., Ye, M., & Ju, X. (2007). Hydraulic characteristics of vertical vortex at hydraulic intakes. *Journal of Hydrodynamics, 19*(2), 143–149.
23. Spalart, P. R., & Shur, M. L. (1997). On the Sensitization of Turbulence Models to Rotation and Curvature. *Aerospace Science and Technology, 1*(5), 297–302.
24. Raffel, M., Willert, C.E., Wereley, S.T., & Kompenhans, J. (2007). *Particle Image Velocimetry: A Practical Guide* (2nd ed., pp. 15–18). Springer.

Calibration of an Air Entrainment Model for CFD Spillway Applications

Daniel Valero and Rafael García-Bartual

1 Introduction

High-velocity free surface flows are frequent in hydraulic structures. In large enough spillways, turbulent boundary layer growth reaches free surface where a critical point can be found, then significant quantities of air are trapped into the free surface and bubbles are then convected with the main flow. This air–water flow becomes a compressible mixture with macroscopic properties differing from those of water flow. In hydraulic engineering, flow aeration may induce some flow bulking [17, 39] and turbulence modulation [12, 14]. This turbulence modulation in multiphase flows can reduce drag over a rough surface [9, 29, 39] or enhanced turbulent kinetic energy dissipation depending on the flow and bubble-particle characteristics [1, 15, 16, 19]. Air bubbles in these flows are used for cavitation protection of hydraulic structures such as chutes, spillways, and bottom outlets [18, 26], and also for energy dissipation devices. Thus, aeration has become one of the main design variables in hydraulic structures. However, there is no currently available analytical solution or commonly accepted general method for the determination of the air quantities trapped.

Extensive experimental research has been made to characterize aerated flows past hydraulic structures obtaining variables such as air concentration, bubbles characteristics, and velocity distributions [6, 9, 12, 20, 26, 33]. Some attempts have also been made to study the air–water structure in an aerated supercritical flow [7, 10, 32, 38]. Nevertheless, air–water flows observed in prototypes are difficult to reproduce in laboratory physical models due to scale effects [11, 12, 21]. In addition, air–water measurements require expensive instrumentation with significant drawbacks [4]. Therefore, combined use of computational fluid dynamics

D. Valero (✉) · R. García-Bartual
Instituto Universitario de Investigación de Ingeniería del Agua y Medio Ambiente (IIAMA), Universitat Politècnica de València, Cno. de Vera s/n, 46022 València, Spain
e-mail: davahue@upv.es

P. Gourbesville et al. (eds.), *Advances in Hydroinformatics*,
Springer Water, DOI 10.1007/978-981-287-615-7_38

(CFD) and physical modeling approaches offer a powerful tool for multiphase flow analyses and reliable representation of hydrodynamic features in large hydraulic structures [2, 3, 30], hence taking into account dispersed phase effect over the carrier phase [25]. However, lack of validation and verification is still an issue pointed out by several researchers [12, 13, 27, 28, 31].

In this paper, a RANS model has been employed assessing its accuracy for self-aerated spillway flows. Hence, an extensive calibration of a turbulent air entrainment model coupled with a drift-flux model is presented. VOF method for free surface capturing is used [23], together with a RNG $\kappa - \varepsilon$ turbulence model [41]. Calibration has been carried out employing prototype data of mean air concentrations in uniform aerated flows over steep smooth invert chutes. Other variables have been compared in order to correctly assess the performance of the calibrated model. In addition, simulations for lower slopes have been conducted comparing as well the results with prototype data.

2 Model Description

Reynolds Averaged Navier-Stokes equations (RANS) [3, 34] have been numerically solved by means of the Finite Volume Method [35]; coupled with a RNG $\kappa - \varepsilon$ turbulence model, being κ the turbulent kinetic energy and ε the turbulent dissipation rate, both modeled by their respective transport equations [37, 41]. VOF method [23] as included in the commercial code FLOW-3D® has been used for free surface representation.

Turbulent air entrainment and a drift-flux model are also employed in order to take into account air entrained. The air entrainment model is responsible for predicting entrainment of air pockets smaller than the finest cell resolution while drift-flux model adds the dispersed air effect upon the carrier phase by adding a drag component to the governing equations [5]. Thus, it is not necessary to solve smaller scales of the fluid dynamics allowing coarser computational grids which help avoiding unaffordable, too costly simulations.

For the turbulent air entrainment model, a characteristic size of turbulent eddies can be defined by

$$L_T = C_\mu \sqrt{\frac{3}{2}} \frac{\kappa^{3/2}}{\varepsilon} \tag{1}$$

with $C_\mu = 0.085$ for the RNG $\kappa - \varepsilon$ turbulence model, which also calculates κ and ε in every step at every cell. This length scale should be taken as an approximation to a length scale of perturbations, for which no unanimous formulation is available [30]. L_T value depends strongly on the chosen turbulence model, while κ and ε quantities are also affected by the air entrainment model. Therefore, both models are implicitly coupled.

According to [22], the energy density associated with a disturbed fluid element raised over the free surface to a height L_T, can be expressed considering two components (gravity and surface tension)

$$P_d = \rho g_n L_T + \frac{K\sigma}{L_T} \tag{2}$$

where ρ is the macroscopic fluid density, g_n is the gravity component normal to the free surface, K is a calibration parameter, and σ is the liquid–gas surface tension. P_d represents thus a surface stabilizing force, while P_t (turbulent kinetic energy per unit volume) represents the perturbing component that makes the flow unstable.

$$P_t = \rho\kappa \tag{3}$$

Air entrainment occurs when $P_t > P_d$. Corresponding air entrained volume per unit time can be computed as

$$\delta V = C_{\text{air}} A_s \sqrt{2\frac{P_t - P_d}{\rho}} \tag{4}$$

where C_{air} is another calibration parameter and A_s is the free surface area at each cell. This air volume δV is taken into account affecting macroscopic density of the mixture and producing bulking of the flow. This macroscopic density is computed as

$$\rho = (1 - C)\rho_w + C\rho_a \tag{5}$$

where C is the computed entrained air at every cell, ρ_w the water density and ρ_a the air density. It is also assumed that air entrained form bubbles of a characteristic diameter. Thus, bubbles produce a drag force upon the carrier phase which opposes to the water movement. A relative velocity between both phases is computed and a so-called drift-flux model is introduced. More details about the drift-flux model can be found in [5].

3 Model Calibration

3.1 Model Setup

The USBR ogee spillway of 53.13° slope (0.75H:1V) [8, 36] was chosen for calibration purposes. According to [10, 39], a mean air concentration C_{mean} of 0.65 is expected to be naturally established in the downstream uniform flow region. The water level over the crest is fixed to $h_d = 1$ m, which gives as a result an specific flow rate of 2.18 m^2/s. The numerically modeled spillway is 20 m height thereby ensuring the existence of the inception point and the fully development of the

aerated uniform region. For validation purposes, different slope spillways of the same height have been used. Surface roughness of all the spillways has been set to 1 mm.

The employed 2D meshes consist on regular square cells. A 2D mesh is expected to reproduce correctly the flow patterns [31]. Numerical experiments were carried out using cell sizes ranging 2–10 cm. A structured Cartesian grid is defined independently of the spillway geometry and subsequently the geometry is embedded in the grid by the FAVOR technique [24]. This technique computes the fractional areas and corresponding fractional volumes open to the flow.

Flow rate is imposed at the upstream boundary condition and outflow is allowed for the flow leaving the domain at the downstream boundary condition. Velocity profiles convergence has been verified through comparison of results with different meshes. Figure 1 shows velocity profiles for different mesh resolutions in simulations conducted with the turbulent air entrainment model switched off. Whereas velocity profiles converge even for coarser meshes for the crest section, do not converge at the end of the spillway for cell sizes over 6 cm. However, 8 cm cell resolution simulations have been also included in the calibration procedure in order to assess a sensitivity analysis.

Characteristic values of the turbulent kinetic energy (κ) are shown in Fig. 2. The maximum value over the crest is considered as well as the value at the free surface cell at the totally developed region. Turbulent kinetic energy has shown a lower convergence rate; therefore, the air entrained model is expected to be very sensitive to cell resolution due to its strong dependence on this variable.

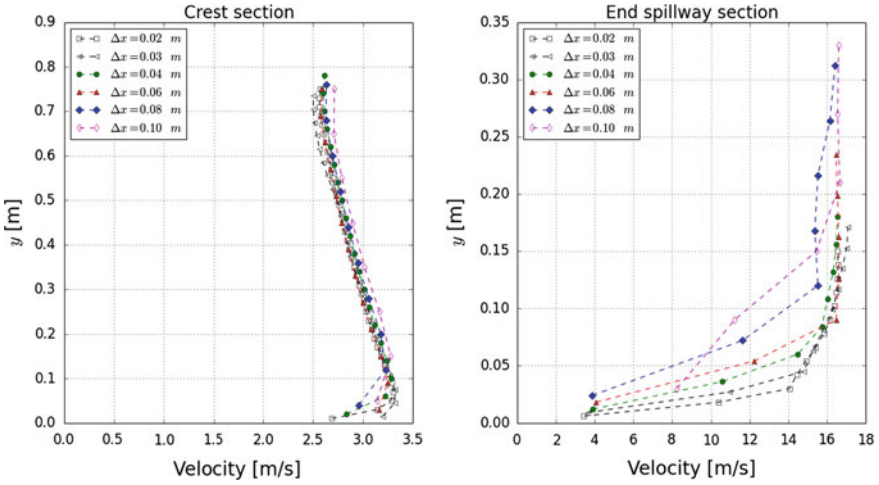

Fig. 1 Velocity profiles over the crest (*left*) and at the end of the spillway (*right*) for different mesh resolutions

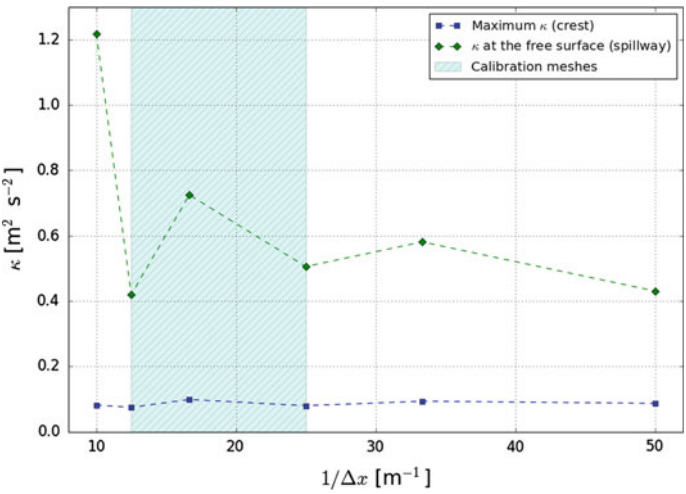

Fig. 2 Turbulent kinetic energy over the crest (maximum value) and at the end of the spillway (at the free surface cell) for different mesh resolutions

3.2 Calibration Data

Two calibration variables have been selected: mean air concentration (C_{mean}) at the uniform flow region, and spatial location of inception point (x_I). The first one has been considered the most important one, since it affects directly the flow bulking, spillway protection and the limit velocity. Although, inception point location must be also considered. Mean air concentration is dependent on spillway slope for a given discharge, while inception point location is very sensitive to flow conditions [39].

The boundary layer thickness δ is given by

$$\frac{\delta}{x_s} = 0.021 \left[\frac{x_s}{h_s}\right]^{0.11} \left[\frac{k_s}{x_s}\right]^{0.10} \tag{6}$$

where x_s is the curvilinear distance measured from spillway vertex, h_s is taken as indicated in Fig. 3, and k_s the surface roughness. For the simulations carried out, k_s was taken equal to 1 mm, as in the numerical model.

The inception point location can be estimated combining Eqs. (6) and (7) [39]:

$$d = \delta + {}^{(q - q_\delta)}/_{u_{fs}} \tag{7}$$

In this equation, d is the flow depth, u_{fs} is the velocity outside the boundary layer, while q and q_δ are computed as follows:

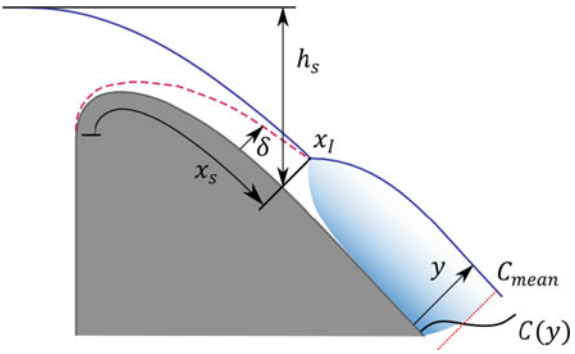

Fig. 3 Air–water flow characteristics over a spillway surface. Inception point location x_I and uniform aerated flow

$$q = \frac{(6n+1)}{5(n+1)}\delta\sqrt{2gh_s} \tag{8}$$

$$q_\delta = \frac{n}{n+1}\delta\sqrt{2gh_s} \tag{9}$$

In both equations, n is taken equal to 6.3 as recommended in [40].

3.3 Calibration Methodology

A total of 205 2D numerical simulations have been carried out employing a specific flow rate of 2.18 m^2/s as the inflow boundary condition. Structured finite volume mesh is made of cubic cells with uniform size Δx all over the entire domain. The inlet boundary condition is located upstream far enough from the spillway vertex in order to ensure it is not affecting the final solution where the supercritical aerated flow takes place.

These 205 flow numerical simulations have been implemented using pairs of possible values of the two parameters: C_{air} ranging from 0 to 1, and $K \cdot \sigma$ varying from 0 to 5 N/m. For each of them, the inception point position and the mean air concentration value in the uniform flow along the spillway were estimated. Initially, three cell sizes were used for the numerical simulations: 4, 6, and 8 cm. Additional simulations with cell sizes $\Delta x = 10$ cm and $\Delta x = 2$ cm were also conducted to confirm trends of the optimal estimated parameters.

In Fig. 4 it is shown the mean air concentration error surface for the size cell $\Delta x = 8$ cm case. In Fig. 5 it is shown the surface error for the inception point location for the same case. Other cases have similar error surfaces but are not shown for clarity reasons. In both figures, a least squared error surface has been fitted. As

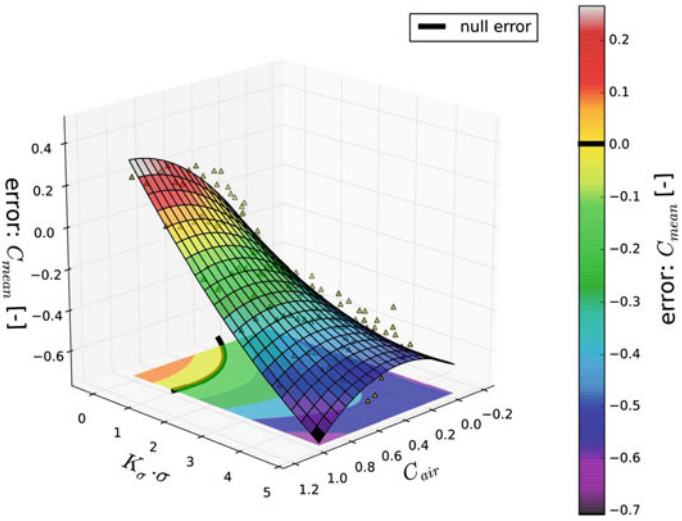

Fig. 4 Mean air concentration surface error for $\Delta x = 8$ cm. *Solid black lines* are null error lines

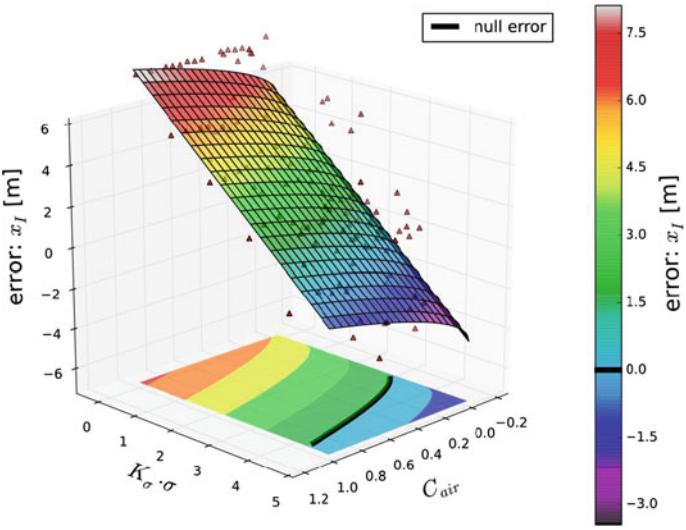

Fig. 5 Inception point location surface error for $\Delta x = 8$ cm. *Solid black lines* are null error lines

shown in the graphics, there is no actual solution for (C_{air}, $K \cdot \sigma$) yielding simultaneous reproduction of both, mean air concentration (C_{mean}) and inception point location (x_I). In order to estimate optimal values in the calibration, variable C_{mean} is given priority, ensuring that the estimated parameters reproduce the expected mean air concentration in the flow. For such condition, error in x_I is then minimized.

Table 1 Optimal values obtained in the calibration

Δx (cm)	4	6	8
C_{air} (–)	0.525	0.619	0.631
$K \cdot \sigma$ (N/m)	0.073	0.570	0.978

Table 2 Optimal values obtained in the calibration enforcing $K = 1$

Δx (cm)	4	6	8
C_{air} (–)	0.525	0.291	0.334
$K \cdot \sigma$ (N/m)	0.073	0.073	0.073

3.4 Calibration Results

Table 1 shows the optimal parameters found, as a function of the cell size used for the numerical simulations.

For the case $K = 1$, the original formulation of Eq. (2) stands, as formulated initially by [22] and thus there is only one calibration parameter. In such case $K \cdot \sigma = 0.073$ N/m and the resulting optimal values of C_{air} as a function of the cell size are shown in Table 2.

The trend of C_{air} values is in agreement with those of the kinetic turbulent energy (κ) corresponding to each cell size simulation (Fig. 2). Thus, when the value of κ at the free surface cell does not vary with cell size, C_{air} is not expected to change. It may be noticed as well that for $\Delta x = 4$ cm cell size simulations, physically based surface tension value properly yields the correct air concentration minimizing the error in the inception point location.

4 Model Validation

For the optimal parameters found, air concentration profiles in 2D simulations were compared with the theoretical ones reported by Chanson [10]. As shown in Fig. 6, a reasonably good agreement for the profile shape is found, while some more significant deviations are identified in the region closer to the free surface and the bottom. In Fig. 6, y_{90} states for the depth where concentration C reaches 0.90.

Additionally, further 2D simulations have been carried out for validation purposes, introducing spillway slopes ranging from 30° to 48.5° and the same flow rate as in the calibration tests, using cell sizes of 4 cm with the prior obtained optimal air-entrainment model parameters, namely $C_{air} = 0.525$ and $K \cdot \sigma = 0.073$ N/m. Table 3 shows the obtained results. In Fig. 7 it is shown the equilibrium concentration values proposed by [10, 20] and the obtained in the validation simulations.

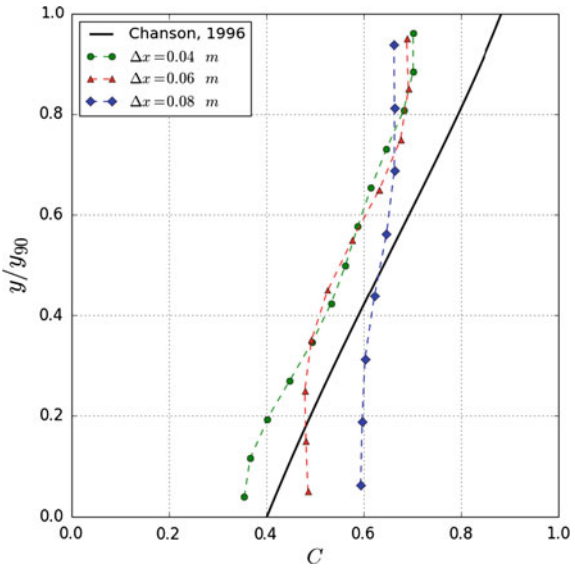

Fig. 6 Air concentration profile for different computational cell sizes

Table 3 Equilibrium concentration values in validation simulations (FLOW-3D), proposed by Chanson [10] (*) and proposed by Hager [12] (**)

Slope	30.00	34.62	39.25	43.88	48.50
C_{mean} (FLOW-3D)	0.38	0.47	0.52	0.56	0.63
C_{mean} (*)	0.41	0.51	0.58	0.61	0.63
Error (%) (**)	7.13	8.20	10.57	9.04	1.36
C_{mean} (**)	0.39	0.43	0.46	0.49	0.52
Error (%) (**)	1.38	−9.70	−12.80	−13.16	−19.81

Relative errors to the values proposed by the previous authors are also presented

It has been observed that the calibrated model is predicting values in agreement with the prototype data found in the literature. The model is also predicting the decrease of the equilibrium concentration with the reduction of the spillway slope. All the relative errors remain below 20 % with an average value of 9.32 %, which is consistent with the error magnitude of the prototype data measurements.

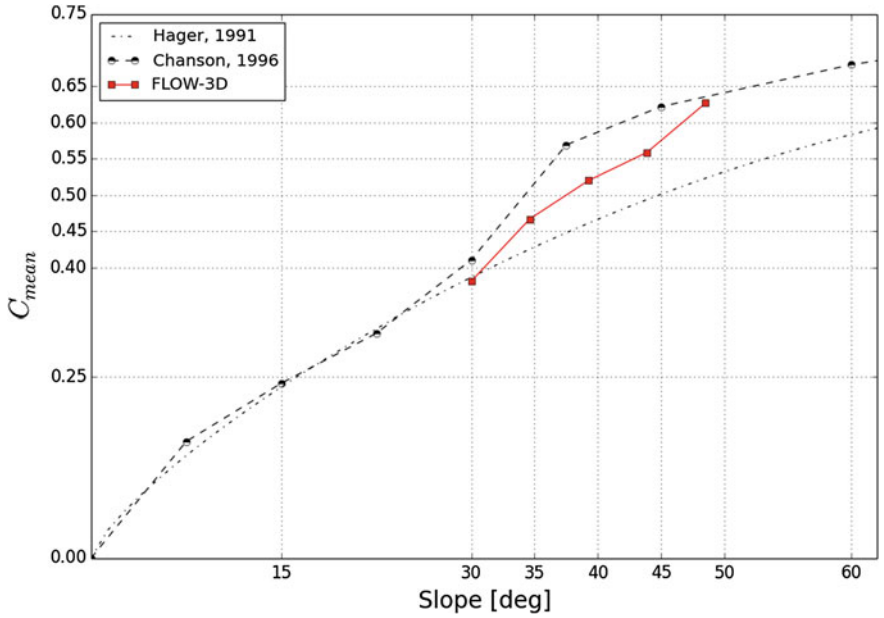

Fig. 7 Equilibrium air concentration versus spillway slope

5 Conclusions

A turbulent air entrainment model coupled with RNG $\kappa - \varepsilon$ turbulence model and VOF representation for free surface has been calibrated with over 200 numerical simulations. The spillway flow in the USBR ogee spillway of 53.13° slope [8, 36] was chosen for calibration purposes.

Results show significant cell size dependence, which can be explained by the lower convergence rate of the turbulent kinetic energy, main input variable of the calibrated model. In general, there is a reasonable agreement in the air concentration profiles. The values obtained for the two parameters involved in the turbulent air entrainment model allow realistic spillway flow simulations, being thus a useful tool for analysis of large hydraulic structures in order to optimize its operation.

Accurate laboratory measurements concerning air concentration profiles are difficult to obtain, but they can actually yield important benefits in engineering practice. Calibrated CFD models as the one presented herein, can be very useful to understand and expand such results, improving the basis for hydraulic design and actual performance of spillways and stilling basins.

Acknowledgments The authors thank Dr. Fabian Bombardelli, UC Davis, for his kind attention and advice.

The research described in this paper has been carried out under the research project "Natural and forced air entrainment in dam spillways and potential range of operation enlargement for hydraulic jump energy dissipators", BIA2011-28756-C03-01, supported by the Spanish Ministry of Economy and Competitiveness and by ERDF funding of the European Union.

References

1. Balachandar, S., & Eaton, J. K. (2010). Turbulent dispersed multiphase flow. *Annual Review of Fluid Mechanics*, *42*, 111–133.
2. Bombardelli, F. A. (2012). Computational multi-phase fluid dynamics to address flows past hydraulic structures. In *4th IAHR International Symposium on Hydraulic Structures*, February 9–11, 2012, Porto, Portugal. ISBN: 978-989-8509-01-7.
3. Bombardelli, F. A., Meireles, I., & Matos, J. (2011). Laboratory measurements and multi-block numerical simulations of the mean flow and turbulence in the non-aerated skimming flow region of steep stepped spillways. *Environmental Fluid Mechanics, 11*(3), 263–288.
4. Borges, J. E., Pereira, N. H., Matos, J., & Frizell, K. H. (2010). Performance of a combined three-hole conductivity probe for void fraction and velocity measurement in air–water flows. *Experiments in Fluids, 48*(1), 17–31.
5. Brethour, J. M., & Hirt, C. W. (2009). Drift model for two-component flows. *FSI-09-TN83Rev. Flow Science, Inc*.
6. Bung, D. B. (2011). Developing flow in skimming flow regime on embankment stepped spillways. *Journal of Hydraulic Research, 49*(5), 639–648.
7. Bung, D. B. (2013). Non-intrusive detection of air–water surface roughness in self-aerated chute flows. *Journal of Hydraulic Research, 51*(3), 322–329.
8. Bureau, O. R. (1977). *Design of small dams*. Washington, DC: US Department of the Interior.
9. Chanson, H. (1994). Drag reduction in open channel flow by aeration and suspended load. *Journal of Hydraulic Research, 32*(1), 87–101.
10. Chanson, H. (1996). *Air bubble entrainment in free-surface turbulent shear flows*. London: Academic Press.
11. Chanson, H. (2009). Turbulent air–water flows in hydraulic structures: dynamic similarity and scale effects. *Environmental Fluid Mechanics, 9*(2), 125–142.
12. Chanson, H. (2013). Hydraulics of aerated flows: Qui pro quo? *Journal of Hydraulic Research, 51*(3), 223–243.
13. Chanson, H., & Lubin, P. (2010). Discussion of "Verification and validation of a computational fluid dynamics (CFD) model for air entrainment at spillway aerators". *Canadian Journal of Civil Engineering, 37*(1), 135–138.
14. Chanson, H., & Toombes, L. (2002). Air-water flows down stepped chutes: Turbulence and flow structure observations. *International Journal of Multiphase Flow, 28*(11), 1737–1761.
15. Chen, J.-H., Wu, J.-S., & Faeth, G. M. (2000). Turbulence generation in homogeneous particle-laden flows. *AIAA Journal, 38*(4), 636–642.
16. Crowe, C. T. (2000). On models for turbulence modulation in fluid–particle flows. *International Journal of Multiphase Flow, 26*(5), 719–727.
17. Falvey, H. T. (1980). *Air-water flows in hydraulic structures*. USBR Engineering Monograph, No. 41, Denver, CO.
18. Falvey, H. T. (1990). *Cavitation in chutes and spillways*. USBR Engineering Monograph, No. 42, Denver, CO.

19. Gore, R. A., & Crowe, C. T. (1989). Effect of particle size on modulating turbulent intensity. *International Journal of Multiphase Flow, 15*(2), 279–285.
20. Hager, W. H. (1991). Uniform aerated chute flow. *Journal of Hydraulic Engineering, 117*(4), 528–533.
21. Heller, V. (2011). Scale effects in physical hydraulic engineering models. *Journal of Hydraulic Research, 49*(3), 293–306.
22. Hirt, C. W. (2003). Modeling turbulent entrainment of air at a free surface. *FSI-03-TN61-R. Flow Science, Inc*.
23. Hirt, C. W., & Nichols, B. D. (1981). Volume of fluid (VOF) method for the dynamics of free boundaries. *Journal of Computational Physics, 39*(1), 201–225.
24. Hirt, C. W., & Sicilian, J. M. (1985). A porosity technique for the definition of obstacles in rectangular cell meshes. In *Proceedings of International Conference on Numerical Ship Hydrodynamics* (19 p.). Washington, DC: National Academy of Science.
25. Jha, S. K., & Bombardelli, F. A. (2010). Toward two-phase flow modeling of nondilute sediment transport in open channels. *Journal of Geophysical Research: Earth Surface*, *115* (F3), 2003–2012.
26. Kramer, K., & Hager, W. H. (2005). Air transport in chute flows. *International Journal of Multiphase Flow, 31*(10), 1181–1197.
27. Ma, J., Oberai, A. A., Drew, D. A., Lahey, R. T., & Hyman, M. C. (2011). A comprehensive sub-grid air entrainment model for RaNS modeling of free-surface bubbly flows. *The Journal of Computational Multiphase Flows, 3*(1), 41–56.
28. Ma, J., Oberai, A. A., Lahey, R. T., Jr, & Drew, D. A. (2011). Modeling air entrainment and transport in a hydraulic jump using two-fluid RANS and DES turbulence models. *Heat and Mass Transfer, 47*(8), 911–919.
29. Madavan, N. K., Deutsch, S., & Merkle, C. L. (1984). Reduction of turbulent skin friction by microbubbles. *Physics of Fluids, 27*(2), 356–363.
30. Meireles, I. C., Bombardelli, F. A., & Matos, J. (2014). Air entrainment onset in skimming flows on steep stepped spillways: An analysis. *Journal of Hydraulic Research, 52*(3), 375–385.
31. Oertel, M., & Bung, D. B. (2012). Initial stage of two-dimensional dam-break waves: Laboratory versus VOF. *Journal of Hydraulic Research, 50*(1), 89–97.
32. Pfister, M. (2008). Bubbles and waves description of self-aerated spillway flow. *Journal of Hydraulic Engineering, 46*(3), 420–423.
33. Pfister, M., & Hager, W. H. (2010). Chute aerators. I: Air transport characteristics. *Journal of Hydraulic Engineering, 136*(6), 352–359.
34. Pope, S. B. (2000). *Turbulent flows*. Cambridge: Cambridge University Press.
35. Versteeg, H.K., & Malalasekera, W. (2007). *An introduction to computational fluid dynamics: the finite volume method*. Harlow: Pearson Education.
36. Vischer, D., Hager, W. H., & Cischer, D. (1998). *Dam hydraulics*. Chichester, UK: Wiley.
37. Wilcox, D. C. (1998). *Turbulence modeling for CFD*. La Canada, CA: DCW industries.
38. Wilhelms, S. C., & Gulliver, J. S. (2005). Bubbles and waves description of self-aerated spillway flow. *Journal of Hydraulic Research, 43*(5), 522–531.
39. Wood, I. R. (1991). Air entrainment in free-surface flows. In *IAHR Hydraulic design manual No. 4, hydraulic design considerations*. Rotterdam, The Netherlands: Balkema Publications.
40. Wood, I. R., Ackers, P., & Loveless, J. (1983). General method for critical point on spillways. *Journal of Hydraulic Engineering, 109*(2), 308–312.
41. Yakhot, V., Orszag, S. A., Thangam, S., Gatski, T. B., & Speziale, C. G. (1992). Development of turbulence models for shear flows by a double expansion technique. *Physics of Fluids A: Fluid Dynamics, 4*, 1510.

3D Numerical Simulations of Particle–Water Interaction Using a Virtual Approach

Varvara Roubtsova and Mohamed Chekired

1 Introduction

The hydraulic conductivity of porous media is often predicted either based on empirical relationships or hydraulic radius theories, or using capillary models or statistical models, and, more recently, network or fractal models. A great deal of experimental work has been performed by several investigators [1–8], in an effort to reflect the complexity of permeability in models with general applicability. These widely used models represent simplified macroscopic approaches in which the porous medium is treated as an easy-to-use continuum. However, the continuum approach suffers from a major limitation, which is to disregard the physics of flow at pore level, because all its complexities and fine details at the pore scale are hidden in bulk terms, such as empirical coefficients [2], shape coefficients, permeability, tortuosity, etc. In fact, although these investigations give us a clearer understanding of some of the factors that control permeability, a universal relationship between permeability and all these factors seems to be an illusion.

1.1 Permeability Models

To model the flow rate through a porous medium, we need to know the parameters of the pore structure, such as the pore sizes throughout the medium, the connectivity of the pore channels, and the tortuosity of these channels (morphology and

V. Roubtsova (✉) · M. Chekired
Hydro-Quebec Research Institute (IREQ), Quebec, Canada
e-mail: roubtsova.varvara@ireq.ca

M. Chekired
e-mail: chekired.mohamed@ireq.ca

P. Gourbesville et al. (eds.), *Advances in Hydroinformatics*,
Springer Water, DOI 10.1007/978-981-287-615-7_39

topology). An accurate description of the pore space is a crucial, and rich, source of information about the porous medium. This information is required to investigate the velocity, pressure, and distribution of the fluid flow. Modeling flow rate is an indispensable task, as it is vital to know what occurs inside the porous medium, which is a complex structure consisting of a solid skeleton and pores through which the flow occurs. However, this task is a difficult one. Numerous studies have been carried out to link the microscopic structural quantities to macroscopic properties. One of the most widely accepted relationships between permeability and the properties of pores was proposed by Kozeny and later modified by Carman. The well-known semi-empirical Kozeny-Carman model [2, 9] relates permeability to porosity, specific surface, tortuosity, and the shape factor. This model was developed based on Poiseuille flow through bundled parallel tubes of equal length and constant cross-section for which the Navier-Stokes equation can be solved. However, this model does not work accurately for all types of porous medium, and it gives very poor predictions for complex porous media. Many empirical models have been proposed [1, 4, 6–8, 10–12], but their correlations all have a significant drawback, which is that fully empirical models are technically valid only for the samples for which the results have been collected. A reasonable prediction can be generated by semi-empirical models of permeability, and are an alternative to permeability tests for granular soils. These models relate permeability to parameters like porosity, specific surface area, tortuosity, the shape factor, and particle size distribution. However, not only do they have limitations, they also lack accuracy.

1.2 Tortuosity

Because the shape of the pore space is highly chaotic, the concept of tortuosity has been introduced to represent the complex structure of porous media. Tortuosity is an important feature of the flow through such media, and serves as an adjustable parameter for matching experimental results to those predicted by bundled parallel tubes. It is governed mainly by the topology of the pore network, and defined as the ratio of the length of the fluid streamlines to the shortest path in the direction of the flow. To date, it has not been possible to measure tortuosity directly. Several attempts have been made, among them the development of models of fluid movement in soils which idealize the intricate structures of soil in the form of fractals [13] or networks [14]. These models represent void space in a regular two- or three-dimensional lattice of pores connected by throats. However, in a three-dimensional model, the shape of every pore or throat is generally simplified to either a sphere or cylinder, while natural systems have a random topology.

Frequently, tortuosity has been assumed to be responsible for discrepancies between predictions and observed behavior in various porous systems, and, as such, tends to have been used largely as a fitting parameter. In contrast, the use of the Kozeny–Carman equation involves a key factor which gathers together all the geometrical features, such as pore shape and pore size distribution, particle shape,

tortuosity, pore throat, pore interconnectivity, etc. The literature dealing with tortuosity is very broad. Although the concept of tortuosity is used in various areas of science, it is not yet well understood, mainly because the theoretical research includes simplifications that do not reflect the complex reality encountered in porous media. An examination of this research reveals that no consensus has yet been reached.

1.3 Inaccuracy of Experimental Tests

The accuracy of laboratory permeability tests involving coarse-grained materials is often open to discussion, as there are many factors that affect the measurement of hydraulic conductivity. Chapuis and Aubertin [15] note that the experimental hydraulic conductivity values obtained from just three replicate tests may vary broadly. This lack of precision partially depends on the test equipment and procedures applied, in addition to the natural variability of the material tested. Dunn and Mitchell [16] point out in a practice review of hydraulic conductivity measurements that, in addition to test apparatus and procedural errors, such as head and flow measurement errors, temperature variations, and non-uniform specimen sizes, there are many other factors that contribute to hydraulic conductivity estimation inaccuracy, such as (1) the influence of specimen preparation methods; (2) water quality; (3) consolidation during the test; (4) the influence of hydraulic gradient; and (5) methods of specimen saturation and verification of the degree of saturation. The wall effect is another source of errors. Strizhov and Khalilov [17] demonstrate that the non-curvature of a smooth wall causes a decrease in resistance in its vicinity and an increase in flow velocity (by a factor of 1.5–2, in the case of gas flows), which leads to the wall effect. In addition, the use of small samples with a diameter of less than 15 cm would lead to an underestimation of the in situ hydraulic conductivity by a factor of 10–10,000 [18].

An additional source of error is the laboratory test procedure itself, which forces the flow in a prescribed direction that probably does not represent the actual direction of the flow encountered in the field. This is because the laboratory test usually checks the vertical hydraulic conductivity, whereas the soil is anisotropic.

2 3D Virtual Laboratory: Simsols

Until the late of 1970s, when computer processing power increased dramatically, the pore-scale modeling of porous medium processes was considered a fruitless undertaking. To overcome the difficulties associated with the inherent complexity of porous media, a three-dimensional virtual laboratory, called SIMSOLS, was developed by IREQ to simulate the flow through porous media at a micro level. The pore sizes throughout the medium, the connectivity of the pore channels, and the

tortuosity of these channels were generated using the virtual laboratory, creating a virtual porous medium made up of idealized particles. This approach can provide a high level of detail, which would be impossible to acquire in any other way. Subsequently, a more accurate representation of the flow through porous media was realized using the full Navier–Stokes equations, involving inertial terms that are significant in high speed flows.

The primary purpose of this study is to demonstrate the ability of the virtual laboratory to mimic reality, and then to achieve a better understanding of the tortuosity of streamlines through a porous medium made up of multisized glass beads. This paper addresses the following topics: (1) the discrete element method used to model the motion of glass beads during generation of the porous medium; (2) the sample generation process; (3) the Navier–Stokes equations solved by the Marker and Cell method; (4) the representative elementary volume; and (5) the results obtained and a discussion.

2.1 Discrete Element Method

The three-dimensional Discrete Element Method (3D DEM), a common approach to the numerical modeling of non cohesive granular materials, is used in this study. In this approach, which was first introduced by Cundall and Strack [19], every particle in the system is modeled as a rigid body subject to various body and surface forces. The method is presented in detail in [20]. However, combining the DEM approach for granular materials with pore network methods remains a difficult task. Although the investigations carried out by various researchers have been limited mostly to 2D models, with a few involving 3D models with an idealized pore space, these models may not reflect the random nature of a real porous space. The main drawback of the DEM approach is its high computational cost. To address this drawback, we parallelized the model using GPU (Graphics Processing Units), and, for portability, we used the OpenCL (Open Computing Language) framework, which provides an abstract view of the parallel architecture. This allowed us to use CPU (Central Processing Units) with a GPU backend.

2.2 Sample Generation Process

The samples, consisting of spherical particles, were virtually generated layer by layer according to the particle size distribution shown in Fig. 1. This procedure was conducted randomly to ensure homogeneity. Each layer of particles (Fig. 2a) was generated so that the sample surface would be as flat as possible, but in such a way as to fill the gaps in the vicinity of the edges of the sample. To accomplish this, each

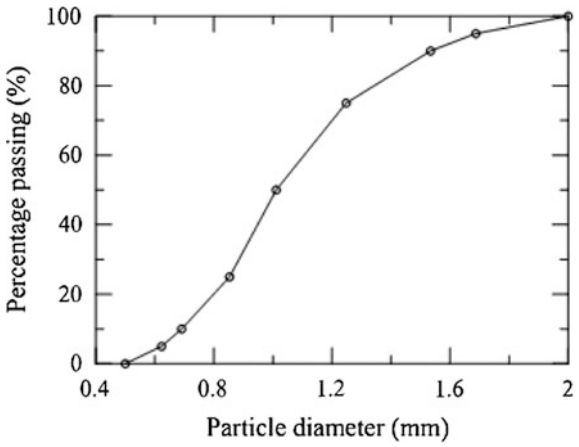

Fig. 1 Particle size distribution curve

layer was generated with a rotation of 90º in the horizontal plane with respect to the previous layer. In the first step, the sample was generated with a minimum density (e_{max}). At this stage, before a layer is subjected to gravity, it is important to confirm that the particles in the previous layer are all steady (Fig. 2b). The loosest possible packing is then achieved by carefully pouring the glass beads into a container, avoiding any disturbance, which gives e_{max}. This procedure avoids the possibility of segregation. From Fig. 2c, we can see that there was no segregation. Once the sample had been completely generated, it was vibrated until the maximum density (e_{min}) was achieved. A constant surcharge (dead weight) of 14 kPa was maintained at the surface during vibration, with a predominant frequency of 60 Hz and a double amplitude of 0.33 mm, based on the test procedures found in ASTM D 4253. To ensure total densification of the sample, the sample height was calculated at different time intervals during the vibration process. Figure 3 shows the evolution of the sample height with the time of vibration, and reveals that the height of the sample decreases throughout the process of vibration and stabilizes after 15 s. When

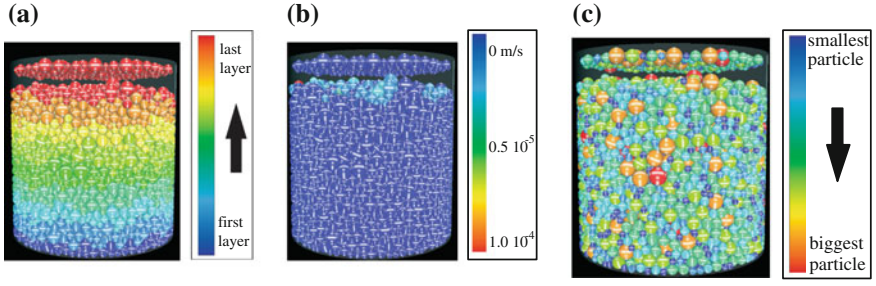

Fig. 2 Generation of porous media with different colors representing: **a** successive layers, **b** velocity, and **c** particle size

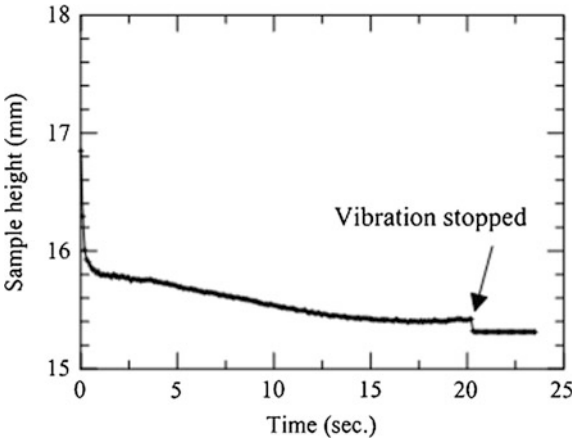

Fig. 3 Sample height variation during and after vibration

vibration is complete (after 20 s), the height of the sample suddenly decreases by 0.1 mm, as shown in Fig. 3.

2.3 Marker and Cell Method

The water flow through a pore channel is described by the Navier-Stokes equations for a viscous-incompressible fluid. One of the more successful methods for solving the Navier–Stokes equations in physical variables is the Marker and Cell (MAC) method, developed at the Los Alamos Laboratory in 1965 [21]. This method uses a staggered grid. Since its initial success, many modified schemas have been introduced. SIMSOLS uses the schema based on the splitting of physical parameters [22, 23], and is described in detail in [24].

The boundary conditions for the solid cylindrical walls and the particle boundaries are nonslip and non penetration, as proposed in [25]. In the simplest case, all liquid grid velocities located 'inside' the particles are forced to equal the particle velocity, or zero in the case of fixed obstacles, prior to evaluation of the temporary velocity, while all other points retain the old values. The 'interior' points are updated once the pressure has been determined in the same way as for all the other points, in order to ensure incompressibility.

To arrive at the proper particle–liquid interaction, the fluid stress tensor is integrated over the particle surface.

With the aim of verifying and validating this model, many experimental tests have been conducted in the 3D configuration [26]. Examples of an experiment and the corresponding numerical simulation of spherical particle–particle collision and rebound in a Newtonian fluid are shown in Fig. 4. The experimental and numerical results obtained are compared in Fig. 5. These results demonstrate the validity of our approach.

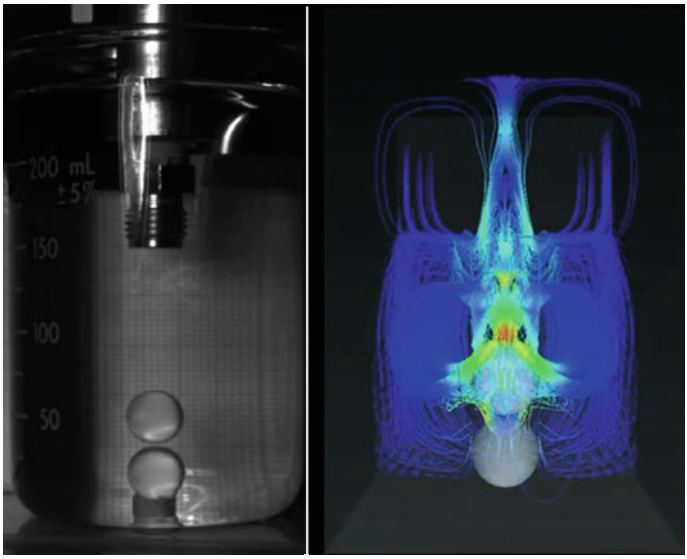

Fig. 4 Close view of the experimental and numerical tests

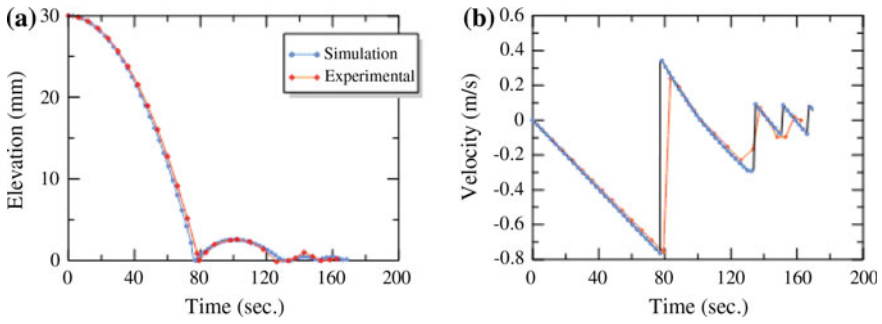

Fig. 5 Comparison of the experimental and numerical results as a function of time: **a** elevation; and **b** velocity

2.4 Representative Elementary Volume

To ensure the representativeness of the sample in terms of size, and then to set the volume as a representative parameter, simulations were performed on samples of different dimensions (height and diameter) to obtain the Representative Elementary Volume (REV). The REV that represents the continuous scale for which the macroscopic properties of a porous medium are reached when the parameter studied did not change with a further increase in sample size [27]. The REV must be sufficiently large to contain enough elements of the microstructure, and the effects of boundary conditions (wall effect) must be not significant. This approach, which

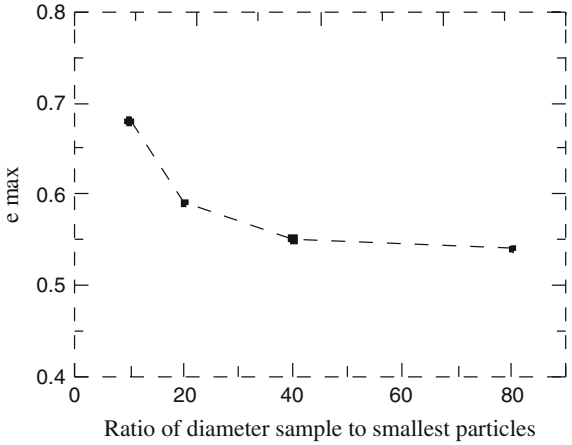

Fig. 6 The dependency of the maximum void ratio on the ratio of the sample diameter to the diameter of the smallest particle

has been applied for void ratio, particle size distribution, and permeability, as suggested by many authors [28–34], allows us to reduce the dimensions of the sample by reducing the number of particles involved. The handling of a large number of particles tends to compromise the computation times.

The sample diameter was determined through simulation for different ratios of the sample diameter to the smallest particle diameter (Fig. 6). A view of the sample we generated is shown in Fig. 7. The smallest particles, with a 623 micron diameter, are in blue. The sample height was determined by calculating the void radio, defined as the ratio of the volume of the pores to the volume of the solids, for 20 slices 2 mm in height along the sample, starting from the bottom, as shown in Fig. 8. Using this procedure, we can see the evolution of the void ratio as a function of height, and so define the minimum height of the sample. This exercise was carried out with two increments of height (2 and 4 mm) to make sure that all the information along the sample was captured and that identical results would be produced. The sample is 25 mm in diameter and 16.7 mm in height. Note that the

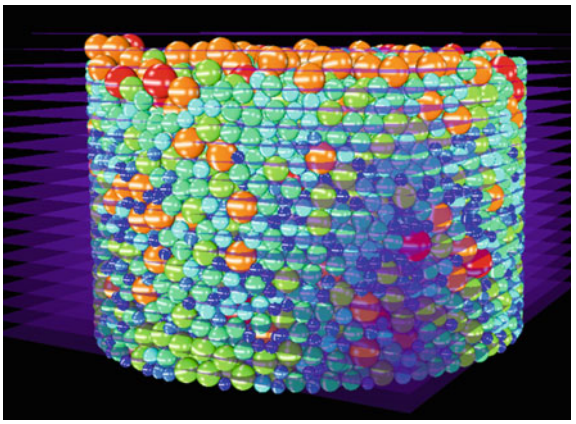

Fig. 7 View of the sample generated, consisting of spherical particles

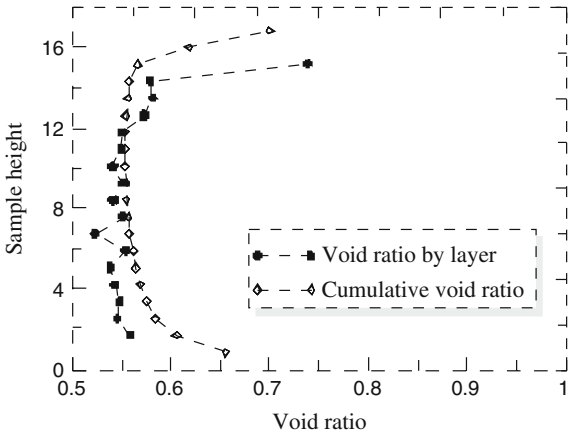

Fig. 8 Variation in void ratio along the sample height

sample height is more than 25 times the diameter of the smallest particle. The smallest particles are considered to affect tortuosity the most, since they can occupy the most space between the larger particles.

The void ratio of the sample is 0.61, when the voids created in the upper and lower parts of the sample are considered, and 0.56 if the sections at the top and bottom of the sample are not taken into account. To simulate the real behavior in the laboratory, the upper and lower parts of the sample were not removed in the current analysis.

3 Results and Perspectives

Our achievement is the direct measurement of the flow path length in porous media. Figure 9 shows an example of a three-dimensional view of the streamline patterns obtained by numerical simulations. A streamline is a path traced by a massless

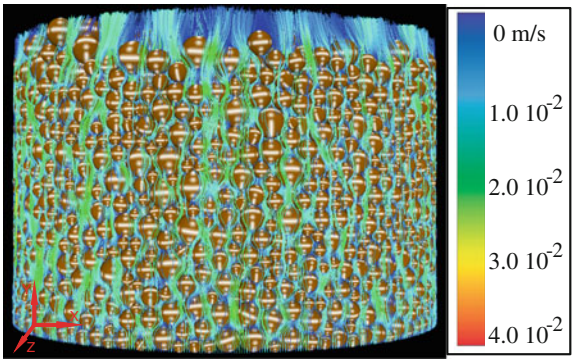

Fig. 9 Front view of the streamlines in the sample with the loosest packing

particle as it moves with the flow. Figure 10a, b show a projection of the streamlines of the loosest sample onto the XY and YZ planes respectively. Figure 11a, b present similar views for the densest sample.

In order to analyze the data obtained from images, the tortuosity values were subdivided into 30 ranges. Figure 12 presents the distribution of more than 30,000 tortuosity values. The tortuosity values before and after compaction show that the tortuosity does not vary significantly. The results given in Table 1 show that there is no significant difference between the tortuosity evaluated in the projections onto the XY and ZY planes. The hydraulic conductivity (m/s) is calculated as follows [35]:

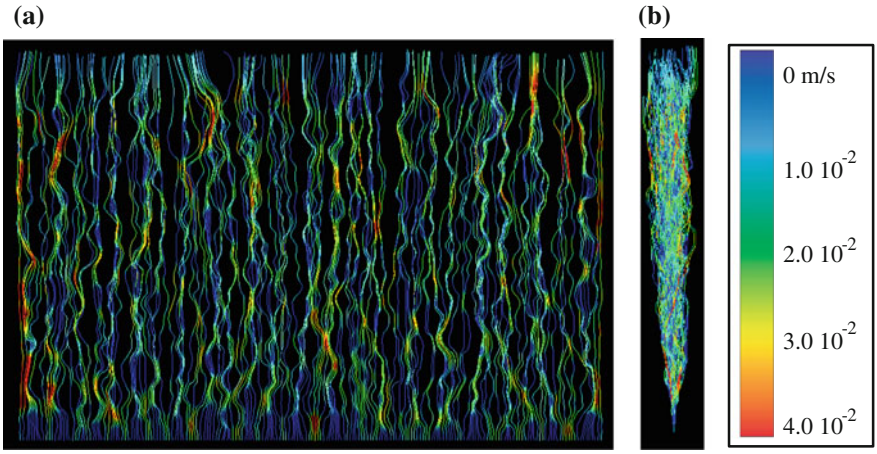

Fig. 10 The middle range of the projection of streamlines onto the: **a** XY; and **b** YZ planes for the loosest packing

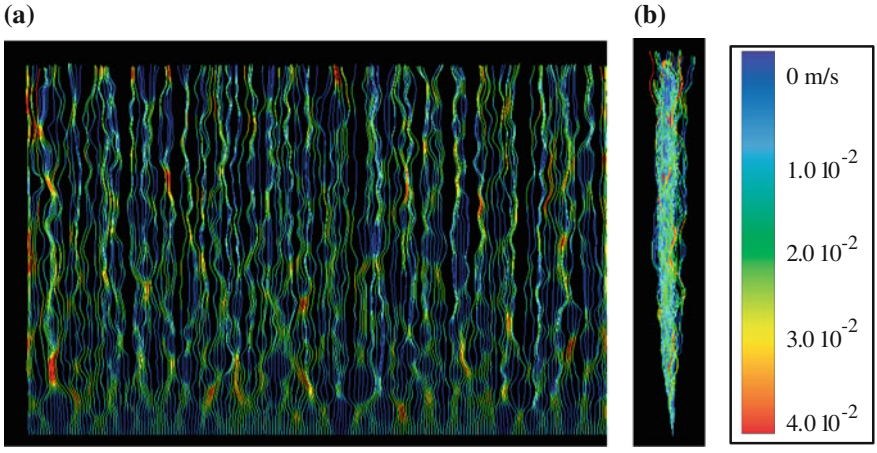

Fig. 11 The middle range of the projection of streamlines onto the: **a** XY; and **b** YZ planes for the densest packing

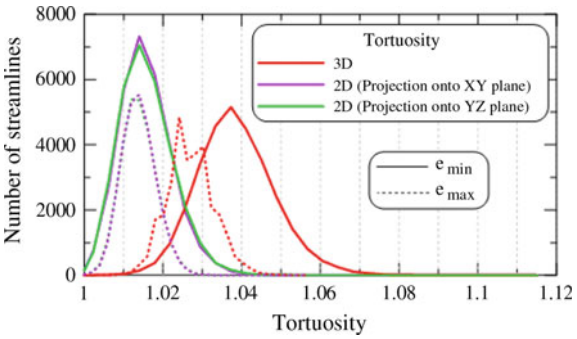

Fig. 12 Streamline distribution as a function of tortuosity

$$K = \frac{-\langle v \rangle s \rho g}{\Delta p} \tag{1}$$

where $\langle v \rangle$ is the average velocity in the soil (m/s), s is the length of the sample in the direction of flow (m), Δp is the pressure drop (Pa), g is the acceleration due to gravity, and ρ is the fluid density.

From these results, it is clear that the flow path does not take any preferential direction, and therefore is isotropic in nature. Naturally, the fluid flow will follow the path of least resistance, where the lowest amount of energy is required to produce the motion of the fluid particle. However, the hydraulic conductivity values obtained, which were computed for e_{min} and e_{max}, are not consistent with those presented in the literature in which hydraulic conductivity is related as a power-law of porosity (or void ratio). However, it should be noted that, to our knowledge, no pore-scale studies have been conducted for calculating the permeability of a granular medium in both loose and dense state to confirm our results.

Table 1 Numerical results for both loose (e_{max}) and dense (e_{min}) samples

Void ratio (%)	e_{max} = 0.68	e_{min} = 0.55
Sample height (mm)	16.7	15.4
Pressure gradient (Pa)	40	40
Average seepage velocity through the sample, m/s	6.5×10^{-4}	5.9×10^{-4}
Hydraulic conductivity (m/s)	1.8×10^{-3}	2.255×10^{-3}
Number of streamlines	30,322	30,011
Average length of streamlines in XY projection (mm)	17.14	15.70
Average length of streamlines in ZY projection (mm)	17.14	15.70
Average length of streamlines in 3D configuration (mm)	17.53	15.91
Average tortuosity in XY projection	1.01	1.006
Average tortuosity in ZY projection	1.01	1.006
Average tortuosity in 3D configuration	1.04	1.019
Ratio of average tortuosity to 2D projection (%)	2.21	1.28

It must be noted that the computed tortuosity does not depend only on spatial discretization, but also on the number of streamlines in each pore channel. In this work, we assume that the streamlines have been uniformly seeded over the inlet plane, and that the starting positions of each streamline were centered in the cell of that plane. There are still many improvements to be made in this area, such as refinement in both space and time, which will result in greater precision in evaluating tortuosity.

The results indicate that compaction of the multisized porous media leads to less tortuous pore channels. However, the influence of particle size distribution needs further investigation.

At the same time, considering the particle size distribution chosen, we may be able to conclude that the difference between the total streamline length and the streamline lengths computed on the plane projections is small. If confirmed, the flow in porous media can be investigated in two-dimensional simulations with confidence.

4 Conclusion

In this preliminary part of a research project currently under way, we presented a simulation tool, called SIMSOLS, which can generate a granular medium by means of the discrete element method, consisting of polydispersed spherical particles. This tool also simulates the flow of a fluid, in order to define its permeability, but other properties as well, such as tortuosity. The medium is generated according to the principle of gravitational deposition. The samples are initially generated in their loosest state, and then densified by means of vibration, as in laboratory tests.

This simulation tool enables us to extract the streamlines in three dimensions. However, the results obtained do not correspond to those already widely published, in which hydraulic conductivity can be approximated by a power-law function of the porosity. Refinement, in the form of simulations associated with laboratory tests performed on porous media with different size distributions, will allow us to better understand the various aspects of flow through a porous medium and the contradictions noted. We have no doubt that the work presented here is a realistic approach to mimicking reality, and that our approach will better quantify the effect of the parameters involved in flow in porous media. The use of three-dimensional simulations of the phenomena of fluid flowing directly into the pore spaces will relax a number of the simplifications inherent in network modeling, and is a promising avenue for the use of the complex morphology of pore spaces.

SIMSOLS seems to be the most realistic numerical tool available for generating granular media and modeling flow through these media, even though it is not yet able to account for all complexities involved and to make accurate predictions. Despite the fact that the results are controversial, we hope that this work will motivate further research exploring more types of granular media. Three-dimensional visualization through the virtual laboratory appears to be a promising approach.

References

1. Hazen, A. (1892). Some physical properties of sands and gravels, with special reference to their use in filtration. In *24th Annual Report, Massachusetts State Board of Health, Publication*. Doc. No. 34 (pp. 539–556).
2. Carman, P. C. (1956). *Flow of gases through porous media*. London: Butterworths Scientific Publications.
3. Shepherd, R. G. (1989). Correlations of permeability and grain size. *Ground Water, 27*(5), 633–638.
4. Alyamani, M. S., & Sen, Z. (1993). Determination of hydraulic conductivity from grain size distribution curves. *Ground Water, 31*, 551–555.
5. Terzaghi, K., Peck, R. B., & Mesri, G. (1996). *Soil mechanics in engineering practice*. New York: Wiley.
6. Kenney, T. C., Lau, D., & Ofoegbu, G. I. (1984). Permeability of compacted granular materials. *Canadian Geotechnical Journal, 21*, 726–729.
7. Chapuis, R. P. (2004). Predicting the saturated hydraulic conductivity of sand and gravel using effective diameter and void ratio. *Canadian Geotechnical Journal, 41*, 787–795.
8. Kresic, N. (1998). *Quantitative solutions in hydrogeology and groundwater modeling*. Florida: Lewis Publishers.
9. Carman, P. C. (1937) Fluid flow through granular bed. *Transactions of the Institution of Chemical Engineers*, *London*, *15*, 150–166.
10. Slichter, C. S. (1898). Theoretical investigation of the motion of ground waters. In *19th Annual Report*. U.S. Geology Survey, USA.
11. Vukovic, M., & Soro, A. (1992). *Determination of hydraulic conductivity of porous media from Grain-Size composition*. USA: Water Resources Publications.
12. Odong, J. (2007). Evaluation of the empirical formulae for determination of hydraulic conductivity based on grain size analysis. *Journal of American Science, 3*, 54–60.
13. Zinovik, D., & Poulikakos, D. (2012). On the permeability of fractal tube bundles. *Transport in Porous Media, 94*, 747–757.
14. Andrey, P. J., Cathy, H., Friday, E., Samuel, A. Mc D, & Philip, J. W. (2013). A novel architecture for pore network modelling with applications to permeability of porous media. *Journal of Hydrology, 486*, 246–258.
15. Chapuis, R. P., & Aubertin, M. (2003). On the use of the Kozeny-Carman equation to predict the hydraulic conductivity of soils. *Canadian Geotechnical Journal, 40*(3), 616–628.
16. Dunn, R. J., & Mitchell, J. K. (1984). Fluid Conductivity Testing of Fine-Grained Soil. *Journal of Geotechnical Engineering, 110*(11), 1648–1665.
17. Strizhov, A. A., & Khalilov, V. S. (1994). Structure of wall flow through a channel with a granular bed. *Fluid Dynamics, 29*(6), 745–748.
18. Daniel, D. E. & Trautwein, S. J. (1986). Field permeability test for earthen liner. In *Proceedings Institute 86, ASCE Specialty Conference on Use of In-situ Tests in Geotechnical Engineering. Virginia Polytechnic Institute and State University Blacksburg, New York* (pp. 146–160).
19. Cundall, P., & Strack, O. (1979). A Discrete numerical model for granular assemblies. *Geotechnique, 29*(1), 47–65.
20. Roubtsova, V., Chekired, M., Morin B., & Karray, M. (2011). 3D virtual laboratory for geotechnical applications: An other perspective. In *Particles 2011, II International Conference on Particle-based Methods Fundamentals and Applications, Barcelona, Spain, October 26–28, 2011*.
21. Harlow, F. H., & Welch, J. E. (1965). Numerical calculation of time-dependent viscous incompressible flow of fluid with a free surface. *The Physics of Fluids, 8*, 2182–2189.
22. Fortin, M., Peyret, R., & Temam, R. (1971). Résolution numériques des équations de Navier-Stokes pour un fluide incompressible. *Journal de Mécanique, 10*(3), 357–390.

23. Belotserkovsky, O. M. (1994). *Numerical modeling in the mechanics of continuous media*. Moscow: Physico-matematic literature. (in Russian).
24. Chekired, M. & Roubtsova, V. (2013) Virtual reality 3D interaction of fluid-particle simulations. In *V International Conference on Coupled Problems in Science and Engineering, Ibiza, Spain, June 17–19*.
25. Kalthoff, W., Schawarzer, S., & Herrmann, H. J. (1997). Algorithm for the simulation of particle suspension with inertia effects. *Physical Review E, 56*, 2234–2242.
26. Roubtsova, V., Chekired, M., Ethier, Y., & Avendano, F. (2012). SIMSOLS: A 3D virtual laboratory for geotechnical applications. In *ICSE6 Paris, August 27–31*.
27. Bear, J. (1972) *Dynamics of fluids in porous media*. New York: American Elsevier Publishing Company, Inc.
28. Baveye, P., & Sposito, G. (1984). The operational significance of the continuum hypothesis in the theory of water movement through soils and aquifers. *Water Resources Research, 20*(5), 521–530.
29. Mayer, A. S., & Miller, C. T. (1992). The influence of porous medium characteristics and measurement scale on pore-scale distributions of residual nonaqueous-phase liquids. *Journal of Contaminant Hydrology, 11*, 189–213.
30. Zhang, D., Zhang, R., Chen, S., & Soll, W. E. (2000). Pore scale study of flow in porous media: Scale dependency, REV, and statistical REV. *Geophysical Reseach Letters, 27*(8), 1195–1198.
31. Razavi, M. R., Muhunthan, B., & Al Hattamleh, O. (2007). Representative elementary volume analysis of sands using x-ray computed tomography. *Geotechnical Testing Journal, 30*(3), 212–219.
32. Nordahl, K., & Ringrose, P. S. (2008). Identifying the representative elementary volume for permeability in heterolithic deposits using numerical rock models. *Mathematical Geosciences, 40*, 753–771.
33. Salama, A., & Van Geel, P. J. (2008). Flow and solute transport in saturated porous media: 1. The continuum hypothesis. *Journal of Porous Media, 11*(4), 403–413.
34. Li, J. H., Zhang, L. M., Wang, Y., & Fredlund, D. G. (2009). Permeability tensor and representative elementary volume of saturated cracked soil. *Canadian Geotechnical Journal, 46*, 928–942.
35. Scheidegger, A. E. (1963). *The Physics of Flow Through Porous Media*. Toronto: University of Toronto Press.

A Stochastic Model for Particle Deposition in Turbulent Flows and Clogging Effects

Céline Caruyer, Jean-Pierre Minier, Mathieu Guingo and Christophe Henry

1 Introduction

Particle deposition in turbulent flows is a phenomenon met in various applications which can lead to fouling and affect normal operating conditions of key components of industrial processes. Particle deposition is due to several thermohydraulic or chemical processes. Fouling can be divided into different stages: with first deposition of single particles on a clean surface, then formation of a multilayer deposit, up to a possible complete blocking of the fluid cross section.

In our modeling approach, the complete fouling phenomenon is separated into four elementary phenomena (Fig. 1) which are:

- Deposition: governed by particle–fluid interactions and particle–surface interactions.
- Resuspension: a particle initially deposited on a wall loses contact with it. This phenomenon depends on the balance between the hydrodynamic efforts exerted on a deposited particle by the flow and the adhesion forces between the particle and the wall. These adhesion forces can be of different natures (van der Waals, electrostatic forces) and depend on parameters that can be difficult to know precisely, such as the characteristics of surface roughness.

C. Caruyer (✉) · J.-P. Minier · M. Guingo
EDF R&D, 6 Quai Watier, 78401 Chatou, France
e-mail: celine.caruyer@edf.fr

J.-P. Minier
e-mail: jean-pierre.minier@edf.fr

M. Guingo
e-mail: mathieu.guingo@edf.fr

C. Henry
Institute of Fluid Flow Machinery, 80-231 Gdańsk, Poland
e-mail: christophe.henry@mines-paris.org

P. Gourbesville et al. (eds.), *Advances in Hydroinformatics*,
Springer Water, DOI 10.1007/978-981-287-615-7_40

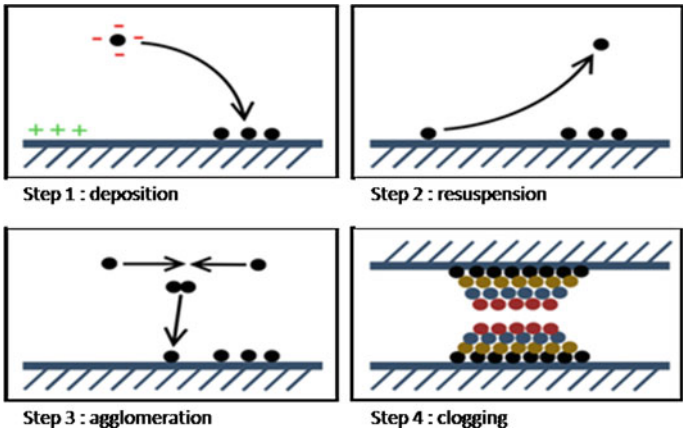

Fig. 1 Elementary phenomena of fouling

- Agglomeration: for a high concentration of particles in the flow, particle–particle interaction must be taken into account. For instance, the formation of aggregates can modify the particle mass flowrate towards the wall (since particle aggregates have a different inertia compared to "elementary" particles, their response to near-wall turbulence is also different, and thus their probability to reach the wall).
- Clogging: several layers of particle can accumulate on the surface, forming a multilayer deposit. Particle–particle interactions are important in this phenomenon. For a sufficiently significant particle deposit, the influence of the deposit morphology on the local flow structure must be modeled; an example of this influence being the acceleration of the local flow velocity during its passage through a cross section reduced by fouling.

In this model, the interactions between particles and near-wall coherent structures are explicitly simulated [7]. The modeling approach is not limited to particle–turbulence interactions, and particle–surface interactions are accounted for using an energy balance method: particles impacting the wall (or particle already deposited) deposit if their wall-normal kinetic energy is high enough to overcome the energy barrier, otherwise they rebound on the surface [8, 9].

The model accounts accurately for two major fundamental mechanisms: first, the hydrodynamic transport of particles (which describes particle–fluid interactions such as particle–turbulence interactions) and, second, the attachment mechanism (where physico-chemical interactions between two bodies occur). Roughness is also specifically included in the stochastic description of the surface since it plays an important role, in particular in repulsive cases where the energy barrier can be lowered [9].

The present article deals with the clogging issue and, more precisely, with the influence of multilayer deposits on the flow. The first part describes the multilayer deposition model while the second part is dedicated to the influence of a deposit on the fluid flow. Different approaches that are able to perform this coupling are briefly described. Then a calculation which brings out the impact of a deposit on the flow is performed, using a porous medium approach.

2 Multilayer Deposition

Recent developments [8] have shown that the model is not only able to reproduce single-particle deposition and resuspension but can also be applied to simulate the formation and the growth of multilayer deposits. Such deposits result from the competition between particle–fluid, particle–surface, and particle–particle interactions. According to the chemical properties of the surfaces involved (both particles and walls), different morphologies of the deposit can exist (monolayer, dentrite, multilayer) and this is well captured qualitatively by the present model. For the cases considered in the present paper, we neglect particle–particle interactions in the bulk of the fluid and particle detachment is also not taken into account.

2.1 Modeling Approach

When modeling the formation of multilayer deposits, the transport step is not modified and only the attachment step is extended to account for particles interacting with fouled surfaces.

The deposition of a particle on a fouled surface is given by an energy balance approach in the wall-normal direction. The wall-normal kinetic energy of incoming particles is the result of the transport step while the wall-normal energy barrier between a particle and a fouled surface is determined according to the attachment model. This means that the interaction between a particle and a fouled surface is similar to the interaction between a particle and a rough substrate (covered by hemispherical asperities).

Then, various cases can appear: if the particle interacts with a clean surface, the energy barrier is given by the model developed previously whereas, if deposited particles are present inside the contact area, the energy barrier is determined using the DLVO theory [12], named after Derjaguin-Landau [2] and Verwey-Overbeek [17], assuming interaction energies to be additive:

$$U_{\text{part}-\text{surf}} = U^{\text{DLVO}}_{\text{part}-\text{plate}}(1 - S_{\text{cov}}) + \sum U^{\text{DLVO}}_{\text{part}-\text{part}},$$

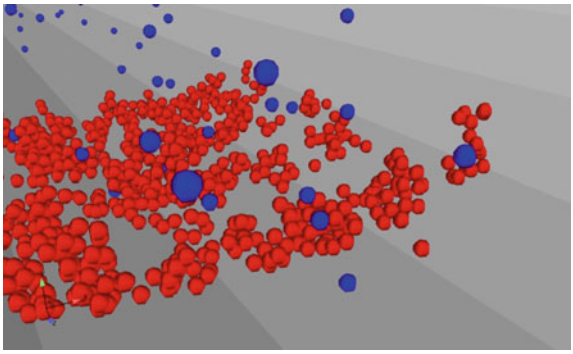

Fig. 2 Multilayer deposition of particles on the wall. Calculation with a low jamming limit and particle–particle attraction

with S_{cov} the surface coverage, $U_{part–plate}$ the interaction between a particle and the plane, and $U_{part–part}$ the interaction between particles.

The contact surface S_{cont} defining the contact area is:

$$S_{cont} = \pi(2\sqrt{R_{part}R_{dep}} + R_{dep})^2,$$

where R_{part} is the particle radius and R_{dep} is the deposited particle radius.

If deposited particles are present inside the contact area, a particle is chosen randomly among them and the incoming particle is deposited on this one with a random angle.

Two parameters have been introduced in the simulation of fouling: the jamming limit and the minimal porosity. The jamming limit corresponds to the maximum attainable surface coverage of deposited particles. This parameter has been introduced since the use of a probabilistic approach allows single-particle deposition to occur until a surface coverage of 100 % whereas, in reality, the packing of spheres on a surface cannot be higher than a jamming limit (equal to 90 % for a 2-D hexagonal close packing of spheres). Once the surface coverage reaches limit value, incoming particles are always considered to deposit on adhering particles (Fig. 2). The minimal porosity of a cell is equal in 0.366 for a structure obtained by random deposition of monodispersed particles.

2.2 Numerical Results

2.2.1 Effect of the Ionic Strength

Bacchin et al. [1] studied the deposition of 4.9-μm latex particles under Brownian motion on polymer substrates (PDMS). In this experiment, multilayer deposition was observed with an ionic force of I = 100 mM but no multilayer deposition occurred at I = 10 mM or lower (Fig. 3). Particle–particle interactions have been calculated using a zeta potential of –52 mV at pH 7 for the two ionic strength considered and a

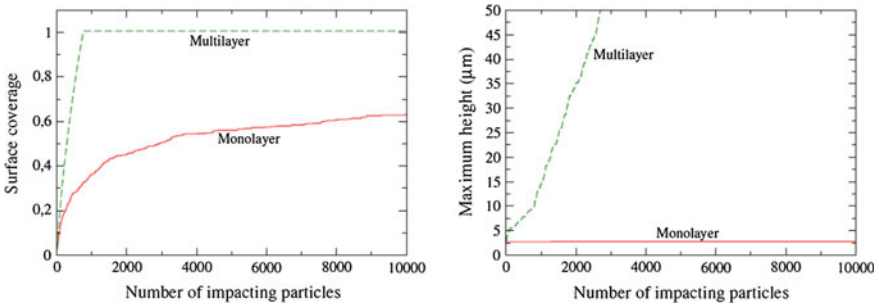

Fig. 3 Clogging behavior of polymer substrates by 4.9 µm latex particles at various solution conditions: I = 10 mM (*red line*), I = 100 mM (*green dashed line*)

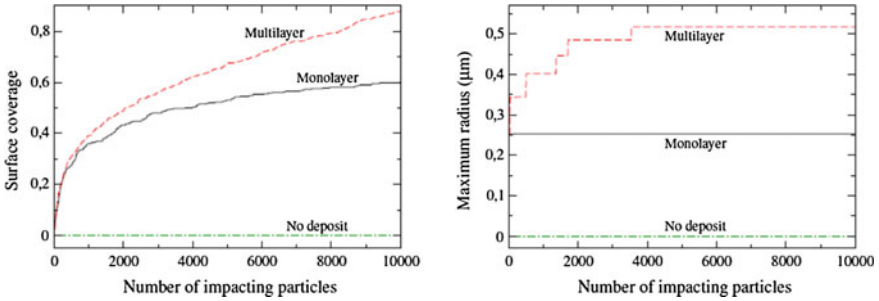

Fig. 4 Clogging behavior of silicon substrates by 250 nm alumina particles at various solution conditions: pH = 3 (*black line*), pH = 9 (*red dashed line*), pH = 10 (*green dot-dash line*)

Hamaker constant of 4.10^{-20} J. Particle–substrate interactions were not considered. Numerical results confirm that the model is able to predict the formation of multilayers: multilayer deposition occurs at an ionic strength of 100 mM, while only monolayers can be formed at an ionic strength lower than 60 mM.

2.2.2 Effect of the pH

Perry et al. [14] studied the deposition of 250-nm alumina particles on silicon substrates. The study was performed for different pH and showed that the first layer is determined by particle–surface interactions, while next layers are piloted by particle–particle interactions. For a pH of 3, a monolayer deposit was obtained because particle–surface interactions are attractive but particle–particle interactions are repulsive. At pH = 9, a multilayer deposit develops due to particle–particle attraction (close to the point of zero charge of alumina particles). At a pH of 10, there is no deposit on the substrate due to high particle–surface repulsion. These qualitative results have been confirmed numerically (Fig. 4).

3 Influence of the Multilayer Deposit on the Fluid Flow

When the size of multilayer deposit becomes significant which means that the fluid section is reduced, it is important to account for the influence of the deposit on the fluid flow in order to obtain more realistic evolutions, both of the fluid flow and of the deposit formation.

3.1 Possible Approaches

Different methods can be applied to address this issue, such as Arbitrary Lagrangien Eulerien (ALE) methods [3, 11], porous medium approaches [15, 16], hybrid methods or Smoothed Particle Hydrodynamics (SPH) approach [6, 13].

The choice of a modeling approach is based on two criteria: first, it needs to be consistent with models already developed within the framework of statistical or stochastic models; second, it must be sufficiently open to allow future developments (in particular the deposit cohesion and multilayer resuspension) to be introduced. According to these criteria, we have retained the porous medium approach.

3.2 Chosen Modeling Approach: Porous Medium Approach

The impact of the deposit on the flow can be taken into account at the mesh size by the use of a porous media approach (Fig. 5). Indeed, the number of deposited particles is known at the end of each time step and each wall-bounded cell can then be described by its porosity which represents the volume fraction not occupied by the deposited particles. As particle deposition goes on and the resulting deposit grows in size, the cell porosity is decreased (from one down to zero when the cell if completely clogged or blocked). A head loss coefficient is added in the equation of momentum for concerned cells in order to represent the pressure variation induced by the passage of fluid through a porous medium. This method has the advantage of being rather simple to implement since it does not require important numerical developments. However, the use of a single head loss coefficient in every cell implies that the deposit formed is properly described by the porosity only. This may appear as a restrictive assumption since the deposit morphology (dentrite or compact clusters) can change. Yet, it is believed that in simple geometry (such as in a parallel-plate channel), the interactions at play in fouling are not highly dependent on the cell position and the resulting deposit morphology is rather homogeneous and thus properly described by its porosity. It should be borne in mind that this assumption may become unrealistic in complex geometries (such as impacting jet or sudden reduction of the fluid cross section) due to specific hydrodynamic conditions (this remains to be studied both numerically and experimentally though).

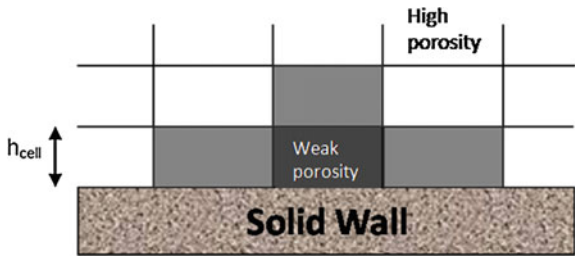

Fig. 5 Mesh and cell porosity

A fluid flow in a porous medium is modeled using the Darcy law:

$$\underline{u} = -\frac{k}{\mu}\underline{\nabla} P,$$

with $\underline{u}$ the velocity (m/s), p the pressure (Pa), μ the dynamic viscosity (Pa.s) and k the permeability (which depends only on the porous medium, in m^2). The hydraulic conductivity or the permeability coefficient of the porous medium (m/s) is written as follows:

$$K = \frac{k\rho g}{\mu}.$$

The momentum equation with the head loss term K_{pdc} is

$$\rho \frac{\partial \underline{u_i}}{\partial t} + \rho \underline{u_i} \frac{\partial \underline{u_i}}{\partial x_j} = -\frac{\partial P}{\partial x_i} + \mu \frac{\partial^2 \underline{u_i}}{\partial x_j^2} - \rho K_{\text{pdc}} \cdot \underline{u_i}.$$

The head loss coefficient is given by correlations according to different configurations, such as a flow through a pile of spheres or in cylinders with a section restriction. Laws have a phenomenological origin and are obtained from experiments realized in a macroscopic scale.

This method remains simple enough to be implemented in a straightforward manner and does not require extensive numerical developments. However, as mentioned previously, it should be borne in mind that the underlying assumption is that the deposit is homogeneous in space so as to describe it using only its porosity.

According to the literature, the regular head loss in a duct is

$$\Delta P = \lambda \frac{l}{D} \rho \frac{\overline{U^2}}{2},$$

where λ is a head loss coefficient (m^{-1}) dependent of the flow nature, l the duct length, D the hydraulic diameter, ρ the fluid density, and U the velocity.

The head loss coefficient K_{pdc} is defined as

$$\Delta P = K_{\text{pdc}} \rho \overline{U},$$

where

$$K_{\text{pdc}} = \lambda \frac{l}{D} \frac{\overline{U}}{2}.$$

The cell porosity ε can be defined by

$$\varepsilon = \frac{V_{\text{cel}} - V_{\text{part}}}{V_{\text{cell}}},$$

where V_{cel} corresponds to the volume of the cell, V_{part} to the particle volume given by $V_{\text{part}} = N_{\text{dep}} \frac{4}{3} \pi r_p^3$, with r_p the particle radius and N_{dep} the number of deposited particles in the cell (considering a monodispersed case, i.e., all particles have the same diameter).

The head loss, according to the porosity, for a pile of spheres of the same diameter, is given by the Ergun formula [5]:

$$\begin{aligned} \frac{\Delta P}{H} &= \left[\frac{150 \mu_f}{\rho_f d_p^2} \frac{(1-\varepsilon)^2}{\varepsilon^3} + 1.75 \frac{1-\varepsilon}{\varepsilon} \frac{1}{d_p} |U| \right] \rho_f U \\ \Delta P &= K_{\text{pdc}} \rho_f U \\ K_{\text{pdc}} &= \frac{150 \mu_f H}{\rho_f d_p^2} \frac{(1-\varepsilon)^2}{\varepsilon^3} + 1.75 * \frac{1-\varepsilon}{\varepsilon^3} \frac{H}{d_p} |U|, \end{aligned} \tag{1}$$

with H a characteristic length of the granular medium, μ_f the fluid dynamic viscosity, ρ_f the fluid density.

The head loss is the sum of two terms representing, respectively, the losses of viscous and kinetic energy of the fluid. This law is valid for fluid flows through porous media formed by pile of homogeneous, fixed and spherical particles from laminar to turbulent flows.

The necessary data to calculate the head loss coefficient are

- the porosity (determined from the number of deposited particles in each cell),
- the characteristic length H, and
- the diameter of the particles d_p.

Initially, the cells of the fluid domain have a porosity of 1 and thus a head loss coefficient equal to 0. The cell porosity decreases according to the number of

deposited particles in this cell. The head loss term is calculated with the Ergun law (1) according to the cell porosity at each time step.

The maximal compactness of sphere pile with a same diameter is $c = 0.74$ thus a minimal porosity of $\varepsilon_p = 1 - c = 0.26$. For a random deposit, the compactness is between 0.591 and 0.634 [8].

Other formulae exist to take into account the polydispersion by a mean diameter and the standard deviation [4] or the mean Sauter diameter [10]. The non-sphericity of particles can be also considered using appropriate formulae. Some improvements have still to be provided to have a head loss coefficient more representative of general cases. The porosity is homogeneous in the cell; it is calculated from the number of deposited particles and does not depend on the deposit morphology. At the moment, developments are performed for monodispersed particles.

4 Results and Discussion

4.1 Particle Injection in a Cylindrical Duct

This test case is performed with the deposition and clogging models, while no resuspension is considered. The flow is calculated at each time step in order to take into account the impact of the deposit on the fluid flow. The geometry is a cylindrical duct with a diameter of 1.27 cm and a length of 1.22 m. The mesh is composed of 159040 hexahedra, a radial cut of the mesh is represented on the Fig. 6. Ten particles are injected onto the flow at each time step ($\Delta t = 10^{-4}$ s) from the center of the inlet with an initial velocity directed towards the wall (Fig. 8). Large particles with a diameter of 8.10^{-5} m (monodispersed) are injected in order to obtain a multilayer deposit more rapidly and observe the effect on the flow. Only, a

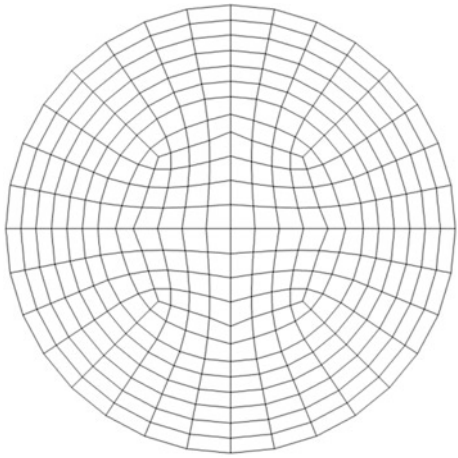

Fig. 6 Radial cut of the mesh

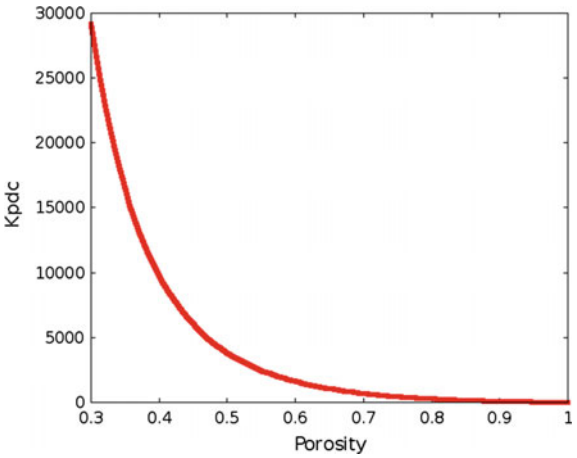

Fig. 7 Head loss coefficient according to the cell porosity

part of the wall between 0.025 and 0.03 m is considered favorable for deposit growth, somewhere else particles impacting the wall are removed.

The head loss coefficient is calculated by the Ergun formula (1) according to the cell porosity (Fig. 7).

In Figs. 8, 9 and 10, we can see the injection of particles and the growth of a deposit as a function of time. The flow is perturbed by the multilayer deposit and the bulk velocity increases with time since a part of the section is blocked by the deposit.

4.2 Evolution of Fluid Velocity and Pressure with Time

Figure 11 displays the fluid velocity along the duct at different times, at the center of the flow and near the wall. At the initial moment, the flow velocity at the center

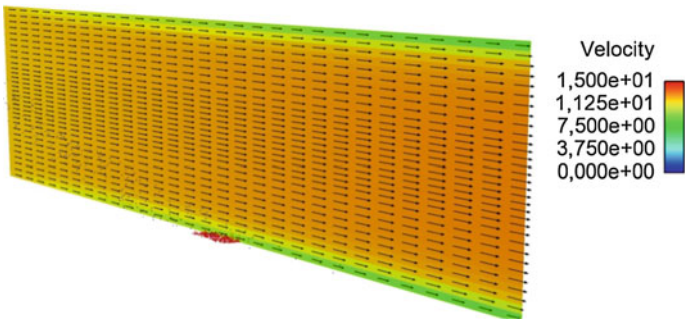

Fig. 8 Deposit of particles and velocity at $t = 0.1$ s

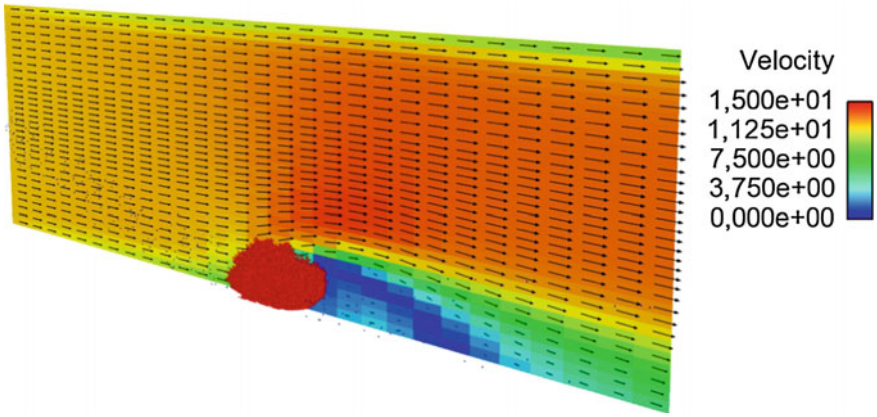

Fig. 9 Deposit of particles and velocity at t = 10 s

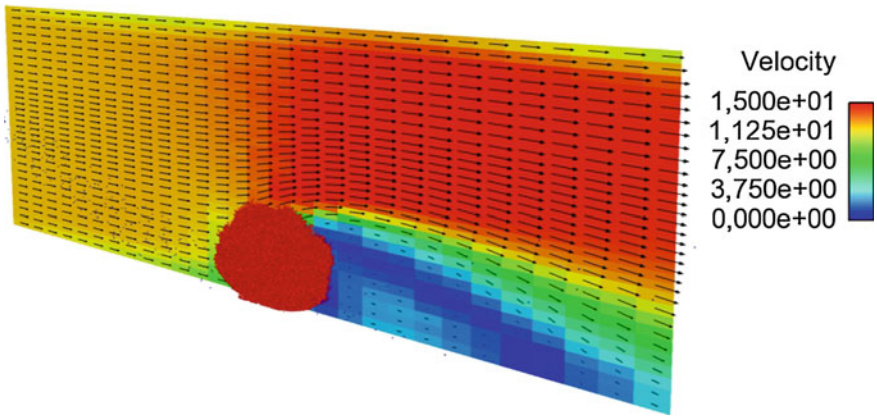

Fig. 10 Deposit of particles and velocity at t = 30 s

of the flow increases along the duct because the flow is still in a transition state. The velocity at the center of the flow increases from 12.5 to 15 m/s when the deposit grows (between 0 and 30 s). The multilayer deposit reduces indeed the pipe cross section resulting in an increased fluid velocity (for a constant flow rate). On the contrary, the velocity near the wall decreases inside the deposit and also downstream. The velocity just downstream the deposit is very low and increases again further away (4 m/s at the exit of the domain). A zone of recirculation is observed downstream from the deposit around z = 0.025–0.03 m (Fig. 12).

Figure 13 shows pressure profiles along the duct at different times at the center of the flow and near the wall. Near the wall, there is a small pressure rise upstream from the deposit and a depression downstream. The pressure gap through the deposit is about 106 Pa. At the center of the flow, the pressure is also perturbed by the deposit.

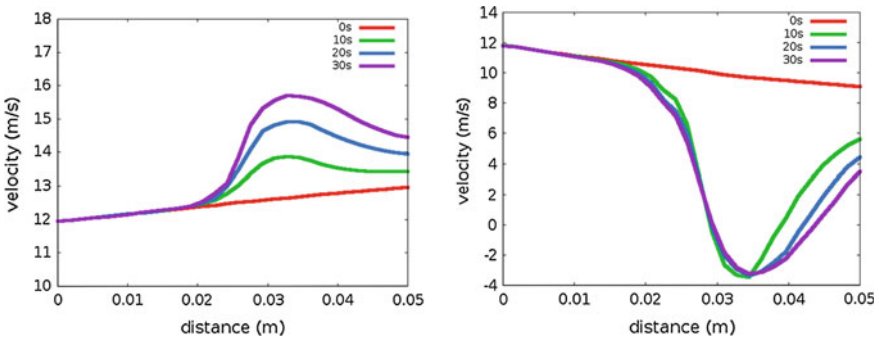

Fig. 11 Velocity along the cylindrical duct for 4 different times t = 0, 10, 20 and 30 s (*left* at the middle of the flow, *right* near the wall)

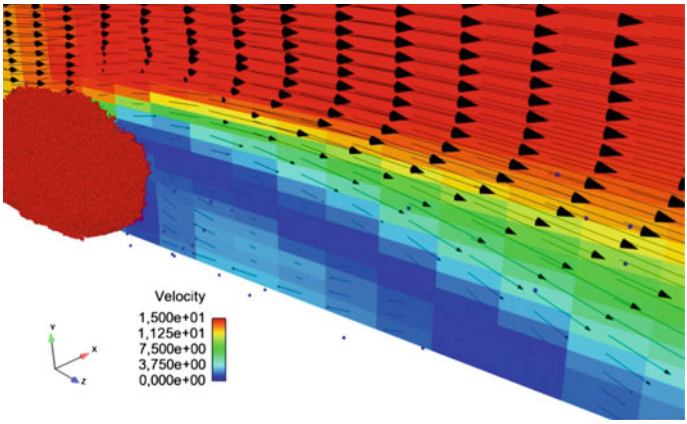

Fig. 12 Zone of recirculation downstream of the multilayer deposit

The cell porosity is determined from the number of deposited particles in a cell. If the cell porosity becomes inferior to a limit value (equal to 0.366 for a structure obtained by random deposition of monodispersed particles), we prevent particles from depositing in this cell and a rebound condition is applied (Fig. 14).

4.3 Sensitivity Study

To test the influence of the head loss coefficient on the flow velocity, different parameters such as the particle diameter or the fluid velocity are modified in the Ergun formula (1). The head loss coefficient is represented in 3 cases according to three porosities (Fig. 15). The red curve corresponds to a head loss coefficient calculated with the initial velocity, the blue one to the previous case, and the green one to a particle cluster.

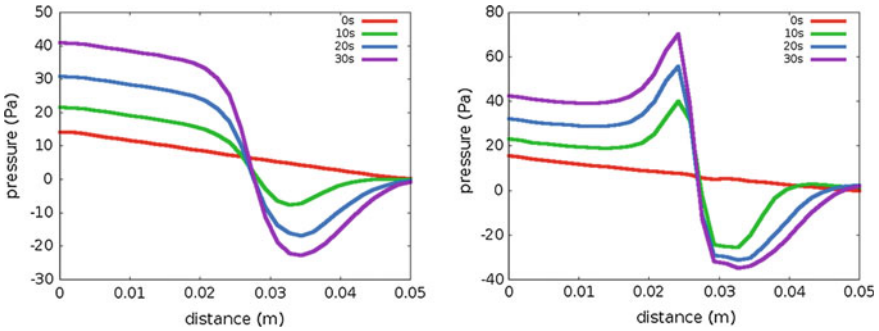

Fig. 13 Pressure along the cylindrical duct for 4 different times (*left* at the middle of the flow, *right* near the wall)

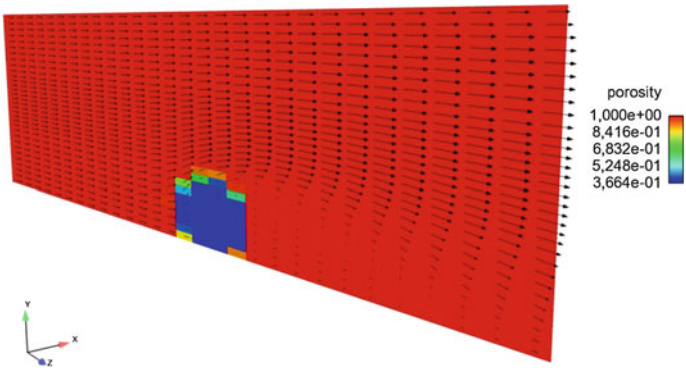

Fig. 14 Cell porosity at t = 30 s

Fig. 15 Head loss coefficient according to the porosity for different parameters

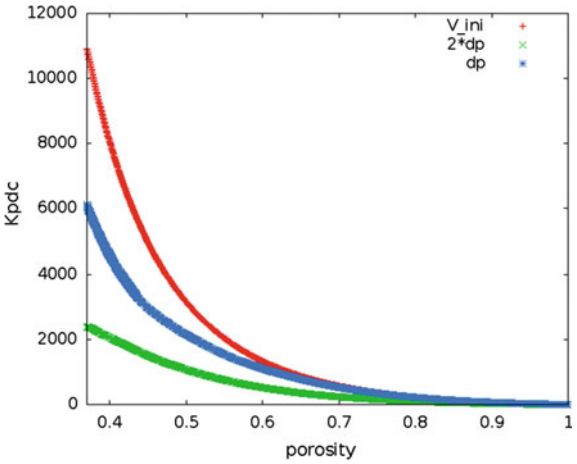

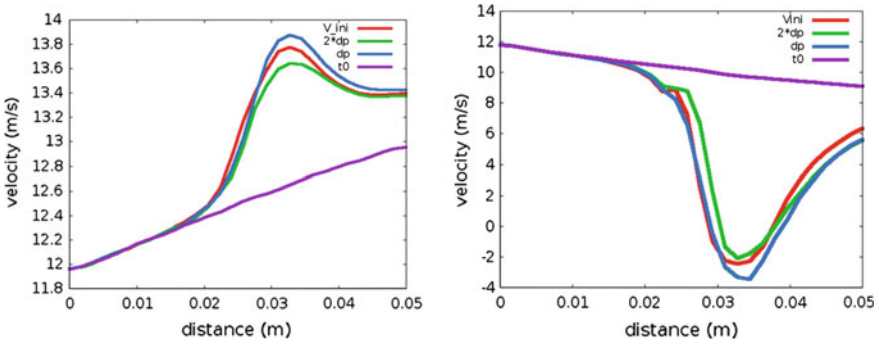

Fig. 16 Velocity along the cylindrical duct at $t = 10$ s for different head loss coefficients (*left* at the middle of the flow, *right* near the wall)

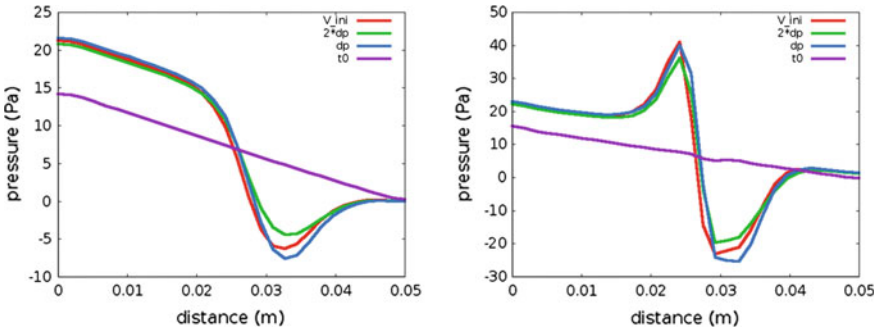

Fig. 17 Pressure along the cylindrical duct at $t = 10$ s for different head loss coefficients (*left* at the middle of the flow, *right* near the wall)

A ratio of almost 5 is obtained for the maximal value of the head loss coefficient.

A difference of about 2 % is observed on velocities at the center of the flow for the various head loss coefficients (Fig. 16 left). An increase about 10 % exists between the initial velocity and the velocity at $t = 10$ s. In Fig. 16 (right), we observe a reduction of the velocity in the zone corresponding to the deposit (around $z = 0.025$–0.03 m). According to the value of the head loss coefficient applied, the velocity which is obtained in the deposit is in the range within –2 and –3.5 m/s against approximately 10 m/s upstream of the deposit formation. For pressure, differences of about 24 % are found near the wall downstream of the deposit (Fig. 17).

For the 3 conditions, the evolution of the multilayer deposit is slightly different because of the velocity difference.

The deposit morphology has an influence on the prediction of the head loss coefficient applied in the momentum equation and thus on the fluid flow calculations.

5 Conclusion and Perspectives

The present work has presented new coupled approaches to address the influence of a particle deposit on the carrier-fluid motion. Among the methods presented here, the porous medium approach seems well adapted to capture the coupled effects between the fluid flow and the particle deposits. In this approach, fluid velocities modified by multilayer deposits are predicted using a head loss coefficient in the momentum equation. However, there are some limitations due to the uncertainty on some parameters and even to the formulation of a physically relevant law for the head loss coefficient. At the moment, an Ergun law has been retained but additional developments are needed to come up with accurate expressions. Furthermore, it is difficult to have experimental data to validate the results. On the other hand, our understanding of particulate fouling remains incomplete. Significant efforts are still required to comprehend resuspension in multilayer deposits and to explore the influence of the deposit morphology on inter-particle cohesion. To put forward one example, the deposit morphology plays also an important role and must be correctly included in the modeling picture. Thus, this is clearly a subject which is currently evolving, with some uncharted aspects, and, in that sense, it appears justified to select an approach (such as the porous medium one) which allows first developments to be made without too many complications. It is believed that with new insights provided by experimental studies and feedbacks from additional numerical works, a proper framework will be outlined. Finally, it is worth recalling that particle resuspension must also be accounted for and, in turn, this represents an additional challenge as particle reentrainment from multilayer deposits is more intricate than single-particle reentrainment.

References

1. Bacchin, P., Aimar, P., & Sanchez, V. (1995). Model for colloidal fouling of membranes. *AICHE, 41*, 368–376.
2. Derjaguin, B., & Landau, L. (1941). Theory of the stability of strongly charged lyophobic sols and of the adhesion of strongly charged particles in solution of electrolytes. *Acta Physicochimica URSS, 14*, 633–662.
3. Donea, J. (1983). *Arbitrary Lagrangian-Eulerian finite element methods* (pp. 473–516). Computational Methods for Transient Analysis Amsterdam: North-Holland.
4. Endo, Y., Chen, D.-R., & Pui, D. Y. H. (1998). Effects of particle polydispersity and shape factor during dust cake loading on air filters. *Powder Technology, 98*, 241–249.
5. Ergun, S. (1952). Fluid flow through packed columns. *Chemical Engineering Progress, 48*(2), 89–94.
6. Gingold, R. A., & Monaghan, J. J. (1977). smoothed particle hydrodynamics: Theory and application to non-spherical stars. *Monthly Notices of the Royal Astronomical Society, 181*, 375–389.
7. Guingo, M., & Minier, J. P. (2008). A stochastic model of coherent structures for particle deposition in turbulent flows. *Physics of Fluids, 20*, 053303.

8. Henry, C., Minier, J. P., & Lefebvre, G. (2012). Towards a description of particulate fouling: From single particle deposition to clogging. *Advances in Colloid and Interface Science, 185–186*, 34–76.
9. Henry, C., Minier, J. P., & Lefebvre, G. (2012). Numerical study of the adhesion and reentrainment of nondeformable particles on surfaces: The role of surface roughness and electrostatic forces. *Langmuir, 28*, 438–452.
10. Holdich, R. G. (2002). *Fundamentals of particle technology*. Department of Chemical Engineering, Loughborough University, UK.
11. Hughes, T. J. R., Liu, W. K., & Zimmermann, T. K. (1981). Lagrangian-Eulerian finite element formulation for incompressible viscous flows. In *Interdisciplinary finite element analysis* (p. 179). College of Engineering and School of Civil & Environmental Engineering of Cornell University.
12. Israelachvili, J. N. (2011). *Intermolecular and surface forces* (3rd ed.). London: Academic Press.
13. Lucy, L. B. (1977). A numerical approach to the testing of the fission hypothesis. *Astronomical Journal, 82*, 1013–1024.
14. Perry, J. L., & Kandlikar, S. G. (2008). Fouling and its mitigation in silicon microchannels used for IC chip cooling. *Microfluidics and Nanofluidics, 5*, 357–371.
15. Szewc, K. (2013). *Development of smoothed particle hydrodynamics approach for modeling of multiphase flows with interfaces*. Ph.D. Thesis, Institute of fluid flow machinery, polish academy of sciences, Gdansk, Poland.
16. Szewc, K., Pozorski, J., & Minier, J.-P. (2012). Analysis of the incompressibility constraint in the smoothed particle hydrodynamics method. *International Journal for Numerical Methods in Engineering, 92*, 343–369.
17. Vervey, E., & Overbeek, J. T. G. (1948). *Theory of stability of lyophobic colloids*. Amsterdam: Elsevier.

Towards Numerical Simulation of Snow Showers in Jet Engine Fuel Systems

Ewen Marechal, Sofiane Khelladi, Florent Ravelet, Farid Bakir and Olivier Delepierre-Massue Snecma

1 Introduction

Ice in flight can be disastrous. A thin layer on the airfoil degrades its ability to lift and increases its drag, leading the airplane to stall even at high speeds. Ice collected on wing can also broke off and be sucked into the engines, damaging the fan blades. An airplane can roll or pitch uncontrollably if icing occurs on the horizontal or vertical stabilizer. Obstruction of Pitot tube will cause the airspeed indicator to give wrong information. These events are related to weather (moisture, snow, freezing rain and drizzle) and caused hundreds of casualties over decades.

However, fuels used in jet aircraft contain significant quantities of water. Investigation of the Boeing 777-236ER, G-YMMM crash at Heathrow in 2008 revealed that this water can create ice structures in aircraft fuel ducts at low temperatures and moderate flow rates. If the latter is increased, shear stress may tear off the ice resulting in high concentrations of particles in the fuel. Such sudden releases of large amount of ice are often referred as "snow showers" [1].

E. Marechal (✉) · S. Khelladi · F. Ravelet · F. Bakir
DynFluid Laboratory, Ecole Nationale Supérieure des Arts et Métiers,
151, Boulevard de l'Hôpital, 75013 Paris, France
e-mail: ewen.marechal@ensam.eu

S. Khelladi
e-mail: sofiane.khelladi@ensam.eu

F. Ravelet
e-mail: florent.ravelet@ensam.eu

F. Bakir
e-mail: farid.bakir@ensam.eu

O. Delepierre-Massue Snecma
Rond-Point René Ravaud, 77550 Réau, France
e-mail: olivier.delepierre-massue@snecma.fr

P. Gourbesville et al. (eds.), *Advances in Hydroinformatics*,
Springer Water, DOI 10.1007/978-981-287-615-7_41

Jet engines have complex fuel systems, involving several hydraulic components sensitive to clogging, e.g. filters, valves or heat exchanger inlet screens. When a snow shower occurs, ice particles settle in seconds to form a porous layer which is likely to occasion fuel flow restrictions. Nowadays, aviation safety authorities require that the fuel systems must be designed so that any accumulation of water which may separate from the fuel will not cause engine malfunctioning [2]. Hence, understanding of such flow has become a rising matter of interest among jet engines manufacturers over last years.

In this paper, we propose a numerical approach to investigate dynamics of transient clogging of hydraulic components. Simulation strategies for particulate flows can be roughly classified into two categories. The first one is the Eulerian–Eulerian approach. The fluid phase and the dispersed phase are considered as interpenetrating continuum and updated using mass, momentum and energy conservation laws. Additional constitutive equations may be required to describe interactions between particles. This approach is well suited for very small particles moving with the fluid, but is not adapted to packed beds involved in clogging.

Therefore, we chose the second approach known as Eulerian–Lagrangian approach. Each particle, or group of similar particles (called parcel), is considered with its own position and velocity which are updated with the equation of motion. The effect of particles on the flow field is accounted through momentum and energy sources. Collisions between particles can be treated deterministically. Therefore, it is possible to describe how they stack on each other [3].

2 Modelling Snow Shower

2.1 A Multiphysic, Multiscale Phenomenon

Snow showers are three-stage events. The first step is a slow (several hours) growth of ice crystal within the aircraft fuel pipes. Then, accumulated snow is unexpectedly released and carried by the fuel into the jet engine fuel system. At last, ice particles will choke fuel system components in seconds.

2.1.1 Ice Accretion onto Sub-Cooled Surfaces

Icing is influenced by several parameters, e.g. surface properties, temperature variations of fuel and fluid velocity. Laboratory observations show that accretion process involves the combination of growth of ice crystal from the water dissolved in the fuel (frost) and deposit of supercooled droplets (rime) [4, 5]. Crystal growth is driven by thermodynamics: higher molecular diffusion favours adsorption of water molecules to the growing crystal, while thermal diffusion removes latent heat released by water solidification [6].

2.1.2 Ice Shedding

The mechanical strength of an ice sample at a given temperature depends of the shape and size of the specimen, the way ice is formed, and how the load is applied. The fracture is initiated by the formation of a crack, depending on the crystallographic orientation, which then spread through the specimen. A generally fracture law has yet to be agreed upon, but correlations were proposed by several authors. Ice present weak tensile and shear strengths [7, 8]. Investigations following the 2008 accidents demonstrated that release of accretion occurs when the fuel velocity is increased to the range of 0.7–0.8 m/s. Hence, ice shedding is likely caused by shear stress resulting from a drag increase [9].

2.1.3 Clogging

Components with small holes are obviously threatened by ice particles. This includes filters, strainers, injectors and heat exchanger inlets. It is usual to provide by-pass means to such components so that if they were to be obstructed, fuel will continue to flow at an acceptable rate through the rest of the system. Accumulation of a significant quantity of ice will form a thin layer. Resulting pressure drop may cause by-pass valves to open. Therefore, it is critical to know in which extent ice particles will follow the flow through the by-pass and propagate in the fuel system. Given a carrier fluid, the dynamic is driven by the shape, size and density of ice particles. According to recent studies, ice particle size is in the range of 1–0 μm and may be considered almost neutrally buoyant in fuel [10].

2.2 Replicating Snow Showers

The European Aviation Safety Agency (EASA) issues certification specifications to ensure the tolerance of fuel systems to high concentration of ice particles. CS-E 560 states: “The fuel system must be designed so that any accumulation of likely quantities of water which may separate from the fuel will not cause engine malfunctioning.” [2].

2.2.1 Experimental Setup

In order to comply with international safety standards, an experimental setup was designed by the French jet engine manufacturer SNECMA. The equipment used to make such tests is described in more detail previously [11]. Briefly, pure water is introduced in cold kerosene fuel flow through a homemade injector. The system regulation ensures that a given quantity of water is injected at the desired volumetric

flow rate (around 10,000 ppm). It was observed that injected water froze almost immediately when the fuel temperature is below –20 °C.

2.2.2 Collected Ice

80 mL of water were introduced in a –45 °C jet engine fuel, and ice was collected downstream by a 25 µm filter. The flow decreased by about 20 % though the filter appeared to be completely obstructed. Figure 1 shows the layer of ice accumulated on the filter and a close-up on ice particles.

Ice was collected as dry as possible from the deposit and left to melt. A volume fraction up to 50 % of fuel was still observed. This implies that permeability of the ice layer is a combination of compactness from particle stacking and porosity of particles themselves.

2.3 Assumptions

Complete modelling of a snow shower is outside of this research scope. This paper focuses on the clogging of system components by ice, which is the most critical step of the phenomenon. Furthermore, we mean to keep the model close to what have been observed in previously described tests in the perspective of future validation of the method. Hence, several assumptions are made in this study:

1. Supercooling droplets are not considered.
2. Injected water is considered as already frozen. We do not consider any freezing or melting.
3. Particles are considered already released and created at flow inlet.
4. Particle initial velocity is set equal to the fuel one.
5. Particle radius is evenly distributed within the range of 150–250 µm.
6. Particle radius is assumed to remain constant throughout the simulation.

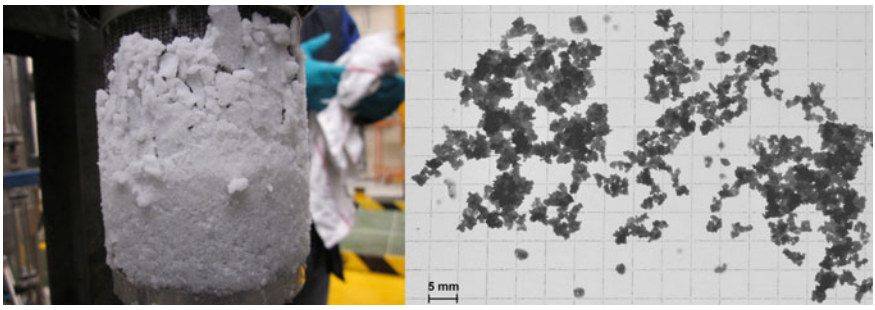

Fig. 1 *Left* Clogging of a filter—*Right* Picture of particles

7. Particle porosity is in the range of 0.1–0.5.
8. The carrier fluid is incompressible.
9. We restrict our study to laminar flow.

3 Numerical Method

3.1 Numerical Simulation of Solid Dynamics

3.1.1 Particle Equation of Motion

Let us consider a rigid body of mass m and inertia matrix $\mathbf{J}$ submitted to total forces $\mathbf{F}$ and torques $\mathbf{T}$. Its centre of mass has for coordinate and orientation ($\mathbf{X}$, $\mathbf{W}$). Its motion is governed by the following equations:

$$\begin{cases} m\frac{\mathrm{d}\dot{\mathbf{x}}}{\mathrm{d}t} = \mathbf{F} \\ \mathbf{J}\frac{\mathrm{d}\dot{\mathbf{w}}}{\mathrm{d}t} = \mathbf{T} \end{cases}. \tag{1}$$

Modelling total forces $\mathbf{F}$ and torques $\mathbf{T}$ applied on a solid particle in an infinite medium has been studied extensively. Various forces are involved: drag, buoyancy, Magnus, Suffman and Basset forces, virtual mass force. In this study, we only consider drag $\mathbf{F_D}$, buoyancy $\mathbf{F_B}$ and contact forces $\mathbf{F_C}$. Rotation of the particle is discarded. Let n denote the simulation time step of length Δt. The discretized equation of motion for a particle is

$$\mathbf{X}^{n+1} = \mathbf{X}^n + \dot{\mathbf{X}}^n \Delta t + \frac{1}{2} m^{-1} (\mathbf{F_D} + \mathbf{F_B} + \mathbf{F_C})^n \Delta t^2. \tag{2}$$

3.1.2 Drag in a Multiparticle System

In the following, subscript M denotes the mixture, C is the fluid continuum and P is the particle. Drag arises from the relative motion $\mathbf{V}_R$ between the particle and the flow:

$$\mathbf{V}_R = \dot{\mathbf{X}}_P - \dot{\mathbf{X}}_C. \tag{3}$$

A standard relation for drag is force is

$$\mathbf{F_D} = -\frac{C_D}{2} \rho_C S_P |\mathbf{V}_R| \mathbf{V}_R. \tag{4}$$

In a multiparticle system, the effect of others particles on the drag force is modelled as an increase of viscosity resulting from additional stress in the flow. We use the mixture viscosity model proposed by Clift et al. [12]:

$$\mu_M = \mu_C (1 - \alpha)^{-2.5}, \tag{5}$$

where μ denotes the mixture viscosity and α is the fraction of volume occupied by particles. Two similarity hypotheses are introduced. First, the particle Reynolds number is defined as

$$\mathrm{Re}_P = \frac{\rho_C d_P |\mathbf{V}_R|}{\mu_M}. \tag{6}$$

Then it is assumed that a similarity exists between a single-particle system and a multiparticle system. The relation for the drag coefficient is given by

$$C_D = \frac{24}{\mathrm{Re}_P}\left(1 + \frac{\mathrm{Re}_P^{0.75}}{10}\right). \tag{7}$$

This equation holds for particle Reynolds number lesser than 1000. Above this value, the drag coefficient C_D should be set to a constant value of 0.44 [12]. It is also necessary to set a maximum value for C_D. Otherwise, particle velocity may exceed fluid velocity at the end of a step. Maximum drag coefficient value is related to the time step. It has been found that sedimentation speed is sensitive to this parameter.

3.1.3 Particle Interactions

The mixture viscosity model only holds for moderate solid volume fractions. In dense flow and packed bed, we need to take into account contact forces between particles. In this paper, we derive a discrete contact model from equation of motions. Let i and j denote two particles of radiuses r_i and r_j. Let $\mathbf{X}_i^n$ and $\mathbf{X}_j^n$ be their centres of mass.

We define the directional unit vector between i and j as

$$\mathbf{E_{ij}} = \left(\mathbf{X}_j^n - \mathbf{X}_i^n\right)\left\|\mathbf{X}_j^n - \mathbf{X}_i^n\right\|^{-1}. \tag{8}$$

Let $\mathbf{F}_{ij} = -\mathbf{F}_{ji}$ be a force exerted by particle j on particle i over a time step. This force is directed along $\mathbf{E}_{ij}$. Writing equation of motion (2) for each particle and taking into account $\mathbf{F}_{ij}$ give the following system:

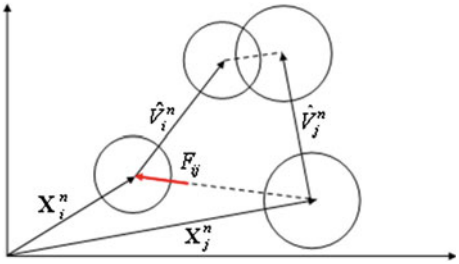

Fig. 2 Particles initial position, directional vector, and a priori velocities and particles final positions given $\mathbf{F}_{ij} = 0$

$$\begin{cases} \mathbf{X}_i^{n+1} = \mathbf{X}_i^n + \dot{\mathbf{X}}_i^n \Delta t + \frac{\Delta t^2}{2m_i}\left(\mathbf{F}_i - \mathbf{F}_{ij}\right) = \mathbf{X}_i^n + \hat{\mathbf{V}}_i^n \Delta t + \frac{\Delta t^2}{2m_i}\mathbf{F}_{ij} \\ \mathbf{X}_j^{n+1} = \mathbf{X}_j^n + \dot{\mathbf{X}}_j^n \Delta t + \frac{\Delta t^2}{2m_j}\left(\mathbf{F}_j + \mathbf{F}_{ij}\right) = \mathbf{X}_j^n + \hat{\mathbf{V}}_j^n \Delta t - \frac{\Delta t^2}{2m_j}\mathbf{F}_{ij} \end{cases}, \tag{9}$$

where $\hat{\mathbf{V}}_i^n$ and $\hat{\mathbf{V}}_j^n$ are called "a priori" velocity of particles i and j. These velocities can be such that if no force is exerted between particles, there may be interpenetration (Fig. 2).

Subtracting equations of motion for particles i and j in (9) give the following relation:

$$\mathbf{X}_j^{n+1} - \mathbf{X}_i^{n+1} = \left(\mathbf{X}_j^n - \mathbf{X}_i^n\right) + \left(\hat{\mathbf{V}}_j^n - \hat{\mathbf{V}}_i^n\right)\Delta t - \frac{\Delta t^2}{2m_{ij}}\mathbf{F}_{ij}, \tag{10}$$

where $m_{ij} = \left(m_i^{-1} + m_j^{-1}\right)^{-1}$. Now we perform the dot product of (10) with the directional vector $\mathbf{E}_{ij}$:

$$\left(\mathbf{X}_j^{n+1} - \mathbf{X}_i^{n+1}\right) \cdot \mathbf{E}_{ij} = \left(\mathbf{X}_j^n - \mathbf{X}_i^n\right) \cdot \mathbf{E}_{ij} + \left(\hat{\mathbf{V}}_j^n - \hat{\mathbf{V}}_i^n\right) \cdot \mathbf{E}_{ij}\Delta t - \frac{\Delta t^2}{2m_{ij}}\left|\mathbf{F}_{ij}\right|. \tag{11}$$

Let l_{ij}^n denote the projected distance between particle centres of mass and $\hat{\mathbf{V}}_{ij}^n$ denote the relative a priori velocity. To guarantee that no interpenetration occurs at the end of a time step, we need to set a constraint $l_{ij}^{n+1} \geq r_i + r_j$. Introduction of this constraint in Eq. (11) give

$$l_{ij}^n - r_i - r_j + \hat{\mathbf{V}}_{ij}^n \cdot \mathbf{E}_{ij}\Delta t - \frac{\Delta t^2}{2m_{ij}}\left|\mathbf{F}_{ij}\right| \geq 0. \tag{12}$$

According to the velocity projection method introduced by Lefebvre in [13], finding the non-overlapping velocity field is equivalent to minimizing the following function:

$$J(\mathbf{V},\lambda)=\left|\mathbf{V}-\hat{\mathbf{V}}^{n}\right|^{2}-\sum_{i<j}\lambda_{ij}\left(l_{ij}^{n}-r_{i}-r_{j}+\hat{\mathbf{V}}_{ij}^{n}\cdot\mathbf{E}_{ij}\Delta t\right). \tag{13}$$

Solution of this saddle-point problem is obtained iteratively by the Uzawa algorithm:

$$\begin{cases}\mathbf{V}_{i}^{k+1}=\hat{\mathbf{V}}_{i}^{n}+\sum_{i<j}\lambda_{ij}^{k}\mathbf{E}_{ij}\\ \lambda_{ij}^{k+1}=\max\left(0,\lambda_{ij}^{k}-\frac{\omega}{\Delta t}\left(l_{ij}^{n}-r_{i}-r_{j}+\hat{\mathbf{V}}_{ij}^{n}\cdot\mathbf{E}_{ij}\Delta t\right)\right)\end{cases}. \tag{14}$$

The real ω is the non-dimensional artificial time parameter. Comparison of Eqs. (12) and (14) shows the relation between contact force and Lagrange multipliers:

$$\lambda_{ij}=-\frac{\Delta t}{2m_{ij}}\left|\mathbf{F}_{ij}\right|. \tag{15}$$

3.2 Numerical Simulation of Fluid Dynamics

Flow simulation is performed using a homemade finite volume code. The geometry is meshed so that computational cells remain greater than particles. This is essential to get cell-averaged quantities as solid volume fraction, but can lead to rather coarse meshes.

3.2.1 Moving Least Squares Approximation

In order to have a good accuracy of the solution, we use a high-order formulation based on Moving Least Squares (MLS) approximants, a technique widely used in the meshless community. Let $u(\mathbf{x})$ be a function. Its MLS approximation $\hat{u}(\mathbf{x})$ is computed from a set of Ns neighbouring points called stencil where the value u_j of $u(\mathbf{x})$ is known. The number of neighbours depends on the order of accuracy, and the stencil should be as compact as possible, centred around the node. The MLS approximation $\hat{u}(\mathbf{x})$ is written as

$$\hat{u}(\mathbf{x})=\sum_{j=1}^{Ns}N_{j}u_{j}. \tag{16}$$

High-order approximate derivatives can be expressed in terms of the derivatives of the MLS shape function. The n-th derivative of $u(\mathbf{x})$ can be expressed as

$$\frac{\partial^n \hat{u}}{\partial x_i^n} = \sum_{j=1}^{Ns} \frac{\partial^n N_j}{\partial x_i^n} u_j. \tag{17}$$

We refer the reader to [14] for a complete description of the computation of MLS shape functions and derivatives.

3.2.2 Navier–Stokes Equations

Fluid motion is governed by the well-known Navier–Stokes equations. Let $\mathbf{U} = (u, v, w)^T$ denotes the velocity vector (m.s^{-1}), ρ_0 is the fluid density (kg.m^{-3}) and p is the pressure (Pa). In order to achieve two-way coupling between particles and fluid, we replace the fluid viscosity by previously defined mixture viscosity and introduce a source term $\mathbf{S_V}$ to account for viscous loss within the porous layer [15]:

$$\mathbf{S_V} = \frac{\mu_M}{\varepsilon} \mathbf{U}. \tag{18}$$

Let $\bar{d}_P$ denotes the mean particle diameter and α denotes the volumetric solid fraction. Parameter ε is defined as

$$\varepsilon = \frac{\bar{d}_P^2 (1-\alpha)^3}{150\alpha^2}. \tag{19}$$

The continuity and momentum conservation equations integrated over a control volume Ω can be written as

$$\oint_\Gamma \rho_0 \mathbf{U} \cdot \mathbf{n} \, d\Gamma = 0, \tag{20}$$

$$\int_\Omega \rho_0 \frac{\partial \rho \mathbf{U}}{\partial t} \, d\Omega + \oint_\Gamma \mathbf{U} \cdot (\rho_0 \mathbf{U} \cdot \mathbf{n}) d\Gamma = -\oint_\Gamma p \cdot \mathbf{n} \, d\Gamma + \oint_\Gamma \mu_M (\nabla \mathbf{U} \cdot \mathbf{n}) \, d\Gamma + \int_\Omega \mathbf{S_V} \, d\Omega. \tag{21}$$

Equations (20) and (21) are discretized using a formulation based on MLS approximants introduced previously. The solution procedure is based on the SIMPLE algorithm [16].

4 Application: Clogging of a Filter

By the way of application we consider the simple 2D case of a filter clogged by a snow shower. An ideal filter (permeable to the flow but blocking any kind of particle) is located in the middle of rectangular domain representing a segment of pipe. Domain dimensions are 2.5 cm (the diameter) by 10 cm (the length).

As inlet condition, we set the fluid velocity to 0.1 m/s, and up to 1000 particles are seed in order to have a concentration of water close to 10,000 ppm. The carrier fluid has a density of 850 kg/m^3 and a viscosity of 1.10–3 Pa.s. Ice particles have a density of 917 kg/m^3, and porosity is set to 0.5. We set the time step to 1 ms and perform up to 3000 iterations.

Figure 3 shows the evolution of the velocity field **U** and solid fraction α over time. Particles seem to be influenced by buoyancy, though this could be due to the maximum value imposed on drag coefficient. The deposit starts building on the bottom of the pipe, but contact forces push particles upward until equilibrium is

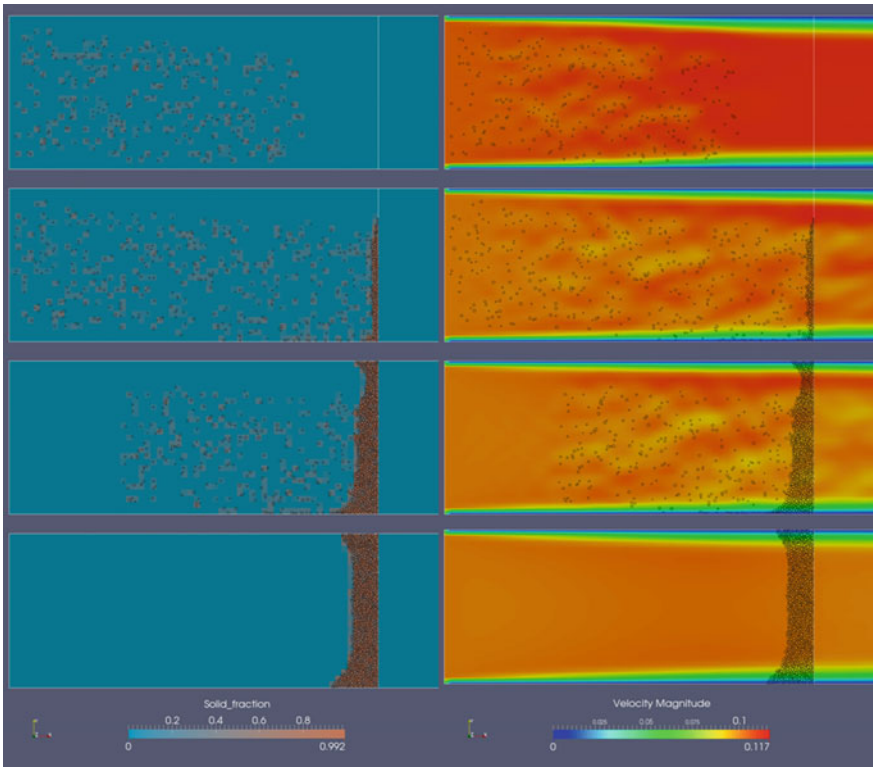

Fig. 3 2D simulation of transient clogging of a filter. *Left* Solid volume fraction field. *Right* Velocity magnitude field. Snapshots taken at time = 0.5, 1.0, 2.0 and 3.0 s

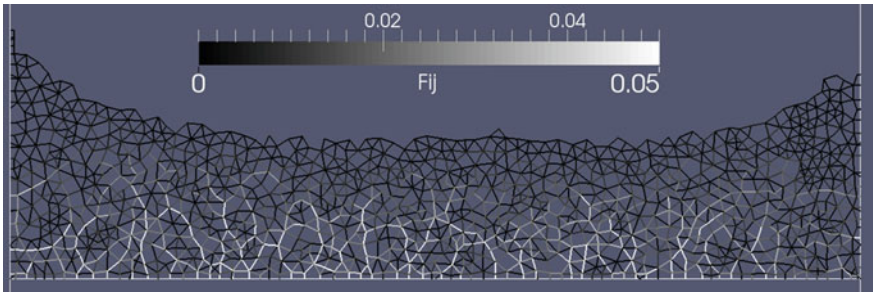

Fig. 4 2D simulation of transient clogging of a filter. Network of contact forces between particles

reached. The velocity field is disturbed by particles, and a global decrease of the velocity is observed as particles settle to form a porous layer.

Figure 4 shows the network of contact forces between particles. Because diameters are randomly generated between 150 and 250 μm, the stack is irregular. Therefore, some particles close to the filter are under the full load of the drag cumulated by the stack of particles while others are not.

5 Conclusion

We proposed a method to simulate clogging of components by snow showers. A standard formulation is used to describe particle dynamics and retroaction of particles on the flow. Contact forces between particles are introduced to describe the behaviour of the packed bed formed by accumulating particles. We emphasize that the results presented here are preliminary. For purpose of illustration, a simulation is performed on the simple case of a 2D ideal filter in a pipe. The clogging is qualitatively consistent with experimental observations of snow shower dynamics. However, the method requires be extending in 3D, and confronting quantitatively to available experimental data. The novel high-order formulation used for computation of fluid dynamics should allow handling of complex geometries.

Acknowledgments This research was carried out within the framework of a joint supervised doctoral thesis (grant #2011/0411).

The first author is grateful to SNECMA for funding and would like to thank colleagues of DynFluid laboratory for their support.

References And Citations

1. Sleight P. A., & Carter, R. D. G. (2010). Report on the accident to Boeing 777-236ER, G-YMMM, at London Heathrow Airport on 17 January 2008. Air Accidents Investigation Branch, Department of Transport (UK).
2. Certification Specification for Engines CS-E, Amendment 3. (2010). European Aviation Safety Agency. http://easa.europa.eu/system/files/dfu/CS-E_Amendment%203.pdf
3. Zhangxin, C., Guanren, H., & Yuanle, M. (2006) *Computational methods for multiphase flows in porous media*. Philadelphia: Society for Industrial and Applied Mathematics.
4. Baena, S., Lawson C. P., & Lam J. K.-W. (2012). Cold fuel test rig to investigate ice accretion on different pump inlet filter-mesh screens. *28th International Congress of the Aeronautical Sciences*, ICAS paper.
5. Murray, B. J., Broadley, S. L., & Morris, G. J. (2011). Supercooling of water droplets in jet aviation fuel. *Fuel, 90*, 433–435.
6. Hobbs, P. V. (2010). *Ice physics, Oxford classic texts in the physical sciences*. Oxford: Oxford University Press.
7. Butkovich, T. R. (1945). The ultimate strength of ice. USA Snow Ice and Permafrost Research Establishment Res. Rep 9, 12.
8. Jellinek, H.H.G., (1958) The influence of imperfections on the strength of ice. *Proceedings of the Physical Society*, *71,* 797.
9. Reid, M. (2013). Engine fuel system tolerance to fuel born ice. *Managing Water and Ice in Aviation Fuel Under Low Temperature Conditions, Seminar Proceedings*.
10. Lam, J. K.-W. (2013). WAFCOLT—Water behavior in aviation fuel under low temperature conditions. EASA Reasearch Project 2010/01.
11. Marechal, E., Perrin, J. Y. (2014). Dispositif de simulation d'une introduction de paquets de glace dans un moteur. Patent WO2014006297 A1.
12. Clift, R., Grace, J. R., Weber, M. E. (1978). *Bubbles, drops and particles*. New York: Academic Press.
13. Lefebvre A. (2007). Modélisation numérique d'écoulements fluide/particules. PhD Thesis.
14. Khelladi, S., Nogueira, X., Bakir, F., & Colominas, I. (2011). Toward a Higher-order unsteady finite volume solver based on reproducing kernel particle method. *Computer Methods in Applied Mechanics and Engineering, 200*, 2348–2362.
15. Ergun, S. (1952). Fluid flow through packed columns. *Chemical Engineering Progress, 48*(2), 89–94.
16. Patankar, S. V., & Spalding, D. B. (1972). A calculation procedure for heat, mass and momentum transfer in three dimensional parabolic flows. *International Journal of Heat Mass Transfer, 15*, 1787–1806.